The Influence of Side Chain Modifications on the Properties of Imine Based Organic Cage Compounds

Ke Tian

田科

Dissertation

Heidelberg

2023

Dissertation

Submitted to the
Combined Faculty of Mathematics,
Engineering and Natural Sciences
Heidelberg University, Germany
for the degree of
Doctor of Natural Sciences (Dr. rer. nat.)

presented by
Ke Tian, M. Sc.

Oral examination: December 1st, 2023

The Influence of Side Chain Modifications on the Properties of Imine Based Organic Cage Compounds

Referee: Prof. Dr. Michael Mastalerz

Prof. Dr. Milan Kivala

Publications

Die vorliegende Arbeit wurde von November 2018 bis October 2023 in dem Arbeitskreis von Herrn Prof. Dr. Michael Mastalerz an der Ruprecht-Karls-Universität Heidelberg angefertigt.

Teile dieser Arbeit wurden bereit veröffentlicht:

Ke Tian, Sven M. Elbert, Xin-Yue Hu, Tobias Kirschbaum, Wen-Shan Zhang, Frank Rominger, Rasmus R. Schröder, and Michael Mastalerz. *Adv. Mater.* **2022**, *34*, 2202290: **"Highly Selective Adsorption of Perfluorinated Greenhouse Gases by Porous Organic Cages"**.

Ke Tian, Xubin Wang, Moritz P. Schuldt, Sven M. Elbert, Frank Rominger, and Michael Mastalerz. *Org. Mater.* **2023**, *5*, 91-97: **"[4+ 4]-Imine Cage Compounds with Nitrogen-Rich Cavities and Tetrahedral Geometry"**.

Poster:

Ke Tian, Xin-Yue Hu, Sven M. Elbert, and Michael Mastalerz. *International symposium on porous organic polymers (POPs)*, **2019**, Heidelberg, Germany (September 9^{th}-12^{th}): **"[2+3] Imine Cages with Different Degree of Side-Chain Fluorination"**.

Abstract

This thesis mainly aims to investigate the influence of side chain modifications on the properties of imine based organic cage compounds.

A series of [2+3] isostructural POCs with *n*-butyl, perfluorinated *n*-butyl, and partially fluorinated *n*-butyl groups, is synthesized by precursor modification strategy and the structure-property relationship between the degree of fluorination of the alkyl chains and gas sorption properties for perfluorocarbons (PFCs) is studied in detail. The cage with fluorinated side chains shows excellent selectivities for PFCs over N_2 (e.g., S_H = 41475 for *c*-C_4F_8 vs N_2), due to fluorine-fluorine interactions.

This strategy extends to introducing *n*-fluorinated alkyl chains of different lengths from perfluoromethyl to perfluorohexyl into [2+3] POCs. The impact of chain lengths on gas uptakes and selectivities for PFCs, sulphur hexafluoride (SF_6), and nitrogen trifluoride (NF_3) over not only N_2 but also O_2 or CO_2 is explored. The cage with perfluoropentyl chains displays outstanding selective adsorption properties for these fluorinated gases (F-gases) over N_2 or O_2, while the cage with perfluorobutyl chains still remained the most selective for F-gases over CO_2 (e.g., S_H = 19631 for *c*-C_4F_8 vs CO_2).

Moreover, the solid packing of POCs significantly influences gas sorption. [2+3] POC with perfluoromethyl groups exhibits different porous and non-porous polymorphic forms, influenced by crystallographic packing and the orientation of middle flexible phenyl groups in terphenyl units. The specific surface of [2+3] POC can be significantly enhanced by elongated π systems of terphenyl units and the optimization of activation conditions.

Lastly, a series of [4+4] truncated tetrahedral nitrogen-rich POCs, synthesized from prochiral tripyrroltrialdehyde and side chain-modified amines, reveals face-oriented polyhedra in the crystalline state through X-ray crystallography.

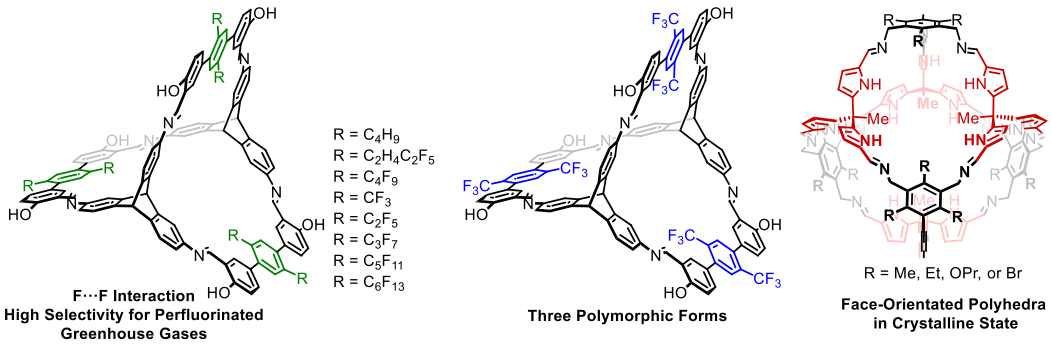

Kurzzusammenfassung

In dieser Arbeit soll der Einfluss der Seitenkettenmodifikation auf die Eigenschaften von organischen Käfigverbindungen auf Iminbasis untersucht werden.

Eine Reihe von [2+3] isostrukturellen POC mit nicht fluoriert, perfluoriert und teilweise fluorierten *n*-Butylgruppen wurde durch eine Strategie zur Modifizierung von Vorläufermolekülen synthetisiert und die Struktur-Eigenschafts-Beziehung zwischen dem Fluorierungsgrad der Alkylketten und den Gassorptionseigenschaften für Perfluorkohlenwasserstoffe (PFCs) im Detail untersucht. Der Käfig mit fluorierten Seitenketten zeigte aufgrund von Fluor-Fluor-Wechselwirkungen ausgezeichnete Selektivitäten für PFCs gegenüber N_2 (z. B. S_H = 41475 für *c*-C_4F_8 ggü. N_2).

Diese Strategie wurde auf die Einführung von n-fluorierten Alkylketten unterschiedlicher Länge, von Perfluormethyl bis Perfluorhexyl, in [2+3]-POC erweitert. Die Auswirkungen der Kettenlängen auf die Gasaufnahme und die Selektivität für PFCs, Schwefelhexafluorid (SF_6) und Stickstofftrifluorid (NF_3) nicht nur ggü. N_2, sondern auch O_2 oder CO_2 wurden untersucht. Der Käfig mit Perfluorpentyl-Ketten zeigte hervorragende selektive Adsorptionseigenschaften für diese fluorierten Gase (F-Gase) ggü. N_2 oder O_2, während der Käfig mit Perfluorbutyl-Ketten die höchste Selektivität für F-Gase ggü. CO_2 aufweist (z. B. S_H = 19631 für *c*-C_4F_8 ggü. CO_2).

Außerdem beeinflusst die Packung im Festkörper von POC die Gassorption erheblich. [2+3] POC mit Perfluormethylgruppen wiesen unterschiedliche poröse und nicht poröse polymorphe Formen auf, die durch die kristallografische Packung und die Orientierung der mittleren flexiblen Phenylgruppen in den Terphenyleinheiten beeinflusst werden. Die spezifische Oberfläche von [2+3] POC kann durch verlängerte π-Systeme der Terphenyleinheiten und die Optimierung der Aktivierungsbedingungen erheblich verbessert werden.

Schließlich zeigte eine Reihe von [4+4]-abgestumpft tetraedrischen, stickstoffreichen POC, die aus prochiralem Tripyrroltrialdehyd und Aminen mit modifizierten Seitenketten synthetisiert wurden, durch Röntgenkristallstrukturanalyse flächenorientierte Polyeder im kristallinen Zustand.

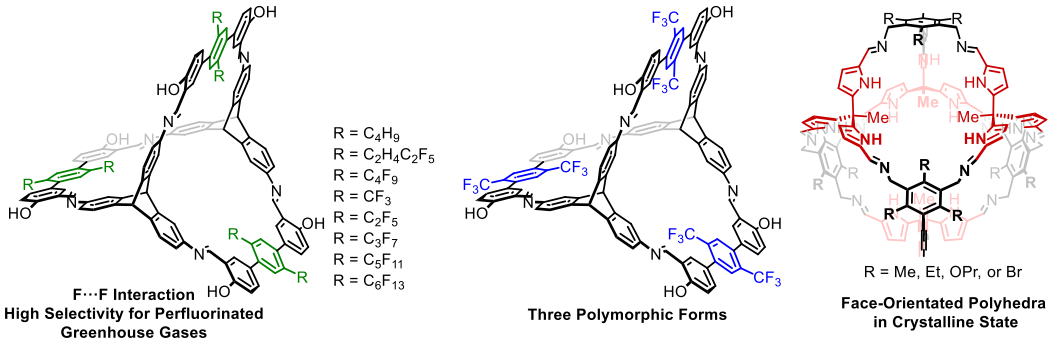

Table of Contents

I. Introduction

1. Global Warming and Greenhouse Gases

In the Fifth and Sixth Assessment Report on the science of climate change, the Intergovernmental Panel on Climate Change (IPCC) concluded that "*Human influence on the climate system is clear, and recent anthropogenic emissions of greenhouse gases are the highest in history.*"[1]. According to these reports, the global temperature has increased by >1.2°C since the 1850 to 1900 baseline period, with accelerating tendency in the post industrial age due to human activity.[1b, 2] Strong correlations are observed between the evolution of greenhouse gases concentrations in the atmosphere and global temperature rise (Figure 1).[1b, 2] Greenhouse gases (GHGs) can trap heat in the atmosphere by reflecting a fraction of the earth's long-wave (infrared) heat radiation, which reduces outgoing thermal radiation to space. This property is responsible for the well-known greenhouse effect.[1b] Naturally present greenhouse gases, like water vapor, maintain the Earth's warmth and temperature stability.[1b] However, the global-scale anthropogenic emission of GHGs into the atmosphere unbalances the Earth's energy system and lead to various environmental issues, including the increase of global surface temperature, deglaciation or glacial termination, and the occurrence of more frequent extreme weather events such as droughts, ocean storms and floods, etc.[2a, 3] Therefore, the enhanced global warming caused by the anthropogenic GHGs is alarming.

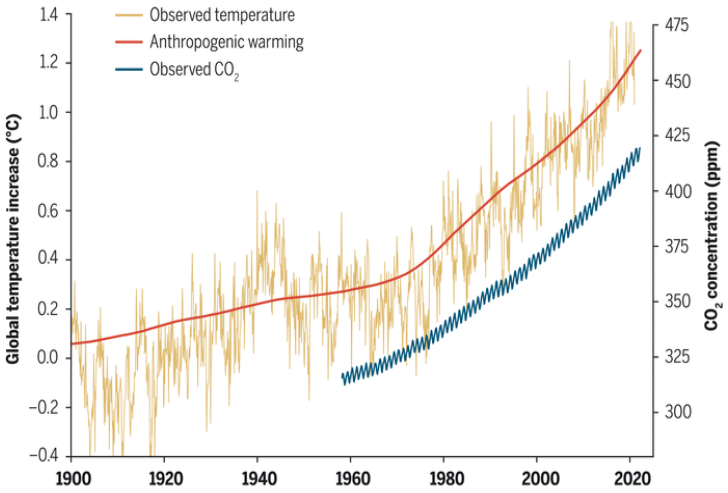

Figure 1. Global temperature and atmospheric CO_2 change. Observed global temperature (thin beige line; monthly temperature observations). Virtually all of this increase can be attributed to anthropogenic driving force (red line). The observed atmospheric CO_2 increase (blue line) is the primary driver of anthropogenic global warming. Reproduced with permission from Ref.[2c]. Copyright © 2022 American Association for the Advancement of Science.

The main GHGs whose concentrations are rising are carbon dioxide (CO_2), methane (CH_4), nitrous oxide (N_2O), and fluorinated gases.[1b, 4] Each gas's effect on climate change depends on three main factors: concentration in the air, lifetime in the atmosphere, and radiative efficiency. To compare the global warming impacts of different gases, the concept of the global warming potential (GWP) was developed and defined as the integration of the radiative forcing of a unit mass of a given substance over a chosen time horizon, normally 20 or 100 years, relative to that of CO_2, as stated by the IPCC.[1b] The larger the GWP value, the more the gas contributes to warming the Earth compared to CO_2 over that specific time period. For instance, methane has a GWP_{100} of 28, indicating one ton of methane has a equivalent impact to 28 tons of CO_2 over 100 years. However, methane has a relatively short lifetime of 12 years in the atmosphere, much shorter than carbon dioxide whose lifetime is unspecific due to varying time scales according to IPCC.[1a] Despite this, the vast quantity of non-naturally generated CO_2 mainly from the combustion of fossil fuels, remains the most significant contributor to global warming (Figure 1).[2c]

2. Emissions of Fluorinated Gases

Fluorinated gases (F-gases) mainly include chlorofluorocarbons (CFCs) hydrochlorofluorocarbons (HCFCs), hydrofluorocarbons (HFCs), and perfluorocarbon (PFCs), sulfur hexafluoride (SF_6), and nitrogen trifluoride (NF_3).[4] Compared with other greenhouse gases especially CO_2, most F-gases have significantly longer lifetimes resulting in higher GWP, thus small atmospheric concentrations can nevertheless contribute strongly to the greenhouse effect.[4] These gases have no significant natural sources and are almost entirely human-made for various application.[1b] In 1930s, F-gases, such as CFCs and HCFCs were originally produced and widely used for refrigerants in commercial, home and vehicle air conditioners.[5] However, they were linked to the depletion of the Earth's ozone layer and thus phased out from most applications by the Montreal protocol in 1987.[6] HFCs were subsequently adapted as substitutes for ozone-depleting substances due to their ozone-friendly properties.[5] The use of HFCs resulted in a substantial increase in emissions since 1990. To address this issue, the reduction of HFCs was agreed upon in the Kyoto Protocol and further specified in the Kigali Amendment to the Montreal Protocol. The amendment outlines plans to reduce HFC emissions by 80% over the next 30 years.[1a]

Table 1. Physical properties of various perfluorinated greenhouse gases.[1-2] Adapted with permission from Ref.[7]. Copyright © 2022 Wiley-VCH.

	PFC-14	**PFC-116**	**PFC-218**	**PFC-318**	**Sulphur hexafluoride**	**Nitrogen trifluoride**
Formula	CF_4	C_2F_6	C_3F_8	*c*-C_4F_8	SF_6	NF_3
Atmos. Lifetime	50000	10000	2600	3200	3200	500
Radiative Efficiency ($W \cdot m^{-2} \cdot ppb^{-1}$)	0.09	0.25	0.28	0.32	0.57	0.2
GWP_{20}	4880	8210	6640	7110	17500	12800
GWP_{100}	6630	11100	8900	9540	23500	16100
Historical abundance 2000 (ppt)	71.5	3.11	0.28	0.98	4.56	0.17
Historical abundance 2019 (ppt)	85.5	4.85	0.68	1.75	9.95	2.05
Increase in the historical abundance from 2000-2019 (%)	19.6	55.9	142.9	78.6	118.2	1106
Effective Radiative forcing ($mW \cdot m^{-2}$)	5.1	1.3	0.2	0.5	5.6	0.4

PFCs are hydrocarbons that are fully fluorinated. Commercially, PFCs mainly include tetrafluoromethane (CF_4, R-14, PFC-14), hexafluoroethane (C_2F_6, R-116, PFC-116), octafluoropropane (C_3F_8, R-218, PFC-218) or octafluorocyclobutane (*c*-C_4F_8, RC-318, PFC-318), etc. As a group of high chemically stable greenhouse gases, PFCs, and non carbon based analogues, such as SF_6 and NF_3 have lifetimes ranging from thousands to tens of thousands of years and possess among the highest GWPs known, with values ranging from 6630 to 23500 (Table 1).[8] Surprisingly, these F-gases haven't received sufficient public attention yet, despite their significant threat on climate change. To the best of our knowledge, they have not yet been completely phased out officially, leading to the constantly increasing growth rates of PFCs, SF_6 and NF_3 over the last ≈10 years, with abundances rising by approximately ≈1106% from 2000 to 2019 (e.g., for NF_3, Table 1) according to data from the Advanced Global Atmospheric Gases Experiment (AGAGE).[8] PFCs, SF_6, and NF_3 emissions primarily come from manufacturing processes for aluminum, magnesium, electronics (e.g. semiconductors), and electrical transmission and distribution equipment.[8c, 8e, 9] For instance, PFCs are produced as a byproduct of aluminum smelting industry and widely used in the flourishing semiconductor industry for the etching of silicon wafers and cleaning of chemical vapor deposition (CVD) chambers.[9b, 10] PFCs are also used

in the medical field, such as in eye surgeries or as ultrasound contrast agents.[11] *c*-C_4F_8 emissions are also related to thermal decomposition of polytetrafluoroethylene (PTFE, “Teflon”) and other fluoropolymers.[8a] SF_6 has a historical application in the aluminum and magnesium smelting industry as a blanketing gas.[8e] More recently, SF_6 and SF_6/N_2 mixture have been utilized as an insulating gas in electrical transmission equipment, including circuit breakers thanks to their dielectric strength and excellent insulating properties.[8e] NF_3, on the other hand, has emerged as a replacement for PFCs in the semiconductor industry due to its superior process performance and the potential for reducing carbon dioxide equivalent emissions.[8d]

3. Selective Adsorption of Perfluorinated Greenhouse Gases

The approaches available for reducing the emissions of F-gases, especially from semiconductor industries may include: thermal destruction, chemical conversion, plasma destruction, and recovery/reclamation.[5, 12] Due to the high chemical stability and GWPs of PFCs, SF_6, and NF_3, it seems reasonable to recover/recycle/reuse these gases.[12-13] Among some available recovery/recycle technologies, pressure swing adsorption/desorption processes using a suitable porous material offer significant energy savings over cryogenic condensation/distillation technology for obtaining ultrahighly pure gas from a gas mixture. However, this requires highly selective PFCs, SF_6, and NF_3 adsorptions.[14]

The selective adsorption process is one in which adsorbents prefer to adsorb certain components of a gas mixture. Accurate experimental measurements of mixture isotherms can be time-consuming and relatively expensive.[15] In 1965, Myers and Prausnitz introduced a straightforward technique for calculating adsorption equilibria among components in a gaseous mixture.[16] This method relies on the principles of the Ideal Adsorption Solution Theory (IAST). What makes this technique particularly valuable is its ability to predict isotherms that closely match experimental data, all while utilizing only pure-component adsorption equilibria data obtained at the same temperature and on the same adsorbent. Its simplicity and the fact that it doesn’t require any data specific to the mixture make it especially well-suited for engineering applications. As a result, it has become a widely adopted method for determining selectivity.

IAST is analogous to Raoult's law for vapor-liquid equilibrium. To meet the ideal requirement, it is hypothsied that there are no interactions between the adsorbate molecules within the adsorbed phase mixture, and the spreading pressures of the components are equal at a constant temperature.[17]

$$P_i = y_i P = x_i p_i^0 \quad i = 1, \dots, N \tag{1}$$

$$\frac{\pi A}{RT} = \int_0^{p_i^0} \frac{n_i}{P_i}\, dP_i \tag{2}$$

$$\frac{1}{n_t} = \sum_{i=1}^{N} \frac{x_i}{n_i^0\left(p_i^0\right)} \tag{3}$$

$$n_i = x_i n_t \tag{4}$$

with: π:spreading pressure

P_i : partial pressure

x_i : mole fraction of component *i* in the adsorbed phase

p_i^0 : partial pressure of component *i* at given temperature and spreading pressure π

n_i : amount of adsorbed component *i* at pressure *p*

A : surface area of the adsorbent, and *R* is the ideal gas constant

n_t : total amount adsorbed of the mixture

N : total species of the gas mixture

n_i^0 : amount of component *i* adsorbed at constant temperature and spreading pressure in the absence of the other components.

Solving these equations for p_i^0 provides a comprehensive insight into the system's composition. This can be achieved through either numerical integration of the isotherms or by fitting the isotherms to a model and subsequently conducting analytical integration. In the simpler case of two-component gas mixture, a fundamental approach involves obtaining the single volumetric isotherm in equilibrium. Subsequently, the isotherm of every single adsorbate is fitted by the appropriate model and the selectivity coefficient S_{IAST} of gas A over gas B can be calculated with the following equation:

$$S_{IAST} = \frac{x_A / y_A}{x_B / y_B} \tag{5}$$

with: x_i: molar fraction of compound i in the adsorbed phase

y_i: molar fraction of compound i in the gas phase

While IAST calculations are useful to suggest the selectivity of porous materials simply by single-component adsorption equilibria result, the breakthrough experiment is a kinetics characterization to investigate the actual practice of gas separation by passing a gas mixture of controlled composition through a column or bed of adsorbents at a defined rate and specific temperature.[18] The longer breakthrough time suggests the higher affinity of the adsorbent towards the adsorbate under the same measurement conditions.[19]

Since CO_2 has the largest effect on global warming, most studies on porous materials, such as zeolite,[20] metal-organic frameworks (MOFs),[21] amorphous porous organic polymers (POPs),[22] covalent organic frameworks (COFs),[23] and porous organic molecular materials (POMs),[24] like porous organic cages (POCs)[25] for selective gas removal focus on this gas. In contrast, there are only a few reports for selective PFCs, SF_6, and NF_3 capture in porous materials until now.[13] In these reports, SF_6 is the most investigated gas in terms of selective adsorption, followed by CF_4 and NF_3. The gas pairs of PFCs, SF_6 or NF_3 with N_2 are often been investigated due to their industrially relevant compositions.[26]

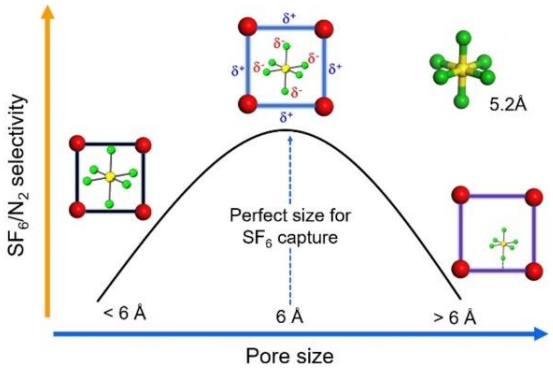

Figure 2. The proposed strategy for SF_6 capture. Reproduced with permission from Ref.[27]. Copyright © 2022 Wiley-VCH.

Precise control of pore size is an effective approach to achieve highly selective adsorption of PFCs, SF_6, and NF_3.[28] Too small pores prevent the entry of not only certain component of a gaseous mixture but also targeted gas molecule while oversize pores minimize the binding affinity and thus reduce gas selectivity. One of the widely used strategies is to perfectly match pore size with targeted molecule by precise control over structures to generate better overlap of attractive potential fields of opposite walls in the relatively narrower pores.[29] Following this concept, Yang and co-workers designed three MOFs with fine-tuning pore sizes (12 Å for **Cu(peba)$_2$**, 8.2 Å for

Ni(pba)$_2$, and 6 Å for **Ni(ina)$_2$**).[27] Among them, the pore size of **Ni(ina)$_2$** is well-suited to the kinetic diameter of SF_6 (5.1 Å),[28a] along with the formation of multiple C-H···F interactions between gas molecules and pore wall (Figure 2). Consequently, **Ni(ina)$_2$** possesses the highest SF_6 selectivity (375 at 298 K and 1 bar) for a SF_6/N_2 mixture (10/90, v/v) and SF_6 uptake capacity (63.7 $cm^3\ g^{-1}$ at 298 K and 1 bar) at ambient conditions. In breakthrough experiments charging with the same ration of the gas mixture, the breakthrough time of SF_6 for **Ni(ina)$_2$** was ~1500 s g^{-1}. Bao and co-workers prepared a group of ultra-microporous carbon adsorbents with relatively uniform pore size distributions (5.2 to 5.3 Å), which could facilitate a strong confinement effect for SF_6 and CF_4 (CF_4 kinetic diameter = 4.7 Å[28a]).[28b] This strong interaction between the narrow channel walls and SF_6 was also discovered in some porous carbons, MOF and zeolite materials, such as **PhxM(10-x)Ay**,[30] **UiO-66-Zr**,[31] **MIL-100(Fe)** granule,[32] **CAU-17**,[33] **SIFSIX-2-Cu**,[34] **SBMOF-1**,[35] **NaX** (**zeolite 13X**)[14a, 36].

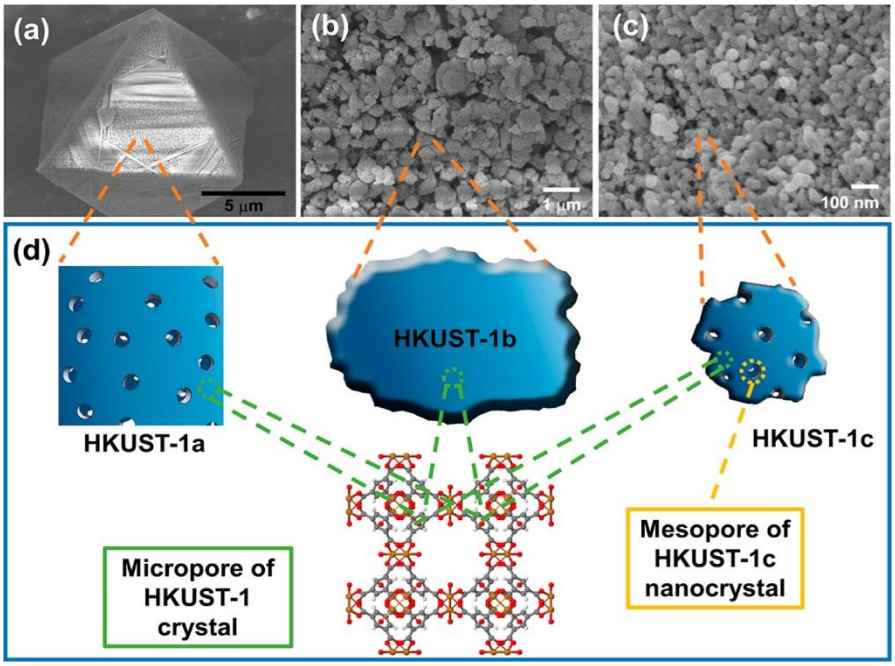

Figure 3. FESEM images and structural scheme of **HKUST-1** crystals: (a) bulk crystal (**HKUST-1a**), (b) nanocrystal (**HKUST-1b**), and (c) nanocrystals with hierarchical structure (**HKUST-1c**). Reproduced with permission from Ref.[37]. Copyright © 2017 American Chemical Society.

Narrow channel can significantly enhance gas molecule interactions with adsorbents but limit the kinetic diffusion of gas molecules in channel, thus leading to a slow adsorption-desorption cycling in industrial operations. Bae and colleagues overcame this problem using hierarchically structured POP **PPNx**,[38] zeolite **MFI**,[39] and MOF **HKUST-1** (Figure 3).[37] These materials demonstrated an IAST selectivity of ~51, 70 and 80, respectively, at 298 K and 1 bar for a 10:90 SF_6/N_2 mixture. The

presence of mesopores facilitates the faster transport of SF_6 to the abundant active sites located in microporous spaces without significantly sacrificing the selectivity. Addtionally, larger pore size is suitable for highr pressure selective adsorption above 1 bar. Isostructural MOFs **UiO-66** and **UiO-67** were formed via coordination bonding between $Zr_6O_4(OH)_4$ and benzene-1,4-dicarboxylic acid (BDC) and longer linkers biphenyl-4,4'-dicarboxylate (BPDC), respectively.[40] **UiO-67** with larger pores (12 and 23 Å) exhibited higher SF_6/N_2 selectivity (S_{IAST} = 30) at 10 bar for a 10:90 SF_6/N_2 mixture.

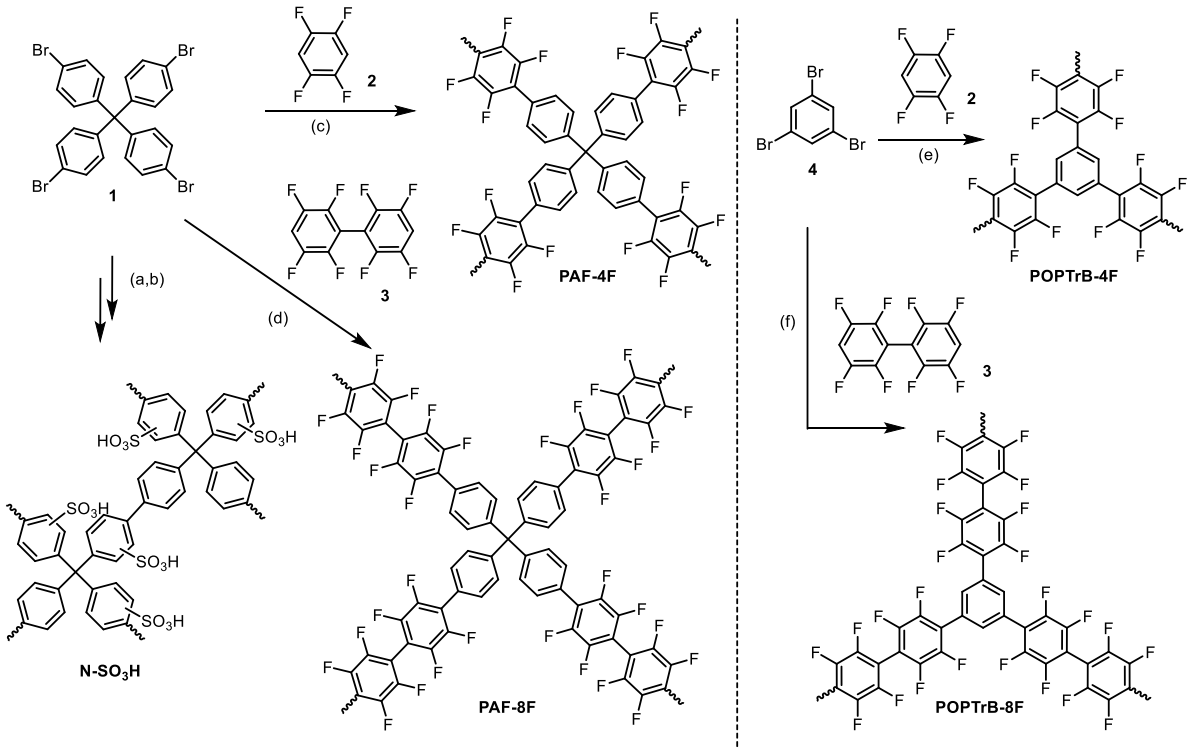

Scheme 1. Synthesis of PAFs **N-SO_3H**, **PAF-4F**, **PAF-8F**, **POPTrB-4F**, and **POPTrB-8F**.[41] Reaction condition: (a) 2,2'-bipyridyl (bpy), $NiCl_2$, Mg, DMF, rt, 48 h; (b) chlorosulfonic acid, DCM, rt, 3 d; (c-f) $Pd(OAc)_2$, $P^tBu_2Me\text{-}HBF_4$, K_2CO_3, dimethylacetamide, 120 °C, 48 h.

Besides pore design, the properties of the internal surface of porous materials, such as polarizability, play a key role in deciding the strength of the interaction with the targeted gas molecules.[42] For example, a series of isostructural **M-MOF-74** materials (M = Mg, Co, and Zn) with pore sizes (11-12 Å) and highly dense unsaturated metal sites was synthesized and tested for SF_6 adsorption.[43] The inclusion of open-metal sites in MOFs enhances SF_6 adsorption and selectivity by serving as Lewis acids, which polarize the S-F bonds in SF_6 molecules.[9a] The utilization of MOFs with open-metal sites has also been investigated on **HKUST-1**.[37, 44]

The functionality of internal surface can be specifically tuned by introducing various

functional sites on the organic building blocks via either pre-synthetic or post-synthetic modification. Ma *et al*. reported the synthesis of four 3D fluorinated porous aromatic frameworks (PAFs) via the C-H arylation polycondensation between aryl bromides **1** or **4** with aryl fluorides **2** or **3** for selective separation of SF_6, NF_3, and CF_4 over N_2 (Scheme 1).[41b, 41c] It was discovered that the selective adsorption of these F-gases is driven by fluorine-induced electropositive field sites within PAFs, which exhibit a strong affinity for electronegative F-gases. Bae and co-workers synthesized a series of **UiO-66-X** (X = NO_2, NH_2, Cl, Br, I, Br_2) MOF compounds by using six different functionalized ligands and investigated the effect of the polarizability of the pore surface on the adsorption of SF_6 and CF_4. **UiO-66-Br_2** with the highest polarizability exhibited the best SF_6 and CF_4 adsorption, and highest SF_6 selectivity over N_2 with S_{IAST} = 220 for a SF_6/N_2 mixture (10/90, v/v) at 1 bar. The polar sulfonic acid group was introduced by post-modification of pre-synthetic porous aromatic framework **New-PAF-1** to enhance the interactions between the skeleton and F-gas molecules (Scheme 1).[41a] Obtained PAF **N-SO_3H** demonstrated improved selective adsorption of NF_3, SF_6, and CF_4 over N_2 or O_2.

As for other PFCs, there have been mainly theoretical studies on the physical adsorption of C_2F_6 and its mixtures with nitrogen on model graphite slit micropores, which indicates the potential use of microporous carbon materials as selective adsorbents.[45] Indeed, individual adsorption experiments of C_2F_6 and C_3F_8 have been conducted, but their selectivities, e.g., against nitrogen or oxygen or carbon dioxide, haven't yet to be discussed in these investigations.[46] Furthermore, there is currently no *c*-C_4F_8-sorption report.

4. Fluorinated Porous Materials

As aforementioned, fluorinated PAFs have been studied for their application in selectively separating F-gases from N_2.[41b, 41c] Other fluorinated porous materials, such as MOFs, COFs, POMs or cages also have been described in literature due to their excellent thermal, hydrophobicity and chemical stability and unique physical properties.[47] However, the vast majority of these materials incorporate fluorine in aromatic units, methyl group or fluorinion rather than long fluorocarbon chains.[48] While theoretical calculations on fluorine-fluorine interactions of perfluorinated alkyl chains in the solid state suggest that "....*it is possible to design solid phase recovery systems for*

[...] pollutants based on fluorous interactions. The weakness of fluorous interactions relative to other intermolecular forces is an advantage for such applications because, as shown in our experiments, it allows for ease of desorption/recovery.", few perfluoroalkyl-functionalized porous materials were synthesized and mainly focused on CO_2 adsorption or separation, anhydrous proton conduction and the accommodation of long perfluoroalkanes.[49] Farha *et al*. synthesized a series of perfluoroalkyl-functionalized Zr-based MOFs **SALI-*x*** to enhance CO_2 adsorption and water stability. This was achieved through post-modification of known mesoporous MOF **NU-1000** with terminal -OH ligands (molecular formula: $Zr_6(\mu_3\text{-}OH)_8(\text{-}OH)_8(TBAPy)_2$, TBAPy: 1,3,6,8-tetrakis(*p*-benzoic acid)pyrene **5**) (Figure 4a-b).[49d, 50] The incorporation of perfluoroalkane relied on acid-base chemistry between the hydroxyl groups and the carboxylate group of the perfluorinated chain. Notably, with increasing chain length, these MOFs exhibited higher affinity for CO_2.

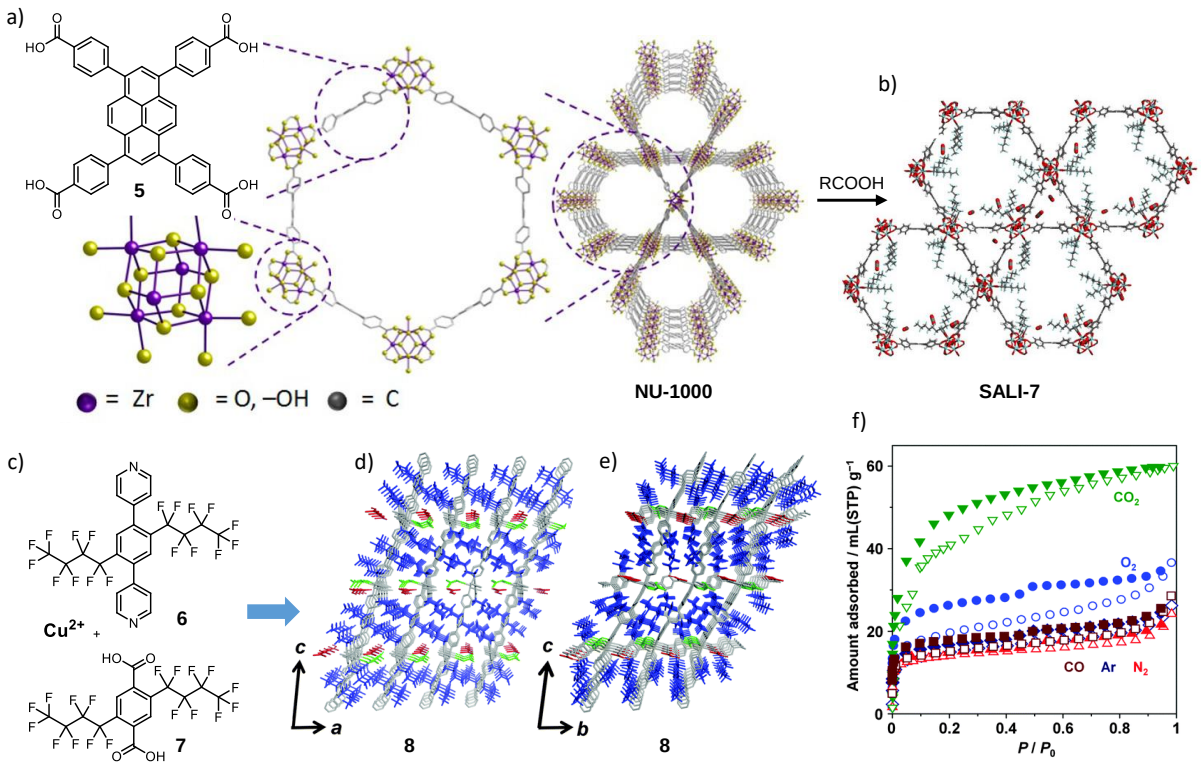

Figure 4. (a) Molecular representations of **NU-1000**. (b) Ligand incorporation and simulated snapshot of CO_2 adsorption in **SALI-*x*** (**SALI-7** as an example). **SALI-*x*** [RCOOH]: **SALI-1** [CF_3COOH], **SALI-3** [$CF_3(CF_2)_2COOH$], **SALI-7** [$CF_3(CF_2)_6COOH$], **SALI-9** [$CF_3(CF_2)_8COOH$], **SALI-1'** [$CF_3(CH_2)_3COOH$], **SALI-3'** [$CF_3(CF_2)_2(CH_2)_2COOH$]. Adapted with permission from Ref.[49d]. Copyright © 2013 American Chemical Society. (c) Schematic representation of the preparation of perfluorobutyl-functionalized PCP **8**. (d) Guest-accommodating crystal structure of PCP viewed along the *b* axis and (e) viewed along the *a* axis. Perfluorobutyl group, metal-coordinated DMF, and guest DMF are colored in blue, green, and red, respectively in (d) and (e). Hydrogen atoms are omitted for clarity. (f) Gas sorption isotherms of **8**. CO_2, O_2, CO, Ar, and N_2 were measured at 195, 90, 82, 87 and 77 K, respectively. STP is standard temperature and pressure. Adapted with permission from Ref.[49a]. Copyright © 2014 Royal Society of Chemistry.

A similar postsynthetic functionalization approach was also successfully performed on another Zr-based MOF, **DUT-67** (molecular formula: $Zr_6O_6(OH)_2(tdc)_4(CH_3COO)_2$, tdc = 2,5-thiophenedicarboxylate) and COF material to enhance the hydrophobicity of the inner surface of the network.[49e, 49g] In a different approach, another group of perfluoroalkyl-functionalized Zr-based **MOF-808** was synthesized by a one-pot method using a series of fluorinated carboxylic acids [trifluoroacetic acid (TFA), pentafluoropropionic acid (PFPA), and heptafluorobutyric acid (HFBA)] as a CO_2-philic modulator.[49h]

Another approach to introduce perfluoroalkane is through ligand functionalization.[49a] Kitagawa *et al*. reported the synthesis of a perfluorobutyl-functionalized 2D porous coordination polymer (PCP) **8**, (molecular formula: $\{[Cu(bpbtp)(L)(DMF)](DMF)\}_n$, ($H_2$bpbtp = 2,5-bis(perfluorobutyl)terephthalic acid **7**, L = 2,5-bis(perfluorobutyl)-1,4-bis(4pyridyl)benzene **6**, DMF = N,N-dimethylformamide) based on two perfluorobutyl modified ligands and investigated its preferential adsorption of CO_2 and O_2 (Figure 4c-f).[49a] This same strategy was also employed to construct perfluoroalkyl-functionalized hydrazone-linked 2D COFs, allowing for the investigation of their acid stability and proton conductivity.[49f]

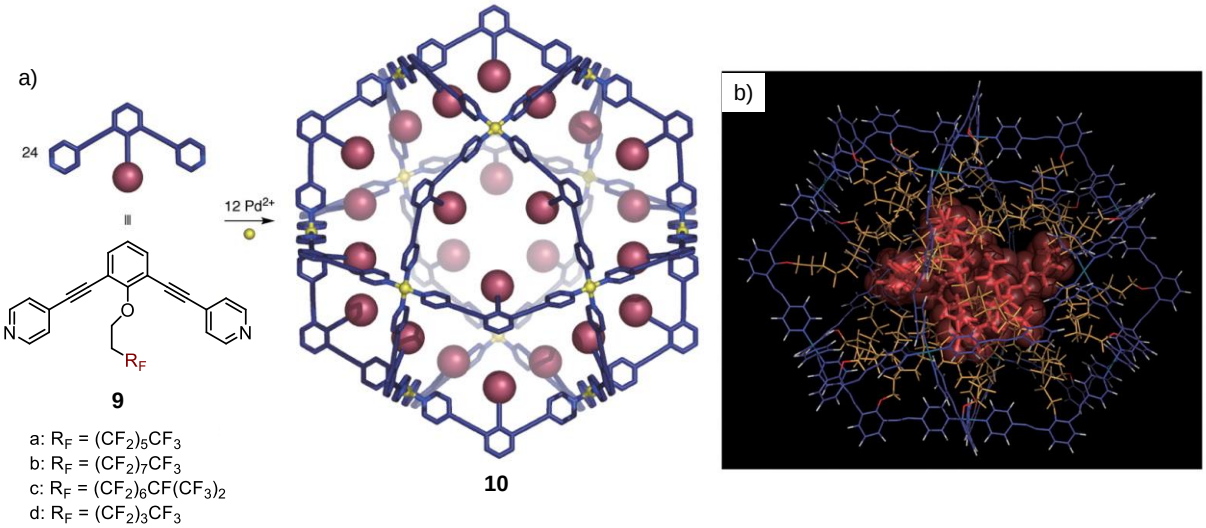

Figure 5. (a) Self-assembly of endofluorous $M_{12}L_{24}$ molecular spheres **10**. (b) Molecular structure of **10a** with six molecules of perfluorooctane (red) at the central void, and structural annealing was conducted from 2000 to 300 K by molecular dynamics (MD) simulation. The host **10a** is represented by wire frames, whereas the accommodated guest molecules are represented by space-filling models. Adapted with permission from Ref.[49b]. Copyright © 2006 American Association for the Advancement of Science.

Fujita and co-workers reported that complexation of pyridine-capped banana-shaped bridging ligands **9** with Pd^{2+} or Co^{2+} results in a coordination network **10** containing fluorous pores, which can accommodate long perfluoroalkanes such as

perfluorohexane and perfluorooctane through fluorophilic host-guest interactions between the terminal $CF_3CF_2CF_2$-portions of the perfluoroalkyl side chains and the guest molecules (Figure 5).[49b, 49c] This suggests the design of perfluoroalkyl-functionalized porous material for adsorbing small F-gases selectively could be very feasible.

5. Organic Cages Compounds

Extended porous frameworks like MOFs, COFs, or POPs have intrinsic limitations, primarily their insolubility, which poses challenges in terms of characterization, processability, and reproducibility, with only a few exceptions.[51] In contrast, porous molecules are miscible in solution enabling adjustment of the properties of the material and standard molecular chemistry methods (NMR spectroscopy, mass spectrometry, etc.) can be employed during characterization.[52] Moreover, porous molecules can be processed into functional devices like quartz crystal microbalances for volatile analyte sensing[53] and can be embedded in membranes.[54] As a result, porous materials constructed from discrete molecules have received extensive attention.

POCs is a subclass of porous molecules.[24-25, 55] According to the IUPAC, cage compounds are defined as “polycyclic compounds with the shape of a cage”.[56] This very broad definition technically includes even platonic hydrocarbons[57] or coordination cages.[58] To distinguish them, porous organic cages are defined as typical organic molecules, with three-dimensional structures featuring cavities large enough to accommodate molecular guests. These organic cages are synthesized and subsequently assembled in the solid state in two independent steps.[25d] Overall porosity of POCs is from the inefficient packing of molecules (extrinsic porosity) or/and intrinsic cavity voids (intrinsic porosity) in the molecule itself.[48h]

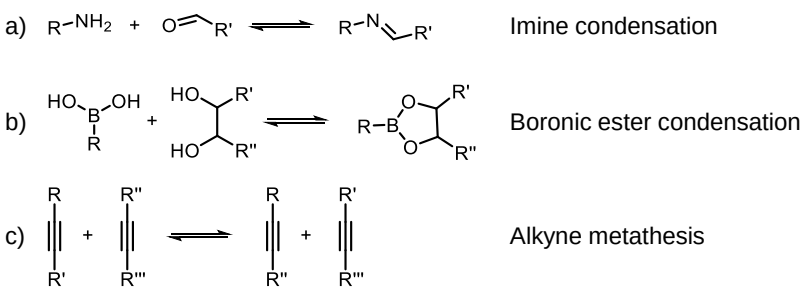

Scheme 2. DCC used for porous organic cage formation.

The synthesis of POCs can be divided into two categories: irreversible and reversible routes.[25a] Irreversible reactions are sparse for porous organic cages. Some examples include carbon-carbon bond formation through metal-catalyst-assisted cross-coupling,[59] nucleophilic aromatic substitution,[60] and azide-alkyne Huisgen cycloaddition.[61] Reversible routes are based on dynamic covalent chemistry (DCC).[25a] The main advantage of reversible routes is that they allow the self-correction of the errors in the multistep self-assembly reaction pathway, which finally gives a thermodynamically stable cage product in high yield.[25a, 25c] One of the most frequently used motif in DCC is the formation of imine bonds by the condensation of amines and aldehydes,[25c] though some other DCC has all been used, such as boronic ester[62] or boroxine formation[63] and dynamic alkyne metathesis[64] (Scheme 2).

5.1. Imine Cage Compounds

The imine condensation reaction, first discovered by Hugo Schiff nearly 150 years ago,[65] found its initial application in the synthesis of cage compounds in 1991.[66] Cram and Quan reported the creation of a molecular container, specifically a hemicarcerand, through a [2+4] condensation involving a tetraformylcavitand and 1,3-diaminobenzene.[66] Since then, numerous imine cage compounds with different cage geometries[67] and sizes[68] have been successfully synthesized by leveraging this DCC motif for applications such as stabilizing reactive compounds[69] or the selective recognition of guest molecules.[70]

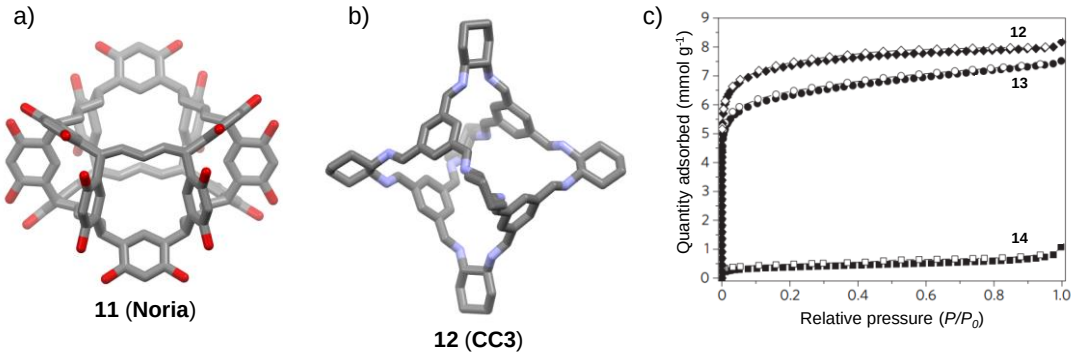

Figure 6. SCXRD structures of **11** (**Noria**)[71] (a) and **12** (**CC3**)[72] (b) as stick models. H atoms are omitted for the sake of clarity. Blue, red, and gray spheres represent N, O, and C atoms, respectively. (c) Nitrogen sorption isotherms (77 K) of Cooper's cage compounds **12**-**14**. Three imine-linked **12**-**14** tetrahedral cages were synthesized by the condensation reaction of 1,3,5-triformylbenzene with (*R*, *R*)-1,2-diaminocyclohexane, 1,2-propylenediamine and1,2-ethylenediamine, respectively. Full symbols: adsorption. Empty symbols: desorption. Adapted with permission from Ref.[72]. Copyright © 2009 Springer Nature.

In 2009, Atwood and his colleagues pioneered the development of amorphous, double-cyclic ladder-type organic cage compounds designed for gas adsorption under isothermal conditions (Figure 6a).[71] One of these compounds **11**, known as Noria exhibits adsorption of 11 wt% CO_2 at 30 bar and 298 K, along with a surface area of SA_{BET} = 350 m^2 g^{-1}. In parallel, Cooper *et al*. independently reported a group of crystalline organic cages with remarkable specific surface areas (SA_{BET} = 624 m^2 g^{-1} for **12**, known as **CC3**, Figure 6b-c). These cages were formed through the [4+6] (4 aldehyde units and 6 diamine units) cycloimination of trialdehydes with diamines.[72] The crystalline pore structures within this series were found to depend on diamines used and multiple polymorphs.

The rapid development of this field since 2009 is evident in the increased surface areas achieved for triptycene-based organic cages, as reported by Mastalerz *et al.* (Scheme 3). Mastalerz and his co-workers successfully created the *endo*-functional adamantanoid [4+6] cage **19** and the cubic [4+4] cage **21**.[73] These structures exhibited even higher specific surface areas of 2071 m^2 g^{-1} and 1680 m^2 g^{-1}, respectively.[73c, 73d] By using dihydroxydialdehyde **17**, they achieved an imine cage with *exo*-functionality **20** while maintaining the adamantoid geometry.[74] These large, complex cage structures demonstrated permanent shape-persistence and porosity, attributed to the rigidity of the precursors and the formation of cyclic six-membered intramolecular hydrogen bonding between the hydroxy groups and neighboring imine bonds.

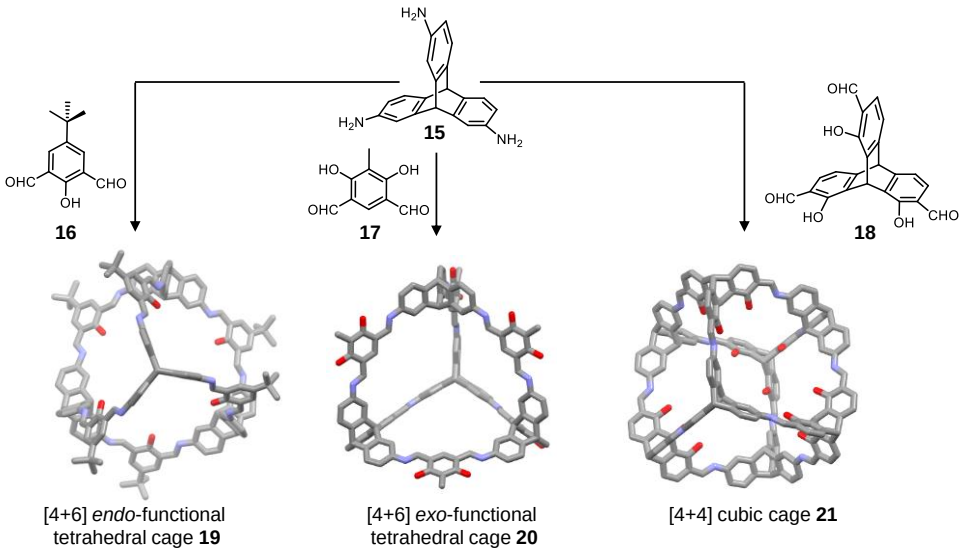

Scheme 3. Schematic representation of the preparation of various imine cage compounds starting from triaminotriptycene **15**. SCXRD structures of imine cage **19**[73c]; MM2 optimized structures of imine cages **20**[74] and **21**[73b]. H atoms are omitted for the sake of clarity. Blue, red, and gray spheres represent N, O, and C atoms, respectively.

The impact of molecular rigidity on the formation of permanent porosity is demonstrated through a pair of *exo*-functionalized shape-persistent [2+3] cage compounds **22** and **23** (Figure 7a).[75] The condensation reaction between triaminotriptycene and biphenylsalicylaldehyde resulted in the formation of the [2+3] cage compound **22**. A crystalline cage compound **22** exhibited permanent pores with a specific surface area of SA_{BET} = 744 m^2 g^{-1}. In contrast, the more flexible cage **23**, featuring a flexible ethyl bridge, not only had a significantly lower surface area of only 30 m^2 g^{-1} but also generated a noticeably higher number of byproducts during its synthesis, negatively affecting the yield and complicating the purification process.

These [2+3] cage compounds possess unique structural characteristics. Through the use of linear bis(salicylaldehydes) in the reaction with triptycene triamine **15**, a series of isostructural *exo*-functionalized [2+3] cage compounds **22**-**25** with adjustable cavity dimensions in the longitudinal direction has been synthesized and made accessible (Figure 7a).[76] These cages can be processed into thin films on quartz crystal microbalances (QCMs) to enhance their sensitivity for detecting volatile aromatic compounds.[53] The [2+3] cage compounds offer multiple modification sites where chemical functionality can be introduced (Figure 7b). This can be achieved through post-synthetic modifications at reactive sites or by incorporating functional sites into the molecular precursors.[77] For instance, the [2+3] imine cage **22** has been converted into a chemically stable carbamate cage in a two-step approach by first reduction of the imine bonds to amine bonds, followed by a cyclization reaction with N' N'-carbonyldiimidazole.

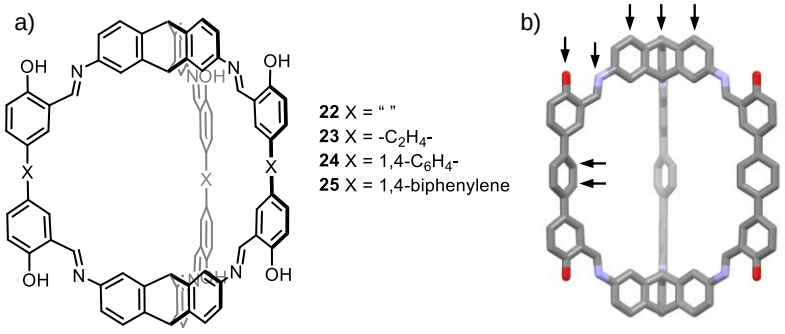

Figure 7. (a) Chemical structures of [2+3] imine cages reported by Mastalerz *et al*., starting from triamino triptycene **15**.[53, 75] (b) MM2 optimized structures of imine cages **24**. The arrows point possible modification sites. H atoms are omitted for the sake of clarity. Blue, red, and gray spheres represent N, O, and C atoms, respectively.

5.2. Solid-State Cage Packing

After discrete cages are synthesized, they are precipitated or crystallized into the solid state. Discrete cages are held together by relatively weak intermolecular forces, rather than strong covalent bond or coordinated bond, leading to an abundant possibility for the structure, especially, when exposed to an external stimulus. For example, cages can crystallize into alternative polymorphs (α or β phase) on account of small changes to the solvent or go to an amorphous phase after the removal of the solvent (Scheme 4).[78] When exposed to certain gases or vapors, cages can interchange between different polymorphs in their solid form (Scheme 4). By altering the chemical functionality, the three-dimensional connection between the cage windows can be regulated, resulting in either non-porous or permanently porous structures.

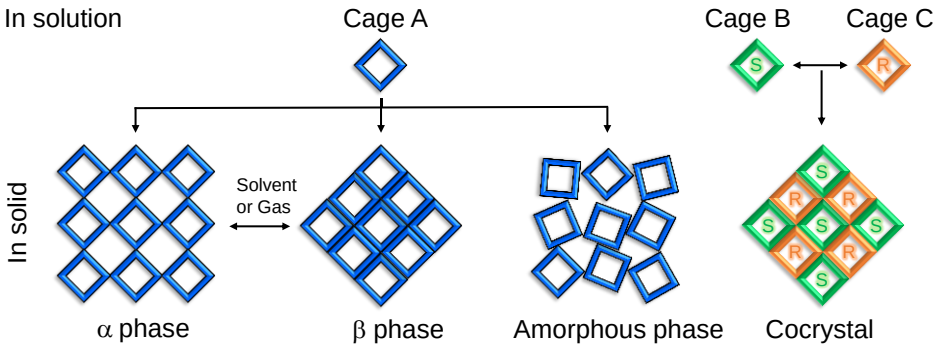

Scheme 4. Different solid-state phases for a single molecular cage A (left). Cages B and C with opposing chirality *S* and *R* can be combined to make binary co-crystals (right).[25a]

Cooper *et al*. has demonstrated that non-porous [4+6] cage **14** (**CC3** analogue) as synthesized from ethyl acetate (SA_{BET} = 24 m^2 g^{-1}), can be recrystallized from a mixture solvent of dichloromethane and *o*-xylene to form a permanently porous polymorph (SA_{BET} = 550 m^2 g^{-1}).[72] It was further found that desolvated cage **14** can even exist in three different polymorphic forms (α´, β´, and γ´ phase) which are nonporous to N_2 and H_2, selectively porous to H_2, and non-selectively porous to both gases, respectively.[79] The first two forms can even be interconverted reversibly in the solid state by exposure to organic trigger molecules (ethyl acetate or dichloromethane). This “on-off” porosity switching in polymorphic porous organic cages was also observed in Rahul Banerjee’s imine cage **TpOMe-CDA**, which is a **CC3** cage analogue.[80] Because POCs are soluble in common solvent, porous co-crystalline solids can be produced by mixing different prefabricated organic cages in the same solution that self-assemble by means of chiral recognition (Scheme 4).[81] By this method, mutilfunctionality from different

cages could be engineered into the cocrystalline solids.[82] For example, guest selectivity and capacity are usually opposite nature in one porous solid but might be combined by co-crystallizing one cage that favours binding of a specific guest with a second cage provided enough pore space.

5.3. Porous Organic Cages for Selective Gas Adsorption

Cages in solid-state packing are commonly utilized for gas adsorption purposes.[24] These cage systems have demonstrated selectivity for various gas pairs, such as CO_2/N_2, CO_2/CH_4, C_2H_6/C_2H_4, C_2H_6/C_2H_2, C_2H_4/C_2H_2, C_3H_4/C_3H_6, C_3H_4/C_3H_8, D_2/H_2, Xe/Kr.[25b, 48k, 73a, 73b, 82-83] However, among these examples, there is only one reported instance of selective adsorption of SF_6, as reported by Cooper *et al*.[84] They found that a series of porous organic cages could adsorb SF_6, despite the fact that the kinetic diameter of this gas (5.5 Å) is larger than the static window diameter of ~3.6 Å in the cages, which contribute to the flexibility of the molecular crystal (Figure 8).[84] The investigation of the selective adsorption of SF_6 over nitrogen revealed that **CC3** had the IAST selectivity of 178 at 273 K and 1 bar for a mixture gas of SF_6/N_2 (v/v, 10/90). In breakthrough experiments, SF_6 starts to break through at 6.5 min and completely breaks through until approximately 20 min while nitrogen accomplishes this process within only 1 min, demonstrating high affinity of **CC3** toward SF_6 (Figure 8d).

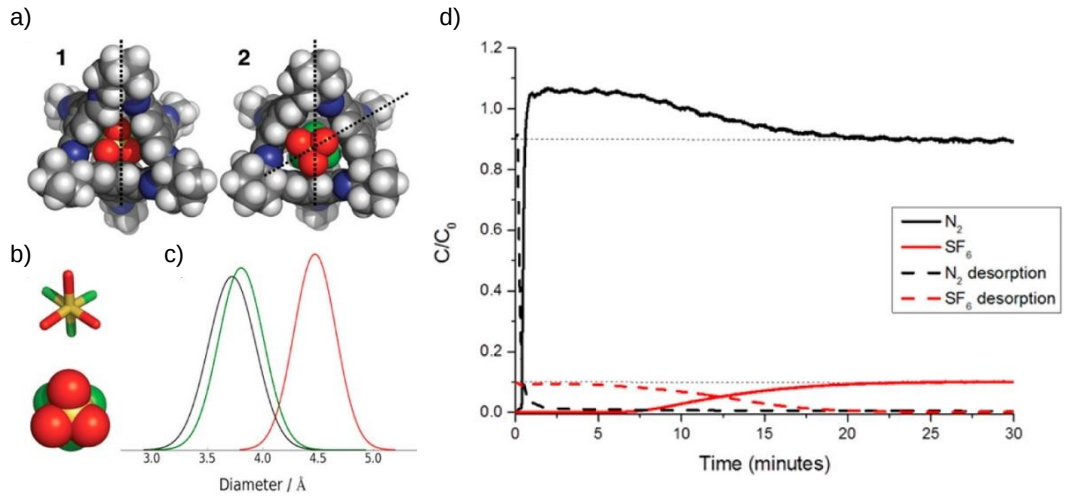

Figure 8. (a) **CC3** and SF_6 configurations. Structure 1 corresponds to the global minimum orientation with SF_6 in the **CC3** cavity, and structure 2 represents the structure at the highest point of the free energy surface, when SF_6 is placed exactly in the center of the window. (b) Stick and space fill representations of the SF_6 molecule. The three fluorine atoms that diffuse through the window first are colored red. (c) Comparison of the pore envelope of the **CC3** window, for an empty cage (black), for **CC3** with SF_6 occupying the cage cavity (green), and for cage where SF_6 is positioned in the window (red). (d) N_2/SF_6 (90:10) breakthrough curve for **CC3** at 298 K. Total flow rate was 25 mL min^{-1}, and pressure was 1 bar. Desorption was performed by flowing helium through the bed at the same flow rate and pressure. Adapted with permission from Ref.[84]. Copyright © 2016 American Chemical Society

5.4. Fluorinated Organic Cages

The subtle difference in structures can change porosity and gas sorption properties of cages.[48f, 48j, 85] One common pair of cages studied in this regard involves fluorinated organic cages and non-fluorinated analogues. Mastalerz and colleagues explored the direct synthesis of both fluorinated and non-fluorinated shape-persistent [4+6] tetrahedral boronic ester cages.[48k] After desolvation, fluorinated cages **26** and its analogue **27** exhibit significantly lower BET surface areas of 60 and 28 $m^2 g^{-1}$ (N_2, 77 K), respectively, in contrast to non-fluorinated cages (511 $m^2 g^{-1}$) (Figure 9a and b). In a different approach, Cooper *et al*. introduced phenyl and fluorophenyl bulkier groups at the vertices of cages to create additional, extrinsic pore volume.[48h] Fluorinated imine cage **28** has a lower BET surface area of 460 $m^2 g^{-1}$ compared to unfunctionalized cages of the same dimensions (550 $m^2 g^{-1}$) (Figure 9c). A similarly sized fluorinated cage **29** with an improved fluorination grade was synthesized by Schmidt and co-workers and displays an enhanced BET surface area of 536 $m^2 g^{-1}$, along with the capacity to adsorb 19.0 wt% CO_2 (273 K and 1 bar) and 1.5 wt% H_2 (77 K and 1 bar) (Figure 9d).[48i] These findings suggest that higher degrees of fluorination could benefit gas adsorption.

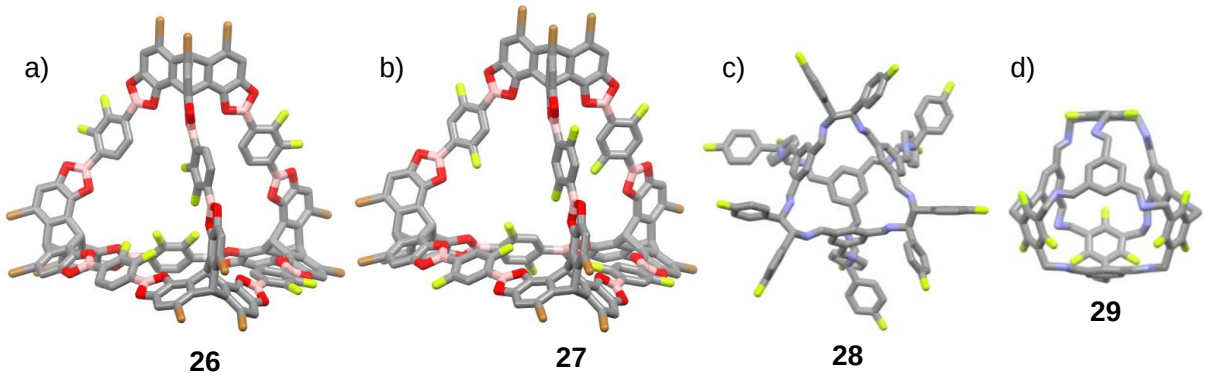

Figure 9. Molecule structures of fluorinated cages as stick models.[48h, 48i, 48k] **26** and **28**: SCXRD structures. **27** : edited SCXRD structure of **26**. **29** : edited structure from Dr. Bernd M. Schmidt (Heinrich-Heine-Universität)'s SCXRD data. H atoms are omitted for the sake of clarity. Green, brown, blue, red, gray, and pink spheres represent F, Br, N, O, C, and B atoms, respectively.

Research on MOFs and COFs has also demonstrate that the introduction of the fluorine can fine-tune crystallinity, porosity, and gas sorption property.[48f, 48j, 85] In a related study within our research group, Dr. Xin-Yue Hu synthesized a series of side chain-modified [2+3] cages including long alkyl and perfluoroalkyl chains, and so on.[86] Interestingly, an opposite phenomenon was observed. **F-cage** with perfluorobutyl chains has much higher BET-surface areas (588 $m^2 g^{-1}$) than **H-cage** with *n*-butyl

chains (28 m^2 g^{-1}). Notably, **F-cage** exhibits IAST selectivity of 28 and 10 at 273 K and 1 bar for gas mixtures of SF_6/N_2 (v/v, 10/90 and 50:50, respectively) (Figure 10).[86] Although a comprehensive study regarding the structure-property relationship at the molecular level has not been presented yet, this finding provides a strong hint towards the potential selective adsorption of F-gases using this fluorinated cage.

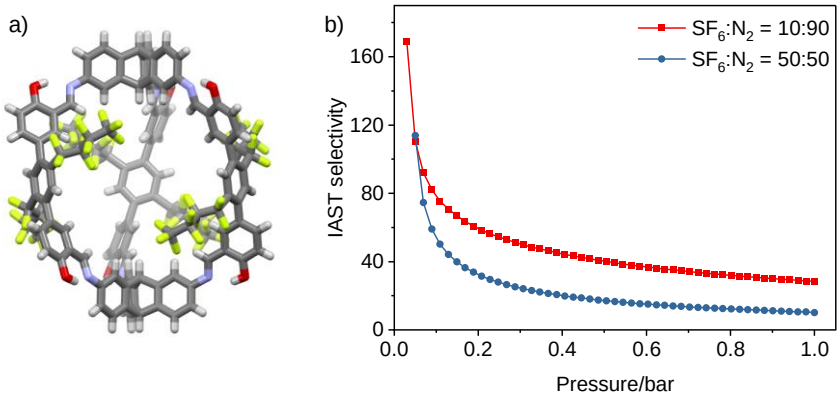

Figure 10. (a) Single crystal structure of **F-cage** as the stick model. Green, blue, red, white and gray spheres represent F, N, O, H, and C atoms, respectively. The IAST selectivity of **F-cage** for SF_6 over N_2 at ratios of 50:50 and10:90.[86]

II. Objective

The aim of this thesis is to introduce functional side chains into imine cages, and to investigate how these functional side chains affect the properties of the cages (crystallinity, packing, porosity, selectivity, chirality, etc.) and develop highly selective adsorption of perfluorinated greenhouse gases using fluorinated POCs. Therefore, a series of isostructural [2+3] imine cages with different degrees of fluorination and different lengths of fluorinated side chains will be synthesized by side chain modification strategy and investigated for their structure-property relationship in detail (Scheme 5).

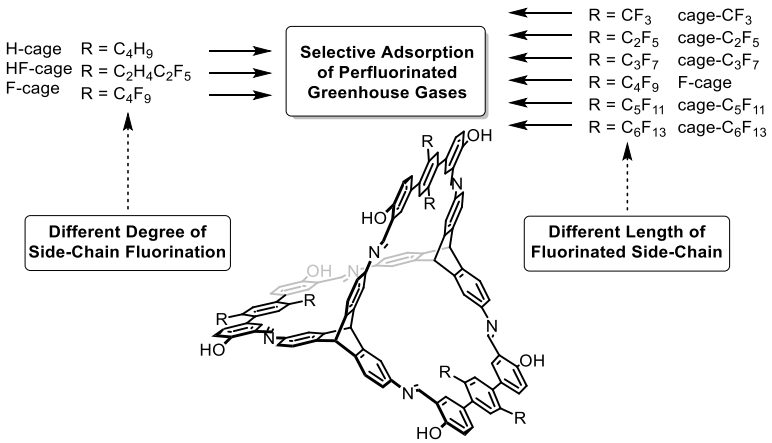

Scheme 5. [2+3] imine cages with different side chains for selective adsorption of perfluorinated greenhouse gases.

POCs can exhibit polymorphism, potentially impacting porosity and gas properties of the cages materials.[79-80, 87] Varied crystalline polymorphs of the same molecules can result in entirely disparate structural organizations, so the influence of the crystal packing of [2+3] imine cages on gas adsorption will be studied.

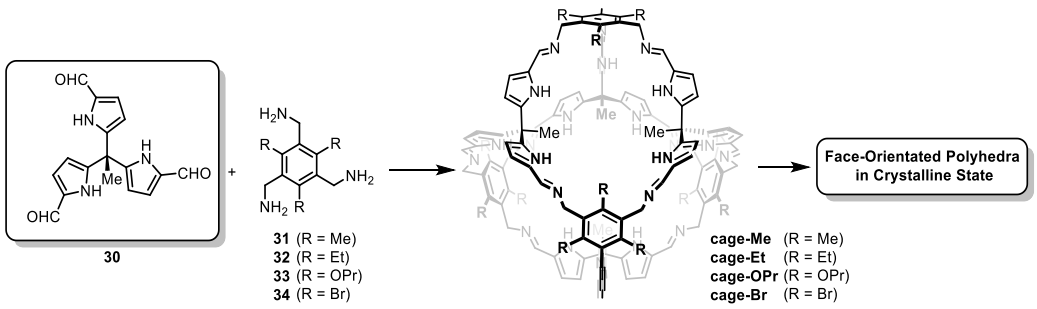

Scheme 6. Synthesis of [4+4] imine cages derived from chiral C_3-symmetrical building block **30**, followed into face-orientated polyhedral in crystalline state.

Another group of side chain-modified amine is also designed, which made it possible to examine the chiral change of cages with the side chain modification in the crystalline state in detail (Scheme 6).

III. Results and Discussion

1. The Influnce of the Degree of Side Chain Fluorination on Perfluorocarbon Adsorption

As aforementioned, Dr. Xin-Yue Hu has used 2,7,14-triaminotriptycene and modified terphenyl-based bis-salicylaldehydes to construct successfully the fluorinated and nonfluorinated butyl functionalized [2+3] imine cages.[86] Fluorinated cage demonstrated promising potential for selectively adsorbing F-gases. Expanding upon this prior work, the current chapter presents a small series of [2+3] porous imine cages functionalized with different types of *n*-butyl groups, including n-butyl, perfluorinated *n*-butyl, and partially fluorinated *n*-butyl groups.[7] The main focus of this chapter is to explore the relationship between the degree of fluorination in the alkyl chains and the gas sorption properties for PFCs and investigate their selective uptakes in comparison to other, nonfluorinated gases in detail.

1.1. Synthesis of [2+3] Cages with Different Degree of Fluorination of *n*-Butyl Chains

In order to introduce different degrees of fluorination of *n*-butyl side chains into the [2+3] cage, the salicyldialdehyde terphenyl building blocks were initially modified following the method established by Dr. Xin-Yue Hu (Figure 11).[86] Prior to the synthesis of these building blocks, three dibromide compounds bearing different degree of fluorination of *n*-butyl side chains (**35**-**37**) were firstly prepared according to the routes outlined in Scheme 7. Referring to a modified procedure from the literature[88], pure 1,4-dibutyl benzene **40** was obtained in 39% yield [Lit.: 81% crude product] by nickel-phoshpine complex-catalyzed Kumada coupling of 1,4-dichlorobenzene **38** and a pre-prepared Grignard reagent (*n*-butylmagnesium bromide) (Scheme 7a). Subsequently, 1,4-dibutyl benzene was brominated in liquid bromine for 20 h to give the dibrominated compound **41** in 61% yield [Lit.: 88% crude product].[88a]

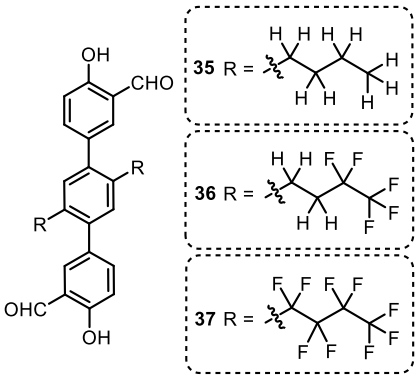

Figure 11. Chemical structures of salicyldialdehyde terphenyls **35**-**37**.

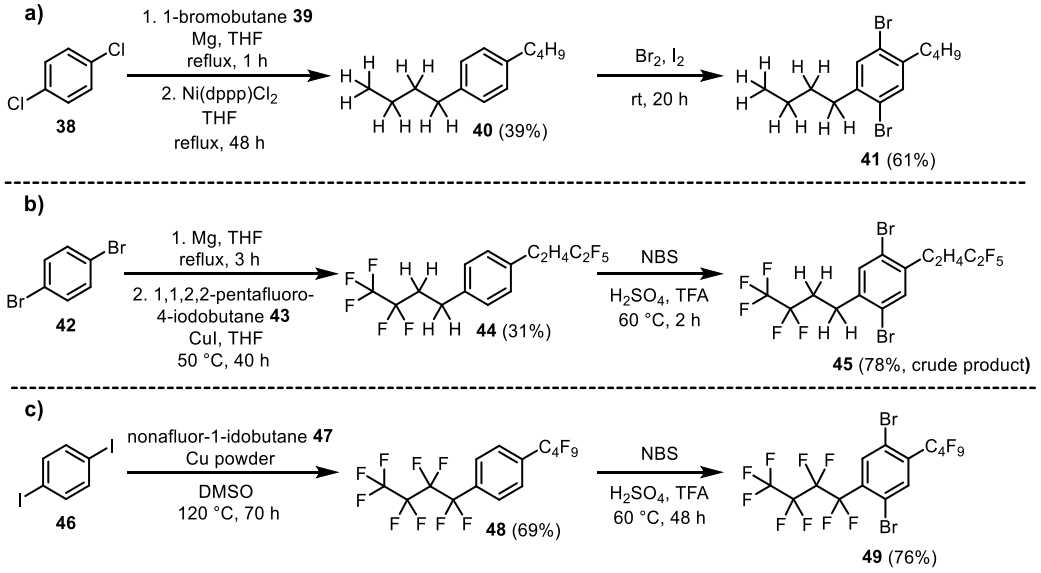

Scheme 7. Synthesis of dibromides **41**, **45**, and **49**.

Starting with 1,4-bromobenzene **42**, partially fluorinated *n*-butyl groups were introduced in 31% yield by copper-catalyzed cross-coupling reaction of *β*-perfluoroalkyl-substituted alkyl halide **43** with pre-prepared di-Grignard reagent 1,4-bis(bromomagnesium)-benzene (Scheme 7b).[89] Subsequent bromination was carried out in a mixture strong acid of sulfuric acid (H_2SO_4) and trifluoroacetic acid (TFA) with NBS, instead of liquid bromine, and produced a crude product in 78% yield. It cannot be purified further, even by recystallization and chromatography, and thus was used in the next step directly. The synthesis of dibromide compounds with perfluorobutyl group **49** was reported as a precursor for preparing both dicarboxylate and dipyridyl ligands of aforementioned perfluorobutyl-functionalized PCPs (Scheme 7c).[49a] Nonafluoro-1-iodobutane **47** as a source of the fluorobutyl moiety was reacted with copper powder in DMSO at 120 °C to form the corresponding perfluoroalkyl copper intermediate, which participated in the coupling reaction with 1,4-diiodobenzene **46** to produce the perfluorinated butyl chain modified benzene **48** in 69% yield [Lit.: 83%].[49a] It was brominated further under similar condition as previously employed for the preparation of **45** to give dibromide compounds **49** in 76% yield [Lit.: 77%].[49a]

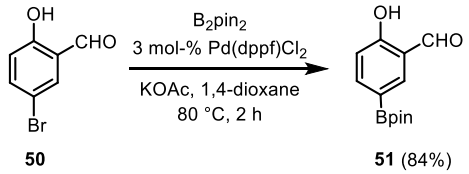

Scheme 8. Synthesis of **51**.

Pinacol boronic ester **51** was synthesized by Miyaura borylation of bromosalicylaldehyde **50** in 84% yield [Lit.: 88%] (Scheme 8) as previously demonstrated,[90] and then subjected to palladium-catalyzed Suzuki-Miyaura cross-coupling reaction with different dibromo derivatives to obtain salicyldialdehyde terphenyls with non-, partially-, and fully- fluorinated *n*-butyl groups in yields of 54% [Lit.: 40%] for **35**, 39% for **36** and 32% [Lit.: 30%] for **37** (Scheme 9).[86]

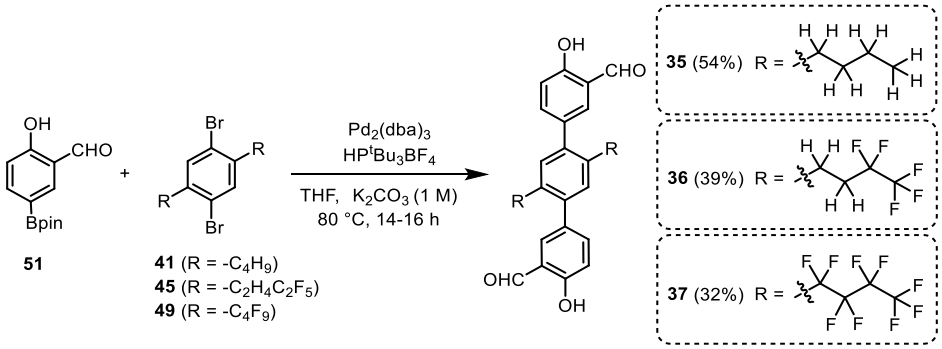

Scheme 9. Synthesis of terphenyl bis-salicyl aldehydes **35**-**37** by Suzuki-Miyaura reaction.

The other building block for the envisioned [2+3] imine cages, 2,7,14-triaminotriptycene **15** was synthesized through a two-step process involving nitration of triptycene **52** and followed by reduction of the introduced nitro groups (Scheme 10). According to a literature protocol by Chen *et al.*, triptycene can be converted to the trinitro compounds **53** and **54** in a 3:1 statistical mixture, using concentrated nitric acid at 70 °C for one day.[91]

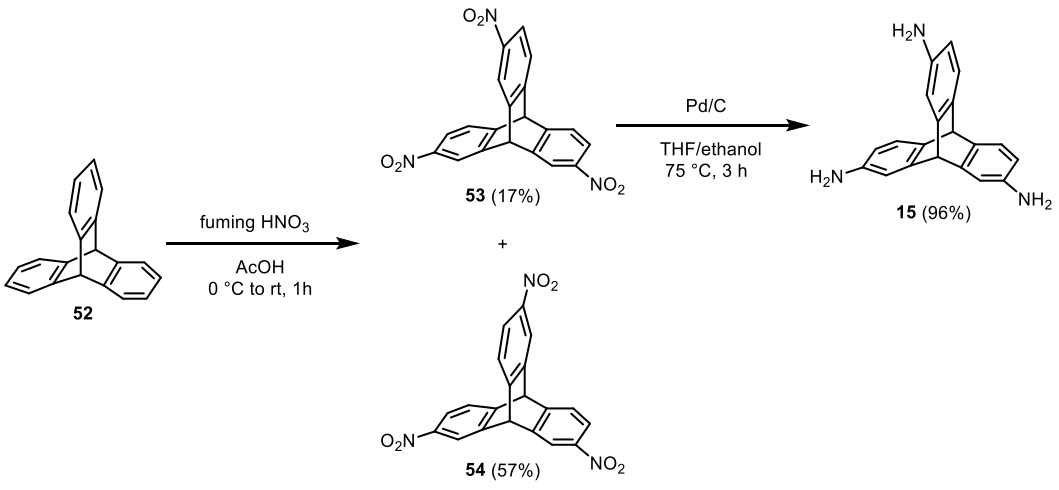

Scheme 10. Synthesis of triamino triptycene **15**.

A more effective method reported in Markus W. Schneider's doctoral thesis for producing the trinitro isomer mixture is to use glacial acetic acid and fuming nitric acid as nitration reagents for just one hour.[76] The desired isomer **53** was isolated in 17%

yield [Lit.: 21%] by repeated column chromatography of the isomer mixture and then almost quantitatively [Lit.: quant.] reduced to 2,7,14-triaminotriptycene **15** in the presence of hydrazine and palladium on charcoal (Scheme 10).[86, 92]

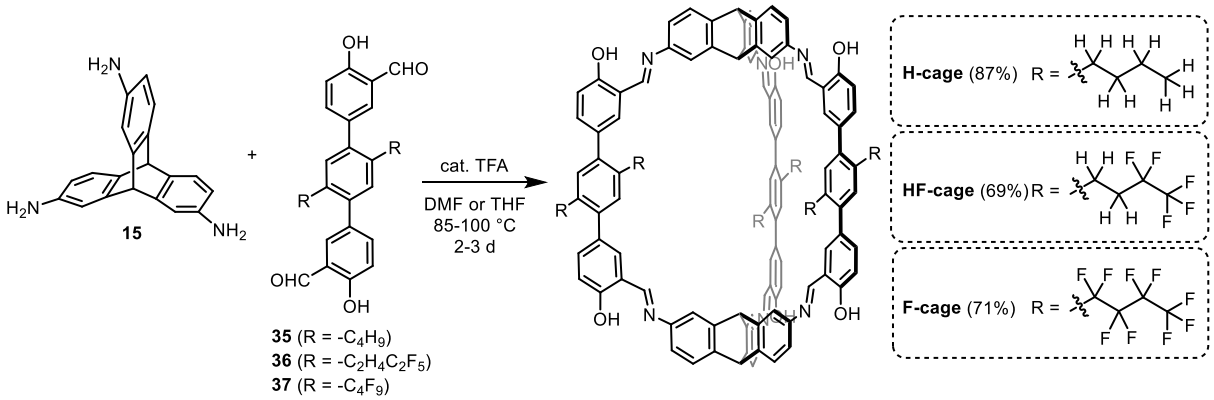

Scheme 11. Synthesis of **H-cage**, **HF-cage**, and **F-cage** by imine condensation reaction of triamino triptycene **15** and terphenyl bis-salicyl aldehydes **35-37** (condition: DMF, 100°C, TFA, 3 d for **H-cage**; DMF, 100°C, TFA, 2 d for **HF-cage**; THF, 85°C, TFA, 2 d for **F-cage**).

The isostructural [2+3] cages **H-cage** (with non-fluorinated *n*-butyl chains), **HF-cage** (with partially fluorinated *n*-butyl chains) and **F-cage** (with perfluorinated *n*-butyl chains) were synthesized by a six-fold condensation reaction of triamino triptycene **15** with the terphenyl-based bis-salicylaldehydes **35**-**37** with a catalytic amount of TFA at elevated temperatures (85-100 °C) for 2-3 days (Scheme 11 and Table 2).[86] After cooling to room temperature, the reaction mixtures were filtered through syringe filters and concentrated to a certain volume by rotary evaporation. Methanol was added, acting as an anti-solvent to precipitate the pure cages in yields of 87% [Lit.: 68%] (**H-cage**), 69% (**HF-cage**), and 71% [Lit.: 67%] (**F-cage**).[86]

Table 2. Reaction condition of cage synthesis.

Cages	Solvent	Temperature	Time	Catalyst amount[a]	Yield
H-cage	DMF	100 °C	3 d	3 mol-%	87%
HF-cage	DMF	100 °C	2 d	3 mol-%	69%
F-cage	THF	85 °C	2 d	4.5 mol-%	71%

[a] based on the amount of **15**.

The chemical structures of three cages were investigated by ^{1}H and ^{19}F NMR spectroscopy in THF-d_8 (Figure 12-13). The disappearance of the aldehyde singlets at 9.95-10.02 ppm and the appearance of all imine singlets at 9.15 ppm indicates the formation of pure cages. With a higher degree of side-chain fluorination, the peaks of the hydroxy protons shift slightly from 13.13 to 13.36 ppm due to increasing electro-withdraw effect of the side chains located in the middle of the terphenyl units.

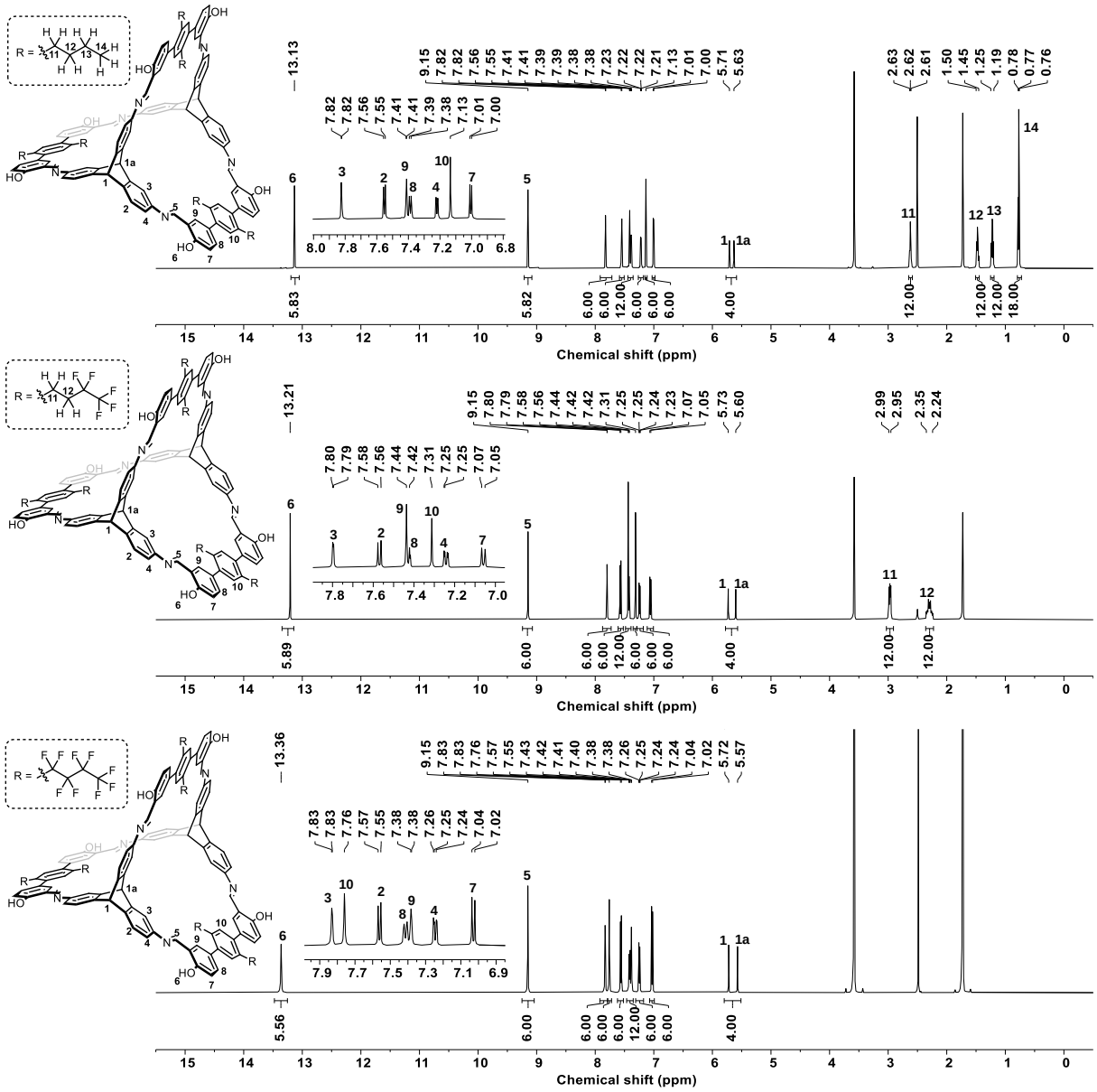

Figure 12. ^{1}H NMR spectra of **H-cage**(top, 700 MHz), **HF-cage**(middle, 500 MHz), and **F-cage**(bottom, 500 MHz) in THF-d_8. Adapted with permission from Ref.[7]. Copyright © 2022 Wiley-VCH.

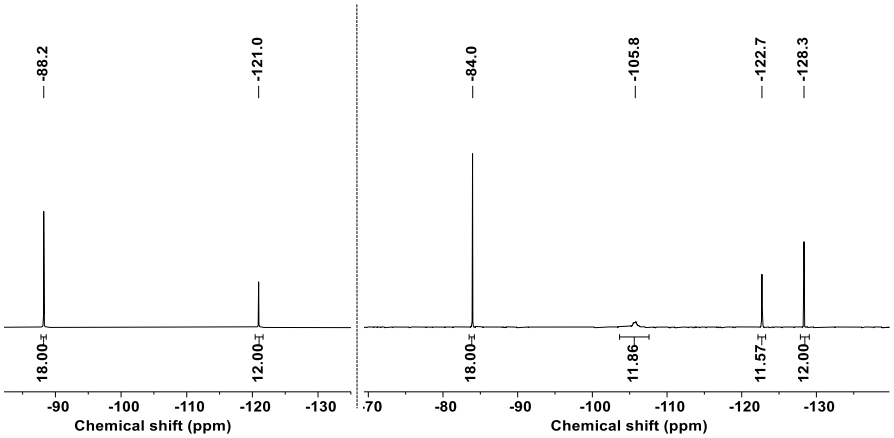

Figure 13. ^{19}F NMR spectra of **HF-cage**(left) and **F-cage**(right)(471 MHz, THF-d_8). Adapted with permission from Ref.[7]. Copyright © 2022 Wiley-VCH.

The chemical shift between 7.00-8.00 ppm are clearly assigned to aromatic protons of triptycene and terphenyl units while two bridgehead protons of the triptycene part appear at 5.71-5.73 ppm and 5.57-5.63 ppm as singlets, respectively. The distinctive side-chain regions can be readily discerned in the low chemical shift region through the presence of four sets of proton peaks for the butyl chain, two sets of proton peaks for partially fluorinated butyl chains, and the absence of proton peaks for perfluorinated butyl chains (Figure 12). This observation gains additional affirmation in ^{19}F NMR spectra by the presence of zero, two, and four fluorine peak groups corresponding to non-fluorinated, partially fluorinated, and perfluorinated butyl chains, respectively (Figure 13).

DOSY-NMR spectra of the cage compounds were recorded at 400 MHz and 295 K. Calibration was performed using the self-diffusion of the solvent (THF; D_{solv} = $2.33 \cdot 10^{-9}$ $m^2 \cdot s^{-1}$, η = $0.47 \cdot 10^{-3}$ $kg \cdot m^{-1} \cdot s^{-1}$).[93] The solvodynamic radii r_s of the cage compounds were calculated from the measured diffusion coefficients D using the semi-empirical modification of the Stokes-Einstein equation.[94]

$$r = \frac{k_B T}{6\pi\eta D} \quad (6)$$

D is the measured diffusion coefficient ($m^2 \cdot s^{-1}$)

k_B is Boltzmann constant ($1.3806485 \cdot 10^{-23}$ $m^2 \cdot kg \cdot s^{-2} \cdot K^{-1}$)

T is the temperature (K)

r is the hydrodynamic radius of the analyte (m)

η is the viscosity of the solvent at temperature T ($kg \cdot m^{-1} \cdot s^{-1}$)

DOSY-NMR investigations of the cage compounds show well-defined signal traces, which can be clearly identified and assigned (Figure 14). Calculated hydrodynamic radii r_s for the cage compounds are 1.10-1.28 nm, which are in good agreement to the dimensions obtained by SCXRD (see discussion below). Three cage compounds were further investigated by MALDI-TOF mass analysis (Figure 15). Only a strong peak of the molecular ions $[M+H]^+$ (m/z = 1781.913 for **H-cage**, 2321.604 for **HF-cage**, 2753.413 for **F-cage**) and a small peak of $[M+DCTB]^+$ (m/z = 2032.054 for **H-cage**, 2571.749 for **HF-cage**, 3003.583 for **F-cage**) are detected for three corresponding cages in the m/z range from 1000 to 4000 Da. Experimental isotope distributions for the molecular ions $[M+H]^+$ were in good agreement with simulated ones. All these cage were also characterized by ^{13}C NMR, 2D NMR, elemental analysis (EA) and infrared spectroscopy (IR).

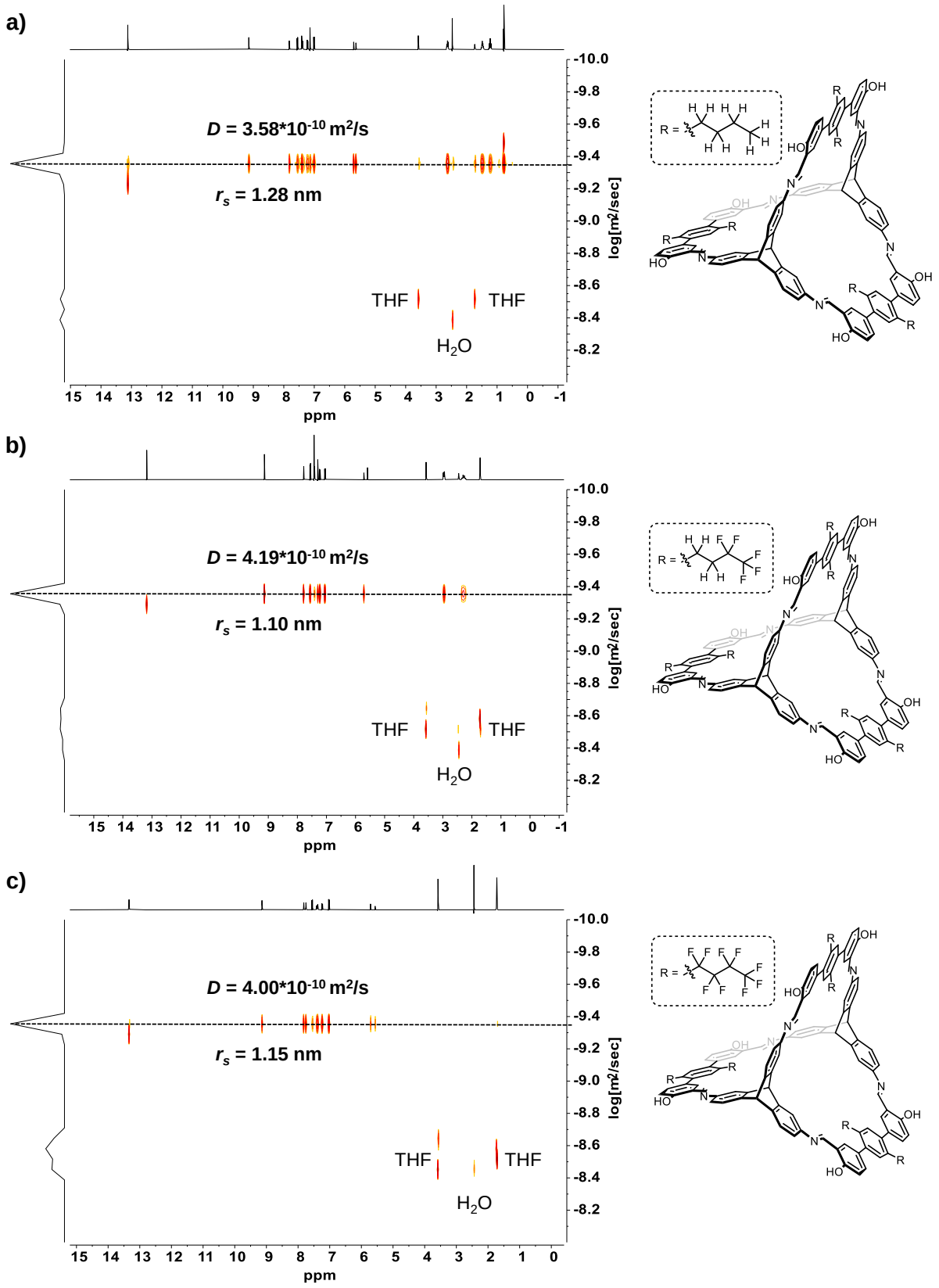

Figure 14. DOSY-NMR spectra (THF-d_8, 400 MHz, 295 K) of **H-cage** (a), **HF-cage** (b), and **F-cage** (c)**.** Adapted with permission from Ref.[7]. Copyright © 2022 Wiley-VCH.

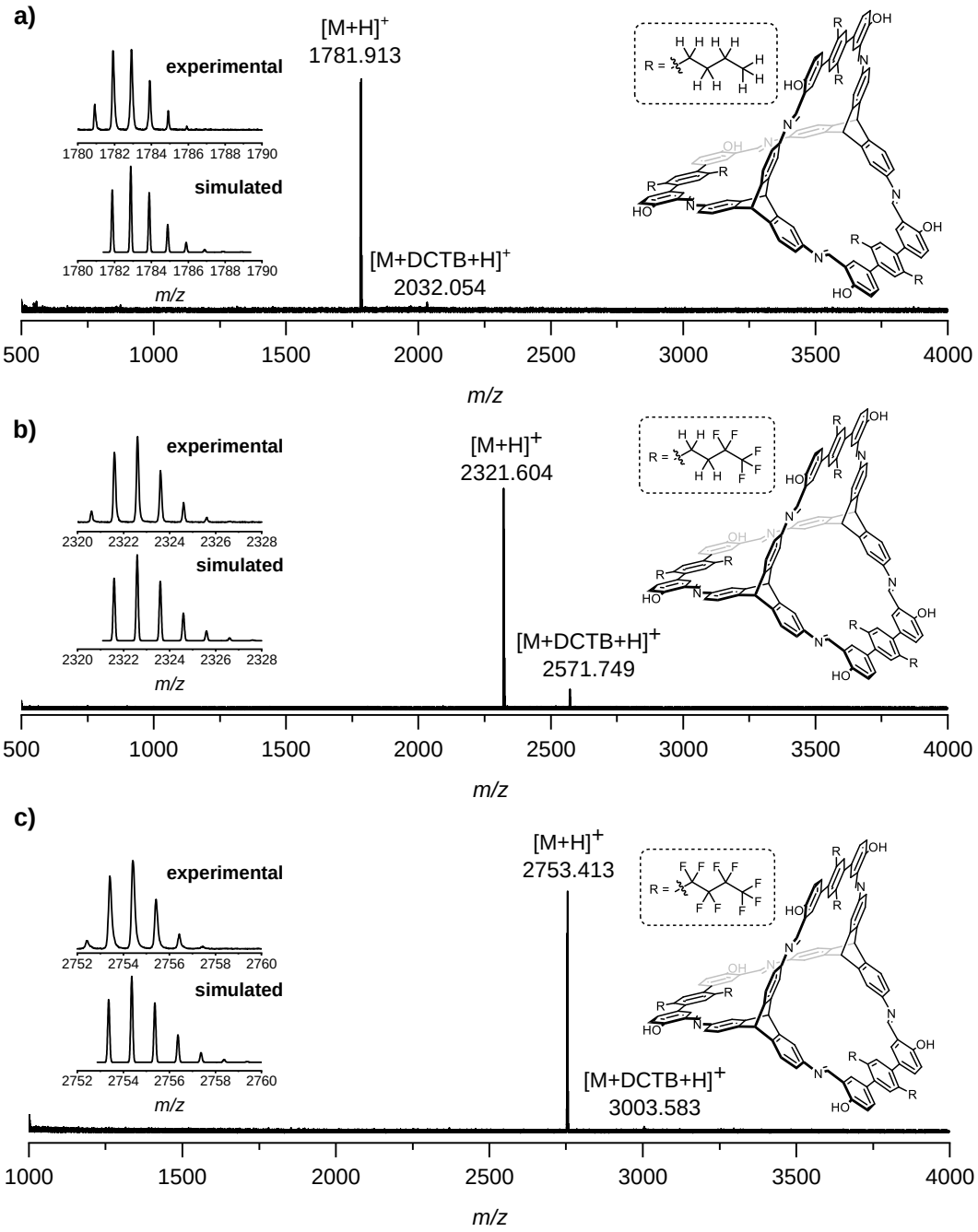

Figure 15. MALDI-TOF mass spectra of **H-cage** (a), **HF-cage** (b), and **F-cage** (c) (matrix: DCTB). Adapted with permission from Ref.[7]. Copyright © 2022 Wiley-VCH.

1.2. Single Crystal Structure Investigation

Given the better solubility of the **F-cage** in tetrahydrofuran (THF) in comparison to some other solvents like dichloromethane (DCM), chloroform ($CHCl_3$), and dimethylformamide (DMF), the crystals of the three cages were acquired through by slow vapor diffusion of methanol into THF solutions. All cages crystallized in the trigonal space group $R\bar{3}c$ with similar cell volumes of 18052.3 Å^3 (**H-cage**), 19985 Å^3

(**HF-cage**), and 20049.6 Å^3 (**F-cage**), demonstrating the isomorphism in the crystalline state (Figure 16). Structural details will only be discussed for **F-cage**, since they are isomorphous. The size of the cages, measured between the outer triptycene bridgehead carbons, is 1.8 nm (Figure 16a-c). This is in agreement with the solvodynamic radii of 1.10-1.28 nm calculated from DOSY NMR experiments (Figure 14). Additionally, the cages possess almost spherical voids, which are determined by a distance of 1.3 nm between the inner triptycene bridgehead carbons and 1.4 nm between the centroids of the central benzene rings of the terphenyl units.

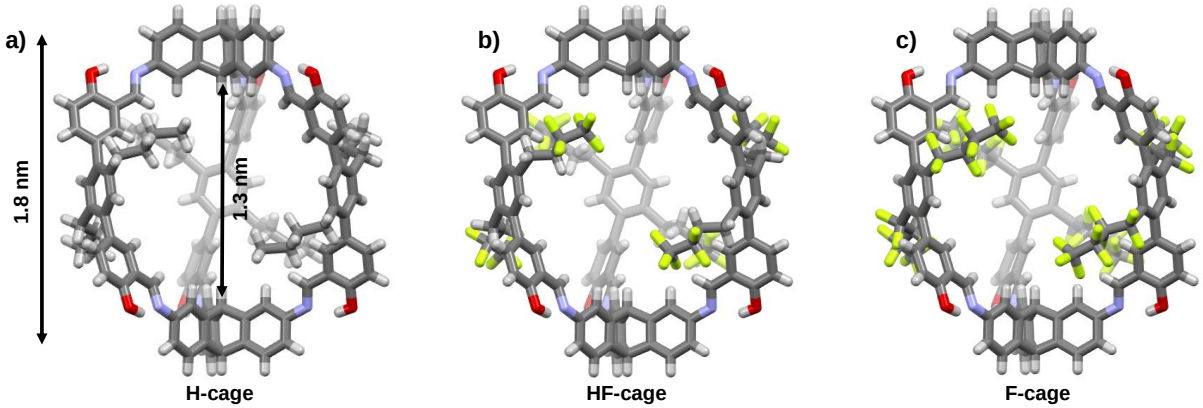

d)

Parameter	**H-cage**	**HF-cage**	**F-cage**
Crystal system	Trigonal	Trigonal	Trigonal
Space group	*R*$\bar{3}$*c*	*R*$\bar{3}$*c*	*R*$\bar{3}$*c*
Z	6	6	6
Cell volume [Å^3]	18052.3	19985	20049.6
endo-population	61%	63%	68%
exo-population	39%	37%	32%
$d_{\pi\text{-}\pi}$[a] (Å)	3.70	3.56	3.68
Rel.π-π-stacking Energy[b] (kJ/mol)	0	4	-1
Dispersion energy[c] (kJ/mol)	-438	-485	-560
Cage void volume[d]	518	650	625

Figure 16. Single crystal X-ray structures of **H-cage** (a), **HF-cage** (b), and **F-cage** (c) (only one enantiomer of each racemic crystal structure is depicted). The inner and outer diameter (measured between two carbon atoms) is depicted for **H-cage**. (d) Selected crystallographic parameters. [a] Crystallographic parameters, π-stacking distance $d_{\pi\text{-}\pi}$ according to Figure 17k-m. [b] Relative π-stacking energy per dimeric unit. (**H-cage** is set as reference) of the substructure shown in Figure 17l-m calculated using the XDM method (B3LYP/aug-cc-pVDZ). [c] per hexameric side chain alignment. [d] Crystalline voids per cage represented as contact surface, created by Mercury 2020.1 with a probe radius of 1.82 Å and a grid spacing of 0.5 Å. Quantumchemical calculations of this section were performed by Dr. Tobias Kirschbaum (Institute of Organic Chemistry (OCI), Heidelberg University). Adapted with permission from Ref.[7].

Due to the flexibility of the long perfluoroalkyl side chains, the central (and substituted) phenyl part of the terphenyl units, which are contorted by 71.4-75.0° to the neighboring ring, can be found in one of two possible main conformations (Figure 17a-h). The conformations in which a side chain points into the cage's window and points outward are termed "*endo*" and "*exo*", respectively. The populations of the *"endo"* and "*exo*" states are 61-68% and 39-32% on average, respectively (Figure 16d). This *endo*/*exo* ratio of approximately 2:1 cannot be differentiated further to determine if 2/3 of the cages are *endo* or if four of the six chains are *endo* in a single cage, or a combination of both. For simplicity, only the two extreme states of full-*endo* and full-*exo* will be discussed here. The overlay of both extremes indicated the average atomic positions of the whole cage backbone are equal (Figure 17i-j). The two triptycene scaffolds of the cage backbones are rotated by 29.0° with respect to one another, resulting in helical chirality for the cage molecules, labeled as "*endo-M"* and "*endo-P",*

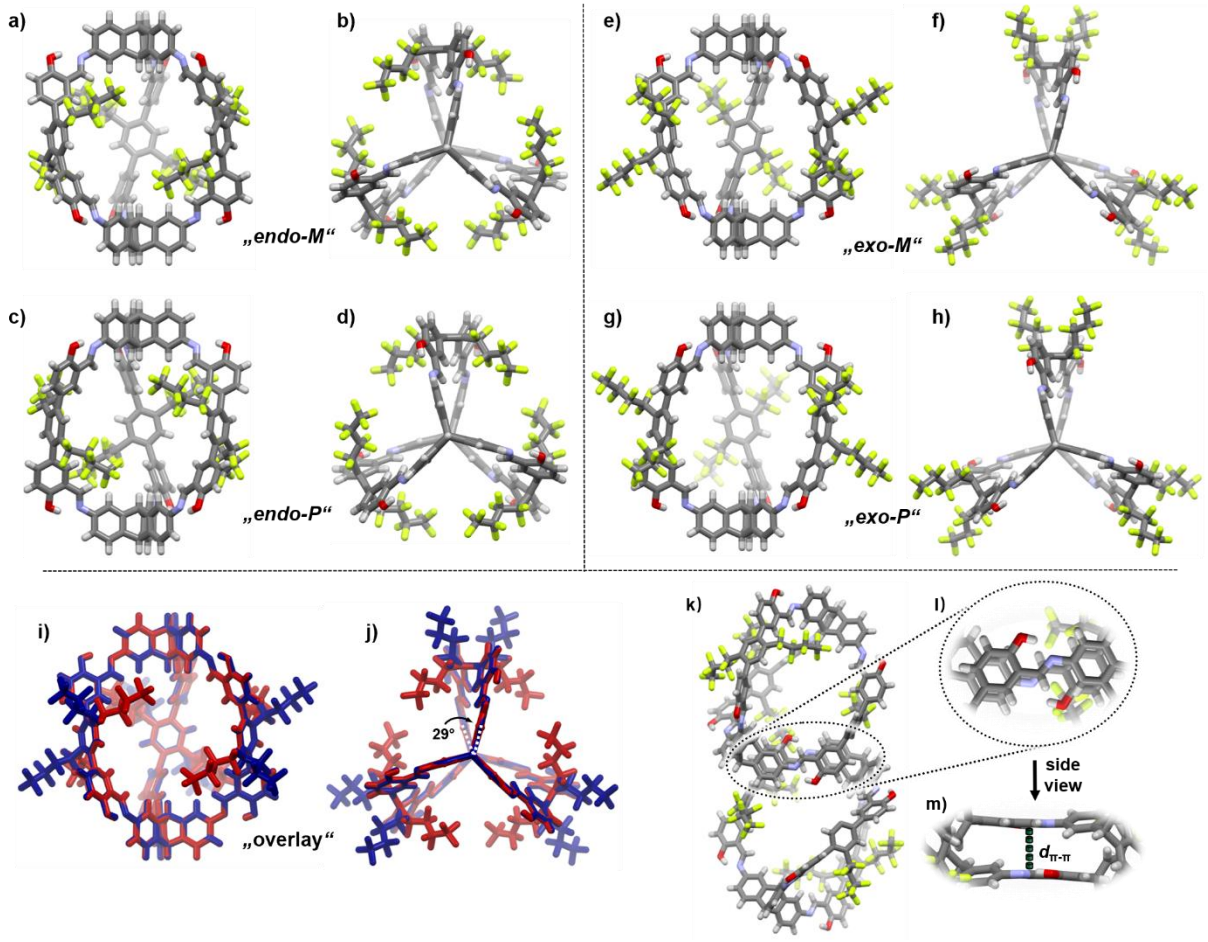

Figure 17. Side-views (a and c) and top-views (b and d) on the two helical isomers *endo-M* (a and b) and *endo-P* (c and d) of **F-cage**. Side-views (e and g) and top-views (f and h) on the two helical isomers *exo-M* (e and f) and *exo-P* (g and h) of **F-cage**. Side-view (i) and top-view (j) of on an overlay of the full *endo-M* (red) and full *exo-M* (blue) conformer. (k) π-stacked dimer of two cage molecules. (l) Zoom-in of the π-stacking motif as top view. (m) Zoom-in of the π-stacking as side view. Colors: carbon, grey; hydrogen, white; oxygen, red; nitrogen, blue; fluorine, lime. Adapted with permission from Ref.[7]. Copyright © 2022 Wiley-VCH.

"*exo-M"* and "*exo-P"* (Figure 17a-h).

The cage packing is dominated by π-π stacking of the salicylimine substructures (Figure 17k-m). The distance $d_{\pi\text{-}\pi}$ is 3.70 Å for **H-cage**, 3.56 Å for **HF-cage**, and 3.68 Å for **F-cage** (Figure 16d). Every cage is surrounded by six adjacent cages (Figure 18). Six adjacent side chains from six cage molecules interact with each other to form a hexagonal array for both full-*endo* and full-*exo* states. Quantumchemical calculations were performed by Dr. Tobias Kirschbaum (OCI, Heidelberg University) to investigate the relative π-stacking energy of the dimeric unit and the dispersion interactions of hexameric side-chain alignment. Relative π-stacking energy ΔE is -1 to 4 kJ/mol (**H-cage** is set to 0), demonstrating that the effect of side chains on the π-stacking energy of these subunits is minimal (Figure 16d). Furthermore, the calculations reveal an increase in dispersion energies with a higher degree of fluorination of the side chains (-438 kJ/mol for **H-cage**, -485 kJ/mol for **HF-cage**, and -560 kJ/mol for **F-cage**) (Figure 16d). This trend is further supported by a recent report by Robert Pollice and Peter Chen, which demonstrate that perfluoroalkanes have a higher intrinsic ability for dispersive interactions than their alkane counterparts and that dispersion in perfluoroalkane dimers primarily arise from F···F interactions.[95]

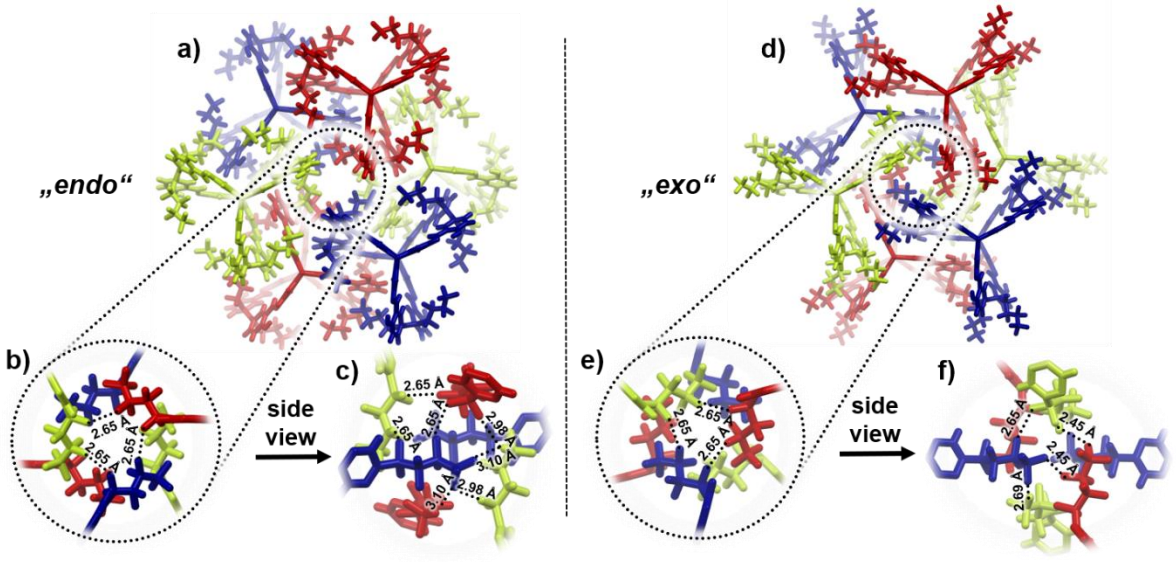

Figure 18. Hexameric alignment of full *endo* (a) and full *exo* (d) along the crystallographic c-axis. Cages depicted in the same color are equal by inversion symmetry. Zoom-in to the hexameric side-chain alignment of full *endo* (b and c) and full *exo* (e and f) as top view and side view with F···F-distances measured. Adapted with permission from Ref.[7]. Copyright © 2022 Wiley-VCH.

Somewhat surprisingly, F···F noncovalent interactions, recognized for their stabilizing nature and substantial energy contributions to structures, initially seem counterintuitive due to the low polarizability of fluorine, as Pauling's principle.[96]

However, an increasing number of experimental and theoretical studies on F···F interactions in the solid state has emerged.[95, 96b, 97] These investigations identify two distinct types of F···F interactions (Figure 19a): Back in 1986, Ramasubbu *et al*. noted that type II X···X interactions stem from halogen atom polarization, while type I arises from close packing without forming stabilizing interactions.[98] Considering all this together, the following criteria for classification of type I and type II contacts are suggested: (1) contacts with $0° \leq |\theta_1 - \theta_2| \leq 15°$ are classified as type I; (2) contacts with $30° \leq |\theta_1 - \theta_2|$ are categorized as type II; (3) contacts with $15° \leq |\theta_1 - \theta_2| \leq 30°$ are considered quasi-type I/type II.[99] Upon inspecting the crystallographic data, it becomes evident that multiple F···F noncovalent interactions exist in side chains of **F-cage** (Figure 18 and 19). Among them, the shortest interactions (2.65 Å for *endo* and 2.45 Å for *exo*) between neighboring perfluorobutyl groups correspond to typical Type II (∠C-F···F-C = 122° and 156°) and Type I contacts (∠C-F···F-C = 122° and 121°), respectively (Figure 19b and c). In addition, Type I, Type II, and quasi-type I/type II halogen-halogen contacts are also observed in relatively longer F···F interactions.

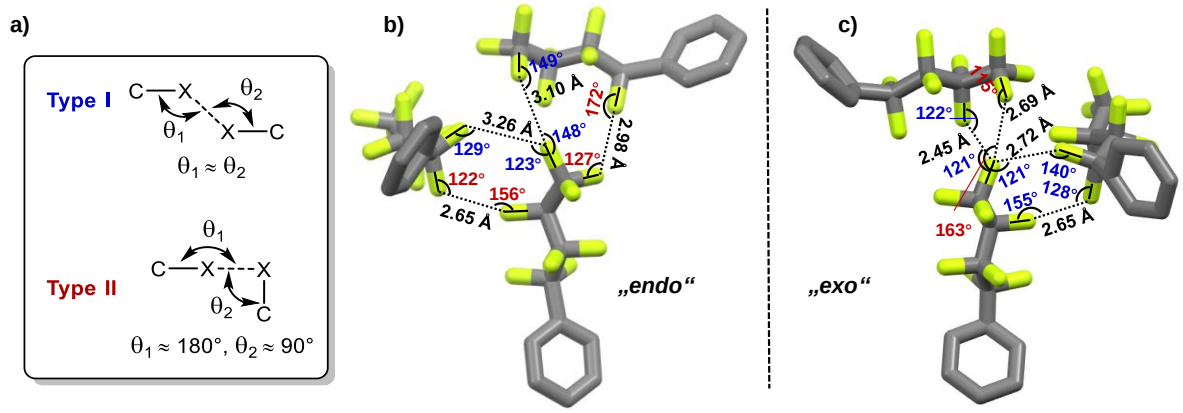

Figure 19. (a) Classification of halogen···halogen interactions. (b) Selected adjacent side-chain alignment of full *endo* (b) and full *exo* (c) with F···F-distances and C-F···F-C angles measured. Colors: carbon, grey; fluorine, lime.

In the racemic crystalline packing, enantiopure layers can be found. The single layers are connected by the π-stacking described before, resulting in intrinsic porous strctures (Figure 20). To analyze crystalline voids, the *endo* and *exo* conformers were examined using the “voids” tool of the Mercury 2020.1 software where the approx. grid spacing was chosen to be 0.5 Å with a probe radius from 1.6 Å to 2.0 Å (Appendix, Figure 201).[100] Intrinsic pores of cages are observed in both conformers. However, the pores aren’t interconnected in the case of the *exo*-conformer. For the *endo*-conformer, connected pores seem present when probe radii is less than 1.8 Å. A slight side view on the crystalline packing proves that even at a probe radius of 1.6 Å the full

endo cages actually only have isolated pores (Appendix, Figure 202). In conclusion, all cages have only isolated intrinsic pores, which are kept apart by hexameric side-chain alignments held together by dispersion interactions. Therefore, permanent porosity is only possible by gas diffusion[101] through the side-chains and/or gate-opening mechanisms.[102]

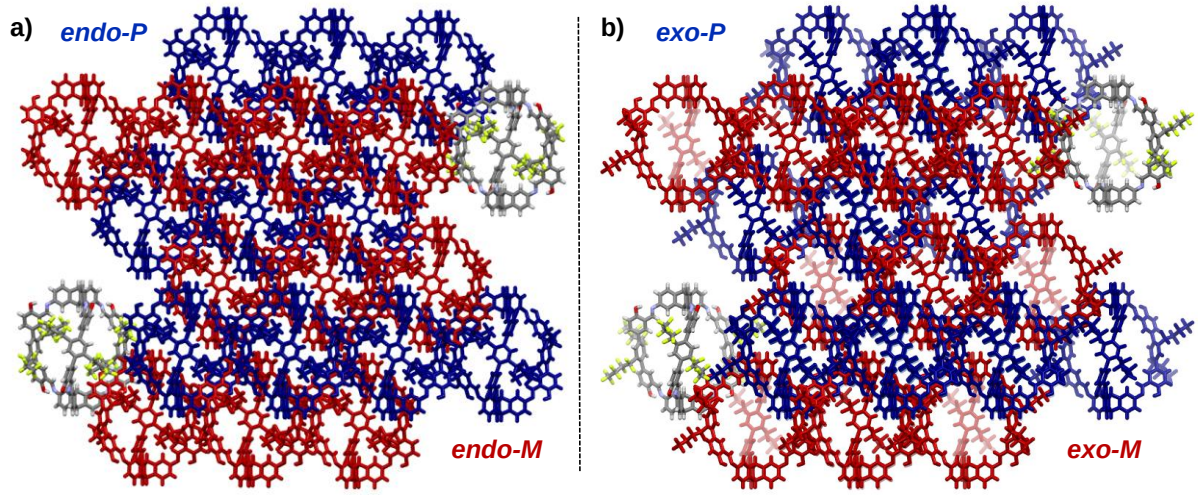

Figure 20. Crystalline packing motif of (a) *endo*-**F-cage** and (b) *exo*-**F-cage** with the *P* isomer depicted in blue and the *M* isomer depicted in red. Two cage molecules are shown in elemental colours. Adapted with permission from Ref.[7]. Copyright © 2022 Wiley-VCH.

1.3. Activation Investigation

To prevent the influence of enchlathrated solvent on the subsequent gas sorption investigation, it is essential to ensure the complete removal of all solvents (THF and MeOH) from the crystalline cages. After the crystalline cages were washed with the mixture solvent of methanol and THF, they were immediately activated at high vacuum at room temperature for 9-14 h first and then analyzed by thermogravimetric analysis (TGA) under a flow of N_2 (20 mL/min) with a heating rate of 10 K/min. As shown in Figure 21, a weight loss of 1.4 wt.% for **H-cage** and 2.5 wt.% for **HF-cage** was detected between 80 and 175 °C while no weight loss for **F-cage** was observed before thermal decomposition. It suggests small molecules can escape from the crystalline lattice of **F-cage** more easily than **HF-** and **H-cage**, thus giving the clue to explain following gas adsorption behaviors. This organophobic interactions with enclathrated guest molecules were also observed in fluorous pores of coordination networks.[49b, 49c] Additionally, it is proven that all solvent has been removed from **F-cage**.

As for the weight loss for **H-cage** and **HF-cage**, they are suspected to be enchlatrated solvent molecules from the crystallization. To confirm the assumption, **H-cage** and **HF-cage** samples prior to and after further thermal activation were investigated by ^{1}H-NMR spectroscopy in $CDCl_3$. In ^{1}H-NMR spectra, only singnals of THF and pure cages were observed (Figure 22). By integration, one molecule of THF (integration 4 on the corresponding peaks at δ = 3.75 and 1.85 ppm) is found per 2.8 **H-cage** molecules before further thermal activation (integration of 11.20 for the four bridgehead atoms, 11.2/4 = 2.8). By the following equation:

$$\frac{1 \cdot M_{\mathrm{THF}}}{2.8 \cdot M_{\text{H-cage}} + 1 \cdot M_{\mathrm{THF}}} = \frac{1 \cdot 72.11\ \mathrm{g \cdot mol^{-1}}}{2.8 \cdot 1782.30\ \mathrm{g \cdot mol^{-1}} + 1 \cdot 72.11\ \mathrm{g \cdot mol^{-1}}} \cdot 100\% = 1.4\% \quad (6)$$

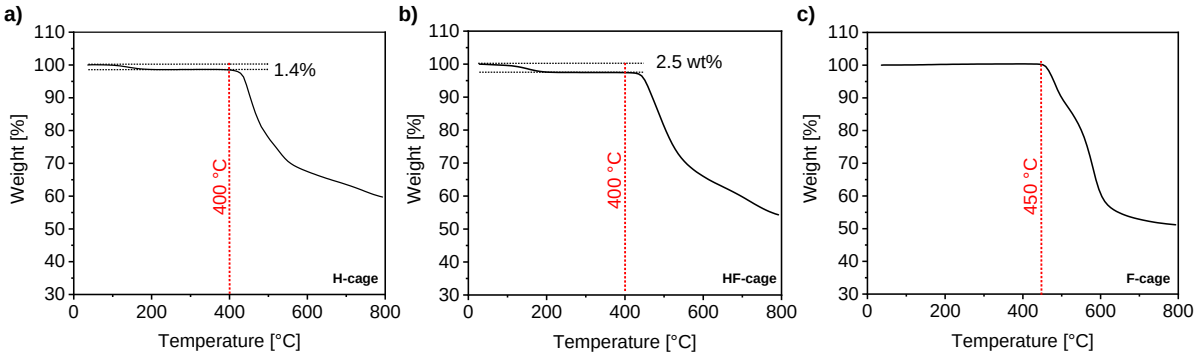

Figure 21. TGA curves of crystalline **H-cage**, **HF-cage**, and **F-cage** before thermal activation for gas sorption (N_2, flow rate: 20 mL/min, heating rate: 10 K·min^{-1}). Adapted with permission from Ref.[7]. Copyright © 2022 Wiley-VCH.

Referring to the TGA results, it is proven that 1.4 wt.% of THF remains within the crystalline lattice. Furthermore, ^{1}H-NMR spectroscopic investigations in $CDCl_3$ of **H-cage** after activation at 50 or 100 °C at 3·10^{-2} mbar for 14h show no residual THF molecules and indicated a sufficient activation at these temperatures.

The same method is applied to **HF-cage**. It is found that one THF molecule is present for every 1.25 **HF-cage** molecules before thermal activation (integration of 4.98 for the four bridgehead atoms, which is calculated as 4.98/4 = 1.25) (Figure 23). By the following equation:

$$\frac{1 \cdot M_{\mathrm{THF}}}{1.25 \cdot M_{\text{H-cage}} + 1 \cdot M_{\mathrm{THF}}} = \frac{1 \cdot 72.11\ \mathrm{g \cdot mol^{-1}}}{1.25 \cdot 2322.01\ \mathrm{g \cdot mol^{-1}} + 1 \cdot 72.11\ \mathrm{g \cdot mol^{-1}}} \cdot 100\% = 2.4\% \quad (7)$$

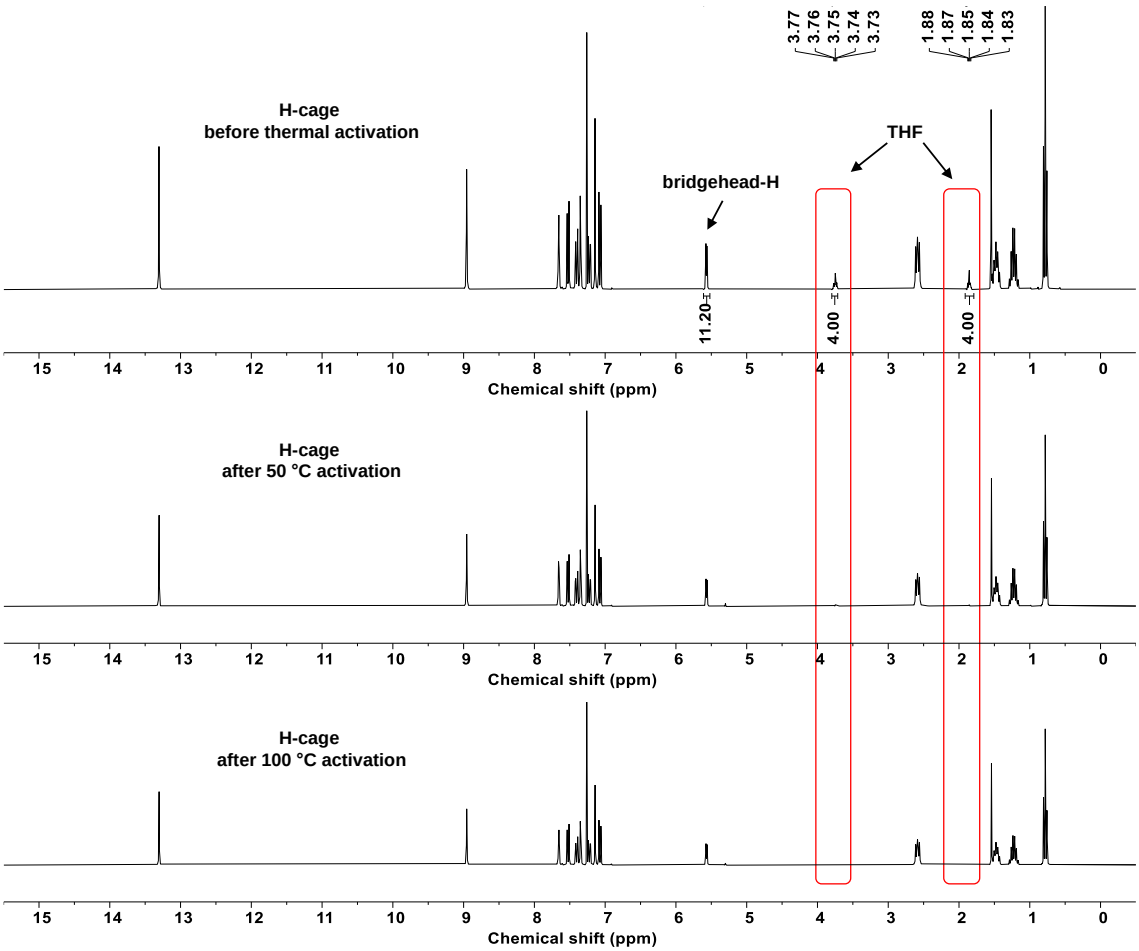

Figure 22. ^{1}H NMR spectra of **H-cage** before thermal activation and after thermal activation at 50°C and 100 °C ($CDCl_3$, 301 MHz). Reproduced with permission from Ref.[7]. Copyright © 2022 Wiley-VCH.

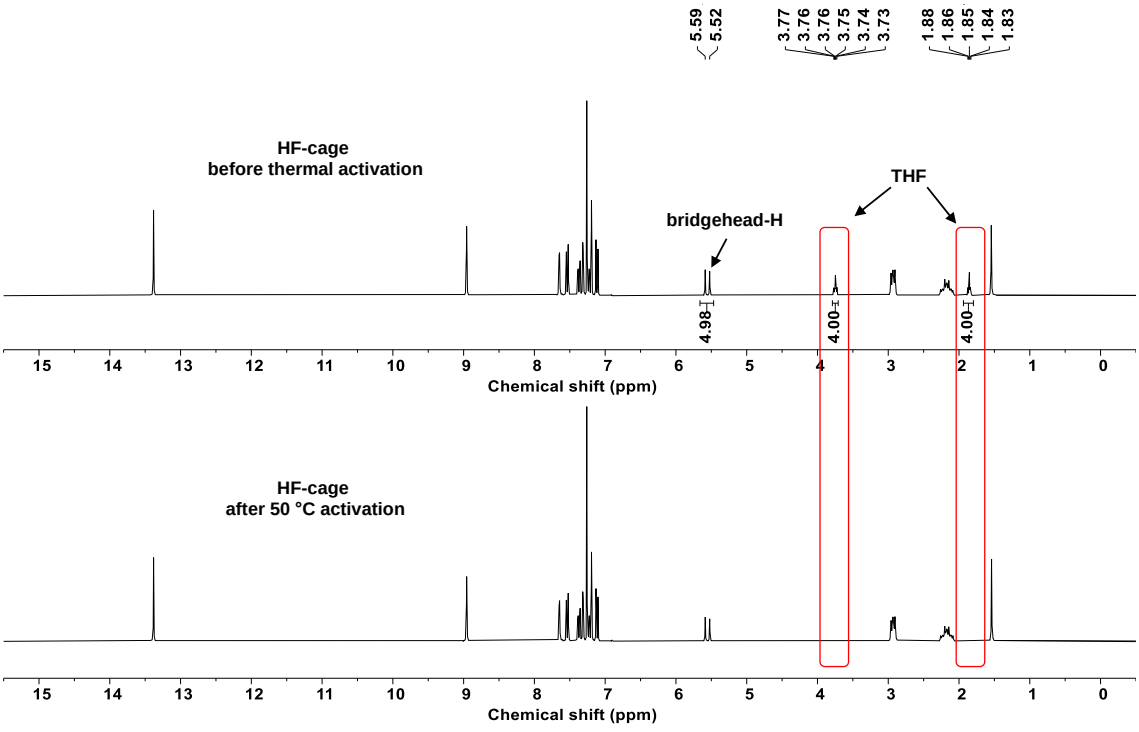

Figure 23. ^{1}H NMR spectrum of **HF-cage** before thermal activation and after thermal activation at 50°C ($CDCl_3$, 301 MHz). Reproduced with permission from Ref.[7]. Copyright © 2022 Wiley-VCH.

The ^{1}H-NMR and TGA result confirms the hypothesis, that the 2.5 wt.% correspond to enchlatrated THF molecules in the crystalline lattice. Investigations of ^{1}H-NMR spectroscopy in $CDCl_3$ of **HF-cage** after activation at 50 °C and $3 \cdot 10^{-2}$ mbar for 14 hours showed no residual THF molecules and also confirmed sufficient activation at the given temperature. For the sake of consistency, all cages were thermally activated before the gas adsorption experiments.

The crystallinity of three cages in mother liquor, prior to and after thermal activation and after gas adsorption is investigated by optical and scanning electron microscopy (SEM) (Figure 24). All SEM pictures in this dissertation were taken by Dr. Wen-Shan Zhang (BioQuant, Heidelberg University). In the mother liquor, all cages have their characteristic shape, with **H-cage** being dipyramidal, and **HF-cage** and **F-cage** being rhombohedral. Upon activation and gas adsorption, the crystals still keep their typical morphology and display well-defined edge, though some of the crystals broke into smaller fragments. Interestingly, more cracks are visible in **H-cage** than in **HF-cage** and **F-cage**. This is likely due to the strong dispersion interactions of the hexameric fluorine-containing side-chain units.

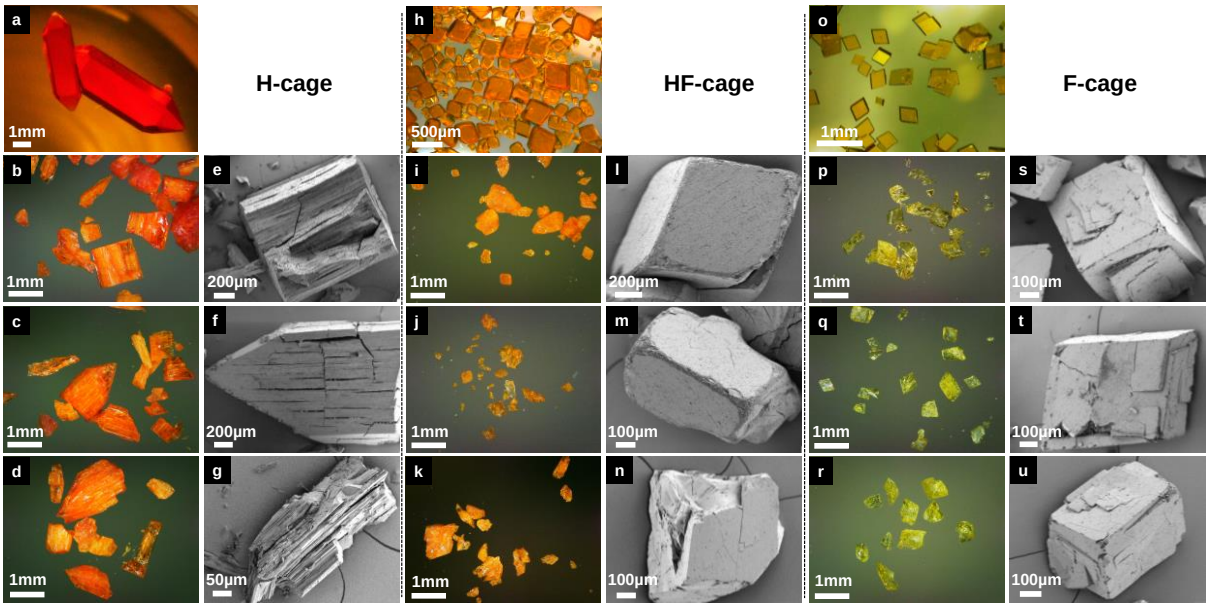

Figure 24. Light microscope and SEM images of **H-cage**, **HF-cage**, and **F-cage**. (a), (h), (o) Crystals in the THF/MeOH mother liquor for **H-cage**, **HF-cage**, and **F-cage**, respectively. (b) and (e), (i) and (l), (p) and (s) filtered crystal before thermal activation for **H-cage**, **HF-cage**, and **F-cage**, respectively. (c) and (f), (j) and (m), (q) and (t) Thermally activated crystals for **H-cage**, **HF-cage**, and **F-cage**, respectively. (d) and (g), (k) and (n), (r) and (u) Crystals after gas adsorption experiments for **H-cage**, **HF-cage**, and **F-cage**, respectively. Pictures (a-d), (h-k), (o-r) have been obtained by light microscope, pictures (e-g), (l-n), (s-u) have been obtained by SEM. SEM pictures were taken by Dr. Wen-Shan Zhang (BioQuant, Heidelberg University). Reproduced with permission from Ref.[7]. Copyright © 2022 Wiley-VCH.

The crystallinity of the three cages was further confirmed by the powder X-ray diffraction (PXRD). The results obtained by calculations from single crystal structures,

and experiments before and after thermal activation, as shown in Figure 25, reflect the same trend observed in SEM analysis. Cages after desolvation and activation have narrower peaks with a higher degree of fluorination of side chains. This observation is consistent with the presence of more flexible and amorphous alkyl units that freely rotate within the pores.[103] Specifically, for **F-cage**, the calculated diffraction pattern is almost identical to the experimental one upon desolvation and activation. This stable crystalline nature of the cages facilitates the acquisition of reliable diffraction data when the cages are loaded with guest molecules, to delve deeper into the intricate interactions between the host and guest molecules at the molecular level in the following gas adsorption investigation.

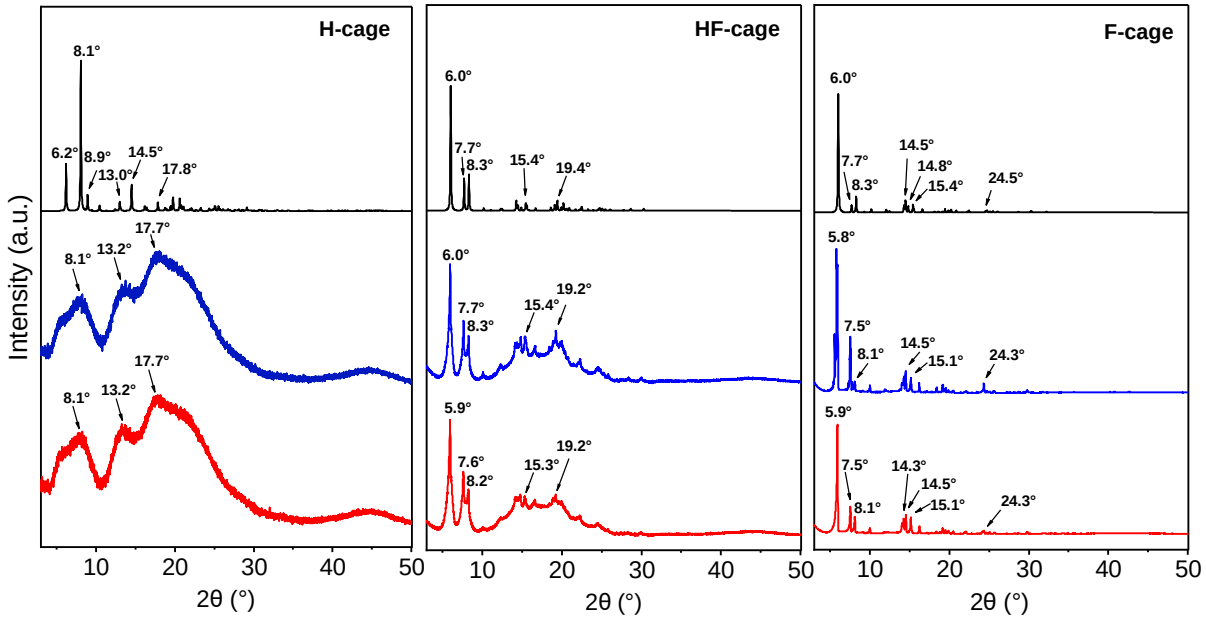

Figure 25. PXRD patters of **H-cage**, **HF-cage**, and **F-cage**. Black: Calculated from the single crystal X-ray structure; Blue: samples before thermal activation; red: samples after thermal activation. The PXRD measurements were performed under Dr. Sven M. Elbert's help at the Institute for Molecular Systems Engineering and Advanced Materials (IMSEAM) (Heidelberg University). Adapted with permission from Ref.[7]. Copyright © 2022 Wiley-VCH.

1.4. The Influence of Side-Chain Fluorination on Gas Sorption Properties

To investigate the porosity of cages, gas sorption experiments at cryogenic condition was carried out. The obtained nitrogen (at 77 K) and argon (at 87 K) sorption isotherms of **F-cage** can be best described as type I according to the International Union of Pure and Applied Chemistry (IUPAC) definition (Figure 26a-b).[104] The specific surface area is 752 $m^2\ g^{-1}$ and 728 $m^2\ g^{-1}$, respectively, when the BET model[105] is considered (Figure 26e). In contrast, **H-cage** and **HF-cage** hardly took up gases and seemed to be non-porous under those conditions (5 $m^2\ g^{-1}$ (N_2) and 7 $m^2\ g^{-1}$ (Ar) for **H-cage**, 0

(N_2) and 4 m^2 g^{-1} (Ar) for **HF-cage**). However, when the measurement temperature is increased to 195 K, all three cages were found to adsorb notable and comparable amounts of both nitrogen (**H-cage:** 0.58 mmol g^{-1}; **HF-cage:** 0.67 mmol g^{-1}; **F-cage:** 0.93 mmol g^{-1}) and carbon dioxide (**H-cage:** 6.63 mmol g^{-1}; **HF-cage:** 8.92 mmol g^{-1}; **F-cage:** 8.66 mmol g^{-1}) at 1 bar (Figure 26e). The BET surface area derived from carbon dioxide adsorption at 195 K is 372 m^2 g^{-1} for **H-cage,** 653 m^2 g^{-1} for **HF-cage**, and 605 m^2 g^{-1} for **F-cage,** demonstrating permanent porosity for all three cages (Figure 26c).

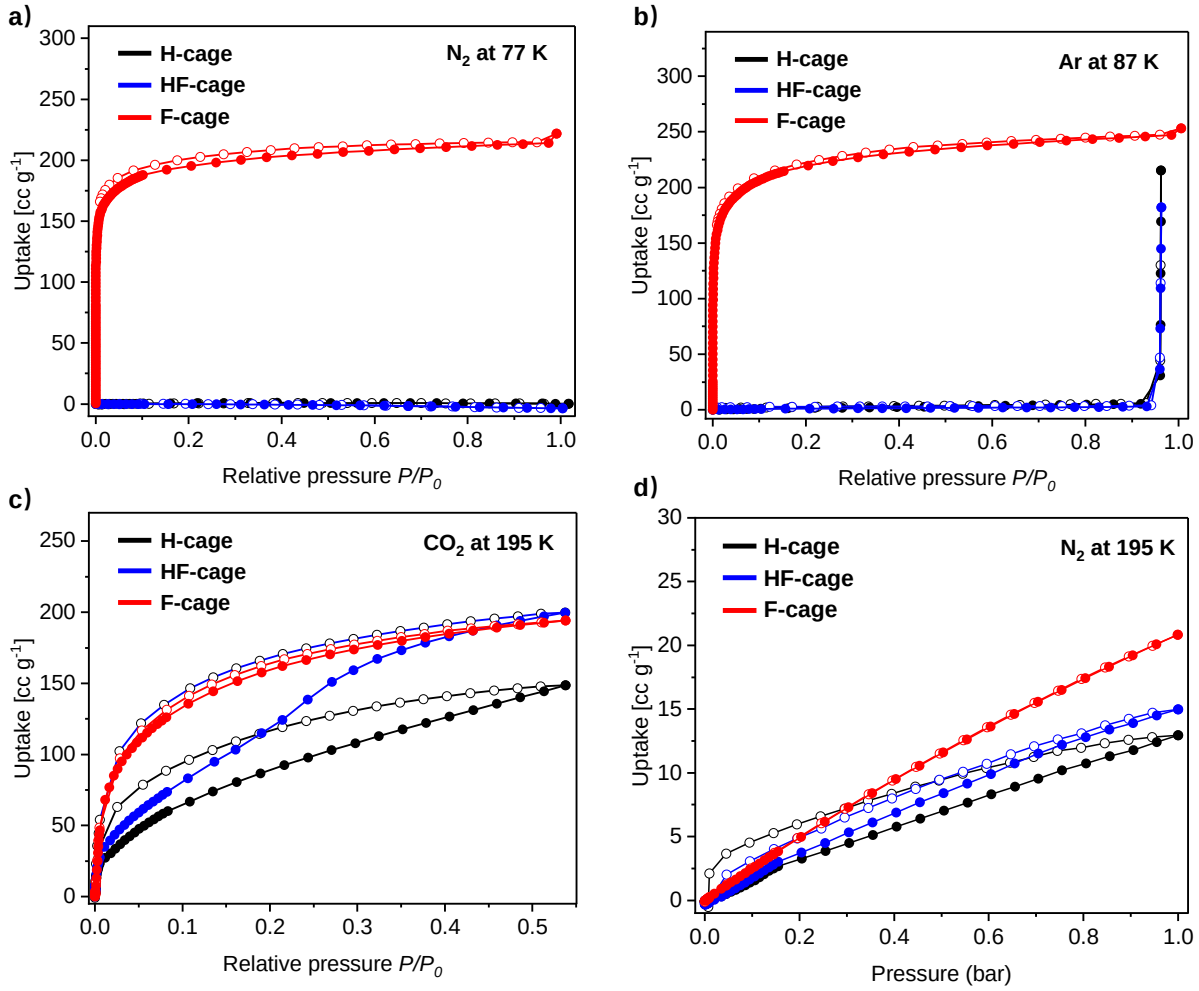

e)

	BET surface area (m^2 g^{-1})			Uptake (mmol g^{-1})	
	N_2 (77 K)	Ar (87 K)	CO_2 (195 K)	CO_2 (195 K)	N_2 (195 K)
H-Cage	5	7	372	6.63	0.58
HF-Cage	0	4	653	8.92	0.67
F-Cage	752	728	605	8.66	0.93

Figure 26. a) N_2 sorption isotherms at 77 K; b) Ar sorption isotherms at 87 K; c) CO_2 and d) N_2 sorption isotherms at 195 K of **H-cage** (black), **HF-cage** (blue), and **F-cage** (red): Adsorption: full circles; desorption: empty circles. e) Table comparing the adsorption properties derived from N_2 sorption at 77 K, Ar sorption at 87 K as well as CO_2 and N_2 sorption at 195 K. Adapted with permission from Ref.[7]. Copyright © 2022 Wiley-VCH.

It should be noted that the isotherms of **H-cage** and **HF-cage** have pronounced hystereses, whereas the **F-cage** does not**.** This difference in the gas sorption behaviour could be explained by the fact that gas molecules are kinetically hindered by the alkyl units in **H-cage** and **HF-cage** compared to fluorinated alkanes in **F-cage** at cryogenic conditions, but this hindered behavior disappears with increasing temperature to 195 K, thus allowing all three cages to have permanent porosity.[103a, 106] To further prove permanent porosity, alkane (methane, ethane, and propane) and perfluorocarbon (CF_4, C_2F_6, and C_3F_8) sorption of three cages was investigated at 273 K and all results are shown in Figure 27 and Table 3. The adsorption behaviors of alkanes at higher temperatures resemble those observed during nitrogen and carbon dioxide sorption at 195 K. For instance, the propane isotherms for **H-cage** and **HF-cage** display prominent hysteresis, while the **F-cage**'s isotherm does not (Figure 27e). The three cages show comparable uptakes of 0.7-1.0 wt.% (0.46-0.61 mmol g^{-1}) of methane, 5.6-7.5 wt.% (1.50-2.49 mmol g^{-1}) of ethane and 10.5-14.6 wt.% (2.37-3.30 mmol g^{-1}) propane at 1 bar (Table 3). The uptake of three cages increases with longer alkanes. Each **F-cage** is capable of adsorbing up to 9.09 propane molecules on average, taking up 84% of the cage void (Table 3).

In addition to alkane sorption, perfluorocarbon adsorption of the three cages was also investigated at 273 K (Figure 27b, d, and f). **F-cage** exhibits considerably high adsorption amounts of perfluorocarbons; for instance, it adsorbs more than double the amount of CF_4 (8.2 wt.%, 0.93 mmol g^{-1}) than both **H-cage** (3.3 wt.%, 0.38 mmol g^{-1}) and **HF-cage** (3.4 wt.%, 0.39 mmol g^{-1}) (Figure 27 b and Table 3). Additionally, **F-cage** absorbs 2.9-4.0 times the amount of C_2F_6 (1.8 mmol g^{-1}, 25 wt.%) than **H-cage** (0.62 mmol g^{-1}, 8.6 wt.%) and **HF-cage** (0.44 mmol g^{-1}, 6.1 wt.%), and even 7.0 to 11 times more C_3F_8 (2.1 mmol g^{-1}, 39 wt.%) than the **H-cage** (0.30 mmol g^{-1}, 5.6 wt.%) and the **HF-cage** (0.19 mmol g^{-1}, 3.6 wt.%) at 1 bar (Figure 27d, f and Table 3). In particular, the C_3F_8 adsorption of **F-cage** corresponds to 5.8 mmol/mmol, or 5.8 propane molecules per cage compound, filling the cage void to 76% (Table 3). Furthermore, **H-cage** and **HF-cage** exhibit a nearly linear adsorption isotherm, while **F-cage** demonstrates a more and more evident type I-like shape isotherm with larger PFCs, which suggests a high affinity of **F-cage** towards fluorinated guests (Figure 27b, d and f).

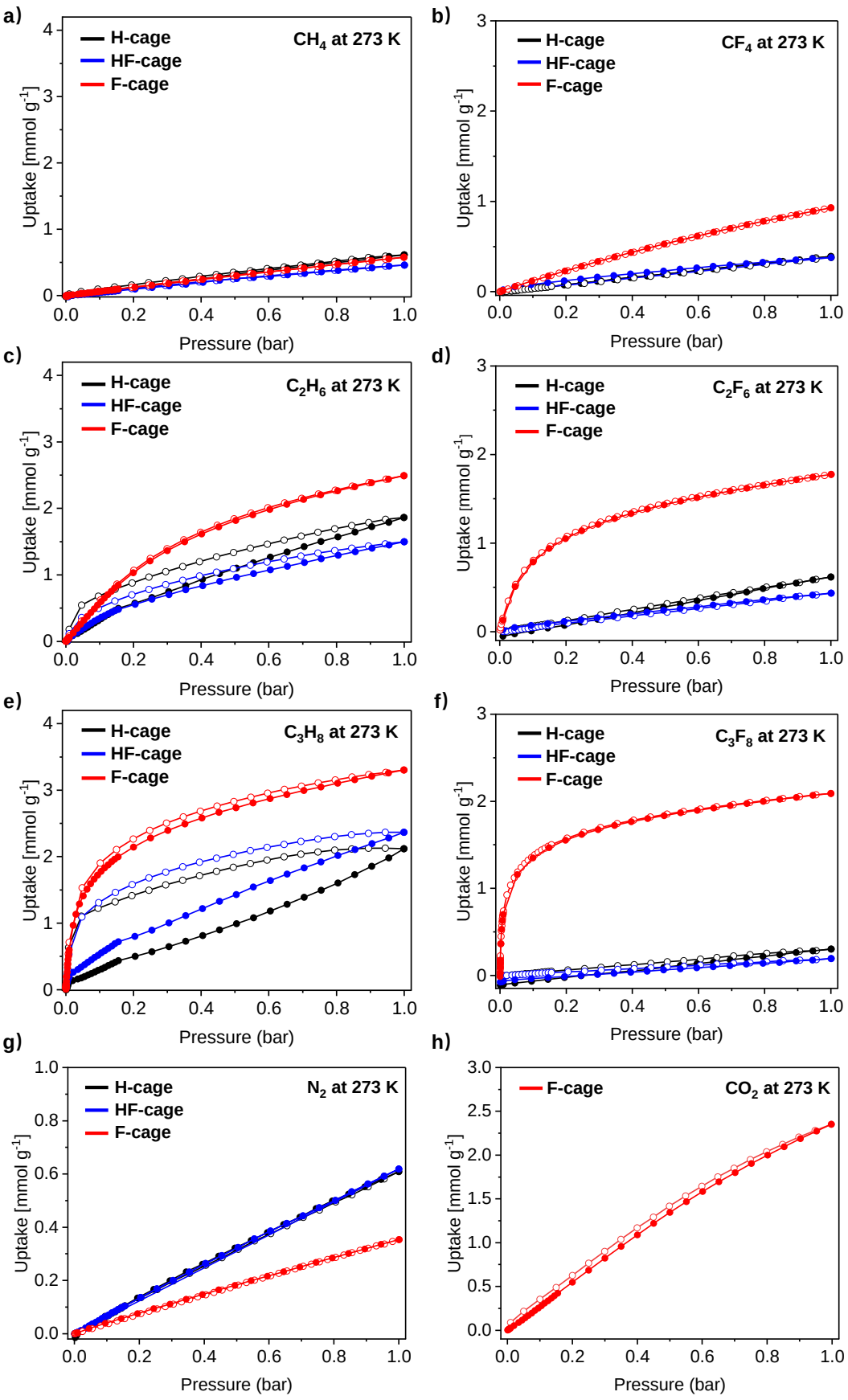

Figure 27. Gas sorption isotherms of **H-cage**, **HF-cage**, and **F-cage** at 273 K. (a) CH_4, (c) C_2H_6, e) C_3H_8, b) CF_4, d) C_2F_6, f) C_3F_8, g) CO_2 and h) N_2. Full circles: adsorption; empty circles: desorption. Adapted with permission from Ref.[7]. Copyright © 2022 Wiley-VCH.

Table 3. Filling percentage of **H-cage**, **HF-cage**, and **F-cage** for alkanes and PFCs at 273 K and 1 bar. Reproduced with permission from Ref.[7]. Copyright © 2022 Wiley-VCH.

Cage	Gas	Uptake (mmol g^{-1})	Uptake (wt%)	Uptake (mmol/mmol)	$V_{per\ gas}$ (Å^3)	$V_{gas\ per\ cage}$ (Å^3)	$V_{per\ cage}$ (Å^3)	Filling percentage(%)
H-cage	CH_4	0.61	1.0	1.09	25	27.3	518	5.27
	C_2H_6	1.86	5.6	3.32	42	139		26.8
	C_3H_8	2.76	12.2	4.92	58	285		55.0
	CF_4	0.39	3.4	0.70	35	24.5		4.73
	C_2F_6	0.62	8.6	1.11	60	66.6		12.9
	C_3F_8	0.30	5.6	0.53	82	43.5		8.40
HF-cage	CH_4	0.46	0.7	1.07	25	26.8	650	4.12
	C_2H_6	1.50	4.5	3.48	42	146		22.5
	C_3H_8	2.37	10.5	5.50	58	319		49.1
	CF_4	0.38	3.3	0.88	35	30.8		4.74
	C_2F_6	0.44	6.1	1.02	60	61.2		9.42
	C_3F_8	0.19	3.6	0.44	82	36.1		5.55
F-cage	CH_4	0.58	0.9	1.60	25	40	625	6.40
	C_2H_6	2.49	7.5	6.86	42	288		46.1
	C_3H_8	3.30	14.6	9.09	58	527		84.3
	CF_4	0.93	8.2	2.56	35	89.6		14.3
	C_2F_6	1.78	24.6	4.90	60	294		47.0
	C_3F_8	2.09	39.3	5.76	82	472		75.5

The adsorption behaviour of two gases in comparison was investigated using two different selectivity models. The experimental isotherms possessing a type I like behaviour have been fitted with the non-linear Tóth equation:

$$q_{eq} = q_{max} \frac{K \cdot p}{(1 + (K \cdot p)^t)^{\frac{1}{t}}} \quad (8)$$

With: p: pressure

q_{eq}: experimental uptake (mmol·g^{-1})

q_{max}: maximum uptake (mmol·g^{-1})

K: affinity constant (1·bar^{-1})

t: heterogeneity (or Tóth) parameter (dimensionless)

Since gases with lower adsorption tendencies differ from a typical type I like behaviour, other isotherm models had to be used for them. Isotherms with a non-linear yet non-pronounce type I like behaviour have been fitted using the non-linear Tóth equation with t = 1 which is known as Langmuir adsorption isotherm:

$$q_{eq} = q_{max} \frac{K \cdot p}{1 + (K \cdot p)} \quad (9)$$

with: p: pressure

q_{eq}: experimental uptake (mmol·g^{-1})

q_{max}: maximum uptake (mmol·g^{-1})

K: affinity constant (1·bar^{-1})

Linear isotherms can be thus interpreted as Langmuir isotherms with $q_{max} \rightarrow \infty$, which transfers the Langmuir isotherm to a standard Henry isotherm:

$$q_{eq} = K \cdot p \quad (10)$$

with: p: pressure

q_{eq}: experimental uptake (mmol·g^{-1})

K: affinity constant (1·bar^{-1})

For this purpose, the max. uptake was set to 1000 mmol·g^{-1} to obtain restricted Langmuir isotherm.

The parameters q_{max}, K, t, obtained by the described fittings (see Appendix) using 3P's 3P Sim software, where then applied in the IAST-theory, as introduced in the Introduction section (equations 1-4) to calculate the selectivity $S_{A/B}$ of gas A over gas B by

$$S_{A/B} = \frac{x_A / y_A}{x_B / y_B} \quad (5)$$

with: x_i: molar fraction of compound i in the adsorbed phase

y_i: molar fraction of compound i in the gas phase

For pressures of $p \rightarrow 0$, the IAST-selectivity can be seen as a frontier selectivity which is commonly known as Henry selectivity with the simplified Tóth equation:

$$q_{eq} = q_{max} \cdot K \cdot p \quad (11)$$

By the definition of Henry's law, this means the Henry constant K_H is now defined as:

$$K_H = q_{max} \cdot K \quad (12)$$

And the Henry selectivity S_H of a gas A over gas B can be now calculated as the quotient of the corresponding Henry constants.

While the IAST-selectivity is considering the competition of two gases and thus gives insights in the bulk behaviour of an adsorbent, the Henry selectivity is only taking the most selective binding sites into account.

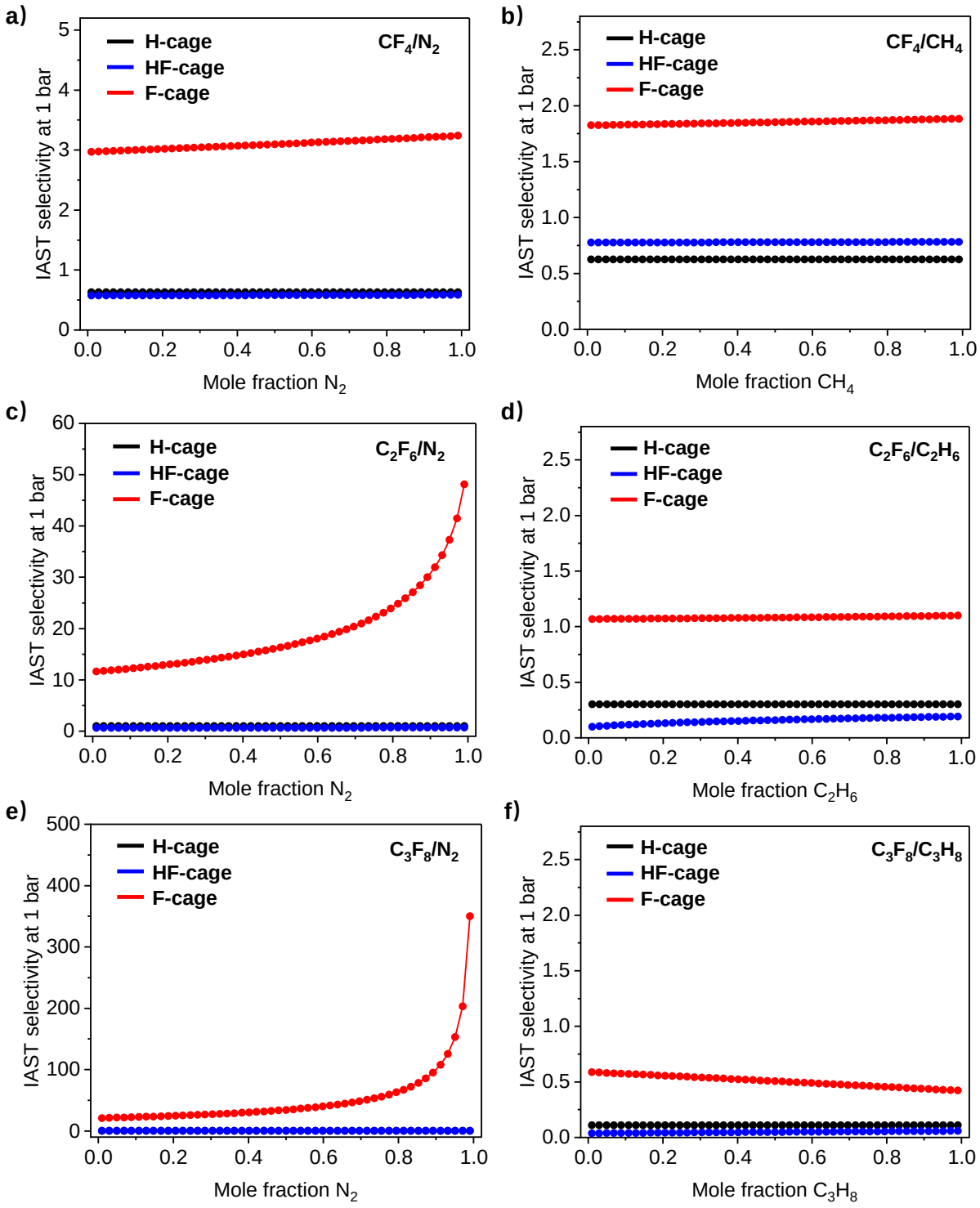

Figure 28. IAST selectivities of the corresponding PFC over nitrogen and hydrocarbon analogue at variable composition at 273 K and 1 bar. Adapted with permission from Ref.[7]. Copyright © 2022 Wiley-VCH.

By fitting experimentally obtained isotherms using Tóth-, Langmuir- or restricted Langmuir isotherm models, corresponding IAST theory,[16] S_{IAST} have been calculated at 273 K and 1 bar (Figure 28 and Table 4). S_{IAST} values of **F-cage** are much higher than those of **H-cage** and **HF-cage** for every fluorinated gas tested over in the entire range of mole fraction. Similar and even near-overlapping S_{IAST} curves of **H-cage** and

HF-cage indicate that **HF-cage** is more behaving like the **H-cage** and less than the **F-cage**. With the increase of mole fraction N_2, S_{IAST} of **F-cage** increases while S_{IAST} of **H-cage** and **HF-cage** remains almost unchanged. For CF_4, the increasing trend of **F-cage** is not obvious. However, for the higher homologue C_2F_6, the selectivity of **F-cage** appears to increase sharply as the relative amount of C_2F_6 decreases (S_{IAST} $(CF_4/N_2)_{50:50}$ = 16.3 vs S_{IAST} $(C_2F_6/N_2)_{10:90}$ = 30.8 vs S_{IAST} $(CF_4/N_2)_{1:99}$ = 48.1, both at 1 bar and 273 K). The highest selectivity within the investigated series is found for the adsorption C_3F_8, with a faster growth from S_{IAST} $(CF_4/N_2)_{50:50}$ = 34 to S_{IAST} $(C_2F_6/N_2)_{10:90}$ = 100 to S_{IAST} $(CF_4/N_2)_{1:99}$ = 350 at 1 bar and 273 K, indicating well-defined high affinity adsorption sites contributing to the bulk selectivity.

Table 4. IAST[a] and Henry gas selectivity at 273 K (Tóth model). Reproduced with permission from Ref.[7]. Copyright © 2022 Wiley-VCH.

			H-Cage	**HF-Cage**	**F-Cage**
CF_4	CF_4/N_2	IAST 50:50	0.63	0.58	3.10
		IAST 10:90	0.63	0.58	3.21
		IAST 1:99	0.63	0.58	3.24
		Henry	0.63	0.56	3.37
	CF_4/CO_2	IAST 50:50	-	-	0.35
		Henry	-	-	0.44
	CF_4/CH_4	IAST 50:50	0.63	0.78	1.85
		Henry	0.63	0.76	1.95
C_2F_6	C_2F_6/N_2	IAST 50:50	1.00	0.67	16.3
		IAST 10:90	1.00	0.68	30.8
		IAST 1:99	1.00	0.68	48.1
		Henry	1.00	0.65	85.6
	C_2F_6/CO_2	IAST 50:50	-	-	1.96
		Henry	-	-	11.2
	C_2F_6/C_2H_6	IAST 50:50	0.30	0.16	1.08
		Henry	0.30	0.03	4.60
C_3F_8	C_3F_8/N_2	IAST 50:50	0.50	0.29	34.4
		IAST 10:90	0.50	0.30	100
		IAST 1:99	0.50	0.30	350
		Henry	0.50	0.29	4977
	C_3F_8/CO_2	IAST 50:50	-	-	6.47
		Henry	-	-	650
	C_3F_8/C_3H_8	IAST 50:50	0.11	0.05	0.51
		Henry	0.11	0.04	8.80

[a] at 1 bar. - : did't measure.

The corresponding IAST selectivities S_{IAST} of the bulk can converge to the Henry selectivities S_H at hypothetical zero pressure revealing the affinity of the most selective adsorption sites (Table 4). Henry selectivities of three cages for PFCs have similar trends as the IAST selectivities. **F-cage** has much higher S_H values than **H-cage** and **HF-cage**. The highest Henry selectivity of **F-cage** is found for C_3F_8 adsorption, with S_H (C_3F_8/N_2) = 4977, in agreement with the IAST result. When contrasting the fluorinated alkanes with their non-fluorinated counterparts, the S_{IAST} value of **F-cage** surpasses that of **H-cage** and **HF-cage**. Amongst these cages, **F-cage** stands alone, exhibiting higher affinities for perfluorinated alkanes as opposed to their nonfluorinated counterparts. This is evident through the values (S_H (CF_4/CH_4) = 2.0, S_H (C_2F_6/C_2H_6) = 4.6 and S_H (C_3F_8/C_3H_8) = 8.8), which consistently depict an escalating trend of selectivity for larger PFCs.

1.5. Hirshfeld Analysis of PFC-Loaded cage

For a more in-depth understanding of the interactions between adsorbed PFCs with **F-cage**, an activated single crystal was subjected to SCXRD analyses before and after keeping under an atmosphere of C_3F_8 for 19 h. Despite a slightly enlarged unit cell, the single crystal structure was fully maintained not only upon activation but also upon gas loading. The highly disordered residual electron density of two C_3F_8 molecules was determined inside the cage voids. Accroding to the physical structure of C_3F_8, the fluorine atoms shield the C-C skeleton sterically, thus the surface of residual electron density is treated as a fluorine cluster.[103a] To analyze the interaction between the cage and the residual electron density, Hirshfeld surface and two-dimensional fingerprint plots analysis[107] were conducted with three residual electron densities taken into account at >0.15 $e^- \cdot Å^{-3}$, >0.17 $e^- \cdot Å^{-3}$ and >0.20 $e^- \cdot Å^{-3}$ (Figure 29). The Hirshfeld surfaces display quite clearly close muti-intermolecular contacts to the CF_2-unit at C2 of the perfluorobutyl side chains and the triptycene bridgehead atoms (indicated by red area) at the electron density >0.15 $e^- \cdot Å^{-3}$. At a relatively high electron density >0.17 $e^- \cdot Å^{-3}$ and >0.20 $e^- \cdot Å^{-3}$, the short intermolecular contact between the residual electron density and the CF_2-unit at C2 of the perfluorobutyl side chains still remain whereas the interaction of the triptycene bridgehead atoms disappear. Therefore, the former can be attributed as the main interaction.

In two-dimensional fingerprint plots, corresponding to close contacts (red area) of Hirshfeld surface, a short intermolecular F···F distance of $d_{F\cdots F}$ = 2.8 Å is measured exactly in the range of attractive F···F interactions found in single crystal X-ray structures[108] and intermolecular F···F interactions found by NMR-spectroscopy.[109] This supports the hypothesis that F···F interactions are the main force behind the high selectivities observed for **F-cage**. It also explains the non-selective behavior of **H-cage** and **HF-cage** because they both have a CH_2-unit, rather than CF_2-unit at C2 position.

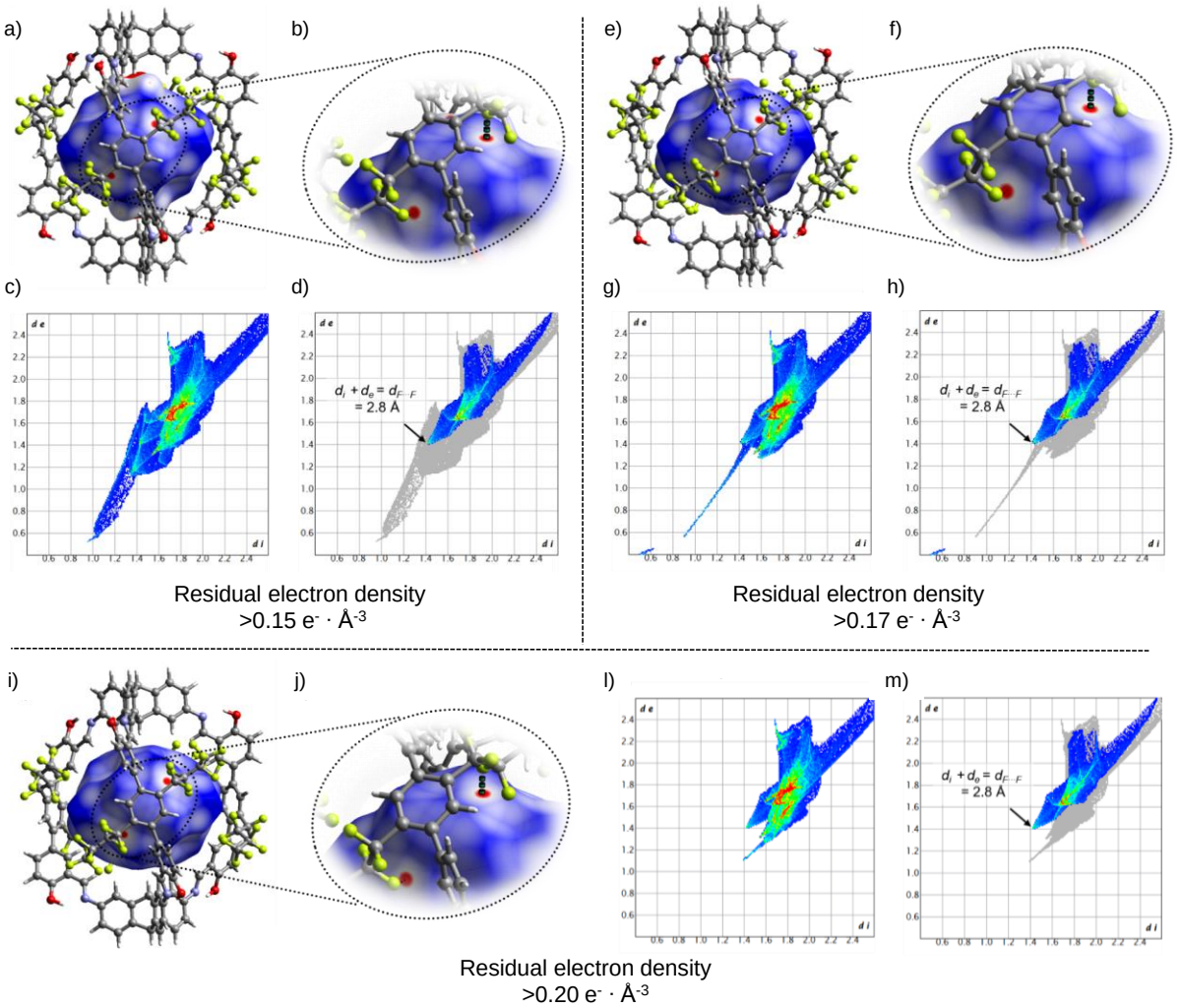

Figure 29. Hirshfeld surface analyses of the single-crystal X-ray structure of C_3F_8 loaded **F-cage**. The residual electron density (a-d) >0.15 e⁻ · Å⁻³, (e-h)>0.17 e⁻ · Å⁻³, (i-m) >0.20 e⁻ · Å⁻³ was replaced by fluorine dummy atoms and the corresponding Hirshfeld surface d_{norm} (isovalue: 0.5; quality: very high) was plotted with a rescaled surface property of -0.05 to 1.0. Red areas represent short d_i-d_e distances; blue areas long d_i-d_e distances. (a), (e), (i) Side view on one cage molecule filled with C_3F_8. (b), (f), (j) Zoom-in on the $CF_2\cdots F$ interactions. (c), (g), (l) Hirshfeld fingerprint plot taking all elements into account. (d), (h), (m) Hirshfeld fingerprint plot taking only fluorine atoms into account. The highlighted spot corresponds to the short $CF_2\cdots F$ distance. Images were made by Dr. Sven M. Elbert (OCI, Heidelberg University). Reproduced with permission from Ref.[7]. Copyright © 2022 Wiley-VCH.

1.6. Selective PFC-Adsorption at Variable Temperatures

The promising characteristics of the **F-cage** in selectively adsorbing PFCs at 273 K led to a further exploration of the adsorption behavior across varying temperatures (Figure 30). Furthermore, the sorption of perfluorocyclobutane *c*-C_4F_8 (PFC-318) was also examined because of its notably escalated historical abundance in recent years, even more than C_3F_8, and high GWP_{100} of 9540 as described in Introduction.[110]

As the temperature increases from 273 K to 313 K **F-cage** takes up lower amounts of PFCs, and the adsorbed amounts of *c*-C_4F_8 is always highest at each temperature (Table 5). The uptake at 273 K (0.93 mmol g^{-1}, 8.2 wt.% for CF_4; 1.78 mmol g^{-1}, 25 wt.% for C_2F_6; 2.09 mmol g^{-1}, 39 wt.% for C_3F_8; 4.41 mmol g^{-1}, 88 wt.% for *c*-C_4F_8) was approximately 73%-36% lower than that at 313 K (0.25 mmol g^{-1}, 2.2 wt.% for CF_4; 0.94 mmol g^{-1}, 13 wt.% for C_2F_6; 1.34 mmol g^{-1}, 25 wt.% for C_3F_8; 1.66 mmol g^{-1}, 33 wt.% for *c*-C_4F_8).

The gas adsorption selectivities show a nearly monotonic increase with rising temperature, except for a few selectivities of linear PFCs which fluctuate slightly at 273 K and 283 K, before increasing towards their peaks at 313 K (Figure 30 and Table 6). The selectivity at 313 K is 3.4-9.3 times higher than that at 273 K, which is attributed to the N_2-phobic effects at higher temperatures.[111] For a 10:90 PFC/N_2 mixture, which is of industrial relevance,[112] high selectivities are observed for C_2F_6 ($S_{IAST,\ 10:90}$ = 143), C_3F_8 ($S_{IAST,\ 10:90}$ = 658) and *c*-C_4F_8 ($S_{IAST,\ 10:90}$ = 1268). The selectivity climbs even further with lower PFC concentrations for the PFC/N_2 mixture, with S_{IAST} $(C_2F_6/N_2)_{1:99}$ = 164; S_{IAST} $(C_3F_8/N_2)_{1:99}$ = 1522 and S_{IAST} $(C_4F_8/N_2)_{1:50}$ = 4385, displaying the presence of strongly selective adsorption sites that are occupied even at low PFC gas loadings.

Henry selectivities follow the same trend (CF_4 < C_2F_6 < C_3F_8 < *c*-C_4F_8) as the IAST selectivities at each temperature (Figure 30 and Table 6). However, with varying temperatures, the selectivities drop until 298 K before increasing again at 313 K, where very high selectivities are observed for C_3F_8 (S_H = 3243) and *c*-C_4F_8 (S_H = 41475).

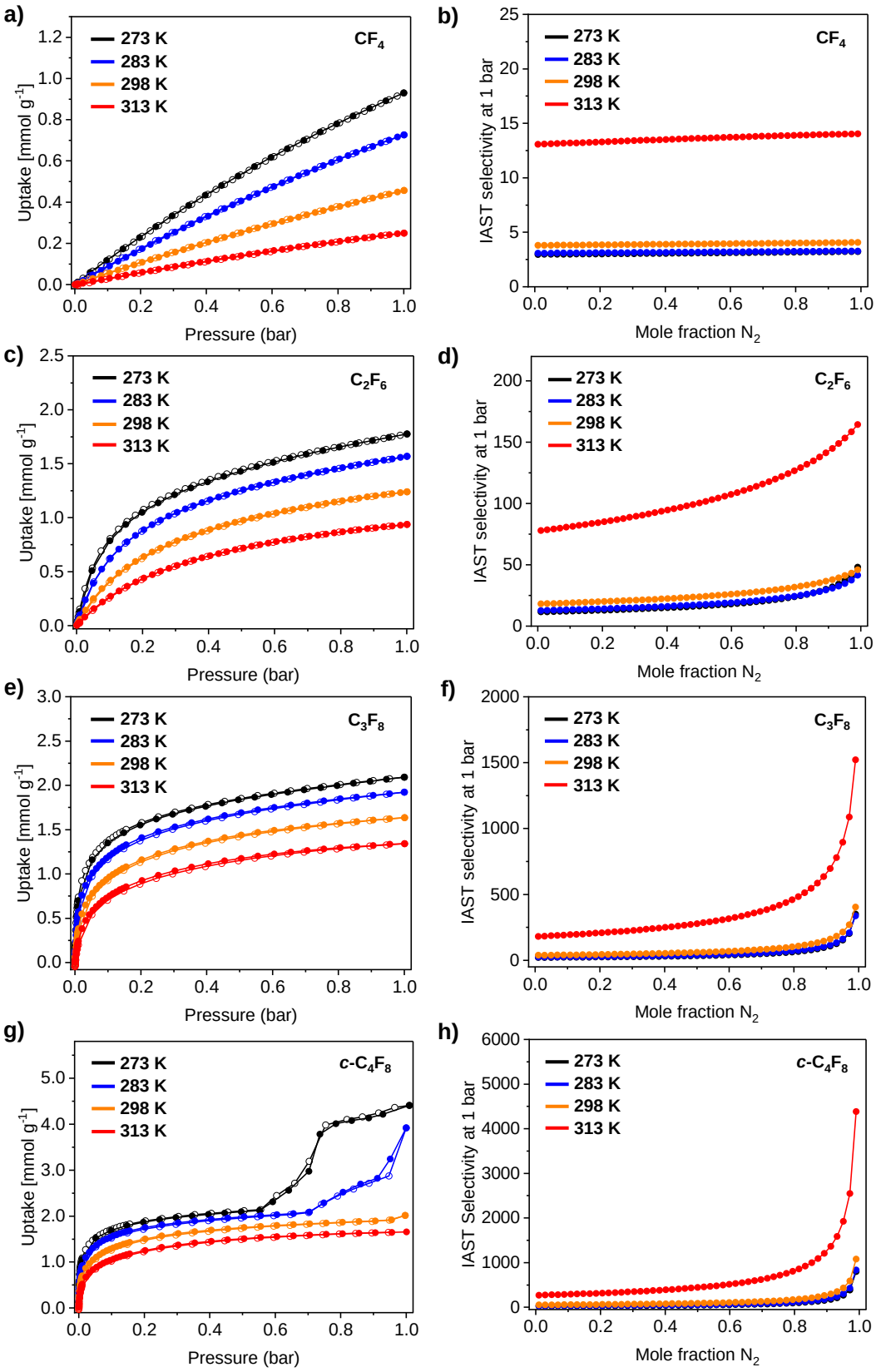

Figure 30. Gas sorption isotherms and IAST curves of **F-cage** at variable gas compositions (PFC over nitrogen) at 273 K (black), 283 K (blue), 298 K (orange), and 313 K (red) and 1 bar. Full circles: adsorption; empty circles: desorption. Note: The isotherm shapes of *c*-C_4F_8 at 273 K and 283 K are related to pore condensation processes. Adapted with permission from Ref.[7]. Copyright © 2022 Wiley-VCH.

Table 5. Filling percentage of **F-cage** for PFCs at different temperatures and 1 bar. Reproduced with permission from Ref.[7]. Copyright © 2022 Wiley-VCH.

Temp. (K)	Gas	Uptake (mmol g^{-1})	Uptake (wt%)	Uptake (mmol/mmol)	$V_{per\ gas}$ (Å^3)	$V_{gas\ per\ cage}$ (Å^3)	$V_{per\ cage}$ (Å^3)	Filling percentage (%)
273	CF_4	0.93	8.2	2.56	35	89.6	625	14.3
	C_2F_6	1.78	24.6	4.90	60	294		47.0
	C_3F_8	2.09	39.3	5.76	82	472		75.5
	c-C_4F_8	4.41	88.2	12.1	91	1101		176[a]
283	CF_4	0.73	6.4	2.01	35	70.4		11.3
	C_2F_6	1.57	21.7	4.32	60	259		41.4
	C_3F_8	1.92	36.1	5.29	82	434		69.4
	c-C_4F_8	3.92	78.4	10.8	91	983		157[a]
298	CF_4	0.46	4.0	1.27	35	44.5		7.12
	C_2F_6	1.24	17.1	3.41	60	205		32.8
	C_3F_8	1.64	30.8	4.52	82	371		59.4
	c-C_4F_8	2.02	40.4	5.56	91	506		81.0
313	CF_4	0.25	2.2	0.69	35	24.2		3.87
	C_2F_6	0.94	13.0	2.59	60	155		24.8
	C_3F_8	1.34	25.2	3.69	82	303		48.5
	c-C_4F_8	1.66	33.2	4.57	91	416		66.6

[a] Pore condensation was observed at 1 bar (see Figure 30).

Table 6. IAST[a] and Henry gas selectivity of **F-cage** at variable temperatures (Tóth model). Reproduced with permission from Ref.[7]. Copyright © 2022 Wiley-VCH.

		273 K	283 K	298 K	313 K
CF_4/N_2	IAST 50:50	3.10	3.18	3.93	13.6
	IAST 10:90	3.21	3.27	4.04	14.0
	IAST 1:99	3.24	3.29	4.07	14.0
	Henry	3.37	3.36	4.15	14.1
C_2F_6/N_2	IAST 50:50	16.3	17.5	24.1	101
	IAST 10:90	30.8	30.0	37.2	143
	IAST 1:99	48.1	41.5	46.0	164
	Henry	85.6	58.9	53.8	171
C_3F_8/N_2	IAST 50:50	34.4	39.5	59.9	278
	IAST 10:90	100	108	152	658
	IAST 1:99	350	338	404	1522
	Henry	4977	2767	1537	3243
c-C_4F_8/N_2	IAST 50:50	47.5	57.3	90.9	443
	IAST 10:90	163	187	277	1268
	IAST 1:99	801	836	1079	4385
	Henry	150374	59278	24459	41475

[a] at 1 bar

To estimate the average binding energy of PFCs to **F-cage**, isosteric heats of adsorption (Q_{st}) have been calculated at different temperatures by fitting a virial expression to the adsorption isotherms (Table 7). At hypothecial zero uptake, the heat of adsorption for linear PFCs increases with increasing chain lengths of the adsorbate. This trend is in line with the observed selectivities. When examining isotherms at higher temperatures (298 K and 313 K), significantly higher values were observed for more selectively bound C_3F_8 (34.2 ± 1.1 kJ/mol) and *c*-C_4F_8 (33.2 ± 1.4 kJ/mol) compared to CF_4 (29.2 ± 2.87 kJ/mol) and C_2F_6 (30.9 ± 0.38 kJ/mol).

Table 7. Q_{st} data of **F-cage**[a]. Reproduced with permission from Ref.[7]. Copyright © 2022 Wiley-VCH.

Gas	CF_4	C_2F_6	C_3F_8		*c*-C_4F_8	
Q_{st}(kJ/mol)	29.2±2.87	30.9±0.38	35.5±1.06[b]	34.2±1.13[c]	30.4±0.65[b]	33.2±1.40[c]

[a] Zero coverage heat of adsorption.

[b] Calculated from 273 K and 283 K isotherms.

[c] Calculated from 298 K and 313 K isotherms.

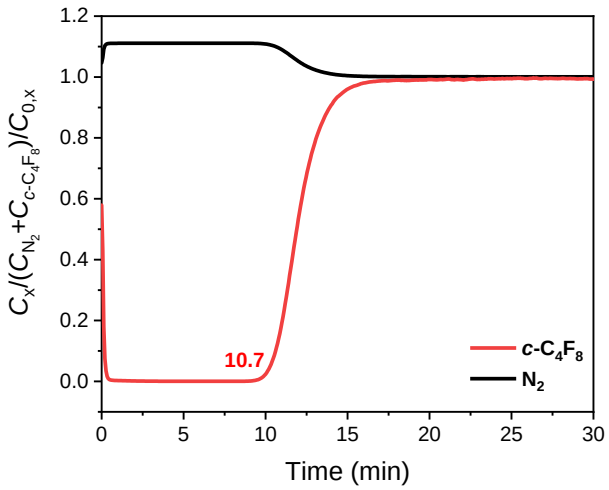

Figure 31. Breakthrough curve of a 10:90 *c*-C_4F_8/N_2 mixture with 50% Helium as carrier gas. The measurement was performed by Dr. Sebastian Ehrling and Francesco Walenszus (3P instruments). Reproduced with permission from Ref.[7]. Copyright © 2022 Wiley-VCH.

While calculations involving IAST, Henry coefficients, and isosteric heats of adsorption offer valuable insights into thermodynamic equilibrium adsorption, the breakthrough experiment serves as a crucial tool for characterizing kinetics, closely simulating the actual gas separation process. To establish the practical potential of **F-cage** for PFC/N_2 separations, real breakthrough experiments were conducted by Dr. Sebastian Ehrling and Francesco Walenszus of 3P Instruments at 298 K, utilizing a 90:10 (v/v) N_2/*c*-C_4F_8 mixture in a 50% Helium carrier gas stream. The setup maintained an overall pressure of 1 bar and a flow rate of 10 mL/min. The resulting

breakthrough curves, representing N_2 and *c*-C_4F_8 passing through a **F-cage** bed, were plotted to showcase the relative adsorbate concentration against real time (Figure 31). Nitrogen breaks through the column quickly, whereas *c*-C_4F_8 does not start to break through until after 10.7 min and does not completely break through until approximately 15 min. The large difference in breakthrough time between N_2 and *c*-C_4F_8 reflects the much higher affinity of **F-cage** toward *c*-C_4F_8.

1.7. Reproducibility, Stability and Recyclability

Batch-to-batch variations are often observed in materials.[113] To investigate the reproducibility of the cage materials presented here, at least two independent batches (batch 1 and batch 2) of **H-**, **HF-**, and **F-cage** crystals were obtained under identical experimental conditions. The two independent batches (batch a and batch b) were activated from one same batch (batch 1 or batch 2).

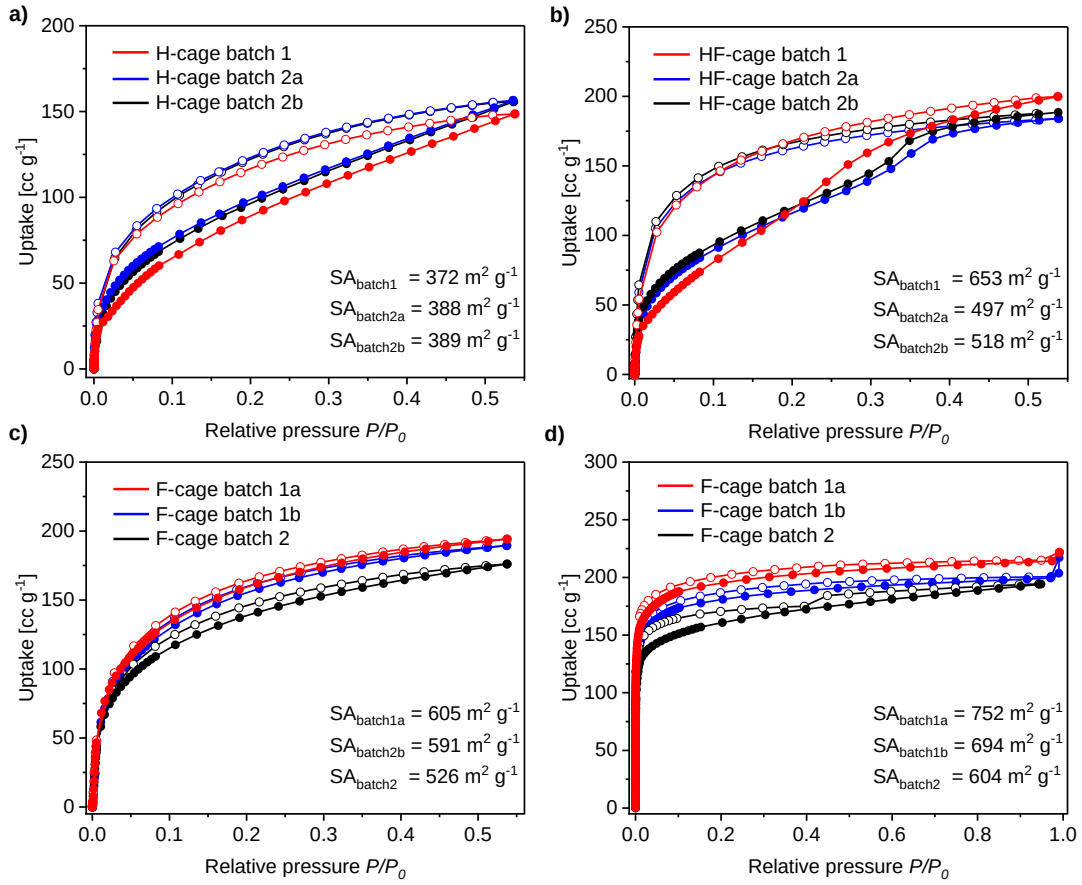

Figure 32. CO_2 sorption isotherm of different batches of **H-cage** (a), **HF-cage** (b) and **F-cage** (c) at 195 K. d) N_2 sorption isotherm of different batches of **F-cage** at 77 K. Filled circles: adsorption; empty circles: desorption. Adapted with permission from Ref.[7]. Copyright © 2022 Wiley-VCH.

The reproducibility of the three cages was investigated by gas sorption analysis. Carbon dioxide sorption experiments at 195 K show that the different batches of cages have reproducible isotherm and BET surface areas of 372-389 $m^2 g^{-1}$ for **H-cage**, 497-653 $m^2 g^{-1}$ for **HF-cage**, and 526-605 $m^2 g^{-1}$ for **F-cage** (Figure 32). The reproducibility of **F-cage** was further demonstrated by BET surface areas of 604 $m^2 g^{-1}$-752 $m^2 g^{-1}$ from nitrogen at 77 K.

Table 8. Gas uptake[a] and IAST[a] and Henry gas selectivity of different batches of **F-cage** at 273 K (Tóth model). Reproduced with permission from Ref.[7]. Copyright © 2022 Wiley-VCH.

		Batch 1a	Batch 1b	Batch 2
CF_4 Uptake	(mmol g^{-1})	0.93	0.86	0.72
CF_4/N_2	IAST 50:50	3.10	3.74	5.33
	IAST 10:90	3.21	3.87	5.59
	IAST 1:99	3.24	3.90	5.65
	Henry	3.37	3.99	5.80
C_2F_6 Uptake	(mmol g^{-1})	1.78	1.71	1.42
C_2F_6/N_2	IAST 50:50	16.3	20.6	30.0
	IAST 10:90	30.8	38.5	58.8
	IAST 1:99	48.1	59.0	95.6
	Henry	85.6	90.2	145
C_3F_8 Uptake	(mmol g^{-1})	2.09	1.92	1.63
C_3F_8/N_2	IAST 50:50	34.4	40.0	62.4
	IAST 10:90	100	112	190
	IAST 1:99	350	356	728
	Henry	4977	2373	13232

[a] at 1 bar.

Due to the excellent selectivity of **F-cage**, more gas adsorption experiments of different batches of **F-cage** were conducted at 273 K. The comparable adsorption properties of three batches of **F-cage** at 273 K were verified by similar PFC adsorption behaviors, with uptakes of 0.72-0.93 mmol g^{-1} of CF_4, 1.42-1.78 mmol g^{-1} of C_2F_6, 1.63-2.09 mmol g^{-1} of C_3F_8 (Figure 33 and Table 8). The gas adsorption selectivities of PFCs over nitrogen at 273 K also shows a similar rising trend at higher nitrogen concentrations, demonstrating satisfactory reproducibility for different batches of **F-cage**. The highest selectivities within the investigated series are found for the adsorption of C_3F_8, with an IAST selectivity of S_{IAST} $(C_3F_8/N_2)_{10:90}$ = 190 and S_{IAST} $(C_3F_8/N_2)_{1:99}$ = 728 at 1 bar and a Henry selectivity of S_H (C_3F_8/N_2) = 13232.

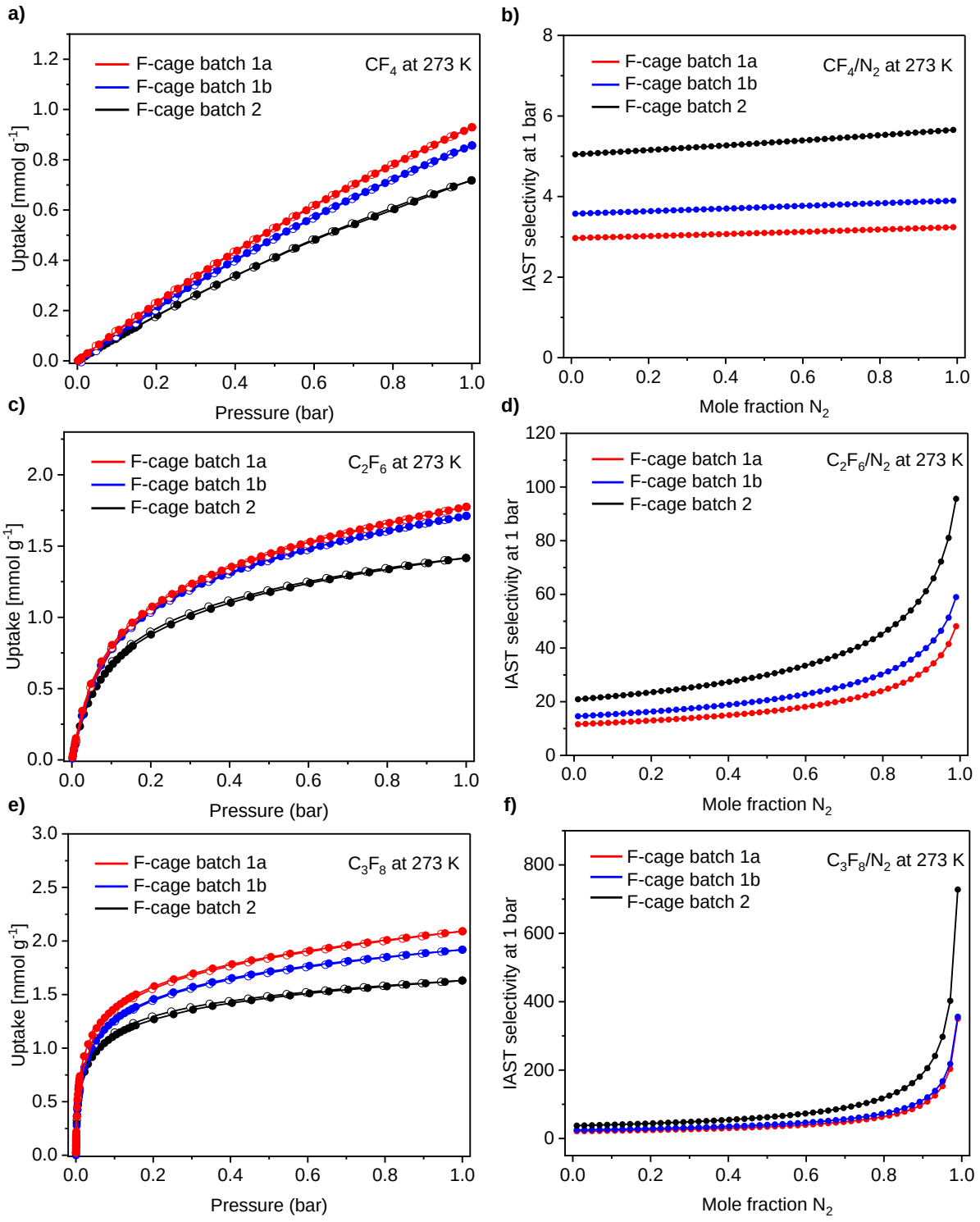

Figure 33. CF_4 (a), C_2F_6 (c) and C_3F_8 (e) sorption isotherms of different batches of **F-cage** at 273 K. Filled circles: adsorption; empty circles: desorption. IAST selectivity curves of different batches of **F-cage** for CF_4 (b), C_2F_6 (d) and C_3F_8 (f) over N_2 at different mole ratios at 273 K and 1 bar. Adapted with permission from Ref.[7]. Copyright © 2022 Wiley-VCH.

Most imine-based molecules are known to be unstable in acidic, basic, or even water environments.[25c] Therefore, the stability of **F-cage** was examined by stirring the crystalline material in water or in HCl_{aq} (0.1 mM) or $NaOH_{aq}$ (1 mM) solutions and then drying and analyzing with TGA, NMR spectroscopy, and nitrogen sorption at 77 K. No

weight loss was observed up to ~400 °C, revealing that all water had been removed (Figure 34a). Three overlapped TGA curves indicate the same chemical sturcture of crystals after the different treatments.

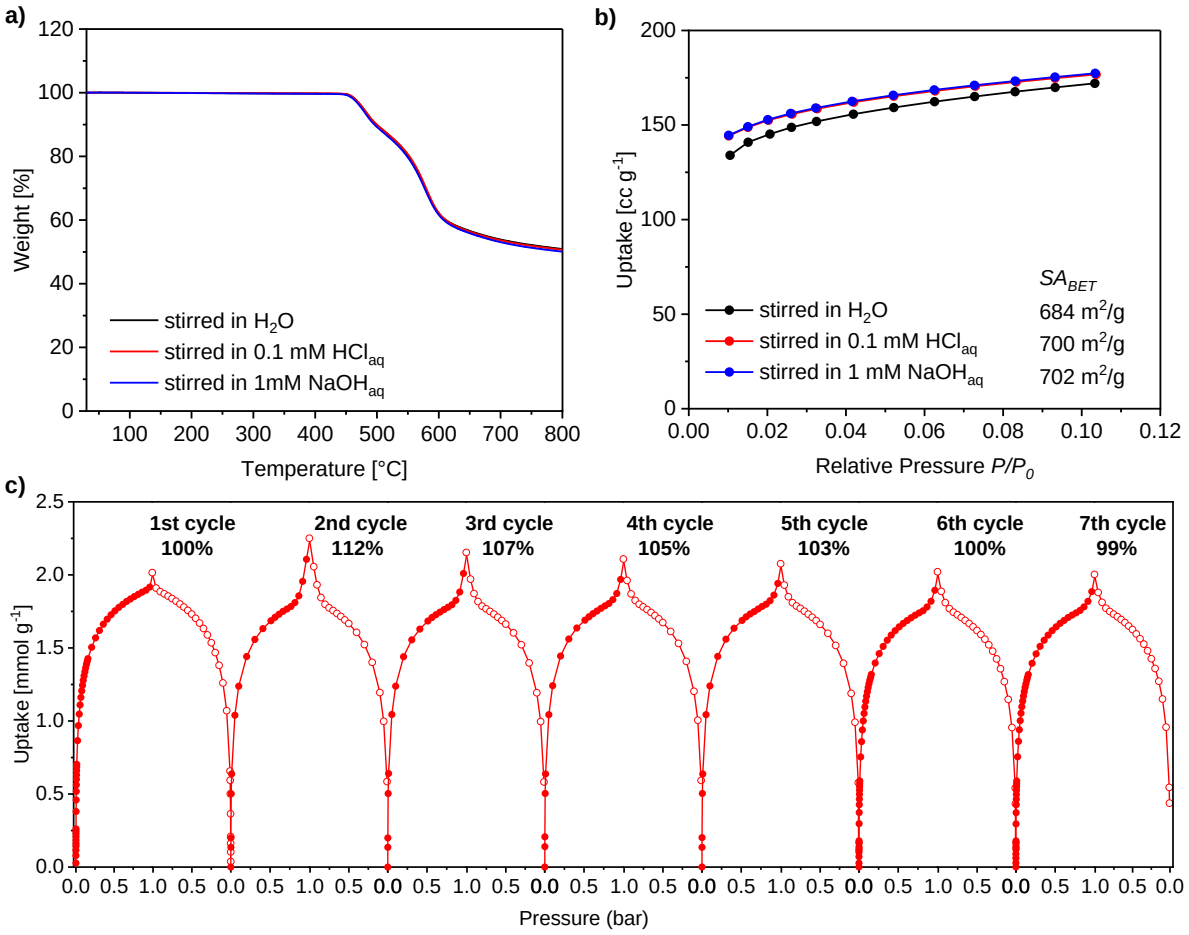

Figure 34. (a) TGA of **F-cage** after water, acid, and base treatment (20 mL/min under N_2; heating rate: 10 K/min). (b) N_2 isotherms at 77 K (12 points in the typical BET-region) after stirring **F-cage** in water for 18 h (black), HCl_{aq} (0.1 mM) for 24 h (red) or $NaOH_{aq}$ (1 mM) for 24 h (blue). (c) recyclability test of **F-cage** demonstrated for seven adsorption and desorption cycles of *c*-C_4F_8 at 298 K. Reproduced with permission from Ref.[7]. Copyright © 2022 Wiley-VCH.

Both ^{1}H- and ^{19}F-NMR spectroscopy before and after the treatments showed the same chemical shift, proving the high chemical stability of **F-cage** (Appendix, Figure 190-191). These acid/base/water treatments did not affect the porosity in the material, as shown by the N_2 isotherms in Figure 34b, which yielded BET surface areas of 684-702 $m^2\ g^{-1}$ comparable to the surface area of the original material (752 $m^2\ g^{-1}$). The chemical stability of **F-cage** is attributed to strongly hydrophobic perfluorinated side chains. Furthermore, the recyclability of **F-cage** was evaluated via adsorption and desorption cycles with *c*-C_4F_8 (Figure 34c). The uptake at 1 bar in cycle 1 was set to 100%. After the material was stored for 204 days in ambient atmosphere, six more

cycles were carried out. *c*-C_4F_8 uptakes ranged from 99-112%, demonstrating the potential recyclability of **F-cage** in real separations.

1.8. Conclusion

To conclude, a series of [2+3] porous imine cages with various degrees of side-chain fluorination was synthesized and assembled into isomorphic crystalline materials. By examination of the influence of the side-chains on gas sorption properties, the fluorinated **F-cage** demonstrated unprecedented uptakes and selectivities for PFCs over N_2, which was further underlined by theoretical as well as experimental breakthrough analyses. These excellent properties have been attributed to F···F interactions between host and guest, supported by Hirshfeld analysis of a single-crystal of **F-cage** containing C_3F_8. Moreover, the excellent reproducibility, recyclability, and acid/base/water stability of **F-cage** makes it a promising candidate for practical applications in real life environments. The findings of this research are anticipated to stimulate further exploration into the creation of porous materials designed for the purpose of effectively capturing and removing PFCs from the environment.

2. The Influence of the Lengths of Fluorinated Side Chains and Solid Packing on the Gas Sorption Behaviour of Porous Organic Cages

In Chapter III, Section 1, [2+3] porous imine cages with perfluorobutyl chains demonstrated unprecedented uptakes and selectivities for PFCs over N_2. The perfluorobutyl chains play a key role in structure and performance investigation. Therefore, a new series of cages with different lengths of perfluorinated *n*-alkyl chains was presented (Scheme 12). Gas uptakes and selectivities for a range of F-gases, such as CF_4, C_2F_6, C_3F_8, *c*-C_4F_8, SF_6, and NF_3, over three major atmospheric components (O_2, N_2, and CO_2) were explored in detail herein.

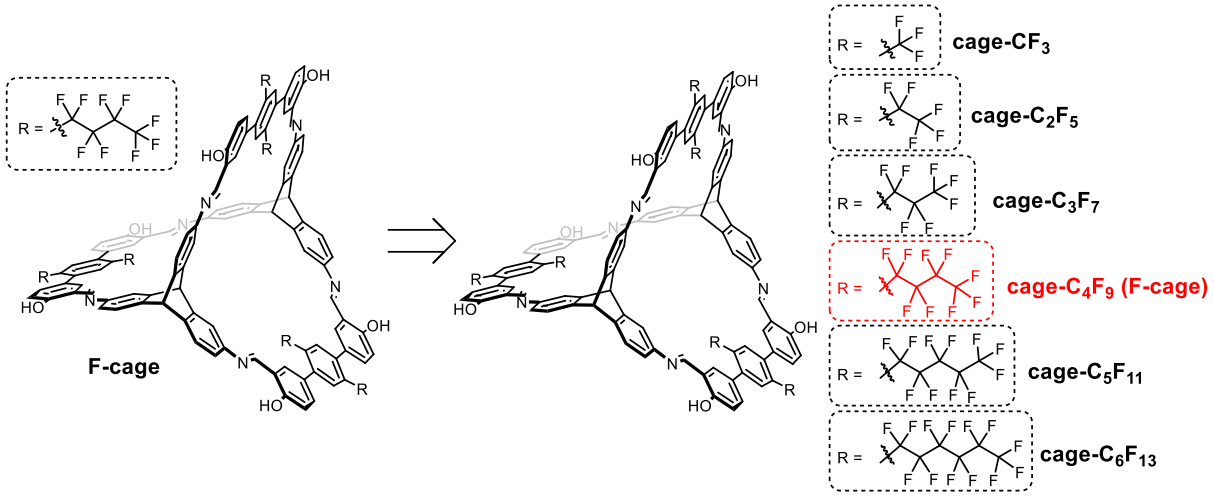

Scheme 12. Scheme description of this chapter. (**F-cage** = **cage-C_4F_9**)

2.1. The Influence of the Lengths of Fluorinated Side Chains on Fluorinated Gas Adsorption

2.1.1. Synthesis of [2+3] Cage with Different Lengths of Perfluoroalkyl Chains

The synthesis of **F-cage** has been described in Chapter III, Section 1. The same strategy used in the synthesis of **F-cage**, was applied to synthesize the other five new cages with different lengths of perfluoroalkyl chains. The starting materials 1,4-bis(perfluoroalkyl)benzenes (**56**-**59**) were synthesized, except for 1,4-bis(perfluoromethyl)benzene **63** which was commercially available (Scheme 13). According to the report of Gillian et al.[114], sodium pentafluoropropionate, in the

presence of copper(I) iodide under high temperature, is used as a source of pentafluoroethyl group to replace halogens in 1,4-diiodobenzene and produce 1,4-bis(perfluoroethyl)benzene **56**. The crude product wasn't purified further and used directly in the next step. Perfluoro-1-iodoalkanes and diiodobenzene are smoothly coupled utilizing copper metal in DMSO at 120 °C to produce 1,4-bis(perfluoroalkyl)benzenes (**57**-**59**) in high yields (75%, 77%, and 93% [Lit.:78%], respectively) (Scheme 13).[115]

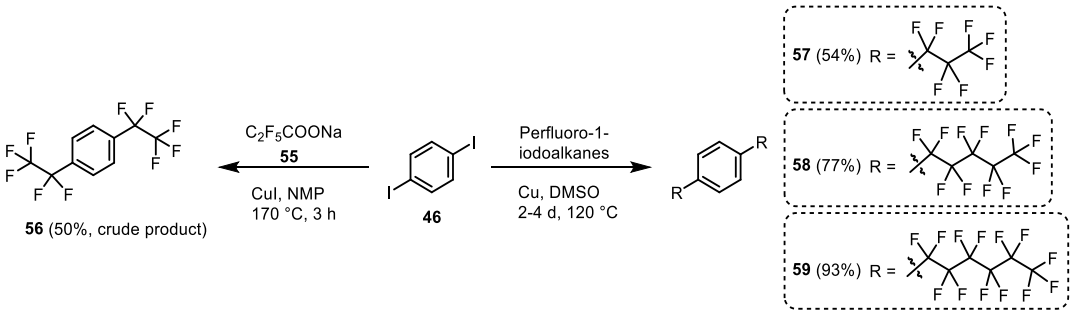

Scheme 13. Synthesis of 1,4-bis(perfluoroalkyl)benzenes **57**-**59**. Perfuoro-1-iodoalkanes: perfuoro-1-iodopropan (**60**), perfuoro-1-iodopentane (**61)**, and perfuoro-1-iodohexan (**62**) used in the synthesis of **57**-**59**, respectively.

The series of 1,4-bis(perfluoroalkyl)benzenes (**63** and **56-59**) was brominated further in a mixture of H_2SO_4 and TFA with NBS, and subsequently coupled with boronic ester **51** in a palladium-catalyzed Suzuki-Miyaura cross-coupling reaction to obtain the salicyldialdehyde terphenyl building blocks bearing fully-fluorinated methyl (**69**), ethyl (**70**), *n*-propyl (**71**), *n*-pentyl (**72**), and *n*-hexyl (**73**) groups at 2,5-positions of the middle benzene ring in yields of 38%-65% (Scheme 14).

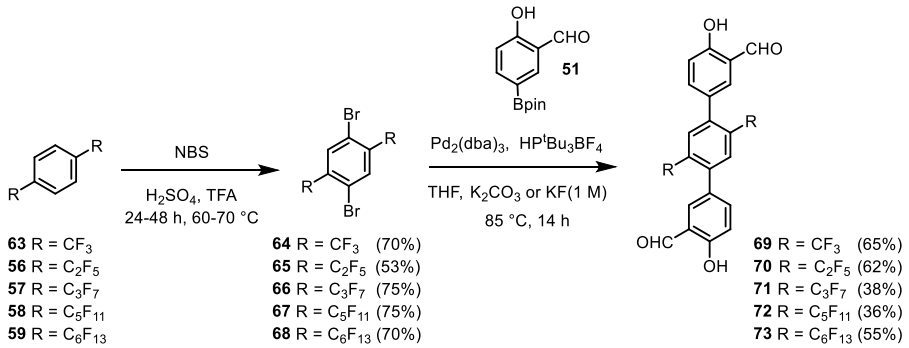

Scheme 14. Synthesis of terphenyl bis-salicylaldehydes with different lengths of perfluoroalkyl chains.

The isostructural imine cages **cage-CF_3** (with perfluorinated methyl chains), **cage-C_2F_5** (with perfluorinated ethyl chains), **cage-C_3F_7** (with perfluorinated *n*-propyl chains), **cage-C_5F_{11}** (with perfluorinated *n*-pentyl chains), and **cage-C_6F_{13}** (with perfluorinated *n*-hexyl chains) were synthesized by six fold condensation reactions between triptycenetriamine **15** and the corresponding terphenyl-based bis-salicylaldehydes **69**-

73 in a 2 : 3 ratio with a catalytic amount of TFA at room temperature or 100 °C for 24 hours to 2 days (Scheme 15 and Table 9). In comparison to the **F-cage** synthesis, an improved work-up method was implemented. This improved approach took into consideration the varying solubility of cage and noncage components. As a result, two different solvents, namely DCM and DMF, were utilized. This strategic solvent selection eliminated the need for procedures involving the concentration of crude reaction mixtures and the subsequent addition of anti-solvents. The pure cages were directly precipitated from the crude reaction mixture. The obtained yields were as follows: 49% for **cage-CF_3**, 70% for **cage-C_2F_5**, 63% for **cage-C_3F_7**, 60% for **cage-C_5F_{11}**, and 59% for **cage-C_6F_{13}**.

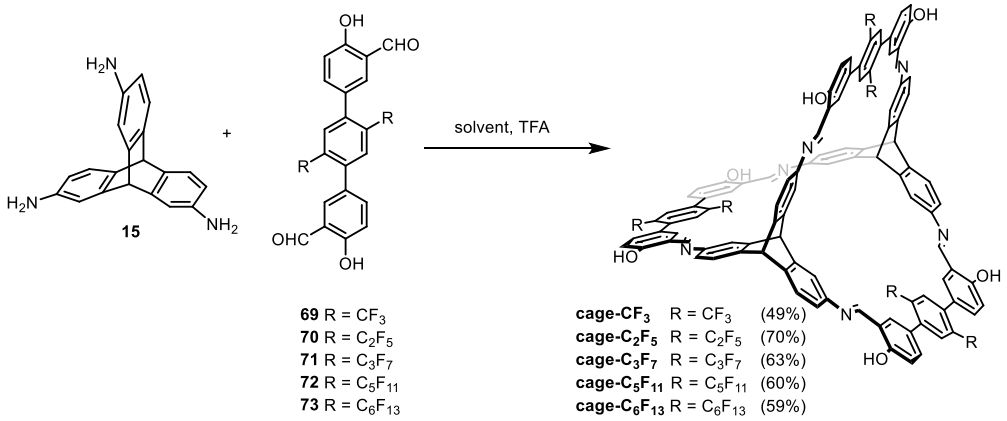

Scheme 15. Synthesis of [2+3] cages with different lengths of perfluoroalkyl chains.

Table 9. Summary of reaction conditions of fluorinated [2+3] cages.

Cages	Solvent	Temperature	Time	TFA amount[a]	Yield
cage-CF_3	DCM	rt	24 h	4.5 mol-%	49%
cage-C_2F_5	DCM	rt	2 d	3 mol-%	70%
cage-C_3F_7	DCM	rt	2 d	3 mol-%	63%
cage-C_5F_{11}	DMF	100 °C	24 h	3 mol-%	60%
cage-C_6F_{13}	DMF	100 °C	36 h	4.5 mol-%	59%

[a] based on the amount of **15**.

All cages are soluble in THF allowing the characterization by ^{1}H and ^{19}F NMR-spectroscopy in THF-d_8 (Figure 35-36). The singlets at 9.95-10.03 ppm and 13.27-13.37 ppm are assigned to the imine and hydroxy protons, respectively. Signals associated with aromatic protons from the triptycene and terphenyl subunits appear in the range of 7.00-8.00 ppm.

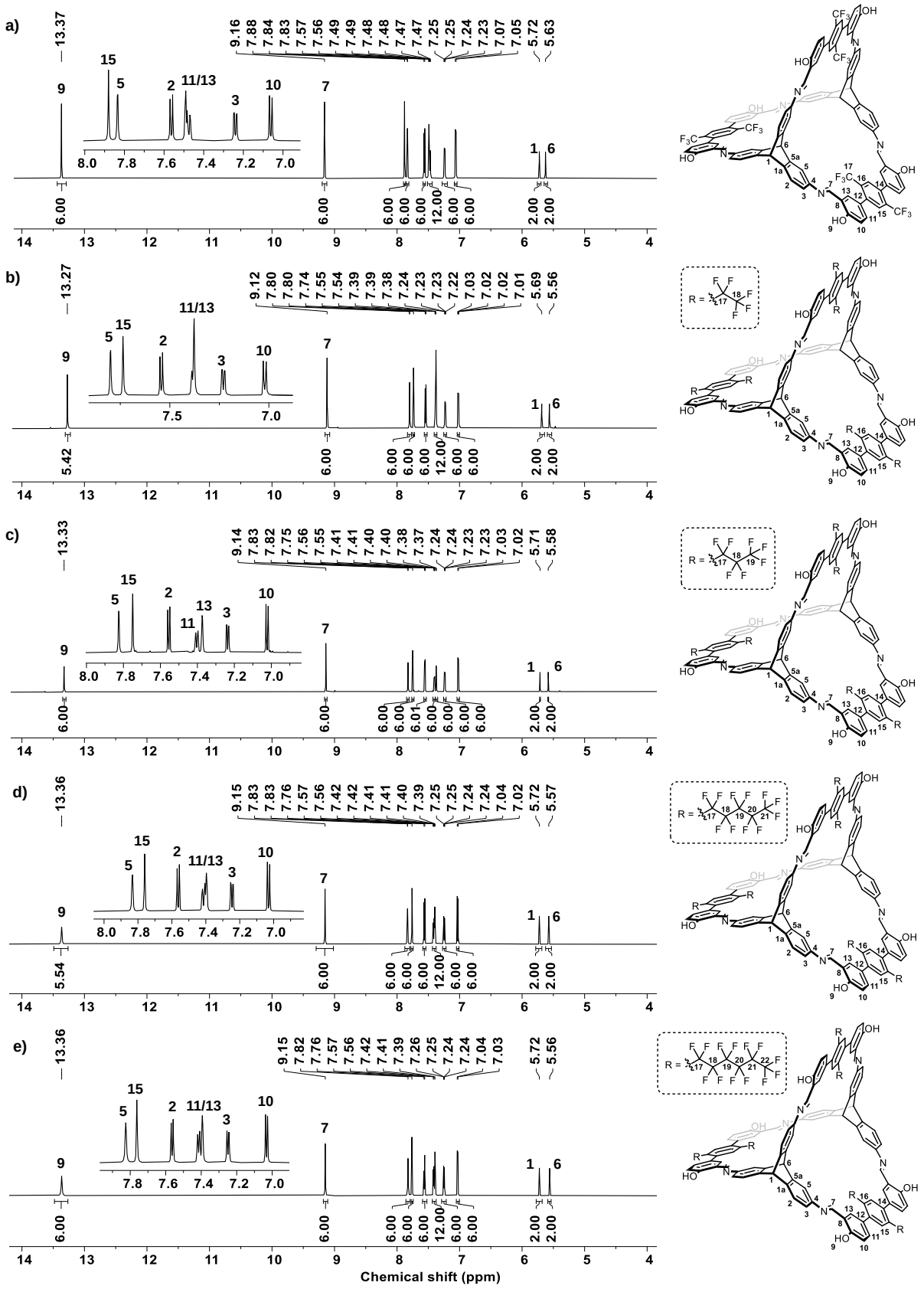

Figure 35. ^{1}H NMR of fluorinated [2+3] cages in THF-d_8. (a) **cage-CF$_3$** (600 MHz), (b) **cage-C$_2$F$_5$** (600 MHz), (c) **cage-C$_3$F$_7$** (700 MHz), (d) **cage-C$_5$F$_{11}$** (600 MHz), (e) **cage-C$_6$F$_{13}$** (700 MHz).

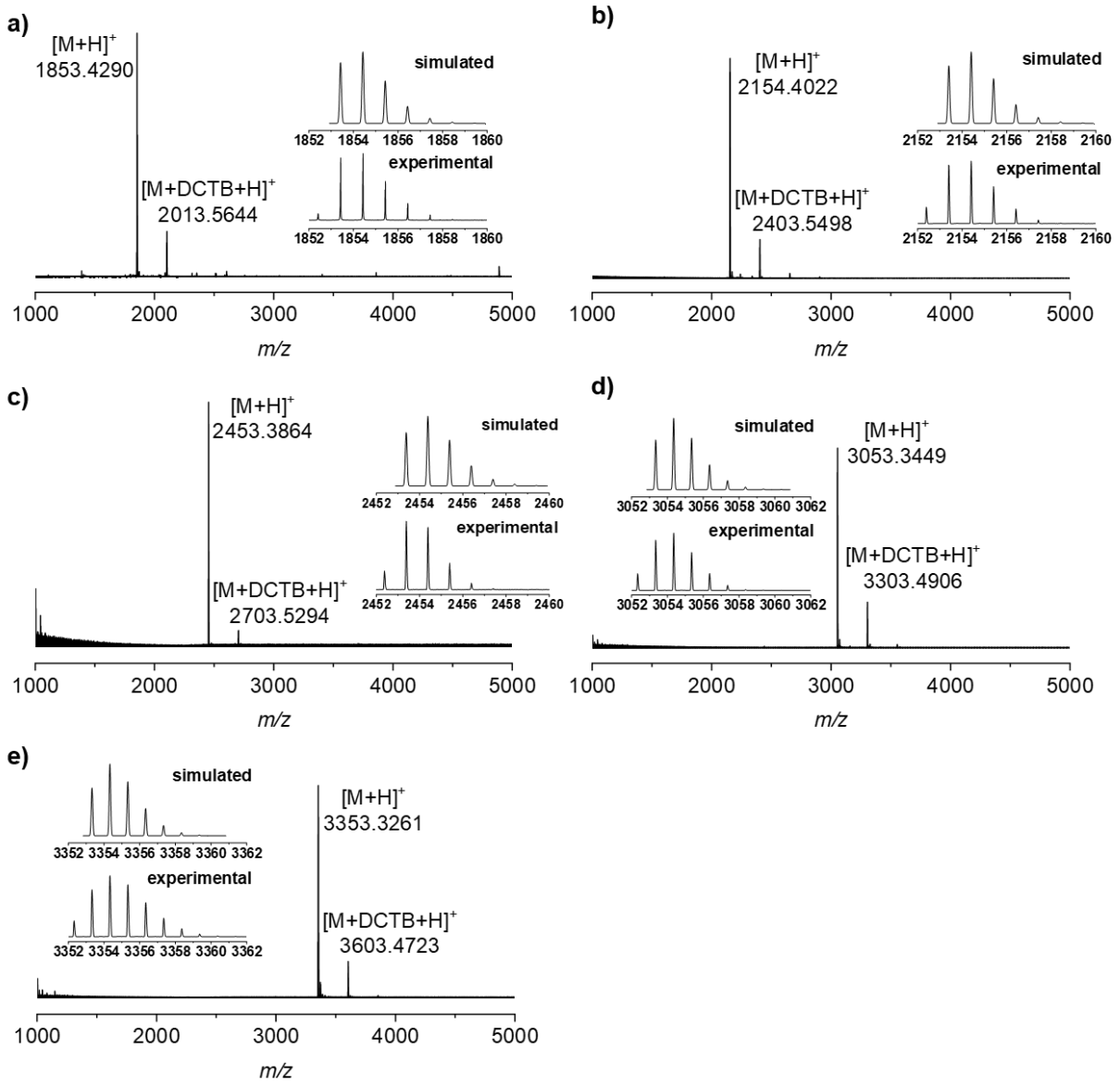

Figure 36. MALDI-TOF spectra of **cage-CF_3** (a), **cage-C_2F_5** (b), **cage-C_3F_7** (c), **cage-C_5F_{11}** (d), and **cage-C_6F_{13}** (e) (matrix: DCTB).

Notably, a different chemical shift pattern is observed for the proton located closest to the side-chain substitution position (H-15). This proton exhibits a higher chemical shift compared to the proton (H-5) for **cage-CF_3** featuring -CF_3 groups. With the increase in the length of fluorinated chains, the proton (H-15) demonstrates a lower chemical shift than the proton (H-5). This phenomenon is attributed to the stronger electron-withdrawing effect of -CF_3 groups than -CF_2- groups.[116] Additionally, two bridgehead protons are identifiable at approximately 5.70 and 5.60 ppm.

In ^{19}F NMR spectroscopy, the side-chain region can be identified clearly by single or multiple groups of peaks: **cage-CF_3** (δ = -59.9 ppm), **cage-C_2F_5** (δ = -86.1 and -109.4 ppm), **cage-C_3F_7** (δ = -81.1, -104.4, and -124.6 ppm), **cage-C_5F_{11}** (δ = -82.0, -

103.7, -120.0, -123.1, -126.9 ppm), **cage-C_6F_{13}** (δ = -83.9, -105.5, -121.8, -124.2, -124.9, -128.8 ppm) (Appendix). By DOSY experiments in THF-d_8 at 295 K, diffusion coefficients of D = 3.66 × 10^{-10} m^2 s^{-1} for **cage-CF_3**, 3.98 × 10^{-10} m^2 s^{-1} for **cage-C_2F_5**, 4.27 × 10^{-10} m^2 s^{-1} for **cage-C_3F_7**, 2.75 × 10^{-10} m^2 s^{-1} for **cage-C_5F_{11}**, and 3.25 × 10^{-10} m^2 s^{-1} for **cage-C_6F_{13}** are determined, which corresponds to a solvodynamic radii of r_s = 0.93-1.45 nm (Appendix, Figure 188-189). These are in good agreement to the dimensions obtained by SCXRD (see discussion below). MALDI-TOF mass spectrometry in positive mode shows signals correlated to the molecular ions of the desired cage compounds at *m*/*z* = 1853.4290 for **cage-CF_3** (calc. for $[C_{106}H_{59}F_{18}N_6O_6]^+$ *m*/*z* = 1853.4203), *m*/*z* = 2154.4022 for **cage-C_2F_5** (calc. for $[C_{112}H_{59}F_{30}N_6O_6]^+$ *m*/*z* = 2154.4012), *m*/*z* = 2453.3864 for **cage-C_3F_7** (calc. for $[C_{118}H_{59}F_{42}N_6O_6]^+$ *m*/*z* = 2453.3820), *m*/*z* = 3053.3449 for **cage-C_5F_{11}** (calc. for $[C_{130}H_{59}F_{66}N_6O_6]^+$ *m*/*z* = 3053.3437), and *m*/*z* = 3353.3261 for **cage-C_6F_{13}** (calc. for $[C_{136}H_{59}F_{78}N_6O_6]^+$ *m*/*z* = 3353.3245), having the expected isotope distribution pattern (Figure 36). These results prove that pure cages have been obtained.

2.1.2. Single Crystal Structure Investigation

Single crystal of **F-cage** has been obtained by vapor diffusion of methanol into THF solutions in Chapter III, Section 1. Large single-crystals of the other cages were also obtained using the same method, as seen Figure 40a-f. Unfortunately, for **cage-C_6F_{13}**, single crystal X-ray diffraction did not provide sufficient resolution to elucidate the solid-state structures. Among the crystals that were successfully analyzed, **cage-C_2F_5**, **cage-C_3F_7**, **F-cage**, and **cage-C_5F_{11}** crystallized in the trigonal space group $R\bar{3}c$. It's worth mentioning that **cage-C_2F_5** exhibited relatively larger cell volumes (27369.3 $Å^3$) compared to **cage-C_3F_7** (21183.1 $Å^3$), **F-cage** (20049.6 $Å^3$), and **cage-C_5F_{11}** (21822.8 $Å^3$), as detailed in Table 10. For **cage-CF_3**, the same packing single-crystal with the cell volume of 19852.4 $Å^3$ were obtained by vapor diffusion of methanol into DMF solutions (**cage-$CF_{3\alpha}$**), rather than into THF solutions (**cage-$CF_{3\beta}$**, see Chapter III, Section 2.2). Compared with **F-cage**, all cages have a similar outer size in a range of 1.8-1.9 nm (measured between the outer triptycene bridgehead carbons) and inner size in a range of 1.3-1.4 nm (measured between the inner triptycene bridgehead carbons), which fits well to corresponding solvodynamic radii of 0.93-1.45 nm from DOSY-NMR (Figure 37e and Appendix, Figure 188-189).

Table 10. Selected crystallographic parameters.

Parameter	**cage-$CF_{3\alpha}$**	**cage-C_2F_5**	**cage-C_3F_7**	**F-cage**	**cage-C_5F_{11}**
Solvent	DMF/ Methanol	THF/ Methanol	THF/ Methanol	THF/ Methanol	THF/ Methanol
Crystal system	Trigonal	Trigonal	Trigonal	Trigonal	Trigonal
Space group	*R*$\bar{3}$*c*	*R*$\bar{3}$*c*	*R*$\bar{3}$*c*	*R*$\bar{3}$*c*	*R*$\bar{3}$*c*
Z	6	6	6	6	6
Cell volume [Å^3]	19852.4	27369.3	21183.1	20049.6	21822.8
endo/*exo* population	no	endo/exo 46%/54%	exo1/exo2 50%/50%	endo/exo 68%/32%	endo1/endo2/ exo 36%/33%/31%
$d_{\pi\text{-}\pi}$ [Å]	3.5	3.3	3.5	3.5	3.6

With side chain lengths varying, the flexible side chains of the cages can adopt one or multiple potential conformations. Importantly, these conformations are independent of the cage backbones, as demonstrated by the overlay structures (Figure 37q-x). For **cage-$CF_{3\alpha}$**, the side chains exclusively adopt a singular conformation (Figure 37a and f).

As the length of the side chains increases, a diversity of conformations becomes apparent. As aforementioned, the conformations in which a side chain points into the window of the cage and point outward are termed "*endo*" and "*exo*", respectively. In the case of **cage-C_2F_5** and **F-cage**, side chains exhibit two primary possible conformations ("*endo*" and "*exo*") in roughly equal proportions (Figure 37b, g, k, n, Figure 17, and Table 10). Similarly, **cage-C_3F_7** demonstrates two predominant exo conformations ("*exo1*" and "*exo2*") present in approximately a 1:1 ratio (Figure 37c, h, l, o, and Table 10). In the *exo1* conformation, two side chains of the same phenyl group are slightly closer than they are in the *exo2* conformation.

Notably, **cage-C_5F_{11}** showcases three principal conformations – "*endo1*", "*endo2*" and "*exo*" – distributed in an approximate 1:1:1 ratio (Table 10 and Figure 37d-e, i-j, m, and p). In the *endo1* conformation, the side chains exhibit a zig-zag configuration, while in the *endo2* conformation, they assume a U shape. It's important to note that these *endo*/*exo* conformations cannot be further differentiated to determine whether a certain ratio of the cages are *endo* or if certain ratio of side chains are *endo* in a single cage, or a combination of both. For simplicity, only the extreme states of full-*endo* and full-*exo* will be discussed, as with the **F-cage**.

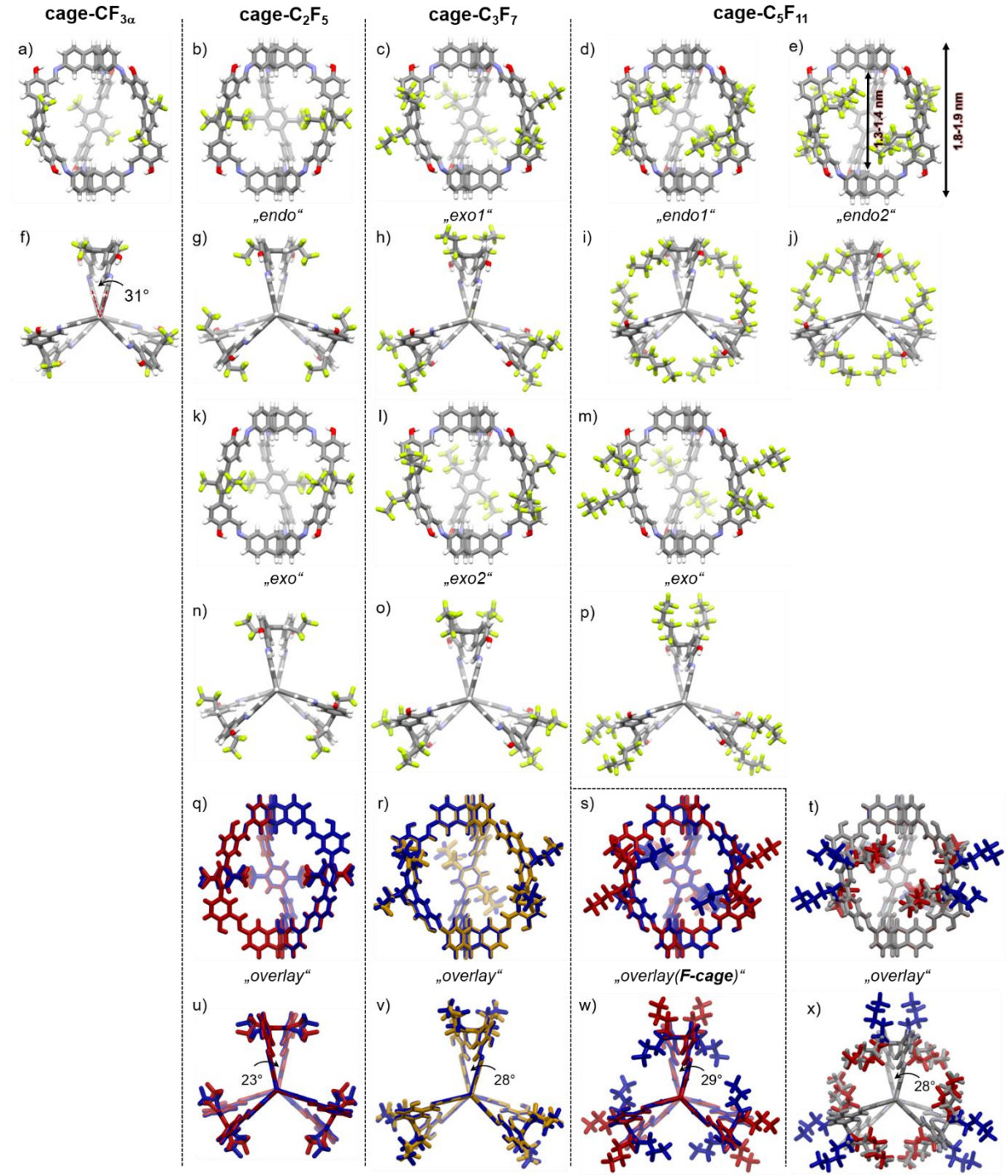

Figure 37. Side-view (a) and top-view (f) of one enantiomer for **cage-CF$_{3\alpha}$**. Side-view of one enantiomer for full *endo* **cage-C$_2$F$_5$** (b), full *exo* **cage-C$_2$F$_5$** (k), full *exo1* **cage-C$_3$F$_7$** (c), full *exo2* **cage-C$_3$F$_7$** (l), full *endo1* **cage-C$_5$F$_{11}$** (d), full *endo2* **cage-C$_5$F$_{11}$** (e), full *exo* **cage-C$_5$F$_{11}$** (m). The inner and outer diameter (measured between two carbon atoms) is depicted for all cages. Top-view of one enantiomer for full *endo* **cage-C$_2$F$_5$** (g), full *exo* **cage-C$_2$F$_5$** (n), full *exo1* **cage-C$_3$F$_7$** (h), full *exo2* **cage-C$_3$F$_7$** (o), full *endo1* **cage-C$_5$F$_{11}$** (i), full *endo2* **cage-C$_5$F$_{11}$** (j), full *exo* **cage-C$_5$F$_{11}$** (p). Side-view (q) and top-view (u) of on an overlay of the full *endo* (red) and full *exo* (blue) conformer of **cage-C$_2$F$_5$**. Side-view (r) and top-view (v) of on an overlay of the full *exo1* (red) and full *exo2* (blue) conformer of **cage-C$_3$F$_7$**. Side-view (s) and top-view (w) of on an overlay of the full *endo* (blue) and full *exo* (red) conformer of **F-cage**. Side-view (t) and top-view (x) on an overlay of the full *endo1* (grey), full *endo2* (red), and full *exo* (blue) conformer of **cage-C$_5$F$_{11}$**. (*Note:* For the discussion on the enantiomeric cage isomers of **F-cage** see Chapter III, Section 1.)

All cages exhibit the same packing pattern as **F-cage** (Figure 38). Within the context of six adjacent cage molecules, an alignment of one side-chain per cage molecule is observed, resulting in the formation of a hexagonal array in extreme cases. Notably, the shortest F···F distance between adjacent side chains within **cage-CF$_{3\alpha}$** measures 4.7 Å. As the side chains lengthen, they occupy more space, leading to a gradual reduction in the distance between side chains. For instance, the shortest F···F distance between side chains progressively shortens from 2.9 Å in **cage-C$_2$F$_5$**, to 2.8 Å in **cage-C$_3$F$_7$**, to 2.5 Å in **F-cage**, and finally to 2.1 Å in **cage-C$_5$F$_{11}$** (Figure 17 and 38). This trend implies an increasingly potent F···F interactions between the side chains.

Referring to **F-cage**, the two triptycene scaffolds of the cage backbones are rotated with respect to one another, resulting in helical chirality for the cage molecules. When one enantiomer with side-chain orientations is considered as shown in Figure 37, the rotation degree of two triptycenes of **cage-CF$_{3\alpha}$**, **cage-C$_3$F$_7$**, **F-cage,** and **cage-C$_5$F$_{11}$** is anticlockwise 28.0°-31° from a top view, while for **cage-C$_2$F$_5$** they rotate clockwise by only 23°. The racemic crystalline packing of all cages contains enantiopure layers that are interconnected by π-stacking as described in Chapter III, Section 1. The distances of $d_{\pi\text{-}\pi}$ for **cage-C$_2$F$_5$** is 3.3 Å, shorter than that of 3.5-3.6 Å for **cage-CF$_{3\alpha}$**, **cage-C$_3$F$_7$**, **F-cage,** and **cage-C$_5$F$_{11}$** (Table 10). This discrepancy in triptycene units and π-stacking distances accounts for the notably larger cell volume (27369 Å^3) exhibited by **cage-C$_2$F$_5$** in single crystal parametres, even when packed similarly to the other cages (Table 10).

Analyzing the voids of the crystal structures with a probe of radius 1.6-2.0 Å revealed that **cage-CF$_{3\alpha}$** and **cage-C$_2$F$_5$** contain interconnected solvent-accessible pores within three-dimensional channels (Appendix, Figure 203-204). With longer side chains, the intrinsic pores of **cage-C$_3$F$_7$** and **cage-C$_5$F$_{11}$** in the crystalline states are separated entirely by the hexameric side-chain alignments. Therefore, permanent porosity is also only possible by gas diffusion[101] through the side-chains and/or gate-opening mechanisms, as with **F-cage**.[102]

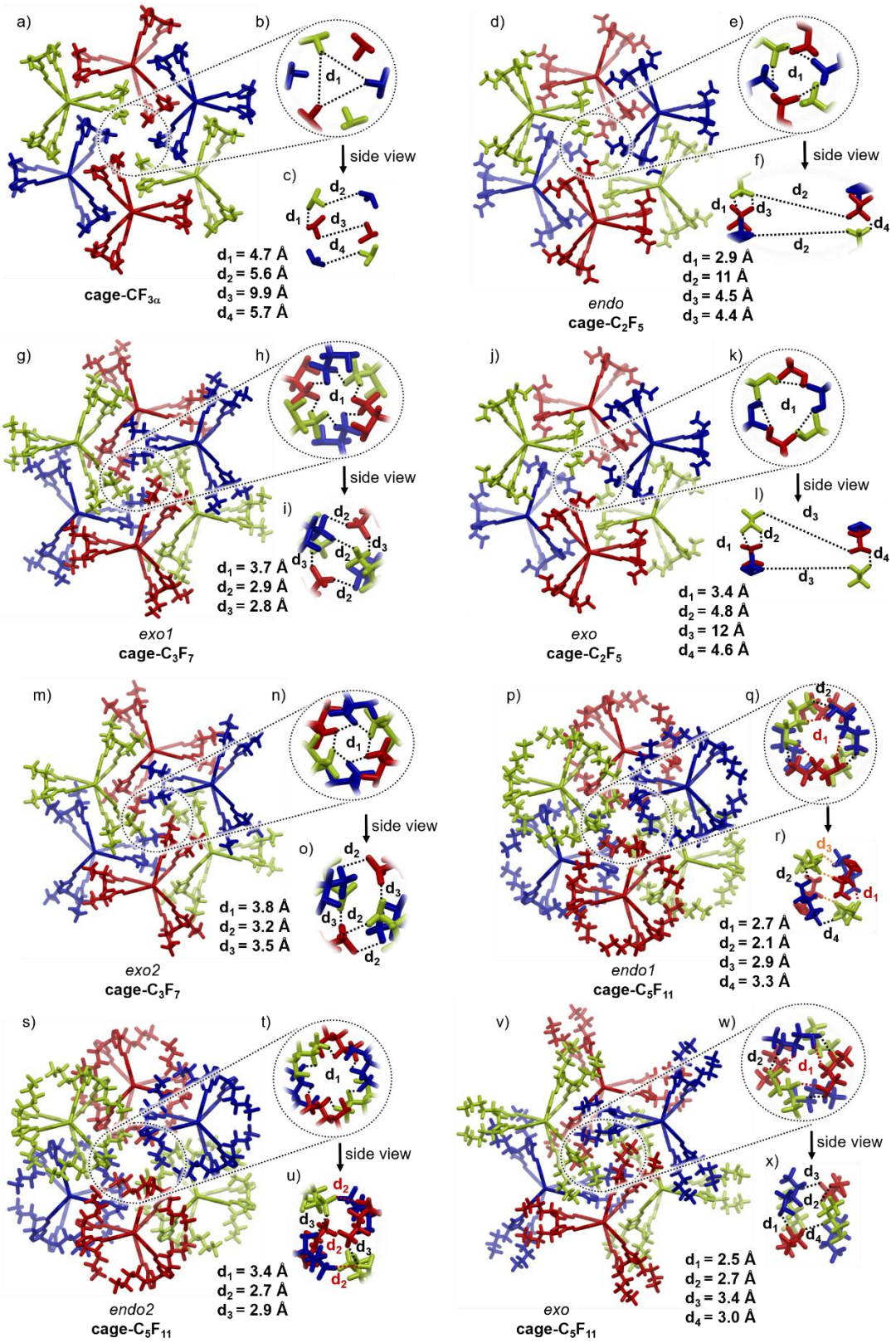

Figure 38. Hexameric alignment of cages along the crystallographic *c*-axis for **cage-CF$_{3\alpha}$** (a), for full *endo* **cage-C$_2$F$_5$** (d), full *exo* **cage-C$_2$F$_5$** (j), full *exo1* **cage-C$_3$F$_7$** (g), full *exo2* **cage-C$_3$F$_7$** (m), full *endo1* **cage-C$_5$F$_{11}$** (p), full *endo2* **cage-C$_5$F$_{11}$** (s), full *exo* **cage-C$_5$F$_{11}$** (v). Cages depicted in the same color are equal by inversion symmetry. Zoom-in to the hexameric side-chain alignment as top view with F···F-distances for **cage-CF$_{3\alpha}$** (b), for full *endo* **cage-C$_2$F$_5$** (e), full *exo* **cage-C$_2$F$_5$** (k), full *exo1* **cage-C$_3$F$_7$** (h), full *exo2* **cage-C$_3$F$_7$** (n), full *endo1* **cage-C$_5$F$_{11}$** (q), full *endo2* **cage-C$_5$F$_{11}$** (t), full *exo* **cage-C$_5$F$_{11}$** (w). Side view with F···F-distances for **cage-CF$_{3\alpha}$** (c), for full *endo* **cage-C$_2$F$_5$** (f), full *exo* **cage-C$_2$F$_5$** (l), full *exo1* **cage-C$_3$F$_7$** (i), full *exo2* **cage-C$_3$F$_7$** (o), full *endo1* **cage-C$_5$F$_{11}$** (r), full *endo2* **cage-C$_5$F$_{11}$** (u), full *exo* **cage-C$_5$F$_{11}$** (x).

2.1.3. Activation Investigation

To remove the enchlatrated solvent for the subsequent gas sorption investigation, all materials were activated in a dynamic vacuum at room temperature, followed by 50°C, and then subjected to NMR analyses. Desolvated **cage-CF$_{3\alpha}$** (crystallized from DMF/methanol) and **cage-C$_6$F$_{13}$** (crystallized from THF/ methanol, denoted as **cage-C$_6$F$_{13\alpha}$**) was dissolved in THF-d_8 and $CDCl_3$, respectively, and no signals of any residue solvent were observed in the NMR spectrum (Appendix, Figure 193-194). For desolvated **cage-C$_2$F$_5$**, **cage-C$_3$F$_7$**, **and cage-C$_5$F$_{11}$**, TGA measurements confirm the absence of the other solvent molecules and show the stability of the cages up to 430°C (Figure 39). The chemical integrities of the desolvated forms were proved by comparing them after activation with their corresponding spectra as synthesized (Appendix, Figure 192).

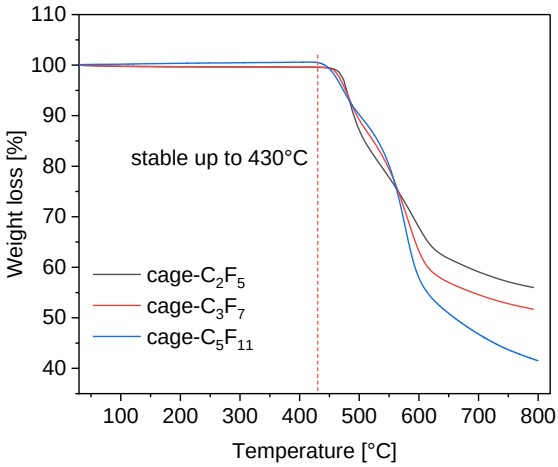

Figure 39. TG curves of **cage-C$_2$F$_5$**, **cage-C$_3$F$_7$**, and **cage-C$_5$F$_{11}$** after thermal activation (N_2, flow rate: 20 mL·min^{-1}, heating rate: 10 K·min^{-1}).

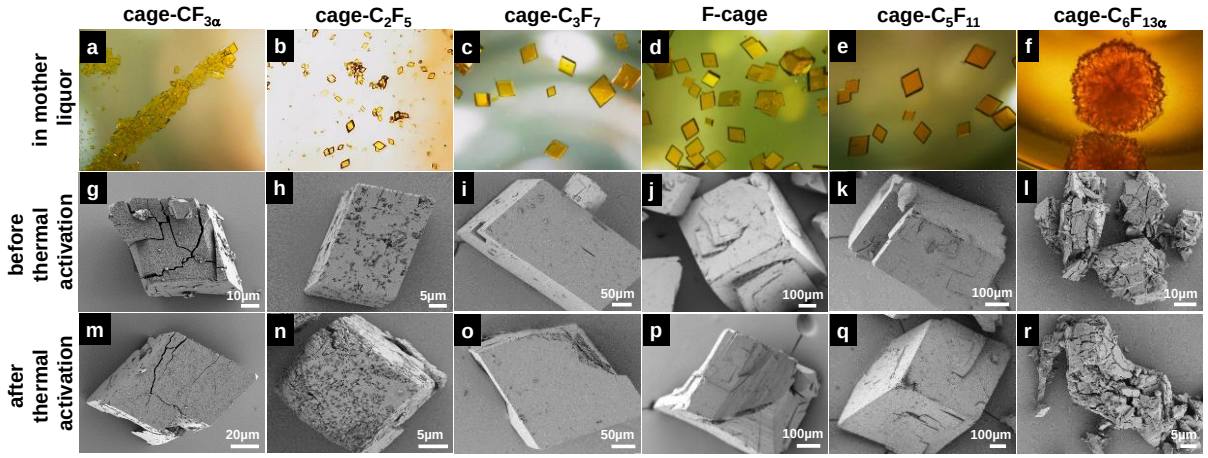

Figure 40. Light microscope and SEM images of fluorinated [2+3] cages: (a-f) All crystals in the THF/MeOH mother liquor except **cage-CF$_{3\alpha}$** in the DMF/MeOH; g-h) filtered crystal prior to thermal activation. m-r) Thermally activated crystals. Pictures (a-f) have been obtained by light microscope, pictures (g-r) have been obtained by SEM. SEM measurements were performed by Dr. Wen-Shan Zhang (BioQuant, Heidelberg University).

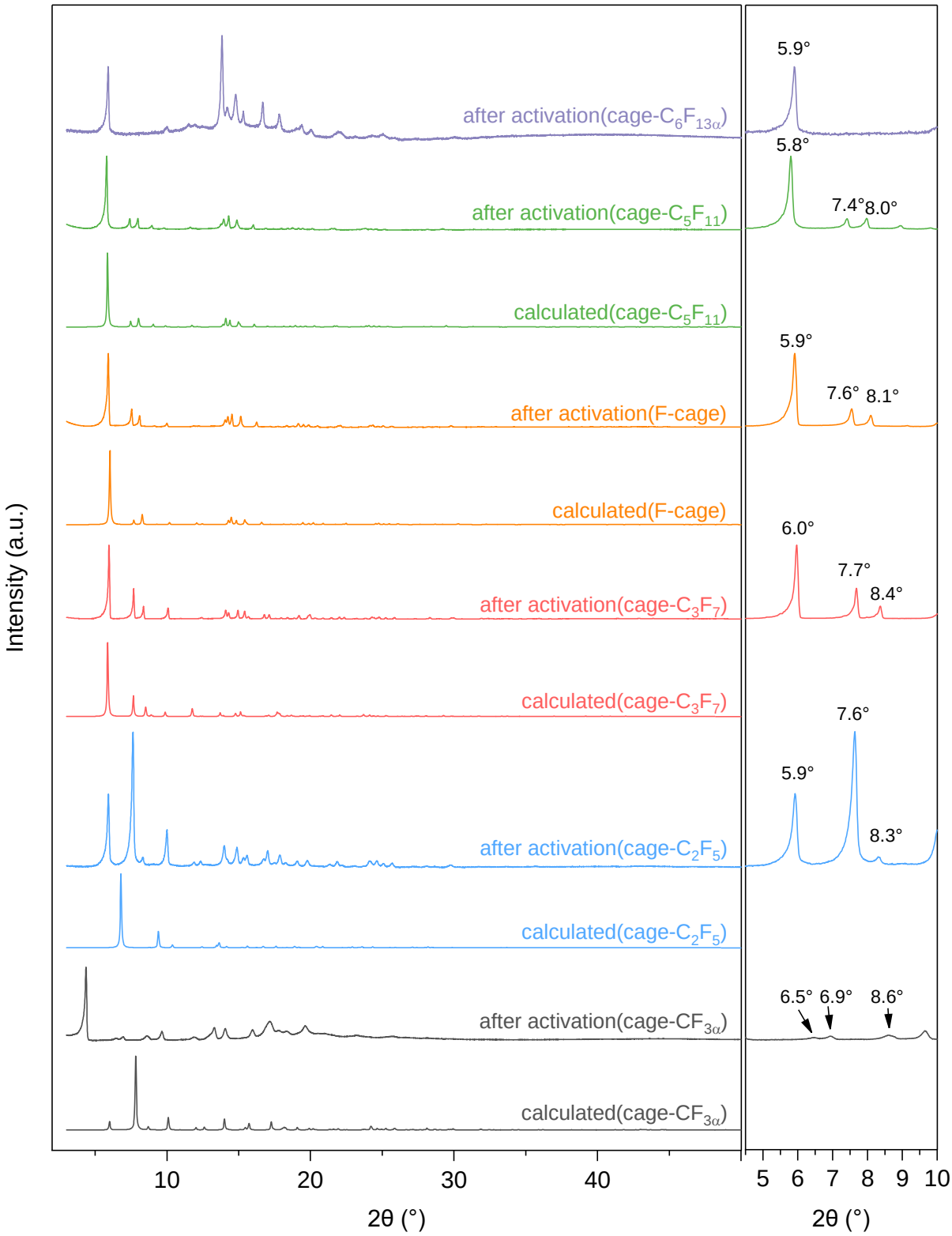

Figure 41. PXRD patterns of fluorinated [2+3] cages after thermal activation for **cage-$CF_{3\alpha}$** (black), **cage-C_2F_5** (blue), **cage-C_3F_7** (red), **F-cage** (yellow), **cage-C_5F_{11}** (blue), and **cage-$C_6F_{13\alpha}$** (purple) and calculated from the single crystal X-ray structure for **cage-$CF_{3\alpha}$** (black), **cage-C_2F_5** (blue), **cage-C_3F_7** (red), **F-cage** (yellow), and **cage-C_5F_{11}** (blue). The right spectrum is zoomed left one after thermal activation. The PXRD measurements were performed under Dr. Sven M. Elbert's help at IMSEAM (Heidelberg University).

The crystallinity of the cages in mother liquor, before and after thermal activation is investigated by optical microscopy and SEM (Figure 40). All cages, except for **cage-**

C_6F_{13}, had a regular rhombohedral shape in the mother liquor, which remained intact before and after thermal activation, although some of the crystals appeared cracked. Notably, more cracks were apparent for **cage-$CF_{3\alpha}$**, indicating that dispersion interactions between the short fluorinated chains were not strong enough to fully maintain original crystallinity for **cage-$CF_{3\alpha}$** upon desolvation and activation.

This observed macroscopic trend is also reflected by PXRD. PXRD results reveal the persistence of the crystallinity of the cages after thermal activation (Figure 41). **cage-C_3F_7**, **F-cage**, and **cage-C_5F_{11}** exhibit diffraction patterns after thermal activation almost identical to simulated ones from corresponding single crystal structures. In contrast, the PXRD peaks of **cage-$CF_{3\alpha}$** and **cage-C_2F_5** differ significantly from their simulated ones. This discrepancy suggests that the structural integrity of **cage-$CF_{3\alpha}$** and **cage-C_2F_5** is not maintained under the evacuation conditions, resulting in a phase transition to another crystalline polymorph. Interestingly, the diffraction pattern of **cage-C_2F_5** closely resemble the simulated patterns of other cages, rather than itself. It is assumed that during desolvation and activation, the two triptycene units of **cage-C_2F_5** rotated reversely to align with the position of those of **cage-C_3F_7**, **F-cage**, and **cage-C_5F_{11}** while maintaining the original packing. As a result, all cages after activation, except for **cage-$CF_{3\alpha}$**, show similar patterns, demonstrating the isomorphism in the desolvated solid state which is necessary to compare the effects of side-chains on gas-sorption properties.

2.1.4. The Influence of the Length of Fluorinated Alkyl on Gas Sorption Properties

In nitrogen sorption experiments at 77 K as well as argon sorption at 87 K, **cage-C_2F_5**, **cage-C_3F_7**, **F-cage** and **cage-C_5F_{11}** were found to have significant amounts of gases adsorbed, resulting in BET-surface areas of 347-921 $m^2\ g^{-1}$ (N_2) and 373-877 $m^2\ g^{-1}$ (Ar) (Figure 42a, b, and d). In contrast, **cage-$CF_{3\alpha}$** and **cage-C_6F_{13}** seem non-porous under these conditions, most likely due to destroyed inter-cage window connectivity in the former and filling of the pore by the excessively long fluoroalkyl in the latter. The nitrogen isotherms of **cage-C_2F_5** and **cage-C_3F_7** are best described as a combination of type I (microporous) and type IV (mesoporous) isotherms,[117] with the desorption isotherm of **cage-C_2F_5** almost retracing the adsorption branch, and the desorption

branch of **cage-C$_3$F$_7$** not tracing the adsorption isotherm, thereby resulting in pronounced hysteresis.

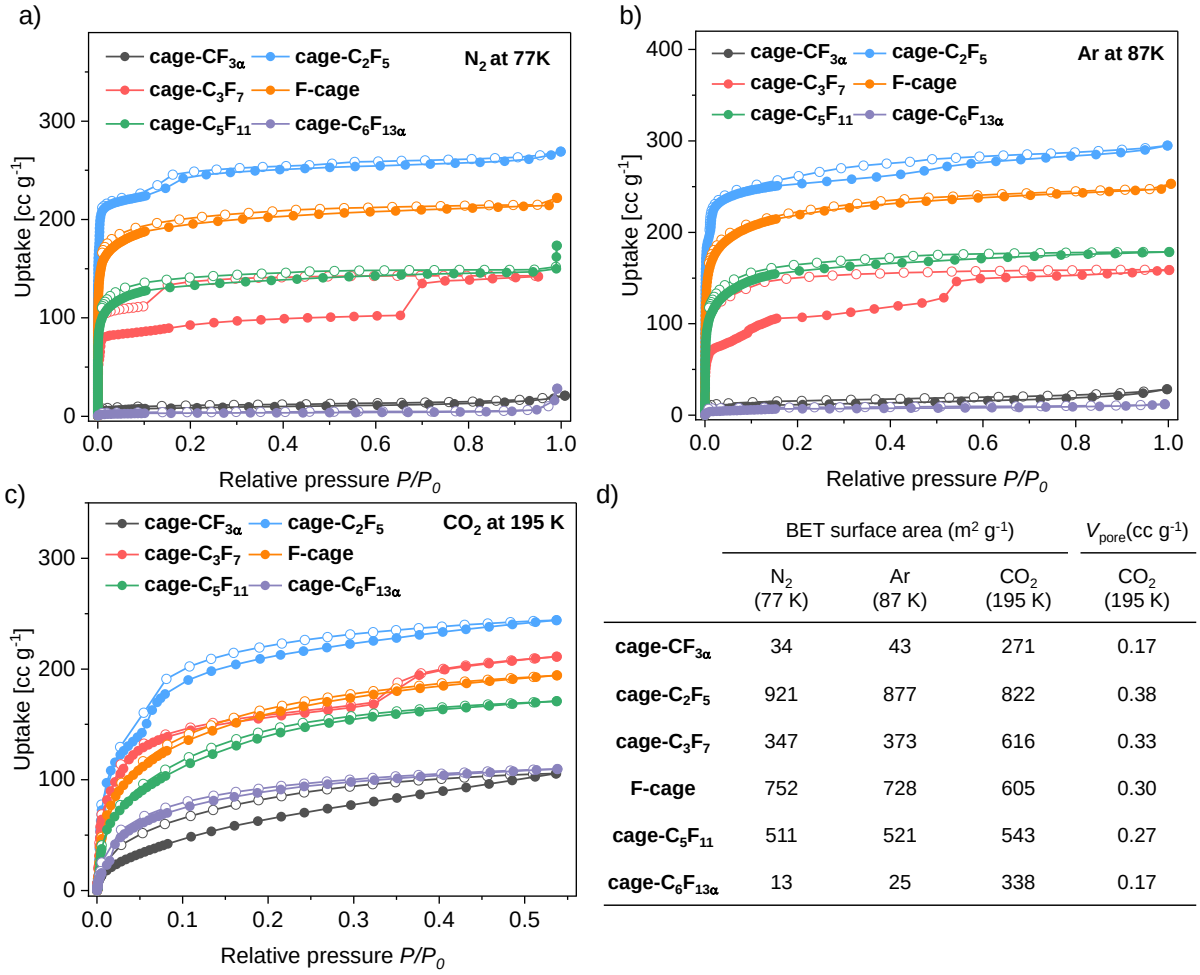

	BET surface area (m^2 g^{-1})			V_{pore}(cc g^{-1})
	N_2 (77 K)	Ar (87 K)	CO_2 (195 K)	CO_2 (195 K)
cage-CF$_{3α}$	34	43	271	0.17
cage-C$_2$F$_5$	921	877	822	0.38
cage-C$_3$F$_7$	347	373	616	0.33
F-cage	752	728	605	0.30
cage-C$_5$F$_{11}$	511	521	543	0.27
cage-C$_6$F$_{13α}$	13	25	338	0.17

Figure 42. (a) Nitrogen sorption isotherms at 77 K; (b) argon sorption isotherms at 87 K; (c) carbon dioxide sorption isotherms at 195 K; of **cage-CF$_{3α}$** (black), **cage-C$_2$F$_5$** (blue), **cage-C$_3$F$_7$** (red), **F-cage** (orange), **cage-C$_5$F$_{11}$** (green), **cage-C$_6$F$_{13}$** (purple): Adsorption: full circles; desorption: empty circles. (d) Table comparing the adsorption properties derived from nitrogen sorption at 77 K, argon sorption at 87 K as well as carbon dioxide and nitrogen sorption at 195 K.

With increasingly larger fluoroalkyl groups, nitrogen gas adsorption of **F-cage** and **cage-C$_5$F$_{11}$** results invariably in Type I isotherms with BET-surface areas of 752 m^2 g^{-1} and 511 m^2 g^{-1}, respectively, which indicates that microporous networks are formed. Argon sorption follows an almost identical trend and similar pattern to that of nitrogen sorption. However, as the side chain length increases, the surface area determined by either nitrogen sorption at 77 K or argon sorption at 87 K does not exhibit a continuous decrease from **cage-C$_2$F$_5$** to **cage-C$_6$F$_{13}$**.

The kinetic dimensions of nitrogen and argon are 3.64 Å and 3.40 Å, respectively.[118] When carbon dioxide, with a kinetic dimension of 3.30 Å,[118] is used as the probe, the observed surface area (ranging from 822 to 338 m^2 g^{-1}) and pore

volume (ranging from 0.38 to 0.17 cc g^{-1}) decrease as the length of the fluoroalkyl substituent increases (Figure 42c-d). The reason behind this distinctive trend remain unclear, but it is assumed that carbon dioxide may access smaller spaces, such as the corner cavities of the pore,[103b] which are not accessible to nitrogen and argon due to their larger kinetic dimensions.

The CO_2 isotherms of **cage-C_2F_5** and **cage-C_3F_7** show a two-step process with a small but noticeable second step observed at 0.05 and 0.32 P/P_0, respectively, further demonstrating the combination of micro and mesoporous networks. In utilizing this analysis method, surfaces that are inaccessible for larger nitrogen and argon molecules can be accessed for **cage-$CF_{3\alpha}$**, thus determining BET-surface areas of 271 $m^2\ g^{-1}$. The reason why **cage-$CF_{3\alpha}$** does not follow the trend observed in **cage-C_2F_5** to **cage-$C_6F_{13\alpha}$** is because **cage-$CF_{3\alpha}$** is not isomorphic with them.

At elevated temperatures of 273 K, the CO_2 uptake at 1 bar is proportional to the calculated surface area and pore volume derived from CO_2 at 195 K (Figure 43-44 and Table 11). Similar adsorption properties at 273 K are also observed in small molecular F-gas adsorption (Figure 43-44 and Table 11). For example, **cage-C_2F_5** adsorbs the most amount of CF_4 at 1.11 mmol g^{-1} and NF_3 at 1.22 mmol g^{-1} at 1 bar while the adsorbed amount initially increases and then decreases from **cage-$CF_{3\alpha}$** to **cage-C_6F_{13}**. For C_2F_6 and SF_6, **cage-C_2F_5** again shows the highest uptake of 1.91 mmol g^{-1} and 2.21 mmol g^{-1} at 1 bar, respectively. However, when adsorbed molecules are larger F-gases, **F-cage** with fluorobutyl side chains demonstrates higher uptake of C_3F_8 (2.09 mmol g^{-1}) and *c*-C_4F_8 (4.14 mmol g^{-1}) at 273 K and 1 bar than **cage-C_2F_5** with fluoroethyl side chains, despite the latter having the highest specific surface area, suggesting high affinity of long fluoroalkyl side chains to big fluorinated guests. On the other hand, too long side chain can fill the pore, reducing pore space. This is evidenced by *c*-C_4F_8 isotherm of **cage-C_5F_{11}**, which shows a steep uptake at low pressure followed by a saturated plateau. Consequently, **cage-C_5F_{11}** with longer fluoroalkyl functionalities than **F-cage** has a lower uptake. All cages have comparable amounts of N_2 and O_2 uptake in a small range of 0.2-0.35 mmol g^{-1}, 0.21-0.44 mmol g^{-1}. These uptakes are obviously lower than those of F-gases under the same condition, suggesting the excellent potential of fluorinated cages for F-gas separation from these gases.

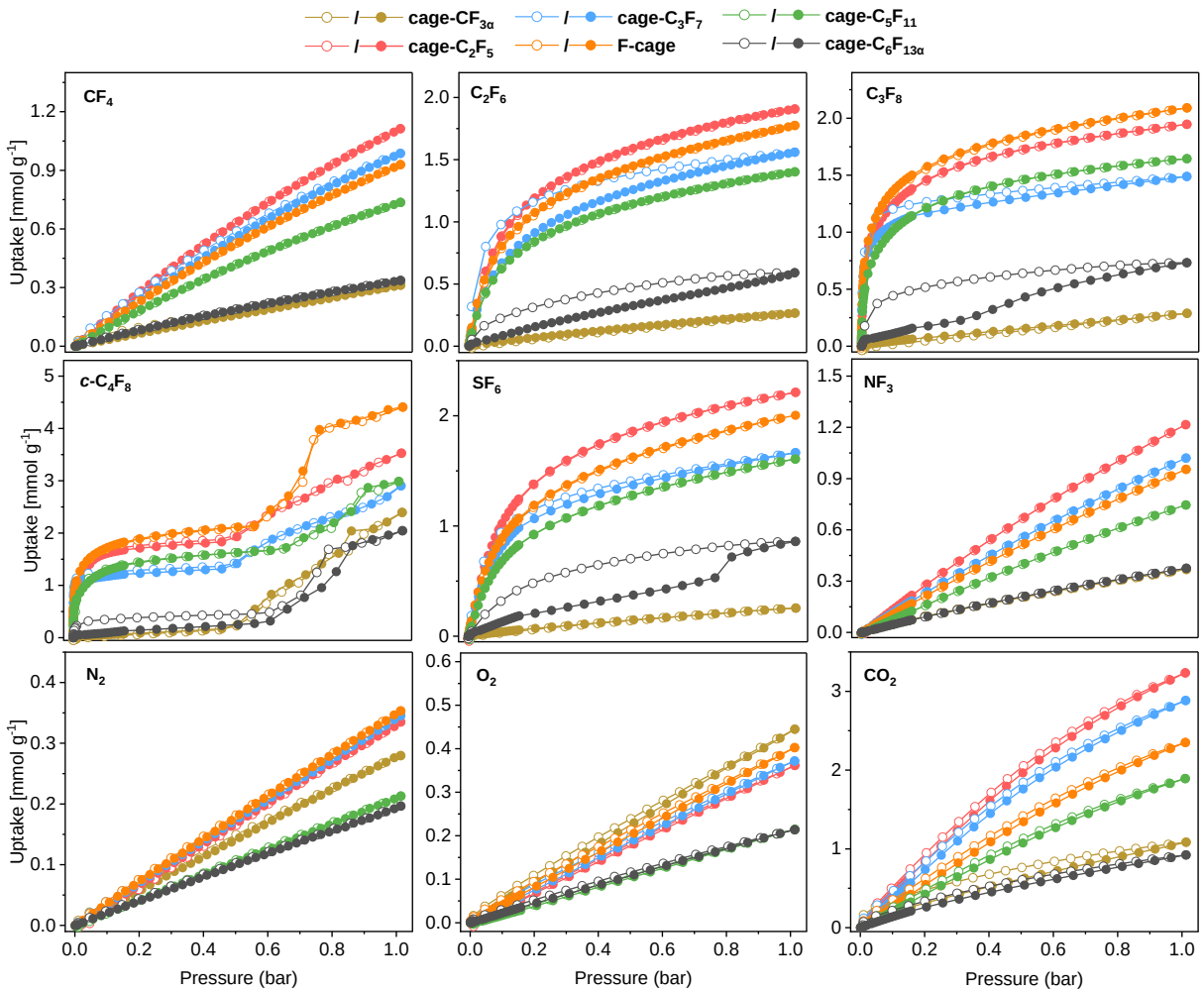

Figure 43. Gas sorption isotherms of **cage-CF$_{3α}$** (brown), **cage-C$_2$F$_5$** (red), **cage-C$_3$F$_7$** (blue), **F-cage** (orange), **cage-C$_5$F$_{11}$** (green), and **cage-C$_6$F$_{13α}$** (black) at 273 K. Note: The isotherm shapes of *c*-C$_4$F$_8$ are related to pore condensation processes.

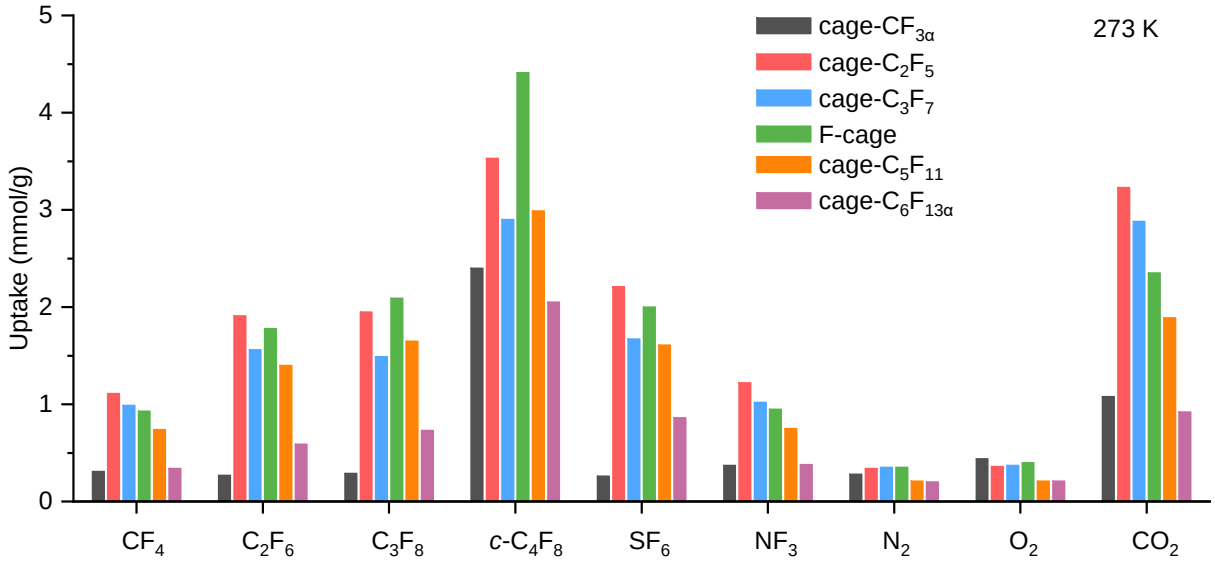

Figure 44. Gas uptake of **cage-CF$_{3α}$** (black), **cage-C$_2$F$_5$** (red), **cage-C$_3$F$_7$** (blue), **F-cage** (green), **cage-C$_5$F$_{11}$** (orange), and **cage-C$_6$F$_{13α}$** (purple) at 273 K and 1 bar.

The adsorption at different temperatures was investigated in more detail. When the temperature increases from 273 K to 283 K, 298 K, and even 313 K, the uptake of the corresponding gases decreases steadily for all cages as anticipated (Figure 43, Table 11 and Appendix, Figure 242-247). Either **cage-$CF_{3\alpha}$** or **cage-C_6F_{13}** has the lowest F-gas uptake among all comparisons. For the other four cages, the uptake of small molecular F-gases CF_4 at 313 K (0.21-0.27 mmol g^{-1}) is approximately 72-76% lower than the uptake at 273 K (0.74-1.11 mmol g^{-1}) and NF_3 at 313 K (0.2-0.31 mmol g^{-1}) is about 73-75% lower than the uptake at 273 K (0.75-1.22 mmol g^{-1}).

Table 11. Summary of gas uptake (mmol g^{-1}) at variable temperature and 1 bar.

	cages	CF_4	C_2F_6	C_3F_8	*c*-C_4F_8	SF_6	NF_3	N_2	O_2	CO_2
273 K	cage-$CF_{3\alpha}$	0.31	0.27	0.29	2.4	0.26	0.37	0.28	0.44	1.08
	cage-C_2F_5	1.11	1.91	1.95	3.53	2.21	1.22	0.34	0.36	3.23
	cage-C_3F_7	0.99	1.56	1.49	2.9	1.67	1.02	0.35	0.37	2.88
	F-cage	0.93	1.78	2.09	4.41	2	0.95	0.35	0.4	2.35
	cage-C_5F_{11}	0.74	1.4	1.65	2.99	1.61	0.75	0.21	0.21	1.89
	cage-$C_6F_{13\alpha}$	0.34	0.59	0.73	2.05	0.86	0.38	0.2	0.21	0.92
283 K	cage-$CF_{3\alpha}$	0.21	0.18	0.21	1.41	0.18	0.26	0.2	0.32	0.86
	cage-C_2F_5	0.84	1.67	1.79	2.81	1.97	0.92	0.25	0.27	2.52
	cage-C_3F_7	0.75	1.46	1.47	2.2	1.53	0.78	0.26	0.28	2.26
	F-cage	0.73	1.57	1.92	3.92	1.77	0.75	0.26	0.3	1.85
	cage-C_5F_{11}	0.56	1.24	1.53	2.09	1.4	0.57	0.15	0.16	1.44
	cage-$C_6F_{13\alpha}$	0.24	0.46	0.7	1.25	0.76	0.27	0.14	0.16	0.72
298 K	cage-$CF_{3\alpha}$	0.1	0.08	0.09	0.13	0.09	0.15	0.11	0.12	0.55
	cage-C_2F_5	0.51	1.27	1.45	1.71	1.53	0.55	0.12	0.14	1.65
	cage-C_3F_7	0.49	1.24	1.37	1.43	1.35	0.51	0.14	0.16	1.49
	F-cage	0.46	1.24	1.64	2.02	1.41	0.45	0.13	0.15	1.17
	cage-C_5F_{11}	0.36	0.98	1.3	1.5	1.11	0.35	0.08	0.08	0.92
	cage-$C_6F_{13\alpha}$	0.13	0.26	0.54	0.6	0.34	0.15	0.06	0.07	0.48
313 K	cage-$CF_{3\alpha}$	-	-	-	-	-	-	-	-	0.3
	cage-C_2F_5	0.27	0.94	1.17	1.45	1.14	0.31	0.01	0.02	1.05
	cage-C_3F_7	0.27	0.98	1.24	1.22	1.09	0.28	0.03	0.04	0.95
	F-cage	0.25	0.94	1.34	1.66	1.06	0.25	0.02	0.02	0.72
	cage-C_5F_{11}	0.21	0.75	1.09	1.28	0.87	0.2	0.01	0.01	0.58
	cage-$C_6F_{13\alpha}$	0.03	0.13	0.43	0.51	0.19	0.04	-	-	0.3

-: no uptake; the red data represents the highest uptake for each gas at each respective temperature.

Similar effects can be observed for the bigger F-gas C_2F_6 (313 K: 0.75-0.98 mmol g^{-1}; 273 K: 1.4-1.91 mmol g^{-1}), SF_6 (313 K: 0.87-1.14 mmol g^{-1}; 273 K: 1.61-2.21 mmol g^{-1}) and C_3F_8 (313 K: 1.09-1.34 mmol g^{-1}; 273 K: 1.49-2.09 mmol g^{-1}), though to a lesser extent. *c*-C_4F_8 shows the highest adsorbed amounts at 1 bar at both 273 K (2.9-4.41 mmol g^{-1}) and 313 K (1.22-1.66 mmol g^{-1}). The adsorption of F-gas in cages with different fluoroalkyl functionalities at higher temperatures follows a trend comparable

to that observed at 273 K. Notably, among these cages, **cage-C_3F_7** exhibits the least decrease in F-gas adsorption with increasing temperature. Thus, **cage-C_3F_7** exhibits the highest uptake of C_2F_6 (0.98 mmol g^{-1}) and greater uptake of C_3F_8 (1.24 mmol g^{-1}) than **cage-C_2F_5** at 313 K, despite having a lower specific surface area than **cage-C_2F_5** (Table 11 and Appendix, Figure 247).

2.1.5. The Influence of the Length of Fluorinated Alkyl on Selective F-gas-Adsorption

The adsorption selectivities of the binary mixtures of F-gas/N_2 were evaluated using IAST and Henry calculations at different temperatures (Figure 45, Table 12, and Appendix, Figure 248). **cage-$CF_{3\alpha}$** and **cage-$C_6F_{13\alpha}$** show significantly lower selective adsorption of any fluorinated gas tested over nitrogen (S_{IAST} and $S_H < 5$) due to to their non-porous structures, as compared with the other four cages. Therefore, more selectivity discussion below is focused on **cage-C_2F_5**, **cage-C_3F_7**, **F-cage**, and **cage-C_5F_{11}**. Selectivities of F-gas/N_2 at 273 K are initially discussed. For small molecular F-gases such as CF_4 and NF_3, the selectivity is low and barely influenced by the gas composition (S_{IAST} $(CF_4/N_2)_{50:50\text{-}1:99}$ = 3.1-4.4, S_{IAST} $(NF_3/N_2)_{50:50\text{-}1:99}$ = 3.0-4.1, all at 1 bar and 273 K). Larger F-gas molecules such as C_2F_6 and SF_6 have higher selectivity and were significantly affected by the F-gas concentration at 273 K and 1 bar. For instance, for a mixture of 50% F-gas and 50% of N_2, the selectivities are S_{IAST} $(C_2F_6/N_2)_{50:50}$ = 16.3-21.4 and S_{IAST} $(SF_6/N_2)_{50:50}$ = 17.7-22.9. When the F-gas concentration decreases to 1%, the selectivities of S_{IAST} $(C_2F_6/N_2)_{1:99}$ and S_{IAST} $(SF_6/N_2)_{1:99}$ increase to 41.7-61.6 and 44.2-55.1, respectively. The most selective echelon among the series studied was observed for the adsorption of C_3F_8 and *c*-C_4F_8, with an IAST selectivity of S_{IAST} $(C_3F_8/N_2)_{1:99}$ = 292-379 and S_{IAST} $(c\text{-}C_4F_8/N_2)_{1:99}$ = 680-937 at 1% F-gas concentration and 1 bar and the Henry selectivities of S_H (C_3F_8/N_2) = 2083-4977 and S_H $(c\text{-}C_4F_8/N_2)$ = 3754-150374 (Table 12). **cage-C_2F_5**, **cage-C_3F_7**, and **cage-C_5F_{11}** have similar trends with **F-cage**, indicating these three cages also have well-defined high-affinity adsorption sites contributing to the bulk selectivity, as discussed **F-cage** (Figure 45 and Appendix, Figure 248).

The incorporation of various long fluoroalkyl functional groups affects the selectivity of these cages (Figure 45, Table 12, and Appendix, Figure 248). For a 10:90 F-gas/N_2 mixture, **cage-C_5F_{11}** appears to be most selective among these cages with

S_{IAST} $(CF_4/N_2)_{10:90}$ = 4.4, S_{IAST} $(C_2F_6/N_2)_{10:90}$ = 40, S_{IAST} $(SF_6/N_2)_{10:90}$ = 39.9, and S_{IAST} $(C_3F_8/N_2)_{10:90}$ = 117 at 273 K and 1 bar. Additionally, although the S_{IAST} (c-C_4F_8/N_2) of **cage-C_5F_{11}** is lower than the highest one (S_{IAST} (c-C_4F_8/N_2) $_{10:90}$ = 247 for **cage-C_3F_7**), its Henry selectivities (S_H = 38486) at hypothetical zero pressure, which reveals the affinity of the most selective adsorption sites, is higher than that of the same cage. For selectivity of NF_3 over nitrogen, S_{IAST} $(NF_3/N_2)_{10:90}$ of **cage-C_5F_{11}** is 3.8, closest to the highest of 4.1 for **cage-C_2F_5**. This relative trend remains constant even when the temperature is elevated.

For the other F-gases including CF_4, C_2F_6, SF_6, C_3F_8, c-C_4F_8, the selectivity changes differently with an increase in temperature. However, at 283 K and 298 K, **cage-C_5F_{11}** is the most selective adsorber of the other F-gases over nitrogen among all cages, while **cage-C_2F_5** becomes the most selective at 313 K (Figure 45 and Table 12).

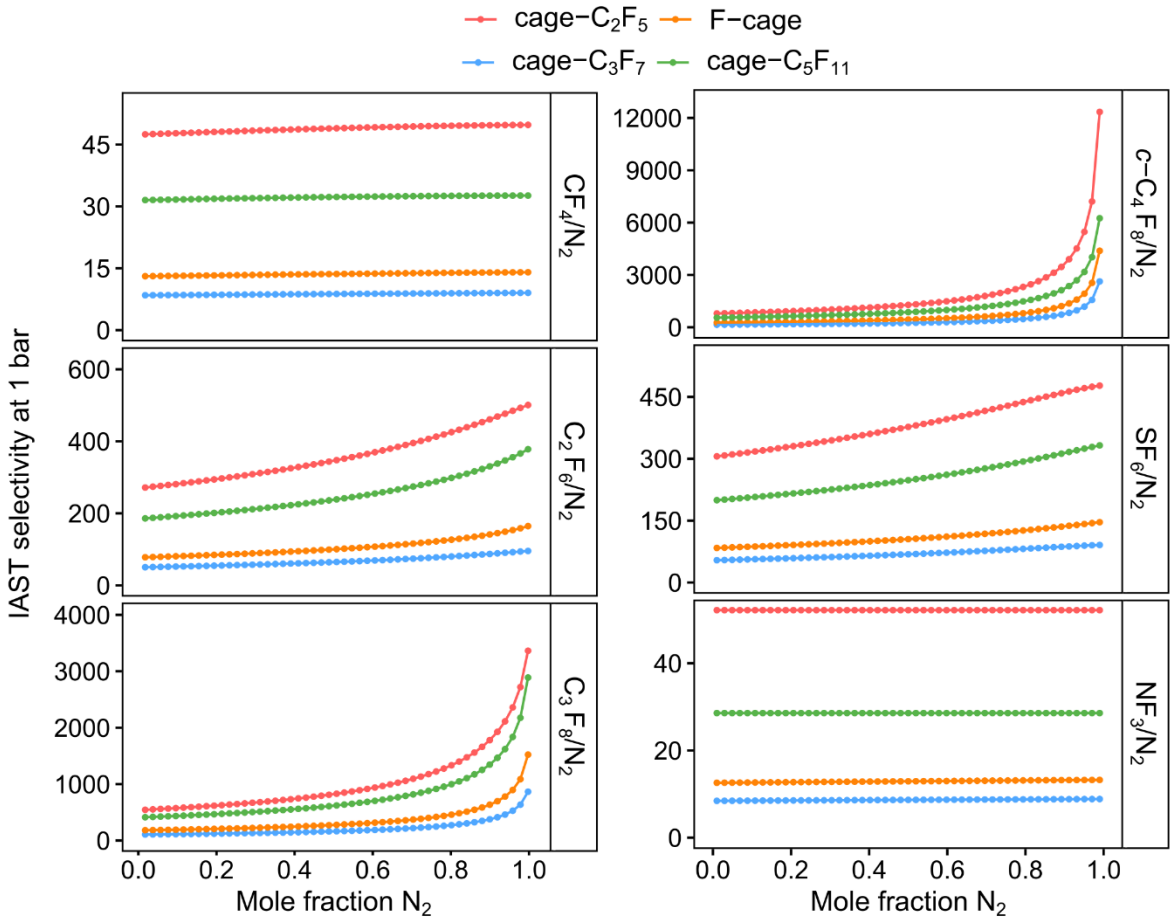

Figure 45. IAST curves (F-gas over nitrogen) of **cage-C_2F_5** (red), **cage-C_3F_7** (blue), **F-cage** (orange), and **cage-C_5F_{11}** (green), at 313 K and 1 bar. Note: The selectivity of F-gas over nitrogen for **cage-$CF_{3\alpha}$** and **cage-$C_6F_{13\alpha}$** can't be calculated because there is no valid nitrogen uptake data available at 313 K.

This shift in selectivity may be attributed to the stronger N_2-phobic effect of **cage-C_2F_5** at elevated temperatures.[119] As a whole, IAST selectivity of F-gas over nitrogen for all cages slightly fluctuates initially with increasing temperature and then sharply rises to its maximum at 313 K, as evidenced by S_{IAST} $(CF_4/N_2)_{1:99}$ = 49.8, S_{IAST} $(C_2F_6/N_2)_{1:99}$ = 501, S_{IAST} $(C_3F_8/N_2)_{1:99}$ = 3364, S_{IAST} $(c\text{-}C_4F_8/N_2)_{1:99}$ = 12345, S_{IAST} $(SF_6/N_2)_{1:99}$ = 477, and S_{IAST} $(NF_3/N_2)_{1:99}$ = 52.2 for **cage-C_2F_5**, while Henry selectivity decreases until 283 K for CF_4 and NF_3, or 298 K for the other F-gases, then increases at 313 K.

For a 10:90 F-gas/N_2 mixture, which is a typical industrially relevant composition,[14b, 43] the selectivities of **cage-C_2F_5** at an elevated temperature of 313 K are as follows: S_{IAST} $(SF_6/N_2)_{10:90}$ = 461 at 1 bar (Table 12). The value surpasses those of other porous materials, including **MIL-100(Fe)** granule (< 30),[32] **CAU-17** (31.0),[33] **HKUST-1a** (< 30),[37] **HKUST-1b** (< 40),[37] **HKUST-1c** (~ 60),[37] **MFI-1** (~60),[39] **MFI-2** (~70),[39] at all 313 K. Additionally, it outperforms **Zn-MOF-74** (~40),[43] **Co-MOF-74** (~30),[43] and **Mg-MOF-74** (~20),[43] at 308 and 318 K. The NF_3/N_2 and CF_4/N_2 IAST selectivities are reported at lower temperature of 298 K. At this temperature, the highest S_{IAST} (NF_3/N_2 and $CF_4/N_2)_{10:90}$ of this group of [2+3] cages is < 6 at 1 bar (Table 12), which is comparable to the reported values for **New-PAF-1** (< 5),[41a] **N-SO_3H** (< 10),[41a] **PAF-4F** and **PAF-8F** (5.35-4.67),[41b] **POPTrB-4F** and **POPTrB-8F** (4.40-7.35),[41c] **α-SiC-CDC1100** (~7).[120] However, they are lower than the S_{IAST} (NF_3/N_2 and $CF_4/N_2)_{10:90}$ = 19.2-30 for **M_3(HCOO)$_6$**,[121] S_{IAST} $(CF_4/N_2)_{10:90}$ = 13.2-18.6 for **C-PVDC**,[28b] ~13 for **PET-K(2)700**[122] and **PC450-K**2,[123] ~12 for **TiC-CDC800H**,[124] and ~11 for **PBPC800**.[125]

Nitrogen and oxygen are two of the primary components of air, and the study of the adsorption selectivity of fluorinated cages with regard to binary mixtures of F-gas/O_2 is important for their potential in the separation of F-gas from other mxitures. Therefore, the adsorption selectivities of F-gas/O_2 were also evaluated using ideal adsorbed solution theory (IAST) and Henry calculations at different temperatures (Figure 46, Table 13, and Appendix, Figure 249).

Note: The IAST and Henry selectivities in this section 2.1.5. were calculated by me and Dr. Anjana Kunhumbadukka Othayoth (OCI, Heidelberg University) together. Images related to this section 2.1.5. were made by Qun Liu (Helmholtz-Centre for Environmental Research-UFZ, Department of Community Ecology, Halle (Saale)) using R package *ggplot2* version 3.4.2 (R Core Team, 2022)

Table 12. Selected IAST and Henry selectivity (F-gas over nitrogen) at variable temperature and 1 bar.[a]

	cages	CF_4/N_2	C_2F_6/N_2	C_3F_8/N_2	$c\text{-}C_4F_8/N_2$	SF_6/N_2	NF_3/N_2
273 K	cage-$CF_{3\alpha}$	1.10/1.10/ 1.10/1.10	1.10/1.10/ 1.11/2.11	1.06/1.06/ 1.06/1.05	1.52/1.51/ 1.51/1.50	1.10/1.10/ 1.10/2.76	1.52/1.54/ 1.55/1.93
	cage-C_2F_5	4.00/4.18/ 4.23/4.39	18.8/34.8/ 51.4/74.0	32.8/91.7/ 292/2261	45.2/151/ 680/30217	21.2/36.5/ 47.3/54.7	4.06/4.13/ 4.14/4.16
	cage-C_3F_7	3.37/3.40/ 3.40/3.40	16.7/27.8/ 41.7/84.8	43.9/111/ 334/2083	77.5/247/ 937/3754	19.7/31.6/ 42.2/54.4	3.36/3.38/ 3.39/3.41
	F-cage	3.10/3.21/ 3.24/3.37	16.3/30.8/ 48.1/85.6	34.4/100/ 350/4977	47.5/163/ 801/150374	17.7/31.5/ 44.5/61.4	2.95/3.00/ 3.02/3.06
	cage-C_5F_{11}	4.19/4.36/ 4.40/4.51	21.4/40.0/ 61.6/96.8	42.3/117/ 379/3863	57.3/185/ 804/38486	22.9/39.9/ 55.1/70.8	3.79/3.81/ 3.81/3.82
	cage-$C_6F_{13\alpha}$	1.98/2.04/ 2.05/2.26	3.07/3.07/ 3.07/3.07	1.32/1.32/ 1.32/1.32	2.96/2.96/ 2.96/2.96	4.13/4.13/ 4.13/4.13	2.21/2.28/ 2.30/2.45
283 K	cage-$CF_{3\alpha}$	1.12/1.13/ 1.13/1.16	1.12/1.13/ 1.14/1.51	1.25/1.27/ 1.28/1.28	1.44/1.44/ 1.44/1.44	1.18/1.20/ 1.20/2.28	1.51/1.54/ 1.54/1.74
	cage-C_2F_5	3.99/4.11/ 4.14/4.23	20.1/33.8/ 44.8/55.9	37.7/99.5/ 280/1295	52.8/166/ 687/30131	22.6/35.4/ 42.4/46.4	4.04/4.07/ 4.07/4.10
	cage-C_3F_7	3.41/3.49/ 3.50/3.53	16.5/27.5/ 36.5/48.9	36.1/104/ 332/1608	46.1/163/ 714/2393	18.6/30.6/ 37.7/42.2	3.37/3.43/ 3.45/3.49
	F-cage	3.18/3.27 /3.29/3.36	17.5/30.0/ 41.5/58.9	39.5/108/ 338/2767	57.3/187/ 836/59278	18.8/30.5/ 39.0/47.8	3.08/3.10/ 3.10/3.11
	cage-C_5F_{11}	4.24/4.34/ 4.36/4.41	23.8/40.9/ 56.9/75.8	50.3/132/ 383/2308	70.0/216/ 864/26324	25.3/40.5/ 50.7/58.0	3.92/3.93/ 3.93/3.93
	cage-$C_6F_{13\alpha}$	1.98/1.99/ 1.99/2.05	4.98/5.46/ 5.72/11.1	5.01/5.20/ 5.26/5.49	7.01/6.34/ 6.23/6.04	5.52/5.12/ 5.05/4.90	2.24/2.24/ 2.25/2.26
298 K	cage-$CF_{3\alpha}$	0.94/0.94/ 0.94/0.90	0.81/0.81/ 0.81/1.07	0.78/0.79/ 0.79/0.71	0.98/0.98/ 0.98/0.89	0.89/0.88/ 0.88/1.19	1.44/1.42/ 1.42/1.34
	cage-C_2F_5	4.73/4.84/ 4.86/4.91	26.9/40.1/ 47.04/51.0	55.6/133/ 299/606	80.8/238/ 896/29832	28.9/38.7/ 41.8/42.8	4.67/4.67/ 4.67/4.67
	cage-C_3F_7	3.91/4.02/ 4.04/4.10	22.6/32.6/ 36.5/38.1	51.5/135/ 360/1040	78.3/263/ 1064/4580	24.2/34.2/ 37.6/38.8	3.75/3.78/ 3.78/3.79
	F-cage	3.93/4.04/ 4.07/4.15	24.1/37.2/ 46.0/53.8	59.9/152/ 404/1537	90.9/277/ 1079/24459	25.7/36.9/ 42.3/45.4	3.70/3.73/ 3.74/3.75
	cage-C_5F_{11}	5.18/5.29/ 5.31/5.36	31.3/47.8/ 58.3/65.4	72.5/174/ 422/1245	106/301/ 1048/14252	33.0/46.2/ 51.8/54.1	4.54/4.54/ 4.54/4.54
	cage-$C_6F_{13\alpha}$	2.26/2.23/ 2.23/2.21	7.10/6.73/ 6.71/6.88	12.7/9.12/ 8.70/8.34	16.8/10.9/ 10.3/9.87	11.5/10.9/ 11.5/17.9	2.62/2.56/ 2.55/2.49
313 K	cage-$CF_{3\alpha}$	-	-	-	-	-	-
	cage-C_2F_5	49.0/49.7/ 49.8/49.8	348/464/ 501/505	829/1836/ 3364/4307	1282/3622/ 12345/117240	377/461/ 477/479	52.2/52.2/ 52.2/52.2
	cage-C_3F_7	8.77/9/ 9.04/9.09	64.9/87.9/ 95.5/97.1	165/390/ 866/1581	250/767/ 2627/8266	68.4/86.9/ 90.9/91.5	8.66/8.83/ 8.86/8.91
	F-cage	13.6/14.0/ 14.0/14.1	101/143/ 164/171	278/658/ 1522/3243	443/1268/ 4385/41475	105/136/ 146/148	12.9/13.2/ 13.2/13.3
	cage-C_5F_{11}	32.3/32.6/ 32.6/32.6	239/334/ 378/388	622/1392/ 2888/4916	864/2216/ 6249/26033	248/314/ 332/335	28.6/28.6/ 28.57/28.6
	cage-$C_6F_{13\alpha}$	-	-	-	-	-	-

[a] $S_{IAST,\ 50:50}/S_{IAST,\ 10:90}/S_{IAST,\ 1:99}/S_{Henry}$; the red and green data represents the highest selectivity of $S_{IAST,\ 50:50}/S_{IAST,\ 10:90}/S_{IAST,\ 1:99}$ and S_{Henry}, respectively, for each gas at each respective temperature. - : The selectivity of F-gas over nitrogen for **cage-$CF_{3\alpha}$** and **cage-$C_6F_{13\alpha}$** can't be calculated because there is no valid nitrogen uptake data available at 313 K.

There are many similarities between $S_{F\text{-}gas/N_2}$ with $S_{F\text{-}gas/O_2}$. **cage-$CF_{3\alpha}$** and **cage-$C_6F_{13\alpha}$** demonstrate again markedly lower selective adsorption of any fluorinated gas tested over oxygen (S_{IAST} and $S_H < 12$), of the six cages tested, with selectivities barely influenced by the gas composition. Therefore, further selectivity discussion is also focused on the other four cages. For these cages, Henry selectivities follow the same trend (CF_4, NF_3 < C_2F_6, SF_6 < C_3F_8 < *c*-C_4F_8) as the IAST selectivities at 1 bar (Table 13). Larger F-gas molecules, more significantly their selectivities increase as the F-gas concentration decreases at 1 bar. Notably, **cage-C_5F_{11}** has outstanding F-gas selective adsorption properties, compared with the other cages. At 273 K, it adsorbs selectively CF_4, C_2F_6, SF_6, and NF_3 over oxygen with highest IAST selectivity of S_{IAST} $(CF_4/O_2)_{1:99} = 4.4$, S_{IAST} $(C_2F_6/O_2)_{1:99} = 61.9$, and S_{IAST} $(SF_6/O_2)_{1:99} = 55.4$ and Henry selectivity of S_H $(CF_4/O_2) = 4.5$, S_H $(C_2F_6/O_2) = 97.2$, and S_H $(SF_6/O_2) = 71.1$, and nearly highest selectivity of both S_{IAST} $(NF_3/O_2)_{1:99}$ and S_H (NF_3/O_2) of 3.8.

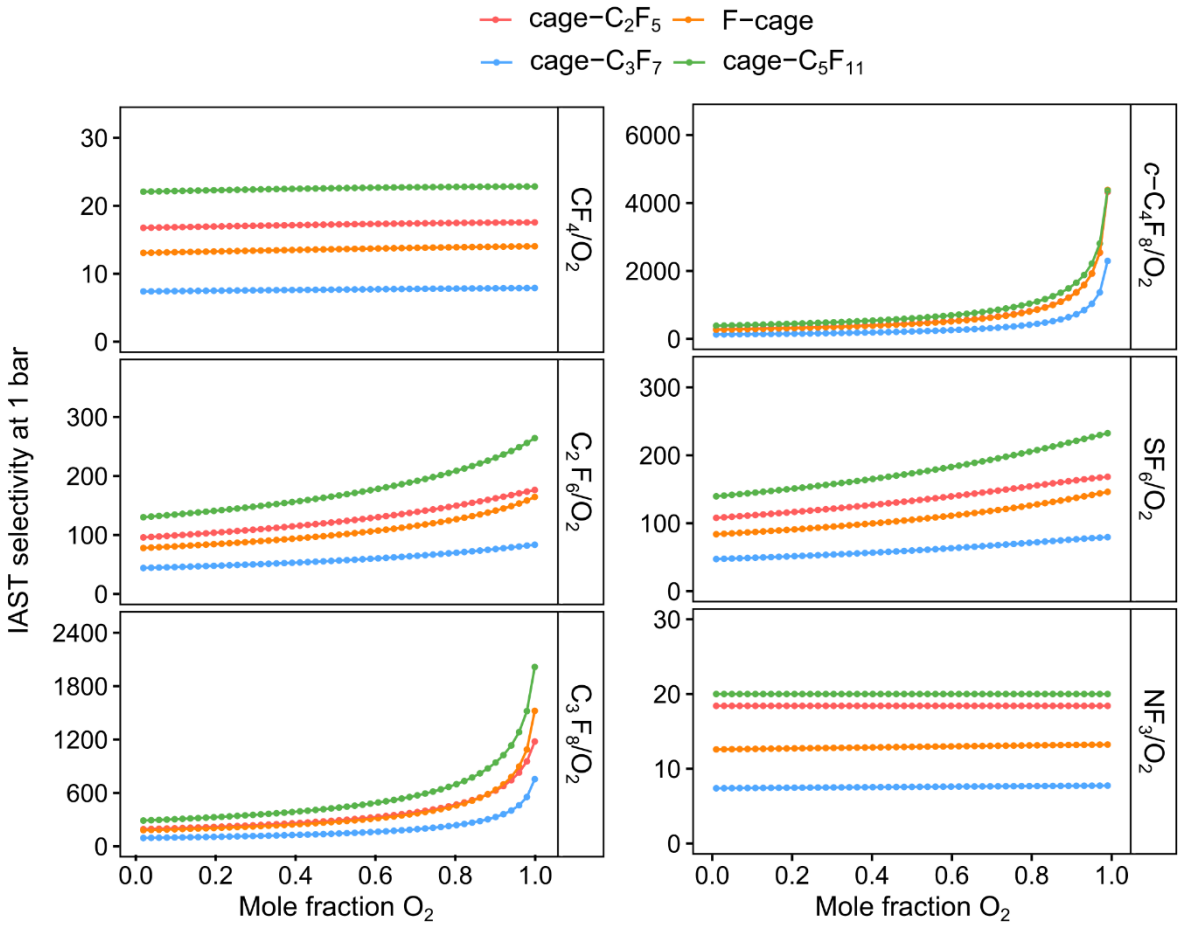

Figure 46. IAST curves (F-gas over oxygen) of **cage-C_2F_5** (red), **cage-C_3F_7** (blue), **F-cage** (orange), and **cage-C_5F_{11}** (green) at 313 K and 1 bar. The selectivity of F-gas over oxygen for **cage-$CF_{3\alpha}$** and **cage-$C_6F_{13\alpha}$** can't be calculated because there is no valid oxygen uptake data available at 313 K.

Table 13. Selected IAST and Henry selectivity (F-gas over oxygen) at variable temperature and 1 bar.[a]

	cages	CF_4/O_2	C_2F_6/O_2	C_3F_8/O_2	$c\text{-}C_4F_8/O_2$	SF_6/O_2	NF_3/O_2
273 K	cage-$CF_{3\alpha}$	0.69/0.69/ 0.69/0.67	0.66/0.64/ 0.64/1.28	0.66/0.66/ 0.66/0.64	0.95/0.95/ 0.95/0.91	0.65/0.63/ 0.62/1.68	0.92/0.92/ 0.91/1.17
	cage-C_2F_5	3.76/3.93/ 3.97/4.13	17.7/32.6/ 47.9/69.6	30.8/86.0/ 272/2127	42.4/141/ 636/28425	19.9/34.2/ 44.3/51.4	3.82/3.88/ 3.89/3.91
	cage-C_3F_7	3.09/3.16/ 3.17/3.21	13.2/24.4/ 38.0/80.1	26.6/80.9/ 287/1966	36.8/141/ 708/3542	15.1/27.6/ 38.7/51.4	3.07/3.14/ 3.16/3.22
	F-cage	2.75/2.81/ 2.83/2.93	16.4/27.9/ 41.4/74.5	43.6/106/ 320/4331	73.8/204/ 809/130872	18.0/28.7/ 38.6/53.5	2.62/2.64/ 2.64/2.66
	cage-C_5F_{11}	4.21/4.38/ 4.42/4.53	21.5/40.2/ 61.9/97.2	42.5/118/ 381/3882	57.6/186/ 808/38671	23.0/40.1/ 55.4/71.1	3.81/3.83/ 3.83/3.83
	cage-$C_6F_{13\alpha}$	1.80/1.84/ 1.85/1.98	2.82/2.79/ 2.78/2.68	3.74/3.68/ 3.66/3.54	2.73/2.69/ 2.69/2.59	3.83/3.76/ 3.75/3.62	2.02/2.06/ 2.07/2.15
283 K	cage-$CF_{3\alpha}$	0.66/0.66/ 0.65/0.61	0.64/0.62/ 0.62/0.80	0.71/0.69/ 0.68/0.82	0.87/0.88/ 0.88/0.76	0.67/0.65/ 0.64/1.21	0.89/0.88/ 0.88/0.92
	cage-C_2F_5	3.74/3.85/ 3.88/3.97	18.8/31.6/ 41.7/52.4	35.4/93.0/ 261/1215	49.5/155/ 641/28270	21.2/33.1/ 39.6/43.5	3.79/3.82/ 3.82/3.83
	cage-C_3F_7	3.06/3.07/ 3.07/3.02	16.2/25.0/ 31.8/41.8	39.6/105/ 304/1376	53.2/176/ 692/2048	18.5/28.1/ 33.1/36.1	3.02/3.02/ 3.02/2.99
	F-cage	2.75/2.76/ 2.77/2.79	18.5/26.9/ 34.6/48.9	62.9/125/ 306/2297	134/292/ 889/49205	20.3/27.4/ 32.7/39.7	2.65/2.63/ 2.62/2.58
	cage-C_5F_{11}	4.10/4.20/ 4.22/4.26	23.0/39.5/ 54.8/73.3	48.7/128/ 369/2234	67.7/209/ 834/25475	24.5/39.2/ 49.0/56.2	3.80/3.80/ 3.80/3.80
	cage-$C_6F_{13\alpha}$	1.71/1.72/ 1.73/1.79	4.14/4.65/ 4.87/9.64	5.81/5.6/ 5.55/5.37	5.72/5.49/ 5.44/5.27	4.59/4.44/ 4.41/4.27	1.93/1.95/ 1.95/1.97
298 K	cage-$CF_{3\alpha}$	0.82/0.81/ 0.81/0.78	0.71/0.70/ 0.70/0.93	0.69/0.70/ 0.70/0.62	0.87/0.87/ 0.87/0.77	0.77/0.76/ 0.76/1.03	1.25/1.25/ 1.25/1.16
	cage-C_2F_5	4.23/4.33/ 4.35/4.40	24.0/35.7/ 41.9/45.7	49.7/119/ 265/543	72.3/212/ 797/26716	25.9/34.6/ 37.3/38.3	0.42/0.42/ 0.42/0.42
	cage-C_3F_7	3.56/3.65/ 3.67/3.74	20.6/29.6/ 33.1/34.7	46.9/122/ 325/948	71.2/239/ 965/4172	22.0/31.0/ 34.1/35.3	3.41/3.44/ 3.44/3.45
	F-cage	3.38/3.47/ 3.49/3.58	20.7/31.8/ 39.1/46.3	51.5/130/ 343/1323	78.2/238/ 922/21057	22.1/31.6/ 36.1/39.1	3.18/3.21/ 3.22/3.23
	cage-C_5F_{11}	5.05/5.16/ 5.18/5.22	30.5/46.6/ 56.8/63.8	70.7/170/ 411/1214	103/294/ 1021/13896	32.1/45.0/ 50.4/52.8	4.43/4.43/ 4.43/4.43
	cage-$C_6F_{13\alpha}$	1.96/1.95/ 1.95/1.81	5.70/5.85/ 5.86/5.66	9.17/7.96/ 7.66/6.86	11.2/9.49/ 9.07/8.11	8.42/9.36/ 9.90/14.7	2.28/2.24/ 2.23/2.05
313 K	cage-$CF_{3\alpha}$	-	-	-	-	-	-
	cage-C_2F_5	17.3/17.5/ 17.6/17.6	123/163/ 176/178	292/646/ 1178/1520	452/1275/ 4327/41379	133/162/ 168/169	18.4/18.4/ 18.4/18.4
	cage-C_3F_7	7.67/7.87/ 7.90/7.95	56.7/76.8/ 83.5/85.0	144/341/ 754/1383	219/671/ 2294/7233	59.8/76.0/ 79.5/80.0	7.58/7.72/ 7.75/7.79
	F-cage	13.6/14.0/ 14.0/14.1	101/143/ 164/171	278/658/ 1522/3243	443/1268/ 4385/41475	105/136/ 146/148	12.9/13.2/ 13.2/13.3
	cage-C_5F_{11}	22.6/22.8/ 22.8/22.8	167/233/ 264/272	435/973/ 2015/3441	605/1550/ 4363/18223	174/220/ 233/234	20.0/20.0/ 20.0/20.0
	Cage-$C_6F_{13\alpha}$	-	-	-	-	-	-

[a] $S_{IAST,\ 50:50}/S_{IAST,\ 10:90}/S_{IAST,\ 1:99}/S_{Henry}$; the red and green data represents the highest selectivity of $S_{IAST,\ 50:50}/S_{IAST,\ 10:90}/S_{IAST,\ 1:99}$ and S_{Henry}, respectively, for each gas at each respective temperature. - : The selectivity of F-gas over oxygen for **cage-$CF_{3\alpha}$** and **cage-$C_6F_{13\alpha}$** can't be calculated because there is no valid oxygen uptake data available at 313 K.

For C_3F_8 and *c*-C_4F_8, its IAST selectivity is comparable to the highest ones, with S_{IAST} (C_3F_8/O_2)$_{10:90}$ = 118 vs 106, S_{IAST} (*c*-C_4F_8)$_{10:90}$ = 186 vs 204 and S_{IAST} (C_3F_8/O_2)$_{1:99}$ = 381 vs 320, S_{IAST} (*c*-C_4F_8)$_{1:99}$ = 808 vs 809 (**cage-C_5F_{11}** vs **F-cage at** 1 bar), and its Henry selectivity of S_H (C_3F_8/O_2) = 3882, S_H (*c*-C_4F_8/O_2) = 38671, is the second highest (Table 13).

With increasing temperature, the IAST selectivity barely changes for CF_4 and NF_3, or slightly increases first for the other F-gases, before sharply reaching its highest value at 313 K with the selectivities being 4.2-5.3 times higher at 313 K compared to those at 273 K, while Henry selectivity decreases until 283 K for CF_4 and NF_3, or 298 K for the other F-gases, before increasing again (Figure 46, Table 13, and Appendix, Figure 249). With increasing temperature to 283 K, 298 K, and even 313 K, the relative trend of all cages still remains the same, with **cage-C_5F_{11}** maintaining top selectivity among the tested cages, with S_{IAST} (CF_4/O_2)$_{1:99}$ = 22.8, S_{IAST} (C_2F_6/O_2)$_{1:99}$ = 264, S_{IAST} (C_3F_8/O_2)$_{1:99}$ = 2015, S_{IAST} (*c*-C_4F_8/O_2) $_{1:99}$ = 4363, S_{IAST} (SF_6/ O_2)$_{1:99}$ = 233, and S_{IAST} (NF_3/O_2)$_{1:99}$ = 20 at 313 K and 1 bar (Figure 46 and Table 13). There are only two PAF materials, **New-PAF-1** and **N-SO_3H**, reported for SF_6 or CF_4, NF_3/O_2 selective adsorption.[41a] At 298 K and 1 bar, with a 10% SF_6 concentration, **cage-C_5F_{11}** achieves the highest SF_6/O_2 adsorption selectivity, which is 45 (Table 13). This value surpasses the selectivity of **New-PAF-1** (< 40) but falls short of a similar framework material **N-SO_3H** (69.9), under the same conditions. The CF_4/O_2 and NF_3/O_2 adsorption selectivity of **cage-C_5F_{11}** remains relatively low at 298 K and 1 bar, similar to these two materials (< 10).

To the best of my knowledge, there has been no report about the selective adsorption of F-gas over CO_2. The adsorption selectivities of the binary mixtures of F-gas/CO_2 were also evaluated using IAST and Henry calculations at different temperatures (Figure 47, Table 14, and Appendix, Figure 250). The overall selectivity of F-gas over carbon dioxide decreases by 1-2 order of magnitude, compared to its selectivity over nitrogen or oxygen. This decrease can be attributed to the fact that perfluoroalkyl side chains can serve as strong binding sites for carbon dioxide, as demonstrated in previous research.[49d] **cage-$CF_{3\alpha}$** and **cage-$C_6F_{13\alpha}$** show no selective adsorption of any fluorinated gas tested over carbon dioxide and all cages show no selective adsorption of CF_4 and NF_3 over carbon dioxide. For **cage-C_2F_5**, **cage-C_3F_7**, **F-cage** and **cage-C_5F_{11}**, Henry selectivity follow the same trend again (C_2F_6, SF_6 < C_3F_8 < *c*-C_4F_8) as the IAST selectivity at 1 bar. For the same cages, the selectivity of

these four F-gases over carbon dioxide increases to a lesser degree than over nitrogen and oxygen as the F-gas concentration decreases at 1 bar. At 273 K, **F-cage** has the highest selectivity of overall F-gas over carbon dioxide with S_{IAST} $(C_2F_6/CO_2)_{1:99}$ = 2.6, S_H (C_2F_6/CO_2) = 11.2; S_{IAST} $(C_3F_8/CO_2)_{1:99}$ = 20.8, S_H (C_3F_8/CO_2) = 650; S_{IAST} $(c\text{-}C_4F_8/CO_2)_{1:99}$ = 72.2, S_H $(c\text{-}C_4F_8/CO_2)$ = 19631; S_{IAST} $(SF_6/CO_2)_{1:99}$ = 2.9, S_H (SF_6/CO_2) = 8.0 (Table 14). **cage-C_5F_{11}** ranks second to it. In the selective adsorption experiments for the binary mixtures of F-gas/CO_2, CO_2 could compete with F-gas about binding sites of fluoroalkyl side chains. As the chain length increases, the increase in CO_2 binding affinity surpasses the increase in F-gas binding affinity, making **F-cage** the most selective for overall F-gas over carbon dioxide instead of **cage-C_5F_{11}**. With the increasing temperature up to 283 K, 298 K, and even 313 K, there is a certain degree of decrease in overall Henry selectivity, but only a slight change in overall IAST selectivity. Nevertheless, **F-cage** retains its position as the most selective cage.

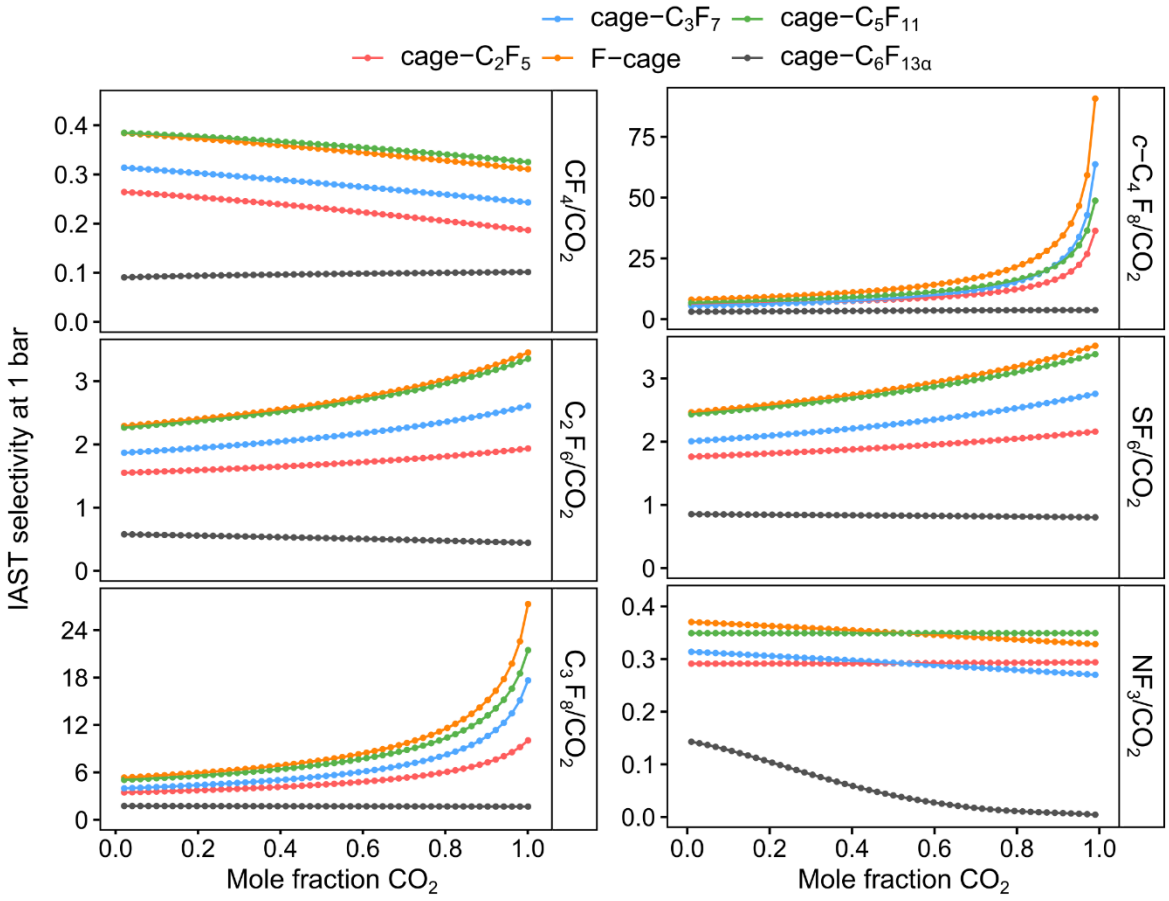

Figure 47. IAST curves (F-gas over carbon dioxide) of **cage-C_2F_5** (red), **cage-C_3F_7** (blue), **F-cage** (orange), **cage-C_5F_{11}** (green), **cage-$C_6F_{13\alpha}$** (black) at 313 K and 1 bar. The selectivity of F-gas over carbon dioxide for **cage-$CF_{3\alpha}$** can't be calculated because there is no valid F-gas uptake data available at 313 K.

Table 14. Selected IAST and Henry selectivity (F-gas over carbon dioxide) at variable temperature and 1 bar.[a]

	cages	CF_4/CO_2	C_2F_6/CO_2	C_3F_8/CO_2	$c\text{-}C_4F_8/CO_2$	SF_6/CO_2	NF_3/CO_2
273 K	cage-$CF_{3\alpha}$	0.27/0.27/ 0.27/0.27	0.23/0.21/ 0.20/0.51	0.26/0.26/ 0.26/0.26	0.37/0.37/ 0.37/0.37	0.22/0.19/ 0.19/0.67	0.32/0.30/ 0.29/0.47
	cage-C_2F_5	0.27/0.25/ 0.24/0.35	1.25/1.35/ 1.38/5.84	2.68/4.28/ 5.92/179	4.63/9.75/ 21.1/2386	1.51/1.69/ 1.76/4.32	0.29/0.26/ 0.25/0.33
	cage-C_3F_7	0.26/0.22/ 0.21/0.32	1.05/1.07/ 1.07/8.07	2.75/4.85/ 7.60/198	4.93/13.2/ 36.4/357	1.26/1.36/ 1.40/5.18	0.28/0.26/ 0.26/0.32
	F-cage	0.35/0.33/ 0.32/0.44	1.96/2.37/ 2.58/11.2	6.47/11.4/ 20.8/650	13.8/27.9/ 72.2/19631	2.20/2.70/ 2.90/8.02	0.36/0.34/ 0.34/0.40
	cage-C_5F_{11}	0.35/0.32/ 0.44/0.44	1.88/2.23/ 2.41/9.49	5.64/9.07/ 14.6/379	11.4/20.5/ 44.0/3773	2.10/2.48/ 2.66/6.94	0.34/0.30/ 0.29/0.37
	cage-$C_6F_{13\alpha}$	0.27/0.26/ 0.26/0.22	0.51/0.53/ 0.54/0.30	0.68/0.70/ 0.71/0.40	0.49/0.51/ 0.52/0.29	0.70/0.72/ 0.72/0.41	0.31/0.30/ 0.3/0.24
283 K	cage-$CF_{3\alpha}$	0.21/0.16/ 0.15/0.25	0.19/0.15/ 0.15/0.33	0.20/0.14/ 0.13/0.34	0.32/0.32/ 0.32/0.32	0.20/0.17/ 0.16/0.50	0.29/0.26/ 0.25/0.38
	cage-C_2F_5	0.29/0.26/ 0.26/0.35	1.42/1.58/ 1.64/4.64	3.15/5.26/ 7.56/108	5.29/11.2/ 24.5/2503	1.70/1.94/ 2.02/3.85	0.31/0.27/ 0.26/0.34
	cage-C_3F_7	0.29/0.24/ 0.24/0.35	1.36/1.48/ 1.53/4.83	3.92/7.05/ 11.7/159	6.07/14.5/ 36.6/237	1.58/1.80/ 1.89/4.17	0.30/0.29/ 0.28/0.35
	F-cage	0.38/0.36/ 0.35/0.45	2.09/2.55/ 2.77/7.83	7.09/12.1/ 21.8/368	16.7/30.9/ 75.7/7874	2.32/2.81/ 3.04/6.35	0.38/0.36/ 0.36/0.41
	cage-C_5F_{11}	0.39/0.36/ 0.35/0.45	2.04/2.60/ 2.86/7.73	4.55/9.44/ 17.5/235	6.48/16.9/ 48.9/2684	2.23/2.82/ 3.08/5.92	0.37/0.33/ 0.31/0.40
	cage-$C_6F_{13\alpha}$	0.27/0.26/ 0.25/0.25	0.63/0.62/ 0.62/1.34	1.01/1.01/ 1.01/0.75	1.05/1.04/ 1.04/0.73	0.84/0.84/ 0.85/0.59	0.30/0.28/ 0.28/0.27
298 K	cage-$CF_{3\alpha}$	0.07/0.03/ 0.02/0.10	0.09/0.08/ 0.07/0.12	0.14/0.15/ 0.15/0.08	0.17/0.18/ 0.18/0.10	0.10/0.09/ 0.09/0.13	0.18/0.15/ 0.14/0.15
	cage-C_2F_5	0.28/0.26/ 0.25/0.33	1.57/1.76/ 1.83/3.47	3.65/6.15/ 8.65/41.2	6.05/12.9/ 28.6/2027	1.78/1.99/ 2.05/2.91	0.32/0.32/ 0.33/0.32
	cage-C_3F_7	0.32/0.29/ 0.28/0.38	1.85/2.14/ 2.25/3.57	5.51/9.48/ 15.6/97.5	13.0/27.0/ 65.0/429	2.02/2.35/ 2.48/3.63	0.32/0.30/ 0.29/0.36
	F-cage	0.40/0.37/ 0.37/0.46	2.48/2.95/ 3.18/5.97	12.8/16.0/ 24.9/170	48.9/52.9/ 88.0/2713	2.75/3.17/ 3.38/5.03	0.38/0.36/ 0.35/0.42
	cage-C_5F_{11}	0.40/0.38/ 0.37/0.46	2.33/2.90/ 3.13/2.33	5.62/11.2/ 19.1/106	8.36/20.9/ 54.7/1212	2.51/3.05/ 3.25/4.60	0.39/0.39/ 0.39/0.39
	cage-$C_6F_{13\alpha}$	0.21/0.18/ 0.17/0.24	0.58/0.54/ 0.53/0.73	1.10/1.10/ 1.10/0.89	1.32/1.30/ 1.30/1.05	0.85/0.83/ 0.83/1.91	0.26/0.23/ 0.23/0.27
313 K	cage-$CF_{3\alpha}$	-	-	-	-	-	-
	cage-C_2F_5	0.23/0.20/ 0.19/0.28	1.69/1.87/ 1.94/2.82	4.48/7.41/ 10.0/24.0	8.12/16.8/ 36.4/654	1.91/2.10/ 2.16/2.67	0.29/0.29/ 0.29/0.29
	cage-C_3F_7	0.28/0.25/ 0.24/0.34	2.12/2.48/ 2.61/3.61	5.55/10.9/ 17.6/58.8	8.60/23.2/ 63.7/307	2.28/2.64/ 2.76/3.40	0.29/0.27/ 0.27/0.33
	F-cage	0.35/0.32/ 0.31/0.41	2.66/3.23/ 3.45/5.04	7.61/15.6/ 27.3/95.5	12.4/32.2/ 90.7/1222	2.83/3.35/ 3.52/4.36	0.35/0.33/ 0.33/0.39
	cage-C_5F_{11}	0.36/0.33/ 0.33/0.40	2.62/3.16/ 3.35/4.74	7.05/13.6/ 21.5/60.1	9.94/22.6/ 48.8/318	2.78/3.24/ 3.38/4.09	0.35/0.35/ 0.35/0.35
	cage-$C_6F_{13\alpha}$	0.10/0.10/ 0.10/0.08	0.52/0.46/ 0.44/0.72	1.71/1.67/ 1.67/1.39	3.47/3.71/ 3.71/3.16	0.83/0.81/ 0.80/1.23	0.04/0.01/ 0.004/0.14

[a] $S_{IAST,\ 50:50}/S_{IAST,\ 10:90}/S_{IAST,\ 1:99}/S_{Henry}$; the red and green data represents the highest selectivity of $S_{IAST,\ 50:50}/S_{IAST,\ 10:90}/S_{IAST,\ 1:99}$ and S_{Henry}, respectively, for each gas at each respective temperature. - : The selectivity of F-gas over carbon dioxide for **cage-$CF_{3\alpha}$** can't be calculated because there is no valid F-gas uptake data available at 313 K.

2.1.6. Hirshfeld and SCXRD Analysis of C_3F_8-Loaded Cage

Similar to **F-cage**, single crystals of **cage-C_5F_{11}** were activated and exposed to an atmosphere of C_3F_8, followed by SCXRD analyses to gain a deeper understanding of the interactions between the adsorbed F-gas and the cage. The highly disordered residual electron density of 1.3 C_3F_8 (121 electrons per cage in average) was then observed inside the cage voids. Hirschfeld surface analysis was performed based on the residual electron density inside the cavity treated as a fluorine cluster (Figure 48). The results indicate that there are multiple F···F interactions between the residual electron density and the CF2-unit at C2 of the perfluoropentyl side chains, with a distance of $d1_{F\cdots F}$ = 1.8 Å, and between the CF2-unit at C2 and C3 of the perfluoropentyl side chains, both with a distance of $d2_{F\cdots F}$ = 3.0 Å. These distances are within the range of attractive F···F-interactions found in single crystal X-ray structures.[96b, 97b, 108c, 126]

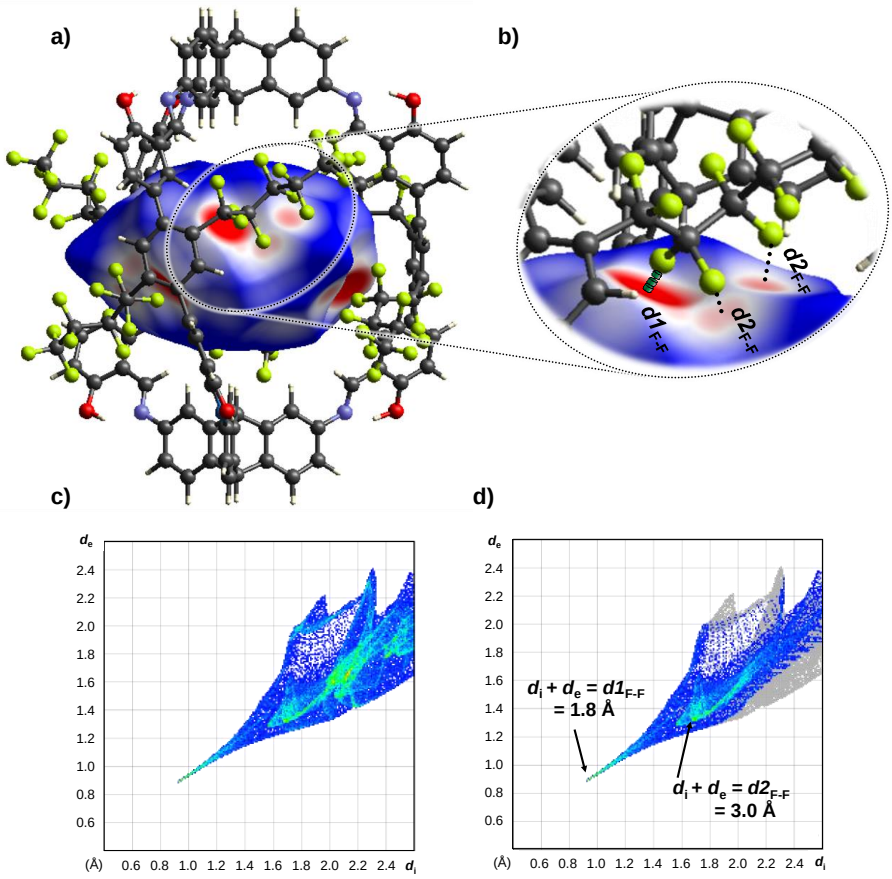

Figure 48. Hirshfeld surface analyses the single X-ray structure of C_3F_8 loaded **cage-C_5F_{11}**. The residual electron density >0.20 $e^- \cdot Å^{-3}$ was replaced by fluorine dummy atoms and the corresponding Hirshfeld surface d_{norm} (isovalue: 0.5; quality: high) was plotted with a rescaled surface property of -0.5 to 1.0. Red areas represent short d_i-d_e distances; blue areas long d_i-d_e distances. a) Side view on one cage molecule filled with C_3F_8. b) Zoom-in on the CF_2-F interactions. c) Hirshfeld fingerprint plot taking all elements into account. d) Hirshfeld fingerprint plot taking only fluorine atoms into account. The highlighted spot corresponds to the short CF_2-F distance depicted in a) and b).

By same approach, single X-ray structure of C_3F_8 loaded **cage-C_3F_7** was obtained. Three C_3F_8 molecules have been observed clearly inside the cage voids (Figure 49). The shortest distance of F···F is 2.9 Å, longer than that of **F-cage** (2.8 Å) and **cage-C_5F_{11}** (1.8 Å). This observation also provides a rational explanation for the higher F-gas selectivity of long fluoroalkyl-functionalized **F-cage** and **cage-C_5F_{11}** than **cage-C_3F_7** in most selectivity investigations of F-gas/N_2, F-gas/O_2, and F-gas/CO_2.

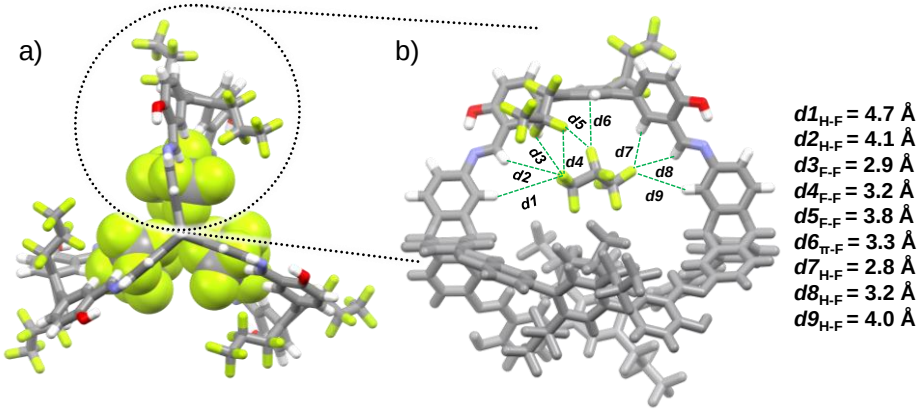

Figure 49. Single X-ray structure analysis of three C_3F_8 loaded **cage-C_3F_7**. (a) cage and C_3F_8 shown as capped sticks and spacefill model from top view. Blue, red, gray, green, and white spheres represent N, O, C, F, and H atoms, respectively. (b) the distances between one C_3F_8 molecule and cage are given from side view (only the upper half part is shown colorful).

2.2. The Influence of Solid Packing on the Gas Sorption of Porous Organic Cages

As mentioned earlier, a series of [2+3] porous imine cages, featuring various degrees of side-chain fluorination and different lengths of perfluorinated side chains was assembled into isomorphic crystalline materials and examined for their gas sorption properties for F-gases and their selective uptakes. It has been demonstrated that the side chains play a key role in both the structural aspects and the performance characteristics of these cages. It's worth noting that POCs are held together by weak intermolecular forces, allowing them to exist in alternative polymorphic forms.[25a] The different crystal packing arrangements of the same set of molecules can result in entirely different porosity and other physical properties.[48k, 79-80, 87] Therefore, given the solubility and the availability of an unambiguously SCXRD structure, **cage-CF_3** was chosen as the subject for investigating its polymorphic forms and the influence of these polymorphs on gas sorption.

2.2.1. The Influence of Polymorphic Forms on Gas Sorption

By slow vapor diffusion in various solvent systems, **cage-CF$_3$** crystallized in three distinct polymorphic forms: α phase from DMF/methanol (as previously discussed in Chapter III, Section 2.1.), β phase from THF/methanol, and γ phase from DCM/Et_2O (Figure 50). **cage-CF$_{3\beta}$** and **cage-CF$_{3\gamma}$** crystallize in a monoclinic crystal system with different space groups ($P2_1/c$ for α, $C2/c$ for γ) and cell volumes (13032.8 Å^3 for α, 15585.1 Å^3 for γ) while **cage-CF$_{3\alpha}$** pack in trigonal $R\bar{3}c$ with a cell volume of 19852.4 Å^3. **cage-CF$_{3\beta}$** and **cage-CF$_{3\gamma}$** share similar geometric shapes with **cage-CF$_{3\alpha}$**, best described as distorted prisms, featuring two triptycene units at each end. These cages have an outer dimension measuring 1.8-1.9 nm (measured between the outer triptycene bridgehead carbons) and an inner diameter of 1.3-1.4 nm (Figure 50).

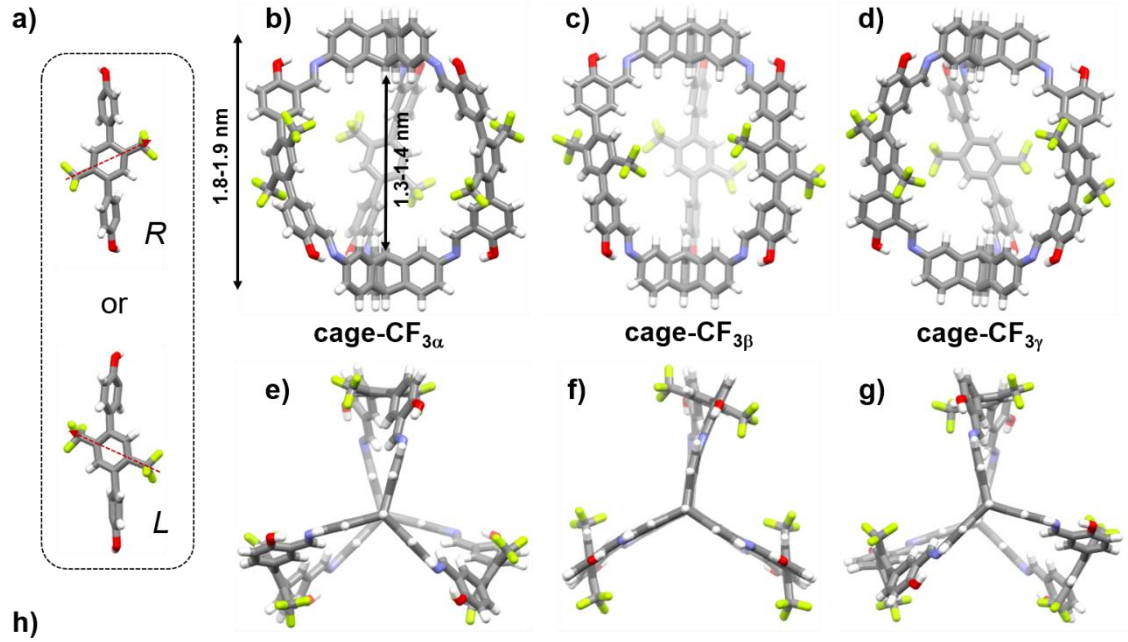

h)

Parameter	**cage-CF$_{3\alpha}$**	**cage-CF$_{3\beta}$**	**cage-CF$_{3\gamma}$**
Solvent	DMF/Methanol	THF/Methanol	DCM/Et_2O
Crystal system	Trigonal	Monoclinic	Monoclinic
Space group	$R\bar{3}c$	$P2_1/c$	$C2/c$
Z	6	4	4
Cell volume [Å^3]	19852.4	13032.8	15585.1
Isomers observed	*R-R-R/L-L-L*	*L-R-L/R-L-R*	*L-R-L/R-L-R*
$d_{\pi\text{-}\pi}$ [Å]	3.5	no	3.6

Figure 50. (a) *L* or *R* Orientation of side chains of the middle phenyl ring of three terphenyl substructures. (b-d) Side view and (e-g) top view of single crystal structures of **cage-CF$_{3\alpha}$**, **cage-CF$_{3\beta}$**, and **cage-CF$_{3\gamma}$**. (h) Selected crystallographic parameters of **cage-CF$_3$**. Colors: carbon, grey; hydrogen, white; oxygen, red; nitrogen, blue; fluorine, lime.

However, there are some small structural differences. Due to steric repulsion, the middle phenyl ring of terphenyl substructure is not coplanar to adjacent ones, which leads to either left (*L*) or right (*R*) conformation of substituted middle phenyl ring (as depicted in Figure 50a, where the orientation from the lower-left -CF_3 group to the upper-right -CF_3 group is denoted as *R*, and the orientation from the lower-right -CF_3 group to the upper-left -CF_3 group is denoted as *L*, for simplicity). Thus, each terphenyl unit is prochiral leading to overall four possible cage isomers (*L*-*L*-*L*, *L*-*R*-*L*, *L*-*R*-*R*, and *R*-*R*-*R*).

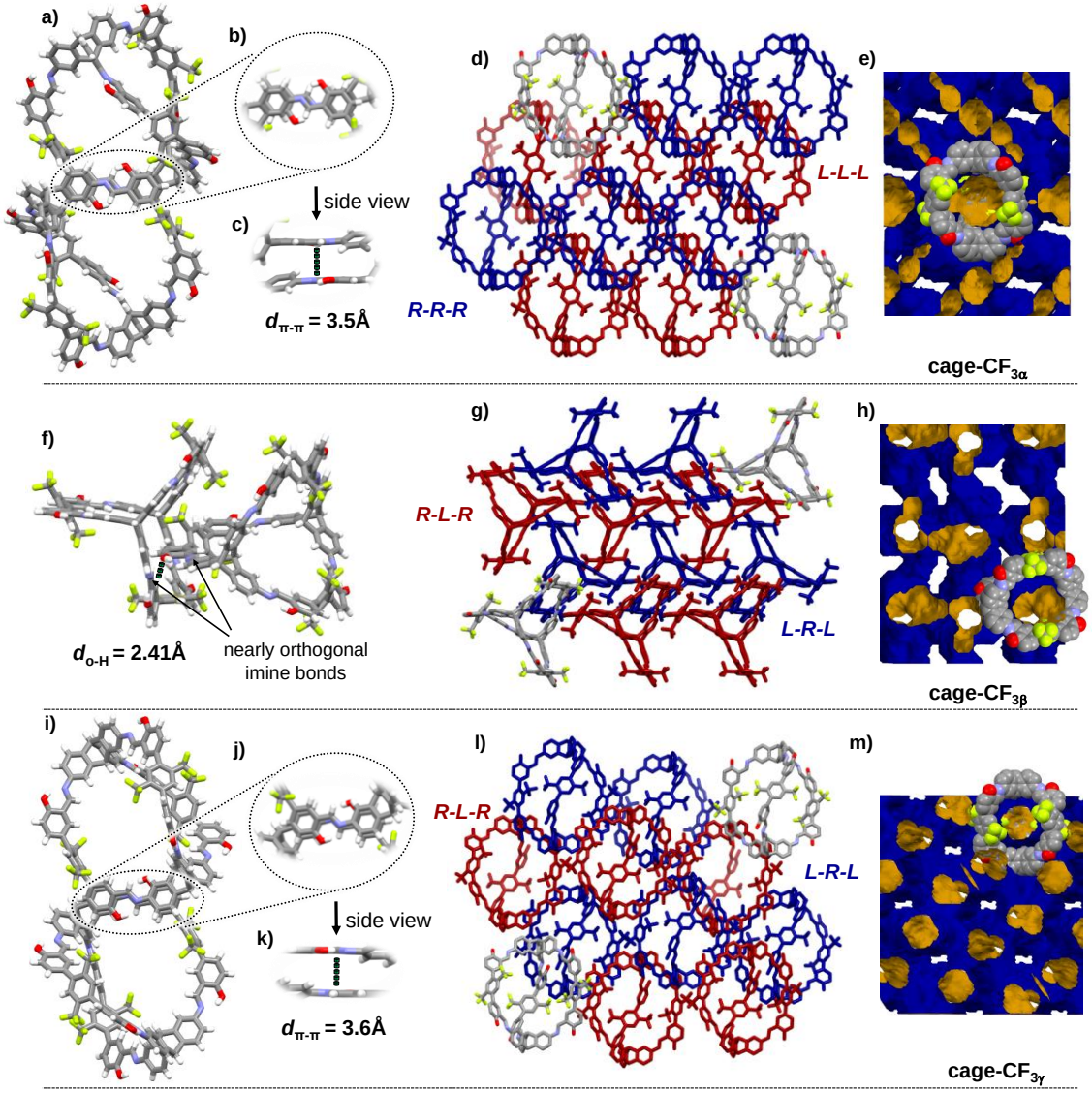

Figure 51. Stacked dimer of two cage molecules for **cage-CF$_{3\alpha}$** (a), **cage-CF$_{3\beta}$** (f), and **cage-CF$_{3\gamma}$** (i). (b and j) Zoom-in of the π-stacking motif as top view for corresponding cages. (c and k) Zoom-in of the π-stacking as a side view for corresponding cages. Crystalline packing motif of **cage-CF$_{3\alpha}$** (d), **cage-CF$_{3\beta}$** (g), and **cage-CF$_{3\gamma}$** (l) with two isomers depicted in blue and red (hydrogen atoms are omitted for clarity). Two cage molecules are shown in elemental colours. Crystalline voids represented as contact surface for **cage-CF$_{3\alpha}$** (e), **cage-CF$_{3\beta}$** (h), and **cage-CF$_{3\gamma}$** (m) (blue outer surface, yellow inner surface, created by Mercury 2020.1 with a probe radius of 1.82 Å and a grid spacing of 0.5 Å). One cage each is shown as space fill model in element colors (hydrogen atoms are omitted for clarity). Colors: carbon, grey; oxygen, red; nitrogen, blue; fluorine, lime; hydrogen, white.

The solid-state structure of **cage-CF$_{3\alpha}$** adopts homo-orientations *L-L-L* and *R-R-R* while hetero-orientations *L-R-L* and *L-R-R* are found in **cage-CF$_{3\beta}$** and **cage-CF$_{3\gamma}$** (Figure 50h). As previously discussed, in **cage-CF$_{3\alpha}$**, the two triptycene scaffolds of the cage backbones are rotated with respect to one another along the axis formed by the four bridge carbons of the two triptycene units, resulting in helical chirality for the cage molecules. Meanwhile, in **cage-CF$_{3\gamma}$**, the two triptycene units are rotated with respect to one another along a dislocated axis, while in **cage-CF$_{3\beta}$**, the two triptycene units almost overlap (Figure 50e-g). The racemic crystalline packing of **cage-CF$_{3\alpha}$** and **cage-CF$_{3\gamma}$** can be rationalized by dominating π-stacking motives with distances of $d_{\pi\text{-}\pi}$ = 3.5-3.6 Å (Figure 51). However, enantiopure layers of **cage-CF$_{3\beta}$** are connected by a hydrogen bond with distances of $d_{O\text{-}H}$ = 2.4 Å, and no π-stacking was observed due to nearly orthogonal imine bonds of the stacked dimer. The analyses of the crystalline voids revealed connected intrinsic pores for solvated **cage-CF$_{3\alpha,\beta,\gamma}$** in three dimensions for the N_2 kinetic probe radius of 1.82 Å (approx. grid spacing of 0.5 Å) (Figure 51e, h, and m).

Prior to gas sorption, the materials were activated in a dynamic vacuum at room temperature, followed by heating to 100°C for **cage-CF$_{3\gamma}$** and 50°C for **cage-CF$_{3\alpha}$**. The crystallized **cage-CF$_{3\beta}$** was treated by subsequent solvent exchange of inclathrated solvent with methanol and activated at 50°C under vacuum. NMR spectra confirm the adequacy of these activation procedures and verified the chemical integrity of the desolvated forms (Appendix, Figure 194-195).

Optical and SEM imaging reveals the persistence of the crystallinity of **cage-CF$_3$** before and after thermal activation (Figure 52). Although some of the crystals appeared cracked, all crystals still show clear facets and smooth surfaces. Investigations by PXRD proved the crystalline nature of the samples by sharp peaks. However, it's worth noting that the fitting between the experimental data and simulated data from the single crystal X-ray structure is different (Figure 53). This disparity suggests that the material's structure is not stable under the evacuation conditions, leading to a phase transition to another crystalline polymorph. Interestingly, the PXRD pattern of **cage-CF$_{3\alpha}$** after activation closely resembled the pattern of **cage-CF$_{3\gamma}$** after activation, indicating their similarity in polymorphic nature.

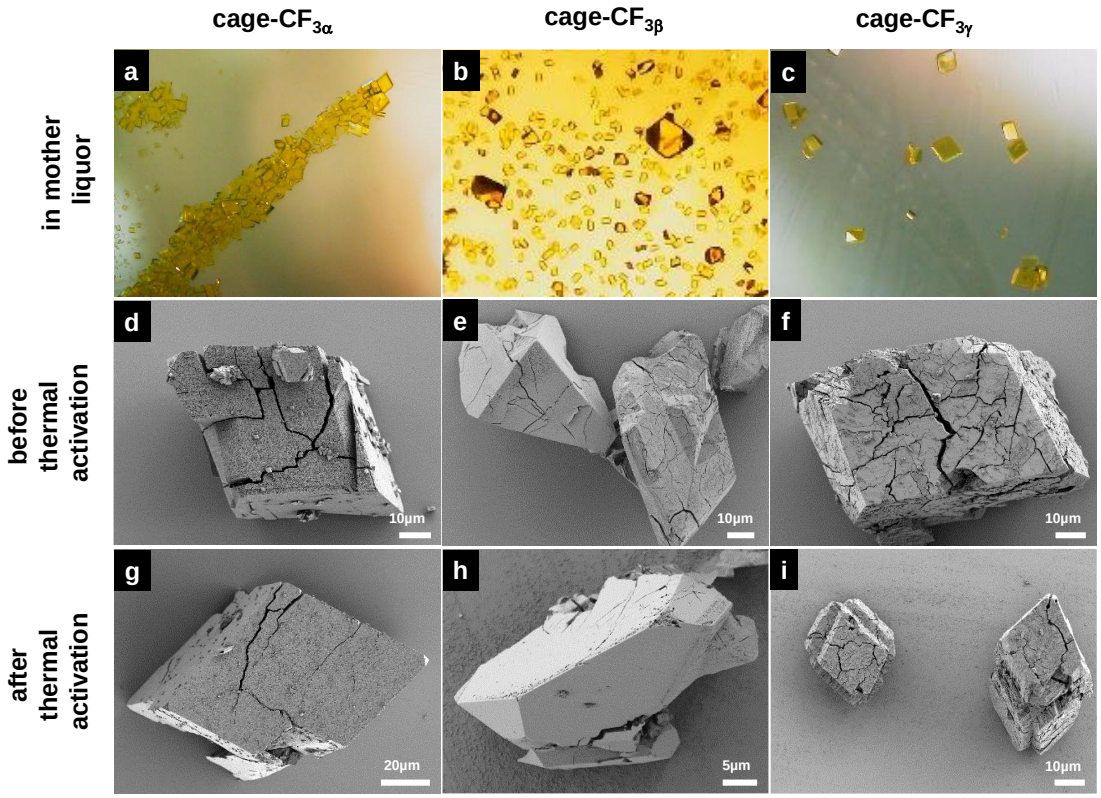

Figure 52. Light microscope and SEM images of crystals. In the mother liquor: solvate **cage-CF$_3$** in (a) DMF/MeOH, in (b) THF/MeOH, and in (c) DCM/Et$_2$O; (d-f) filtered crystal prior to thermal activation. (g-i) Thermally activated crystals. Pictures (a-c) have been obtained by light microscope, and pictures (d-i) have been obtained by SEM. SEM measurements were performed by Dr. Wen-Shan Zhang (BioQuant, Heidelberg University).

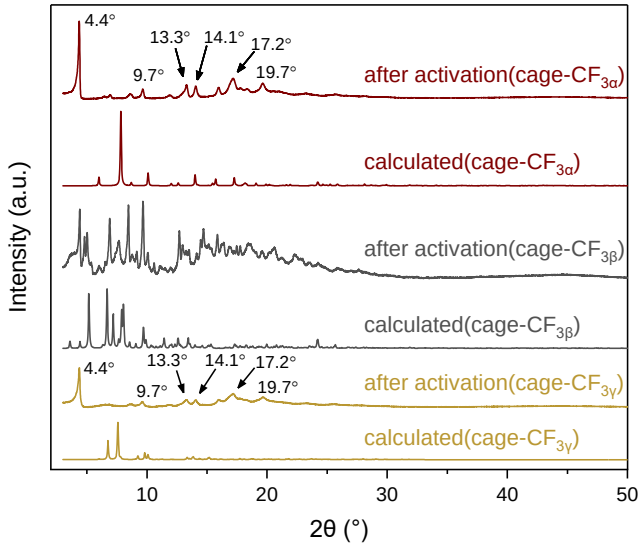

Figure 53. PXRD patterns of **cage-CF$_3$** after thermal activation and calculated from the single crystal X-ray structure. The PXRD measurements were performed under Dr. Sven M. Elbert's help at IMSEAM (Heidelberg University).

In nitrogen sorption experiments at 77 K, **cage-CF$_{3\beta}$** exhibits the highest BET-specific surface area (SA_{BET} = 204 m^2 g^{-1}) among three polymorphs, with pronounced hysteresis (Figure 54a). On the other hand, **cage-CF$_{3\alpha}$** and **cage-CF$_{3\gamma}$** have BET-specific surface area of 34 m^2 g^{-1} and 151 m^2 g^{-1}, respectively. A similar trend is also observed in hydrogen uptake, with the highest adsorbed amounts for **cage-CF$_{3\beta}$** at

93.3 $cm^3\ g^{-1}$ (0.84 wt%) at 760 torr and 77 K (Figure 54b). **cage-CF$_{3\alpha}$** and **cage-CF$_{3\gamma}$** exhibite comparable adsorbed amounts, measuring 43.5 $cm^3\ g^{-1}$ (0.39 wt%) and 53.7 $cm^3\ g^{-1}$ (0.48 wt%), respectively, under the same conditions. These results highlight that the same set of molecules with different crystal packing arrangements, possess different gas sorption properties.

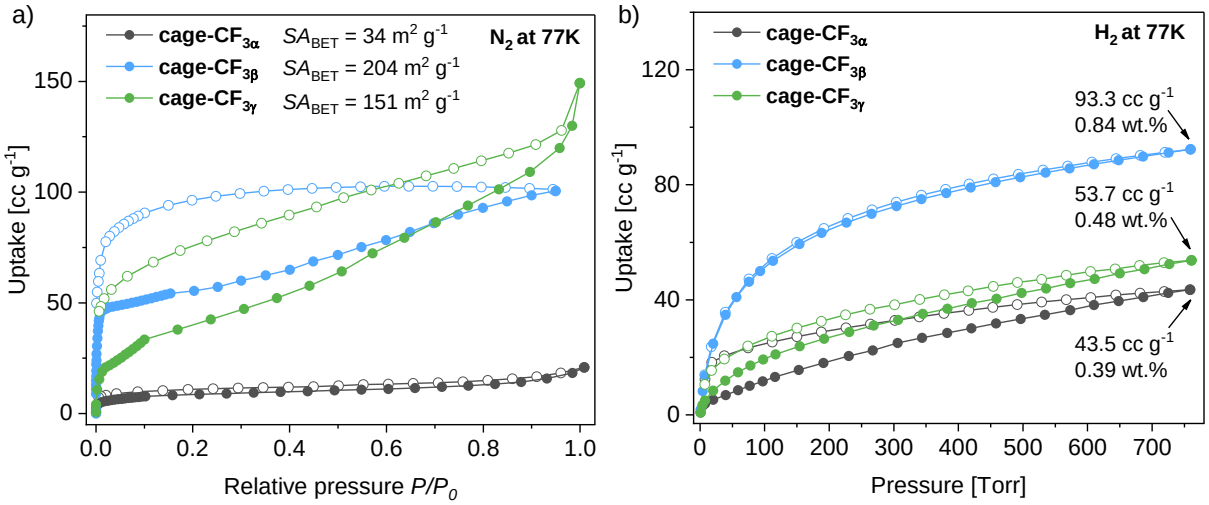

Figure 54. (a) N_2 and (b) H_2 sorption isotherms at 77 K of **cage-CF$_{3\alpha}$** (black), **cage-CF$_{3\beta}$** (blue), and **cage-CF$_{3\gamma}$** (green). Adsorption: full circles; desorption: empty circles.

The intriguing aspect of achieving different crystal packings for the same set of [2+3] cages has already been explored. This diversity in crystal packing can result from minor structural alterations, adding to its overall interest. Therefore, [2+3] cage with methyl groups was design and synthesized. The modified terphenyl salicylaldehyde building block with methyl groups **75** was synthesized initially through Suzuki-Miyaura coupling reaction between boronic ester **51** and dibromo derivatives **74** with a yield of 54% (Scheme 16).

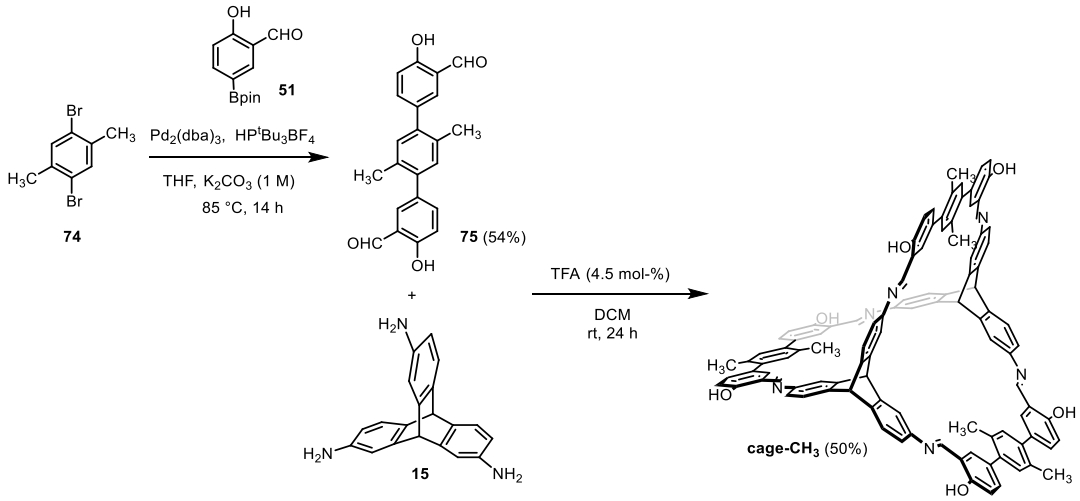

Scheme 16. Synthesis route of **cage-CH$_3$**.

The next step is to construct the cage compound by imine condensation between modified terphenyl salicylaldehyde **75** and triaminotriptycene **15**. The pure cage compound **cage-CH$_3$** precipitated in 50 % yield after stirring of **15** and **75** in a 2:3 stoichiometry in DCM with 4.5 mol-% TFA at room temperature for 24 h (Scheme 16).

The chemical structure of **cage-CH$_3$** is confirmed by NMR spectroscopy and MALDI-MS (Figure 55). The ^{1}H NMR spectrum of **cage-CH$_3$** shows a characteristic singlet at 9.18 ppm for the six imine protons and the signals at 10.01 ppm for the aldehydic protons of the precursor terphenylsalicylaldehyde **75** are no longer detectable. For its MS spectrum, a pronounced signal was observed with a monoisotopic mass of *m*/*z* = 1529.5934, which correlated with the calculated monoisotopic mass expected for **cage-CH$_3$** (*m*/*z* = 1529.5899).

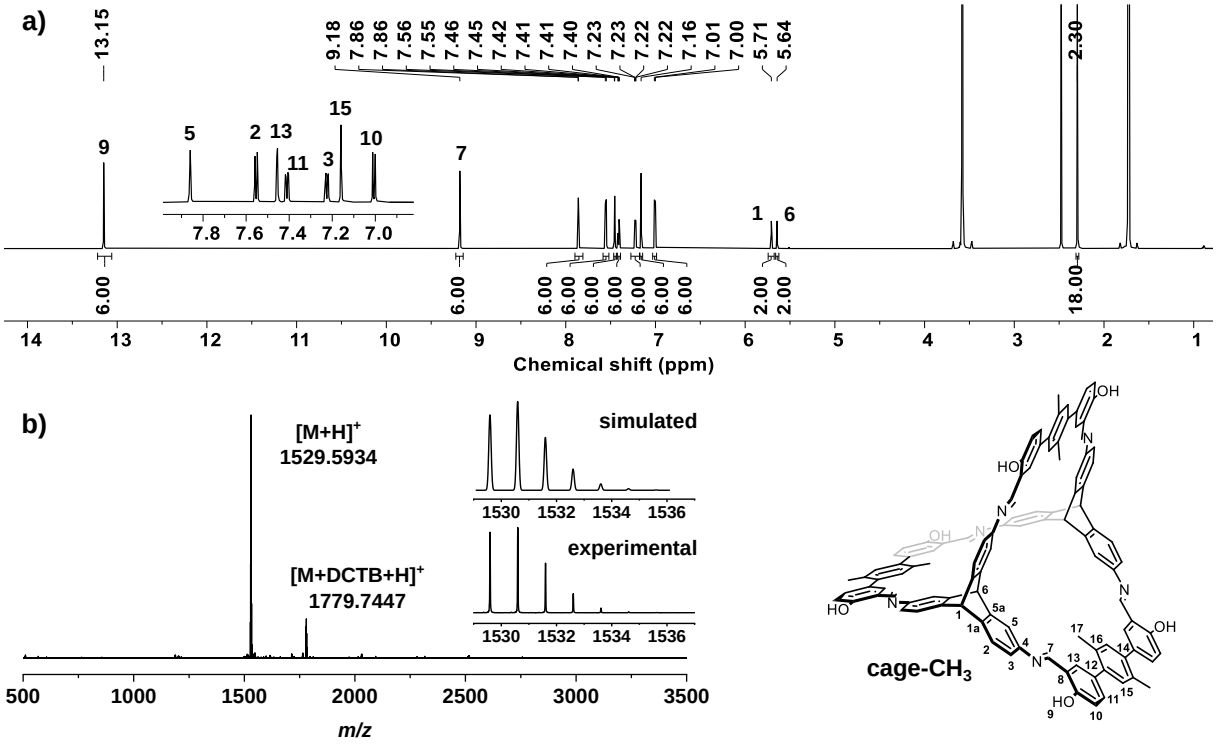

Figure 55. (a) ^{1}H NMR in THF-d_8 (700 MHz) and (b) MALDI-TOF spectrum (matrix: DCTB) of **cage-CH$_3$**.

Single crystal of **cage-CH$_3$** was obtained by vapor diffusion of methanol into THF solutions (Figure 56a). These crystals crystallize in trigonal $R\bar{3}c$ with a cell volume of 16443.4 Å^3. Notably, this crystal system differs from that of **cage-CF$_{3\beta}$** obtained through the same solvent system, even when subjected to minor structural modifications (Figure 50h). According to *L* or *R* orientation principle as aforementioned, the solid-state structures of **cage-CH$_3$** adopt homo-orientations *L*-*L*-*L*/*R*-*R*-*R*.

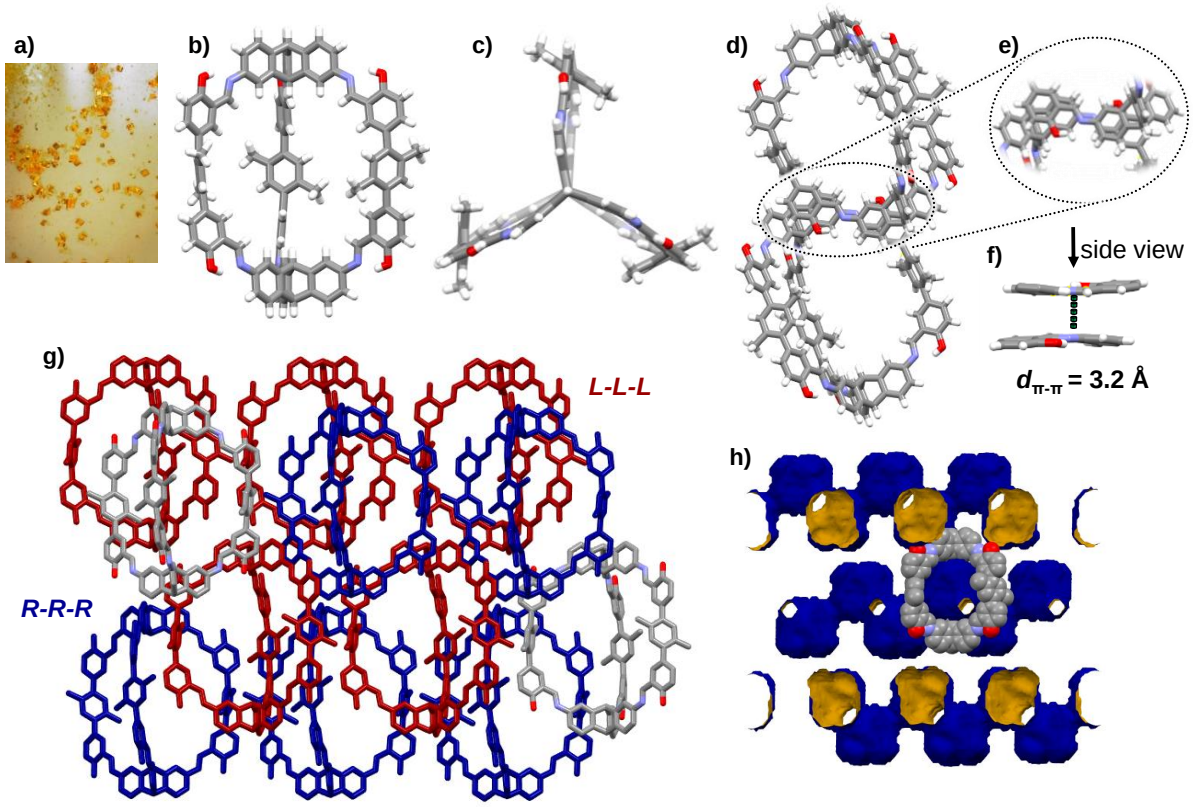

Figure 56. (a) Light microscope image of **cage-CH$_3$** crystals in the mother liquor. (b) Side view and (c) top view of single crystal structures of **cage-CH$_3$**. (d) Stacked dimer of two cage molecules. (e) Zoom-in of the π-stacking motif as top view for corresponding cages. (f) Zoom-in of the π-stacking as a side view for corresponding cages. (g) Crystalline packing motif of **cage-CH$_3$** with two isomers depicted in blue and red (hydrogen atoms are omitted for clarity). Two cage molecules are shown in elemental colours. (h) Crystalline voids represented as contact surface of **cage-CH$_3$** (blue outer surface, yellow inner surface, created by Mercury 2020.1 with a probe radius of 1.82 Å and a grid spacing of 0.5 Å). One cage each is shown as space fill model in element colors (hydrogen atoms are omitted for clarity). Colors: carbon, grey; oxygen, red; nitrogen, blue; fluorine, lime.

The racemic crystalline packing of **cage-CH$_3$** is primarily governed by π-stacking the salicylimine substructures with distances of $d_{\pi\text{-}\pi}$ = 3.2 Å (Figure 56d-f). No π-π interaction was observed between terphenyl subunits due to deliberate frustration of methyl groups. The enantiopure layers *L-L-L*-**cage-CH$_3$** and *R-R-R*-**cage-CH$_3$** can be found in an alternating order (Figure 56g). A detailed analysis of the crystalline voids reveals interconnected 2D intrinsic channels for the N_2 kinetic probe radius of 1.82 Å (approx. grid spacing of 0.5 Å) (Figure 56h).

The crystalline samples of **cage-CH$_3$** underwent activation at a temperature of 50°C, ensuring the complete removal of all solvents for gas sorption. This was confirmed by performing NMR measurements (Appendix, Figure 194). Post-activation, the desolvated crystals retain their integrity, exhibiting clear facets and smooth surfaces although some crystals display minor cracks, as evidenced in the SEM micrograph (Figure 57). Notably, **cage-CH$_3$** crystal exhibits a rhombohedral shape similar to that of **cage-CF$_{3\alpha}$** and **cage-CF$_{3\gamma}$**, but distinct from the shape of **cage-CF$_{3\beta}$**.

Moreover, the presence of strong peaks in the PXRD spectra reveals the high crystallinity of the desolvated crystals although the experimental pattern is different from calculated one (Figure 57).

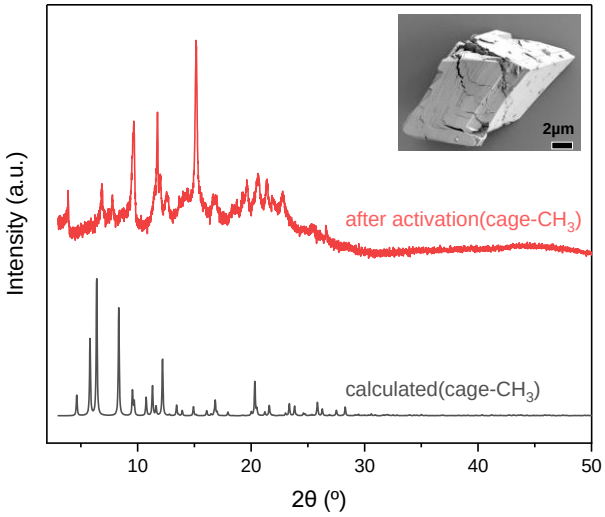

Figure 57. PXRD pattern of **cage-CH$_3$** after activation. Inserted picture: SEM picture of **cage-CH$_3$** after activation. SEM measurements were performed by Dr. Wen-Shan Zhang (BioQuant, Heidelberg University). The PXRD measurements were performed under Dr. Sven M. Elbert's help at IMSEAM (Heidelberg University).

At 77 K **cage-CH$_3$** compound adsorbs 40.7 cm^3 g^{-1} nitrogen (P/P_0 = 0.95) and 16.3 cm^3 g^{-1} hydrogen (corresponds to 0.15 wt%, 760 Torr) (Figure 58). The nitrogen isotherm can best be described as a mixture of a type II isotherm.[117] The calculated specific surface area of **cage-CH$_3$** is 55 m^2 g^{-1} (BET model) comparable with that of **cage-CF$_{3\alpha}$** (SA_{BET} = 34 m^2 g^{-1}) but lower than that of **cage-CF$_{3\beta}$** (SA_{BET} = 204 m^2 g^{-1}) and **cage-CF$_{3\gamma}$** (SA_{BET} = 151 m^2 g^{-1}).

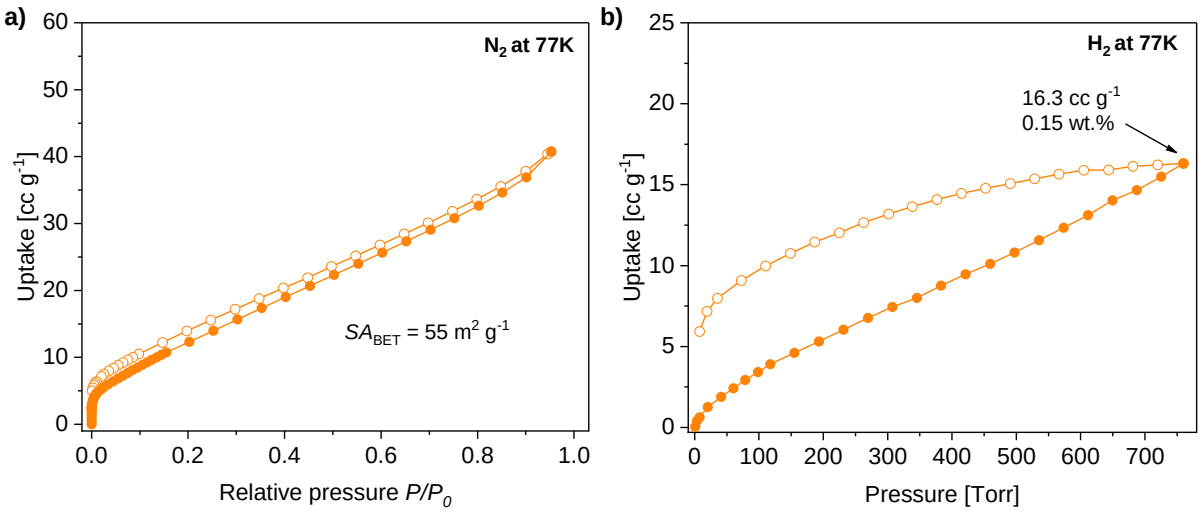

Figure 58. (a) N_2 and (b) H_2 sorption isotherms of **cage-CH$_3$** at 77 K. Adsorption: full circles; desorption: empty circles.

2.2.2. The Influence of Elongated π Systems on Gas Sorption

In Chapter III Section 2.1 and 2.2.1, it was established that π-π stacking of the salicylimine substructures plays a crucial role in the crystalline packing of all [2+3] cages. It is further assumed that elongated π systems could influence the crystalline packing, leading to increased porosity and improved gas sorption performance. To validate this hypothesis, a new [2+3] cage featuring naphthyl groups was designed and synthesized for investigation into its gas sorption capabilities.

According to Scheme 17, new modified salicylaldehydes **77** were synthesized initially through Suzuki-Miyaura cross-coupling reaction between boronic ester **51** and dibromo derivatives **76** with a yield 62%, and then reacted by imine condensation with triaminotriptycene **15** in a 2:3 stoichiometry in THF with 4.5 mol-% TFA at room temperature for 24 h (Scheme 17). Many crude products instead of pure cages percipitated out from THF. To isolate the cage compound from the mixture, the sediment was dissolved in fresh THF, and the insoluble residue was separated through a syringe filter. Methanol then diffused to the clear reddish solution over the gas phase in a closed vessel for three weeks, with small red crystals forming in 14% yield (Scheme 17). Regrettably, the crystal size is insufficient to gather enough data for single crystal X-ray diffraction analysis.

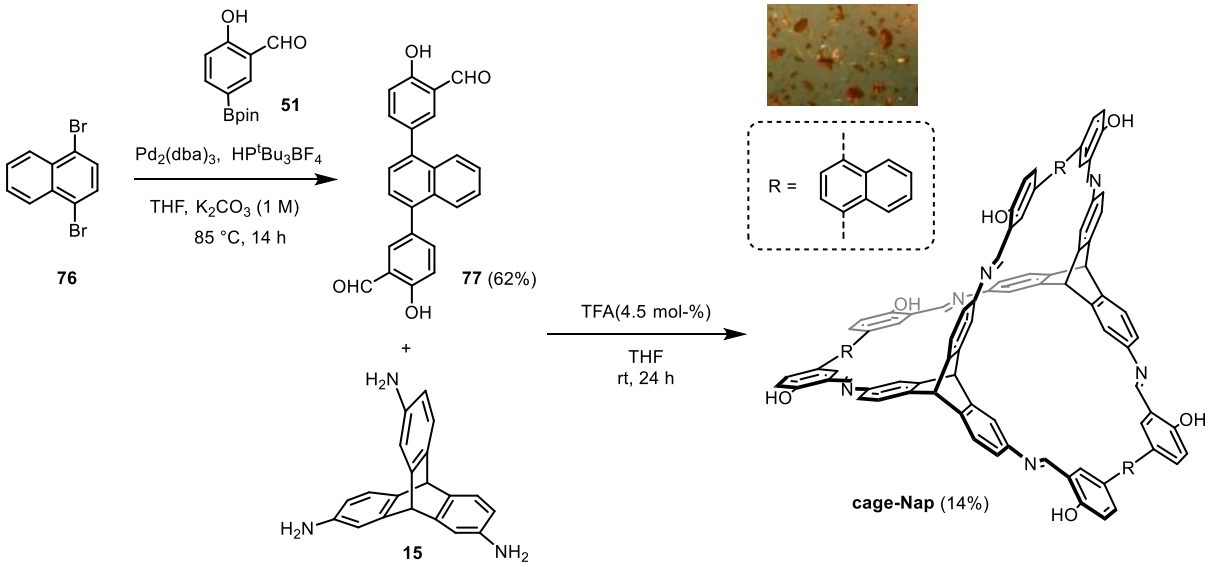

Scheme 17. Synthesis route of **cage-Nap**. Inserted picture: Light microscope images of **cage-Nap** crystal in the mother liquor.

Due to the very poor solubility of **cage-Nap** in THF, DMF, DMSO, $CHCl_3$ and DCM, no NMR spectroscopy could be performed. However, the MALDI-TOF MS proved to be a valuable analytical technique (Figure 59a). Six strong peaks (*m*/*z* = 1595.5410 for

$[M+H]^+$, 1845.6888 for $[M+DCTB+H]^+$, 2095.8365 for $[M+2DCTB+H]^+$, 2346.9902 for $[M+3DCTB+H]^+$, 2597.1383 for $[M+4DCTB+H]^+$, 2847.2885 for $[M+5DCTB+H]^+$) of the desired molecular ions are detected in the *m*/*z* range from 1000 to 5000 Da. The corresponding isotopic distribution matches very well with the calculated values of **cage-Nap** compound.

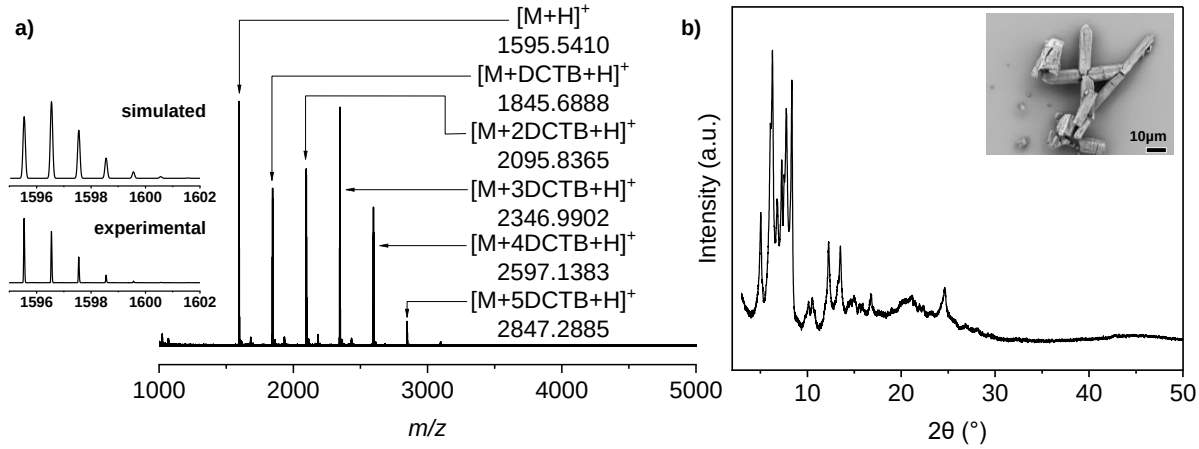

Figure 59. (a) MALDI-TOF spectrum (matrix: DCTB) and (b) PXRD pattern of **cage-Nap** after activation. Inserted picture : SEM picture of **cage-Nap** after activation. SEM measurements were performed by Dr. Wen-Shan Zhang (BioQuant, Heidelberg University). The PXRD measurements were performed under Dr. Sven M. Elbert's help at IMSEAM (Heidelberg University).

The crystalline **cage-Nap** was activated at 50 °C and TG curve confirmed that all solvent was removed out (Appendix, Figure 198). A SEM micrograph of the desolvated crystal of **cage-Nap** are shown in Figure 59b. **cage-Nap** crystals have a hexagonal bipyramid shape, which is different from **cage-CF$_3$** and **cage-CH$_3$** but similar with [2+3] cages without side chains described in the doctoral work of Dr. Markus W. Schneider.[76] Furthermore, strong peaks in PXRD spectra reveal its high crystallinity of desolvated crystal (Figure 59b).

Investigation of **cage-Nap** by nitrogen sorption at 77 K gave a type-I isotherm,[117] revealing the microporous nature of the material with a specific surface of SA_{BET} = 909 $m^2\ g^{-1}$ (Figure 60a). This is much higher than **cage-CH$_3$** (55 $m^2\ g^{-1}$) and the series of [2+3] cages of both Chapter III and Dr. Markus W. Schneider[76], likely due to elongated π systems. In terms of H_2 uptake capacity, **cage-Nap** adsorbs up to 124.3 $cm^3\ g^{-1}$ (1.11 wt%) at 77 K and 760 Torr, much more than **cage-CH$_3$** (Figure 60b). This is comparable to CC2 cage (1.18 wt%) reported by Cooper *et al*.,[72] and slightly higher than the value for [4+6]-exo cage (0.93 wt%)[74], but lower than fluorinated [4+4] cage (1.5 wt%) reported by Schmidt *et al*..[48i]

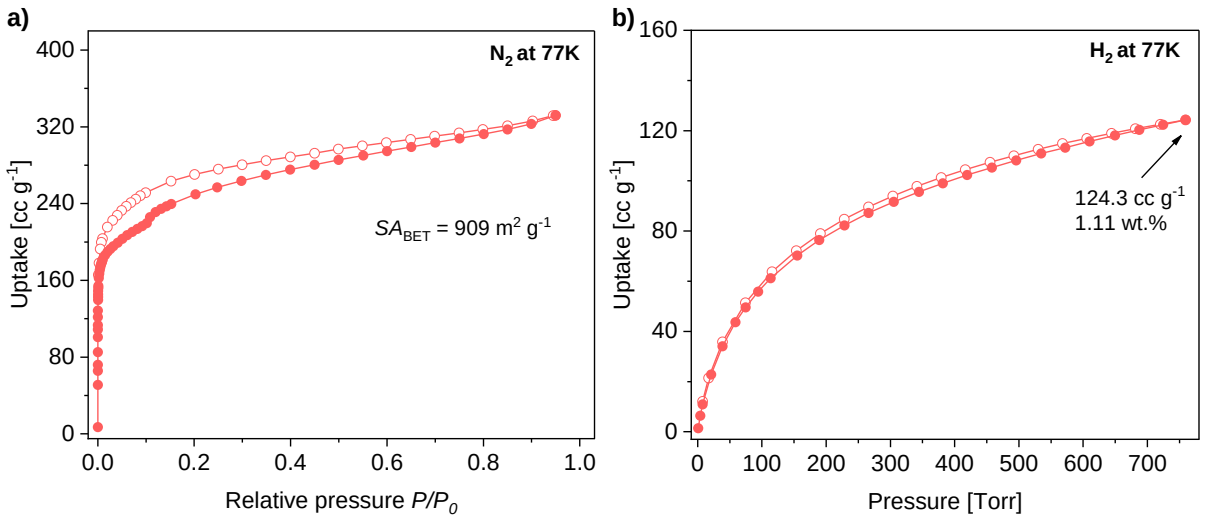

Figure 60. (a) N_2 and (b) H_2 sorption isotherms of **cage-Nap** at 77 K. Adsorption: full circles; desorption: empty circles.

2.2.3. The Influence of Activation Condition on Gas Sorption

In Chapter III Section 2.1., **cage-C_6F_{13}** demonstrates a low specific surface area of only 13 m^2 g^{-1} (N_2) due to the pore being filled by excessively long fluoroalkyl chains. Therefore, various activation conditions for **cage-C_6F_{13}** are also thoroughly investigated to improve its specific surface area. Herein, a new flaky crystal was obtained by directly filtering precipitation from crude DMF reaction solution of the cages (Figure 61a). Directly highly thermal activation at 100°C or rinse with methanol, subsequent activation at room temperature under vacuum afforded materials **cage-$C_6F_{13\beta}$** and **cage-$C_6F_{13\gamma}$**, respectively, with a somewhat lower degree of crystallinity, as indicated by PXRD and SEM micrographs (Figure 61). To confirm that all solvent have been removed before gas sorption, crystalline cages after activation was subjected to NMR analyses. No signal of residue solvent was observed in **cage-$C_6F_{13\alpha,\beta,\gamma}$**, in the NMR spectra (Appendix, Figure 193 and 195).

Furthermore, **cage-$C_6F_{13\gamma}$**, have comparably low BET-specific surface area (37 m^2 g^{-1}) to **cage-$C_6F_{13\alpha}$** (13 m^2 g^{-1}) (Figure 62a). This is likely due to desolvation at high temperatures, which destroyed sufficient packing of cages. However, after rinsing with a lower boiling point solvent followed by activation at room temperature, the specific surface area of **cage-$C_6F_{13\beta}$** increased to SA_{BET} = 317 m^2 g^{-1} with pronounced hysteresis. The same trend was also observed in H_2 uptake with a highest adsorbed amount of 52.3 cm^3 g^{-1} (0.47 wt%) for **cage-$C_6F_{13\beta}$** at 760 torr and 77 K as seen in Figure 62b.

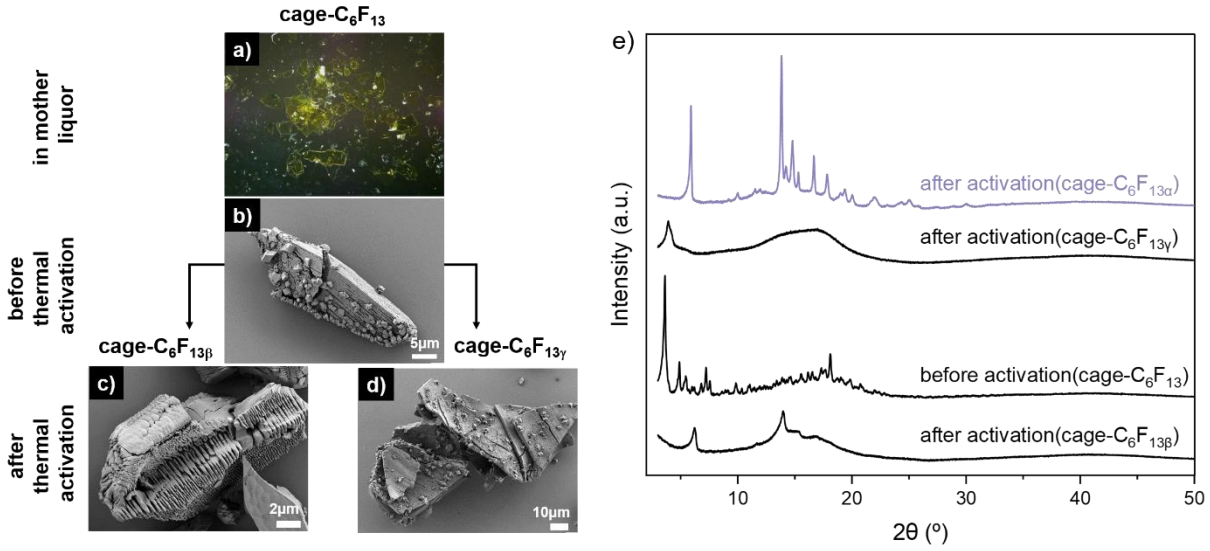

Figure 61. (a) Light microscope image of **cage-C_6F_{13}** crystals in the mother liquor. SEM images of crystals: (b) filtered crystals of **cage-$C_6F_{13\beta}$** and **cage-$C_6F_{13\gamma}$** prior to thermal activation; (c-d) Thermally activated crystals of **cage-$C_6F_{13\beta}$**, and **cage-$C_6F_{13\gamma}$**. (e) PXRD patters of **cage-C_6F_{13}** before and after thermal activation. SEM measurements were performed by Dr. Wen-Shan Zhang (BioQuant, Heidelberg University). The PXRD measurements were performed under Dr. Sven M. Elbert's help at IMSEAM (Heidelberg University).

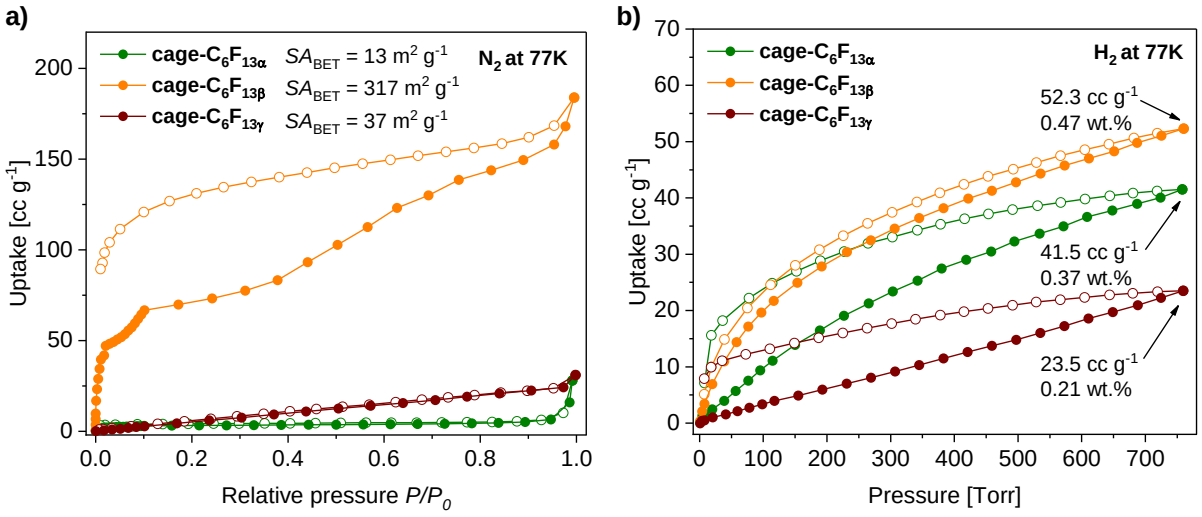

Figure 62. (a) N_2 and (b) H_2 sorption isotherms of **cage-$C_6F_{13\alpha}$**, **cage-$C_6F_{13\beta}$**, and **cage-$C_6F_{13\gamma}$** at 77 K. Adsorption: full circles; desorption: empty circles.

2.3. Conclusion

In summary, different lengths of perfluorinated side chains were successfully incorporated into [2+3] imine cages. NMR, SEM, and PXRD results confirm that isomorphous crystalline materials were produced, providing a platform to study the influence of side chains on F-gas adsorption at variable temperatures. Among the studied cages, **cage-C_5F_{11}** with perfluoropentyl chains demonstrates outstanding F-

gas selective adsorption properties in binary mixtures of F-gas/N_2 (e.g., $S_{IAST(10:90)}$ = 2216 for *c*-C_4F_8 vs N_2) and F-gas/O_2 (e.g., $S_{IAST(10:90)}$ = 1550 for *c*-C_4F_8 vs O_2), while **F-cage** with perfluorobutyl chains is the most selective cage in overall selective adsorption of F-gas over CO_2 (e.g., S_H = 19631 for *c*-C_4F_8 vs CO_2). These selective adsorption studies indicate that perfluoroalkane-functionalized side chains have preferential interaction with F-gases, as supported by single crystal analysis of C_3F_8-loaded cages. It is anticipated that fluorinated cages will be attractive materials for a wide variety of F-gases separations from the gas mixtures coming out of those industial processes.

Furthermore, three different polymorphs of **cage-CF_3** are explored to to investigate the influence of solid packing on the gas sorption. Detailed analysis of single crystal X-ray structures reveals that the prochiral terphenyl unit orient in homo *L-L-L* and *R-R-R* conformations in **cage-$CF_{3\alpha}$** while heteroenantiomeric *L-R-L* and *L-R-R* forms are found in **cage-$CF_{3\beta}$** and **cage-$CF_{3\gamma}$**. Additionally, a pair of new cages **cage-CH_3** and **cage-Nap** were successfully synthesized. Nitrogen and hydrogen sorption experiments at 77 K showed that **cage-Nap** has a much higher specific surface area (909 $m^2\ g^{-1}$) and H_2 uptake (124.3 $cm^3\ g^{-1}$, 1.11 wt% at 760 Torr) than **cage-CH_3** and the series of [2+3] cages presented in this chapter, likely due to the elongated π system. Lastly, for **cage-C_6F_{13}**, a higher specific surface area (SA_{BET} = 317 $m^2\ g^{-1}$) and H_2 uptake (52.3 $cm^3\ g^{-1}$, 0.47 wt% at 760 Torr and 77K) was achieved by crystallization of the cages from DMF, followed by a solvent rinse, and activation at room temperature.

3. [4+4] Pyrrole-Based Imine Cage Compounds with Nitrogen-Rich Cavities and Tetrahedral Geometry

As mentioned earlier, the gas sorption properties of cages are influenced by both the cage's inherent structure and its crystalline packing. Chirality, an intrinsic characteristic found in many imine cages, holds particular significance due to its pivotal role in governing the crystalline arrangement of these molecules.[127] A common approach for incorporating chirality into imine cage systems involves the use of pre-designed chiral amine or aldehyde building blocks with *R-S* (or *P-M*) chirality, which can serve as the edges, vertices, or faces of chiral polyhedra.[128] This strategy effectively transfers the chirality of these components to the resulting chiral structures. For example, combining chiral 1,2-cyclohexanediamine **78** with different chiral or achiral aldehydes has generated numerous chiral cages (Figure 63).[25c, 129] However, it's worth noting that such strategy usually requires additional chemical modifications on the core unit, for example, tribenzotriquinacene (TBTQ)[130] and the chiral substituents may limit the variety of chiralities achievable in the products (Figure 63).[131]

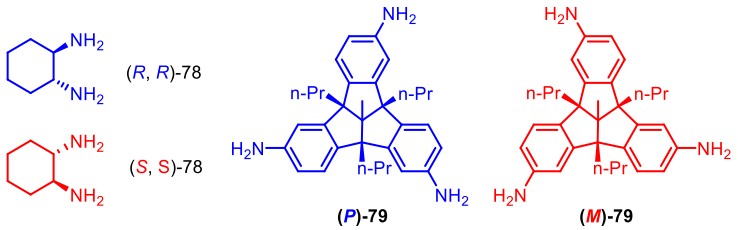

Figure 63. Examples of chiral building blocks for chiral cages.

An alternative strategy for generating chiral imine organic cage polyhedrals involves using achiral components and applying rational design principles based on graph theory.[132] This approach is centered around concepts of configuration restriction and symmetry breaking. Cao *et al.* reported the successful assembly of achiral building blocks, including tetraphenylethylene (TPE) **80**,[131, 132b] truxene derivatives (TR) **82**, [132a, 133] and triazatruxene (TAT) **83**,[134] into organic chiral cages through dynamic covalent chemistry (Figure 64-65). The rectangle motif of TPE presents two orientational configurations of the vinyl bond (i.e., vertical and horizontal as shown in Figure 64a), in addition to the *P* and *M* orientational configurations of the phenyl rings due to the steric hindrance between the phenyl rings, while the propeller-like achiral TR and TAT can exhibit 3D chirality in *P* or *M* orientational congurations upon cage polyhedral formation. Moreover, Li *et al*. have demonstrated the

intramolecular rotation of propeller-shaped trisbenzaldehyde **84**-**85** was restricted by intermolecular CH···π interactions, leading to either a clockwise or counter-clockwise orientational congurations (Figure 65).[135] This innovative strategy offers exciting possibilities for the controlled design and assembly of chiral organic cage polyhedrals with diverse structural and configurational characteristics.

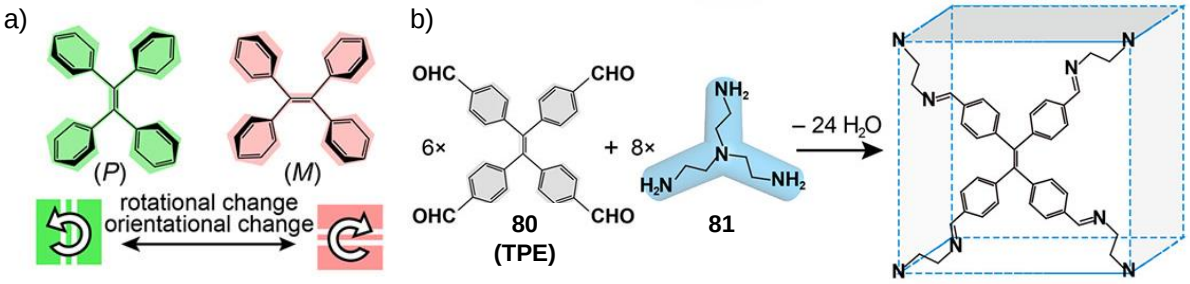

Figure 64. Synthesis of the chiral cubes with different facial rotational and orientational configurations. (a) TPE motif exhibits two rotational modes (*P* or *M*) of the phenyl groups and two orientational modes (horizontal or vertical) of the vinyl group in two dimensions. (b) Schematic of synthesis of organic cubes. Adapted with permission from Ref.[132b]. Copyright © 2017 American Chemical Society.

Trispyrrolaldehyde **30**, employed by Beer and colleagues for the synthesis of flexible [2+3] cages,[136] adopts a C_3-symmetrical conformation (Figure 65). The rotation orientation of the trispyrrol unit around the C-C single bonds to the central carbon atom, as well as the in-out orientation of the methyl group, could lead to various stereoisomers of the assembled structures. Additionally, the impact of side chains on the gas sorption properties of cages has been extensively explored. However, the influence of side chains on the stereochemistry of cages remains an intriguing question. In this chapter, a small series of tetrahedral [4+4] imine cages with nitrogen rich interiors and different side chains is present, based on the condensation of conformationally alterable tris-pyrrol aldehyde **30** and different substituted 1,3,5-trimethylamino benzenes[137] as used in our group before. Their face-oriented polyhedra structures in the crystalline state will be investigated.

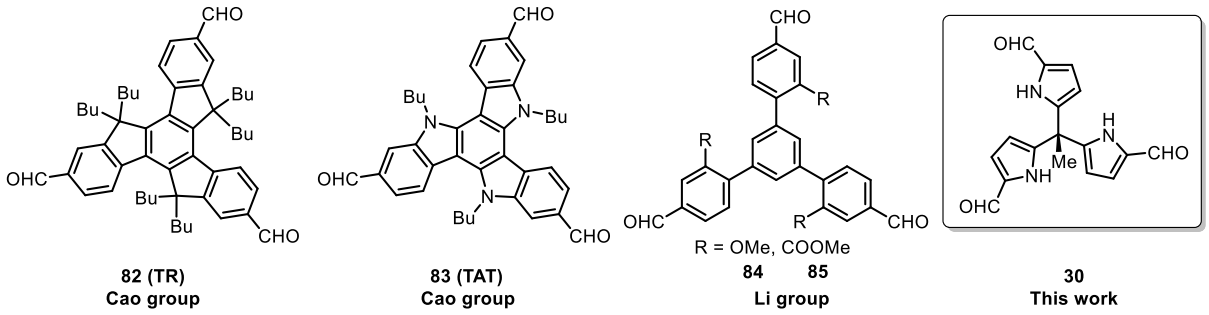

Figure 65. Achiral building blocks for chiral cages.

3.1. Synthesis of [4+4] Cage

The nitrogen-rich building block **30** consists of a central ethane bridge with three pyrrole rings, each bearing a formyl (-CHO) group at the 2-position, creating a symmetrical and trigonal structure. According to Beer *et al.*'s procedure,[136] the building block **30** was synthesized in two steps (Scheme 18). Triethyl orthoacetate **86** was stirred in an excess of pyrrole for only ten minutes under TFA to produce the methyl tripyrrolyl **87** in yield of 61% [Lit.: 59%]. It was subsequently formylated employing standard Vilsmeier-Haack conditions ($POCl_3$ and DMF) to give the triformylpyrrolyl **30** in 75% yield [Lit.: 84%].

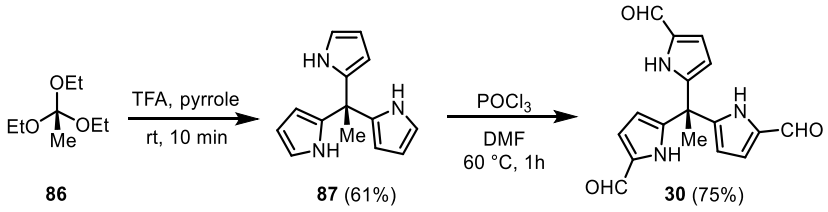

86 **87** (61%) **30** (75%)

Scheme 18. Synthesis of building block **30**.

The four triamine building blocks **31**-**34** have been used before to construct cage compounds for nitrate and ammonium ion binding.[137b, 137c] The primary amine compounds **32** were synthesized by two-step Gabriel synthesis from starting material **88** in yields of 49% [Lit.: 96%] and 92% [Lit.: 89%], respectively (Scheme 19).[138] The low yield in first step is attributed to an additional recrystallization process to obtain highly pure product.

The other three triamine building blocks **31**, **33**, and **34** were gotten from Dr. Jochen C. Lauer (OCI, Heidelberg University) who has used these building blocks to synthesize some [2+3] and [4+4] cages.[137b, 137c]

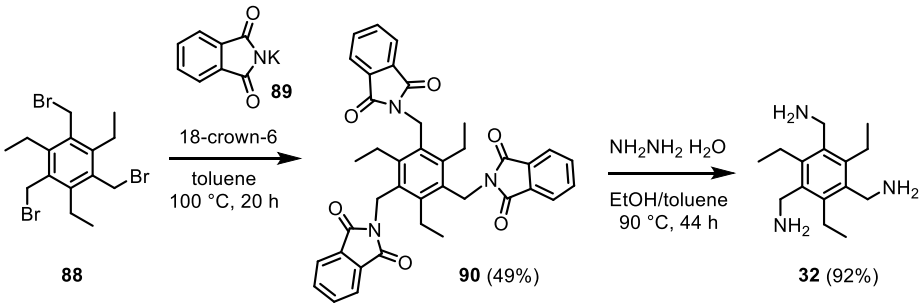

88 **90** (49%) **32** (92%)

Scheme 19. Synthesis of building block **32**.

The isostructurally tetrahedral [4+4] imine cages were synthesized by reacting the methyl-trispyrrolyl-aldehyde with the corresponding substituted 1,3,5-trimethylamino benzenes **31**-**34** in a 1:1 stoichiometry in chloroform at room temperature or 60 °C

(Scheme 20). By applying recycling gel-permeation chromatography (r-GPC) with THF as solvent, pure **cage-Me**, **cage-Et**, and **cage-OPr** were successfully isolated after multiple cycles in yields of 10-18% (Appendix, Figure 199). Due to its low solubility, purifying the **cage-Br** by r-GPC and recrystallization proved unsuccessful, leaving minor impurities behind.

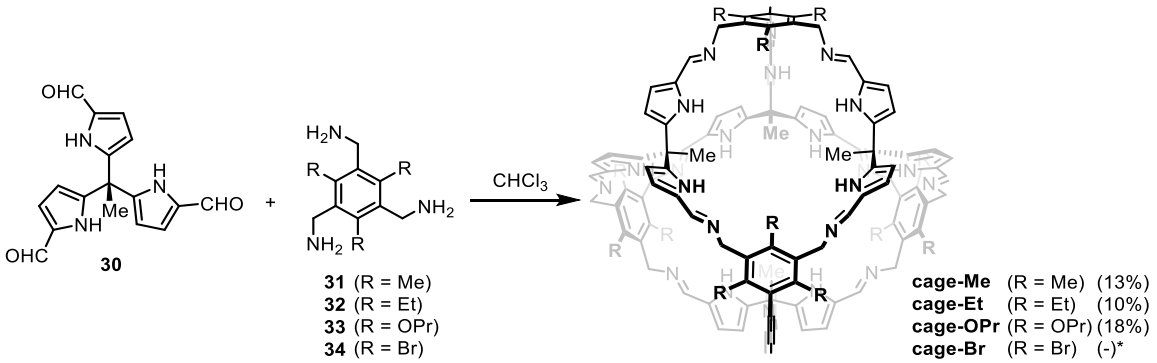

Scheme 20. Synthesis of **cage-Me**, **cage-Et**, **cage-OPr**, and **cage-Br**. (condition: TFA, $CHCl_3$, 60 °C, 2d for **cage-Me**; $CHCl_3$, rt, 2d for **cage-Et**; $CHCl_3$, rt, 2d for **cage-OPr**; TFA, $CHCl_3$, 60 °C, 2d for **cage-Br**)

The isolated cages are fully characterized by NMR spectroscopy and MALDI-TOF MS. In ^{1}H-NMR-spectroscopy, the singlets of the imine protons of cages at 8.15-8.22 ppm were found with the disappearance of aldehyde signals of **30** at 9.13 ppm and the amine units of **31**-**34** at 1.30-1.63 ppm (Figure 66). The chemical shifts of the two protons of the pyrrole groups are located around 6.3 ppm and 5.4 ppm, respectively. The signals of the alkyl groups appear at less than 5.0 ppm. Some solvent still exists in the samples even though were dried in a high dynamic vaccum for more than 7 h.

Furthermore, in MALDI-TOF mass spectrometry, the desired cage ions $[M+H]^+$ appear at *m/z* = 1850.0210 for **cage-Me**, 2018.2058 for **cage-Et**, 2378.3341 for **cage-OPr**, and 2618.7490 for **cage-Br**, which are highly consistent with the simulated ones (Appendix, Figure 200). By DOSY experiments in $CDCl_3$ (T = 295 K) diffusion coefficients of $D = 4.57 \cdot 10^{-10}$ m^2 s^{-1} for **cage-Me**, $3.31 \cdot 10^{-10}$ m^2 s^{-1} for **cage-Et**, and $3.98 \cdot 10^{-10}$ m^2 s^{-1} for **cage-OPr** was measured, corresponding to solvodynamic radii of r_S = 0.87 nm, 1.2 nm, and 1.0 nm, respectively, by exploiting a semi-empirical modification of the Stokes-Einstein equation proposed by Chen et al (Appendix, Figure 197).[139] These are in good agreement to the dimensions obtained by SCXRD (see discussion below).

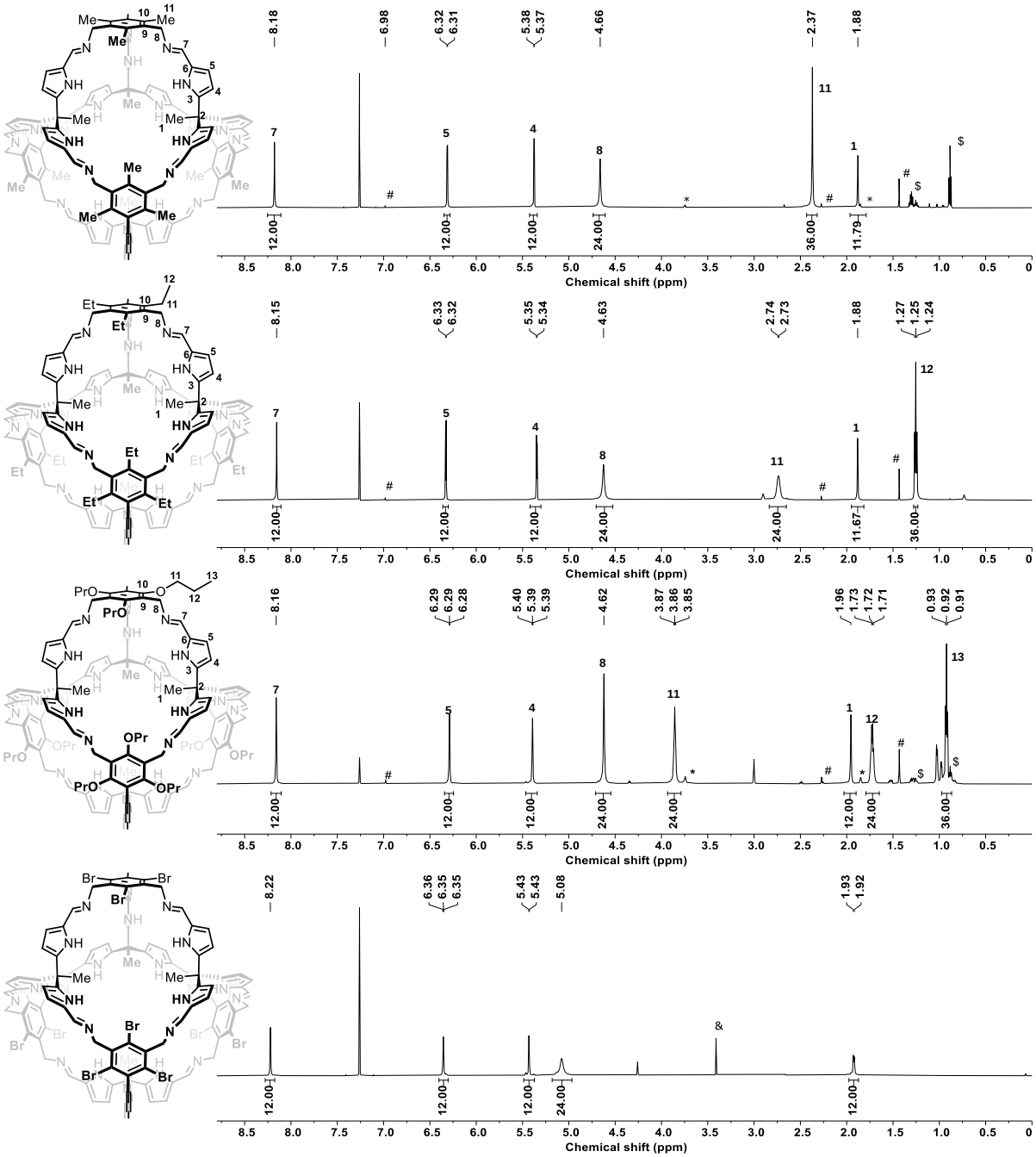

Figure 66. ^{1}H NMR spectra of **cage-Me** (600 MHZ), **cage-Et** (600 MHZ), **cage-OPr** (700 MHZ), **cage-Br** (700 MHZ) in $CDCl_3$. # = BHT, * = THF, $ = pentane, & = methanol. Adapted with permission from Ref.[140]. Copyright © 2023 Thieme Group.

Other fractions of the GPC separation of **cage-Et** from the crude product were also investigated by MS and NMR. In Figure 67, fraction C has been proved to be **cage-Et**. For isolated A fraction, [4+4] condensate is not detected after three cycles while it was detected in isolated B and D fractions after seven and 15 cycles, respectively (Figure 68). It suggests isomeric cage may exist although unsymmetrical GPC pattern and more complex NMR patterns (Appendix, Figure 196) demonstrate it's a mixture.

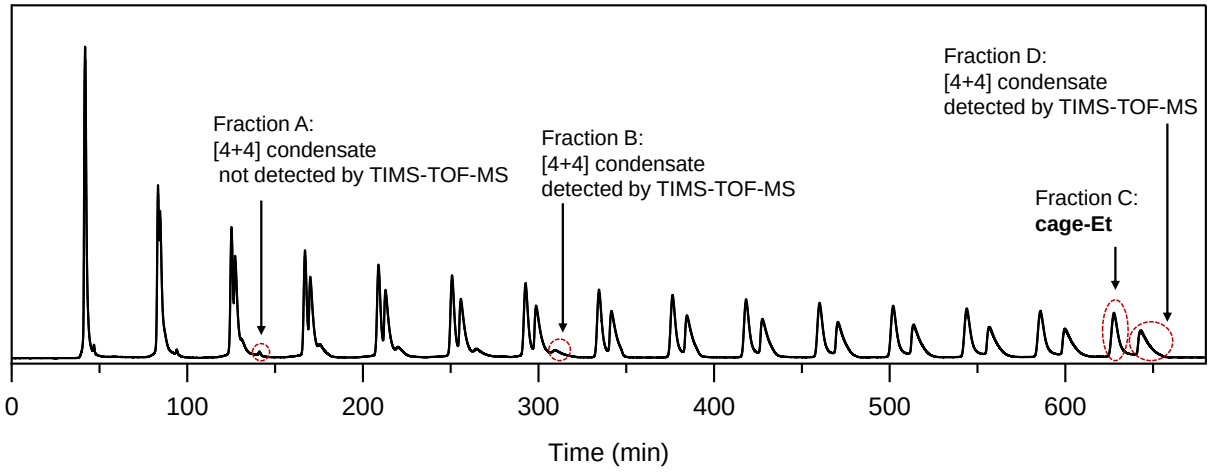

Figure 67. Extended GPC-trace of the separation (THF: flow rate: 5mL/min, temp: 40˚C, wavelength: 254 nm) of **cage-Et** from the crude product with the respective analytical observations. Repetitive injection of the isolated fractions did not lead to further purification, thus structural elucidation was not possible. Adapted with permission from Ref.[140]. Copyright © 2023 Thieme Group.

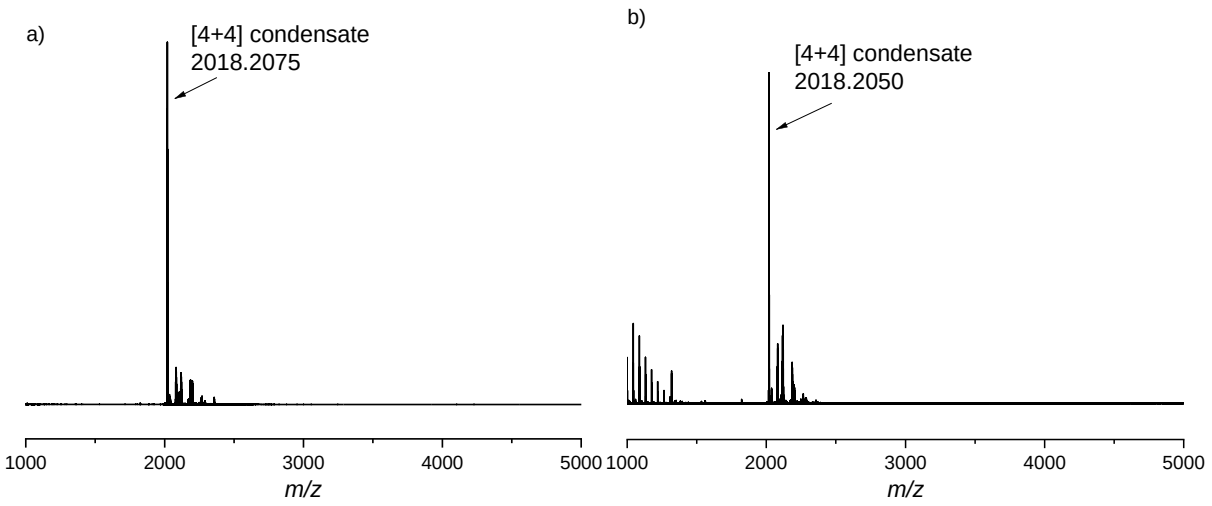

Figure 68. MALDI-TIMS-TOF spectra of the isolated (a) GPC-B fraction after seven cycles and (b) GPC-D fraction after 15 cycles in Figure 67. Adapted with permission from Ref.[140]. Copyright © 2023 Thieme Group.

One potential way to create a mixture of diastereoisomeric cages is the trispyrrol conversion. Quantum chemical calculations at the B3LYP/6-31G(d) level of theory was firstly performed by Moritz Schuldt (OCI, Heidelberg University) to calculate the interconversion energy of a pro-chiral tris-pyrrol unit from *P* (clockwise) to *M* (anticlockwise) orientation (Figure 69). Among this process, the highest energy barrier is 23.7 kJ/mol from intermediate II to transition state III. Even in this case, it would result in a rapid interconversion of $4.35 \cdot 10^8$ s^{-1} and a half-life time of 1.59 ns, suggesting a fast interconversion in solution. Each of three pyrrol units of a [4+4] cage adopts a chiral C_3-symmetrical conformation (*P* or *M*). Every [4+4] cage can adopt one out of five possible conformation-*MMMM*, *PPPP*, *MMMP*, *MMPP*, and *MPPP*.

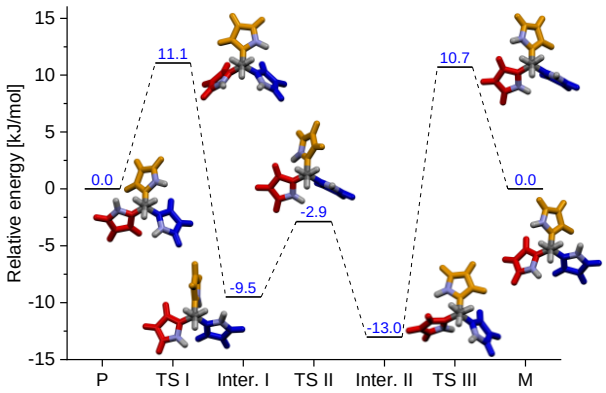

Figure 69. DFT-calculated (B3LYP/6-31G(d)) interconversion of *P*- to *M* trispyrrol. Caculated by Moritz Schuldt (OCI, Heidelberg University). Reproduced with permission from Ref.[140]. Copyright © 2023 Thieme Group.

The comparably low relative energies of these five cages, ranging from 6.7 to 11.1 kJ/mol, independent of the side-chains, further indicate a fast interconversion excluding diastereomeric cages that cause the multiple fractions in r-GPC separation (Figure 70a). Another possibility is that the facial rotation of the tris-pyrrols unit (central methyl-units of the tris-pyrrols point out) leads to the formation of five in-out-isomers. The relative energies of the possible in-out combinations suggest that the all-in isomers should be mainly present in a dynamic equilibrium in solution (Figure 70b). Thus, it can be concluded that the different fractions obtained by r-GPC contain different in-out isomers of the cages that are kinetically trapped.

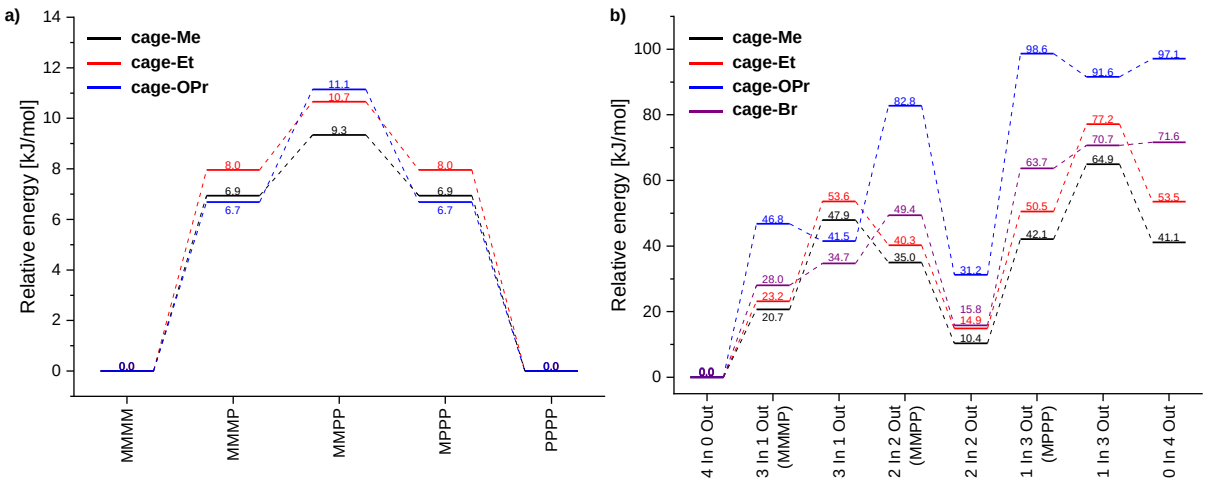

Figure 70. Energy levels of the different In-Out cage isomers calculated at B3LYP/6-31G(d) level of theory. Caculated by Moritz Schuldt (OCI, Heidelberg University). Reproduced with permission from Ref.[140]. Copyright © 2023 Thieme Group.

To get further insight into the kinetics of this series of cages, a sample of pure **cage-OPr** was dissolved in $CDCl_3$, treated with a small amount of TFA and TFA/p-phenylenediamin, and kept at room temperature for 20 hours. Indeed, no signal of the cleavage of imine bonds was witnessed (Figure 71).

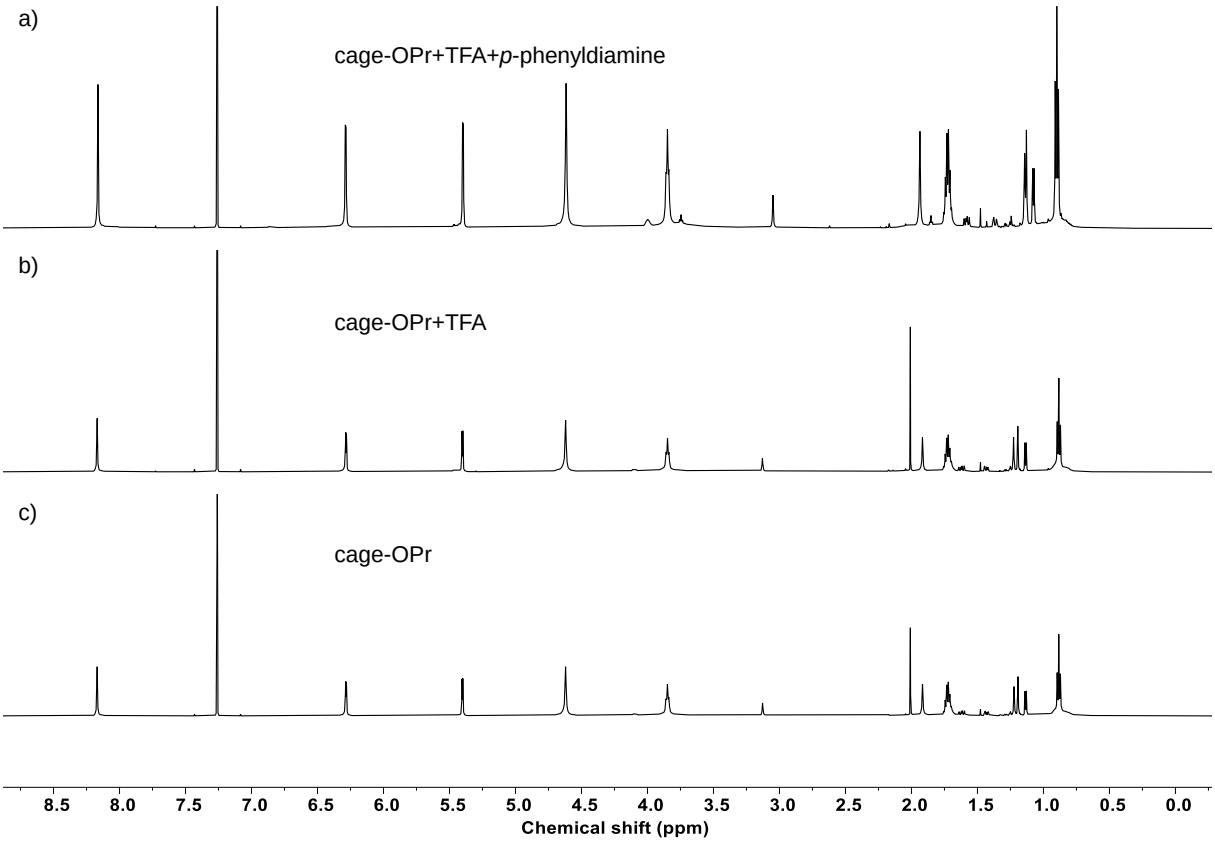

Figure 71. ^{1}H NMR spectra of **cage-OPr** (600 MHZ) in $CDCl_3$. (a) added with two drops of 0.01 M TFA and *p*-phenylenediamine in $CDCl_3$, (b) added with two drops of 0.01 M TFA solution in $CDCl_3$, (c) no add.

3.2. Single Crystal Structure Investigation

Six high-quality single crystals of four cages with various side chains were obtained by vapor diffusion (**cage-Me**, **cage-Et$_\alpha$**, **cage-Et$_\beta$**, **cage-OPr**, and **cage-Br**) or slow evaporation (only **cage-Et$_\gamma$**). In contrast to **cage-Et$_\alpha$** (cubic, $P_a\bar{3}$) and **cage-OPr** (orthorhombic, $A_{ba}2$), all other cages have crystallized in the triclinic space group $P\bar{1}$. The structures of all cages are confirmed by SCXRD, which best describes their geometrical shapes as truncated cubes with tetrahedral symmetry (Figure 72). In all cases, all central methyl groups of the trispyrrols are found in the cage cavities and pointing into phenyl rings opposite. The distances between them are measured to be $d_{Me\text{-}Ph}$ = 1.2-1.3 nm, with an outer diameter of d = 1.5-1.6 nm, which corresponds well with the solvodynamic radii of r_S = 0.87-1.2 nm determined from DOSY NMR. For **cage-Me** and **cage-Br**, it's undisputed that methyl and bromine group is on the plane of phenyl rings. The orientation of the ethyl and propoxy chains, whether pointing towards the cage's window or outward, is referred to as "endo" and "exo", respectively. In the

case of **cage-Et**, all the ethyl groups are oriented in the *exo* fashion, whereas only six of the twelve propoxy chains in cage-OPr are oriented *exo*.

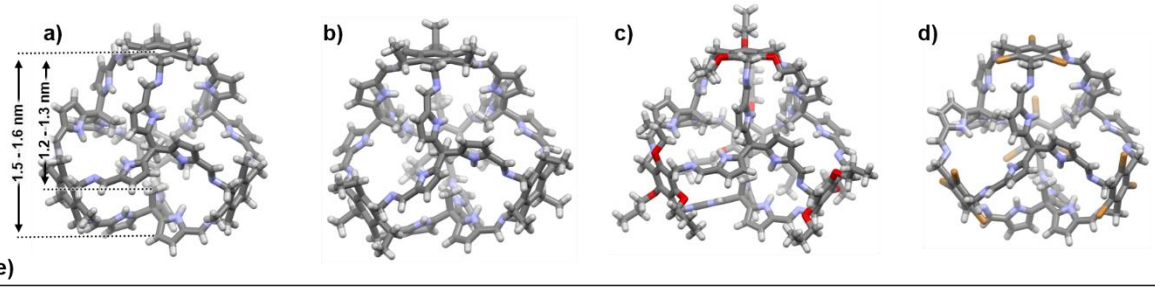

e)

Compound	Solvents	Crystal System	Space Group	Z	Cell Volume	Isomers observed	Packing
cage-Me	$CDCl_3$/MeOH	Triclinic	$P\bar{1}$	2	7578.4 Å^3	*MMMM* / *PPPP*	enantiopure layers
cage-Et$_\alpha$	CH_2Cl_2/C_6H_{14}	Cubic	$P_a\bar{3}$	8	31222.2 Å^3	*MMMP* / *PPPM*	3D-alternating
cage-Et$_\beta$	CH_2Cl_2/MeOH	Triclinic	$P\bar{1}$	2	7646.5 Å^3	*MMMM* / *PPPP*	enantiopure layers
cage-Et$_\gamma$	$CDCl_3$	Triclinic	$P\bar{1}$	2	8142.8 Å^3	*MMMP* / *PPPM*	enantiopure layers
cage-OPr	CH_2Cl_2/MeOH	Orthorhombic	$A_{ba}2$	4	18567.7 Å^3	*MMMM* / *PPPP*	enantiopure layers
cage-Br	CH_2Cl_2/MeOH	Triclinic	$P\bar{1}$	2	7399.5 Å^3	*MMMM* / *PPPP*	enantiopure layers

Figure 72. Single crystal X-ray structures of the cages **cage-Me** (a), **cage-Et** (b), **cage-OPr** (c) and **cage-Br** (d) as capped-sticks models. The distance of a phenyl unit to the opposing internal methyl group and to the outer carbon atoms of the trispyrrol moiety are given for **cage-Me** exemplarily. Colors: carbon, gray; nitrogen, blue; oxygen, red; bromine, brown; hydrogen, white. (e) Selected crystallographic data of **cage-Me**, **cage-Et**, **cage-OPr**, and **cage-Br**. Adapted with permission from Ref.[140]. Copyright © 2023 Thieme Group.

As previously stated, every three-pyrrol unit of the cage adopts a chiral C_3-symmetrical conformation (*P* or *M*) in solid state, resulting in five possibilities of cage isomerization (homo-directional: *MMMM* and *PPPP*; hetero-directional: *MMMP*, *MMPP*, and *MPPP*). The solid-state structures of **cage-Me**, **cage-Et$_\beta$**, **cage-OPr**, and **cage-Br** adopt single enantiomeric *MMMM* or *PPPP* orientation, a phenomenon similar to the assembly of face-oriented polyhedra derived from prochiral building blocks, as reported by the Cao *et al*.[132a] and Li *et al*.[135, 141]. The [4+4] cage molecule consists of four unchiral arene faces linked by four chiral three-pyrrol unit faces. Since four out of eight “faces” of the synthesized [4+4] truncated cubes possess helical chirality, the cages can be understood as semi-face-orientated polyhedral (Figure 73). For **cage-Et**, solvates **cage-Et$_\alpha$** and **cage-Et$_\gamma$** adopt hetero-orientations (*MMMP* and *PPPM*).

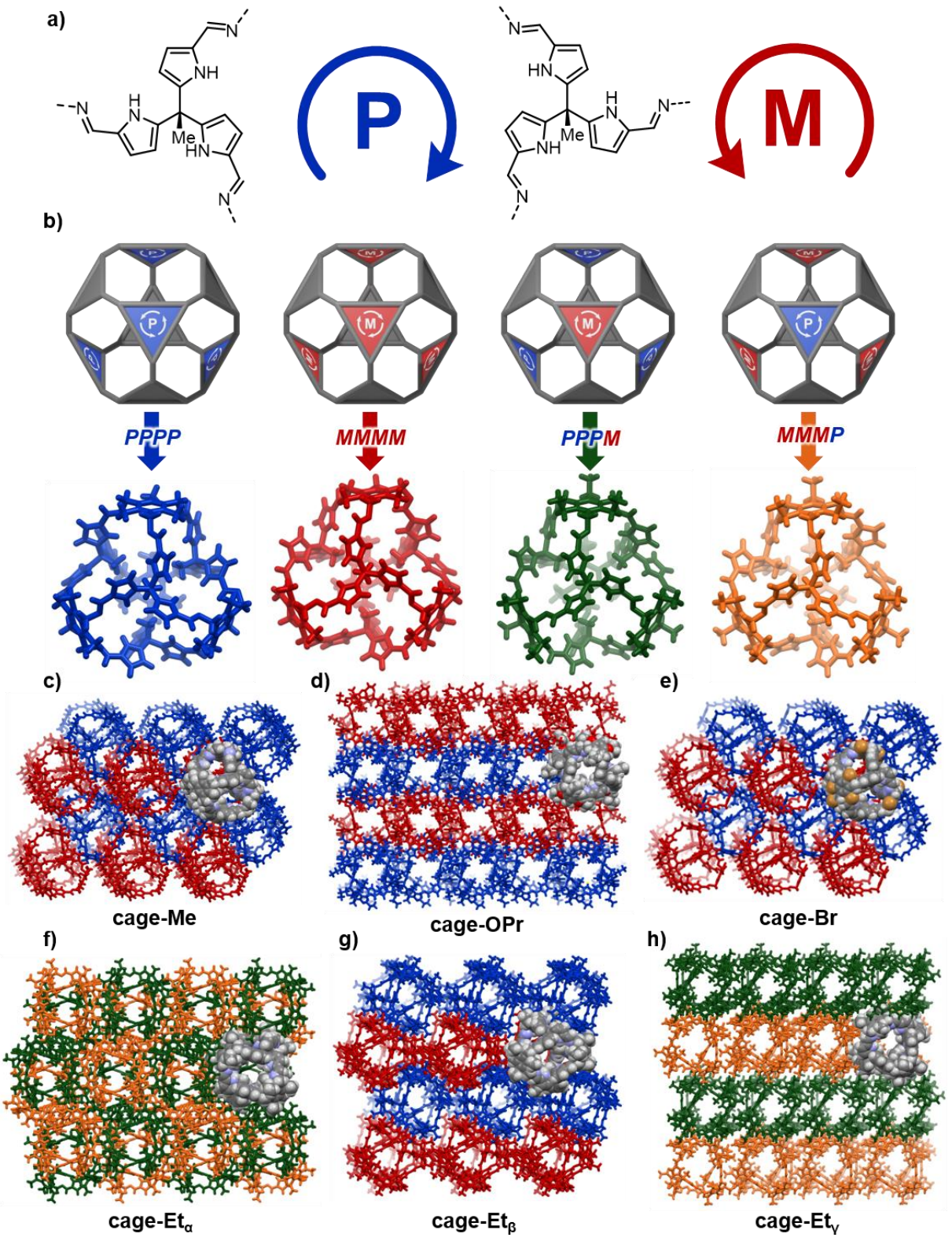

Figure 73. a) Schematical depiction of the *P*- and *M*-alignment of the prochiral tripyrrol units. *Note*: The methyl group pointing out of the paper plane here is pointing inside the cage voids, which has to be taken into account in the following figures. b) Schematic representations of the homochiral *PPPP* (shown in blue for **cage-Me**) and *MMMM* (shown in red for **cage-Me**) as well as heterochiral *PPPM* (shown in green for **cage-Et$_\alpha$**) and *MMMP* (shown in orange for **cage-Et$_\alpha$**) cages. d-h) Packing motifs of the obtained solvates with different enantiomers colored according to Figure 73b as capped sticks model. One cage each is shown as space fill model in element colors. The models of the cages were created by Dr. Tobias Kirschbaum (OCI, Heidelberg University). Reproduced with permission from Ref.[140]. Copyright © 2023 Thieme Group.

The **cage-Me** and **cage-Br** molecule compound assembly into an isomorphism in the solid state with similar unit cell volumes of 7578.4 Å^3 and 7399.5 Å^3, respectively (Figure 72e). The packing is dominated by one face-to-face π-π-stacking and five edge-to-face interactions of substituted phenyl rings for each cage (Figure 74a-d). The distance of face-to-face π-π-stacking $d_{\pi\text{-}\pi}$ is 3.43 Å (**cage-Br**) and 3.48 Å (**cage-Me**). The edge-to-face interactions involve C-H···π-interactions for **3-Me** with $d_{\text{C-H}\cdots\pi}$ = 2.99 Å and C-Br···π-interactions for **cage-Br** with $d_{\text{C-Br}\cdots\pi}$ = 3.26 Å. The packing of both cages generates enantiopure layers of *PPPP* and *MMMM* within the crystallographic *ab*-planes. Similar layers are found in homochiral **cage-OPr**, and the solvate **cage-Et$_\beta$**, as well as heterochiral solvate **cage-Et$_\gamma$** while for solvate **cage-Et$_\alpha$**, the enantiomeric cages ***MMMP*-cage-Et** and ***PPPM*-cage-Et** are arranged in an alternating order in all three dimensions (Figure 73).

A solvent-filled “Russian doll” was discovered in **cage-Me** crystal (Figure 74e-g). Single crystals of **cage-Me** were obtained by vapor diffusion of methanol into $CHCl_3$ solution. The nitrogen-rich cavities of **cage-Me** provide an ideal internal environment for polar guests. Methanol forms H-bonds with the pyrrol-imine subunits of **cage-Me**, with the distance of $d_{\text{N-H}\cdots\text{O}}$ = 2.00 Å and $d_{\text{O-H}\cdots\text{N}}$ = 2.11 Å, respectively, which leads to that twelve methanol molecules self-assemble into a shell in cavities of the cage, with highly polar OH-groups pointing out and less polar methyl groups pointing inwards. One molecule of $CHCl_3$ is stabilized at the center of the shell via van-der-Waals interactions with sixteen methyl groups from both methanol and cages. While molecular-level Russian-doll alignments with three spheres have been achieved previously,[142] as far as our knowledge extends, the structure discussed here represents the first organic cage compound featuring two Russian-doll alignments of three spheres, two of which are two different solvents. Furthermore, the inter-cage voids are filled with seven more methanol and one water molecule.

The single crystals **cage-Et$_\beta$** were obtained by vapor diffusion of methanol into a dichloromethane solution of **cage-Et** (Figure 72). Ten methanol molecules are found in similar alignments as discussed for **cage-Me**, yet due to disorder, the residual solvent molecules had to be SQUEEZED. **cage-OPr** was also crystallized under the same condition (Figure 72). Ten methanol and nine water molecules are found filling one-dimensional channels along the *c*-axis in the crystallographic *bc*-plane (Figure 74h). Water molecules align in a chain-like fashion along the crystallographic *a*-axis.

Owing to rapid exchange, the hydrogen atoms of the water molecules were not observed in the crystallographic data, and thus a detailed discussion of the hydrogen-bonding pattern is not possible.

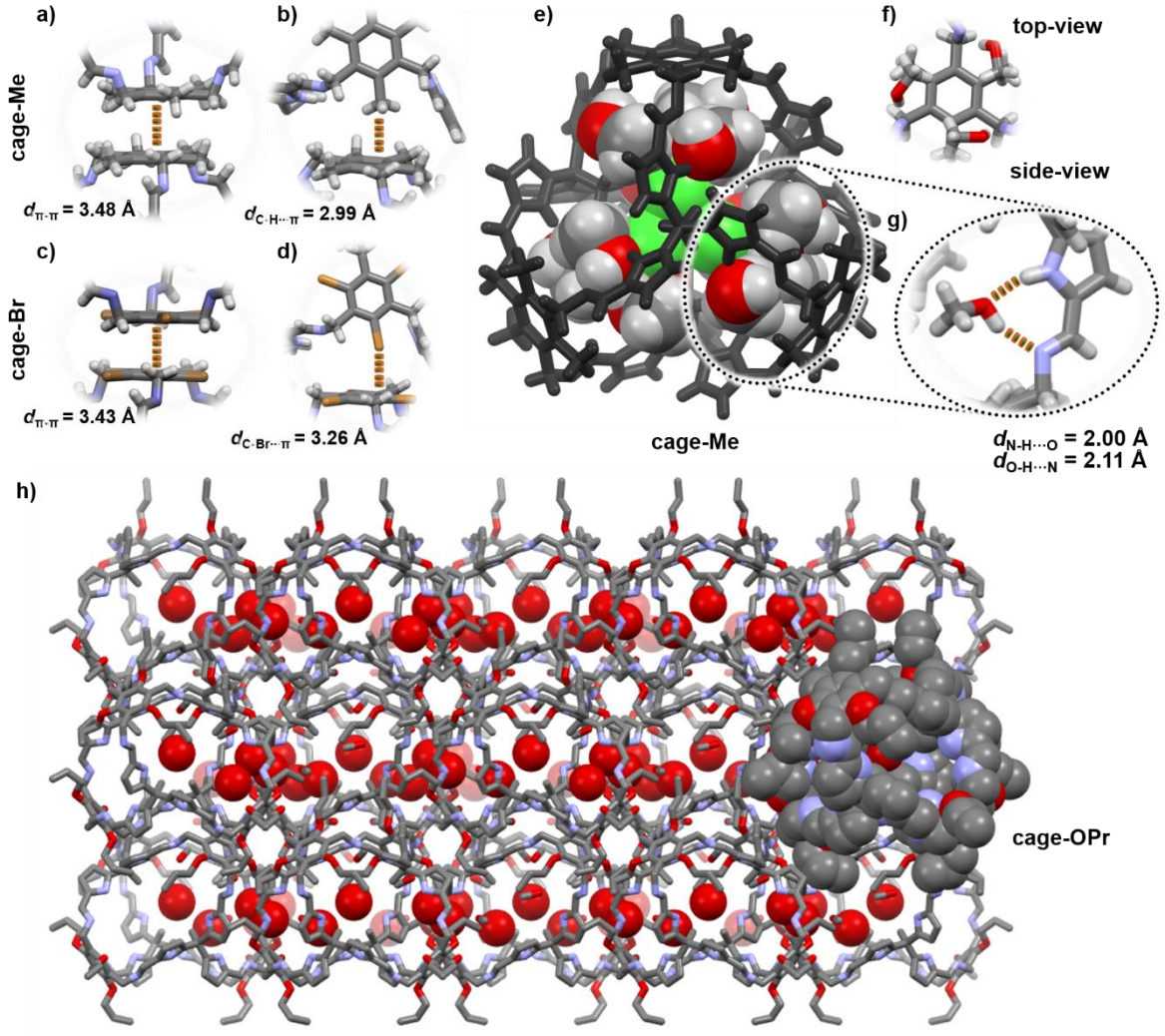

Figure 74. Intermolecular interactions found in the single crystal X-ray structures of **cage-Me** (a-b) and **cage-Br** (c-d). Colors: carbon, gray; nitrogen, blue; oxygen, red; bromine, brown; hydrogen, white. Residual solvent analysis of single crystal X-ray structures of **cage-Me** and **cage-OPr**. e) **cage-Me** (shown in black as capped sticks model) with twelve molecules of methanol and one molecule $CHCl_3$ (shown as space fill models). f) Top-view and g) side-view of the hydrogen bonding pattern in detail. h) Crystal packing of **cage-OPr** (shown as capped sticks models with one molecule shown as space fill model in element colors) with ten methanol molecules (shown as capped sticks model in element colors) and nine water molecules (shown as space fill model in red without hydrogen atoms). H atoms are omitted for the sake of clarity. Adapted with permission from Ref.[140]. Copyright © 2023 Thieme Group.

3.3. Conclusion

In summary, a small series of 4+4 truncated tetrahedral imine cages based on a tripyrroltrialdehyde has been constructed, and their corresponding single-crystal X-ray structures are reported here. Due to steric repulsion, each tripyrroltrialdehyde adopts a chiral C_3-symmetrical conformation (*M* or *P* orientations), generating a chiral face.

Four chiral faces out of eight “faces” orient in homoenantio *PPPP* and *MMMM* form for all cases besides two solvates **cage-Et** in the heteroenantio *MMMP* and *PPPM* form. In addition, the nitrogenous interior of the cages is capable of interacting with polar molecules like methanol or water, leading to molecular self-assemble into shells or chain-like structures. These discoveries can be extened to other cages for the selective binding of polar guests. Furthermore, the nitrogen-rich cavity can be used as cage ligand for transition metal ions or clusters.

IV. Summary and Outlook

In this thesis, a series of [2+3] porous imine cages with various degrees of side-chain fluorination (butyl, fluorobutyl, and partially fluorinated butyl groups) and different lengths of perfluorinated side chains (from perfluoromethyl to perfluorohexyl groups) have been synthesized from triaminotriptycene **15** and side chain modified terphenyl bisalicylaldehydes (Scheme 21). These cages have been assembled into isomorphic crystalline materials and examined for their gas sorption properties for F-gases and their selective uptakes. The cage with relatively long fluoroalkyl side chains displayed outstanding F-gas selective adsorption properties in binary mixtures of F-gas/N_2, F-gas/O_2 and F-gas/CO_2. By exploring the relationship between structure and property from two perspectives, these excellent properties were attributed to F···F interactions between the host and guest, supported by the analysis of C_3F_8-loaded single-crystals. Moreover, the strongly hydrophobic side chains of the fluorinated cages conferred them with excellent acid/base/water stability. These fluorinated cages are promising candidates for practical F-gas separation in harsh environments. The underlying principle of F···F interactions is expected to be extended to other porous materials for the removal of F-gas or to reduce their release into the atmosphere.

The solid packing of POCs significantly influences gas sorption. **cage-CF_3** with fluoromethyl groups exists in three different polymorphic forms (α, β, γ) that are either porous or non-porous, distinguished by their crystallographic packing. Intriguingly, these polymorphs maintain their crystallinity even after desolvation, suggesting the potential for reversible switching in response to external stimuli in future research.[79-80, 87] Additionally, two new [2+3] cages, **cage-CH_3** and **cage-Nap**, have been synthesized (Scheme 21). A detailed study of four single crystal X-ray structures in total revealed, that the prochiral terphenyl unit orient in homo *L-L-L* and *R-R-R* conformations in **cage-$CF_{3\alpha}$** and **cage-CH_3** while heteroenantiomeric *L-R-L* and *L-R-R* forms are found in **cage-$CF_{3\beta}$** and **cage-$CF_{3\gamma}$**. In gas sorption experiments, **cage-Nap** has the highest specific surface area (SA_{BET} = 909 m^2 g^{-1}) in this series of [2+3] cages due to the elongated π system. It is possible that perfluoroalkyl-functionalized **cage-Nap** may exhibit promising F-gas sorption and selective sorption performance in future investigations. Further, optimized activation conditions enabled a higher specific surface area (SA_{BET} = 317 m^2 g^{-1}) and H_2 uptake (52.3 cm^3 g^{-1}, 0.47 wt% at 760 Torr and 77K) for **cage-C_6F_{13}**.

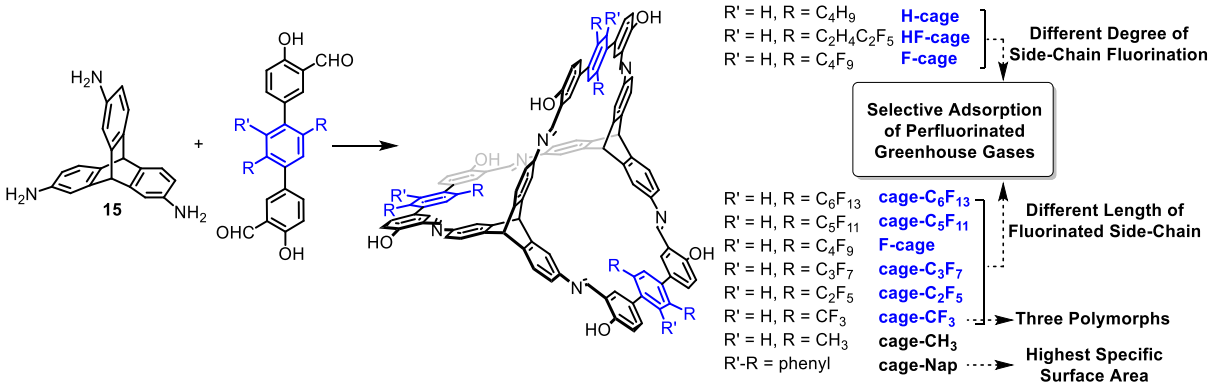

Scheme 21. [2+3] imine cages with different side chains for selective adsorption of perfluorinated greenhouse gases.

A series of [4+4] truncated tetrahedral nitrogen-rich imine cages based on a tripyrroltrialdehyde were synthesized, and their face-orientated polyhedra in the crystalline state were elucidated by X-ray crystallography (Scheme 22). Due to steric repulsion, each tripyrroltrialdehyde adopt a chiral C_3-symmetrical conformation (*M* or *P* orientations), generating a chiral face. Four chiral faces out of eight "faces" orient in homoenatio *PPPP* and *MMMM* for all cases besides two solvates **cage-Et** in the heteroenantio *MMMP* and *PPPM* form. The nitrogen-rich interior of these cages presents a potential application for the selective binding of polar guest.

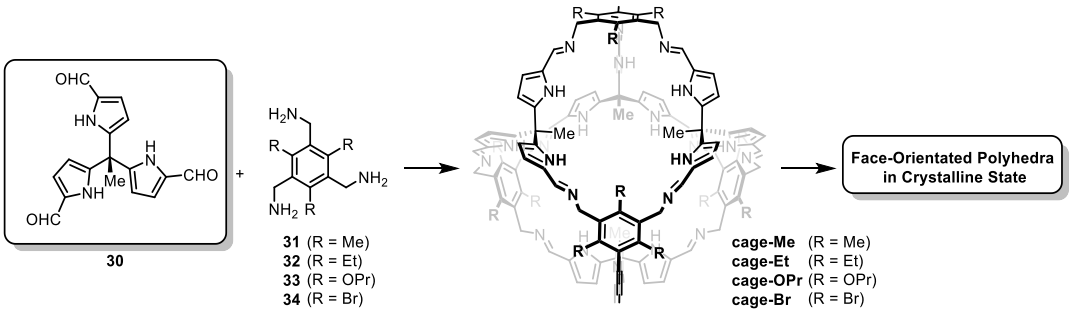

Scheme 22. Synthesis of [4+4] imine cages derived from chiral C_3-symmetrical building block **30**, followed into face-orientated polyhedral in crystalline state.

V. Experimental Section

1. General Remarks

Thin layer chromatography was performed with POLYGRAM® SIL G/UV254 gel plates by Macherey-Nagel. Detection was accomplished using UV-light (254 nm). Flash column chromatography was performed on silica gel from Macherey-Nagel (particle size: 0.040-0.063 mm).

Melting points (not corrected) were measured with a Büchi B-540 melting point analyzer.

NMR spectra were taken on a Bruker DRX 300 (300 MHz), Bruker Avance 300 III (300 MHz), Bruker Avance III 400 (400 MHz), Bruker Avance III 500 (500 MHz), Bruker Avance III 600 (600 MHz) and Bruker Avance III 700 (700 MHz) spectrometer. NMR spectra were internally referenced to residual solvent peaks in $CDCl_3$ (^{1}H-NMR: δ = 7.26 ppm, ^{13}C-NMR: 77.2 ppm) and THF-d_8 (^{1}H-NMR: δ = 1.72, 3.58 ppm, ^{13}C-NMR: 67.2, 25.3 ppm). DMSO-d_6 (^{1}H-NMR: δ = 2.50 ppm, ^{13}C-NMR: 39.5 ppm). NMR signals are reported as (s = singlet, d = doublet, t = triplet, m = multiplet; coupling constant(s) in Hz; integration; assignment). Structural assignments were made with additional information from 2D-NMR experiments (COSY, HSQC, HMBC and NOESY).

IR-Spectra were recorded on a Bruker Tensor 27 spectrometer on a ZnSe ATR crystal. The absorption bands $\tilde{\nu}$ are reported in cm^{-1} using the following abbreviations: s = strong, m = medium, w = weak.

HR-MS experiments were carried out, on a Bruker ApexQe-Fourier Transform Ion Cyclotron Resonance (FT-ICR) instrument equipped with a 9.4 T superconducting magnet and interfaced to an Apollo II MTP ion source and MALDI-TOF experiments were carried out at a Bruker Autoflex speed MALDI-TOF spectrometer, both with DCTB (*trans*-2-[3-(4-*tert*-butylphenyl)-2-methyl-2-propenylidene]malononitrile) as matrix. APCI MS was carried out on a Bruker timsTOFfleX ion mobility-quadupole-time-of-flight (IM-Q-TOF) spectrometer operated in APCI mode. EI MS measurements have been carried out on a JEOL AccuTOX GCx spectrometer.

Elemental analysis was performed by the Microanalytical Laboratory of the University of Heidelberg using an Elementar Vario EL machine.

X-ray crystal structure analysis was accomplished on a STOE Stadivari

diffractometer with a copper source (*λ* CuKα = 1.54178 Å) and a PILATUS detector. Data processing and absorption correction (X-Area LANA 1.83.8.0)[143] were accomplished by standard methods.

TGA was measured on a Mettler-Toledo TGA/DSC1 instrument with a TGA/DSC-Sensor 1100 equipped with a MX1 balance (Mettler-Toledo) and a GC100 gas control box for nitrogen supply.

Powder diffractometry was performed on Rigaku SmartLab diffractometer operated at 9 kW and equipped with a HyPix-3000 detector with incident CuKα radiation at *λ* = 1.54059 Å using a Debye-Scherrer geometry. The samples have been ground prior to measurements and have been measured in special glass mark-tubes with a 0.6 mm inner diameter at a capillary spin stage with 60 rpm. A background was collected using an empty capillary with the same measurement conditions and this was used for baseline correction by substraction. The measurements were performed under Dr. Sven M. Elbert's help at IMSEAM (Heidelberg University).

The surface areas and porosity was characterised by nitrogen, argon and carbon dioxide sorption analyses with autosorb computer-controlled surface analysers (AUTOSORB-IQ2 or AUTOSORB-IQ3, Quantachrome). Cooling was accomplished using a compressed helium CryoCooler (IQ3) or common cooling baths (IQ2); for the latter the temperatures were frequently monitored by a VWR TD 131 digital thermometer. The IQ3 is equipped with 1000, 10 and 0.1 and the IQ2 with 1000, 10 and 1 torr sensors for low pressure measurements. Typically, 10-50 mg of sample were loaded into 9 mm glass tubes (IQ2) or 6 mm cryo cooler tubes (IQ3). The Brunauer-Emmett-Teller (BET) surface areas were calculated assuming a cross sectional area of 0.162 nm^2 for nitrogen molecules, 0.142 nm^2 for argon molecules and 0.164 nm^2 for carbon dioxide molecules at 77 K (N_2), 87 K (Ar) and 195 K (CO_2). The corresponding pressure ranges have been determined using Rouquerol plots; here only the relative pressure values with a positive slope in the Rouquerol plot were taken into account. The specific properties of the corresponding gases can be found in the gas sorption chapter of this section. The measurements of Chapter III, section 1 were performed under Dr. Sven M. Elbert's help at IMSEAM and OCI (Heidelberg University). The measurements at 298 and 313 K of Chapter III, section 2.1. were performed by Dr. Anjana Kunhumbadukka Othayoth (Heidelberg University) under my help at IMSEAM.

Optical microscopy was accomplished using a reflecta digimicroscope flex digital microscope with LED lighting was used. The digital zoom factor was manually chosen

between 60× and 250×. Pictures were taken directly from the as-crystallized sample in the corresponding mother liquor as well as of the crystalline powder after the gas sorption procedure.

Electron micrographs (SEM-pictures) have been obtained with a prototype field emission scanning electron microscope Delta (Carls Zeiss Microscopy), using a landing energy of 1k to 3k eV, a working distance of 3 to 5 mm and a HE-SE2 detector. The powder samples were fixed on the adhesive carbon tabs (Plano) and then sputter-coated with a 3 nm layer of Pt/Pd (weight ratio 80/20, Quorum) using a Quorum sputter coater Q150V ES plus. The measurements were performed by Dr. Wen-Shan Zhang (BioQuant, Heidelberg University). The SEM micrographs presented in the main text were adjusted with brightness and contrast for a easy viewing using MS PowerPoint.

Recycling gel permeation chromatography (r-GPC) was carried out using a Shimadzu Prominence LC20 system with a DGU-20A3R degassing unit, a LC20AD pump unit, a CTO-20AC column oven, Ca BM-20A communication bus module, a SPD-M20A diode array detector, an FRC-10A fraction collector and an FCV-20AH2 valve unit being equipped with a PSS SDV (20 × 50 mm) pre-column and SDV ($d \times L$ = 20 × 300 mm) columns (3 × 100 Å for **cage-Et** cage; 2 × 500 Å and 2 × 1000 for cages **cage-Me** and **cage-OPr**).

Quantumchemical calculations were performed by employing the Gaussian16 program package.[144] The theoretical approach is based on Kohn-Sham density functional methodologies[145] using the B3LYP[146] functional. As basis set the augmented, polarised triple-ζ-basis (aug-cc-pVDZ[147]) was used. For the calculations the quadratic convergence criteria, as implemented in Gaussian16, were applied. The dispersion energies of the corresponding fragments were calculated applying the exchange-hole dipole moment (XDM) model using the postg program package developed by the Johnson group.[148] Quantumchemical calculations of Chapter III, Section 1 and 3 were performed by Dr. Tobias Kirschbaum and Moritz Schuldt (Heidelberg University), respectively.

Software: Microsoft Word 2016 was used to write this thesis, chemical formulas were drawn using ChemDraw 20.0 by Cambridgesoft and graphs were processed with Origin 2020 by OriginLab Corp. and R package *ggplot2* version 3.4.2 (R Core Team, 2022). IR and MS spectra were processed using ACD/Spectrus Processor 2017 by Advanced Chemistry Development, Inc. and mMass (5.5.0), respectively, and then plotted using Origin. NMR spectra were integrated and processed using MestReNova

(v14.0.1-23559). Mercury 4.3.1 (2020) was used to evaluate X-ray structures and generate graphics. Endnote X9 (Bld 12062) was used to manage literature citations. Hirshfeld surface analysis was processed using CrystalExplorer17. Gas selectivities were calculated using 3P's 3P Sim software (Version 1.1.0.9; 2018). Theoretical breakthrough were calculated using the 3P sim software of 3P instruments (Version 1.1.2.3; 2020).

1.1. Solvents

The solvents were used without further purification or drying unless otherwise mentioned. Dry solvents (dichloromethane and tetrahydrofurane) were taken from a MB SPS-800-Benchtop solvent purification system (SPS), using MB-KOL-A and MB-KOL-M as filter materials and MB-KOL-C as catalyst or dried according to standard procedures and stored over molecular sieves (3 Å or 4 Å as appropriate).

Chloroform	99.8% stab. with 0.5-1.5% EtOH	Sigma-Aldrich
Chloroform-d	99.8% atom% D	Sigma-Aldrich
Dichloromethane	≥ 99%, stab. with amylene	Fisher Scientific
Dichloromethane (for SPS)	≥ 99.8%	Honeywell
Diethyl ether	≥ 99.5%	Sigma-Aldrich
Dimethyl sulfoxide	99.9%	Sigma-Aldrich
DMSO-d_6	99.9% atom% D	Sigma-Aldrich
Ethanol	≥ 99.8%	Sigma Aldrich
Ethyl acetate	≥ 99.5%	Honeywell
Methanol	≥ 99.8%	Honerwell
N-Methyl-2-pyrrolidone	99.5%	Sigma-Aldrich
N,N-Dimethylformamide	≥ 99.8%	Sigma-Aldrich
n-Pentane	≥ 99%	Honeywell
Petroleum ether (40-60 °C)	n.d.	Honeywell
THF-d_8	≥ 99.5 atom% D	Sigma-Aldrich
Tetrahydrofurane	≥ 99.9 (stab. with 250 ppm BHT)	Honerwell
Tetrahydrofuran (for SPS)	≥ 99.9%	Honerwell
Toluene	≥ 99.7%	Honerwell
1,4-Dioxane	≥ 99.5%	Sigma Aldrich

Water	deionized	Uni-Heidelberg Institute

1.2. Chemicals

Commercially available reagents were obtained from Acros Organics, Honeywell, Merck, Alfa-Aesar, Sigma-Aldrich or Fluorochem, etc, and have been used without further purification unless otherwise mentioned. Compounds **31**, **33**, **34**, and **88** were obtained from Dr. Jochen C. Lauer (Heidelberg University). Compound **15** was synthesized by bachelor students in AK Mastalerz group (Heidelberg University).

Acetic acid	n.d.	Honeywell
Bromine	reagent grade	Sigma-Aldrich
1-Bromobutene	≥98%	Merck
5-Bromosalicylaldehyde	n.d.	Alfa-Aesar
[1,3-Bis (diphenylphosphino)-propane] nickel (II) chloride	99%	Acros Organics
Copper iodide(I)	≥ 99.5%	Sigma-Aldrich
Cu powder	99.5%	Sigma-Aldrich
18-Crown-6	>99%	Sigma-Aldrich
1,4-Dibromobenzene	98%	Sigma-Aldrich
1,4-Dichlorobenzene	≥99%	Sigma-Aldrich
1,4-Diiodobenzene	99%	Sigma-Aldrich
1,4-Dibromo-2,5-dimethylbenzene	98%	Sigma-Aldrich
1,4-Dibromonaphthalene	98%	Acros Organics
Fuming nitric acid	90%	Acros Organics
Hydrazonium hydroxide	98%	Merck
Hydrochloric acid	36.5%-38%	Honeywell
Iodine	99.8%	Fluka
Magnesium	≥99.5%	Sigma-Aldrich
Magnesium sulfate	>99%	Bernd Kraft
Nonafluoro-1-iodobutane	98%	Sigma-Aldrich
N-Bromosuccinimide	99%	Sigma-Aldrich
1,1,1,2,2-pentafluoro-4-iodobutane	97%	Fluorochem
Perfluoropropyl iodide	98%	Sigma-Aldrich
Perfluoropentyl iodide	98%	Sigma-Aldrich
Perfluorohexyl iodide	99%	Sigma-Aldrich

Pyrrole	>99%	TCI
Phosphoryl chloride	99%	Sigma-Aldrich
Potassium phthalamide	>99%	Sigma-Aldrich
[1,1'-Bis(diphenylphosphino)ferrocene]-dichloropalladium(II)	99%	Carbolution
Palladium on act. Charcoal (5% Pd basis)	n.d.	Degussa
Potassium carbonate	99%	Grüssing
Potassium fluoride	99%	Grüssing
Potassium hydroxide	99.9%	Grüssing
Sodium hydroxide	>98%	Honeywell
Sodium sulfate	>99%	Bernd Kraft
Sodium pentafluoropropionate	98%	Fluorochem
Sulfuric acid (conc.)	95-97%	Sigma-Aldrich
Tris(dibenzylideneacetone)dipalladium(0)	97%	Acros Organics
Tri-*tert*-butylphosphonium Tetrafluoroborate	97%	Sigma-Aldrich
Triethyl orthoacetate	97%	Sigma-Aldrich
Trifluoroacetic acid	99%	Acros Organics

1.3. Gases

Table 15. Gases used in the here presented studies.

Gas	Formula	CAS	Supplier	Quality
Nitrogen	N_2	7727-37-9	Air Liquide	5.0 (99.999%)
Argon	Ar	7440-37-1	Air Liquide	4.8 (99.998%)
Carbon dioxide	CO_2	124-38-9	Air Liquide	4.5 (99.995%)
Oxygen	O_2	7782-44-7	Air Liquide	4.8 (99.998%
Methane	CH_4	74-82-8	Air Liquide	2.5 (99.5%)
Ethane	C_2H_6	74-84-0	Air Liquide	2.5 (99.5%)
Propane	C_3H_8	74-98-6	Air Liquide	2.5 (99.5%)
Perfluoromethane	CF_4	75-73-0	Air Liquide	4.5 (99.995%)
Perfluoroethane	C_2F_6	76-16-4	Air Liquide	4.8 (99.998%)
Perfluoropropane	C_3F_8	76-19-7	Air Liquide	3.7 (99.97%)
Perfluorocyclobutane	*c*-C_4F_8	115-25-3	Air Liquide	3.6 (99.96%)
Sulfur hexafluoride	SF_6	2551-62-4	Air Liquide	5.0 (99.999%)
Nitrogen trifluoride	NF_3	7783-54-2	Air Liquide	3.0 (99.9%)

1.4. Non-Ideality Factors

To express the deviation of the behaviour of a real gas from the ideal one, the so-called non-ideality factor α was calculated and implemented in the parameter files of the operating software of the Quantachrome IQ2 and IQ3 systems used during the here presented studies. Two methods have been taken into account to calculate the non-ideality factors and the average of both values was used for the corresponding measurements. The non-ideality factor calculations were performed by Dr. Sven M. Elbert (OCI, Heidelberg University).

Method 1: Berthelot-Equation [149]

$$pV\,(1 + \alpha p) = nRT \tag{13}$$

with

$$\alpha = \frac{9}{128}\,\frac{1}{p_c}\,\frac{T_c}{T}\left(6\left(\frac{T_c}{T}\right)^2 - 1\right) \tag{14}$$

α: non-ideality factor

p: pressure

p_c: critical pressure

V: volume

R: gas constant

T: temperature

T_c: critical temperature

Method 2: van der Waals Equation[150]

$$\left(p + \frac{a}{V_m{}^2}\right)(V_m - b) = RT \tag{15}$$

with

$$a = \frac{27(RT_c)^2}{64p_c} \tag{16}$$

and

$$b = \frac{RT_c}{8p_c} \tag{17}$$

a: van der Waals parameter (internal pressure)

b: van der Waals parameter (co-volume)

p: pressure

p_c: critical pressure

V_m: molar volume

R: gas constant

T: temperature

T_c: critical temperature

Since the co-volume *b* defines the deviation for ideal behaviour at high pressures. The van-der-Waals parameter *a* is equivalent to the non-ideality factor and taken into account exclusively.

Values for the critical pressure, critical temperature and boiling points have been extracted from the *NIST Chemistry WebBook, SRD 69* of the National Institute of Standards and Technology. [151]

Table 16. Selected physical properties and non-ideality factors.

Gas	bp (K)	T (K)[a]	crit. T (K)	crit. P (Torr)	non-ideality (× 10^{-5} ·$Torr^{-1}$)		
					Berthelot	vdW	average
N_2	77.35	77.35	126	25502	6.70	3.59	5.15
N_2	77.35	195.15	126	25502	0.27	0.37	0.32
N_2	77.35	273.15	126	25502	0.04	0.13	0.08
N_2	77.35	283.15	126	25502	0.02	0.11	0.07
N_2	77.35	298.15	126	25502	0.01	0.09	0.05
N_2	77.35	313.15	126	25502	0.00	0.07	0.03
Ar	87.15	87.3	151	36753	0.27	0.37	0.32
CO_2	194.69[b]	195.15	304.2	55354	2.69	1.50	2.09
CO_2	194.69[b]	273.15	304.2	55354	0.91	0.69	0.8
CO_2	194.69[b]	283.15	304.2	55354	0.81	0.64	0.72
CO_2	194.69[b]	298.15	304.2	55354	0.68	0.56	0.62
CO_2	194.69[b]	313.15	304.2	55354	0.58	0.5	0.54
CH_4	111.0	273.15	190.6	34578	0.27	0.34	0.31
C_2H_6	184.6	273.15	305.3	36753	1.39	1.05	1.22
C_3H_8	231.1	273.15	369.9	31878	2.99	1.9	2.44
CF_4	145.1	273.15	227.5	28090	0.66	0.67	0.67
CF_4	145.1	283.15	227.5	28090	0.58	0.61	0.59
CF_4	145.1	298.15	227.5	28090	0.48	0.54	0.51
CF_4	145.1	313.15	227.5	28090	0.39	0.47	0.43
C_2F_6	195.0	273.15	292.8	22817	1.95	1.54	1.74
C_2F_6	195.0	283.15	292.8	22817	1.73	1.41	1.57

C_2F_6	195.0	298.15	292.8	22817	1.45	1.25	1.35
C_2F_6	195.0	313.15	292.8	22817	1.23	1.11	1.17
C_3F_8	234.0	273.15	345.1	20064	3.80	2.57	3.19
C_3F_8	234.0	283.15	345.1	20064	3.38	2.36	2.87
C_3F_8	234.0	298.15	345.1	20064	2.86	2.10	2.48
C_3F_8	234.0	313.15	345.1	20064	2.43	1.87	2.15
c-C_4F_8	267.3	273.15	388.5	20882	5.34	3.24	4.29
c-C_4F_8	267.3	283.15	388.5	20882	4.76	2.98	3.87
c-C_4F_8	267.3	298.15	388.5	20882	4.04	2.65	3.34
c-C_4F_8	267.3	313.15	388.5	20882	3.44	2.37	2.91
SF_6	209.3	273.15	568.8	18677	19.65	8.41	14.03
SF_6	209.3	283.15	568.8	18677	17.58	7.78	12.68
SF_6	209.3	298.15	568.8	18677	14.99	6.95	10.97
SF_6	209.3	313.15	568.8	18677	12.87	6.24	9.56
NF_3	144.1	273.15	233.8	33458	0.61	0.6	0.61
NF_3	144.1	283.15	233.8	33458	0.54	0.55	0.54
NF_3	144.1	298.15	233.8	33458	0.44	0.48	0.46
NF_3	144.1	313.15	233.8	33458	0.37	0.42	0.4

[a] Measurement temperature. [b] Sublimation point.

2. Synthetic Procedures

2.1. Compounds of Chapter III, Section 1

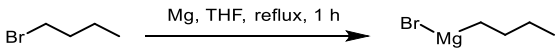

39 **39a**

Butylmagnesium bromide (39a): In a 500 mL three-necked round-bottom flask, magnesium flakes (11.7g, 481 mmol) were covered with anhydrous THF (50 mL) under argon atmosphere. A solution of 1-brombutane **39** (48 mL, 400 mmol) in anhydrous THF (170 mL) was added in portions under reflux. After the initiation of the reaction (approx. after added 10 mL of solution) the rest of 1-brombutane solution in THF was added dropwise and the resulting mixture was refluxed for additional 1 h to give a THF solution Grignard reagent which was used without further characterization.

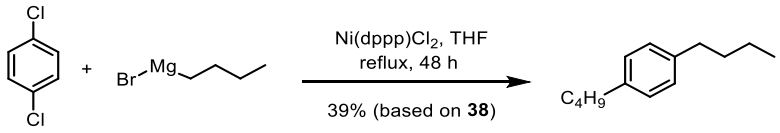

38 **39a** **40**

1,4-Dibutylbenzen (40): A 500 mL flask was charged with 1,4-dichlorbenzene **38** (19.6 g, 133 mmol), [1,3-bis(diphenylphosphino)propane]dichloronickel(II) ($Ni(dppp)Cl_2$) (83.3 mg, 153 µmol) and anhydrous THF (100 mL) under argon and 160 mL of solution of Grignard reagent was added dropwise. The resulting mixture was refluxed for 48 h. After quenching with water (30 mL) and 3 M HCl (30 mL), the mixture was extracted with diethyl ether (3 × 50mL). The combined organic layer was dried over $MgSO_4$ and the solvent removed under reduced pressure. The obtained liquid was distilled under reduced pressure (0.58 mbar) at 70-75 °C to give **40** in 39 % yield (based on **38** over two steps) (10.0 g, 52.5 mmol) as colorless liquid. **^{1}H NMR** (301 MHz, $CDCl_3$): δ = 7.09 (s, 4H), 2.61-2.54 (m, 4H), 1.64-1.53 (m, 4H), 1.42-1.29 (m, 4H), 0.93 (t, J = 7.3 Hz, 6H). The analytical data is in accordance with that previously reported.[88a]

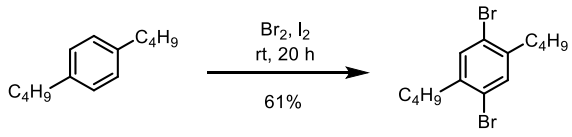

40 **41**

1,4-Dibromo-2,5-dibutylbenzene (41): To ice-cooled 1,4-dibutylbenzen **40** (9.0 g, 47.3 mmol) and iodine (120 mg, 47.3 µmol) was added dropwise bromine (7 mL) under

stirring with rigorous exclusion of light. Afterward, the mixture was stirred at room temperature for 20 h. 50 mL KOH solution (20%) was added, and the aqueous layer was extracted with CH_2Cl_2 (3 × 40 mL). The combined organic layers were dried over $MgSO_4$. After removal of solvent under reduced pressure, the obtained solid was recrystallized from ethanol to give **41** (10 g, 28.7 mmol, 61%). **^{1}H NMR** (301 MHz, $CDCl_3$): δ = 7.35 (s, 2H), 2.71-2.58 (m, 4H), 1.63-1.50 (m, 4H), 1.46-1.32 (m, 4H), 0.95 (t, J = 7.3 Hz, 6H). The analytical data is in accordance with that previously reported.[88a]

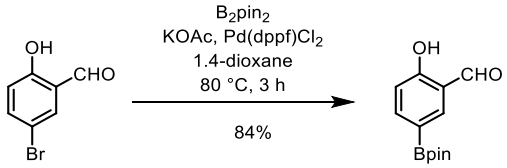

50 **51**

5-Boronicacidpinacolester salicylaldehyde (51): 5-bromosalicylaldehyde **50** (15 g, 74.6 mmol), bis(pinacolato)diboron (21 g, 82.7 mmol) and KOAc (25.8 g, 155 mmol) were added into 150 mL 1,4-dioxane. Then (1,1'-bis(diphenylphosphino)ferrocene)palladium(II) dichloride (1.62 g, 2.21 mmol) was added under argon atmosphere. After stirring for 3 hours at 80°C, the reaction mixture was cooled to room temperature, filtered through celite pad and washed with petroleum ether until the filtrate turned colorless. Purification via flash column chromatography (SiO_2, petroleum ether/ethyl acetate = 10:1, R_f = 0.35) and recrystallization from hot petroleum ether yielded **51** (15.5 g, 62.5 mmol, 84%) as colourless solid. **M.p. =** 109 °C. **^{1}H NMR** (301 MHz, $CDCl_3$): δ = 11.22 (s, 1H), 9.92 (s, 1H), 8.05 (d, J = 1.7 Hz, 1H), 7.94 (dd, J = 8.4, 1.7 Hz, 1H), 6.98 (d, J = 8.4 Hz, 1H), 1.35 (s, 12H). The analytical data is in accordance with that previously reported.[86, 152]

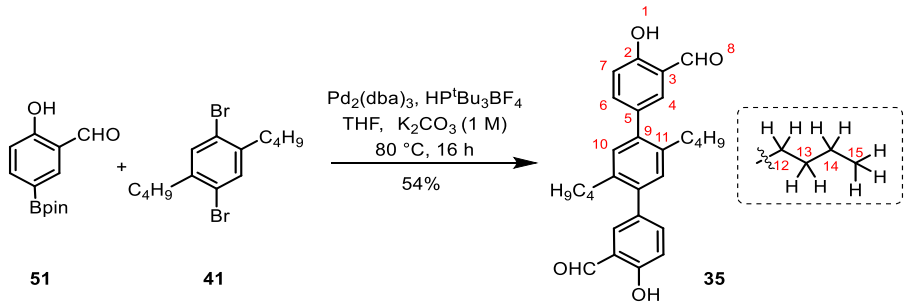

51 **41** **35**

2',5'-Dibutoxy-4,4''-dihydroxy-[1,1':4',1''-terphenyl]-3,3''-dicarbaldehyde (35): In a screw-capped-vessel salicylaldehyde **51** (3.44 g, 13.9 mmol) and dibromide **41** (2.00 g, 5.75 mmol) were suspended in THF (40 mL) and an aqueous K_2CO_3 solution (1 M,

10 mL) under argon atmosphere. 5 mol-% tris(dibenzylideneacetone)dipalladium(0) (266 mg, 290 µmol) and 10 mol-% tri-*tert*-butylphosphonium tetrafluoroborate (168 mg, 579 µmol) were added to the mixture. The suspension was heated to 80 °C and stirred for 16 h. After cooling to room temperature, the suspension was poured on water (20 mL), extracted with CH_2Cl_2 (3 × 40 mL) and the combined organic layer was dried over Na_2SO_4. After removal of solvent under reduced pressure, the obtained crude solid was purified by column chromatography (SiO_2, petroleum ether/ethyl acetate = 5:1, R_f = 0.48) to give **35** as colorless solid in 54% yield (1.36 g, 3.16 mmol). **M.p.** = 166 °C. **^{1}H NMR** (301 MHz, $CDCl_3$): δ = 11.03 ppm (s, 2H, H-1), 9.95 (s, 2H, H-8), 7.52-7.56 (m, 4H, H-4,6), 7.12 (s, 2H, H-10), 7.07 (t, *J* = 4.5 Hz, 2H, H-7), 2.59-2.54 (m, 4H, H-12), 1.52-1.42 (m, 4H, H-13), 1.18-1.30 (m, 4H, H-14), 0.81 (t, *J* = 7.3 Hz, 6H, H-15). **^{13}C NMR** (76 MHz, $CDCl_3$): δ = 196.8 (C-8), 160.8 (C-2), 139.4 (C-9), 138.2 (C-6), 138.1 (C-11), 134.1 (C-4), 133.8 (C-5), 131.2 (C-10), 120.5 (C-3), 117.6 (C-7), 33.8 (C-13), 32.5 (C-12), 22.8 (C-14), 14.0 (C-15). **FT-IR** (neat, ATR): $\tilde{\nu}$ = 2957 cm^{-1} (w), 2920 (w), 2856 (m), 1651 (s), 1620 (m), 1585 (m), 1508 (w), 1474 (s), 1445 (m), 1366 (w), 1333 (w), 1304 (m), 1286 (s), 1269 (m), 1252 (m), 1221 (m), 1180 (m), 1161 (s), 1128 (w), 1047 (w), 1009 (w), 962 (w), 920 (m), 903 (m), 839 (s), 812 (w), 779 (m), 768 (m), 741 (s), 723 (s), 700 (s), 654 (m), 635 (s). **MS** (APCI+): $[M]^+$: m/z Calcd. for ($C_{28}H_{31}O_4^+$): 431.2217, found 431.2204. **Elemental Analysis** (%): ($C_{28}H_{30}O_4$) Calcd. C 78.11, H 7.02 found C 78.22, H 7.24.

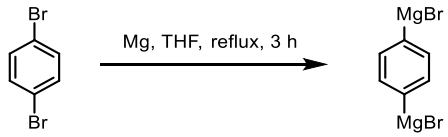

42 **42a**

Phenyl-1,4-di-magnesiumbromide (42a): In a 250 mL three-necked round-bottom flask, magnesium flakes (15.6 g, 640 mmol) were covered with anhydrous THF (70 mL) under argon atmosphere. A solution of dibromobenzene **42** (18.8 g, 79.7 mmol) in anhydrous THF (170 mL) was added in portions under reflux. After the initiation of the reaction (approx. after added 10 mL of solution) the rest of dibromobenzene solution in THF was added dropwise and the resulting mixture was refluxed for additional 3 h to give a THF solution twofold Grignard reagent **42a** which was used without further characterization.

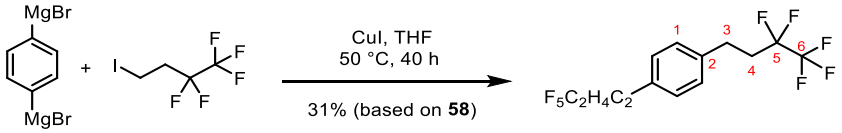

42a **43** **44**

1,4-Bis(3,3,4,4,4-Pentafluorobutyl)benzene (44): A 500 mL flask was charged with 1,1,1,2,2-pentafluoro-4-iodobutane **43** (45.0 g, 0.16 mol), CuI (1.87 g, 9.84 mmol) and anhydrous THF (160 mL) under argon and 136 mL of solution of **42a** was added dropwise. The resulting mixture was stirred at 50 °C for 40 h. After quenching with water (50 mL), the THF was removed using a rotary evaporator and the residual mixture was extracted with CH_2Cl_2 (3 × 50mL). The combined organic layer was dried over $MgSO_4$ and the solvent removed under reduced pressure. The obtained liquid was purified by column chromatography (SiO_2, petroleum ether, R_f = 0.35) to give **44** as colorless solid in 31% yield (based on **42** over two steps) (7.81 g, 21.1 mmol). **M.p.** = 94 °C. **^{1}H NMR** (400 MHz, $CDCl_3$): δ = 7.17 ppm (s, 4H, H-1), 2.91-2.87 (m, 4H, H-3), 2.39-2.26 (m, 4H, H-4). **^{13}C NMR** (101 MHz, $CDCl_3$): δ =137.8 ppm (C-2), 128.8 (C-1), 32.9 (t, J = 21.9 Hz, C-4), 26.3 (t, J = 4.1 Hz, C-3), 115.5 (tq, $^1J_{C\text{-}F}$ = 252.1 Hz, $^2J_{C\text{-}F}$ = 37.7 Hz, C-5), 119.3 (qt, $^1J_{C\text{-}F}$ = 285.3 Hz, $^2J_{C\text{-}F}$ = 36.1 Hz, C-6). **^{19}F NMR** (283 MHz, $CDCl_3$): δ = -85.4 ppm (s, F-6), -118.5 (s, F-5). **FT-IR** (neat, ATR): $\tilde{\nu}$ = 2958 cm^{-1} (w), 1519 (w), 1459 (w), 1426 (w), 1351 (m), 1317 (m), 1295 (m), 1282 (m), 1175 (s), 1116 (w), 1059 (s), 979 (s), 961 (s), 861 (m), 801 (m), 764 (m), 692 (s), 607 (m). **MS** (EI+): $[M]^+$: *m/z* Calcd. for ($C_{14}H_{12}F_{10}^+$): 370.0799, found 370.0769. **Elemental Analysis** (%): ($C_{14}H_{12}F_{10}$) Calcd. C 45.42, H 3.27, found C 45.56, H 3.69.

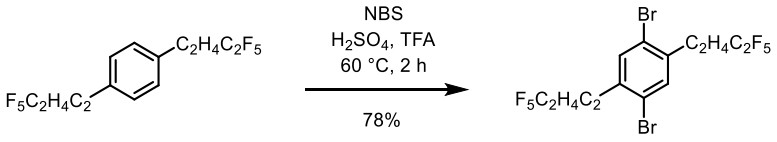

44 **45**

1,4-Dibromo-2,5-bis(3,3,4,4,4-pentafluorobutyl)benzene (45): **44** (9.00 g, 24.3 mmol) was added to a mixture of trifluoroacetic acid (120 mL) and concentrated sulfuric acid (36 mL). The mixture was stirred at 60 °C, and *N*-bromosuccinimide (NBS) (8.87 g, 49.8 mmol) was added in portions (1.48 g h^{-1}) over 5 h. After stirring for additional 2 hours at 60 °C, the mixture was cooled to roomtemperature and ice water (500 mL) was added. The resulting suspension was diluted with CH_2Cl_2 (500 mL) and washed with water (100 mL). After removal of solvent under reduced pressure, the crude solid was purified by column chromatography (SiO_2, petroleum) to give **45** as colorless solid

in 78% yield (10.0 g, 18.9 mmol). It was used in the next step without further purification.

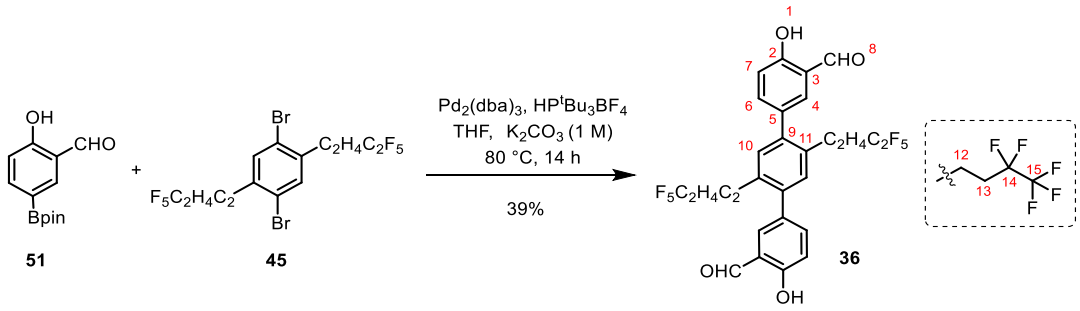

4,4''-Dihydroxy-2',5'-bis(3,3,4,4,4-pentafluorobutyl)-[1,1':4',1''-terphenyl]-3,3''-dicarbaldehyde (36): In a screw-capped vessel salicylaldehyde **51** (2.25 g, 9.07 mmol) and dibromide **45** (2.00 g, 3.79 mmol) were suspended in THF (32 mL) and an aqueous K_2CO_3 solution (1 M, 8 mL) under argon. 5 mol-% tris(dibenzylideneacetone)dipalladium(0) (173 mg, 189 µmol) and 10 mol-% tri-*tert*-butylphosphonium tetrafluoroborate (110 mg, 379 µmol) were added and the mixture stirred at 80 °C for 14 h. After cooling the reaction mixture to room temperature, it was poured on water (20 mL), extracted with CH_2Cl_2 (3 × 50 mL) and the combined organic layer was dried over $MgSO_4$. After removal of solvents under reduced pressure, the crude product was purified by column chromatography (SiO_2, petroleum ether/ethyl acetate/AcOH = 100:20:1, R_f = 0.36) to give **36** as colorless solid in 39% yield (900 mg, 1.47mmol). **M.p.** = 189 °C. **^{1}H NMR** (700 MHz, $CDCl_3$): δ = 11.08 ppm (s, 2H, H-1), 9.96 (s, 2H, H-8), 7.52 (d, J = 2.2 Hz, 2H, H-4), 7.50 (dd, J = 8.3, 2.2 Hz, 2H, H-6), 7.17 (s, 2H, H-10), 7.12 (d, J = 8.3 Hz, 2H, H-7), 2.91-2.89 (m, 4H, H-12), 2.21-2.13 (m, 4H, H-13). **^{13}C NMR** (176 MHz, $CDCl_3$): δ = 196.5 ppm (C-8), 161.3 (C-2), 140.3 (C-9), 137.6 (C-6), 135.7 (C-11), 133.8 (C-4), 132.1 (C-5), 131.7 (C-10), 120.6 (C-3), 119.1 (qt, $^1J_{C\text{-}F}$ = 286.0 Hz, $^2J_{C\text{-}F}$ = 36.5 Hz, C-15),118.3 (C-7), 115.2 (tq, $^1J_{C\text{-}F}$ = 252.5 Hz, $^2J_{C\text{-}F}$ = 37.8 Hz, C-14), 32.2 (t, J = 21.6 Hz, C-13), 23.8 (t, J = 4.1 Hz, C-12). **^{19}F NMR** (471 MHz, $CDCl_3$): δ = -85.4 ppm (6F, F-15), -118.6 (4F, F-14). **IR** (neat, ATR): $\tilde{\nu}$ = 2972 cm^{-1} (w), 2862 (w), 1659 (s), 1622 (w), 1587 (w), 1479 (m), 1464 (w), 1443 (w), 1394 (w), 1371 (w), 1356 (w), 1337 (w), 1319 (w), 1302 (w), 1283 (m), 1252 (w), 1229 (m), 1202 (s), 1186 (s), 1167 (s), 1128 (w), 1109 (w), 1084 (m), 1057 (m), 1014 (w), 989 (m), 962 (m), 922 (w), 901 (w), 843 (m), 771 (m), 741 (m), 721 (s), 702 (s), 671 (w), 658 (w), 635 (w). **MS** (APCI+): $[M]^+$: m/z Calcd. For ($C_{28}H_{21}F_{10}O_4^+$): 611.1275, found 611.1255. **Elemental Analysis** (%): ($C_{28}H_{20}F_{10}O_4$) Calcd. C 55.09, H 3.30, found C 55.38, H 3.46.

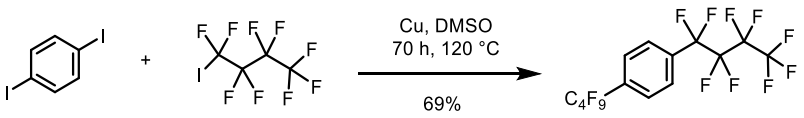

46 47 48

1,4-Bis(perfluorobutyl)benzene (48): Nonafluoro-1-iodobutane **47** (20.9 g, 60.4 mmol) was added to a mixture of 1,4-diiodobenzene **46** (9.07 g, 27.5 mmol) and Cu powder (7 g, 110 mmol) in anhydrous DMSO (70 mL). The mixture was stirred for 70 h at 120 °C. After cooling to room temperature, water (70 mL) and diethyl ether (50 mL) were added to the mixture and stirred for 30 min. The mixture was filtered, and the filtrate was extracted with diethyl ether (2 × 150 mL). The combined organic layers were dried over $MgSO_4$. After removal of solvent under reduced pressure, the resulting residue was subjected to flash silica gel column chromatography eluting with petroleum ether to give **48** in 69% yield (9.7 g, 18.9 mmol) as transparent liquid. **^{1}H NMR** (301 MHz, $CDCl_3$): δ = 7.76 ppm (s, 4H). **^{19}F NMR** (283 MHz, $CDCl_3$): δ = -81.2 ppm (m), -111.7 (m), -122.8 (m), -125.7(m). The analytical data is in accordance with that previously reported.[49a]

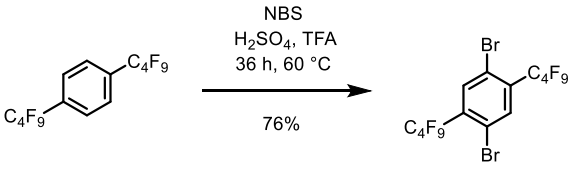

48 49

1,4-Dibromo-2,5-bis(perfluorobutyl)benzene (49): 48 (12.1 g, 23.5 mmol) was added to a mixture of trifluoroacetic acid (100 mL) and concentrated sulfuric acid (30 mL). The mixture was heated to 60 °C, and *N*-bromosuccinimide (12.6 mg, 70.8 mmol) was added in portions (2.09 g h^{-1}) over 6 h. The stirring was continued for 36 h at 60 °C After cooling to room temperature, the reaction mixture was poured into ice water (500 mL). The precipitate was collected, washed with water (300 mL), and recrystallized in ethanol to give **49** (12.0 g, 17.9 mmol, 76%) as colorless solid. **^{1}H NMR** (400 MHz, $CDCl_3$): δ = 7.94 (s, 2H). **^{19}F NMR** (283 MHz, $CDCl_3$): δ = -80.8(m), -107.8(m), -120.3 (m), -125.8 (m). The analytical data is in accordance with that previously reported.[49a]

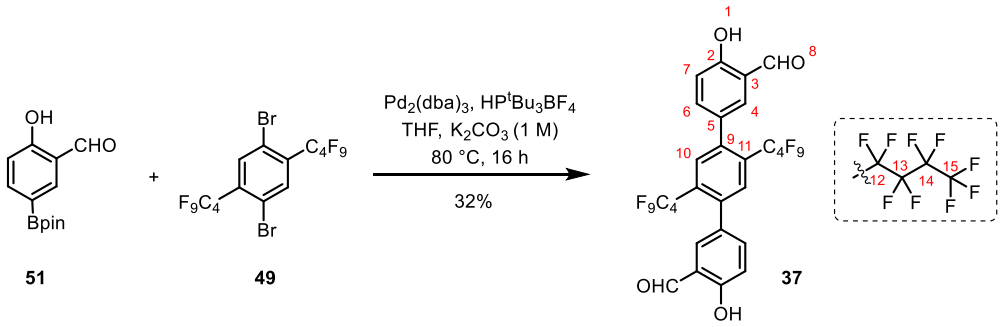

4,4''-Dihydroxy-2',5'-bis(perfluorobutyl)-[1,1':4',1''-terphenyl]-3,3''-dicarbaldehyde (37): In a screw-capped vessel salicylaldehyde **51** (1.60 g, 6.45 mmol) and dibromide **49** (1.80 g, 2.68 mmol) were suspended in THF (32 mL) and K_2CO_3 solution (1 M, 8 mL) under argon. 10 mol-% tris(dibenzylideneacetone)dipalladium(0) (245 mg, 268 µmol,) and 20 mol-% tri-*tert*-butylphosphonium tetrafluoroborate (156 mg, 538 µmol,) were added to the mixture and heated to 80 °C for 16 h. After cooling to room temperature, the suspension was poured on water (40 mL), was extracted with CH_2Cl_2 (3 × 100 mL) and the combined organic layer was dried over Na_2SO_4. After removal of solvents under reduced pressure, the obtained crude solid was purified by column chromatography (SiO_2, petroleum ether /CH_2Cl_2 = 5:4, R_f = 0.32) to give **37** as colorless solid in 32% yield (646 mg, 856 µmol). **M.p.** = 216 °C. **^{1}H NMR** (500 MHz, THF-d_8): δ = 10.99 ppm (s, 2H, H-1), 10.02 (s, 2H, H-8), 7.74 (s, 2H, H-10), 7.69 (d, J = 2.5 Hz, ^{1}H, H-4), 7.52 (dd, J = 8.5, 2.5 Hz, 2H, H-6), 7.04 (d, J = 8.5 Hz, 2H, H-7). **^{13}C NMR** (126 MHz, THF-d_8): δ = 196.4 ppm (C-8), 162.1 (C-2), 142.2 (C-9), 137.7 (C-6), 134.3 (C-4), 134.2(C-10), 130.4 (C-5), 121.2 (C-3), 117.5 (C-7). **Note:** Due to strong and multiple ^{19}F-^{13}C coupling, the signals of the perfluorinated side chains were not visible in ^{13}C-NMR spectra. **^{19}F NMR** (283 MHz, THF-d_8): δ = -82.0 ppm (t, J = 10.1 Hz, 6F, F-15), -104.1 (t, J = 15.1 Hz, 4F, F-12), -121.0 (m, 4F, F-13), -126.5 (m, 4F, F-14). **FT-IR** (neat, ATR): $\tilde{\nu}$ = 3057 cm^{-1} (w), 2866 (w), 1682 (w), 1664 (m), 1624 (w), 1593 (w), 1477 (m), 1371 (w), 1350 (m), 1306 (w), 1288 (m), 1275 (m), 1231 (s), 1205 (s), 1190 (s), 1167 (s), 1150 (s), 1132 (s), 1103 (m), 1059 (m), 1018 (w), 957 (w), 943 (w), 912 (m), 837 (m), 824 (s), 771 (m), 752 (s), 727 (s), 673 (m), 642 (w), 631 (w). **MS** (APCI+): $[M]^+$: m/z Calcd. For ($C_{28}H_{13}F_{18}O_4^+$): 755.0521, found 755.0500. **Elemental Analysis** (%): ($C_{28}H_{12}F_{18}O_4$) Calcd. C 44.58, H 1.60, found C 45.33, H 2.21.

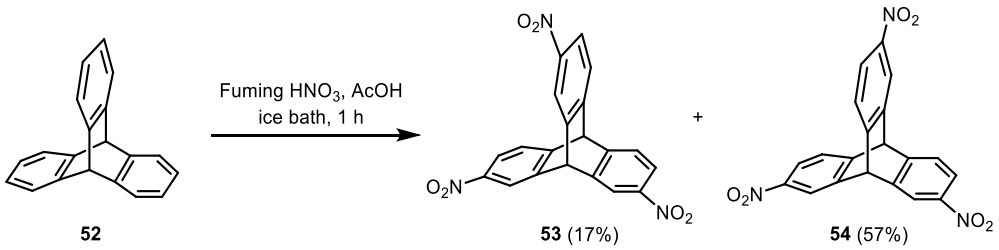

52 **53** (17%) **54** (57%)

2, 7, 14-Trinitotriptycene (53) and **2,7,13-trinitrotriptycene (54):** Triptycene **52** (10 g, 39.3 mmol) was dissolved in 56 mL acetic acid in ice bath. 50 mL fuming nitric acid was added in less than one minute. After stirred for 1 h in ice bath, the mixture was poured into 600 mL ice. When all ice has melted, the precipitate was filtered, washed with water and purified by column chromatography (SiO_2, petroleum ether/ethyl acetate = 4:1) to give **53** as colorless solid in 17% yield (2.60 g, 6.68 mmol) and **54** as light yellow soild in 57% yield (8.72 g, 22.4 mmol). **53**: **M.p.** > 300 °C. **^{1}H NMR** (301 MHz, $CDCl_3$): δ = 8.34 (d, J = 2.0 Hz, 3H), 8.05 (dd, J = 8.1, 2.2 Hz, 3H), 7.62 (d, J = 8.1 Hz, 3H), 5.84 (s, 1H), 5.80 (s, 1H). **54**: **M.p.** = 179 °C. **^{1}H NMR** (301 MHz, $CDCl_3$): δ = 5.80 (s, 1H), 5.84 (s, 1H), 7.62 (m, 3H), 8.05 (m, 3H), 8.34 (m, 3H). The analytical data is in accordance with that previously reported.[76, 86]

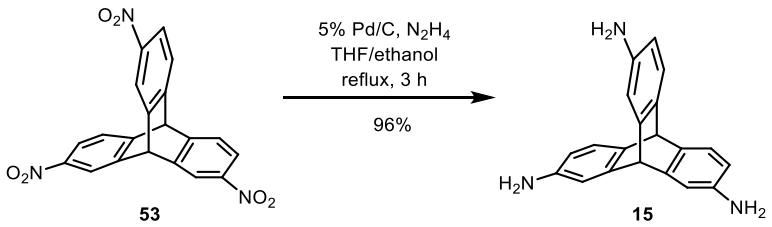

53 **15**

2, 7, 14-Triaminotriptycene (15): Trinitotriptycene **53** (1 g, 2.56 mmol) was dissolved in 40 mL anhydrous THF and added with 5% Pd/C (0.75 g) and 10 mL ethanol. The solution was stirred in ice bath for 30 min under under argon atmosphere. After 1.5 mL hydrazonium hydroxide was added dropwise, the mixture was kept stirring for 20 min in ice bath, follwing 30 min in room temperature, and refluxing for 3 h. The mixture was cooled down to room temperature and filtered with celite pad. After removal of solvent under reduced pressure, the obtained crude solid was purified by column chromatography (SiO_2, DCM/Methanol = 40:1 to 20:1) to give **15** as colorless solid in 96% yield (0.74 g, 2.47 mmol). **M.p.** > 150 °C. **^{1}H NMR** (301 MHz, DMSO-d_6): δ = 6.87 (d, J = 7.7 Hz, 3H), 6.61 (d, J = 2.2 Hz, 3H), 6.08 (dd, J = 7.7, 2.2 Hz, 3H), 4.88 (s, 2H), 4.74 (s, 6H). The analytical data is in accordance with that previously reported.[76, 86]

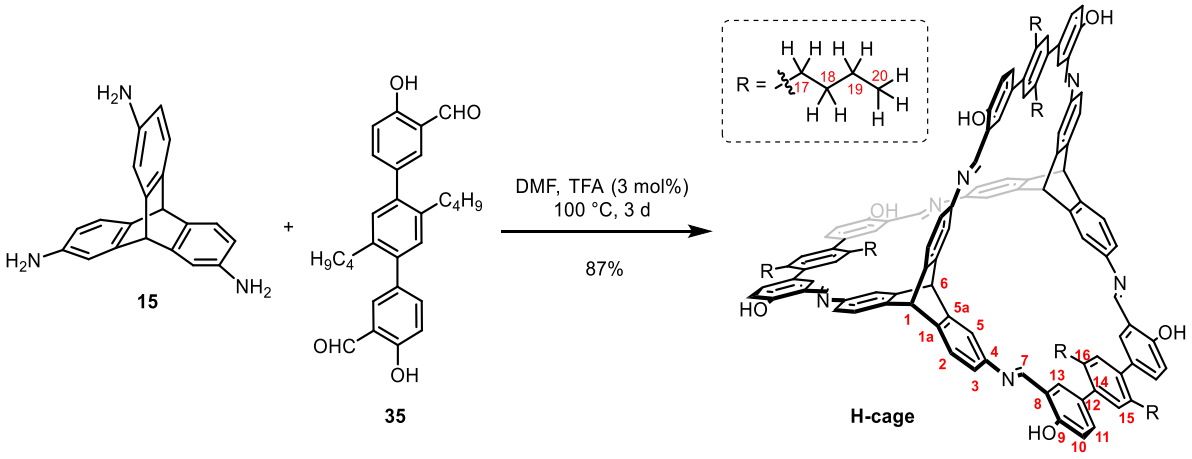

H-Cage: In six individual reactions, triamino triptycene **15** (24.0 mg, 80.0 µmol) and salicylaldehyde **35** (51.7 mg, 120 µmol) were dissolved each in anhydrous DMF (18 mL) in six 25 mL screw-capped vessels and 3 mol-% TFA (0.1 M in anhydrous DMF, 24 µL) was added to the individual solutions. The mixtures were stirred at 100 °C for 3 days. After cooling to room temperature, the reaction mixtures were combined, filtered through syringe filters (0.2 µm pore) and concentrated to approx. 48 mL by rotary evaporation (55 °C). Methanol (80 mL) was added and the obtained suspension was stirred for 30 minutes. The orange precipitate was filtered, washed with methanol (4 × 20 mL) and dried under high vacuum (1.4 mbar) for 14 h at room temperature to give **H-cage** as orange solid in 87% yield (370 mg, 208 µmol). **M.p.**: >350 °C. **^{1}H NMR** (700 MHz, THF-d_8): δ = 13.13 ppm (s, 6H,9-OH), 9.15 (s, 6H, imine-H-7), 7.82 (d, J = 2.0 Hz, 6H, H-5), 7.55 (d, J = 7.8 Hz, 6H, H-2), 7.41 (d, J = 2.3 Hz, 6H, H-13), 7.39 (dd, J = 8.0, 2.3 Hz, 6H, H-11), 7.22 (dd, J = 7.7, 2.1 Hz, 6H, H-3), 7.13 (s, 6H, H-15), 7.00 (d, J = 8.1 Hz, 6H, H-10), 5.71 (s, 2H, bridgehead-H-1), 5.63 (s, 2H, bridgehead-H-6), 2.63-2.61 (m, 12H, H-17), 1.47 (tt, J = 7.9, 6.6 Hz, 12H, H-18), 1.22 (q, J = 7.3 Hz, 12H, H-19), 0.77 (t, J = 7.3 Hz, 18H, H-20). **^{13}C NMR** (176 MHz, THF-d_8): δ = 161.1 ppm (C-9), 160.5 (C-7), 146.8 (C-5a), 145.2 (C-1a), 144.7 (C-4), 140.8 (C-14), 138.2 (C-16), 134.2 (C-11), 133.8 (C-12), 133.5 (C-13), 131.7 (C-15), 125.6 (C-3), 125.4 (C-2), 119.8 (C-8), 117.3 (C-10), 111.5 (C-5), 56.0 (bridgehead-C-6), 53.3 (bridgehead-C-1), 34.4 (C-18), 33.0 (C-17), 23.2 (C-19), 14.0 (C-20). **FT-IR** (neat, ATR): $\tilde{\nu}$ = 2953 cm^{-1} (m), 2926 (m), 2868 (m), 2858 (m), 1624 (m), 1607 (s), 1578 (s), 1502 (w), 1475 (s), 1429 (m), 1377 (m), 1360 (m), 1317 (w), 1277 (s), 1231 (m), 1178 (s), 1130 (s), 1088 (m), 957 (m), 885 (m), 856 (s), 829 (s), 791 (s), 775 (s), 744 (s), 725 (s), 690 (m), 656 (s), 642 (s). **MS** (MALDI-TOF): $[M+H]^+$: *m/z* calcd. For ($C_{124}H_{113}O_6N_6^+$): 1781.872, found 1781.913. **MS** (MALDI-FT-ICR): $[M+H]^+$: *m/z* calcd. For ($C_{124}H_{113}O_6N_6^+$): 1781.8716,

found 1781.8622. **Elemental Analysis** (%): ($C_{124}H_{112}N_6O_6$) Calcd. C 83.56, H 6.33, N 4.72, found C 82.97, H 6.42, N 4.64.

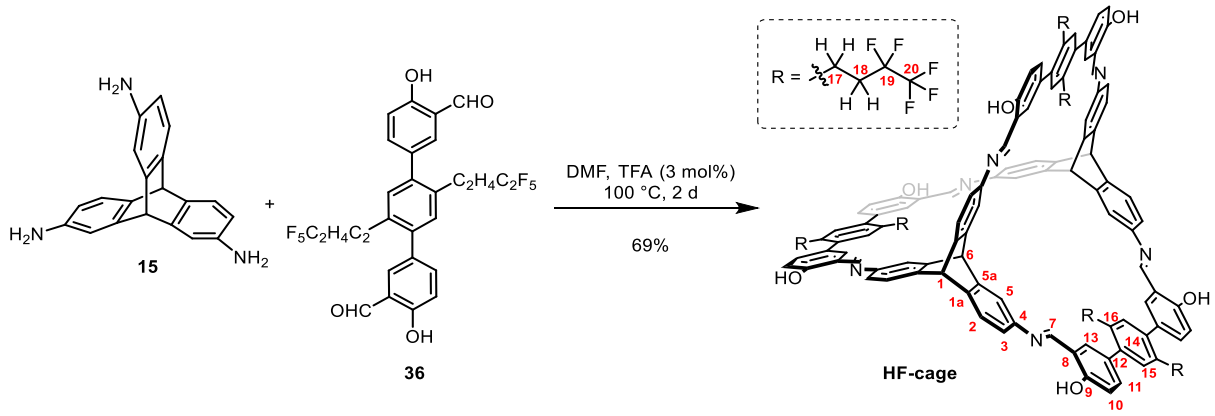

HF-Cage: In six individual reactions, triamino triptycene **15** (24.0 mg, 80.0 µmol) and salicylaldehyde **36** (73.3 mg, 120 µmol) were dissolved each in anhydrous DMF (18 mL) in six 25 mL screw-capped vessels and 3 mol-% TFA (0.1 M in anhydrous DMF, 24 µL) was added to the solutions. The mixtures were stirred at 100 °C for 2 days. After cooling to room temperature, the reaction mixtures were combined, filtered through syringe filters (0.2 µm pore) and concentrated to approx. 28 mL by rotary evaporation (55 °C). Methanol (100 mL) was added and the obtained suspension was stirred for 30 minutes. The orange precipitate was filtered, washed with methanol (4 × 20 mL) and dried under high vacuum (1.4 mbar) for 14 h at room temperature to obtain **HF-cage** as orange solid in 69% yield (386 mg, 166 µmol). **M.p.**: > 350 °C. **^{1}H NMR** (500 MHz, THF-d_8)**:** δ = 13.21 (s, 6H, 9-OH), 9.15 (s, 6H, imine-H-7), 7.80 (d, J = 2.0 Hz, 6H, H-5), 7.58 (d, J = 7.8 Hz, 6H, H-2), 7.44 (s, 6H, H-13), 7.42 (d, J = 2.3 Hz, 6H, H-11), 7.31 (s, 6H, H-15), 7.25 (dd, J = 7.8, 2.0 Hz, 6H, H-3), 7.07 (d, J = 7.9 Hz, 6H, H-10), 5.73 (s, 2H, bridgehead-H-1), 5.60 (s, 2H, bridgehead-H-6), 2.99-2.95 (m, 12H, H-17), 2.30 (dq, J = 18.2, 9.7, 9.0 Hz, 12H, H-18). **^{13}C NMR** (126 MHz, THF-d_8)**:** δ = 161.5 (C-9), 160.1 (C-7), 146.7 (C-5a), 145.3 (C-1a), 144.5 (C-4), 141.5 (C-14), 136.1 (C-16), 133.9 (C-12/15/11), 133.5 (C-13), 132.1 (C-12), 132.1 (C-12/15/11), 125.7 (C-3), 125.5 (C-2), 120.1 (C-8), 119.9 (C-20),117.8 (C-10), 116.3 (C-19), 111.5 (C-5), 56.1 (bridgehead-C-6), 53.3 (bridgehead-C-1), 32.2 (C-18), 24.2 (C-17). ***Note:*** The peaks at 119.9 and 116.3 ppm can be assigned to the -CF_2- and -CF_3 groups in the side chains. While in proton-decoupled ^{13}C spectra, the C-F-coupling is suggested to be similar to the corresponding precursor **36**, the insufficient signal-to-noise ratio (even at 6400 scans) did not allow a detailed discussion on coupling constances. The exact

peak position was assured by ^{19}F decoupled ^{13}C spectra. **^{19}F NMR** (471 MHz, THF-d_8)**:** δ = -88.2 (18F, F-20), -121.0 (12F, F-19). **FT-IR** (neat, ATR): $\tilde{\nu}$ = 2980 cm^{-1} (w), 2961 (w), 2951 (w), 1626 (w), 1607 (w), 1580 (m), 1477 (m), 1387 (w), 1352 (w), 1317 (w), 1285 (m), 1277 (m), 1232 (w), 1184 (vs), 1128 (m), 1086 (m), 1059 (m), 959 (m), 887 (w), 856 (m), 829 (m), 793 (m), 775 (m), 727 (m), 704 (m), 656 (m), 642 (m). **MS** (MALDI-TOF): $[M+H]^+$: *m/z* calcd. For ($C_{124}H_{83}F_{30}O_6N_6^+$): 2321.590, found 2321.604. **MS** (MALDI-FT-ICR): $[M+H]^+$: *m/z* calcd. For ($C_{124}H_{83}F_{30}O_6N_6^+$): 2321.5890, found 2321.5789. **Elemental Analysis** (%): ($C_{124}H_{82}F_{30}N_6O_6$) Calcd. C 64.14, H 3.56, N 3.62, found C 63.97, H 3.79, N 3.71.

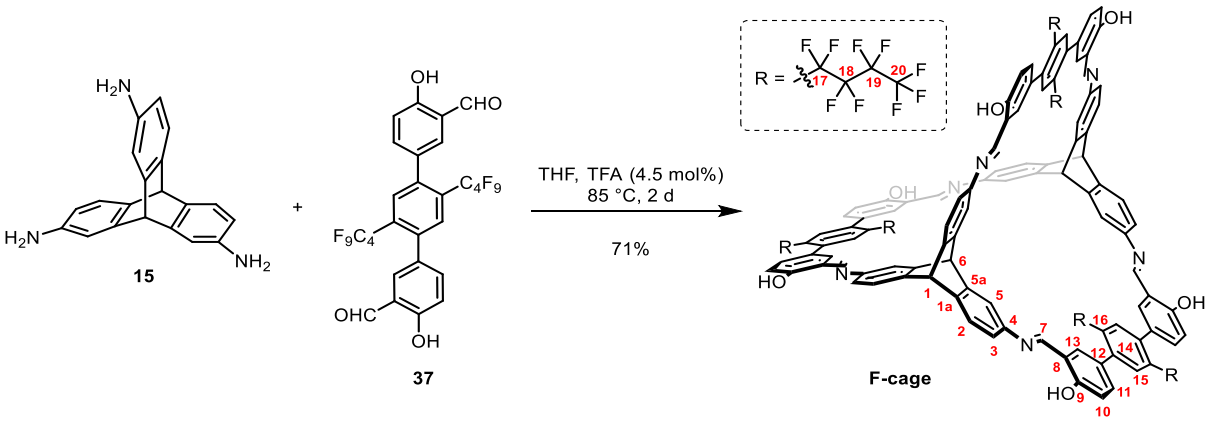

F-Cage: In four individual reactions, salicylaldehyde **37** (90.5 mg, 120 µmol each) was heated and stirred in anhydrous THF (10 mL) in four 25 mL screw-capped vessels until it dissolved. After cooling to room temperature, triamino triptycene **15** (24.0 mg, 80.0 µmol each) was added to the individual solution. After complete dissolution, additional anhydrous THF (8 mL) and 4.5 mol-%TFA (0.1 M in anhydrous THF, 36 µL,) were added. The mixtures were stirred at 85 °C for 2 days. After cooling to room temperature, the reaction mixtures were combined, filtered through syringe filters (0.2 µm pore) and concentrated to ~22 mL by rotary evaporation. Methanol (20 mL) was added and the obtained suspension was stirred for 30 minutes. The yellow precipitate was filtered, washed with methanol (3 × 20 mL) and dried under high vacuum (1.4 mbar) for 14 h at room temperature to give **F-cage** as light yellow solid in 71% yield (313 mg, 114 µmol,). **M.p.**: >350 °C. **^{1}H NMR** (500 MHz, THF-d_8)**:** δ = 13.36 (s, 6H, 9-OH), 9.15 (s, 6H, imine-H-7), 7.83 (d, *J* = 2.2 Hz, 6H, H-5), 7.76 (s, 6H, H-15), 7.56 (d, *J* = 7.8 Hz, 6H, H-2), 7.41 (dd, *J* = 8.1 Hz, 2.3 Hz, 6H, H-11), 7.38 (d, *J* = 2.3 Hz, 6H, H-13),, 7.24 (dd, *J* = 7.8, 2.0 Hz, 6H, H-3), 7.03 (d, *J* = 8.1 Hz, 6H, H-10), 5.72 (s, 2H, bridgehead-H-1), 5.57 (s, 2H, bridgehead-H-6). **^{13}C NMR** (126 MHz, THF-d_8)**:** δ = 162.1 (C-9),

159.7 (C-7), 146.6 (C-5a), 145.3 (C-1a), 144.2 (C-4), 142.7 (C-14), 134.4 (C-15), 134.1 (C-11), 133.6 (C-13), 130.3 (C-16), 129.7 (C-12), 126.0 (C-3), 125.6 (C-2), 119.3 (C-8), 117.2 (C-8), 111.3 (C-5), 56.1 (bridgehead-C-6), 53.3 (bridgehead-C-1). ***Note*:** Due to strong and multiple ^{19}F-^{13}C-coupling, the signals of the perfluorinated side chains where not visible in ^{13}C-NMR spectra. **^{19}F NMR** (471 MHz, THF-d_8)**:** δ = -84.0 (18F, F-20), -105.8 (12F, F-17), -122.7 (12F, F-18), -128.3 (12F, F-19). **FT-IR** (neat, ATR): $\tilde{\nu}$ = 1628 cm^{-1} (w), 1610 (w), 1583 (m), 1481 (m), 1429 (w), 1381 (w), 1350 (m), 1288 (m), 1277 (m), 1231 (vs), 1202 (s), 1173 (s), 1150 (s), 1132 (vs), 1092 (m), 1057 (w), 1009 (w), 957 (w), 895 (w), 860 (m), 839 (m), 831 (m), 818 (s), 798 (m), 777 (m), 737 (s), 679 (m), 654 (w). **MS** (MALDI-TOF): $[M+H]^+$: For ($C_{124}H_{59}F_{54}O_6N_6^+$):*m/z* calcd. 2753.363, found 2753.413. **MS** (MALDI-FT-ICR): $[M+H]^+$: For ($C_{124}H_{59}F_{54}O_6N_6^+$):*m/z* calcd. 2753.3628, found 2753.3671. **Elemental Analysis** (%): ($C_{124}H_{58}F_{54}N_6O_6$) Calcd. C 54.08, H 2.12, N 3.05, found C 54.15, H 2.28, N 3.14.

2.2. Compounds of Chapter III, Section 2

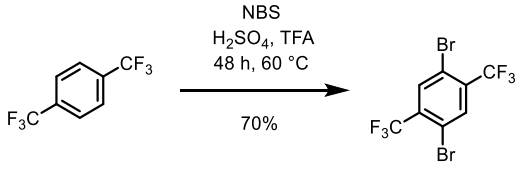

63 **64**

1,4-Dibromo-2,5-bis(trifluoromethyl)benzene (64): 63 (10.7 g, 50.0 mmol) was dissolved in 75 mL trifluoroacetic acid and 18 mL concentrated sulfuric acid in a 250 mL flask,. The mixture was allowed to warm to 60 °C before *N*-bromosuccinimide (26.7 g, 150 mmol) was added to the reaction mixture slowly in 5 h. The stirring was continued for 48 h at 60 °C. After cooling to room temperature, the reaction mixture was poured into ice water (400 mL). The precipitate was collected and dissolved in DCM (200 mL). The organic layer was washed with 3 M K_2CO_3 (40 mL) and water (40 mL). After removal of solvent, the obtained crude solid was sublimated to give **64** in 70% yield (13.0 g, 35.0 mmol) as colorless solid. **M. P.** = 68-70 °C. **^{1}H NMR** (301 MHz, $CDCl_3$): δ = 8.01 (s, 2H) ppm. **^{19}F NMR** (283 MHz, $CDCl_3$): δ = -63.6 ppm. The analytical data is in accordance with that previously reported.[153]

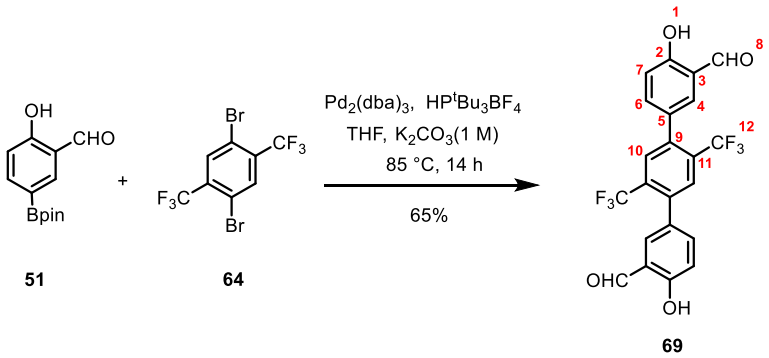

4,4''-Dihydroxy-2',5'-bis(trifluoromethyl)-[1,1':4',1''-terphenyl]-3,3''-dicarbaldehyde (69): In a screw-capped-vessel salicylaldehyde **51** (2.00 g, 5.38 mmol) and dibromide **64** (3.20 g, 12.9 mmol) were suspended in THF (32 mL) and an aqueous K_2CO_3 solution (1 M, 8 mL) under argon atmosphere. 5 mol-% tris(dibenzylideneacetone)dipalladium(0) (246 mg, 269 µmol) and 10 mol-% tri-*tert*-butylphosphonium tetrafluoroborate (156 mg, 538 µmol) were added to the mixture. The suspension was heated to 85 °C and stirred for 14 h. After cooling to room temperature, THF was removed out by rotary evaporation. The suspension was poured on water (40 mL), extracted with CH_2Cl_2 (3 × 30 mL) and the combined organic layer was dried over Na_2SO_4. After removal of solvent under reduced pressure, the obtained crude solid was washed with hexane (15 mL), then recrystallized in mixture solvent of DCM and hexane to give **69** as light yellow solid in 65% yield (1.60 g, 3.52 mmol). **M. P.** = 215 °C **^{1}H NMR** (400 MHz, $CDCl_3$): δ = 11.13 ppm (s, 2H, H-1), 9.95 (s, 2H, H-8), 7.75 (s, 2H, H-10), 7.58 (d, J = 2.3 Hz, 2H, H-4), 7.55 (dd, J = 8.5, 2.4 Hz, 4H, H-6), 7.11 (d, J = 8.5 Hz, 2H, H-7). **^{13}C NMR** (101 MHz, $CDCl_3$): δ = 196.4 ppm(C-8), 161.9(C-2), 139.5(C-9), 137.4(C-6), 134.0(C-4), 131.9 (q, $^2J_{C\text{-}F}$ = 30.6 Hz, C-11), 130.6 (q, $^3J_{C\text{-}F}$ = 5.4 Hz, C-10), 129.7 (C-5), 123.3 (q, $^1J_{C\text{-}F}$ = 274.8 Hz, C-12), 120.3(C-3), 118.0(C-7). **^{19}F NMR** (283 MHz, $CDCl_3$): δ = -57.5 ppm (F-C12). **IR** (neat, ATR): $\tilde{\nu}$ = 1684 (w), 1655 (s), 1622 (m), 1591 (m), 1558 (w), 1541 (w), 1518 (w), 1508 (w), 1475 (m), 1458 (w), 1439 (w), 1420 (w), 1400 (w), 1377 (m), 1344 (w), 1310 (m), 1288 (s), 1261 (m), 1238 (m), 1232 (m), 1138 (s), 1090 (s), 1038 (s), 961 (w), 934 (m), 910 (s), 841 (s), 766 (s), 750 (s), 735 (s), 702 (s), 648 (s). **MS** (EI+): $[M]^+$: *m/z* Calcd. For ($C_{22}H_{12}F_6O_4^+$): 454.0640, found 454.0634. **Elemental Analysis** (%): ($C_{22}H_{12}F_6O_4$) Calcd. C 58.16, H 2.66 found C 58.15, H 2.93.

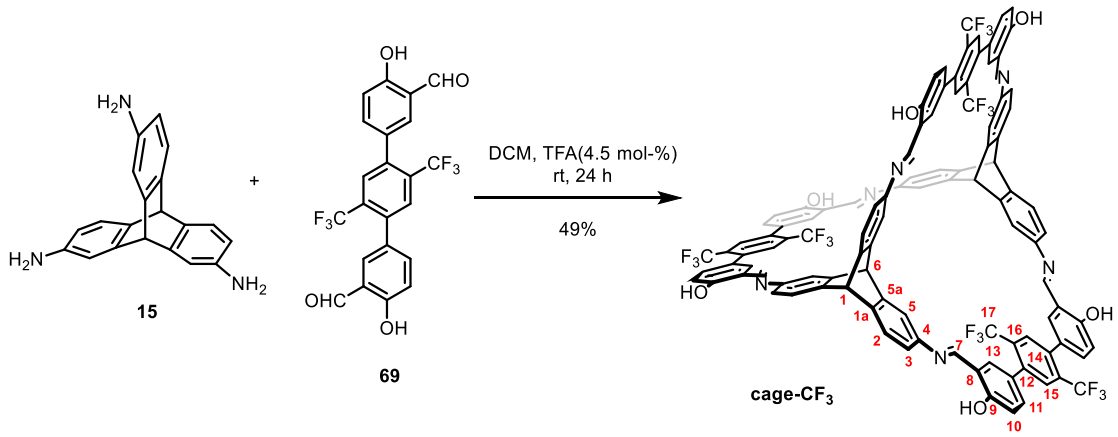

cage-CF$_3$: In six individual reactions, triamino triptycene **15** (29.9 mg, 100 µmol) and salicylaldehyde **69** (68.1 mg, 150 µmol) were dissolved each in anhydrous DCM (20 mL) in six 25 mL screw-capped vessels and 4.5 mol-% TFA (0.1 M in anhydrous DCM, 45 µL) was added to the solutions. The mixtures were stirred at room temperature for 24 h. All precipitate was filtered, washed with pentane (3 × 3 mL) and diethyl ether (2 × 3 mL), dried in the Kugelrohr oven (100 °C, $7.0 \cdot 10^{-2}$ mbar) for 14 h to give **cage-CF$_3$** as light yellow solid in 49% yield (272 mg, 147 µmmol). **M.p.**: >350 °C. **^{1}H NMR** (600 MHz, THF-d_8): δ = 13.37 ppm (s, 6H,9-OH), 9.16 (s, 6H, imine-H-7), 7.88 (s, 6H, H-15), 7.83 (d, J = 2.1 Hz, 6H, H-5), 7.56 (d, J = 7.8 Hz, 6H, H-2), 7.51 – 7.44 (m, 12H, H-11/13), 7.24 (dd, J = 7.8, 2.1 Hz, 6H, H-3), 7.06 (d, J = 8.1 Hz, 6H, H-10), 5.72 (s, 2H, bridgehead-H-1), 5.63 (s, 2H, bridgehead-H-6). **^{13}C NMR** (151 MHz, THF-d_8): δ = 162.3 ppm (C-9), 160.0(C-7), 146.8(C-5a), 145.3(C-1a), 144.3(C-4), 141.0(C-14), 133.8(C-11), 133.7(C-13), 131.9(q, $^1J_{C\text{-}F}$ = 30.4 Hz, C-16), 131.3(C-15), 129.5(C-12), 125.8(C-3), 125.5(C-2), 124.4(q, $^1J_{C\text{-}F}$ = 274.5 Hz, C-17), 119.8(C-8), 117.7(C-10), 111.5(C-5), 56.0(bridgehead-C-6), 53.3(bridgehead-C-1). **^{19}F NMR** (471 MHz, THF-d_8): δ = -59.9 ppm (18F, F-C17). **IR** (neat, ATR): $\tilde{\nu}$ = 1626 (m), 1609 (m), 1582 (m), 1483 (m), 1394 (m), 1364 (w), 1294 (s), 1234 (m), 1167 (s), 1128 (s), 1086 (s), 1040 (s), 959 (m), 920 (w), 887 (m), 866 (m), 852 (m), 827 (m), 793 (m), 777 (m), 744 (m), 733 (w), 687 (w), 662 (m), 615 (w). **MS** (MALDI-FT-ICR): $[M+H]^+$: *m/z* calcd. For ($C_{106}H_{59}F_{18}N_6O_6^+$): 1853.4203, found 1853.4290. **Elemental Analysis** (%): ($C_{106}H_{58}F_{18}N_6O_6$) Calcd. C 68.68, H 3.15, N 4.59, found C 68.62, H 3.49, N 4.43.

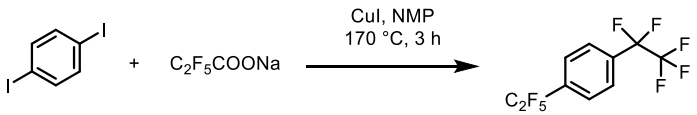

1,4-Bis(perfluoroethyl)benzene (56): A 500 mL flask was charged with 1,4-diiodobenzene **46** (9.90 g, 30.0 mmol), sodium pentafluoropropionate **55** (44.6 g, 240 mmol), CuI (22.9 g, 120 mmol) and anhydrous toluene (80 mL) under argon. Toluene and water were removed out by distillation at 120 °C under argon flow. Then the mixture was cooled down to room temperature and 140 mL anhydrous N-Methyl-2-pyrrolidone(NMP) was added. The mixture was heated to 170 °C and stirred for 3 h. After it was cooled down to 55 °C, the crude product was obtained under reduced pressure in 50% yield as colorless liquid (4.69 g, 14.9 mmol). It was used in the next step without further purification.

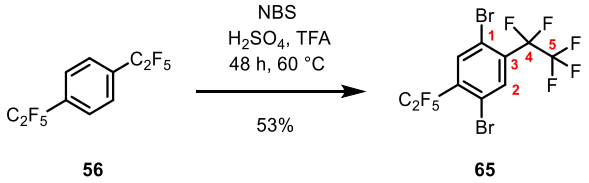

1,4-Dibromo-2,5-bis(perfluoroethyl)benzene (65): 56 (1.26 g, 4.00 mmol) was added to a mixture of trifluoroacetic acid (10 mL) and concentrated sulfuric acid (3 mL). The mixture was stirred at 60 °C, and *N*-bromosuccinimide (NBS) (2.13 g, 12.0 mmol) was added in portions (355 mg × 6 times) over 5 h. After stirring for additional 48 hours at 60 °C, the mixture was cooled to roomtemperature and ice water (100 mL) was added. The resulting suspension was washed with water (40 mL × 3) and sublimated to give **65** as colorless solid in 53 % yield (1.00 g, 2.12 mmol). **M. P.** = 61 °C **^{1}H NMR** (600 MHz, $CDCl_3$): δ = 7.95 ppm (s, 2H, H-2). **^{13}C NMR** (151 MHz, $CDCl_3$) δ = 137.1 ppm (t, $^{3}J_{C\text{-}F}$ = 8.8 Hz, C-2), 133.0(t, $^{2}J_{C\text{-}F}$ = 23.3 Hz, C-3), 120.0(t, $^{4}J_{C\text{-}F}$ = 2.4 Hz, C-1), 118.8(qt, $^{1}J_{C\text{-}F}$ = 287.3 Hz, $^{2}J_{C\text{-}F}$ = 37.5 Hz, C-5), 112.1(tq, $^{1}J_{C\text{-}F}$ = 258.8 Hz, $^{2}J_{C\text{-}F}$ = 40.2 Hz, C-4). **^{19}F NMR** (471 MHz, $CDCl_3$): δ = -82.8 ppm (6F, F-C5), -111.7 (4F, F-C4). **IR** (neat, ATR): $\tilde{\nu}$ = 1487 (w), 1348 (m), 1333 (m), 1321 (s), 1277 (m), 1211 (s), 1188 (s), 1146 (s), 1113 (s), 1069 (vs), 1015 (w), 968 (s), 897 (s), 829 (w), 800 (w), 752 (s), 727 (w), 714 (w), 692 (m), 679 (w). **MS** (EI+): $[M]^+$: *m/z* Calcd. For ($C_{10}H_2F_{10}Br_2^+$): 469.8364, found 469.8340. **Elemental Analysis** (%): ($C_{10}H_2F_{10}Br_2$) Calcd. C 25.45, H 0.43 found C 25.41, H 0.67.

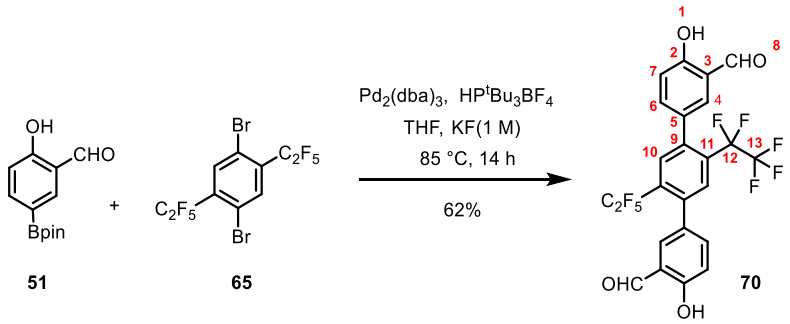

4,4''-Dihydroxy-2',5'-bis(perfluoroethyl)-[1,1':4',1''-terphenyl]-3,3''-dicarbaldehyde (70): In a screw-capped vessel salicylaldehyde **51** (472 mg, 2.40 mmol) and dibromide **65** (572 mg, 1.00 mmol) were suspended in THF (40 mL) and an aqueous KF solution (1 M, 10 mL) under argon. 5 mol-% tris(dibenzylideneacetone)dipalladium(0) (91.6 mg, 10 µmol) and 10 mol-% tri-*tert*-butylphosphonium tetrafluoroborate (58.0 mg, 20 µmol) were added and the mixture stirred at 85 °C for 14 h. After cooling the reaction mixture to room temperature, the organic layer was separated and dried over Na_2SO_4. After removal of solvents under reduced pressure, the crude product was purified by column chromatography (SiO_2, flushed with THF) and recrystallized further from THF/penatne to give **70** as colorless solid in 62% yield (342 mg, 617 µmol). **M. P.** = 276 °C **^{1}H NMR** (700 MHz, THF-d_8): δ = 10.99 ppm (s, 2H, H-1), 10.01 (s, 2H, H-8), 7.73 (s, 2H, H-10), 7.68 (d, J = 2.3 Hz, ^{1}H, H-4), 7.51 (dd, J = 8.3, 2.3 Hz, 2H, H-6), 7.04 (d, J = 8.5 Hz, 2H, H-7). **^{13}C NMR** (176 MHz, THF-d_8): δ = 196.4 ppm (C-8), 162.1 (C-2), 142.0 (C-9), 137.7 (C-6), 134.2 (C-4), 133.7(C-10), 130.4 (C-5), 130.3 (C-11), 121.3 (C-3), 117.5 (C-7), 122.3-112.6(m, C-12/13). **^{19}F NMR** (283 MHz, THF-d_8): δ = -86.2 ppm (6F, F-13), -109.5(4F, F-C12). **IR** (neat, ATR): $\tilde{\nu}$ = 1655 (s), 1624 (w), 1589 (w), 1477 (m), 1441 (w), 1389 (w), 1377 (w), 1331 (m), 1308 (m), 1286 (s), 1258 (w), 1194 (s), 1165 (s), 1148 (s), 1097 (s), 1055 (m), 1018 (w), 980 (s), 930 (s), 908 (m), 895 (w), 845 (m), 771 (m), 741 (vs), 706 (s), 646 (s), 613 (m). **MS** (EI+): $[M]^+$: *m/z* Calcd. For ($C_{24}H_{12}F_{10}O_4^+$): 554.0576, found 554.0559. **Elemental Analysis** (%): ($C_{24}H_{12}F_{10}O_4$) Calcd. C 52.00, H 2.18 found C 52.13, H 2.56.

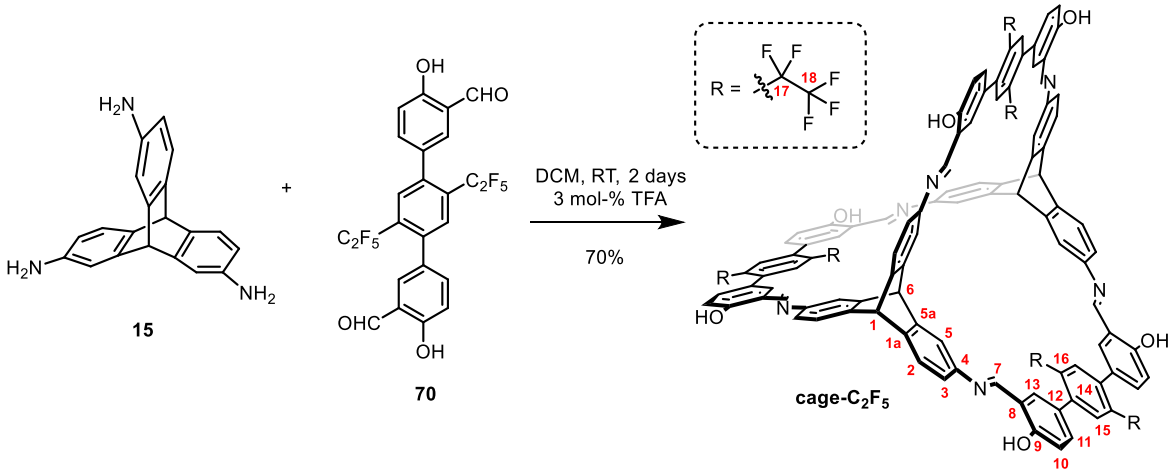

cage-C_2F_5: In a 250 mL flask salicylaldehyde **70** (200 mg, 360 µmol) was stirred in anhydrous DCM (200 mL) until it dissolved. Triamino triptycene **15** (71.9 mg, 240 µmol) was added to the solution. After complete dissolution, 3 mol-% TFA (0.1 M in anhydrous DCM, 108 µL) were added. The mixture was stirred at room temperature for 2 days. The precipitate was filtered, washed with pentane (10 mL) and diethyl ether (3 mL× 2) and dried for 6 h at the Kugelrohr oven (100 °C, $1.0 \cdot 10^{-3}$ mbar) to give **cage-C_2F_5** as light yellow solid in 70% yield (180 mg, 83.6 µmmol). **M.p.**: >350 °C. **^{1}H NMR** (600 MHz, THF-d_8): δ = 13.27 ppm (s, 6H, 9-OH), 9.12 (s, 6H, imine-H-7), 7.80 (d, J = 2.2 Hz, 6H, H-5), 7.74 (s, 6H, H-15), 7.54 (d, J = 7.7 Hz, 6H, H-2), 7.38 (d, J = 6.6 Hz, 12H, H-11/13), 7.23 (dd, J = 7.7, 2.5 Hz, 6H, H-3), 7.02 (d, J = 9.1 Hz, 6H, H-10), 5.69(s, 2H, bridgehead-H-1), 5.56(s, 2H, bridgehead-H-6). **^{13}C NMR** (151 MHz, THF-d_8): δ = 162.2 ppm (C-9), 159.6(C-7), 146.7(C-5a), 145.4(C-1a), 144.3(C-4), 142.5(C-14), 133.9(C-11), 133.8(C-15), 133.6(C-13), 130.4 (t, $^1J_{C\text{-}F}$ = 21.9 Hz, C-16), 129.7(C-12), 125.9(C-3), 125.5(C-2), 119.5(C-8), 117.3(C-10), 111.3(C-5), 56.2(bridgehead-C-6), 53.5(bridgehead-C-1). **^{19}F NMR** (471 MHz, THF-d_8): δ = -86.1 ppm (18F, F-C18), -109.4 (12F, F-C17). ***Note***: Due to strong and multiple ^{19}F-^{13}C-coupling, the signals of the perfluorinated side chains where not visible in ^{13}C-NMR spectra. **IR** (neat, ATR): $\tilde{\nu}$ = 1628 (w), 1609 (w), 1583 (w), 1477 (m), 1385 (w), 1364 (w), 1325 (w), 1279 (m), 1205 (s), 1173 (m), 1151 (m), 1130 (m), 1096 (m), 1084 (s), 1059 (w), 1009 (w), 978 (s), 961 (w), 928 (w), 916 (w), 889 (w), 860 (m), 829 (m), 793 (m), 777 (m), 744 (m), 716 (w), 687 (w), 669 (m), 615 (w). **MS** (MALDI-TOF): $[M+H]^+$: *m/z* calcd. For ($C_{112}H_{59}F_{30}N_6O_6^+$): 2154.4012, found 2154.4022. **Elemental Analysis** (%): ($C_{112}H_{58}F_{30}N_6O_6$) Calcd. C 62.46, H 2.71, N 3.90, found C 62.13, H 3.12, N 3.70.

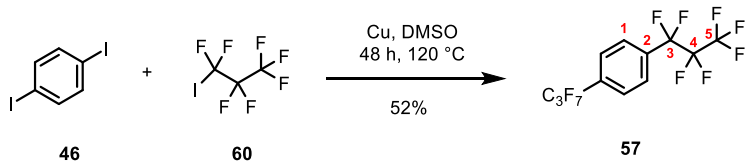

46 60 57

1,4-Bis(perfluoropropyl)benzene (57): In a screw-capped-vessel perfluoropropyl iodide **60** (26.6 g, 90.0 mmol) was added to a mixture of 1,4-diiodobenzene **46** (9.90 g, 30.0 mmol) and Cu powder (11.4 g, 180 mmol) in anhydrous DMSO (80 mL). The mixture was heated to 120 °C and stirred for 48 h. After cooling to room temperature, water (50 mL) and diethyl ether (50 mL) were added to the mixture and stirred additional 30 min. The mixture was filtered, and the filtrate was extracted with diethyl ether (50 mL × 3). The extract was washed with water (40 mL × 2), dried over $MgSO_4$. After removal of solvent under reduced pressure, the resulting residue was purified by column chromatography (SiO_2, petroleum ether, R_f = 0.68) to give **57** as colorless solid in 52% (6.47 g, 15.6 mmol). **M. P.** = 32 °C. **^{1}H NMR** (600 MHz, $CDCl_3$): δ = 7.76 ppm (s, 4H, H-1). **^{13}C NMR** (151 MHz, $CDCl_3$): δ = 132.8 ppm (t, $^1J_{C\text{-}F}$ = 24.6 Hz, C-2), 127.5(t, $^2J_{C\text{-}F}$ = 6.4 Hz, C-1), 118.1(qt, $^1J_{C\text{-}F}$ = 287.7 Hz, $^2J_{C\text{-}F}$ = 34.0 Hz, C-5), 114.9(tt, $^1J_{C\text{-}F}$ = 255.9 Hz, $^2J_{C\text{-}F}$ = 31.3 Hz, C-3), 108.9(m, C-4). **^{19}F NMR** (471 MHz, $CDCl_3$): δ = -80.0 ppm (6F, F-C5), -112.3 (4F, F-C3), -126.32(4F, F-C4). **IR** (neat, ATR): $\tilde{\nu}$ = 1418 (w), 1346 (s), 1277 (m), 1227 (s), 1194 (s), 1177 (s), 1151 (s), 1105 (s), 1082 (s), 1024 (w), 897 (s), 814 (s), 741 (s), 685 (s), 608 (m). **MS** (EI+): $[M]^+$: *m/z* Calcd. For ($C_{12}H_4F_{14}^+$): 414.0084, found 414.0069. **Elemental Analysis** (%): ($C_{12}H_4F_{14}$) Calcd. C 34.80, H 0.97 found C 34.81, H 1.44.

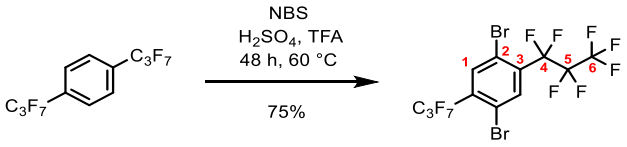

57 66

1,4-Dibromo-2,5-bis(perfluoropropyl)benzene (66): 57 (9.18g, 22.2 mmol) was added to a mixture of trifluoroacetic acid (85 mL) and concentrated sulfuric acid (33 mL). The mixture was stirred at 60 °C, and *N*-bromosuccinimide (NBS) (11.9 g, 66.6 mmol) was added in portions (1.98 g × 6 times) over 5 h. After stirring for additional 48 hours at 60 °C, the mixture was cooled to roomtemperature and ice water (600 mL) was added. The resulting suspension was washed with water (40 mL × 3) and recrystallized in ethanol to give **66** as colorless solid in 75% yield (9.50 g, 16.6 mmol). **M. P.** = 80 °C. **^{1}H NMR** (600 MHz, $CDCl_3$) δ = 7.93 ppm (s, 2H, H-1). **^{13}C NMR** (151

MHz, $CDCl_3$): δ = 137.5 ppm (t, $^1J_{C\text{-}F}$ = 9.0 Hz, C-1), 133.2(t, $^1J_{C\text{-}F}$ = 23.6 Hz, C-3), 120.3(s, C-2), 118.0(qt, $^1J_{C\text{-}F}$ = 287.9 Hz, $^2J_{C\text{-}F}$ = 33.7 Hz, C-6), 114.3(tt, $^1J_{C\text{-}F}$ = 259.7 Hz, $^2J_{C\text{-}F}$ = 33.3 Hz, C-4), 109.3(m, C-5). **^{19}F NMR** (471 MHz, $CDCl_3$) δ = -80.0 ppm (6F, F-C6), -108.5 (4F, F-C4), -123.9(4F, F-C5). **IR** (neat, ATR): $\tilde{\nu}$ = 1483 (w), 1352 (m), 1339 (m), 1277 (m), 1221 (s), 1180 (s), 1146 (s), 1119 (s), 1107 (s), 1047 (s), 916 (s), 866 (s), 744 (s), 706 (m), 623 (m). **MS** (EI+): $[M]^+$: *m/z* Calcd. For ($C_{12}H_2Br_2F_{14}^+$): 569.8300, found 569.8312. **Elemental Analysis** (%): ($C_{12}H_2Br_2F_{14}$) Calcd. C 25.20, H 0.35 found C 25.18, H 0.71.

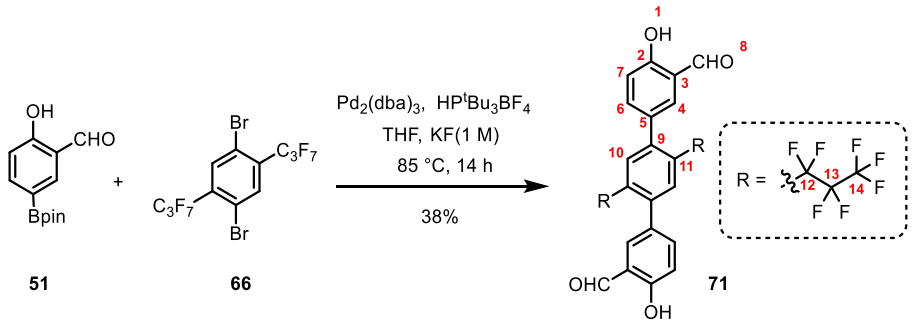

4,4''-Dihydroxy-2',5'-bis(trifluoromethyl)-[1,1':4',1''-terphenyl]-3,3''-dicarbaldehyde (71): In a screw-capped vessel salicylaldehyde **51** (595 mg, 2.40 mmol) and dibromide **66** (572 mg, 1.00 mmol) were suspended in THF (40 mL) and an aqueous KF solution (1 M, 10 mL) under argon. 5 mol-% tris(dibenzylideneacetone)dipalladium(0) (91.6 mg, 10 µmol) and 10 mol-% tri-*tert*-butylphosphonium tetrafluoroborate (58.0 mg, 20 µmol) were added and the mixture stirred at 85 °C for 14 h. After cooling the reaction mixture to room temperature, the organic layer was separated and dried over Na_2SO_4. After removal of solvents under reduced pressure, the crude product was purified by column chromatography (SiO_2, flushed with THF) and recrystallized further from THF/penatne to give **71** as colorless solid in 38% yield (251 mg, 384 µmol). **M. P.** = 232 °C. **^{1}H NMR** (600 MHz, THF-d_8): δ = 10.99 ppm (s, 2H, H-1), 10.02 (s, 2H, H-8), 7.73 (s, 2H, H-10), 7.69 (d, *J* = 2.3 Hz, ^{1}H, H-4), 7.52 (dd, *J* = 8.7, 2.5 Hz, 2H, H-6), 7.04 (d, *J* = 8.5 Hz, 2H, H-7). **^{13}C NMR** (126 MHz, THF-d_8): δ = 196.4 ppm (C-8), 162.1 (C-2), 142.1 (C-9), 137.8 (C-6), 134.2 (C-4), 134.1(C-10), 130.4 (C-5), 130.3(C-11), 121.2 (C-3), 117.4 (C-7). **Note:** Due to strong and multiple ^{19}F-^{13}C coupling, the signals of the perfluorinated side chains were not visible in ^{13}C-NMR spectra. **^{19}F NMR** (471 MHz, THF-d_8): δ = -82.9 ppm (6F), -106.5(4F), -126.6 (4F). **IR** (neat, ATR): $\tilde{\nu}$ = 1661 (m), 1593 (w), 1477 (m), 1371 (w),

1344 (m), 1306 (w), 1288 (s), 1258 (w), 1221 (s), 1204 (s), 1173 (s), 1153 (s), 1132 (m), 1115 (vs), 1094 (m), 1047 (w), 947 (m), 916 (m), 880 (s), 839 (m), 770 (m), 752 (s), 733 (s), 712 (m), 663 (w), 633 (m), 608 (w). **MS** (EI+): $[M]^+$: *m/z* Calcd. For ($C_{26}H_{12}F_{14}O_4^+$): 654.0512, found 654.0478. **Elemental Analysis** (%): ($C_{26}H_{12}F_{14}O_4$* 0.6THF) Calcd. C 47.99, H 2.13 found C 48.19, H 2.19.

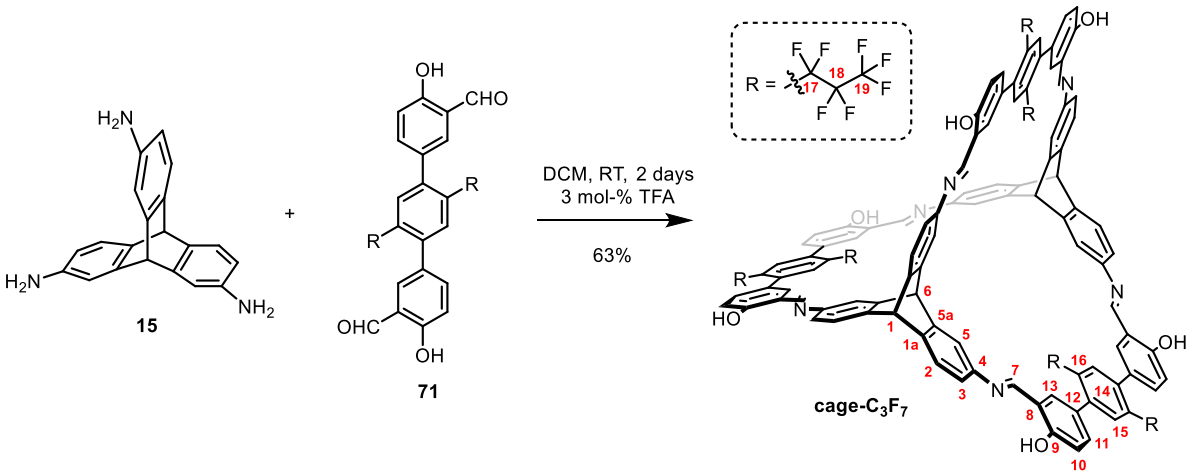

cage-C_3F_7: In a 250 mL flask salicylaldehyde **71** (232 mg, 360 µmol) was stirred in anhydrous DCM (170 mL) until it dissolved. Triamino triptycene **15** (71.9 mg, 240 µmol) was added to the solution. After complete dissolution, 3 mol-% TFA (0.1 M in anhydrous DCM, 108 µL) were added. The mixture was stirred at room temperature for 2 days. The precipitate was filtered, washed with pentane (3 mL× 3) and diethyl ether (5 mL× 3) and dried for 4 h at the Kugelrohr oven (100 °C, $1.0 \cdot 10^{-3}$ mbar) to give **cage-C_3F_7** as light yellow solid in 63% yield (185 mg, 75.4 µmmol). **M.p.**: >350 °C. **^{1}H NMR** (700 MHz, THF-d_8): δ = 13.33 ppm (s, 6H, 9-OH), 9.14 (s, 6H, imine-H-7), 7.83 (d, J = 2.2 Hz, 6H, H-5), 7.75 (s, 6H, H-15), 7.55 (d, J = 7.9 Hz, 6H, H-2), 7.40 (dd, J = 8.0, 2.5 Hz, 6H, H-11), 7.37 (d, J = 2.5 Hz, 6H, H-13), 7.24 (dd, J = 7.9, 2.1 Hz, 6H, H-3), 7.02 (d, J = 8.1 Hz, 6H, H-10), 5.71 (s, 2H, bridgehead-H-1), 5.58 (s, 2H, bridgehead-H-6). **^{13}C NMR** (176 MHz, THF-d_8): δ = 162.1 ppm (C-9), 159.7(C-7), 146.7(C-5a), 145.3(C-1a), 144.2(C-4), 142.6(C-14), 134.2(C-15), 134.0(C-11), 133.7(C-13), 130.3(C-16), 129.7(C-12), 125.9(C-3), 125.5(C-2), 119.4(C-8), 117.2(C-10), 111.4(C-5), 56.1(bridgehead-C-6), 53.4(bridgehead-C-1). ***Note***: Due to strong and multiple ^{19}F-^{13}C-coupling, the signals of the perfluorinated side chains where not visible in ^{13}C-NMR spectra. **^{19}F NMR** (659 MHz, THF-d_8): δ = -81.1 ppm(F-C19), -104.4(F-C18), -124.6(F-C17). **IR** (neat, ATR): $\tilde{\nu}$ = 1629 (m), 1611 (w), 1584 (m), 1480 (m), 1382

(w), 1340 (m), 1279 (m), 1231 (s), 1201 (s), 1182 (s), 1147 (m), 1135 (m), 1129 (m), 1110 (s), 1083 (m), 1061 (w), 1048 (w), 972 (w), 958 (w), 945 (w), 933 (w), 923 (w), 915 (m), 899 (w), 890 (w), 874 (s), 863 (m), 828 (m), 809 (m), 793 (m), 779 (m), 743 (s), 678 (m), 663 (w), 652 (w), 643 (w). **MS** (MALDI-FT-ICR): $[M+H]^+$: *m/z* calcd. For ($C_{118}H_{59}F_{42}N_6O_6^+$): 2453.3820, found 2453.3864. **Elemental Analysis** (%): ($C_{118}H_{58}F_{42}N_6O_6$) Calcd. C 57.76, H 2.38, N 3.43, found C 57.21, H 2.99, N 3.42.

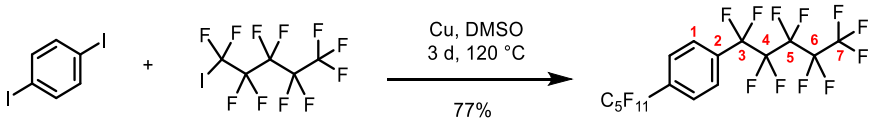

46 **61** **58**

1,4-Bis(perfluoropentyl)benzene (58): In a screw-capped-vessel perfluoropentyl iodide **61** (22.6 g, 57.2 mmol) was added to a mixture of 1,4-diiodobenzene **46** (8.58 g, 26.0 mmol) and Cu powder (6.61 g, 104 mmol) in anhydrous DMSO (80 mL). The mixture was heated to 120 °C and stirred for 3 days. After cooling to room temperature, water (60 mL) and diethyl ether (150 mL) were added to the mixture and stirred additional 20 min. The mixture was filtered, and the filtrate was extracted with diethyl ether (40 mL × 2). The extract was washed with water (40 mL × 2), dried over $MgSO_4$. After removal of solvent under reduced pressure, the resulting residue was purified by column chromatography (SiO_2, petroleum ether, R_f = 0.77) to give **58** as colorless solid in 77% (13.5 g, 22.0 mmol). **M. P.** = 51 °C **^{1}H NMR** (400 MHz, $CDCl_3$) δ = 7.76 ppm (s, 4H, H-1). **^{13}C NMR** (101 MHz, $CDCl_3$) δ = 133.0 ppm (t, $^1J_{C\text{-}F}$ = 24.5 Hz, C-2), 127.6(t, $^2J_{C\text{-}F}$ = 6.6 Hz, C-1) 122.0-105.0(m, C-3/4/5/6). **^{19}F NMR** (283 MHz, $CDCl_3$) δ = -80.9 ppm (6F), -111.4 (4F), -122.0(4F), -122.3(4F), -126.3(4F). **IR** (neat, ATR): $\tilde{\nu}$ = 1417 (w), 1359 (m), 1297 (m), 1232 (s), 1198 (s), 1186 (s), 1137 (vs), 1104 (s), 1084 (s), 1025 (m), 957 (w), 864 (w), 846 (m), 771 (m), 747 (w), 720 (s), 702 (s), 661 (m), 616 (m). **MS** (EI+): $[M]^+$: *m/z* Calcd. For ($C_{16}H_4F_{22}^+$): 594.9972, found 594.9947. **Elemental Analysis** (%): ($C_{16}H_4F_{22}$) Calcd. C 31.29, H 0.66 found C 31.76, H 1.12.

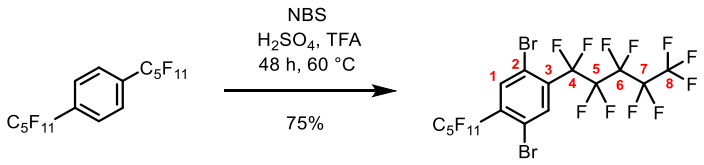

1,4-Dibromo-2,5-bis(perfluoropentyl) benzene (67): 58 (12.3 g, 20 mmol) was added to trifluoroacetic acid (100 mL), and concentrated H_2SO_4 (30 mL). The reaction mixture was heated to 60 °C, and *N*-bromosuccinimide (10.7 g, 60 mmol) was added in portions (1.78 g × 6 times) over 5 h. After stirring for additional 48 hours at 60 °C, the mixture was cooled to room temperature and ice water (100 mL) was added. The precipitate was collected, washed with water (200 mL), dissolved with dichloromethane (500 mL), and dried over $MgSO_4$. After removal of the solvent under reduced pressure the resulting residue was recrystallized in ethanol to give **67** as colorless solid in 75% yield (11.6 g, 15.0 mmol). **M.P.**: 88 °C. **^{1}H NMR** (700 MHz, $CDCl_3$) δ = 7.94 ppm (s, 4H). **^{13}C NMR** (176 MHz, $CDCl_3$): δ = 137.5 ppm (t, $^3J_{C\text{-}F}$ = 9.1 Hz, C-1), 133.2(t, $^2J_{C\text{-}F}$ = 23.6 Hz, C-3), 120.3(C-2), 117.4(qt, $^1J_{C\text{-}F}$ = 288.3 Hz, $^2J_{C\text{-}F}$ = 33.1 Hz, C-8), 114.9(tt, $^1J_{C\text{-}F}$ = 261.3 Hz, $^2J_{C\text{-}F}$ = 33.8 Hz, C-4), 113.0-106.0(m, C-5/6/7). **^{19}F NMR** (283 MHz, $CDCl_3$) δ = -80.7 ppm (6F), -107.7 (4F), -119.5(4F), -122.4(4F), -126.1(4F). **IR** (neat, ATR): $\tilde{\nu}$ =1481 (w), 1359 (m), 1346 (m), 1309 (w), 1285 (w), 1229 (s), 1197 (s), 1137 (s), 1106 (s), 1052 (s), 975 (w), 957 (m), 901 (m), 864 (w), 840 (w), 805 (m), 783 (s), 746 (m), 723 (s), 671 (s), 651 (w), 635 (w). **MS** (EI+): $[M]^+$: *m/z* Calcd. For ($C_{16}H_2Br_2F_{22}^+$): 769.8167, found 769.8168. **Elemental Analysis** (%): ($C_{16}H_2Br_2F_{22}$) Calcd. C 24.89, H 0.26 found C 25.39, H 0.80.

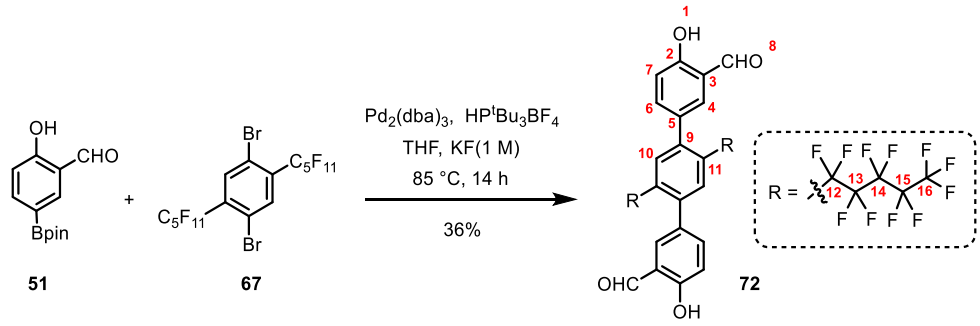

4,4''-Dihydroxy-2',5'-bis(perfluoropentyl)-[1,1':4',1''-terphenyl]-3,3''-dicarbaldehyde (72): In a screw-capped vessel salicylaldehyde **51** (595 mg, 2.40 mmol) and dibromide **67** (772 mg, 1.00 mmol) were suspended in THF (40 mL) and an aqueous KF solution (1 M, 10 mL) under argon. 5 mol-%

tris(dibenzylideneacetone)dipalladium(0) (91.6 mg, 10 µmol) and 10 mol-% tri-*tert*-butylphosphonium tetrafluoroborate (58.0 mg, 20 µmol) were added and the mixture stirred at 85 °C for 14 h. After cooling the reaction mixture to room temperature, the organic layer was separated and dried over Na_2SO_4. After removal of solvents under reduced pressure, the crude product was purified by column chromatography (SiO_2, petroleum ether/ethyl acetate = 5:1, R_f = 0.59, flushed with THF) and recrystallized further from THF/penatne to give **72** as colorless solid in 36% yield (310 mg, 363 µmol). **M. P.** = 210 °C. **^{1}H NMR** (600 MHz, THF-d_8): δ = 11.00 ppm (s, 2H, H-1), 10.03 (s, 2H, H-8), 7.74 (s, 2H, H-10), 7.69 (d, J = 2.5 Hz, 2H, H-4), 7.52 (dd, J = 8.5, 2.5 Hz, 2H, H-6), 7.05 (d, J = 8.5 Hz, 2H, H-7). **^{13}C NMR** (151 MHz, THF-d_8): δ = 196.2 ppm (C-8), 162.1(C-2), 142.2(C-9), 137.7(C-6), 134.2 (C-10), 134.1(C-4), 130.4 (C-5/11), 121.3(C-3), 117.4(C-7). **Note:** Due to strong and multiple ^{19}F-^{13}C coupling, the signals of the perfluorinated side chains were not visible in ^{13}C-NMR spectra. **^{19}F NMR** (283 MHz, THF-d_8): δ = -83.7 ppm (6F), -105.8 (4F), -122.0 (4F), -124.9 (4F), -128.7 (4F). **IR** (neat, ATR): $\tilde{\nu}$ = 1664 (m), 1623 (w), 1593 (w), 1477 (m), 1371 (w), 1357 (m), 1306 (w), 1287 (m), 1251 (m), 1233 (m), 1192 (s), 1165 (s), 1140 (vs), 1110 (s), 1093 (m), 1049 (w), 936 (w), 909 (w), 883 (w), 861 (w), 836 (m), 822 (w), 789 (m), 770 (m), 746 (m), 719 (s), 693 (m), 678 (m), 656 (m), 638 (w), 604 (m). **MS** (APCI+): $[M+H]^+$: *m/z* Calcd. For ($C_{30}H_{13}F_{22}O_4^+$): 855.0457, found 855.0412. **Elemental Analysis** (%): ($C_{30}H_{12}F_{22}O_4$) Calcd. C 42.17, H 1.42 found C 42.04, H 1.93.

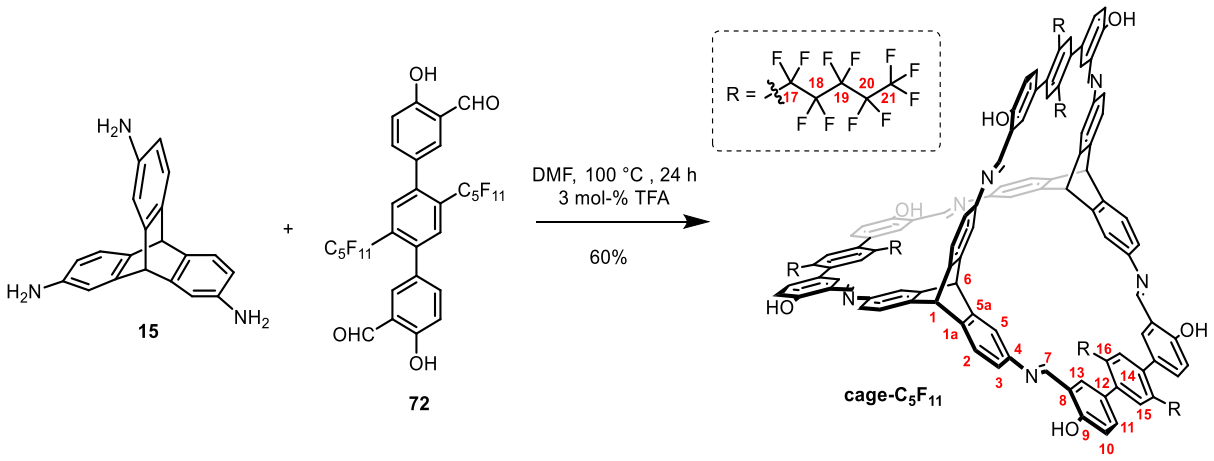

cage-C_5F_{11}: Triamino triptycene **15** (24.0 mg, 80 µmol), salicylaldehyde **72** (103 mg, 120 µmol) were added into 20 mL anhydrous DMF. After complete dissolution, 3 mol-% TFA (0.1 M in anhydrous DMF, 24 µL) was added. The mixture was heated to 100 °C and stirred for 24 h. After cooling the reaction mixture to room temperature, the

precipitate was filtered, washed with methanol (3 mL× 5) and dried for 14 h under high vaccum ($8.9 \cdot 10^{-1}$ mbar) at room temperature to give **cage-C_5F_{11}** as light yellow solid in 60% yield (73 mg, 23.9 µmol). **M.p.**: >350 °C. **^{1}H NMR** (600 MHz, THF-d_8)**:** δ = 13.36 ppm (s, 6H, 9-OH), 9.15 (s, 6H, imine-H-7), 7.83 (d, J = 2.2 Hz, 6H, H-5), 7.76 (s, 6H, H-15), 7.56 (d, J = 7.8 Hz, 6H, H-2), 7.43 – 7.38 (m, 12H, H-11/13), 7.25 (dd, J = 7.8, 2.1 Hz, 6H, H-3), 7.03 (d, J = 8.3 Hz, 6H, H-10), 5.72 (s, 2H, bridgehead-H-1), 5.57 (s, 2H, bridgehead-H-6). **^{13}C NMR** (151 MHz, THF-d_8)**:** δ = 162.1 ppm (C-9), 159.6 (C-7), 146.6 (C-5a), 145.4 (C-1a), 144.1 (C-4), 142.7 (C-14), 134.4 (C-15), 134.0 (C-11), 133.7 (C-13), 130.4 (C-16), 129.7 (C-12), 126.0 (C-3), 125.6 (C-2), 119.3 (C-8), 117.2 (C-8), 111.3 (C-5), 56.1 (bridgehead-C-6), 53.3 (bridgehead-C-1). ***Note*:** Due to strong and multiple ^{19}F-^{13}C-coupling, the signals of the perfluorinated side chains where not visible in ^{13}C-NMR spectra. **^{19}F NMR** (659 MHz, THF-d_8)**:** δ = -82.0 ppm (18F), -103.7 (12F), -120.0 (12F), -123.1 (12F), -126.9 (12F). **IR** (neat, ATR): $\tilde{\nu}$ =1628 (w), 1611 (w), 1584 (m), 1481 (m), 1474 (m), 1382 (w), 1359 (w), 1288 (m), 1231 (s), 1198 (s), 1173 (s), 1142 (s), 1134 (s), 1099 (m), 1085 (m), 1056 (w), 1048 (w), 972 (w), 958 (w), 946 (w), 892 (w), 860 (m), 832 (m), 811 (m), 795 (m), 780 (m), 744 (m), 732 (m), 702 (w), 680 (m), 661 (w), 649 (w). **MS** (MALDI-TOF): $[M+H]^+$: *m/z* calcd. For ($C_{130}H_{59}F_{66}N_6O_6^+$): 3053.3437, found 3053.3449. **Elemental Analysis** (%): ($C_{130}H_{58}F_{66}N_6O_6$) Calcd. C 51.13, H 1.91, N 2.75, found C 50.66 H 2.48, N 2.72.

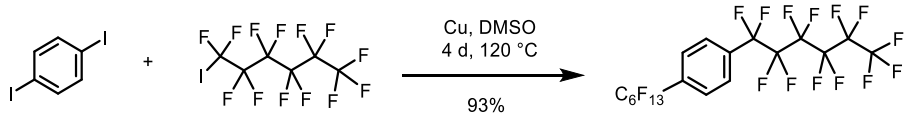

46 **62** **59**

1,4-Bis(perfluorohexyl)benzene (59): In a screw-capped-vessel perfluorohexyl iodide **62** (25.0 g, 56.1 mmol) was added to a mixture of **46** (8.40 g, 25.5 mmol) and Cu powder (6.48 g, 102 mmol) in anhydrous DMSO (60 mL). The mixture was stirred for 4 days at 120 °C and was allowed to cool to room temperature. Water (50 mL) and diethyl ether (50 mL) were added to the mixture and stirred additional 30 min. The mixture was filtered, and the filtrate was extracted with diethyl ether (50 mL × 3). The extract was washed with water (40 mL × 2), dried over $MgSO_4$, and concentrated in vacuo. The resulting residue was subjected to flash silica gel column chromatography eluting with petroleum ether to give **59** in 93% yield (16.9 g, 23.7 mmol) as colorless solid. **M. P.** = 66-67 °C. **^{1}H NMR** (301 MHz, $CDCl_3$): δ = 7.77 (s, 4H). **^{19}F NMR** (283

MHz, $CDCl_3$): δ = -80.8(m), -111.2(m), -121.4(m), -121.7(m), -122.8(m), -126.1(m). The analytical data is in accordance with that previously reported.[115]

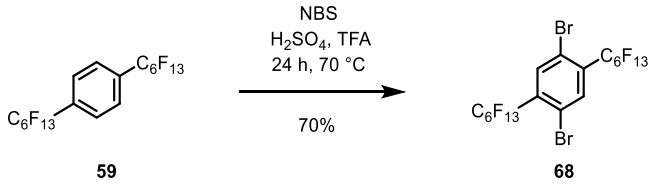

1,4-Dibromo-2,5-bis(perfluorohexyl) benzene (68): **59** (500 mg, 0.70 µmol) was added to trifluoroacetic acid (10 mL), and concentrated H_2SO_4 (3 mL). The reaction mixture was heated to 70 °C, and *N*-bromosuccinimide (374 mg, 2.10 mmol) was added in 6 hours slowly. The stirring was continued for 24 hours at 70 °C. After cooling to room temperature, the reaction mixture was poured into ice water (40 mL). Precipitate was collected by filtration and were recrystallized in ethanol to give **68** in 70% yield as clear crystals (430 mg, 49.3 µmol). **^{1}H NMR** (301 MHz, $CDCl_3$): δ = 7.94 (s, 4H). **^{19}F NMR** (283 MHz, $CDCl_3$): δ = -80.7(m), -107.6(m), -119.3(m), -121.6(m), -122.7(m), -126.0(m). The analytical data is in accordance with that previously reported.[115]

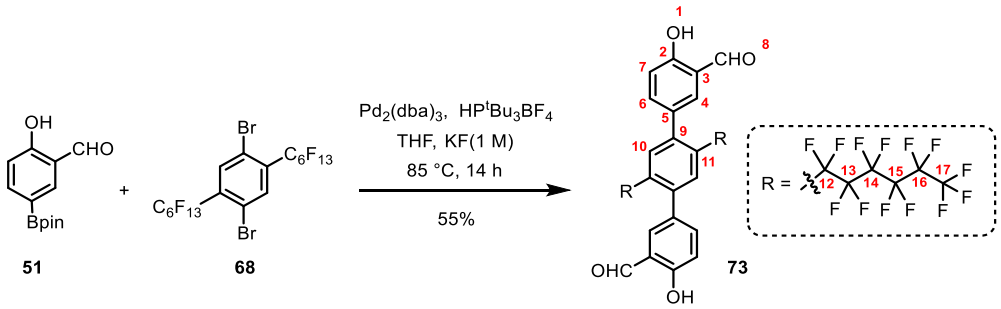

4,4''-Dihydroxy-2',5'-bis(perfluorohexyl)-[1,1':4',1''-terphenyl]-3,3''-dicarbaldehyde (73): In a screw-capped vessel salicylaldehyde **51** (1.43 g, 5.78 mmol) and dibromide **68** (2.10 g, 2.41 mmol) were suspended in THF (40 mL) and an aqueous KF solution (1 M, 10 mL) under argon. 5 mol-% tris(dibenzylideneacetone)dipalladium(0) (111 mg, 121 µmol) and 10 mol-% tri-*tert*-butylphosphonium tetrafluoroborate (69.9 mg, 241 µmol) were added and the mixture stirred at 85 °C for 14 h. After cooling the reaction mixture to room temperature, the organic layer was separated and dried over Na_2SO_4. After removal of solvents under reduced pressure, the crude product was purified by column chromatography (SiO_2, petroleum ether/ethyl acetate = 10:1, R_f = 0.32, flushed with THF) and recrystallized

further from THF/penatne to give **73** as colorless solid in 55% yield (1.26 g, 1.32 mmol). **M. P.** = 195 °C. **^{1}H NMR** (600 MHz, THF-d_8): δ = 11.00 ppm (s, 2H, H-1), 10.02 (s, 2H, H-8), 7.74 (s, 2H, H-10), 7.69 (d, J = 2.5 Hz, 2H, H-4), 7.52 (dd, J = 8.5, 2.6 Hz, 2H, H-6), 7.04 (d, J = 8.5 Hz, 2H, H-7). **^{13}C NMR** (151 MHz, THF-d_8): δ = 196.4 ppm (C-8), 162.1(C-2), 142.2(C-9), 137.7(C-6), 134.3 (C-10/4), 130.4 (C-5/11), 121.2(C-3), 117.5(C-7). **Note:** Due to strong and multiple ^{19}F-^{13}C coupling, the signals of the perfluorinated side chains were not visible in ^{13}C-NMR spectra. **^{19}F NMR** (471 MHz, THF-d_8): δ = -81.8 ppm (6F), -103.9 (4F), -120.0 (4F), -122.2 (4F), -123.4 (4F), -126.8 (4F). **IR** (neat, ATR): $\tilde{\nu}$ = 1661 (m), 1622 (w), 1591 (w), 1477 (m), 1366 (w), 1306 (w), 1286 (s), 1232 (m), 1198 (vs), 1167 (s), 1142 (s), 1123 (s), 1103 (m), 1063 (m), 1032 (m), 1020 (w), 959 (w), 945 (w), 916 (m), 837 (m), 770 (m), 754 (m), 743 (m), 714 (s), 679 (s), 665 (m), 646 (m), 621 (m). **MS** (EI+): $[M]^+$: *m/z* Calcd. For ($C_{32}H_{12}F_{26}O_4^+$): 954.0320, found 954.0336. **Elemental Analysis** (%): ($C_{32}H_{12}F_{26}O_4$) Calcd. C 40.27, H 1.27 found C 40.15, H 1.67.

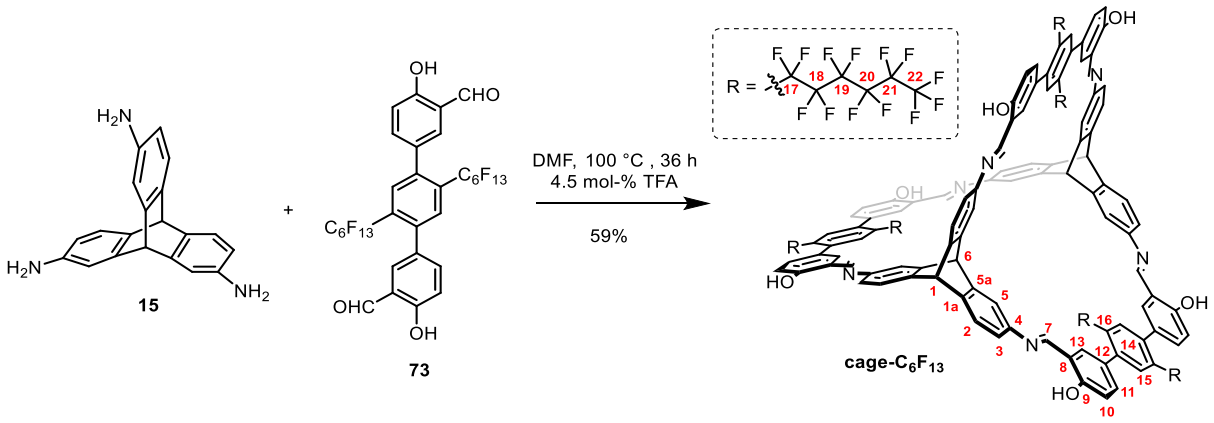

cage-C_6F_{13}: Triamino triptycene **15** (12.0 mg, 40 µmol), salicylaldehyde **73** (57.3 mg, 60 µmol) were added into 20 mL anhydrous DMF. After complete dissolution, 4.5 mol-% TFA (0.1 M in anhydrous DMF, 18 µL) was added. The mixture was heated to 100 °C and stirred for 36 h. After cooling to room temperature, the reaction mixture is filtered through syringe filters (0.2 µm pore) and put at room temperature for 12 h. Much flake crystal precipitated out from reaction solution and was filtered, washed with methanol (5 mL× 3) and dried for 8 h under high vaccum at room temperature to give **cage-C_6F_{13}** (named after **cage-$C_6F_{13\beta}$** according to different activation conditions in chapter III, section 3) as light yellow solid in 59% yield (39.6 mg, 11.8 µmol). **M.p.**: >350 °C. **^{1}H NMR** (700 MHz, THF-d_8)**:** δ = 13.36 ppm (s, 6H, 9-OH), 9.15 (s, 6H, imine-H-7), 7.82

(s, 6H, H-5), 7.76 (s, 6H, H-15), 7.56 (d, *J* = 7.7 Hz, 6H, H-2), 7.44 – 7.37 (m, 12H, H-11/13), 7.25 (dd, *J* = 7.6, 1.9 Hz, 6H, H-3), 7.03 (d, *J* = 8.0 Hz, 6H, H-10), 5.72 (s, 2H, bridgehead-H-1), 5.57 (s, 2H, bridgehead-H-6). **^{13}C NMR** (176 MHz, THF-d_8)**:** δ = 162.1 ppm (C-9), 159.6 (C-7), 146.6 (C-5a), 145.3 (C-1a), 144.1 (C-4), 142.7 (C-14), 134.4 (C-15), 134.0 (C-11), 133.7 (C-13), 130.4 (C-16), 129.7 (C-12), 126.0 (C-3), 125.6 (C-2), 119.3 (C-8), 117.2 (C-8), 111.2 (C-5), 56.2 (bridgehead-C-6), 53.3 (bridgehead-C-1). ***Note*:** Due to strong and multiple ^{19}F-^{13}C-coupling, the signals of the perfluorinated side chains where not visible in ^{13}C-NMR spectra. **^{19}F NMR** (471 MHz, THF-d_8)**:** δ = -83.9 (18F), -105.5 (12F), -121.8 (12F), -124.2 (12F), -124.9 (12F), -128.8 (12F). **M.p.**: >350 °C. **IR** (neat, ATR): $\tilde{\nu}$ = 1628 (w), 1610 (w), 1583 (w), 1481 (m), 1383 (w), 1362 (w), 1281 (m), 1232 (s), 1198 (vs), 1171 (s), 1144 (s), 1119 (s), 1092 (m), 1061 (w), 1034 (w), 1018 (w), 959 (w), 945 (w), 924 (w), 889 (w), 860 (m), 829 (m), 795 (m), 775 (m), 744 (m), 735 (m), 721 (m), 700 (m), 677 (m), 658 (m), 631 (w). **MS** (MALDI-TOF): $[M+H]^+$: *m/z* calcd. For ($C_{136}H_{59}F_{78}N_6O_6^+$): 3353.3245, found 3353.3261. **Elemental Analysis** (%): ($C_{136}H_{58}F_{78}N_6O_6$) Calcd. C 48.70, H 1.74, N 2.51, found C 49.28, H 2.08, N 2.15.

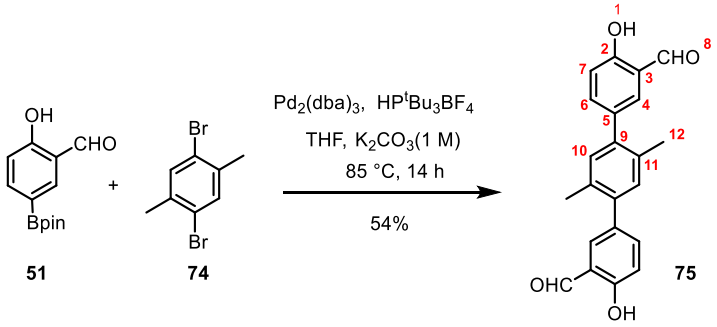

4,4''-Dihydroxy-2',5'-dimethyl-[1,1':4',1''-terphenyl]-3,3''-dicarbaldehyde (75): In a screw-capped-vessel salicylaldehyde **51** (4.17 g, 16.8 mmol) and dibromide **74** (1.85 g, 7.00 mmol) were suspended in THF (32 mL) and an aqueous K_2CO_3 solution (1 M, 8 mL) under argon atmosphere. 5 mol-% tris(dibenzylideneacetone)dipalladium(0) (321 mg, 350 µmol) and 10 mol-% tri-*tert*-butylphosphonium tetrafluoroborate (203 mg, 700 µmol) were added to the mixture. The suspension was heated to 85 °C and stirred for 14 h. After cooling to room temperature, THF and H_2O was removed out by rotary evaporation. , the obtained crude solid was purified by column chromatography (SiO_2, petroleum ether/ethyl acetate = 5:1, R_f = 0.35, then flushed with DCM) and further washed with DCM (10 mL) and pentane (20 mL) to give **75** as off-white solid in 54%

yield (1.30 g, 3.75 mmol). **M.p.** = 227 °C. **^{1}H NMR** (600 MHz, THF-d_8): δ = 10.93 (s, 2H, H-1), 10.01 (s, 2H, H-8), 7.68 (d, J = 2.3 Hz, 2H, H-4), 7.55 (dd, J = 8.5, 2.4 Hz, 2H, H-6), 7.16 (s, 2H, H-10), 7.02 (d, J = 8.5 Hz, 2H, H-7), 2.27 (s, 6H, H-12). **^{13}C NMR** (151 MHz, THF-d_8): δ = 197.1(C-8), 161.3(C-2), 140.2(C-9), 138.1(C-6), 134.2(C-4), 134.1(C-5), 133.4(C-11), 132.4(C-10), 121.7(C-3), 117.7(C-7), 19.8(C-12). **IR** (neat, ATR): $\tilde{\nu}$ = 2968 (w), 2934 (w), 2845 (w), 1678 (w), 1661 (s), 1620 (m), 1587 (m), 1479 (s), 1464 (m), 1450 (m), 1431 (m), 1391 (w), 1379 (m), 1366 (m), 1315 (m), 1279 (s), 1248 (m), 1225 (m), 1186 (m), 1167 (s), 1130 (m), 1047 (w), 989 (w), 918 (m), 905 (m), 889 (m), 839 (s), 770 (m), 735 (s), 714 (vs), 652 (s), 627 (m). **MS** (EI+): $[M]^+$: *m/z* calcd. For ($C_{22}H_{18}O_4^+$): 346.1205, found 3346.1208. **Elemental Analysis** (%): ($C_{22}H_{18}O_4$) Calcd. C 76.29, H 5.24, found C 76.01, H 5.17.

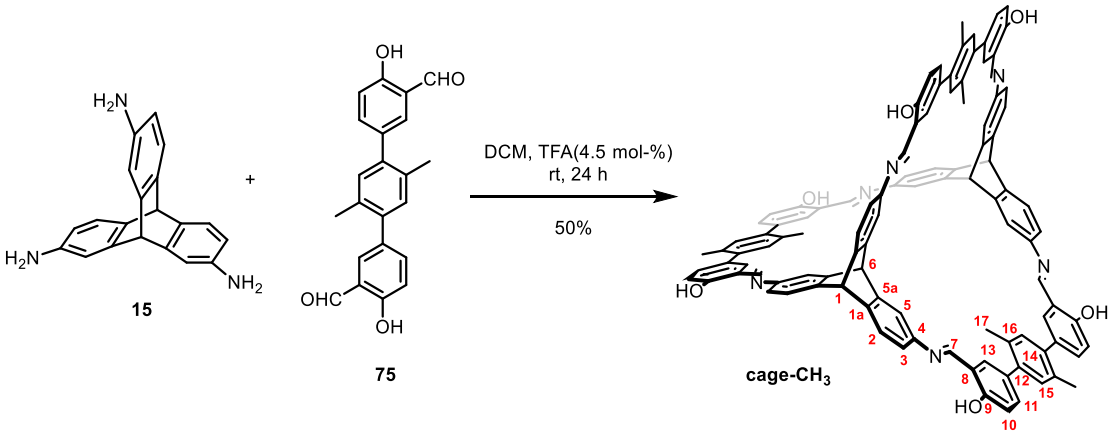

cage-CH$_3$: In three individual reactions, triamino triptycene **15** (29.9 mg, 100 µmol) and salicylaldehyde **75** (52.0 mg, 150 µmol) were dissolved each in anhydrous DCM (20 mL) in three 25 mL screw-capped vessels and 4.5 mol-% TFA (0.1 M in anhydrous DCM, 45 µL) was added to the solutions. The mixtures were stirred at room temperature for 24 h. All precipitate was filtered, washed with pentane (10 mL) and diethyl ether (2 × 3 mL), dried in the Kugelrohr oven (100 °C, $7.0 \cdot 10^{-2}$ mbar) for 12 h to give **cage-CH$_3$** as light yellow solid in 50% yield (115 mg, 75.2 µmol). **M.p.**: >350 °C. **^{1}H NMR** (700 MHz, THF-d_8): δ = 13.15 ppm (s, 6H, 9-OH), 9.18 (s, 6H, imine-H-7), 7.86 (d, J = 2.0 Hz, 6H, H-5), 7.55 (d, J = 7.8 Hz, 6H, H-2), 7.46 (d, J = 2.3 Hz, 6H, H-13), 7.41 (dd, J = 8.0, 2.2 Hz, 6H, H-11), 7.23 (dd, J = 7.7, 2.0 Hz, 6H, H-3), 7.16 (s, 6H, H-15), 7.01 (d, J = 8.1 Hz, 6H, H-10), 5.71 (s, 2H, bridgehead-H-1), 5.64 (s, 2H, bridgehead-H-6), 2.30 (s, 18H, H-17). **^{13}C NMR** (176 MHz, THF-d_8): δ = 161.1 ppm (C-9), 160.3 (C-7), 146.8 (C-5a), 145.2 (C-1a), 144.5 (C-4), 140.6 (C-14), 134.1 (C-11),

133.7 (C-12), 133.3 (C-13/16), 132.4 (C-15), 125.7 (C-3), 125.4 (C-2), 119.9 (C-8), 117.4 (C-10), 111.4 (C-5), 56.0 (bridgehead-C-6), 53.3 (bridgehead-C-1), 20.0 (C-17). **IR** (neat, ATR): $\tilde{\nu}$ = 2947 (w), 1626 (m), 1610 (s), 1582 (m), 1479 (s), 1431 (w), 1396 (w), 1383 (w), 1362 (m), 1321 (w), 1292 (m), 1279 (s), 1258 (w), 1236 (w), 1225 (w), 1182 (s), 1142 (m), 1132 (m), 1088 (w), 1034 (w), 974 (w), 959 (m), 945 (w), 883 (m), 856 (s), 829 (m), 808 (s), 793 (vs), 777 (s), 760 (m), 744 (w), 719 (w), 679 (m), 660 (m), 644 (s). **MS** (MALDI-FT-ICR): $[M+H]^+$: *m/z* calcd. For ($C_{106}H_{77}N_6O_6^+$): 1529.5899, found 1529.5934. **Elemental Analysis** (%): ($C_{106}H_{76}N_6O_6$) Calcd. C 83.22, H 5.01, N 5.49, found C 82.93, H 5.25, N 5.46.

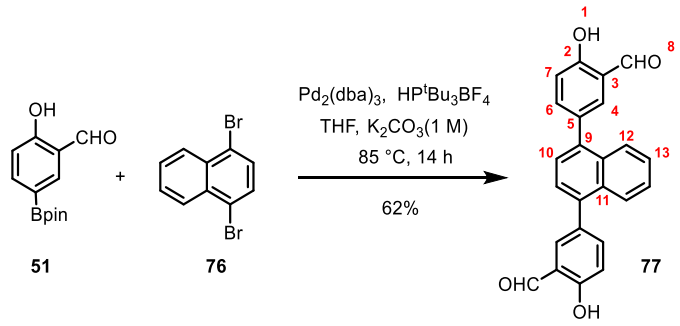

5,5'-(Naphthalene-1,4-diyl)bis(2-hydroxybenzaldehyde) (77): Salicylaldehyde **51** (3.13 g, 12.6 mmol) and dibromide **76** (1.50 g, 5.25 mmol) were suspended in THF (24 mL) and K_2CO_3 solution (1 M, 6 mL) in a screw cap vessel under argon atmosphere. 5 mol-% tris(dibenzylideneacetone)dipalladium(0) (241 mg, 263 µmol) and 10 mol-% tri-*tert*-butylphosphonium tetrafluoroborate (152 mg, 525 µmol) were added to the mixture. The suspension was heated to 85 °C and stirred for 14 h. After cooling to room temperature, the suspension was poured into water (30 mL) and extracted by CH_2Cl_2 (3 × 50 mL) and the combined organic layer was dried over Mg_2SO_4 and filtered with celite pad . After removal of solvent under reduced pressure, the obtained crude solid was washed with DCM (30 mL) and dried in high vacuum to give **77** as colorless solid in 62% yield (1.2 g, 3.16 mmol). **M. P.** >228 °C(decompose) **^{1}H NMR** (400 MHz, THF-d_8): δ = 11.01 (s, 2H, H-1), 10.05 (s, 2H, H-8), 7.93 (m, 2H, H-12), 7.84 (d, *J* = 2.3 Hz, 2H, H-4), 7.70 (dd, *J* = 8.4, 2.3 Hz, 2H, H-6), 7.49 (s, 2H, H-10) 7.46 (m, 2H, H-13), 7.12 (d, *J* = 8.5 Hz, 2H, H-7). **^{13}C NMR** (101 MHz, THF-d_8): δ = 197.1(C-8), 161.7(C-2), 139.2(C-9), 138.8(C-6), 135.1(C-4), 133.1(C-5), 132.9(C-11), 127.2(C-10), 126.8(C-13), 126.7(C-12), 121.9(C-3), 118.0(C-7). **IR** (neat, ATR): $\tilde{\nu}$ = 1624 (s), 1614 (s), 1572 (s), 1512 (w), 1489 (s), 1472 (s), 1425 (w), 1385 (m), 1364 (m), 1273 (s),

1188 (m), 1165 (s), 1130 (m), 1088 (w), 959 (m), 870 (m), 851 (m), 826 (s), 791 (s), 770 (s), 739 (s), 669 (s), 660 (s), 633 (s). **MS** (EI+): $[M]^+$: *m/z* Calcd. For ($C_{24}H_{16}O_4^+$): 368.1049, found 368.1028. **Elemental Analysis** (%): ($C_{24}H_{16}O_4$) Calcd. C 78.25, H 4.38 found C 78.32, H 4.64.

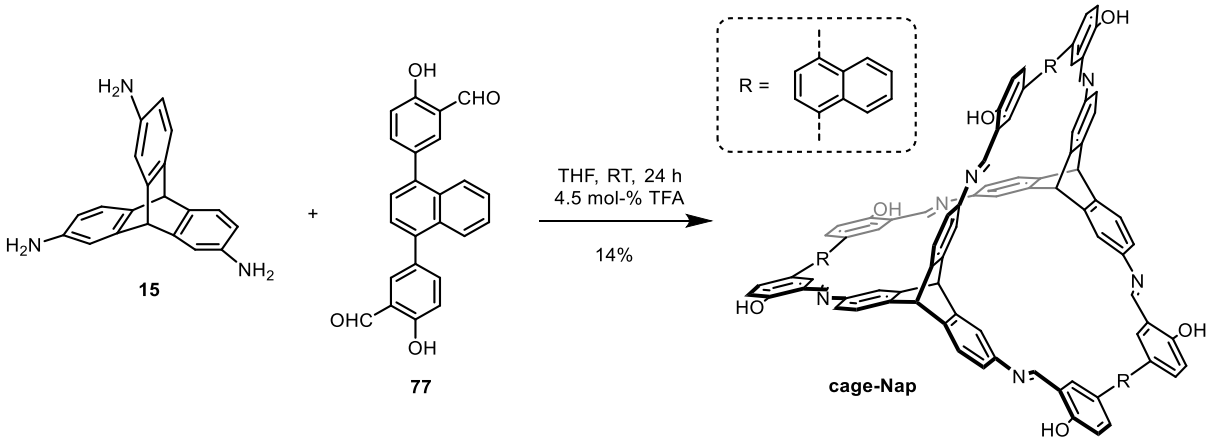

cage-Nap: In ten individual reactions, triamino triptycene **15** (29.9 mg, 100 µmol) and salicylaldehyde **77** (52.0 mg, 150 µmol) were dissolved each in anhydrous THF (18 mL) in ten 25 mL screw-capped vessels and 4.5 mol-% TFA (0.1 M in anhydrous THF, 45 µL) was added to the solutions. The mixtures were stirred at room temperature for 24 h. All precipitate was filtered, washed with pentane (20 mL) and dried in high vacuum for 14 h. The resulting solid was dissolved in 500 mL anhydrous THF. Methanol diffused into the THF solution via the gas phase. Three weeks later a crystalline material was isolated by decantation and washing with methanol to give **cage-Nap** as orange solid in 14% yield (108 mg, 67.7 µmol). **M.p.**: >350 °C. **IR** (neat, ATR): $\tilde{\nu}$ = 1624 cm^{-1} (m), 1607(m), 1578(m), 1489(s), 1470(m), 1385(w), 1362(w), 1273(s), 1186(m), 1165(s), 1130(m), 959(m), 891(w), 868(w), 851(w), 825(s), 791(m), 768(s), 743(m), 735(m), 690(w), 669(m), 660(m), 608(m). **MS** (MALDI-TOF): $[M+H]^+$: *m/z* calcd. For ($C_{112}H_{71}N_6O_6^+$): 1595.5430, found 1595.5410. **Elemental Analysis** (%): ($C_{112}H_{70}N_6O_6$*$3H_2O$) Calcd. C 81.54, H 4.64, N 5.09 found C 81.49, H 4.79, N 4.54.

2.3. Compounds of Chapter III, Section 3

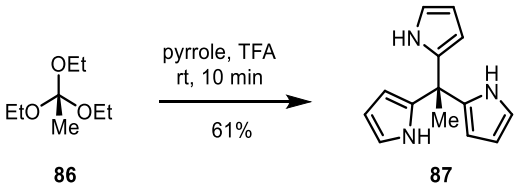

86 **87**

2,2',2''-(Ethane-1,1,1-triyl)tris(1H-pyrrole) (87): Triethyl orthoacetate **86** (7.7 mL) was dissolved in an excess of freshly distilled pyrrole (50 mL). TFA (0.5 mL) was added and the mixture stirred under argon. After 10 minutes, the reaction was quenched with 0.2 M NaOH (50 mL) giving a bright yellow emulsion. Ethyl acetate (50 mL) was added and the organic phase separated and dried over anhydrous $MgSO_4$. Ethyl acetate and unreacted pyrrole were removed under reduced pressure and further purified by silica gel column chromatography (DCM, R_f = 0.33) to give **87** in 61% yield (5.74 g, 25.5 mmol) as a colorless solid. **M.P.**: 168-169 °C. **^{1}H NMR** (301 MHz, $CDCl_3$): δ = 7.87 (s, 3H), 6.66 (s, 3H), 6.18 (m, 3H), 6.06 (s, 3H), 2.00 (s, 3H) ppm. The analytical data is in accordance with that previously reported.[154]

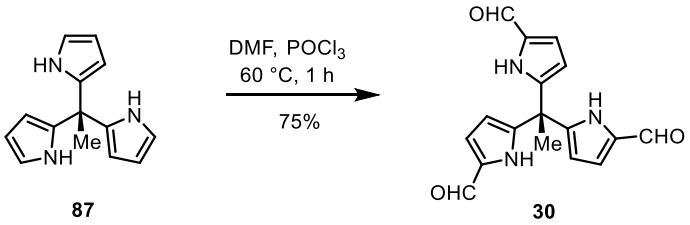

87 **30**

5,5',5''-(Ethane-1,1,1-triyl)tris(1H-pyrrole-2-carbaldehyde) (30): 87 (4.51 g, 20 mmol) was dissolved in dry DMF (180 mL) and cooled to 0 °C. $POCl_3$ (11.2 mL) was added dropwise. The mixture was heated to 60 °C for 1 h after which time the imine salt precipitated out as a fluffy yellow solid, followed by the addition of toluene (140 mL) to ensure complete precipitation. The solid was filtered off and dissolved in 4 M Na_2CO_3 (140 mL) in mixture solvent ($V_{Ethanol}/V_{water}$ = 3/7). The resulting solution was heated to 80 °C at which point the aldehyde precipitated out. This was filtered off and washed with water(15 mL × 3) and EtOH(15 mL × 3) and dried under vacuum to give **30** in 75% yield (4.64 g, 15.0 mmol) as a colorless solid. **M.P.**: 280 °C (decomp.). **^{1}H NMR** (301 MHz, DMSO-d_6): δ = 11.89 (s, 3H), 9.44 (s, 3H), 6.90 (d, J = 3.6 Hz, 3H), 5.81 (d, J = 3.7 Hz, 3H), 2.15 (s, 3H) ppm. The analytical data is in accordance with that previously reported.[154] **^{1}H NMR** (301 MHz, $CDCl_3$): δ = 11.40 (s, 3H), 9.13 (s, 3H), 6.87 (dd, J = 3.9, 2.3 Hz, 3H), 6.21 (dd, J = 3.9, 2.4 Hz, 3H).

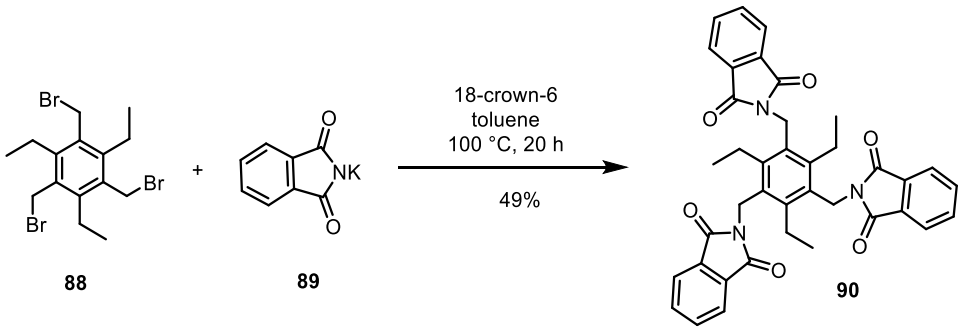

2,2',2''-((2,4,6-Triethylbenzene-1,3,5-triyl)tris(methylene)) tris(isoindoline-1,3-dione) (90): To a solution of **88** (4.0 g, 9.07 mmol) and 18-crown-6 (719 mg, 2.72 mmol) in toluene (110 mL) was added potassium phthalamide **89** (6.05 g, 32.6 mmol). The mixture was heated at 100 °C under Ar for 20 h before being allowed to cool to rt. The mixture was concentrated in vacuo and the resulting solid suspended in water (80 mL) and collected by filtration. The resulting solid was further washed with water (2 × 80 mL) and MeOH (80 mL) before being dried in vacuo. Further purification by recrystallizing in EtOH afforded the desired product **90** in 49% yield (2.85 g, 4.46 mmol) as an off-white solid. **M.P.:** 210-212 °C . **^{1}H NMR** (301 MHz, $CDCl_3$): δ = 7.81 (dd, *J* = 5.5, 3.0 Hz, 6H), 7.68 (dd, *J* = 5.4, 3.1 Hz, 6H), 4.94 (s, 6H), 3.10 (q, *J* = 7.5 Hz, 6H), 0.97 (t, *J* = 7.5 Hz, 9H) ppm. The analytical data is in accordance with that previously reported.[138b]

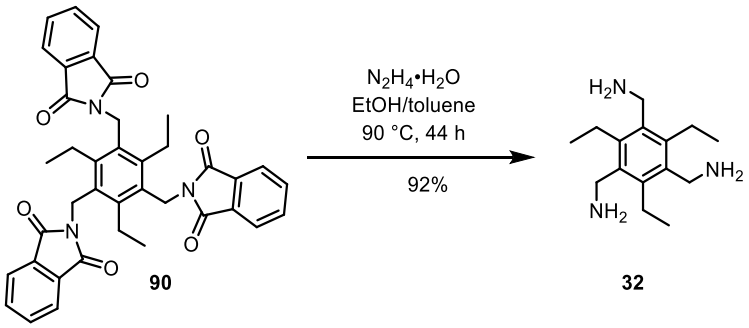

(2,4,6-Triethylbenzene-1,3,5-triyl)trimethanamine (32): To a suspension of **90** (7.68 g, 12 mmol) in a mixture of toluene (80 mL) and EtOH (160 mL) was added hydrazine hydrate in a single portion (3.5 mL, 50 wt% solution in water, 16.88 mmol). The resulting mixture was heated at 90 °C for 44 h, at which point a large amount of solid had precipitated, before being allowed to cool to rt. The reaction mixture was concentrated in vacuo (not to dryness) and portioned between an aqueous KOH solution (40 mL, 40 wt%) and $CHCl_3$ (90 mL). The organic layer was filtered with celite pad to remove the undissolved solid. Aqueous KOH solution (40 mL, 40 wt%) was

further added to the organic layer. H_2O layer was extracted with $CHCl_3$ (60 mL) before the combined organic layers were dried over Na_2SO_4 and concentrated in vacuo to afford **32** in 92% yield (2.75 g, 11.0 mmol) as a pale yellow solid. **M.P.:** 140-141°C . **^{1}H NMR** (301 MHz, $CDCl_3$): δ = 3.88 (s, 6H), 2.83 (q, J = 7.5 Hz, 6H), 1.30 (s, 6H), 1.22 (t, J = 7.5 Hz, 9H) ppm. The analytical data is in accordance with that previously reported.[138b]

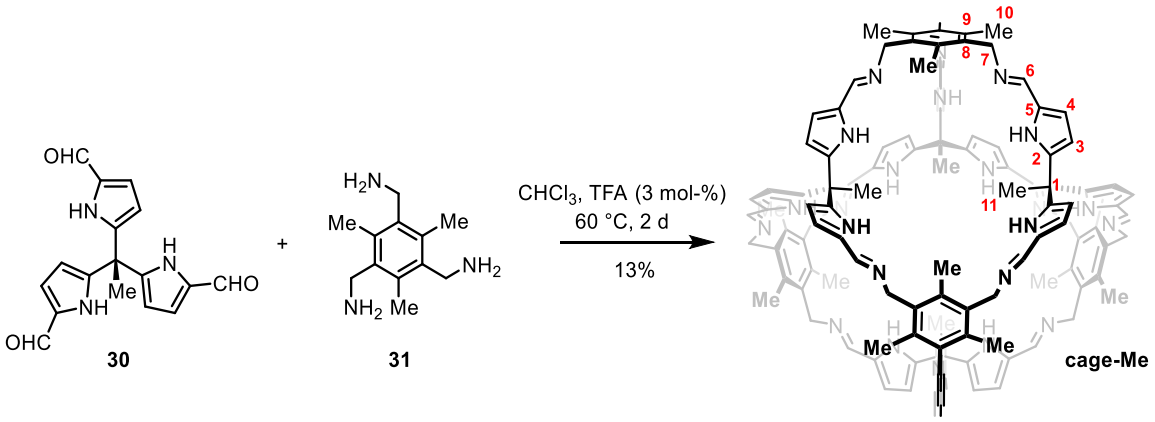

cage-Me: In a 25 mL screw-capped vessel 5,5',5"-(ethane-1,1,1-triyl)tris(1H-pyrrole-2-carbaldehyde) **30** (61.9 mg, 0.2 mmol) and (2,4,6-trimethylbenzene-1,3,5-triyl)trimethanamine **31** (41.4 mg, 0.2 mmol) were suspended in chloroform (20 mL). Trifluoroacetic acid (0.1 M in $CHCl_3$, 60 µL; 3 mol-%) was added to the mixture and heated to 60 °C for 2 days. After cooling to room temperature, the reaction mixture was filtered through a syringe filter (0.2 µm pore) and concentrated by rotary evaporation. The resulting brown solid was immediately dissolved in THF, filtered through a syringe filter (0.2 µm pore) twice and purified by recycling gel permeation chromatography (rGPC) (THF, 40°C, 5 mL/min, see GPC Data section). The obtained GPC solution was concentrated, washed with pentane and dried in high vacuum to give **cage-Me** in 13 % yield (11.9 mg, 6.43 µmol) as colorless solid. **M.P.:** 280 °C (decomp.). **^{1}H NMR** (600 MHz, $CDCl_3$) δ = 8.18 ppm (s, 12H, H-6), 6.31 (d, J = 3.9 Hz, 12H, H-4), 5.38 (d, J = 3.6 Hz, 12H, H-3), 4.66 (s, 24H, H-7), 2.37 (s, 36H, H-10), 1.88 (s, 12H, H-11). **^{13}C NMR** (151 MHz, $CDCl_3$) δ = 152.4 ppm (C-6), 140.9(C-1), 136.6(C-8), 133.8(C-9), 130.0(C-5), 114.7(C-4), 109.6(C-3), 59.8(C-7), 41.7(C-2), 26.6(C-11), 15.8(C-10). **IR** (neat, ATR): $\tilde{\nu}$ = 3602 cm^{-1} (w), 3272 (w), 2978 (w), 2869 (w), 1628 (s), 1561 (m), 1479 (m), 1380 (w), 1354 (w), 1270 (m), 1245 (m), 1204 (m), 1038 (m), 1004 (m), 969 (w), 780 (s), 697 (m), 647 (m), 602 (m). **MS** (MALDI-TOF): $[M+H]^+$ m/z = 1850.0210 (calcd. for $C_{116}H_{121}N_{24}^+$: 1850.0201).

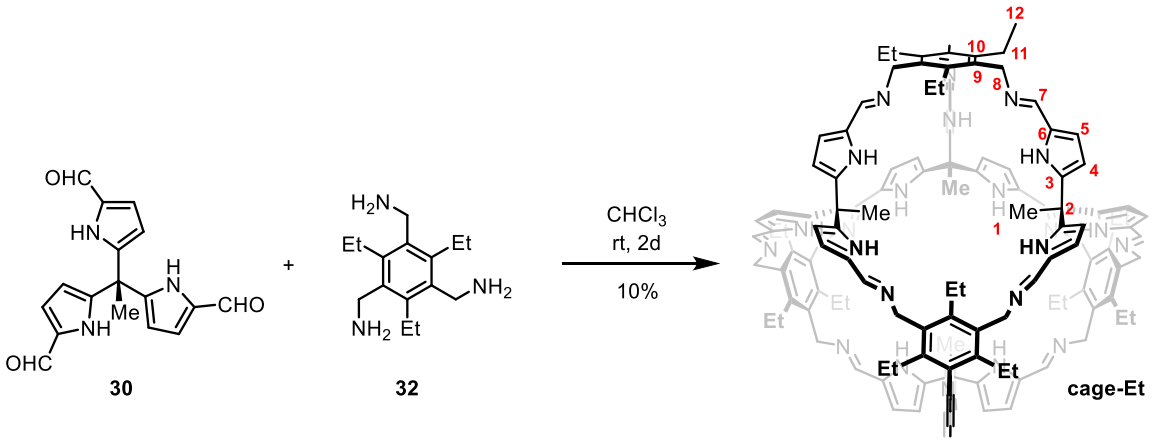

cage-Et: In a 25 mL screw-capped vessel 5,5',5"-(ethane-1,1,1-triyl)tris(1H-pyrrole-2-carbaldehyde) **30** (61.9 mg, 0.2 mmol) and (2,4,6-triethylbenzene-1,3,5-triyl)trimethanamine **32** (49.8 mg, 0.2 mmol) were suspended in chloroform (20 mL). The mixture was stirred at room temperature for 2 days and filtered through a syringe filter (0.2 µm pore) and concentrated by rotary evaporation. The resulting brown solid was immediately dissolved in THF, filtered through a syringe filter (0.2 µm pore) twice and purified by recycling gel permeation chromatography (rGPC) (THF, 40°C, 5 mL/min, see GPC Data section). The obtained GPC solution was concentrated, washed with pentane and dried in high vacuum to give **cage-Et** in 10% yield (9.8 mg, 4.85 µmol) as colorless solid. **M.P.:** 280 °C (decomp.). **^{1}H NMR** (600 MHz, $CDCl_3$) δ = 8.15 ppm (s, 12H, H-7), 6.33 (d, J = 3.6 Hz, 12H, H-4), 5.35 (d, J = 3.9 Hz, 12H, H-5), 4.63 (s, 24H, H-8), 2.74 (d, J = 7.4 Hz, 24H, H-11), 1.88 (s, 12H, H-1), 1.25 (t, J = 7.6 Hz, 36H, H-12). **^{13}C NMR** (151 MHz, $CDCl_3$) δ = 152.5 ppm (C-7), 143.0(C-10), 141.5(C-3), 133.2(C-9), 129.8(C-6), 115.4(C-4), 109.7(C-5), 58.5(C-8), 41.8(C-2), 26.0(C-1), 22.2(C-11), 15.7(C-12). **IR** (neat, ATR): $\tilde{\nu}$ = 3616 (w), 3440 (w), 3294 (w), 3114 (w), 2965 (w), 2871 (w), 2361 (w), 1628 (s), 1561 (m), 1480 (m), 1377 (w), 1354 (w), 1270 (m), 1234 (w), 1204 (m), 1075 (w), 1039 (m), 966 (w), 773 (s), 698 (m), 670 (m), 647 (m), 625 (m), 606 (m). **MS** (MALDI-TOF): $[M+H]^+$ m/z = 2018.2058 (calcd. for $C_{128}H_{145}N_{24}^+$: 2018.2079).

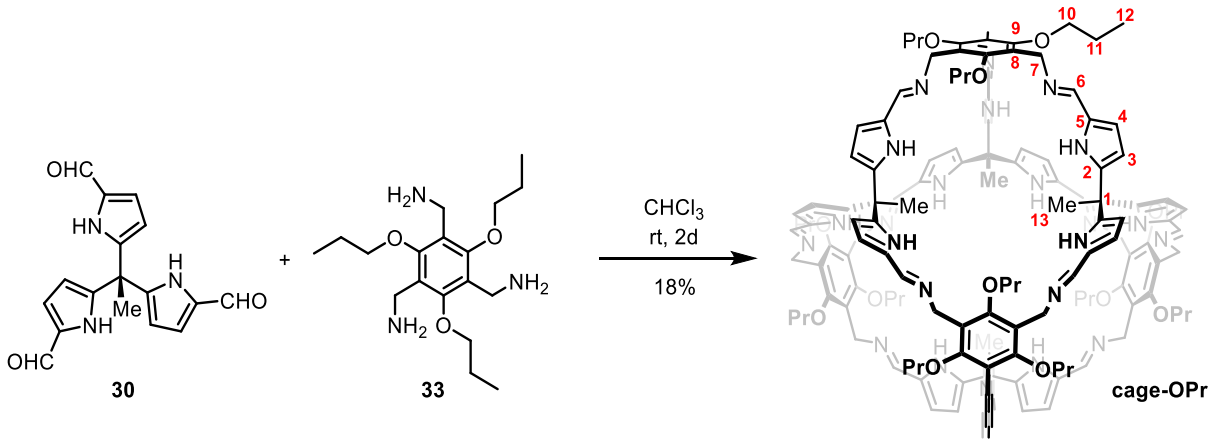

cage-OPr: In a 25 mL screw-capped vessel 5,5',5"-(ethane-1,1,1-triyl)tris(1H-pyrrole-2-carbaldehyde) **30** (61.9 mg, 0.2 mmol) and (2,4,6-tripropoxybenzene-1,3,5-triyl)trimethanamine **33** (67.9 mg, 0.2 mmol) were suspended in 16 mL chloroform. The mixtures were stirred at room temperature for 2 days, filtered through syringe filters (0.2 µm pore) and concentrated by rotary evaporation. The resulting brown solid was immediately dissolved in THF, filtered through a syringe filter (0.2 µm pore) twice and purified by recycling gel permeation chromatography (rGPC) (THF, 40°C, 5 mL/min, see GPC Data section). The obtained GPC solution was concentrated, added with pentane and put at room temperature overnight. The supernatant solvents were removed by a pipette technique and the residual was dried in high vacuum to give **cage-OPr** in 18 % yield (21.5 mg, 9.04 µmol) as colorless solid. **M.P.:** 280 °C (decomp.). **^{1}H NMR** (700 MHz, $CDCl_3$) δ = 8.16 ppm (s, 12H, H-6), 6.29 (d, J = 2.9 Hz, 12H, H-4), 5.39 (d, J = 2.9 Hz, 12H, H-3), 4.62 (s, 24H, H-7), 3.86 (t, J = 6.8 Hz, 24H, H-10), 1.96 (s, 12H, H-13), 1.79 – 1.65 (m, 24H, H-11), 0.92 (t, J = 7.4 Hz, 36H, H-12). **^{13}C NMR** (176 MHz, $CDCl_3$) δ = 158.5 ppm (C-9), 152.8(C-6), 141.1(C-1), 129.8(C-5), 123.3(C-8), 115.0(C-4), 109.6(C-3), 77.0(C-10), 54.6(C-7), 41.6(C-2), 25.9(C-13), 23.5(C-11), 10.7(C-12). **IR** (neat, ATR): $\tilde{\nu}$ = 3602 cm^{-1} (w), 3272 (w), 2978 (w), 2869 (w), 1628 (s), 1561 (m), 1479 (m), 1380 (w), 1354 (w), 1270 (m), 1245 (m), 1204 (m), 1038 (m), 1004 (m), 969 (w), 780 (s), 697 (m), 647 (m), 602 (m). **MS** (MALDI-TOF): $[M+H]^+$ m/z = 2378.3341 (calcd. for $C_{140}H_{169}N_{24}^+$: 2378.3346).

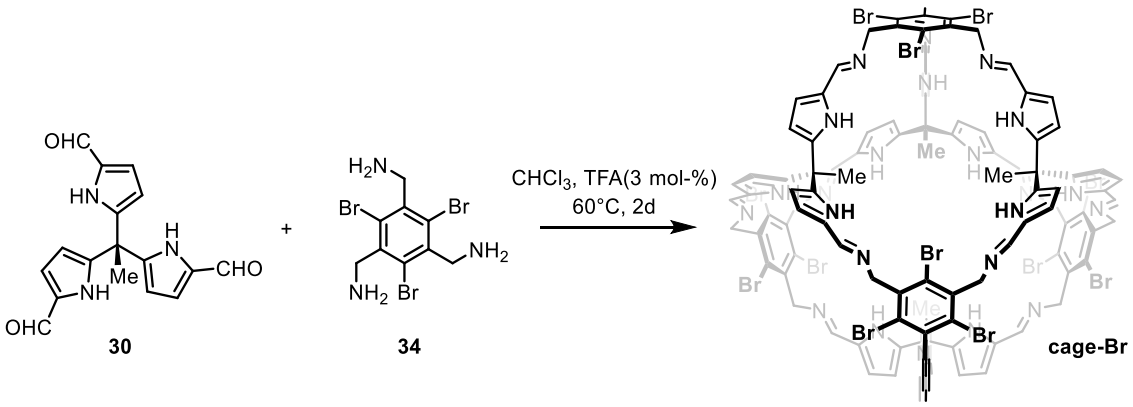

cage-Br: In a 25 mL screw-capped vessel 5,5',5"-(ethane-1,1,1-triyl)tris(1H-pyrrole-2-carbaldehyde) **30** (30.9 mg, 0.1 mmol) and (2,4,6-tribromobenzene-1,3,5-triyl)trimethanamine **34** (40.1 mg, 0.1 mmol) were suspended in 20 mL chloroform. 3 mol-% TFA (0.1 M in $CHCl_3$, 30 µL) was added to the mixture and heated to 60 °C for 2 days. After cooling to room temperature, the reaction mixture was filtered through a syringe filter (0.2 µm pore) and concentrated by rotary evaporation and washed with methanol to give **cage-Br** crude product (14 mg, 5.33 µmol) as colorless solid. **Note**: **cage-Br** can't be purified further due to its too bad solubility. **^{1}H NMR** (700 MHz, $CDCl_3$) δ = 8.22 ppm (12H), 6.35 (12H), 5.43 (12H), 5.08 (24H), 1.92 (12H). **MS** (MALDI-TOF): $[M+H]^+$ *m/z* = 2618.7490 (calcd. for $C_{104}H_{85}Br_{12}N_{24}^+$: 2618.7568).

3. Large Scale Crystal Growth and Activation

H-Cage (1.33 g) was dissolved in dry THF (190 mL, *c* = 7 mg/mL) and filtered through a syringe filter (0.2 µm pore diameter). 10 mL of the filtered cage solution each was added to 19 individual snap-lid jars (*V* = 25 mL, *d* = 3 cm). All vials were capped, the caps pinched with 12 holes each and placed in a desiccator with the ground covered with methanol. After vapour diffusion of methanol into the THF cage solutions at room temperature for 20 days, the mother liquors for every vial were removed by a pipette technique and the residual crystals washed with a methanol/THF mixture ($V_{methanol}/V_{THF}$ = 9/1) (2 × 2 mL), again by a pipette technique. The crystals of the different batches were combined as suspensions and washed again with a methanol/THF mixture ($V_{methanol}/V_{THF}$ = 9/1) (3 × 8 mL). After removing the supernatant solvents, the crystals were dried at high vacuum (1.2 mbar) at room temperature for 14 h to give crystalline **H-cage** (851 mg, 64% efficiency of the crystal growth/activation procedure). Further activation was achieved by drying at a kugelrohr oven at 50 or

100 °C under reduced pressure ($3 \cdot 10^{-2}$ mbar) for 14 h. Prior to gassorption measurements, the cage crystals have been activated again at 40 °C for 3 h at the outgas station of the gas sorption analyser and measured directly.

HF-Cage (1.12 g) was dissolved in dry THF (160 mL, *c* = 7 mg/mL) and filtered through a syringe filter (0.2 µm). 10 mL of the filtered cage solution each was added to 16 individual snap-lid jars (*V* = 25 mL, *d* = 3 cm). All vials were capped, the caps pinched 12 holes each and placed in a desiccator with the ground covered with methanol. After vapour diffusion of methanol into THF/cage solution at room temperature, a gel-like precipitate was observed alongside crystalline material. After 40 days, the gel for every vial was separated from the crystals by tultra-sonication and was removed by a pipette technique. The residual solids were washed with a methanol/THF mixture ($V_{methanol}/V_{THF}$ = 9/1) (5 × 5 mL), again by a pipette technique. The crystals of the different batches were combined as suspensions, the supernatant solvents were removed and the residual dried at high vacuum (2.5 mbar) for 9 h at room temperature to give crystalline **HF-cage** (611 mg, 55% efficiency of the crystal growth/activation procedure). Further activation was achieved by drying at a kugelrohr oven at 50 °C under reduced pressure ($3 \cdot 10^{-2}$ mbar) for 14 h. Prior to gas adsorption measurements, the cage crystals have been activated again at 40 °C for 3 h at the outgas station of the gas sorption analyser and measured directly.

F-cage (1.20 g) was dissolved in dry THF (400 mL, *c* = 3 mg/mL) and filtered through a syringe filter (0.2 µm). 10 mL of the filtered cage solution each was added to 40 individual snap-lid jars (*V* = 25 mL, *d* = 3 cm). All vials were capped, the caps pinched 12 holes each each and placed in two desiccators with the ground covered with methanol. After vapour diffusion of methanol into the THF cage solutions at room temperature for 21 days, the mother liquors for every vial were removed by a pipette technique and the residual crystals washed with a methanol/THF mixture ($V_{methanol}/V_{THF}$ = 4/1) (3 × 2 mL) and methanol (2 mL), again by a pipette technique. The crystals of the different batches were combined as suspensions, the supernatant solvents were removed and the residual dried at high vacuum (1.2 mbar) for 14 h at room temperature to give crystalline **F-cage** (890 mg, 74% efficiency of the crystal growth/activation procedure). Further activation was achieved by drying at a kugelrohr oven at 50 °C under reduced pressure ($3 \cdot 10^{-2}$ mbar) for 14 h. Prior to gas adsorption measurements, the cage crystals have been activated again at 40 °C for 3 h at the outgas station of the gas sorption analyser and measured directly.

cage-CF_3 (210 mg) was dissolved in dry DMF (250 mL, *c* = 0.84 mg/mL) and filtered through a syringe filter (0.2 µm). 10 mL of the filtered cage solution each was added to 25 individual snap-lid jars (*V* = 25 mL, *d* = 3 cm). All vials were capped, the caps pinched 12 holes each each and placed in a desiccator with the ground covered with methanol. After vapour diffusion of methanol into the DMF cage solutions at room temperature for 17 days, the mother liquors for every vial were removed by a pipette technique and the residual crystals washed with methanol (5 × 5 mL) by a pipette technique. The crystals of the different batches were combined as suspensions, the supernatant solvents were removed and the residual dried at high vacuum (7.8 mbar) for 15 h at room temperature to give crystalline **cage-$CF_{3\alpha}$** (125 mg, 60% efficiency of the crystal growth/activation procedure). Further activation was achieved by drying at a kugelrohr oven at 50 °C under reduced pressure ($1.6 \cdot 10^{-1}$ mbar) for 13 h. Prior to gas adsorption measurements, the cage crystals have been activated again at 40 °C for 3 h at the outgas station of the gas sorption analyser and measured directly.

cage-CF_3 (637 mg) was dissolved in dry THF (91 mL, *c* = 7 mg/mL) and filtered through a syringe filter (0.2 µm). 7 mL of the filtered cage solution each was added to 13 individual snap-lid jars (*V* = 25 mL, *d* = 3 cm). All vials were capped, the caps pinched 12 holes each each and placed in a desiccator with the ground covered with methanol. After vapour diffusion of methanol into the THF cage solutions at room temperature for 9 days, the mother liquors for every vial were removed by a pipette technique and the residual crystals washed with a methanol/THF mixture ($V_{methanol}/V_{THF}$ = 9/1) (3 × 4 mL) by a pipette technique. The crystals of the different batches were combined as suspensions, the supernatant solvents were removed and the residual dried at high vacuum (10 mbar) for 16 h at room temperature to give crystalline **cage-$CF_{3\beta}$** (473 mg, 74% efficiency of the crystal growth/activation procedure). Further activation was achieved by drying at a kugelrohr oven at 50 °C under reduced pressure ($1 \cdot 10^{-1}$ mbar) for 12 h. Prior to gas adsorption measurements, the cage crystals have been activated again at 40 °C for 3 h at the outgas station of the gas sorption analyser and measured directly.

cage-CF_3 (210 mg) was dissolved in dry DCM (420 mL, *c* = 0.5 mg/mL) and filtered through a syringe filter (0.2 µm). 14 mL of the filtered cage solution each was added to 30 individual snap-lid jars (*V* = 25 mL, *d* = 3 cm). All vials were capped, the caps pinched 12 holes each each and placed in a desiccator with the ground covered with diethyl ether. After vapour diffusion of diethyl ether into the DCM cage solutions at

room temperature for 8 days, the mother liquors for every vial were removed by a pipette technique and the residual crystals washed with diethyl ether (3 × 3 mL) by a pipette technique. The crystals of the different batches were combined as suspensions, the supernatant solvents were removed and the residual dried at high vacuum (7 mbar) for 15 h at room temperature to give crystalline **cage-$CF_{3\gamma}$** (167 mg, 80% efficiency of the crystal growth/activation procedure). Further activation was achieved by drying at a kugelrohr oven at 50 °C under reduced pressure ($1.4 \cdot 10^{-1}$ mbar) for 10 h. Prior to gas adsorption measurements, the cage crystals have been activated again at 40 °C for 3 h at the outgas station of the gas sorption analyser and measured directly.

cage-C_2F_5 (501 mg) was dissolved in dry THF (167 mL, *c* = 3 mg/mL) and filtered through a syringe filter (0.2 µm). About 8 mL of the filtered cage solution each was added to 20 individual snap-lid jars (*V* = 25 mL, *d* = 3 cm). All vials were capped, the caps pinched 12 holes each each and placed in a desiccator with the ground covered with methanol. After vapour diffusion of methanol into the THF cage solutions at room temperature for 8 days, the mother liquors for every vial were removed by a pipette technique and the residual crystals washed with a methanol/THF mixture ($V_{methanol}/V_{THF}$ = 4/1) (4 × 3 mL) by a pipette technique. The crystals of the different batches were combined as suspensions, the supernatant solvents were removed and the residual dried at high vacuum (10 mbar) for 16 h at room temperature to give crystalline **cage-C_2F_5** (426 mg, 85% efficiency of the crystal growth/activation procedure). Further activation was achieved by drying at a kugelrohr oven at 50 °C under reduced pressure ($2.4 \cdot 10^{-2}$ mbar) for 11 h. Prior to gas adsorption measurements, the cage crystals have been activated again at 40 °C for 3 h at the outgas station of the gas sorption analyser and measured directly.

cage-C_3F_7 (520 mg) was dissolved in dry THF (520 mL, *c* = 1 mg/mL) and filtered through a syringe filter (0.2 µm). About 13 mL of the filtered cage solution each was added to 39 individual snap-lid jars (*V* = 25 mL, *d* = 3 cm). All vials were capped, the caps pinched 12 holes each each and placed in two desiccators with the ground covered with methanol. After vapour diffusion of methanol into the THF cage solutions at room temperature for 19 days, the mother liquors for every vial were removed by a pipette technique and the residual crystals washed with a methanol/THF mixture ($V_{methanol}/V_{THF}$ = 4/1) (3 × 5 mL) by a pipette technique. The crystals of the different batches were combined as suspensions, the supernatant solvents were removed and the residual dried at high vacuum (12 mbar) for 14 h at room temperature to give

crystalline **cage-C_3F_7** (464 mg, 89% efficiency of the crystal growth/activation procedure). Further activation was achieved by drying at a kugelrohr oven at 50 °C under reduced pressure ($7 \cdot 10^{-2}$ mbar) for 11 h. Prior to gas adsorption measurements, the cage crystals have been activated again at 40 °C for 3 h at the outgas station of the gas sorption analyser and measured directly.

cage-C_5F_{11} (920 mg) was dissolved in dry THF (550 mL, *c* = 1.7 mg/mL) and filtered through a syringe filter (0.2 µm). About 13 mL of the filtered cage solution each was added to 42 individual snap-lid jars (*V* = 25 mL, *d* = 3 cm). All vials were capped, the caps pinched 12 holes each each and placed in two desiccators with the ground covered with methanol. After vapour diffusion of methanol into the THF cage solutions at room temperature for 17 days, the mother liquors for every vial were removed by a pipette technique and the residual crystals washed with a methanol/THF mixture ($V_{methanol}/V_{THF}$ = 5/1) (3 × 5 mL) by a pipette technique. The crystals of the different batches were combined as suspensions, the supernatant solvents were removed and the residual dried at high vacuum (7.2 mbar) for 10 h at room temperature to give crystalline **cage-C_5F_{11}** (751 mg, 82% efficiency of the crystal growth/activation procedure). Further activation was achieved by drying at a kugelrohr oven at 50 °C under reduced pressure ($2.7 \cdot 10^{-1}$ mbar) for 19 h. Prior to gas adsorption measurements, the cage crystals have been activated again at 40 °C for 3 h at the outgas station of the gas sorption analyser and measured directly.

cage-C_6F_{13} (336 mg) was dissolved in dry THF (24 mL, *c* = 14 mg/mL) and filtered through a syringe filter (0.2 µm). About 4 mL of the filtered cage solution each was added to 6 individual snap-lid jars (*V* = 10 mL, *d* = 2 cm). All vials were capped, the caps pinched 6 holes each each and placed in a desiccators with the ground covered with methanol. After vapour diffusion of methanol into the THF cage solutions at room temperature for 14 days, the mother liquors for every vial were removed by a pipette technique and the residual crystals washed with a methanol (2 × 3 mL) by a pipette technique. The crystals of the different batches were combined as suspensions, the supernatant solvents were removed and the residual dried at high vacuum (8.7 mbar) for 12 h at room temperature to give crystalline **cage-$C_6F_{13\alpha}$** (200 mg, 60% efficiency of the crystal growth/activation procedure). Further activation was achieved by drying at a kugelrohr oven at 50 °C under reduced pressure ($2.4 \cdot 10^{-2}$ mbar) for 11 h. Prior to gas adsorption measurements, the cage crystals have been activated again at 40 °C for 3 h at the outgas station of the gas sorption analyser and measured directly.

In four individual reactions, triamino triptycene **15** (12.0 mg, 40 µmol), salicylaldehyde **73** (57.3 mg, 60 µmol) were added into 20 mL anhydrous DMF. After complete dissolution, 4.5 mol-% TFA (0.1 M in anhydrous DMF, 18 µL) was added. The mixture was heated to 100 °C and stirred for 36 h. After cooling to room temperature, the reaction mixture is filtered through syringe filters (0.2 µm pore) and put at room temperature for 12 h. Much flake crystal precipitated out from reaction solution and was directly filtered, combined and washed with 1 mL anhydrous DMF to give crystalline **cage-$C_6F_{13\gamma}$** (268 mg with much DMF). The activation was achieved by drying at a kugelrohr oven at 100 °C under reduced pressure ($2 \cdot 10^{-2}$ mbar) for 12 h. Prior to gas adsorption measurements, the cage crystals have been activated again at 40 °C for 3 h at the outgas station of the gas sorption analyser and measured directly.

cage-CH_3 (370 mg) was dissolved in dry THF (370 mL, *c* = 1 mg/mL) and filtered through a syringe filter (0.2 µm). About 14 mL of the filtered cage solution each was added to 27 individual snap-lid jars (*V* = 20 mL, *d* = 3 cm). All vials were capped, the caps pinched 6 holes each each and placed in two desiccators with the ground covered with methanol. After vapour diffusion of methanol into the THF cage solutions at room temperature for 8 days, the mother liquors for every vial were removed by a pipette technique and the residual crystals washed with a methanol (4 × 4 mL) by a pipette technique. The crystals of the different batches were combined as suspensions, the supernatant solvents were removed and the residual dried at high vacuum (10 mbar) for 12 h at room temperature to give crystalline **cage-CH_3** (271 mg, 73% efficiency of the crystal growth/activation procedure). Further activation was achieved by drying at a kugelrohr oven at 50 °C under reduced pressure ($1 \cdot 10^{-1}$ mbar) for 14 h. Prior to gas adsorption measurements, the cage crystals have been activated again at 40 °C for 3 h at the outgas station of the gas sorption analyser and measured directly.

The methods to obtain crystalline **cage-$C_6F_{13\beta}$** and **cage-Nap** have been described in their corresponding synthesis procedures.

4. Stability Experiments of F-cage

Stability against water: A crystalline sample of **F-cage** (45.1 mg) was placed in a vial containing water (0.6 mL) and was slightly stirred for 18 h at room temperature. After filtration, the solid was dried in high vacuum ($1.7 \cdot 10^{-2}$ mbar) for 18 h at room temperature and was investigated by ^{1}H- and ^{19}F-NMR spectroscopy and TGA.

Stability against acid: A crystalline sample of **F-cage** (44.3 mg) was placed in a vial containing HCl_{aq} (0.1 mM; 0.6 mL) and was slightly stirred for 24 h at room temperature. After filtration and washing with 10 mL water, the solid was dried in high vacuum ($8.9 \cdot 10^{-1}$ mbar) for 18 h at room temperature and was investigated by ^{1}H- and ^{19}F-NMR spectroscopy and TGA.

Stability against base: A crystalline sample of **F-cage** (47.0 mg) was placed in a vial containing $NaOH_{aq}$ solution (1 mM; 0.6 mL) and was slightly stirred for 24 h at room temperature. After filtration and washing with 10 mL water, the solid was dried in high vacuum ($8.9 \cdot 10^{-1}$ mbar) for 18 h at room temperature and was investigated by ^{1}H- and ^{19}F-NMR spectroscopy and TGA.

VI. References

[1] a) T. F. Stocker, D. Qin, G.-K. Plattner, M. Tignor, S. K. Allen, J. Boschung, A. Nauels, Y. Xia, V. Bex, P. M. Midgley, (eds.), *IPCC, 2013: Climate Change 2013: The Physical Science Basis. Contribution of Working Group I to the Fifth Assessment Report of the Intergovernmental Panel on Climate Change*, Cambridge University Press, Cambridge, United Kingdom and New York, NY, USA, **2013**; b) V. Masson-Delmotte, P. Zhai, A. Pirani, S. L. Connors, C. Péan, S. Berger, N. Caud, Y. Chen, L. Goldfarb, M. I. Gomis, M. Huang, K. Leitzell, E. Lonnoy, J. B. R. Matthews, T. K. Maycock, T. Waterfield, O. Yelekçi, R. Yu, B. Zhou, (eds.), *IPCC, 2021: Climate Change 2021: The Physical Science Basis. Contribution of Working Group I to the Sixth Assessment Report of the Intergovernmental Panel on Climate Change*, Cambridge University Press, Cambridge, United Kingdom and New York, NY, USA, **2021**.

[2] a) V. Masson-Delmotte, P. Zhai, H.-O. Pörtner, D. Roberts, J. Skea, P. R. Shukla, A. Pirani, W. Moufouma-Okia, R. P. Péan, C. , S. Connors, J. B. R. Matthews, Y. Chen, X. Zhou, M. I. Gomis, E. Lonnoy, T. Maycock, M. Tignor, T. Waterfield, (eds.), *IPCC, 2018: Global Warming of 1.5°C. An IPCC Special Report on the impacts of global warming of 1.5°C above pre-industrial levels and related global greenhouse gas emission pathways, in the context of strengthening the global response to the threat of climate change, sustainable development, and efforts to eradicate poverty*, Cambridge University Press, Cambridge, United Kingdom and New York, NY, USA, **2018**; b) J. Hansen, M. Sato, R. Ruedy, K. Lo, D. W. Lea, M. Medina-Elizade, *Proc. Natl. Acad. Sci. U. S. A.* **2006**, *103*, 14288-14293; c) H. D. Matthews, S. Wynes, *Science* **2022**, *376*, 1404-1409.

[3] a) M. Ishii, A. Shouji, S. Sugimoto, T. Matsumoto, *Int. J. Climatol.* **2005**, *25*, 865-879; b) C. P. Morice, J. J. Kennedy, N. A. Rayner, P. D. Jones, *J. Geophys. Res.-Atmos.* **2012**, *117*, 22; c) N. A. Rayner, D. E. Parker, E. B. Horton, C. K. Folland, L. V. Alexander, D. P. Rowell, E. C. Kent, A. Kaplan, *J. Geophys. Res.-Atmos.* **2003**, *108*, 37; d) T. M. Smith, R. W. Reynolds, T. C. Peterson, J. Lawrimore, *J. Clim.* **2008**, *21*, 2283-2296; e) R. S. Vose, D. Arndt, V. F. Banzon, D. R. Easterling, B. Gleason, B. Y. Huang, E. Kearns, J. H. Lawrimore, M. J. Menne, T. C. Peterson, R. W. Reynolds, T. M. Smith, C. N. Williams, D. B. Wuertz, *Bull. Amer. Meteorol. Soc.* **2012**, *93*, 1677-1685.

[4] S. A. Montzka, E. J. Dlugokencky, J. H. Butler, *Nature* **2011**, *476*, 43-50.

[5] W. T. Tsai, H. P. Chen, W. Y. Hsien, *J. Loss Prev. Process Ind.* **2002**, *15*, 65-75.

[6] UNEP, *Handbook for the Montreal Protocol on Substances that Deplete the Ozone Layer*, UNEP/Earthprint, Nairobi, Kenya, **2006**.

[7] K. Tian, S. M. Elbert, X. Y. Hu, T. Kirschbaum, W. S. Zhang, F. Rominger, R. R. Schroder, M. Mastalerz, *Adv. Mater.* **2022**, *34*, 12.

[8] a) J. Muhle, C. M. Trudinger, L. M. Western, M. Rigby, M. K. Vollmer, S. Park, A. J. Manning, D. Say, A. Ganesan, L. P. Steele, D. J. Ivy, T. Arnold, S. L. Li, A. Stohl, C. M. Harth, P. K. Salameh, A. McCulloch, S. O'Doherty, M. K. Park, C. O. Jo, D. Young, K. M. Stanley, P. B. Krummel, B. Mitrevski, O. Hermansen, C. Lunder, N. Evangeliou, B. Yao, J. Kim, B. Hmiel, C. Buizert, V. V. Petrenko, J. Arduini, M. Maione, D. M. Etheridge, E. Michalopoulou, M. Czerniak, J. P. Severinghaus, S. Reimann, P. G. Simmonds, P. J. Fraser, R. G. Prinn, R. F. Weiss, *Atmos. Chem. Phys.* **2019**, *19*, 10335-10359; b) R. G. Prinn, R. F. Weiss, J. Arduini, T. Arnold, H. L. DeWitt, P. J. Fraser, A. L. Ganesan, J. Gasore, C. M. Harth, O. Hermansen, J. Kim, P. B. Krummel, S. L. Li, Z. M. Loh, C. R. Lunder,

M. Maione, A. J. Manning, B. Miller, B. Mitrevski, J. Muhle, S. O'Doherty, S. Park, S. Reimann, M. Rigby, T. Saito, P. K. Salameh, R. Schmidt, P. G. Simmonds, L. P. Steele, M. K. Vollmer, R. H. Wang, B. Yao, Y. Yokouchi, D. Young, L. X. Zhou, *Earth Syst. Sci. Data* **2018**, *10*, 985-1018; c) D. Say, A. J. Manning, L. M. Western, D. Young, A. Wisher, M. Rigby, S. Reimann, M. K. Vollmer, M. Maione, J. Arduini, P. B. Krummel, J. Muhle, C. M. Harth, B. Evans, R. F. Weiss, R. G. Prinn, S. O'Doherty, *Atmos. Chem. Phys.* **2021**, *21*, 2149-2164; d) T. Arnold, C. M. Harth, J. Muhle, A. J. Manning, P. K. Salameh, J. Kim, D. J. Ivy, L. P. Steele, V. V. Petrenko, J. P. Severinghaus, D. Baggenstos, R. F. Weiss, *Proc. Natl. Acad. Sci. U. S. A.* **2013**, *110*, 2029-2034; e) P. G. Simmonds, M. Rigby, A. J. Manning, S. Park, K. M. Stanley, A. McCulloch, S. Henne, F. Graziosi, M. Maione, J. Arduini, S. Reimann, M. K. Vollmer, J. Muhle, S. O'Doherty, D. Young, P. B. Krummel, P. J. Fraser, R. F. Weiss, P. K. Salameh, C. M. Harth, M. K. Park, H. Park, T. Arnold, C. Rennick, L. P. Steele, B. Mitrevski, R. H. J. Wang, R. G. Prinn, *Atmos. Chem. Phys.* **2020**, *20*, 7271-7290.

[9] a) C. Y. Chuah, Y. Lee, T. H. Bae, *Chem. Eng. J.* **2021**, *404*, 23; b) J. W. Coburn, *Plasma Chem. Plasma Process.* **1982**, *2*, 1-41.

[10] a) T. L. Foecke, *Japca-the International Journal of Air Pollution Control and Hazardous Waste Management* **1988**, *38*, 283-291; b) J. F. Mattrey, J. M. Sherer, J. D. Miller, *Chem. Eng. Prog.* **2000**, *96*, 35-41.

[11] a) X. Chen, Y. Yao, X. Hao, X. Liu, T. Liu, *J. Ophthalmol.* **2018**, *2018*, 1672501; b) M. Claudon, D. Cosgrove, T. Albrecht, L. Bolondi, M. Bosio, F. Calliada, J.-M. Correas, K. Darge, C. Dietrich, M. D'Onofrio, *Ultraschall Med.* **2008**, *29*, 28-44.

[12] M. B. Chang, J. S. Chang, *Ind. Eng. Chem. Res.* **2006**, *45*, 4101-4109.

[13] D. Wanigarathna, J. Gao, B. Liu, *Mater. Adv.* **2020**, *1*, 310-320.

[14] a) W. S. Cho, K. H. Lee, H. J. Chang, W. Huh, H. H. Kwon, *Korean J. Chem. Eng.* **2011**, *28*, 2196-2201; b) H. Murase, T. Imai, T. Inohara, M. Toyoda, *IEEE Trns. Dielectr. Electr. Insul.* **2004**, *11*, 166-173.

[15] N. F. Cessford, N. A. Seaton, T. Duren, *Ind. Eng. Chem. Res.* **2012**, *51*, 4911-4921.

[16] A. L. Myers, J. M. Prausnitz, *AIChE J.* **1965**, *11*, 121-127.

[17] K. S. Walton, D. S. Sholl, *AIChE J.* **2015**, *61*, 2757-2762.

[18] M. Oschatz, M. Antonietti, *Energy Environ. Sci.* **2018**, *11*, 57-70.

[19] L. F. Zou, Y. J. Sun, S. Che, X. Y. Yang, X. Wang, M. Bosch, Q. Wang, H. Li, M. Smith, S. Yuan, Z. Perry, H. C. Zhou, *Adv. Mater.* **2017**, *29*, 1700229.

[20] a) R. B. Bai, X. W. Song, W. F. Yan, J. H. Yu, *Natl. Sci. Rev.*, *9*, nwac064; b) L. H. Chen, M. H. Sun, Z. Wang, W. M. Yang, Z. K. Xie, B. L. Su, *Chem. Rev.* **2020**, *120*, 11194-11294.

[21] a) O. M. Yaghi, G. M. Li, H. L. Li, *Nature* **1995**, *378*, 703-706; b) H. Furukawa, K. E. Cordova, M. O'Keeffe, O. M. Yaghi, *Science* **2013**, *341*, 1230444; c) H. C. Zhou, J. R. Long, O. M. Yaghi, *Chem. Rev.* **2012**, *112*, 673-674; d) H. L. Jiang, Q. Xu, *Chem. Commun.* **2011**, *47*, 3351-3370.

[22] R. S. Sprick, J. X. Jiang, B. Bonillo, S. J. Ren, T. Ratvijitvech, P. Guiglion, M. A. Zwijnenburg, D. J. Adams, A. I. Cooper, *J. Am. Chem. Soc.* **2015**, *137*, 3265-3270.

[23] a) A. P. Cote, A. I. Benin, N. W. Ockwig, M. O'Keeffe, A. J. Matzger, O. M. Yaghi, *Science* **2005**, *310*, 1166-1170; b) C. S. Diercks, O. M. Yaghi, *Science* **2017**, *355*, eaal1585; c) S. Y. Ding, W. Wang, *Chem. Soc. Rev.* **2013**, *42*, 548-568; d) N. Huang, P. Wang, D. L. Jiang, *Nat. Rev. Mater.* **2016**, *1*, 16068; e) J. C. Jiang, Y. B. Zhao, O. M. Yaghi, *J. Am. Chem. Soc.* **2016**, *138*, 3255-3265; f) M. S.

Lohse, T. Bein, *Adv. Funct. Mater.* **2018**, *28*, 1705553; g) P. J. Waller, F. Gandara, O. M. Yaghi, *Acc. Chem. Res.* **2015**, *48*, 3053-3063; h) H. M. El-Kaderi, J. R. Hunt, J. L. Mendoza-Cortes, A. P. Cote, R. E. Taylor, M. O'Keeffe, O. M. Yaghi, *Science* **2007**, *316*, 268-272; i) Q. R. Fang, Z. B. Zhuang, S. Gu, R. B. Kaspar, J. Zheng, J. H. Wang, S. L. Qiu, Y. S. Yan, *Nat. Commun.* **2014**, *5*, 4503; j) P. J. Waller, S. J. Lyle, T. M. O. Popp, C. S. Diercks, J. A. Reimer, O. M. Yaghi, *J. Am. Chem. Soc.* **2016**, *138*, 15519-15522; k) B. Nath, W. H. Li, J. H. Huang, G. E. Wang, Z. H. Fu, M. S. Yao, G. Xu, *CrystEngComm* **2016**, *18*, 4259-4263; l) Z. F. Wang, S. N. Zhang, Y. Chen, Z. J. Zhang, S. Q. Ma, *Chem. Soc. Rev.* **2020**, *49*, 708-735.

[24] M. A. Little, A. I. Cooper, *Adv. Funct. Mater.* **2020**, *30*, 1909842.

[25] a) T. Hasell, A. I. Cooper, *Nat. Rev. Mater.* **2016**, *1*, 16053; b) D. Y. Hu, J. J. Zhang, M. Liu, *Chem. Commun.* **2022**, *58*, 11333-11346; c) G. Montà-González, F. Sancenón, R. Martínez-Máñez, V. Martí-Centelles, *Chem. Rev.* **2022**, *122*, 13636-13708; d) G. Zhang, M. Mastalerz, *Chem. Soc. Rev.* **2014**, *43*, 1934-1947.

[26] N. H. Malik, A. H. Qureshi, *IEEE Trans. Dielectr. Electr. Insul.* **1979**, 70-76.

[27] S. M. Wang, X. T. Mu, H. R. Liu, S. T. Zheng, Q. Y. Yang, *Angew. Chem. Int. Ed.* **2022**, *61*, e202207066.

[28] a) S. Sircar, *Ind. Eng. Chem. Res.* **2006**, *45*, 5435-5448; b) X. L. Huang, F. Q. Chen, H. R. Sun, W. Xia, Z. G. Zhang, Q. W. Yang, Y. W. Yang, Q. L. Ren, Z. B. Bao, *Sep. Purif. Technol.* **2022**, *292*, 8.

[29] a) J. Y. Zhou, T. Ke, F. Steinke, N. Stock, Z. G. Zhang, Z. B. Bao, X. He, Q. L. Ren, Q. W. Yang, *J. Am. Chem. Soc.* **2022**, *144*, 14322-14329; b) B. Y. Li, Z. J. Zhang, Y. Li, K. X. Yao, Y. H. Zhu, Z. Y. Deng, F. Yang, X. J. Zhou, G. H. Li, H. H. Wu, N. Nijem, Y. J. Chabal, Z. P. Lai, Y. Han, Z. Shi, S. H. Feng, J. Li, *Angew. Chem. Int. Ed.* **2012**, *51*, 1412-1415.

[30] Y. Q. Yang, K. L. Goh, C. Y. Chuah, H. E. Karahan, O. Birer, T. H. Bae, *Carbon* **2019**, *155*, 56-64.

[31] M. B. Kim, T. U. Yoon, D. Y. Hong, S. Y. Kim, S. J. Lee, S. I. Kim, S. K. Lee, J. S. Chang, Y. S. Bae, *Chem. Eng. J.* **2015**, *276*, 315-321.

[32] P. J. Kim, Y. W. You, H. Park, J. S. Chang, Y. S. Bae, C. H. Lee, J. K. Suh, *Chem. Eng. J.* **2015**, *262*, 683-690.

[33] M. Koppen, A. Dhakshinamoorthy, A. K. Inge, O. Cheung, J. Angstrom, P. Mayer, N. Stock, *Eur. J. Inorg. Chem.* **2018**, 3496-3503.

[34] I. Skarmoutsos, M. Eddaoudi, G. Maurin, *Microporous Mesoporous Mater.* **2019**, *281*, 44-49.

[35] T. G. Wang, M. Chang, T. A. Yan, Y. P. Ying, Q. Y. Yang, D. H. Liu, *Ind. Eng. Chem. Res.* **2021**, *60*, 5976-5983.

[36] a) D. V. Cao, S. Sircar, *Adsorpt.-J. Int. Adsorpt. Soc.* **2001**, *7*, 73-80; b) J. A. Dunne, R. Mariwals, M. Rao, S. Sircar, R. J. Gorte, A. L. Myers, *Langmuir* **1996**, *12*, 5888-5895.

[37] C. Y. Chuah, K. Goh, T. H. Bae, *J. Phys. Chem. C* **2017**, *121*, 6748-6755.

[38] C. Y. Chuah, Y. Q. Yang, T. H. Bae, *Microporous Mesoporous Mater.* **2018**, *272*, 232-240.

[39] C. Y. Chuah, S. Yu, K. Na, T. H. Bae, *J. Ind. Eng. Chem.* **2018**, *62*, 64-71.

[40] M. B. Kim, T. H. Kim, T. U. Yoon, J. H. Kang, J. H. Kim, Y. S. Bae, *J. Ind. Eng. Chem.* **2020**, *84*, 179-184.

[41] a) S. S. Wang, Y. Wu, Y. Zhang, Z. C. Zhang, W. X. Zhang, X. Y. Li, W. J. Ma, H. P. Ma, *Langmuir* **2022**, *38*, 8667-8676; b) W. X. Zhang, Y. H. Li, S. S. Wang,

Y. Wu, S. H. Chen, Y. Fu, W. J. Ma, Z. H. Zhang, H. P. Ma, *ACS Appl. Mater. Interfaces* **2022**, *14*, 35126-35137; c) W. X. Zhang, Y. Wu, Y. H. Li, S. H. Chen, Y. Fu, Z. H. Zhang, T. Yan, S. S. Wang, H. P. Ma, *Macromolecules* **2022**, *55*, 1435-1444.

[42] J. R. Li, R. J. Kuppler, H. C. Zhou, *Chem. Soc. Rev.* **2009**, *38*, 1477-1504.

[43] M. B. Kim, S. J. Lee, C. Y. Lee, Y. S. Bae, *Microporous Mesoporous Mater.* **2014**, *190*, 356-361.

[44] P. Liu, T. X. Zhao, K. X. Cai, P. Chen, F. Liu, D. J. Tao, *Chem. Eng. J.* **2022**, *437*, 11.

[45] a) X. Peng, J. M. Vicent-Luna, Q. B. Jin, *ACS Appl. Mater. Interfaces* **2020**, *12*, 20044-20055; b) E. A. Muller, *Environ. Sci. Technol.* **2005**, *39*, 8736-8741.

[46] a) A. A. Fomkin, Y. V. Nikiforov, V. A. Sinitsyn, E. G. Savel'ev, *Russ. Chem. Bull.* **2002**, *51*, 2161-2164; b) T. C. Merkel, V. I. Bondar, K. Nagai, B. D. Freeman, I. Pinnau, *J. Polym. Sci. Pt. B-Polym. Phys.* **2000**, *38*, 415-434.

[47] a) D. P. Curran, J. A. Gladysz, *Handbook of Fluorous Chemistry*, Wiley-VCH, **2004**; b) I. T. Horvath, J. Rabai, *Science* **1994**, *266*, 72-75; c) P. T. Nyffeler, S. G. Duron, M. D. Burkart, S. P. Vincent, C. H. Wong, *Angew. Chem. Int. Ed.* **2005**, *44*, 192-212; d) M. Pagliaro, R. Ciriminna, *J. Mater. Chem.* **2005**, *15*, 4981-4991; e) W. B. Li, Y. Z. Cheng, D. H. Yang, Y. W. Liu, B. H. Han, *Macromol. Rapid Commun.* **2022**, *44*, 2200778; f) A. E. Amooghin, H. Sanaeepur, R. Luque, H. Garcia, B. L. Chen, *Chem. Soc. Rev.* **2022**, *51*, 7427-7508; g) Z. Zhang, O. Š. Miljanić, *Org. Mater.* **2019**, *1*, 019-029.

[48] a) J. J. Xie, F. X. Sun, C. R. Wang, Q. K. Pan, *Materials* **2016**, *9*; b) C. Yang, U. Kaipa, Q. Z. Mather, X. P. Wang, V. Nesterov, A. F. Venero, M. A. Omary, *J. Am. Chem. Soc.* **2011**, *133*, 18094-18097; c) C. Yang, X. P. Wang, M. A. Omary, *J. Am. Chem. Soc.* **2007**, *129*, 15454-15455; d) C. Yang, X. P. Wang, M. A. Omary, *Angew. Chem. Int. Ed.* **2009**, *48*, 2500-2505; e) Z. Z. Yang, S. Wang, Z. H. Zhang, W. Guo, K. C. Jie, M. I. Hashim, O. S. Miljanic, D. E. Jiang, I. Popovs, S. Dai, *J. Mater. Chem. A* **2019**, *7*, 17277-17282; f) T. H. Chen, I. Popov, O. Zenasni, O. Daugulis, O. S. Miljanic, *Chem. Commun.* **2013**, *49*, 6846-6848; g) T. H. Chen, W. Kaveevivitchai, A. J. Jacobson, O. S. Miljanic, *Chem. Commun.* **2015**, *51*, 14096-14098; h) M. J. Bojdys, M. E. Briggs, J. T. A. Jones, D. J. Adams, S. Y. Chong, M. Schmidtmann, A. I. Cooper, *J. Am. Chem. Soc.* **2011**, *133*, 16566-16571; i) T. Kunde, E. Nieland, H. V. Schroder, C. A. Schalley, B. M. Schmidt, *Chem. Commun.* **2020**, *56*, 4761-4764; j) T. H. Chen, I. Popov, W. Kaveevivitchai, Y. C. Chuang, Y. S. Chen, A. J. Jacobson, O. S. Miljanic, *Angew. Chem. Int. Ed.* **2015**, *54*, 13902-13906; k) S. M. Elbert, N. I. Regenauer, D. Schindler, W. S. Zhang, F. Rominger, R. R. Schroder, M. Mastalerz, *Chem. Eur. J.* **2018**, *24*, 11438-11443; l) A. Cadiau, K. Adil, P. M. Bhatt, Y. Belmabkhout, M. Eddaoudi, *Science* **2016**, *353*, 137-140; m) B. Li, X. L. Cui, D. O'Nolan, H. M. Wen, M. D. Jiang, R. Krishna, H. Wu, R. B. Lin, Y. S. Chen, D. Q. Yuan, H. B. Xing, W. Zhou, Q. L. Ren, G. D. Qian, M. J. Zaworotko, B. L. Chen, *Adv. Mater.* **2017**, *29*, 1704210.

[49] a) H. J. Jeon, R. Matsuda, P. Kanoo, H. Kajiro, L. C. Li, H. Sato, Y. T. Zheng, S. Kitagawa, *Chem. Commun.* **2014**, *50*, 10861-10863; b) S. Sato, J. Iida, K. Suzuki, M. Kawano, T. Ozeki, M. Fujita, *Science* **2006**, *313*, 1273-1276; c) M. Jang, T. Yamaguchi, K. Ohara, M. Kawano, M. Fujita, *Chem.-Asian J.* **2009**, *4*, 1524-1526; d) P. Deria, J. E. Mondloch, E. Tylianakis, P. Ghosh, W. Bury, R. Q. Snurr, J. T. Hupp, O. K. Farha, *J. Am. Chem. Soc.* **2013**, *135*, 16801-16804; e) N. Han, Z. X. Zhang, H. K. Gao, Y. Q. Qian, L. L. Tan, C. Yang, H. R. Zhang, Z.

Y. Cui, W. Li, X. X. Zhang, *ACS Appl. Mater. Interfaces* **2020**, *12*, 2926-2934; f) X. W. Wu, Y. L. Hong, B. Q. Xu, Y. Nishiyama, W. Jiang, J. W. Zhu, G. Zhang, S. Kitagawa, S. Horike, *J. Am. Chem. Soc.* **2020**, *142*, 14357-14364; g) F. Drache, V. Bon, I. Senkovska, C. Marschelke, A. Synytska, S. Kaskel, *Inorg. Chem.* **2016**, *55*, 7206-7213; h) R. Thur, N. Van Velthoven, V. Lemmens, M. Bastin, S. Smolders, D. De Vos, I. F. J. Vankelecom, *ACS Appl. Mater. Interfaces* **2019**, *11*, 44792-44801.

[50] P. Deria, Y. G. Chung, R. Q. Snurr, J. T. Hupp, O. K. Farha, *Chem. Sci.* **2015**, *6*, 5172-5176.

[51] a) G. Cheng, T. Hasell, A. Trewin, D. J. Adams, A. I. Cooper, *Angew. Chem. Int. Ed.* **2012**, *51*, 12727-12731; b) N. B. McKeown, P. M. Budd, *Chem. Soc. Rev.* **2006**, *35*, 675-683.

[52] A. S. Bhat, S. M. Elbert, W. S. Zhang, F. Rominger, M. Dieckmann, R. R. Schroder, M. Mastalerz, *Angew. Chem. Int. Ed.* **2019**, *58*, 8819-8823.

[53] M. Brutschy, M. W. Schneider, M. Mastalerz, S. R. Waldvogel, *Adv. Mater.* **2012**, *24*, 6049-6052.

[54] a) Q. L. Song, S. Jiang, T. Hasell, M. Liu, S. J. Sun, A. K. Cheetham, E. Sivaniah, A. I. Cooper, *Adv. Mater.* **2016**, *28*, 2629-2637; b) M. Brutschy, M. W. Schneider, M. Mastalerz, S. R. Waldvogel, *Adv. Mater.* **2012**, *24*, 6049-6054.

[55] T. D. Bennett, F. X. Coudert, S. L. James, A. I. Cooper, *Nat. Mater.* **2021**, *20*, 1179-1187.

[56] P. Muller, *Pure Appl. Chem.* **1994**, *66*, 1077-1184.

[57] L. R. MacGillivray, J. L. Atwood, *Angew. Chem. Int. Ed.* **1999**, *38*, 1019-1034.

[58] a) R. Chakrabarty, P. S. Mukherjee, P. J. Stang, *Chem. Rev.* **2011**, *111*, 6810-6918; b) K. Harris, D. Fujita, M. Fujita, *Chem. Commun.* **2013**, *49*, 6703-6712; c) M. M. J. Smulders, I. A. Riddell, C. Browne, J. R. Nitschke, *Chem. Soc. Rev.* **2013**, *42*, 1728-1754.

[59] a) A. Avellaneda, P. Valente, A. Burgun, J. D. Evans, A. W. Markwell-Heys, D. Rankine, D. J. Nielsen, M. R. Hill, C. J. Sumby, C. J. Doonan, *Angew. Chem. Int. Ed.* **2013**, *52*, 3746-3749; b) Z. Wu, S. Lee, J. S. Moore, *J. Am. Chem. Soc.* **1992**, *114*, 8730-8732; c) C. Zhang, C. F. Chen, *J. Org. Chem.* **2007**, *72*, 9339-9341.

[60] C. Zhang, Z. Wang, L. X. Tan, T. L. Zhai, S. Wang, B. Tan, Y. S. Zheng, X. L. Yang, H. B. Xu, *Angew. Chem. Int. Ed.* **2015**, *54*, 9244-9248.

[61] J. H. Zhang, Y. J. Li, W. L. Yang, S. W. Lai, C. J. Zhou, H. B. Liu, C. M. Che, Y. L. Li, *Chem. Commun.* **2012**, *48*, 3602-3604.

[62] S. Ivanova, E. Koster, J. J. Holstein, N. Keller, G. H. Clever, T. Bein, F. Beuerle, *Angew. Chem. Int. Ed.* **2021**, *60*, 17455-17463.

[63] K. Ono, K. Johmoto, N. Yasuda, H. Uekusa, S. Fujii, M. Kiguchi, N. Iwasawa, *J. Am. Chem. Soc.* **2015**, *137*, 7015-7018.

[64] a) C. X. Zhang, Q. Wang, H. Long, W. Zhang, *J. Am. Chem. Soc.* **2011**, *133*, 20995-21001; b) Q. Wang, C. Yu, H. Long, Y. Du, Y. H. Jin, W. Zhang, *Angew. Chem. Int. Ed.* **2015**, *54*, 7550-7554.

[65] H. Schiff, *Justus Liebigs Ann. Chem.* **1864**, *131*, 118-119.

[66] M. L. C. Quan, D. J. Cram, *J. Am. Chem. Soc.* **1991**, *113*, 2754-2755.

[67] V. Santolini, M. Miklitz, E. Berardo, K. E. Jelfs, *Nanoscale* **2017**, *9*, 5280-5298.

[68] a) A. Granzhan, T. Riis-Johannessen, R. Scopelliti, K. Severin, *Angew. Chem. Int. Ed.* **2010**, *49*, 5515-5518; b) K. E. Jelfs, X. F. Wu, M. Schmidtmann, J. T. A. Jones, J. E. Warren, D. J. Adams, A. I. Cooper, *Angew. Chem. Int. Ed.* **2011**, *50*, 10653-10656; c) P. Skowronek, B. Warzajtis, U. Rychlewska, J. Gawronski,

Chem. Commun. **2013**, *49*, 2524-2526; d) J. L. Sun, R. Warmuth, *Chem. Commun.* **2011**, *47*, 9351-9353.

[69] Z. H. Lin, J. L. Sun, B. Efremovska, R. Warmuth, *Chem. Eur. J.* **2012**, *18*, 12864-12872.

[70] a) T. Hasell, M. Schmidtmann, A. I. Cooper, *J. Am. Chem. Soc.* **2011**, *133*, 14920-14923; b) P. S. Huang, C. H. Kuo, C. C. Hsieh, Y. C. Horng, *Chem. Commun.* **2012**, *48*, 3227-3229; c) C. Schouwey, R. Scopelliti, K. Severin, *Chem. Eur. J.* **2013**, *19*, 6274-6281.

[71] J. Tian, P. K. Thallapally, S. J. Dalgarno, P. B. McGrail, J. L. Atwood, *Angew. Chem. Int. Ed.* **2009**, *48*, 5492-5495.

[72] T. Tozawa, J. T. A. Jones, S. I. Swamy, S. Jiang, D. J. Adams, S. Shakespeare, R. Clowes, D. Bradshaw, T. Hasell, S. Y. Chong, C. Tang, S. Thompson, J. Parker, A. Trewin, J. Bacsa, A. M. Z. Slawin, A. Steiner, A. I. Cooper, *Nat. Mater.* **2009**, *8*, 973-978.

[73] a) M. Mastalerz, M. W. Schneider, I. M. Oppel, O. Presly, *Angew. Chem. Int. Ed.* **2011**, *50*, 1046-1051; b) S. M. Elbert, F. Rominger, M. Mastalerz, *Chem. Eur. J.* **2014**, *20*, 16707-16720; c) M. W. Schneider, I. M. Oppel, H. Ott, L. G. Lechner, H. J. S. Hauswald, R. Stoll, M. Mastalerz, *Chem. Eur. J.* **2012**, *18*, 836-847; d) M. Holsten, S. M. Elbert, F. Rominger, W.-S. Zhang, R. R. Schröder, M. Mastalerz, *Chem. Eur. J.* **2023**, e202302116.

[74] M. W. Schneider, H. J. S. Hauswald, R. Stoll, M. Mastalerz, *Chem. Commun.* **2012**, *48*, 9861-9863.

[75] M. W. Schneider, I. M. Oppel, M. Mastalerz, *Chem. Eur. J.* **2012**, *18*, 4156-4160.

[76] M. W. Schneider, Doctoral dissertation thesis, Ulm University **2015**.

[77] F. Beuerle, B. Gole, *Angew. Chem. Int. Ed.* **2018**, *57*, 4850-4878.

[78] M. A. Little, S. Y. Chong, M. Schmidtmann, T. Hasell, A. I. Cooper, *Chem. Commun.* **2014**, *50*, 9465-9468.

[79] J. T. A. Jones, D. Holden, T. Mitra, T. Hasell, D. J. Adams, K. E. Jelfs, A. Trewin, D. J. Willock, G. M. Day, J. Bacsa, A. Steiner, A. I. Cooper, *Angew. Chem. Int. Ed.* **2011**, *50*, 749-753.

[80] S. Bera, K. Dey, T. K. Pal, A. Halder, S. Tothadi, S. Karak, M. Addicoat, R. Banerjee, *Angew. Chem. Int. Ed.* **2019**, *58*, 4243-4247.

[81] a) T. Hasell, S. Y. Chong, K. E. Jelfs, D. J. Adams, A. I. Cooper, *J. Am. Chem. Soc.* **2012**, *134*, 588-598; b) T. Hasell, S. Y. Chong, M. Schmidtmann, D. J. Adams, A. I. Cooper, *Angew. Chem. Int. Ed.* **2012**, *51*, 7154-7157.

[82] M. Liu, L. D. Zhang, M. A. Little, V. Kapil, M. Ceriotti, S. Y. Yang, L. F. Ding, D. L. Holden, R. Balderas-Xicohtencatl, D. L. He, R. Clowes, S. Y. Chong, G. Schutz, L. J. Chen, M. Hirscher, A. I. Cooper, *Science* **2019**, *366*, 613-620.

[83] a) S. Jiang, J. Bacsa, X. F. Wu, J. T. A. Jones, R. Dawson, A. Trewin, D. J. Adams, A. I. Cooper, *Chem. Commun.* **2011**, *47*, 8919-8921; b) M. Mastalerz, *Chem. Commun.* **2008**, 4756-4758; c) H. M. Ding, Y. H. Yang, B. J. Li, F. Pan, G. Z. Zhu, M. Zeller, D. Q. Yuan, C. Wang, *Chem. Commun.* **2015**, *51*, 1976-1979; d) F. Wang, E. Sikma, Z. M. Duan, T. Sarma, C. H. Lei, Z. Zhang, S. M. Humphrey, J. L. Sessler, *Chem. Commun.* **2019**, *55*, 6185-6188; e) Y. H. Jin, B. A. Voss, R. D. Noble, W. Zhang, *Angew. Chem. Int. Ed.* **2010**, *49*, 6348-6351; f) Y. H. Jin, B. A. Voss, A. Jin, H. Long, R. D. Noble, W. Zhang, *J. Am. Chem. Soc.* **2011**, *133*, 6650-6658; g) K. Z. Su, W. J. Wang, S. F. Du, C. Q. Ji, D. Q. Yuan, *Nat. Commun.* **2021**, *12*, 3703; h) Z. F. Wang, N. Sikdar, S. Q. Wang, X. Li, M. H. Yu, X. H. Bu, Z. Chang, X. L. Zou, Y. Chen, P. Cheng, K. Yu, M. J. Zaworotko, Z. J. Zhang, *J. Am. Chem. Soc.* **2019**, *141*, 9408-9414; i) L. Chen, P. S. Reiss,

S. Y. Chong, D. Holden, K. E. Jelfs, T. Hasell, M. A. Little, A. Kewley, M. E. Briggs, A. Stephenson, K. M. Thomas, J. A. Armstrong, J. Bell, J. Busto, R. Noel, J. Liu, D. M. Strachan, P. K. Thallapally, A. I. Cooper, *Nat. Mater.* **2014**, *13*, 954-960.

[84] T. Hasell, M. Miklitz, A. Stephenson, M. A. Little, S. Y. Chong, R. Clowes, L. J. Chen, D. Holden, G. A. Tribello, K. E. Jelfs, A. I. Cooper, *J. Am. Chem. Soc.* **2016**, *138*, 1653-1659.

[85] X. Chen, M. Addicoat, S. Irle, A. Nagai, D. L. Jiang, *J. Am. Chem. Soc.* **2013**, *135*, 546-549.

[86] X.-Y. Hu, Doctoral dissertation thesis, Heidelberg University **2019**.

[87] K. E. Jelfs, F. Schiffmann, J. T. A. Jones, B. Slater, F. Cora, A. I. Cooper, *Phys. Chem. Chem. Phys.* **2011**, *13*, 20081-20085.

[88] a) P. Wessig, M. Gerngross, D. Freyse, P. Bruhn, M. Przezdziak, U. Schilde, A. Kelling, *J. Org. Chem.* **2016**, *81*, 1125-1136; b) K. Tamao, S. Koji, K. Yoshihisa, Z. Michio, F. Akira, K. Shun-ichi, N. Isao, M. Akio, K. Makoto, *Bull. Chem. Soc. Jpn.* **1976**, *49*, 1958-1969.

[89] a) R. Shimizu, E. Yoneda, T. Fuchikami, *Tetrahedron Lett.* **1996**, *37*, 5557-5560; b) X. X. Liu, J. S. Rathore, G. Dubois, L. V. Interrante, *J. Polym. Sci., Part A-1: Polym. Chem.* **2017**, *55*, 1547-1557.

[90] a) D. Reinhard, Doctoral dissertation thesis, Heidleberg University **2021**; b) T. Ishiyama, M. Murata, N. Miyaura, *J. Org. Chem.* **1995**, *60*, 7508-7510.

[91] C. Zhang, C. F. Chen, *J. Org. Chem.* **2006**, *71*, 6626-6629.

[92] A. S. Bhat, Doctoral dissertation thesis, Heidelberg University **2021**.

[93] R. Neufeld, D. Stalke, *Chem. Sci.* **2015**, *6*, 3354-3364.

[94] A. Einstein, *Ann. Phys.* **1905**, *4*, 549-560.

[95] R. Pollice, P. Chen, *J. Am. Chem. Soc.* **2019**, *141*, 3489-3506.

[96] a) L. C. Pauling, *The Nature of the Chemical Bond*, Cornell University Press, NY, **1960**; b) K. Reichenbacher, H. I. Suss, J. Hulliger, *Chem. Soc. Rev.* **2005**, *34*, 22-30.

[97] a) I. Alkorta, J. E. Elguero, *Struct. Chem.* **2004**, *15*, 117-120; b) R. J. Baker, P. E. Colavita, D. M. Murphy, J. A. Platts, J. D. Wallis, *J. Phys. Chem. A* **2012**, *116*, 1435-1444; c) R. Berger, G. Resnati, P. Metrangolo, E. Weber, J. Hulliger, *Chem. Soc. Rev.* **2011**, *40*, 3496-3508; d) Z.-T. Li, L.-Z. Wu, (Eds.), *Hydrogen Bonded Supramolecular Structures*, Springer-Verlag: Berlin, Heidelberg, **2015**; e) R. A. Cormanich, R. Rittner, D. O'Hagan, M. Buhl, *J. Phys. Chem. A* **2014**, *118*, 7901-7910.

[98] N. Ramasubbu, R. Parthasarathy, P. Murray-Rust, *J. Am. Chem. Soc.* **1986**, *108*, 4308-4314.

[99] A. Mukherjee, S. Tothadi, G. R. Desiraju, *Acc. Chem. Res.* **2014**, *47*, 2514-2524.

[100] C. F. Macrae, I. Sovago, S. J. Cottrell, P. T. A. Galek, P. McCabe, E. Pidcock, M. Platings, G. P. Shields, J. S. Stevens, M. Towler, P. A. Wood, *J. Appl. Crystallogr.* **2020**, *53*, 226-235.

[101] M. Liu, L. Zhang, M. A. Little, V. Kapil, M. Ceriotti, S. Yang, L. Ding, D. L. Holden, R. Balderas-Xicohténcatl, D. He, R. Clowes, S. Y. Chong, G. Schütz, L. Chen, M. Hirscher, A. I. Cooper, *Science* **2019**, *366*, 613-620.

[102] a) D. A. Reed, B. K. Keitz, J. Oktawiec, J. A. Mason, T. Runčevski, D. J. Xiao, L. E. Darago, V. Crocellà, S. Bordiga, J. R. Long, *Nature* **2017**, *550*, 96-100; b) J. A. Mason, J. Oktawiec, M. K. Taylor, M. R. Hudson, J. Rodriguez, J. E. Bachman, M. I. Gonzalez, A. Cervellino, A. Guagliardi, C. M. Brown, P. L. Llewellyn, N. Masciocchi, J. R. Long, *Nature* **2015**, *527*, 357-361.

[103] a) J. G. Riess, *Artif. Cells, Blood Substitutes, Biotechnol.* **2005**, *33*, 47-63; b) R.

W. Tilford, S. J. Mugavero, P. J. Pellechia, J. J. Lavigne, *Adv. Mater.* **2008**, *20*, 2741-2746.
[104] K. S. W. Sing, D. H. Everett, R. A. W. Haul, L. Moscou, R. A. Pierotti, J. Rouquerol, T. Siemieniewska, *Pure Appl. Chem.* **1985**, *57*, 603-619.
[105] S. Brunauer, P. H. Emmett, E. Teller, *J. Am. Chem. Soc.* **1938**, *60*, 309-319.
[106] R. Battino, T. R. Rettich, T. Tominaga, *J. Phys. Chem. Ref. Data* **1984**, *13*, 563-600.
[107] a) M. A. Spackman, J. J. McKinnon, *CrystEngComm* **2002**, *4*, 378-392; b) M. A. Spackman, D. Jayatilaka, *CrystEngComm* **2009**, *11*, 19-32; c) J. J. McKinnon, A. S. Mitchell, M. A. Spackman, *Chem. Eur. J.* **1998**, *4*, 2136-2141.
[108] a) R. J. Baker, P. E. Colavita, D. M. Murphy, J. A. Platts, J. D. Wallis, *J. Phys. Chem. A* **2012**, *116*, 1435-1444; b) R. Bayon, S. Coco, P. Espinet, *Chem. Eur. J.* **2005**, *11*, 1079-1085; c) H. R. Khavasi, N. Rahimi, *CrystEngComm* **2017**, *19*, 1361-1365.
[109] I. Alkorta, J. Elguero, *Struct. Chem.* **2004**, *15*, 117-120.
[110] J. Mühle, C. M. Trudinger, L. M. Western, M. Rigby, M. K. Vollmer, S. Park, A. J. Manning, D. Say, A. Ganesan, L. P. Steele, D. J. Ivy, T. Arnold, S. Li, A. Stohl, C. M. Harth, P. K. Salameh, A. McCulloch, S. O'Doherty, M. K. Park, C. O. Jo, D. Young, K. M. Stanley, P. B. Krummel, B. Mitrevski, O. Hermansen, C. Lunder, N. Evangeliou, B. Yao, J. Kim, B. Hmiel, C. Buizert, V. V. Petrenko, J. Arduini, M. Maione, D. M. Etheridge, E. Michalopoulou, M. Czerniak, J. P. Severinghaus, S. Reimann, P. G. Simmonds, P. J. Fraser, R. G. Prinn, R. F. Weiss, *Atmos. Chem. Phys.* **2019**, *19*, 10335-10359.
[111] H. A. Patel, S. Hyun Je, J. Park, D. P. Chen, Y. Jung, C. T. Yavuz, A. Coskun, *Nat. Commun.* **2013**, *4*, 1357.
[112] H. Murase, T. Imai, T. Inohara, M. Toyoda, *IEEE Trans. Dielectr. Electr. Insul.* **2004**, *11*, 166-173.
[113] a) J. H. Zhang, P. J. Zhu, S. M. Xie, M. Zi, L. M. Yuan, *Anal. Chim. Acta* **2018**, *999*, 169-175; b) E. J. Gosselin, G. E. Decker, B. W. McNichols, J. E. Baumann, G. P. A. Yap, A. Sellinger, E. D. Bloch, *Chem. Mat.* **2020**, *32*, 5872-5878; c) S. J. Sun, M. Liu, J. Thapa, N. T. P. Hartono, Y. C. Zhao, D. L. He, S. Wieghold, M. Chua, Y. Wu, V. Bulovic, S. L. Ling, C. J. Brabec, A. I. Cooper, T. Buonassisi, *Chem. Mat.* **2022**, 9384–9391.
[114] G. E. Carr, R. D. Chambers, T. F. Holmes, D. G. Parker, *J. Chem. Soc., Perkin Trans. 1* **1988**, 921-926.
[115] J. Lim, T. M. Swager, *Angew. Chem. Int. Ed.* **2010**, *49*, 7486-7488.
[116] C. Hansch, A. Leo, R. W. Taft, *Chem. Rev.* **1991**, *91*, 165-195.
[117] M. Thommes, K. Kaneko, A. V. Neimark, J. P. Olivier, F. Rodriguez-Reinoso, J. Rouquerol, K. S. W. Sing, *Pure Appl. Chem.* **2015**, *87*, 1051-1069.
[118] D. W. Breck, *Zeolite Molecular Sieves: Structure, Chemistry, and Use*, John Wiley & Sons, Inc.: New York, **1974**.
[119] H. A. Patel, S. Hyun Je, J. Park, D. P. Chen, Y. Jung, C. T. Yavuz, A. Coskun, *Nat. Commun.* **2013**, *4*, 1357.
[120] S. W. Choi, H. J. Yoon, H. J. Lee, E.-S. Lee, D.-S. Lim, K. B. Lee, *Microporous Mesoporous Mater.* **2020**, *306*, 110373.
[121] Y. Wu, T. Yan, W. X. Zhang, S. H. Chen, Y. Fu, Z. H. Zhang, H. P. Ma, *Ind. Eng. Chem. Res.* **2022**, *61*, 13603-13611.
[122] X. Yuan, M.-K. Cho, J. G. Lee, S. W. Choi, K. B. Lee, *Environ. Pollut.* **2020**, *265*, 114868.
[123] X. Yuan, S. W. Choi, E. Jang, K. B. Lee, *Chem. Eng. J.* **2018**, *336*, 297-305.

[124] S. W. Choi, D.-H. Lee, J. Kim, J. Kim, J.-H. Park, H. T. Beum, D.-S. Lim, K. B. Lee, *Chem. Eng. J.* **2017**, *311*, 227-235.
[125] S. W. Choi, S.-M. Hong, J.-H. Park, H. T. Beum, K. B. Lee, *Ind. Eng. Chem. Res.* **2015**, *54*, 8561-8568.
[126] a) G. V. Janjic, S. T. Jelic, N. P. Trisovic, D. M. Popovic, I. S. Dordevic, M. K. Milcic, *Cryst. Growth Des.* **2020**, *20*, 2943-2951; b) H. Omorodion, B. Twamley, J. A. Platts, R. J. Baker, *Cryst. Growth Des.* **2015**, *15*, 2835-2841.
[127] T. Hasell, M. A. Little, S. Y. Chong, M. Schmidtmann, M. E. Briggs, V. Santolini, K. E. Jelfs, A. I. Cooper, *Nanoscale* **2017**, *9*, 6783-6790.
[128] C. L. Li, Y. Zuo, Y. Q. Zhao, S. D. Zhang, *Chem. Lett.* **2020**, *49*, 1356-1366.
[129] A. G. Slater, M. A. Little, M. E. Briggs, K. E. Jelfs, A. I. Cooper, *Mol. Syst. Des. Eng.* **2018**, *3*, 223-227.
[130] a) D. Beaudoin, F. Rominger, M. Mastalerz, *Angew. Chem. Int. Ed.* **2017**, *56*, 1244-1248; b) P. Wagner, F. Rominger, W. S. Zhang, J. H. Gross, S. M. Elbert, R. R. Schroder, M. Mastalerz, *Angew. Chem. Int. Ed.* **2021**, *60*, 8896-8904.
[131] H. Qu, X. Tang, X. C. Wang, Z. H. Li, Z. Y. Huang, H. Zhang, Z. Q. Tian, X. Y. Cao, *Chem. Sci.* **2018**, *9*, 8814-8818.
[132] a) X. C. Wang, Y. Wang, H. Y. Yang, H. X. Fang, R. X. Chen, Y. B. Sun, N. F. Zheng, K. Tan, X. Lu, Z. Q. Tian, X. Y. Cao, *Nat. Commun.* **2016**, *7*, 12469; b) H. Qu, Y. Wang, Z. H. Li, X. C. Wang, H. X. Fang, Z. Q. Tian, X. Y. Cao, *J. Am. Chem. Soc.* **2017**, *139*, 18142-18145.
[133] a) Y. Wang, H. X. Fang, W. Zhang, Y. B. Zhuang, Z. Q. Tian, X. Y. Cao, *Chem. Commun.* **2017**, *53*, 8956-8959; b) X. C. Wang, P. X. Peng, W. Xuan, Y. Wang, Y. B. Zhuang, Z. Q. Tian, X. Y. Cao, *Org. Biomol. Chem.* **2018**, *16*, 34-37.
[134] a) P. Zhang, X. C. Wang, W. Xuan, P. X. Peng, Z. H. Li, R. Q. Lu, S. Wu, Z. Q. Tian, X. Y. Cao, *Chem. Commun.* **2018**, *54*, 4685-4688; b) X. Tang, Z. H. Li, H. L. Liu, H. Qu, W. B. Gao, X. Dong, S. L. Zhang, X. C. Wang, A. C. H. Sue, L. L. Yang, K. Tan, Z. Q. Tian, X. Y. Cao, *Chem. Sci.* **2021**, *12*, 11730-11734.
[135] Y. X. Chen, G. C. Wu, B. B. Chen, H. Qu, T. Y. Jiao, Y. T. Li, C. Q. Ge, C. Zhang, L. X. Liang, X. Q. Zeng, X. Y. Cao, Q. Wang, H. Li, *Angew. Chem. Int. Ed.* **2021**, *60*, 18815-18820.
[136] O. D. Fox, T. D. Rolls, M. G. B. Drew, P. D. Beer, *Chem. Commun.* **2001**, 1632-1633.
[137] a) J. C. Lauer, A. S. Bhat, C. Barwig, N. Fritz, T. Kirschbaum, F. Rominger, M. Mastalerz, *Chem. Eur. J.* **2022**, *28*, e2022015; b) J. C. Lauer, A. S. Bhat, C. Barwig, N. Fritz, T. Kirschbaum, F. Rominger, M. Mastalerz, *Chem. Eur. J.* **2022**, *28*, 9; c) J. C. Lauer, Z. W. Pang, P. Janssen, F. Rominger, T. Kirschbaum, M. Elstner, M. Mastalerz, *ChemistryOpen* **2020**, *9*, 183-190.
[138] a) S. H. Chung, T. J. Lin, Q. Y. Hu, C. H. Tsai, P. S. Pan, *Molecules* **2013**, *18*, 12346-12367; b) R. Greenaway, V. Santolini, M. J. Bennison, B. M. Alston, C. J. Pugh, M. A. Little, M. Miklitz, E. G. B. Eden-Rumps, R. Clowes, A. Shakil, H. J. Cuthbertson, H. Armstrong, M. E. Briggs, K. E. Jelfs, A. I. Cooper, *Nat. Commun.* **2018**, *9*, 2849.
[139] H. C. Chen, S. H. Chen, *J. Phys. Chem.* **1984**, *88*, 5118-5121.
[140] K. Tian, X. Wang, M. P. Schuldt, S. M. Elbert, F. Rominger, M. Mastalerz, *Org. Mater.* **2023**, *5*, 91-97.
[141] T. Y. Jiao, H. Qu, L. Tong, X. Y. Cao, H. Li, *Angew. Chem. Int. Ed.* **2021**, *60*, 9852-9858.
[142] a) S. A. L. Rousseaux, J. Q. Gong, R. Haver, B. Odell, T. D. W. Claridge, L. M. Herz, H. L. Anderson, *J. Am. Chem. Soc.* **2015**, *137*, 12713-12718; b) K. Cai,

M. C. Lipke, Z. C. Liu, J. Nelson, T. Cheng, Y. Shi, C. Y. Cheng, D. K. Shen, J. M. Han, S. Vemuri, Y. N. Feng, C. L. Stern, W. A. Goddard, M. R. Wasielewski, J. F. Stoddart, *Nat. Commun.* **2018**, *9*, 5275; c) D. W. Zhang, T. K. Ronson, J. L. Greenfield, T. Brotin, P. Berthault, E. Leonce, J. L. Zhu, L. Xu, J. R. Nitschke, *J. Am. Chem. Soc.* **2019**, *141*, 8339-8345; d) E. Ubasart, O. Borodin, C. Fuertes-Espinosa, Y. Z. Xu, C. Garcia-Simon, L. Gomez, J. Juanhuix, F. Gandara, I. Imaz, D. Maspoch, M. von Delius, X. Ribas, *Nat. Chem.* **2021**, *13*, 420-427.

[143] J. Koziskova, F. Hahn, J. Richter, J. Kožíšek, *Acta Chim. Slov.* **2016**, *9*, 136-140.

[144] G. W. T. M. J. Frisch, H. B. Schlegel, G. E. Scuseria, M. A. Robb, J. R. Cheeseman, G. Scalmani, V. Barone, G. A. Petersson, H. Nakatsuji, X. Li, M. Caricato, A. V. Marenich, J. Bloino, B. G. Janesko, R. Gomperts, B. Mennucci, H. P. Hratchian, J. V. Ortiz, A. F. Izmaylov, J. L. Sonnenberg, D. Williams-Young, F. Ding, F. Lipparini, F. Egidi, J. Goings, B. Peng, A. Petrone, T. Henderson, D. Ranasinghe, V. G. Zakrzewski, J. Gao, N. Rega, G. Zheng, W. Liang, M. Hada, M. Ehara, K. Toyota, R. Fukuda, J. Hasegawa, M. Ishida, T. Nakajima, Y. Honda, O. Kitao, H. Nakai, T. Vreven, K. Throssell, J. A. Montgomery, Jr., J. E. Peralta, F. Ogliaro, M. J. Bearpark, J. J. Heyd, E. N. Brothers, K. N. Kudin, V. N. Staroverov, T. A. Keith, R. Kobayashi, J. Normand, K. Raghavachari, A. P. Rendell, J. C. Burant, S. S. Iyengar, J. Tomasi, M. Cossi, J. M. Millam, M. Klene, C. Adamo, R. Cammi, J. W. Ochterski, R. L. Martin, K. Morokuma, O. Farkas, J. B. Foresman, and D. J. Fox, Gaussian, Inc., Wallingford CT **2016**.

[145] a) W. Koch, M. C. Holthausen, *A Chemis's Guide to Density Functional Theory*, Wiley-VCH, Weinheim, **2001**; b) R. G. Parr, W. Yang, *Density-Functional Theory of Atoms and Molecules*, Oxford Univ. Press, New York, NY, **1994**; c) P. Hohenberg, W. Kohn, *Phys. Rev.* **1964**, *136*, B864-B871; d) W. Kohn, L. J. Sham, *Phys. Rev.* **1965**, *140*, A1133-A1138.

[146] a) A. D. Becke, *J. Chem. Phys.* **1993**, *98*, 5648-5652; b) C. Lee, W. Yang, R. G. Parr, *Physical Review B: Condensed Matter and Materials Physics* **1988**, *37*, 785-789; c) P. J. Stephens, F. J. Devlin, C. F. Chabalowski, M. J. Frisch, *J. Phys. Chem.* **1994**, *98*, 11623-11627; d) S. H. Vosko, L. Wilk, M. Nusair, *Can. J. Phys.* **1980**, *58*, 1200-1211.

[147] a) T. H. D. Jr., *J. Chem. Phys.* **1989**, *90*, 1007-1023; b) R. A. Kendall, T. H. D. Jr., R. J. Harrison, *J. Chem. Phys.* **1992**, *96*, 6796-6806.

[148] a) A. Otero-de-la-Roza, E. R. Johnson, *J. Chem. Phys.* **2013**, *138*, 204109; b) F. O. Kannemann, A. D. Becke, *J. Chem. Theory Comput.* **2010**, *6*, 1081-1088.

[149] A. F. Saturno, *J. Chem. Educ.* **1962**, *39*, 464.

[150] G. M. Kontogeorgis, R. Privat, J.-N. Jaubert, *J. Chem. Eng. Data* **2019**, *64*, 4619-4637.

[151] P. J. Linstrom, W. G. Mallard, *NIST Chemistry WebBook, NIST Standard Reference Database Number 69, National Institute of Standards and Technology, Gaithersburg MD, 20899, https://doi.org/10.18434/T4D303, (retrieved February 8, 2022).* .

[152] E. F. DiMauro, J. R. Vitullo, *J. Org. Chem.* **2006**, *71*, 3959-3962.

[153] J. D. Pang, Z. Y. Di, J. S. Qin, S. Yuan, C. T. Lollar, J. L. Li, P. Zhang, M. Y. Wu, D. Q. Yuan, M. C. Hong, H. C. Zhou, *J. Am. Chem. Soc.* **2020**, *142*, 15020-15026.

[154] P. D. Beer, A. G. Cheetham, M. G. B. Drew, O. D. Fox, E. J. Hayes, T. D. Rolls, *Dalton Trans.* **2003**, 603-611.

VII. Appendix

The following sections only include the unpublished experimental data. The figures already published in this thesis can be found in the references.[7, 140] All the spectra were recorded at room temperature unless otherwise noted.

1. NMR Spectra

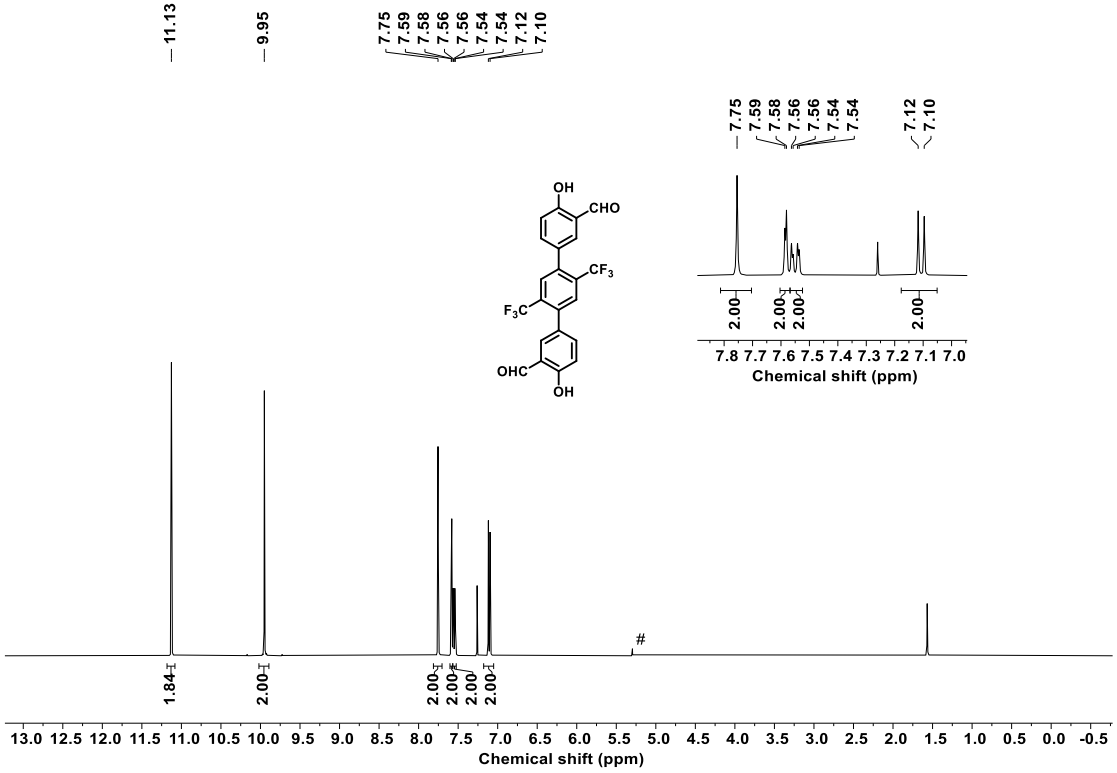

Figure 75. ^{1}H NMR spectrum of **69** ($CDCl_3$, 400 MHz). # marks DCM.

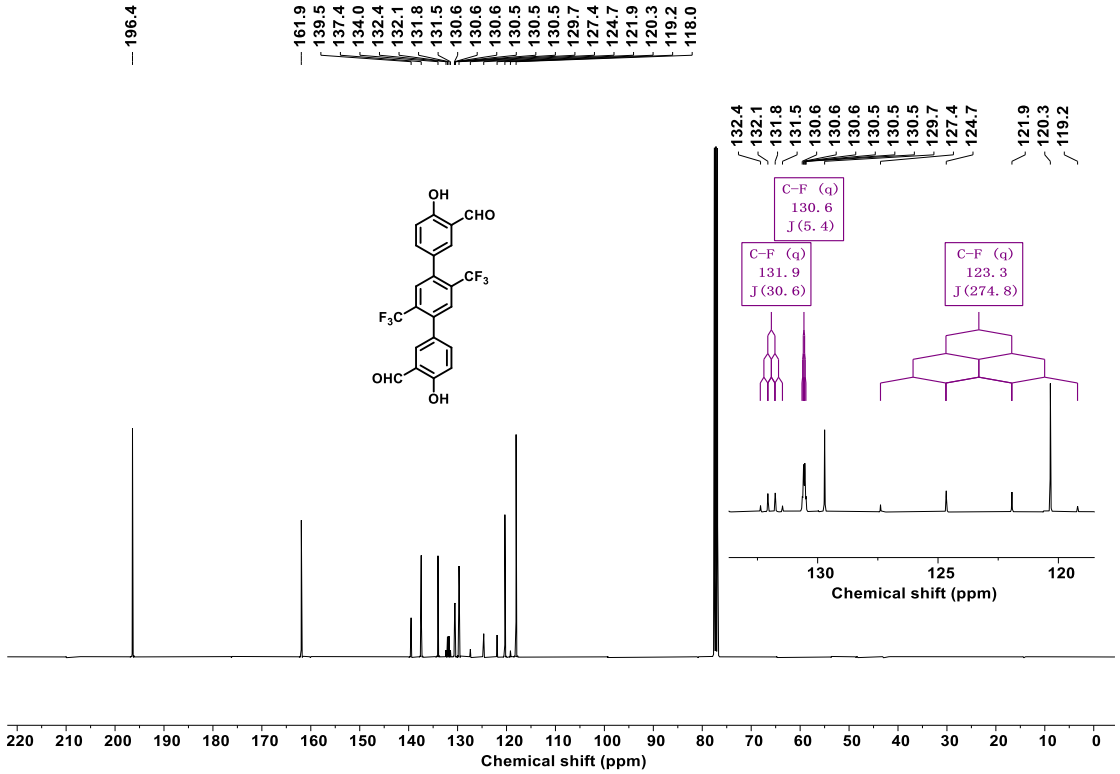

Figure 76. ^{13}C NMR spectrum of **69** ($CDCl_3$, 101 MHz).

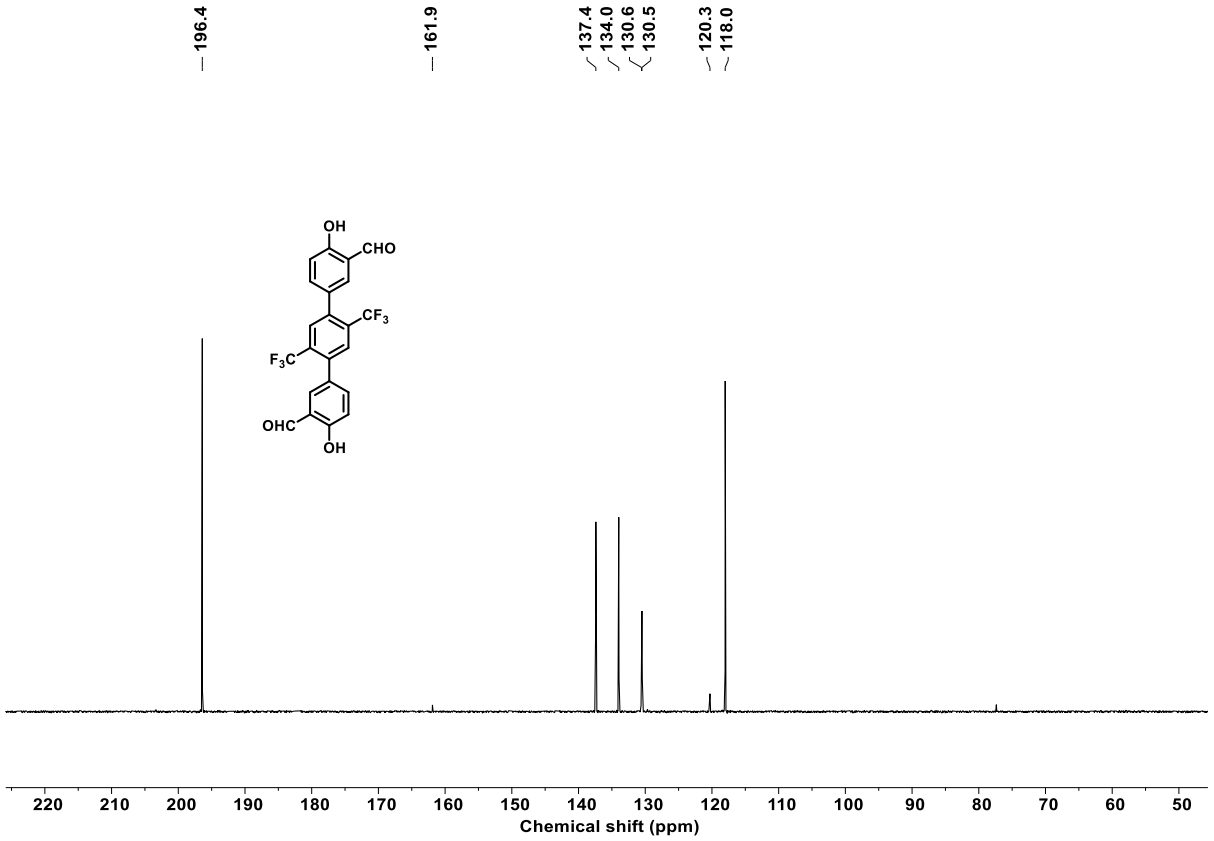

Figure 77. ^{13}C-DEPT135 NMR spectrum of **69** ($CDCl_3$, 101 MHz).

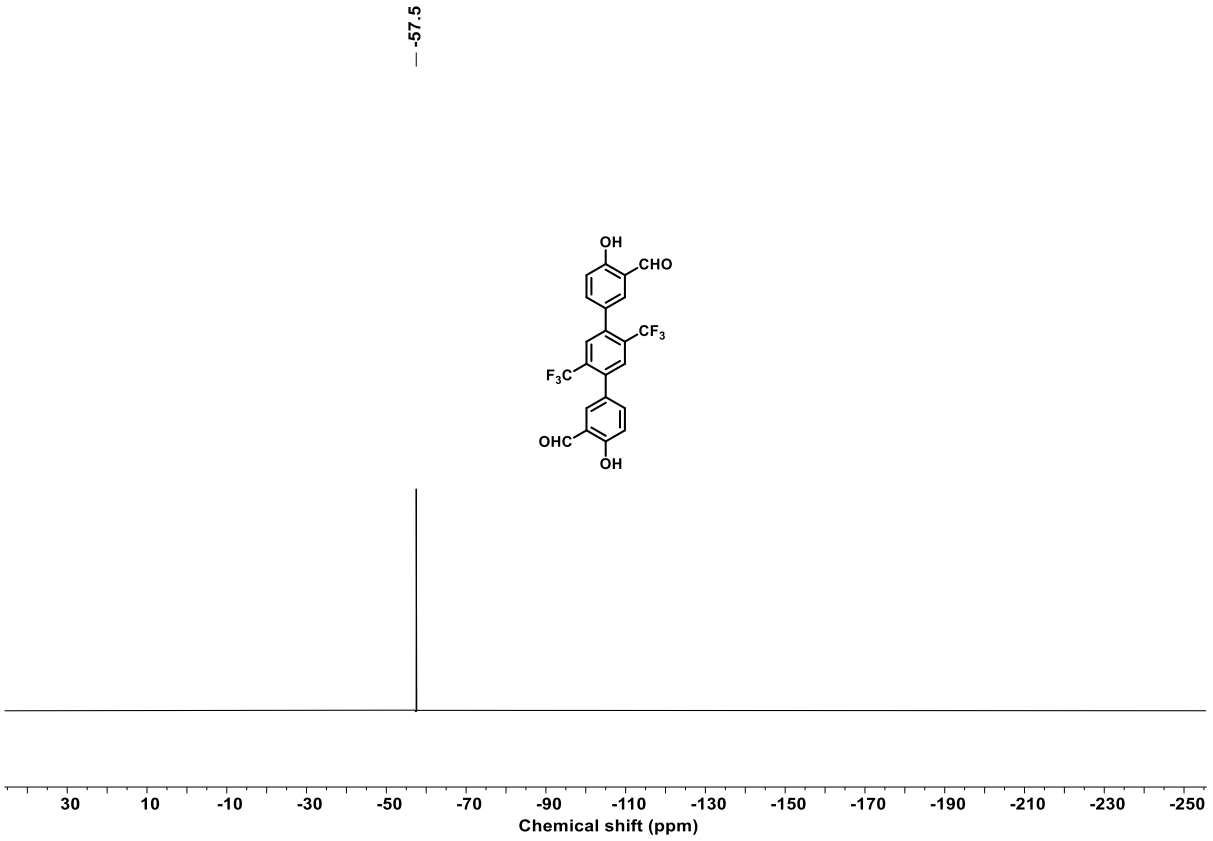

Figure 78. ^{19}F NMR spectrum of **69** (THF-d_8, 471 MHz).

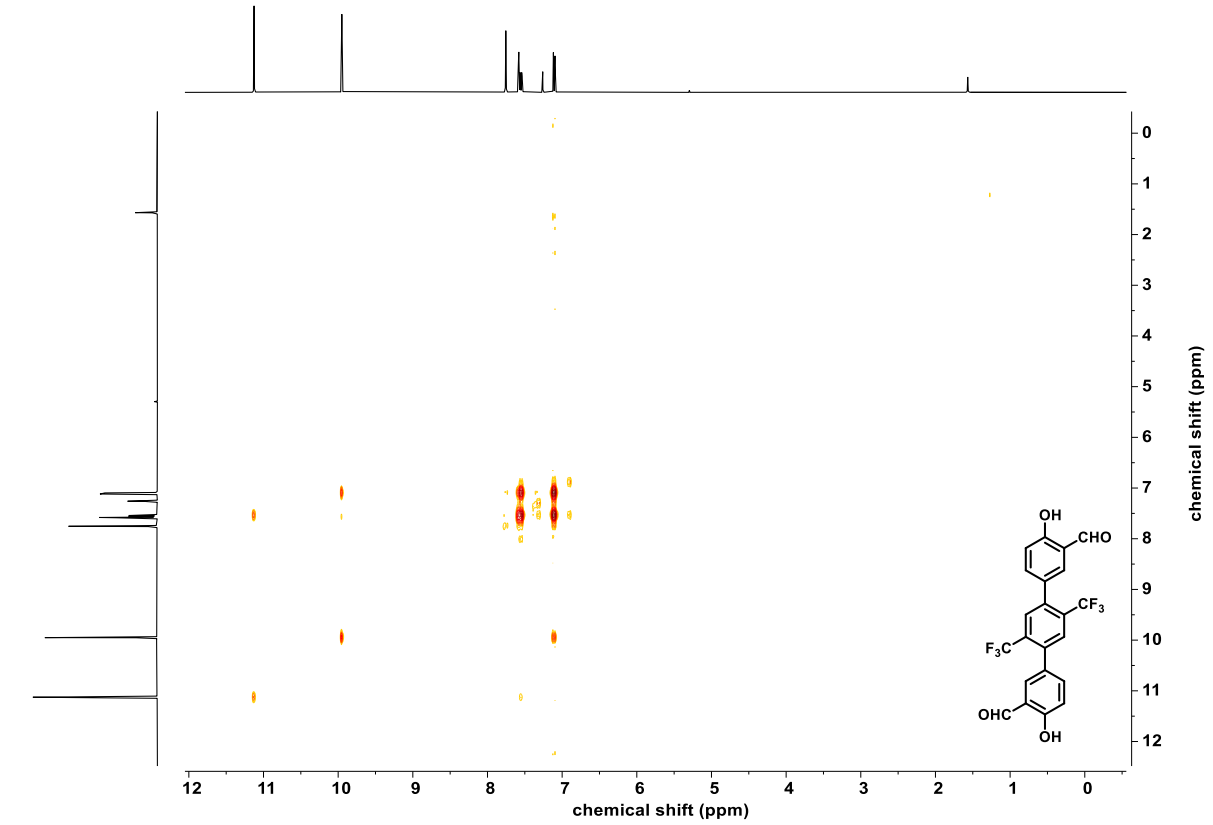

Figure 79. ^{1}H-^{1}H COSY NMR spectrum of **69** ($CDCl_3$, 400 MHz, 400 MHz).

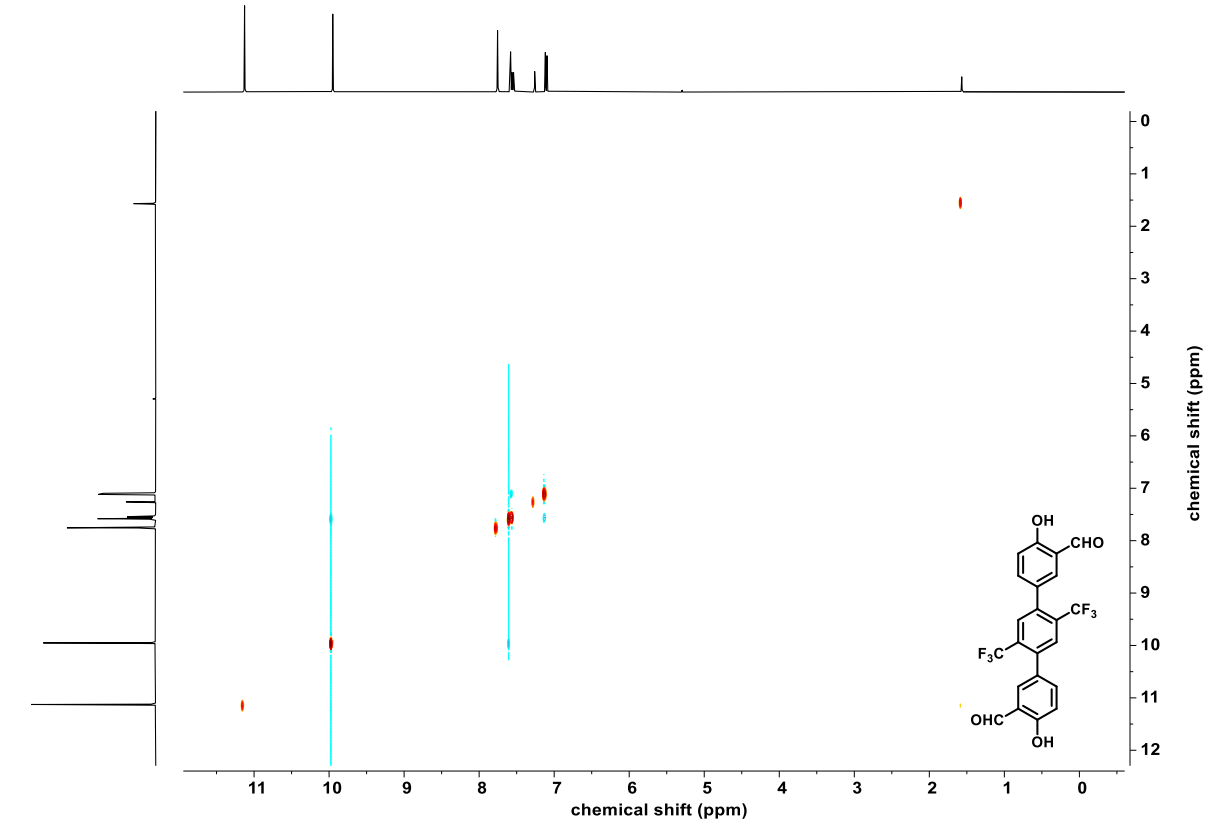

Figure 80. ^{1}H-^{1}H NOSY NMR spectrum of **69** ($CDCl_3$, 400 MHz, 400 MHz).

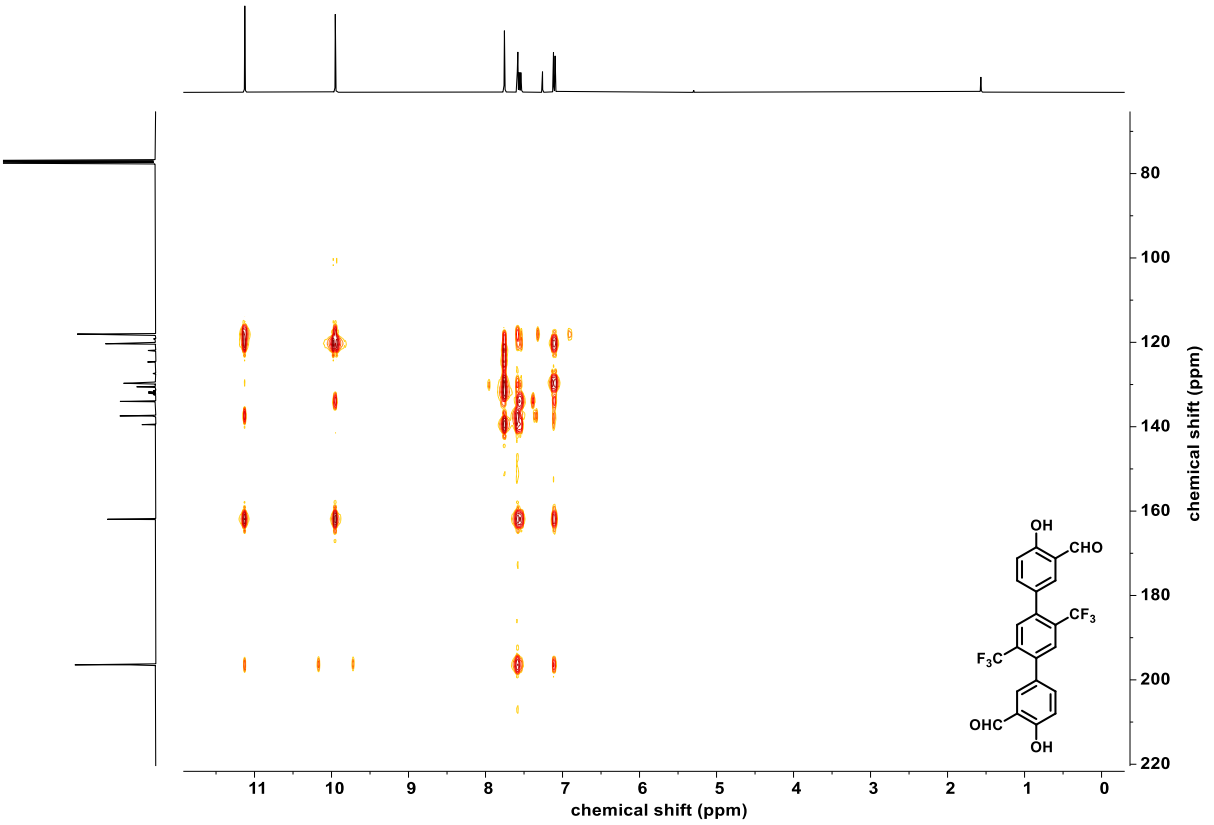

Figure 81. ^{1}H-^{13}C HMBC NMR spectrum of **69** ($CDCl_3$, 400 MHz, 101 MHz).

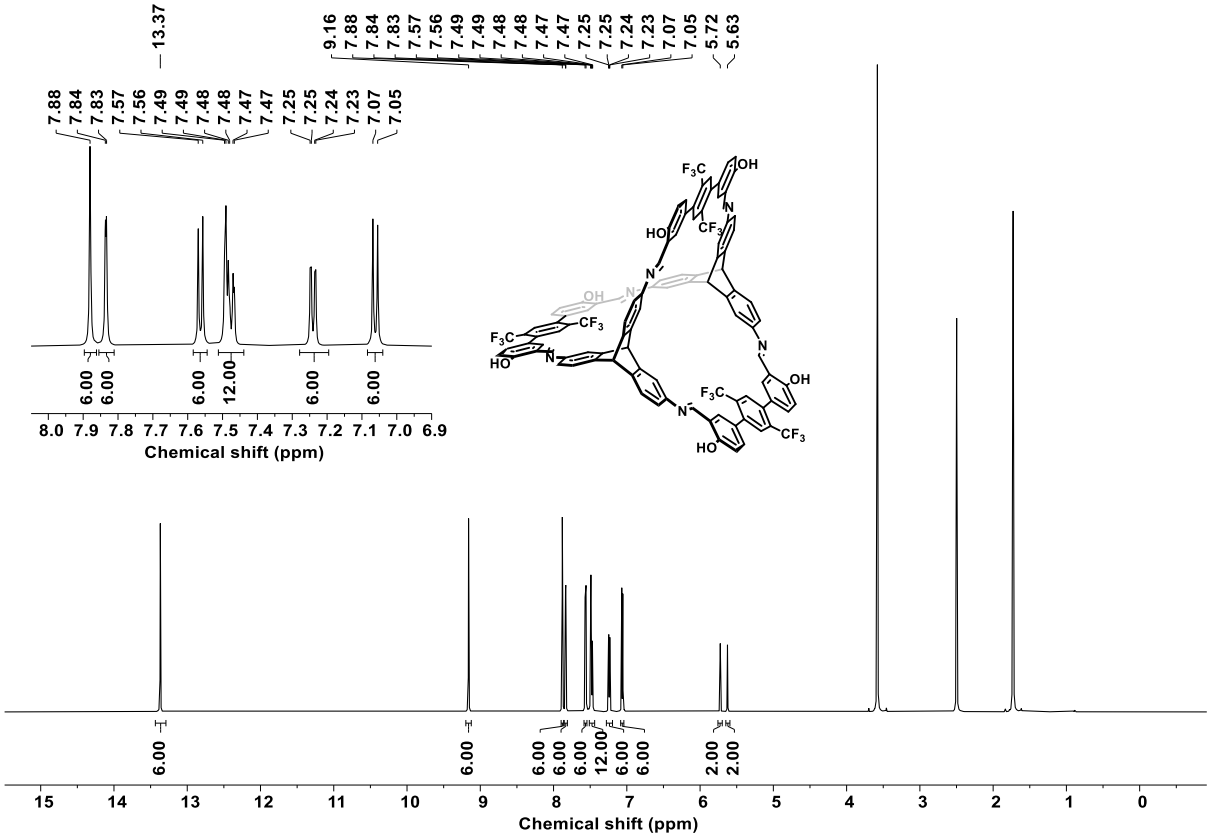

Figure 82. ^{1}H NMR spectrum of **cage-CF$_3$** (THF-d_8, 600 MHz).

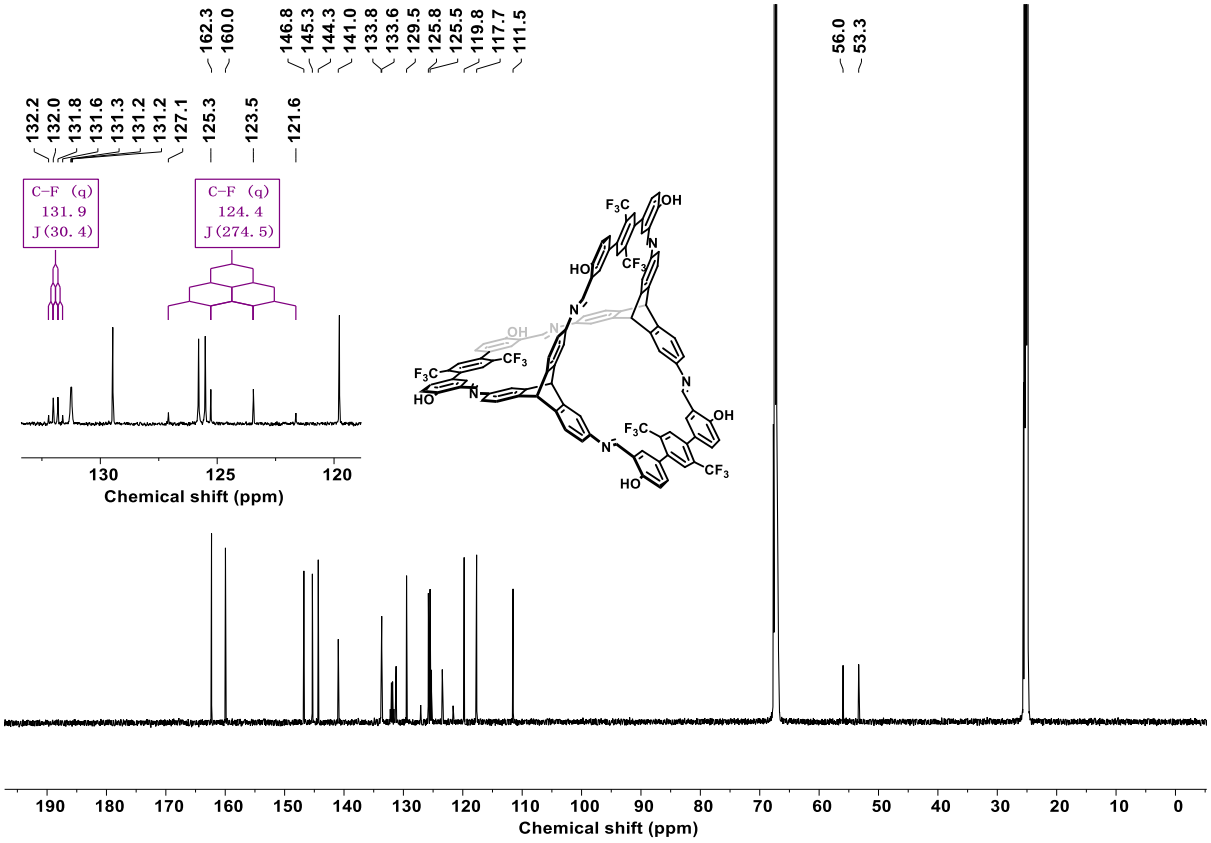

Figure 83. ^{13}C NMR spectrum of **cage-CF$_3$** (THF-d_8, 151 MHz).

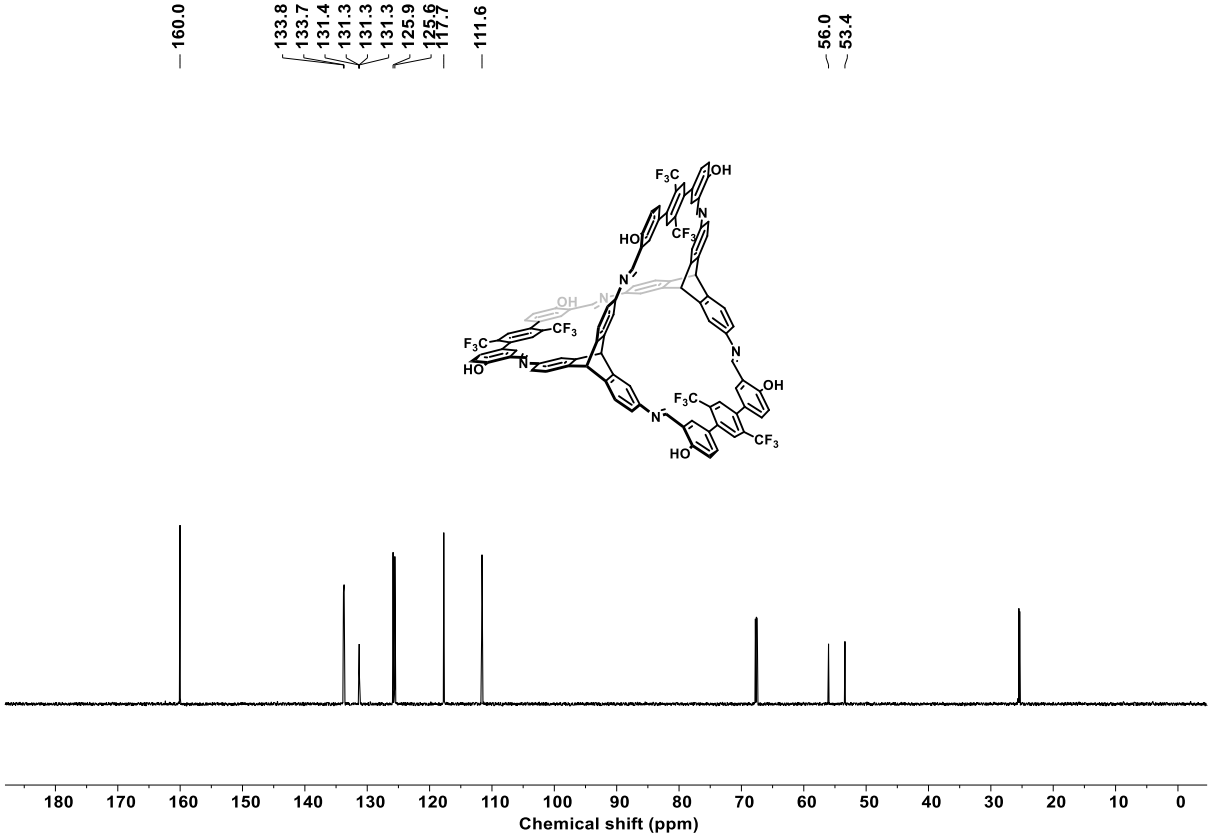

Figure 84. ^{13}C-DEPT135 NMR spectrum of **cage-CF$_3$** (THF-d_8, 151 MHz).

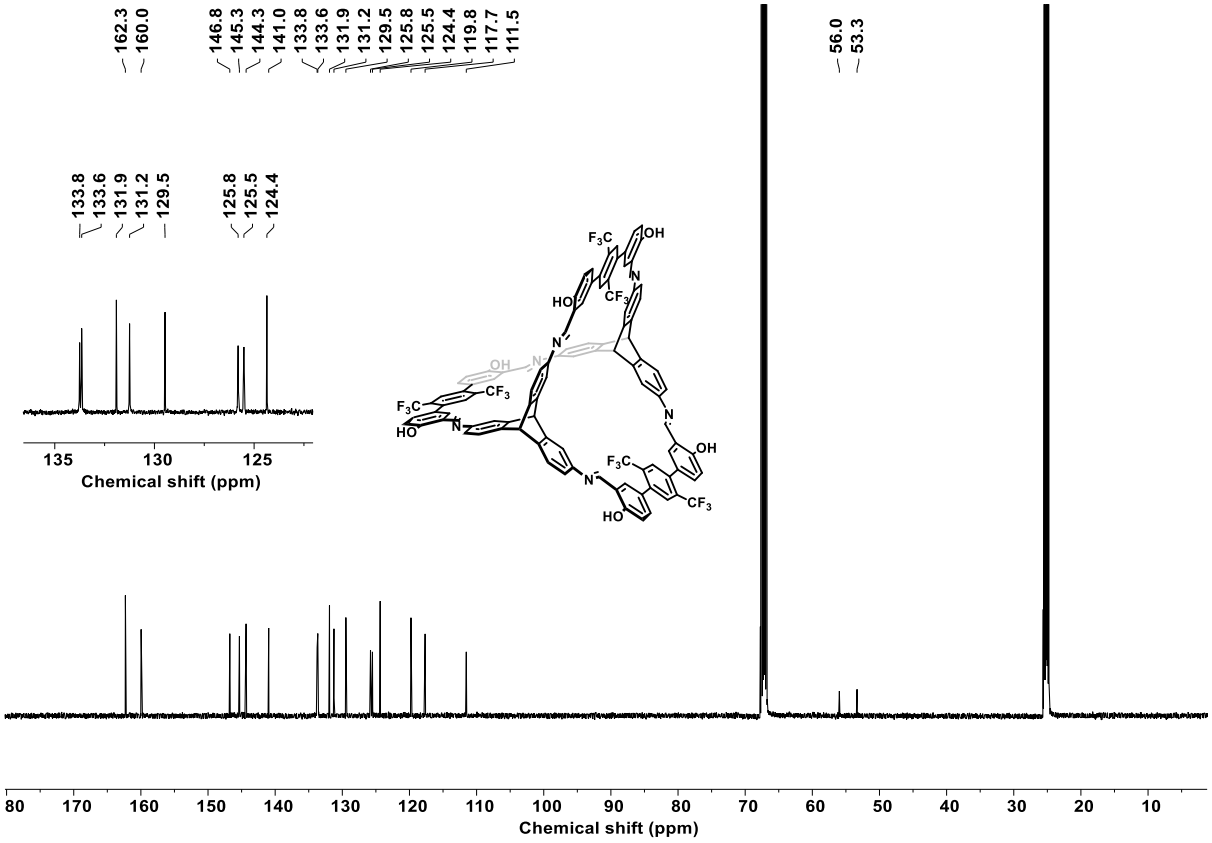

Figure 85. ^{13}C {^{1}H, ^{19}F} NMR spectrum of **cage-CF$_3$** (THF-d_8, 126 MHz).

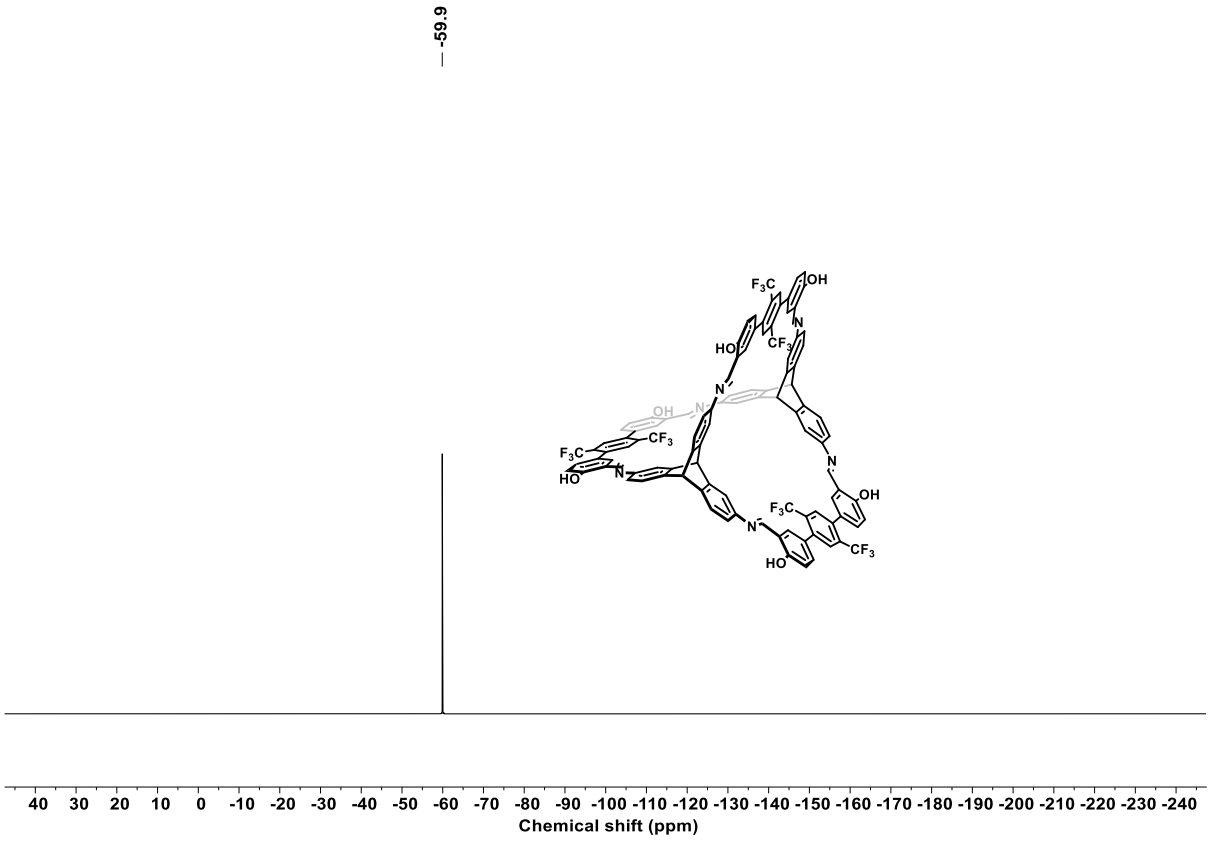

Figure 86. ^{19}F NMR spectrum of **cage-CF$_3$** (THF-d_8, 471 MHz).

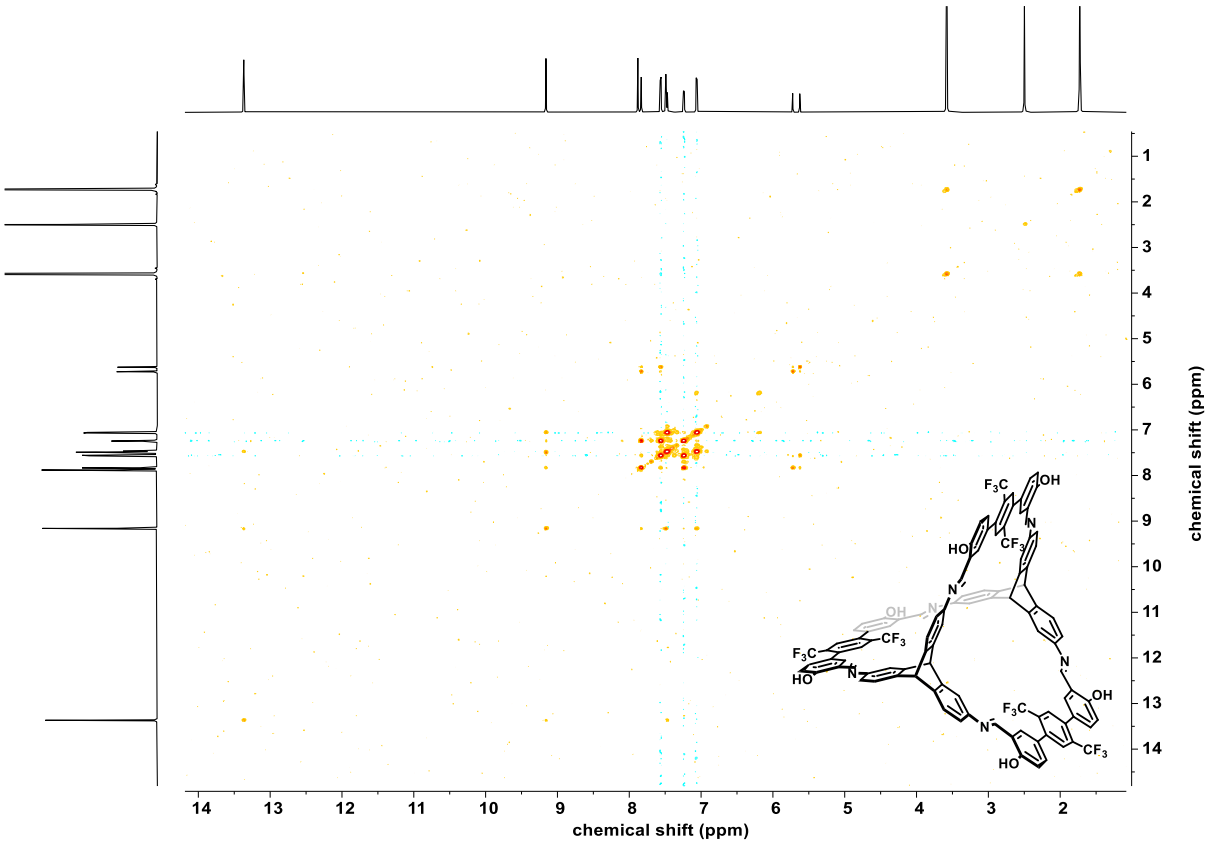

Figure 87. ^{1}H-^{1}H COSY NMR spectrum of **cage-CF$_3$** (THF-d_8, 600 MHz, 600 MHz).

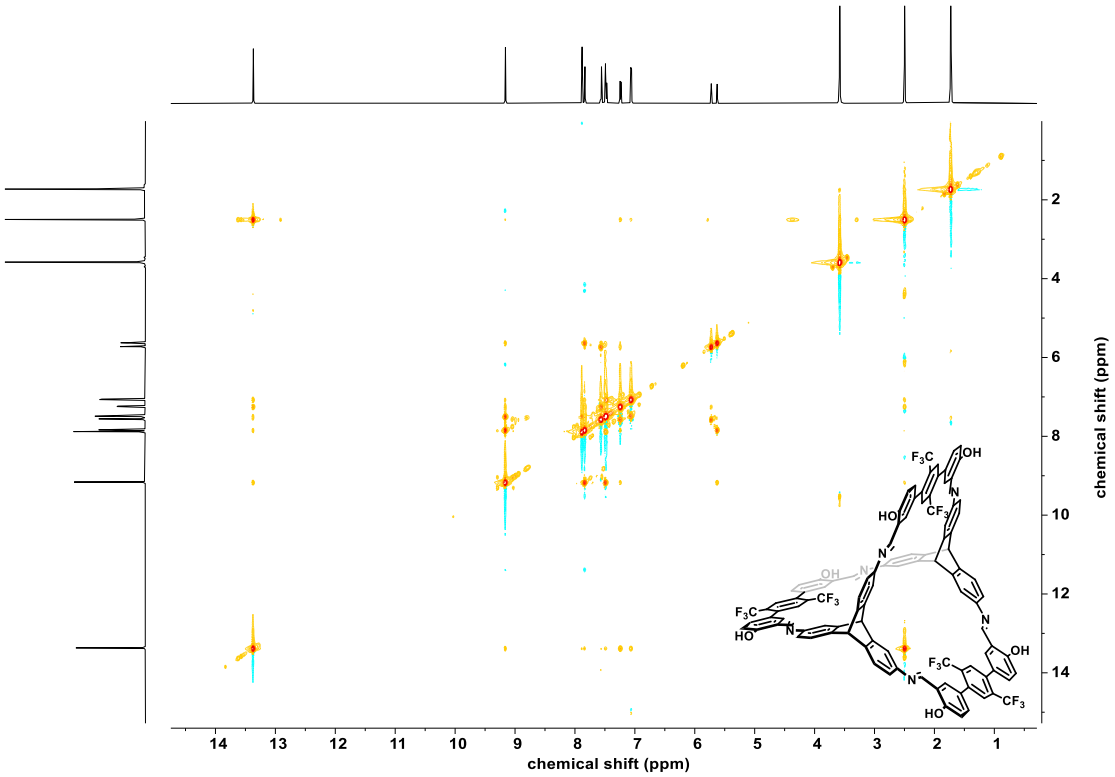

Figure 88. ^{1}H-^{1}H NOSY NMR spectrum of **cage-CF$_3$** (THF-d_8, 600 MHz, 600 MHz).

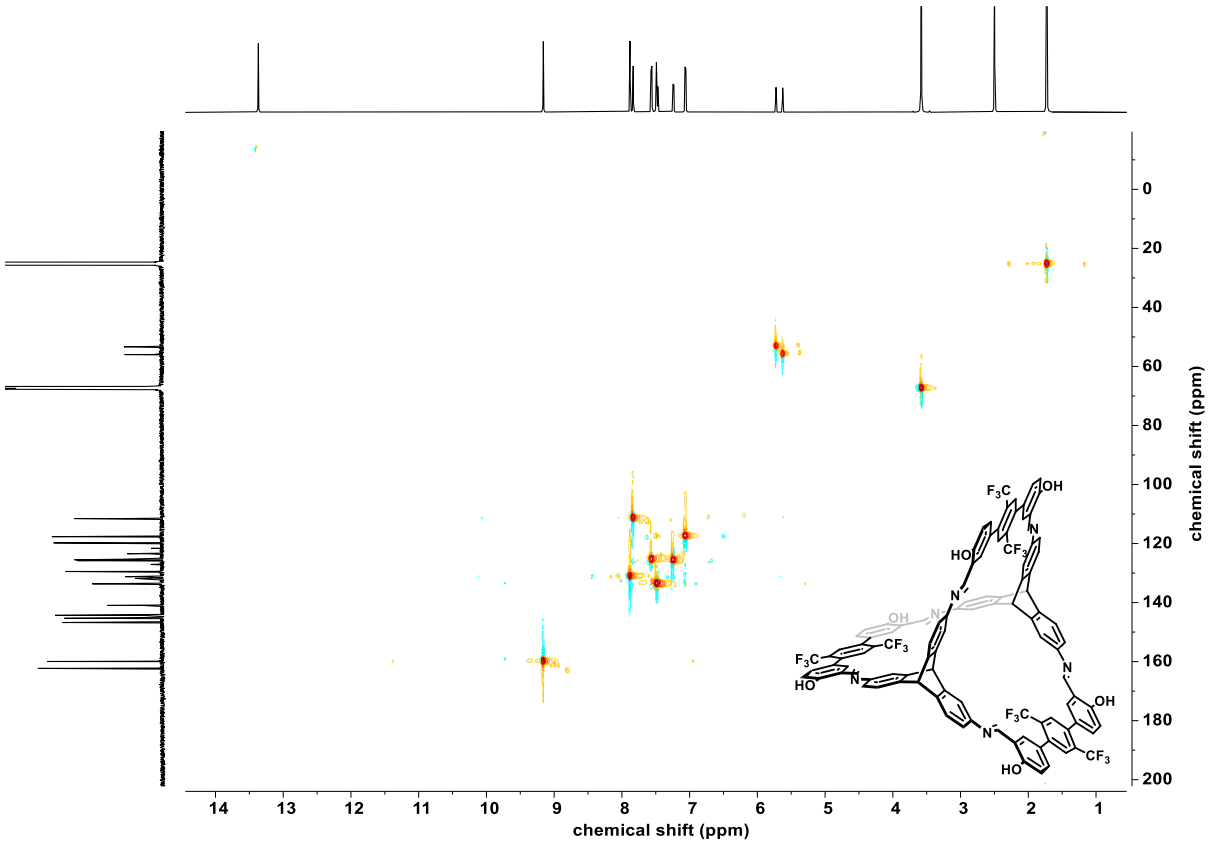

Figure 89. ^{1}H-^{13}C HSQC NMR spectrum of **cage-CF$_3$** (THF-d_8, 600 MHz, 151 MHz).

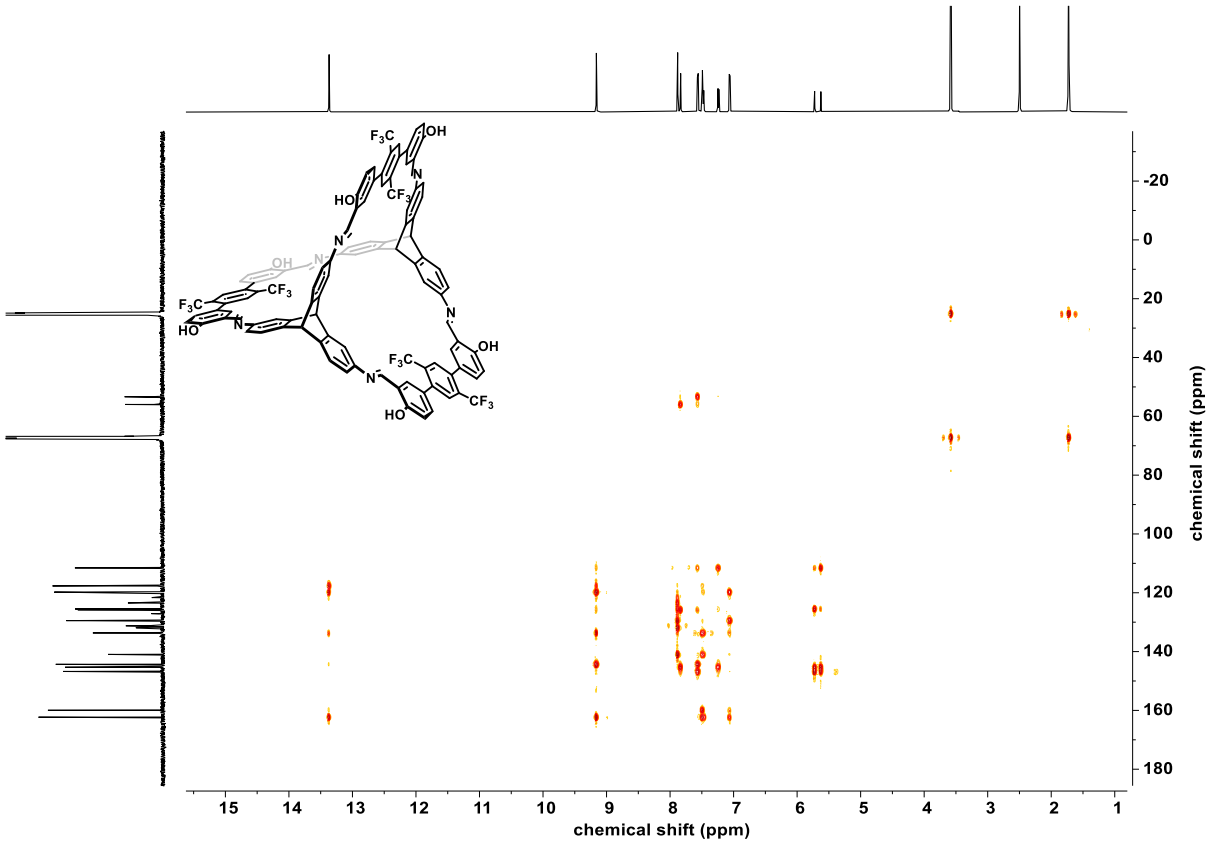

Figure 90. ^{1}H-^{13}C HMBC NMR spectrum of **cage-CF$_3$** (THF-d_8, 600 MHz, 151 MHz).

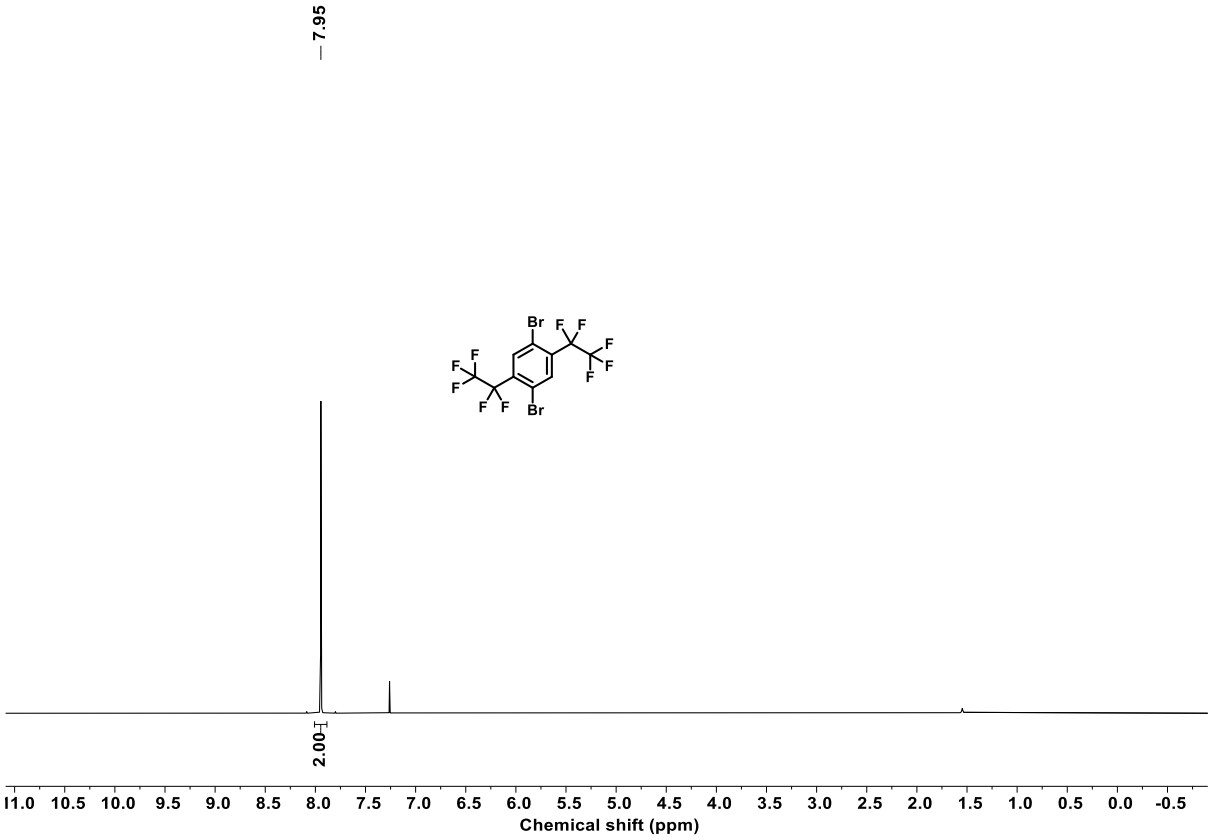

Figure 91. ^{1}H NMR spectrum of **65** ($CDCl_3$, 600 MHz).

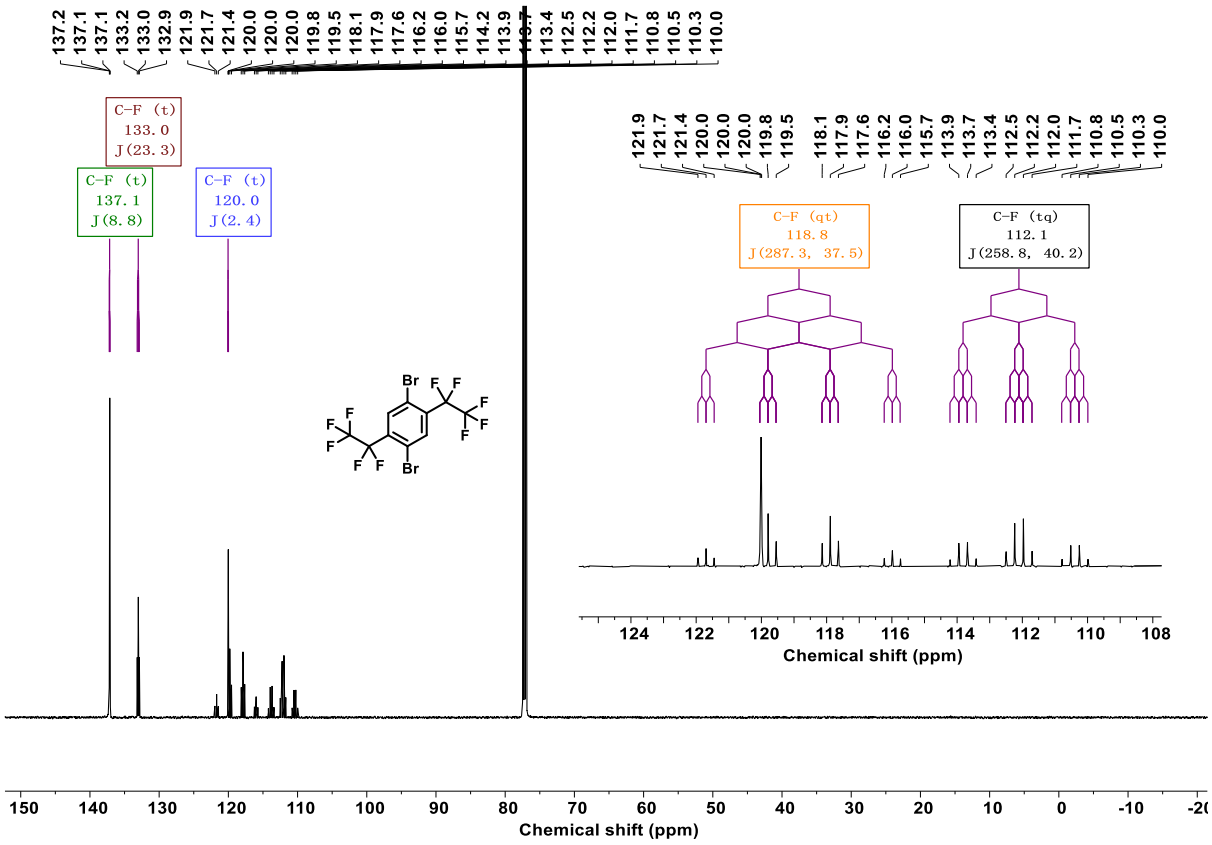

Figure 92. ^{13}C NMR spectrum of **65** ($CDCl_3$, 151 MHz).

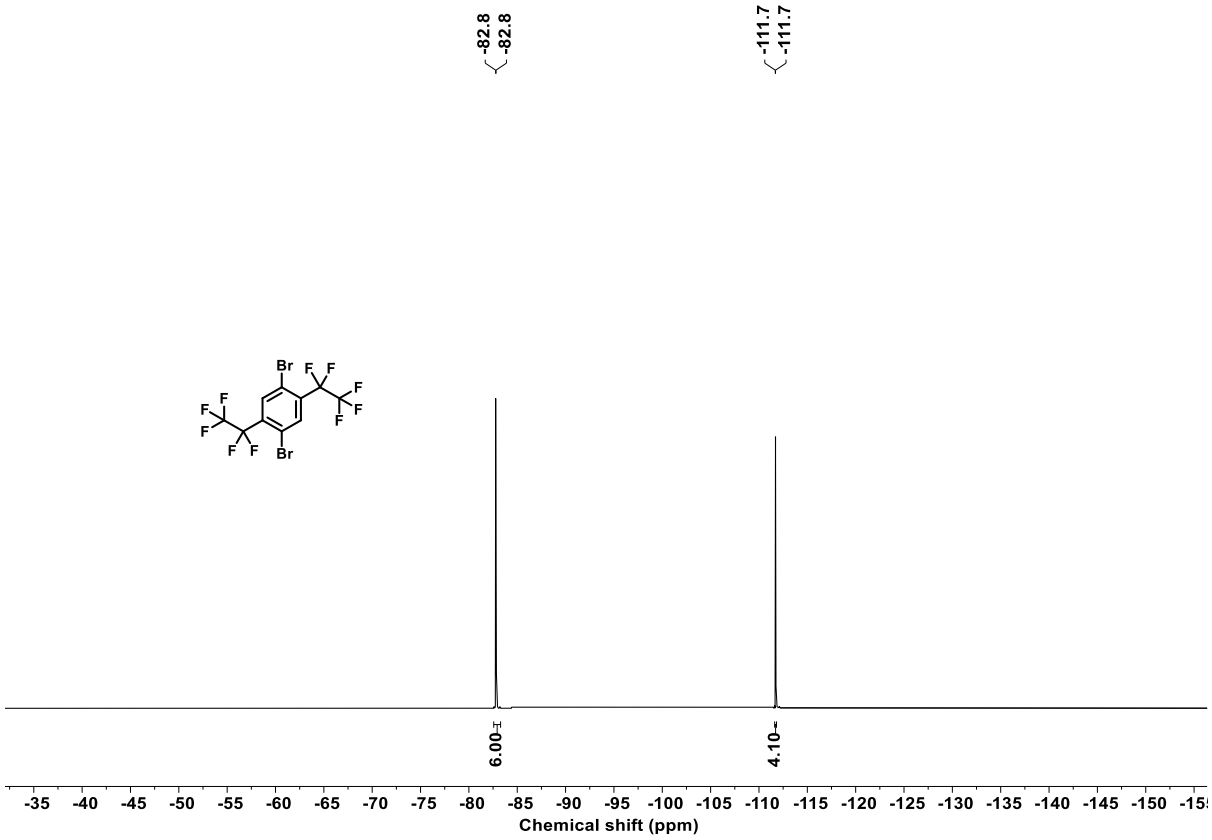

Figure 93. ^{19}F NMR spectrum of **65** ($CDCl_3$, 471 MHz).

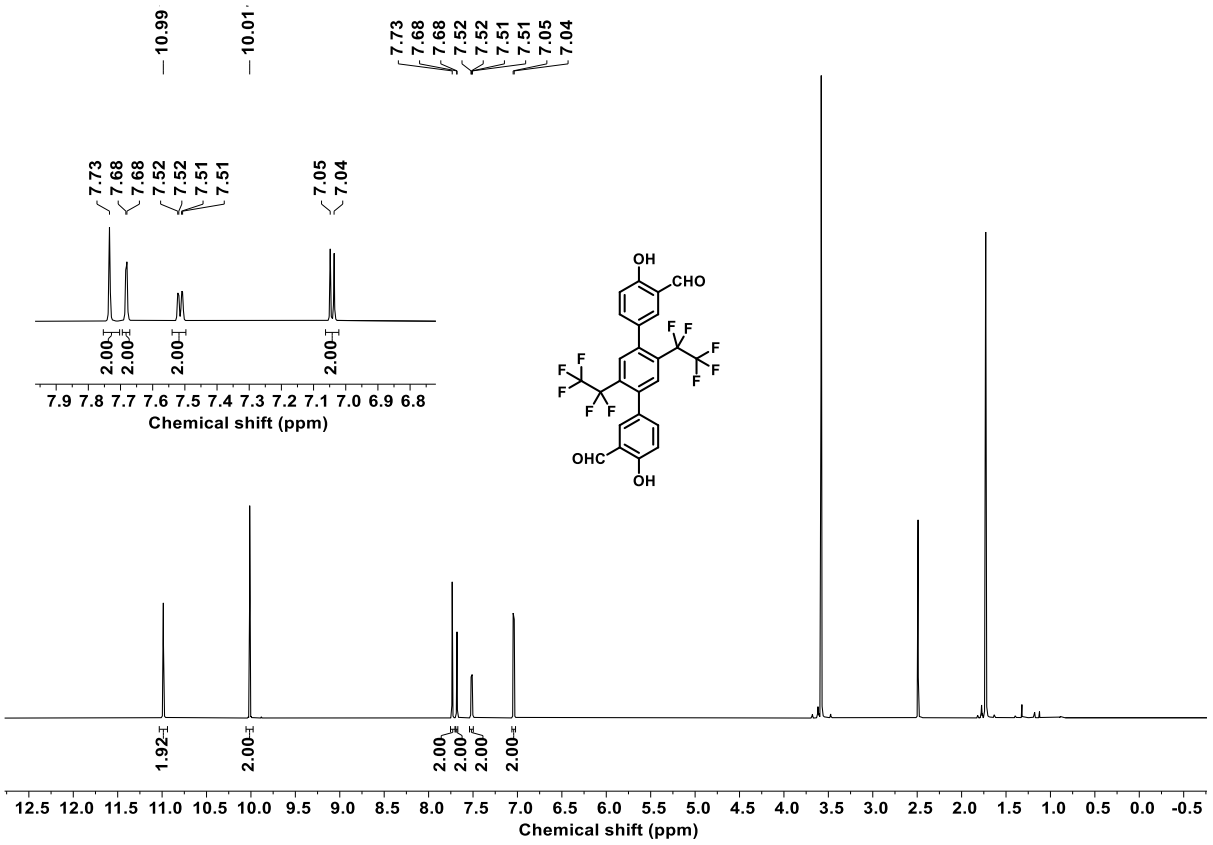

Figure 94. ^{1}H NMR spectrum of **70** (THF-d_8, 700 MHz).

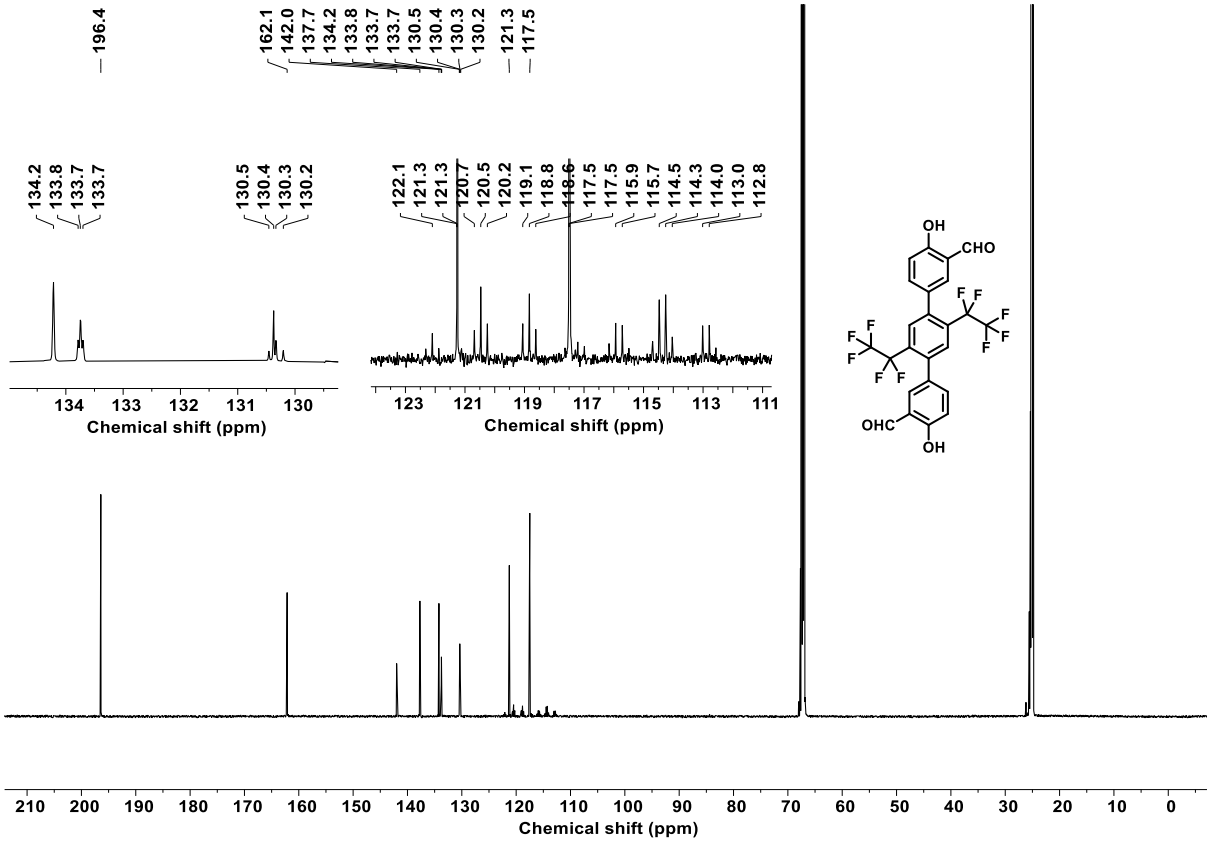

Figure 95. ^{13}C NMR spectrum of **70** (THF-d_8, 176 MHz).

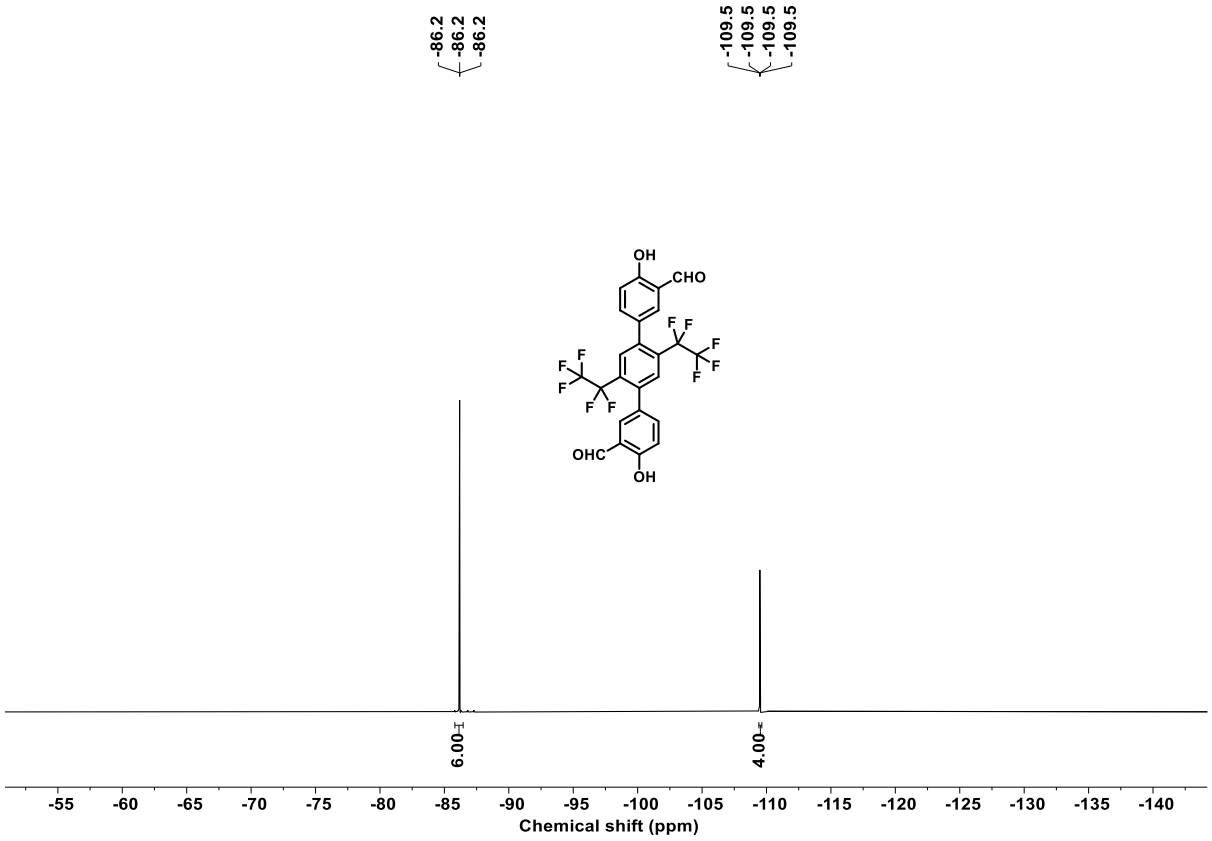

Figure 96. ^{19}F NMR spectrum of **70** (THF-d_8, 283 MHz).

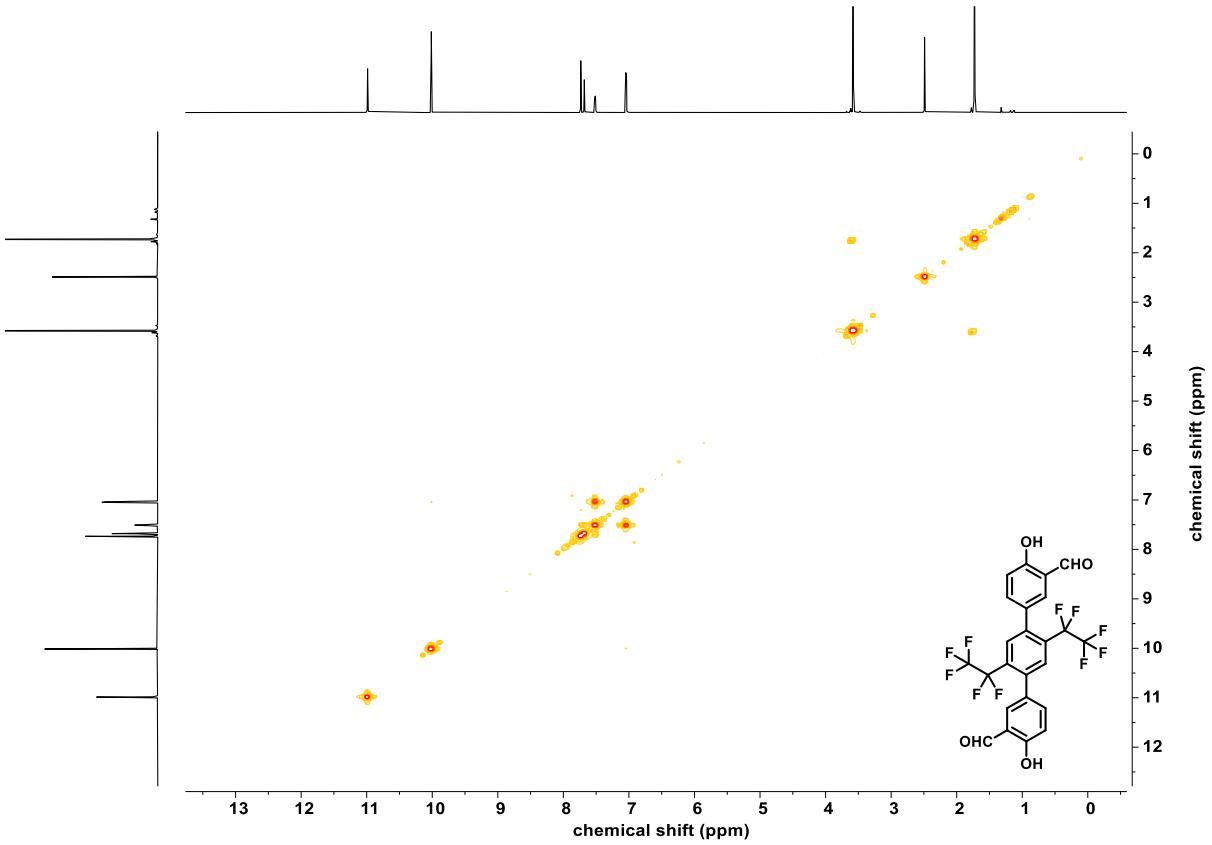

Figure 97. ^{1}H-^{1}H COSY NMR spectrum of **70** (THF-d_8, 700 MHz, 700 MHz).

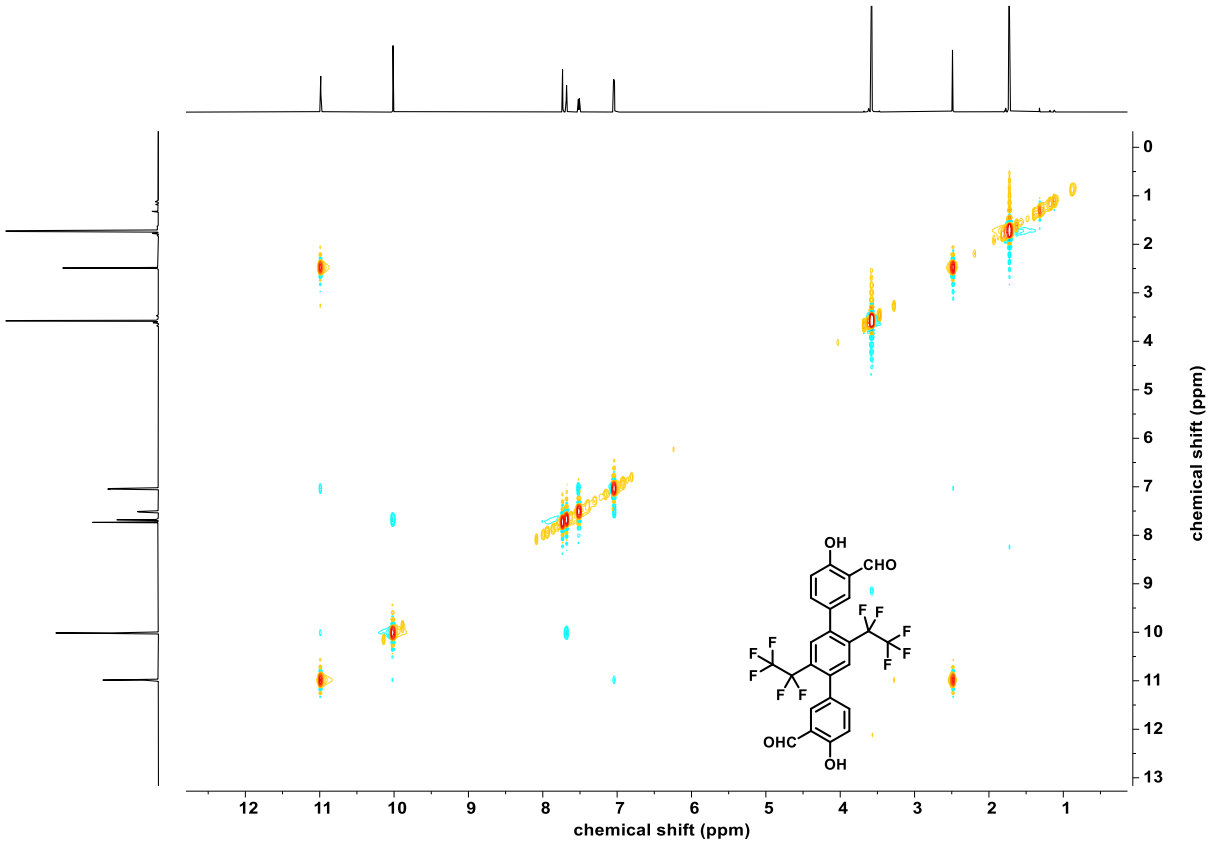

Figure 98. ^{1}H-^{1}H NOSY NMR spectrum of **70** (THF-d_8, 700 MHz, 700 MHz).

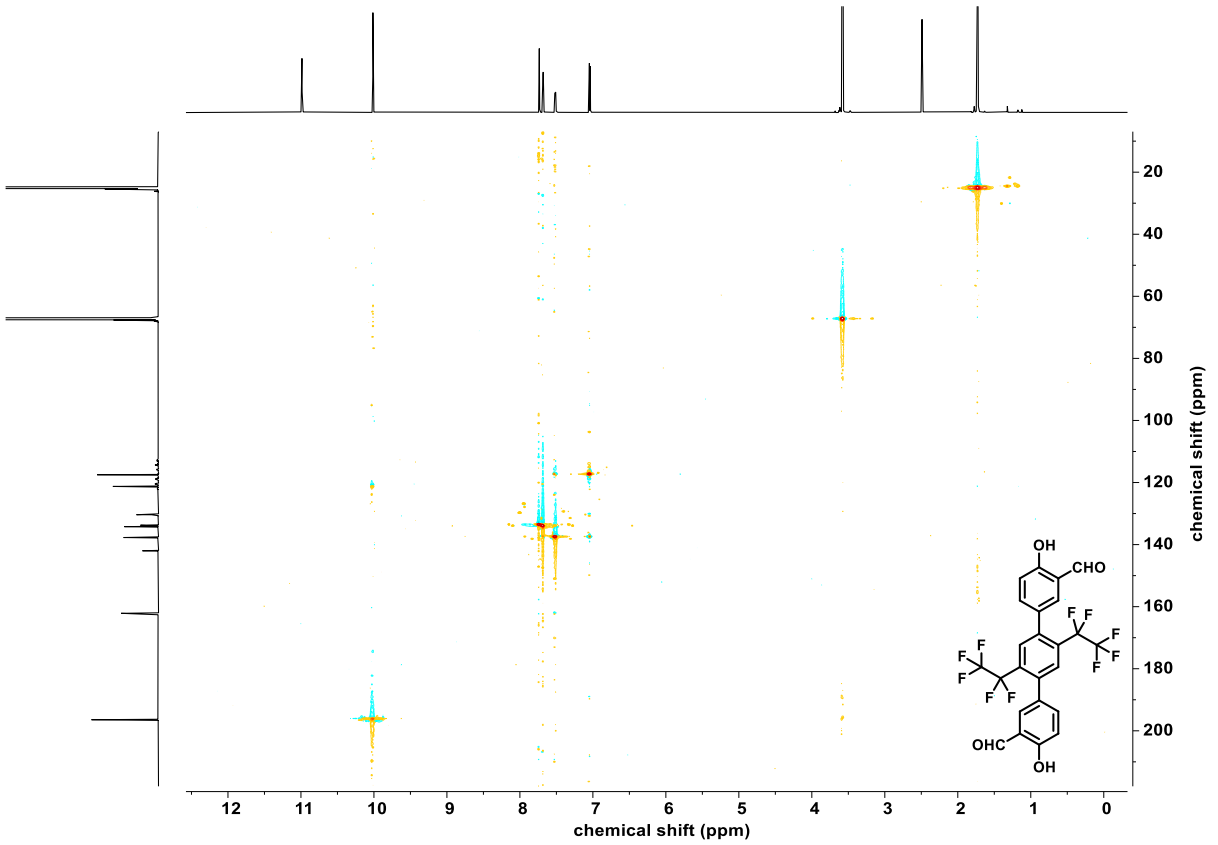

Figure 99. ^{1}H-^{13}C HSQC NMR spectrum of **70** (THF-d_8, 700 MHz, 176 MHz).

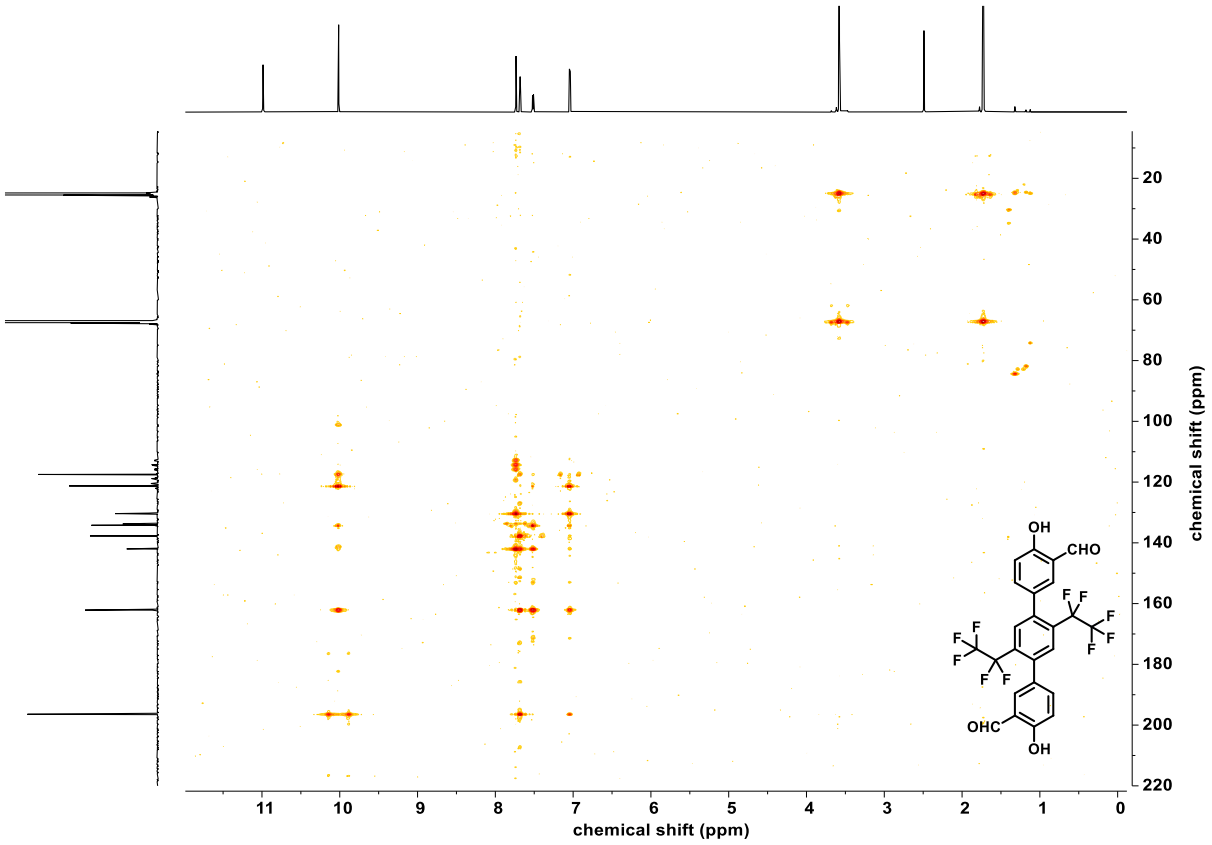

Figure 100. ^{1}H-^{13}C HMBC NMR spectrum of **70** (THF-d_8, 700 MHz, 176 MHz).

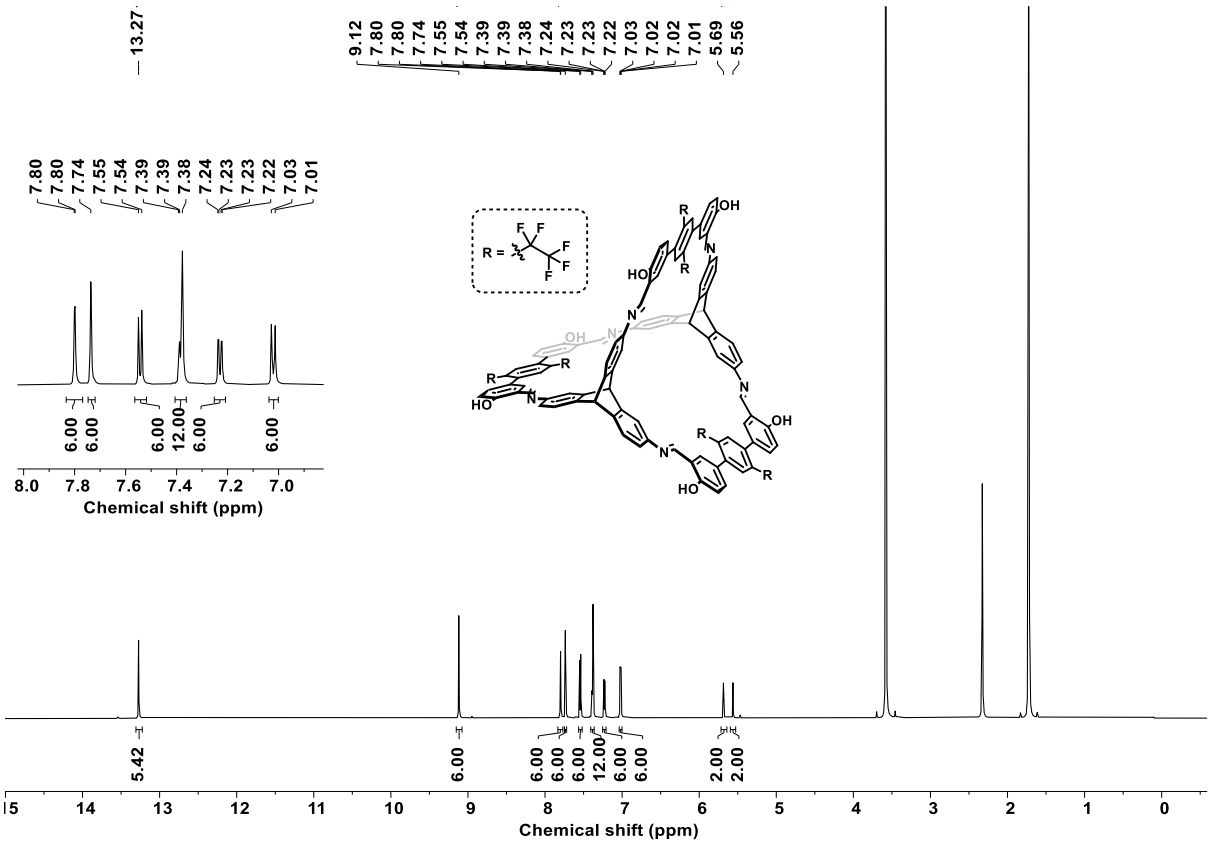

Figure 101. ^{1}H NMR spectrum of **cage-C_2F_5** (THF-d_8, 600 MHz).

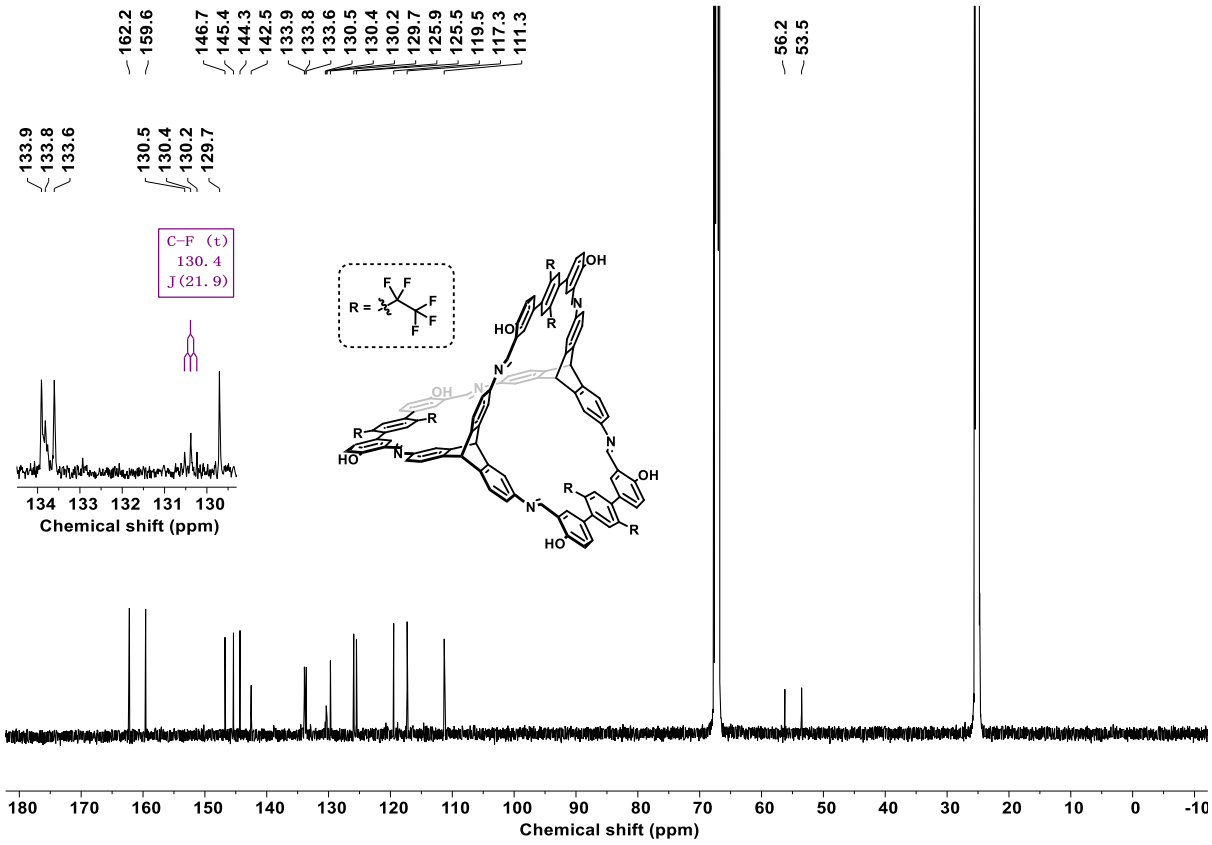

Figure 102. ^{13}C NMR spectrum of **cage-C_2F_5** (THF-d_8, 151 MHz).

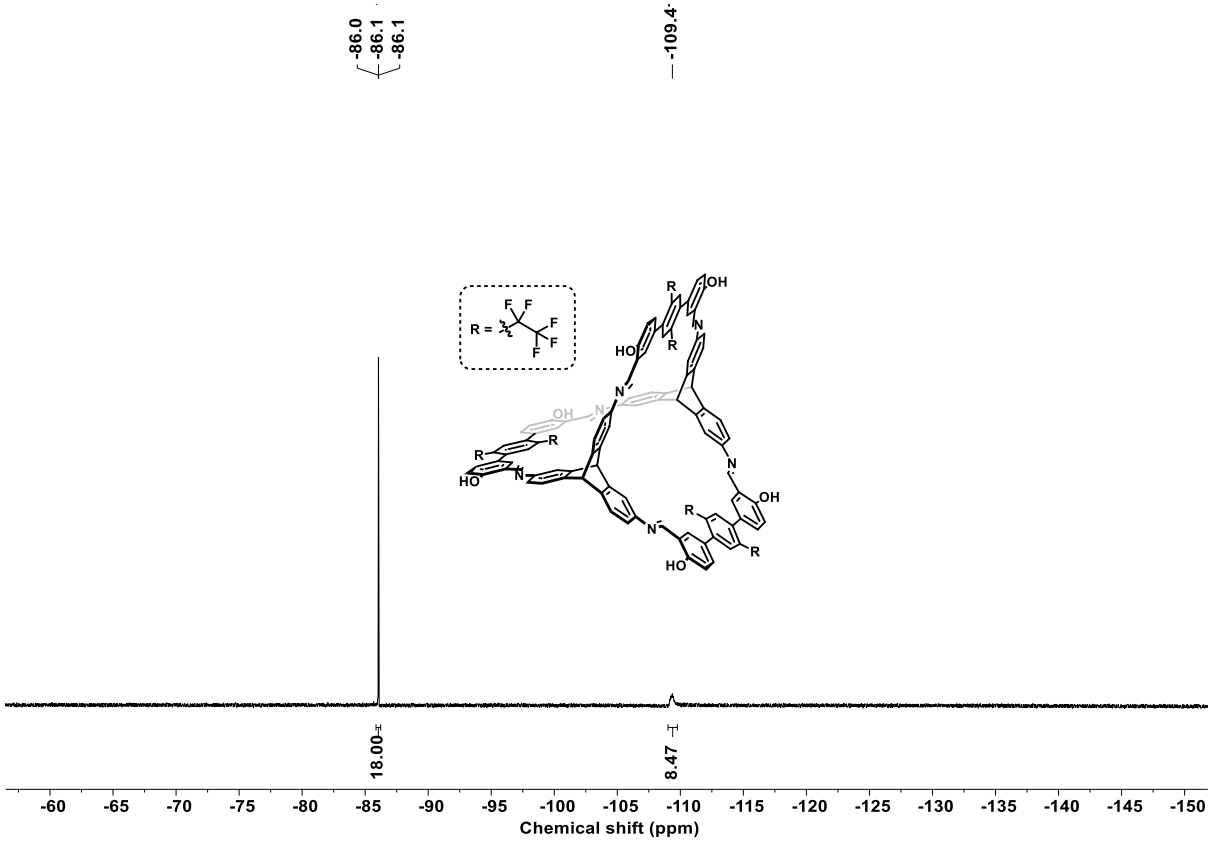

Figure 103. ^{19}F NMR spectrum of **cage-C_2F_5** (THF-d_8, 283 MHz).

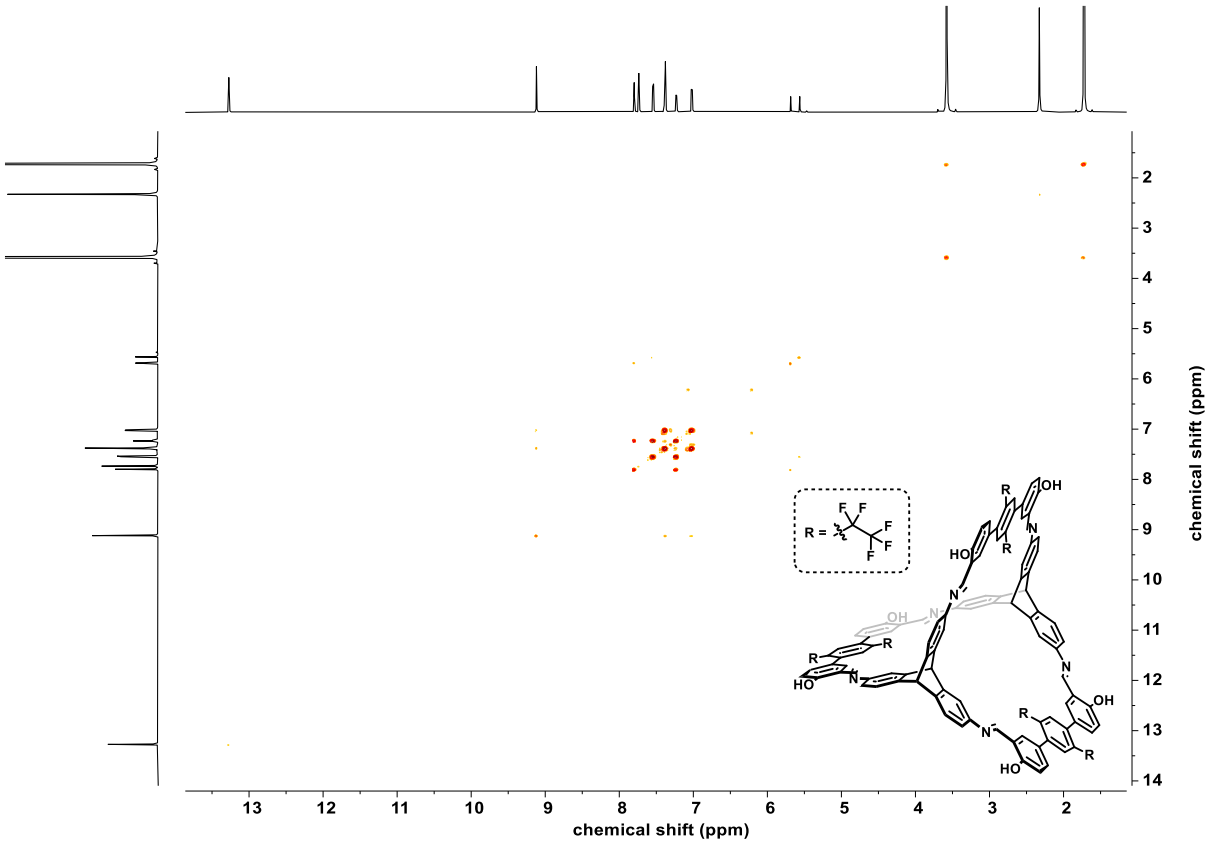

Figure 104. ^{1}H-^{1}H COSY NMR spectrum of **cage-C_2F_5** (THF-d_8, 600 MHz, 600 MHz).

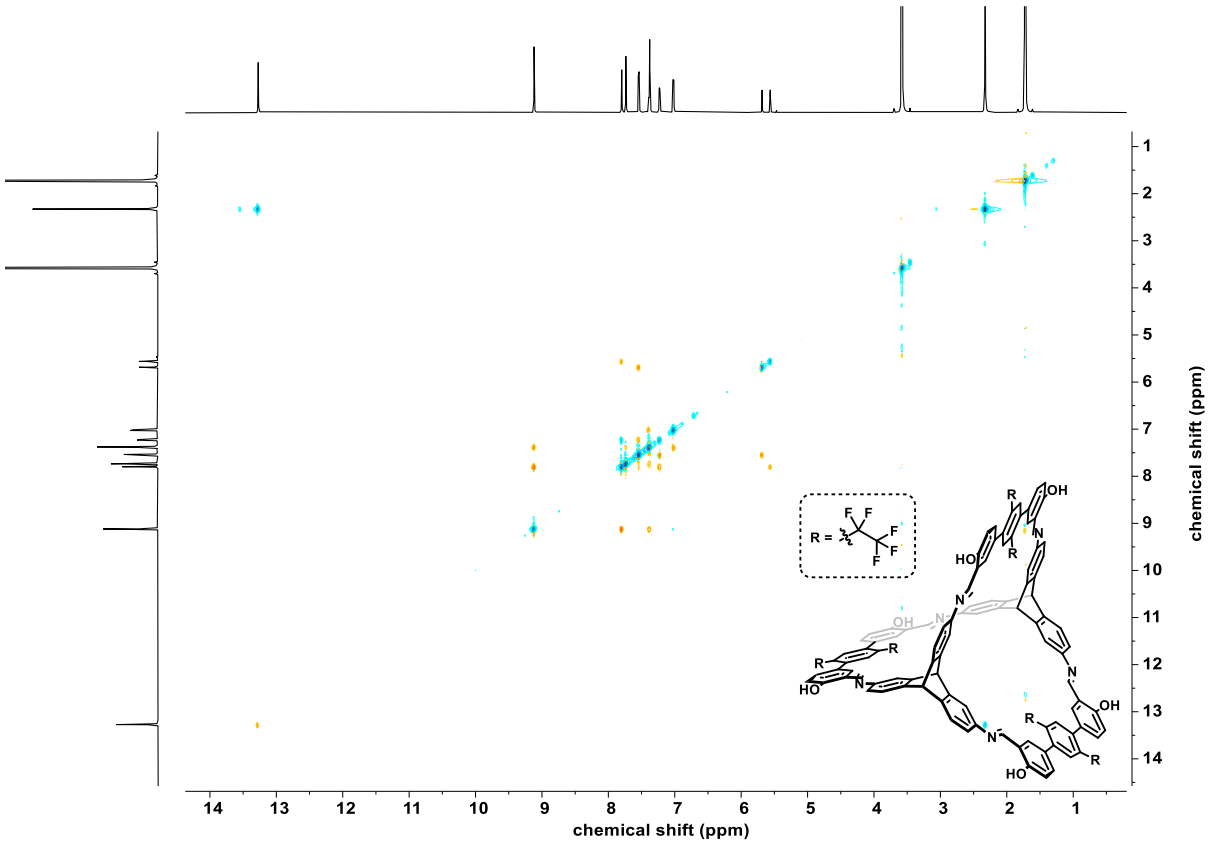

Figure 105. ^{1}H-^{1}H ROSY NMR spectrum of **cage-C_2F_5** (THF-d_8, 600 MHz, 600 MHz).

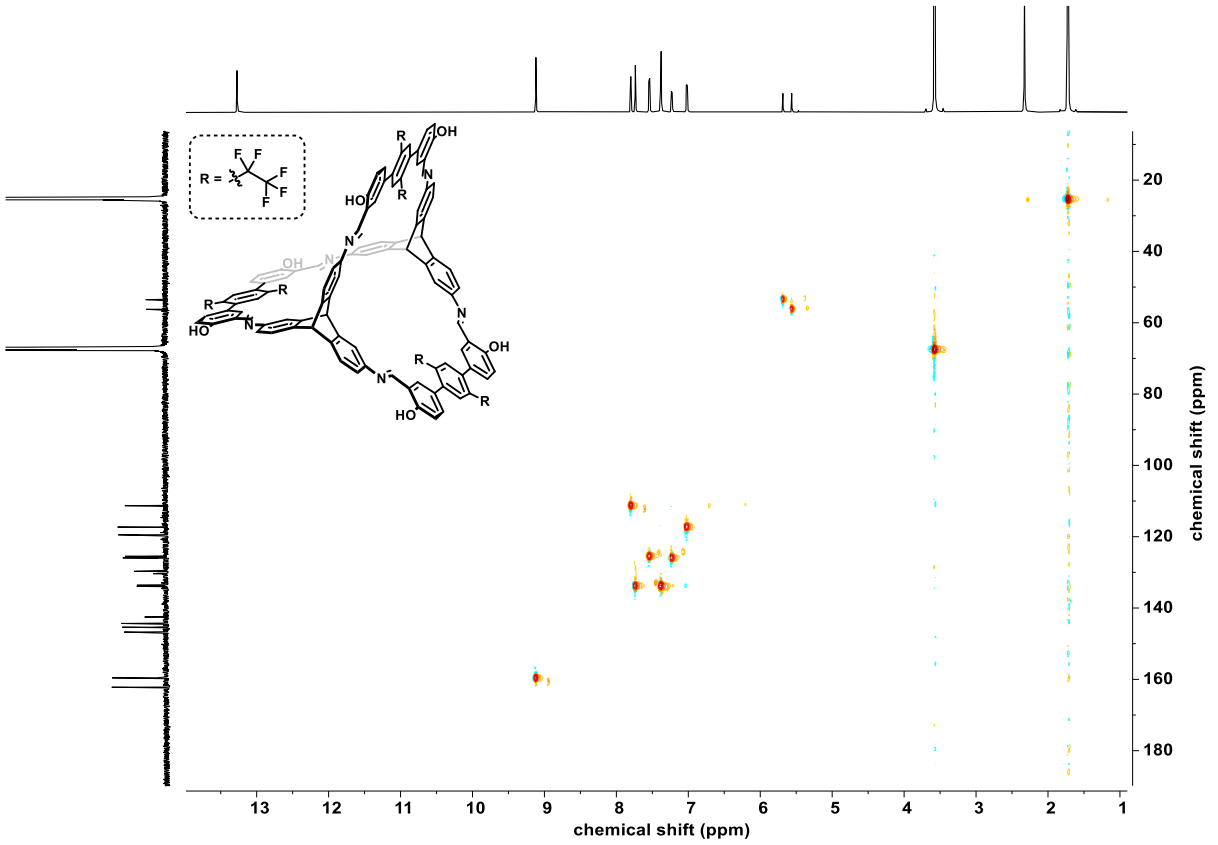

Figure 106. ^{1}H-^{13}C HSQC NMR spectrum of **cage-C_2F_5** (THF-d_8, 600 MHz, 151 MHz).

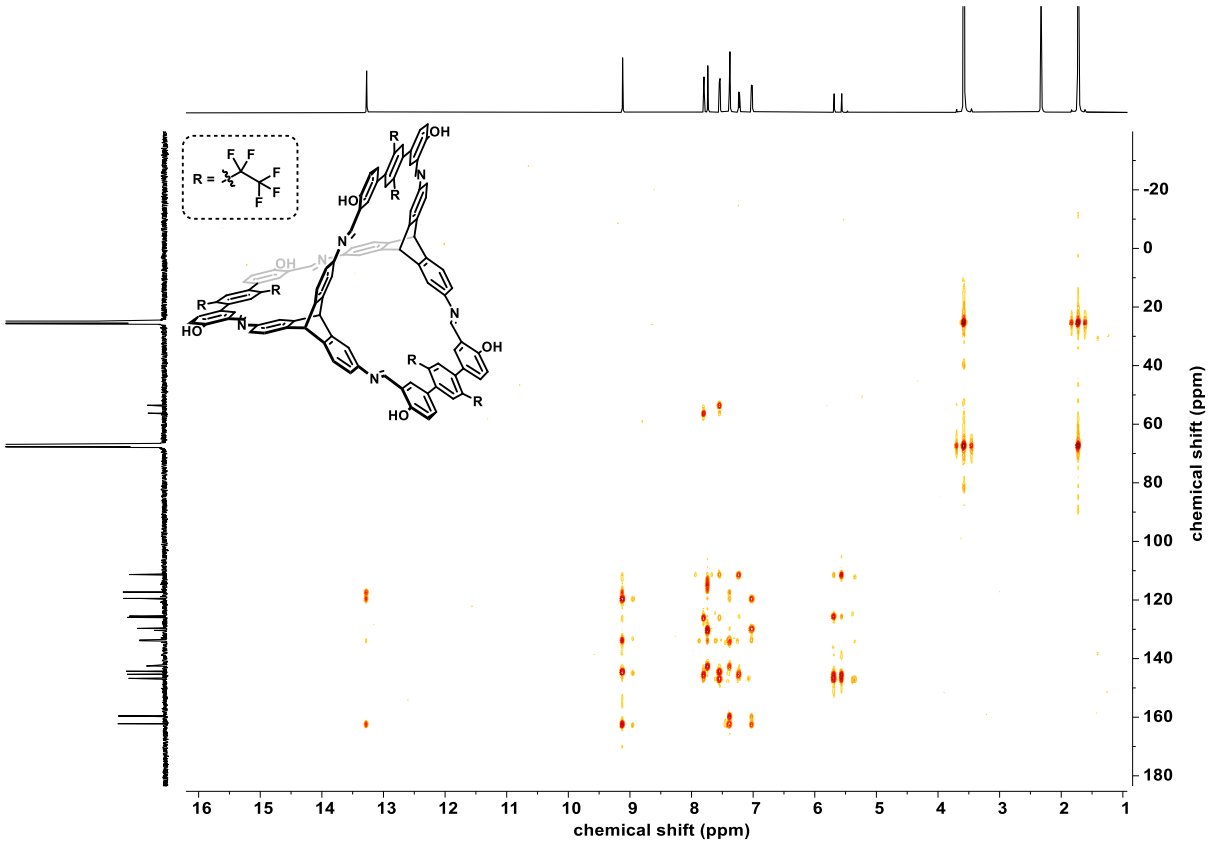

Figure 107. ^{1}H-^{13}C HMBC NMR spectrum of **cage-C_2F_5** (THF-d_8, 600 MHz, 151 MHz).

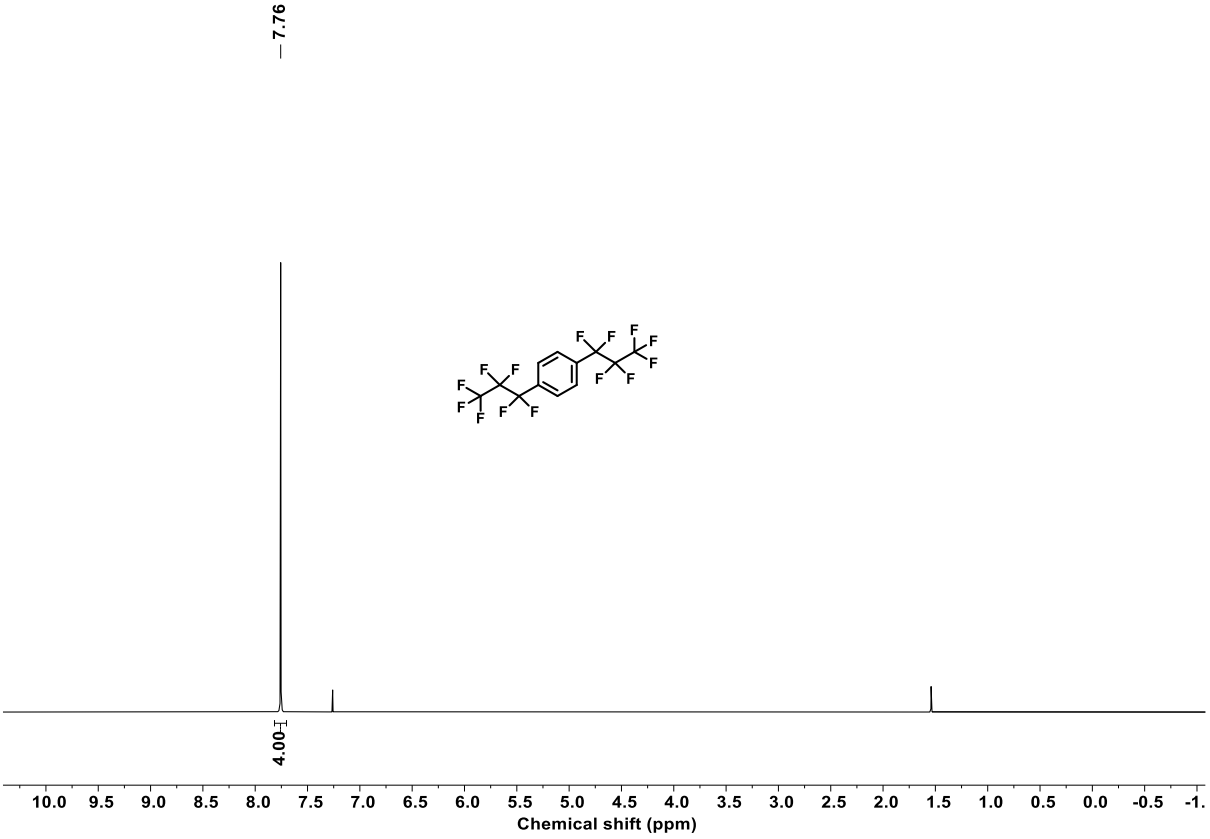

Figure 108. ^{1}H NMR spectrum of **57** ($CDCl_3$, 600 MHz).

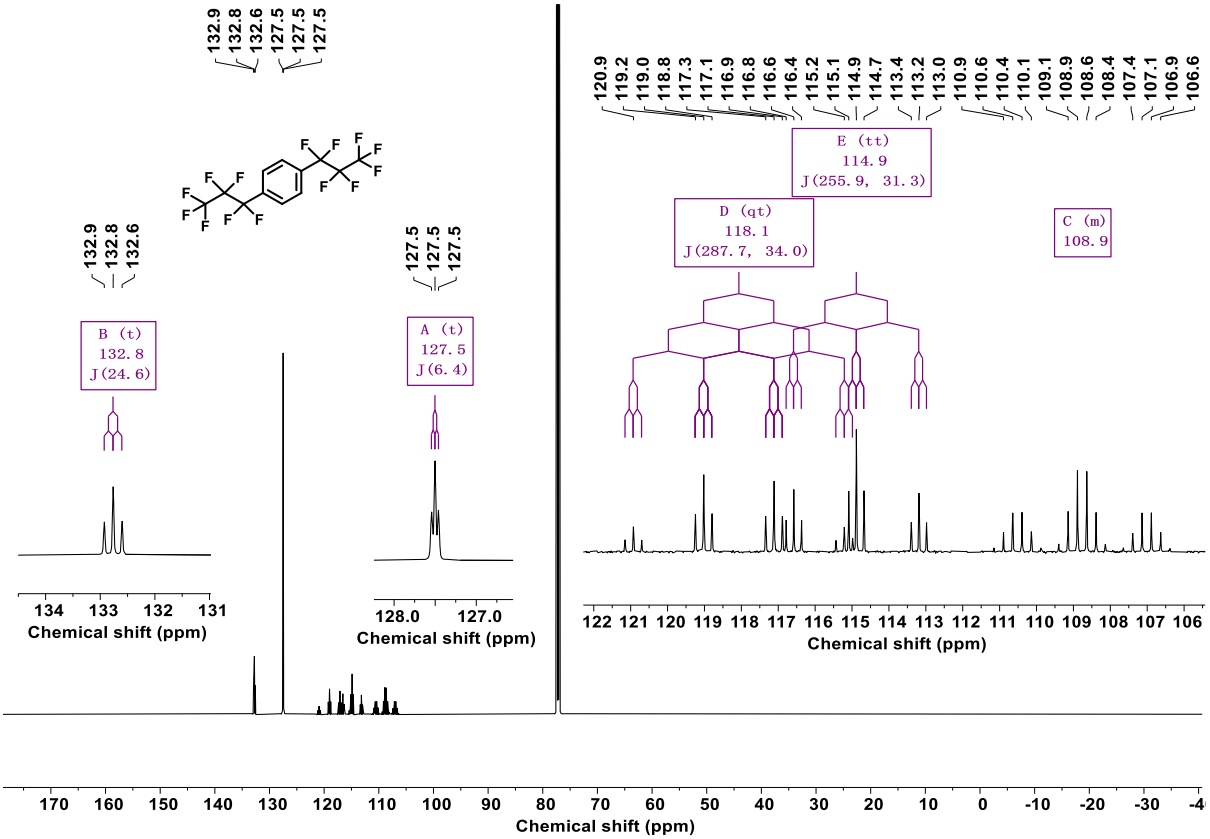

Figure 109. ^{13}C NMR spectrum of **57** ($CDCl_3$, 151 MHz).

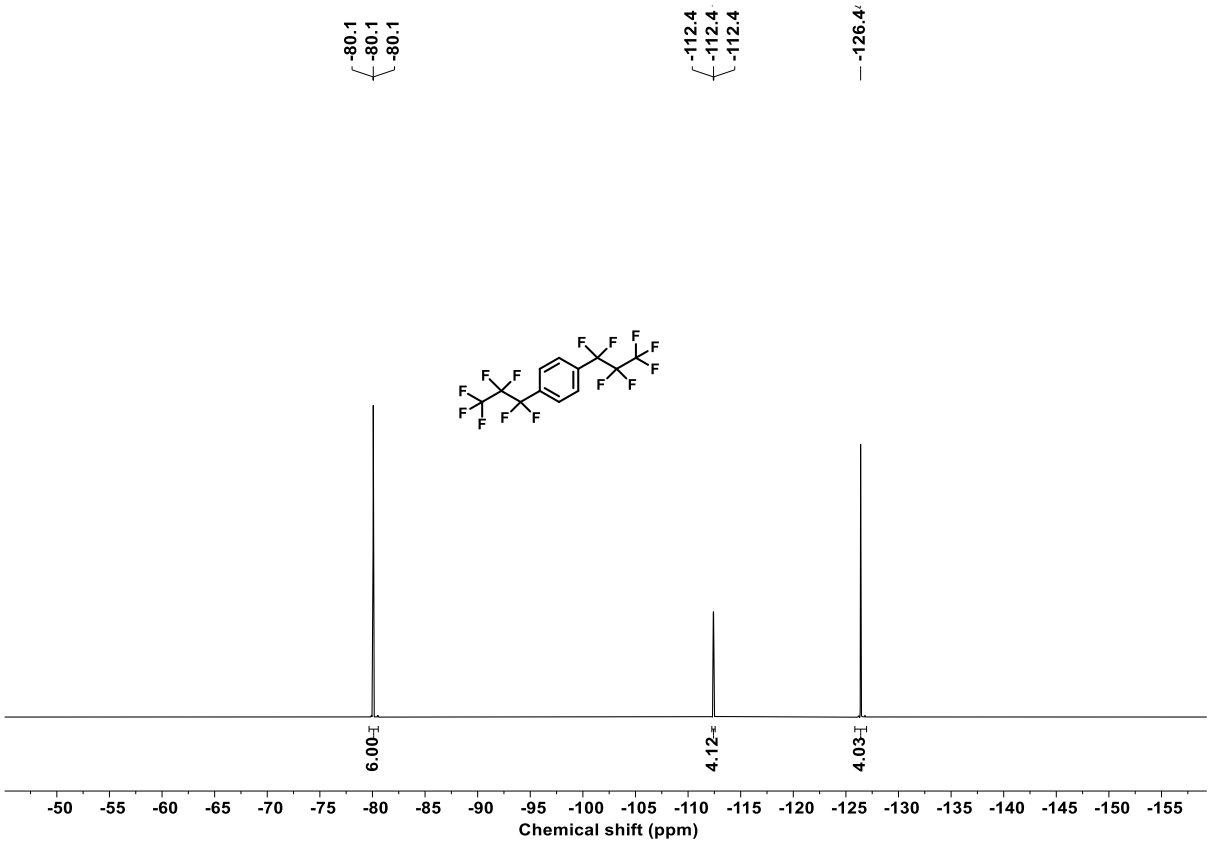

Figure 110. ^{19}F NMR spectrum of **57** ($CDCl_3$, 471 MHz).

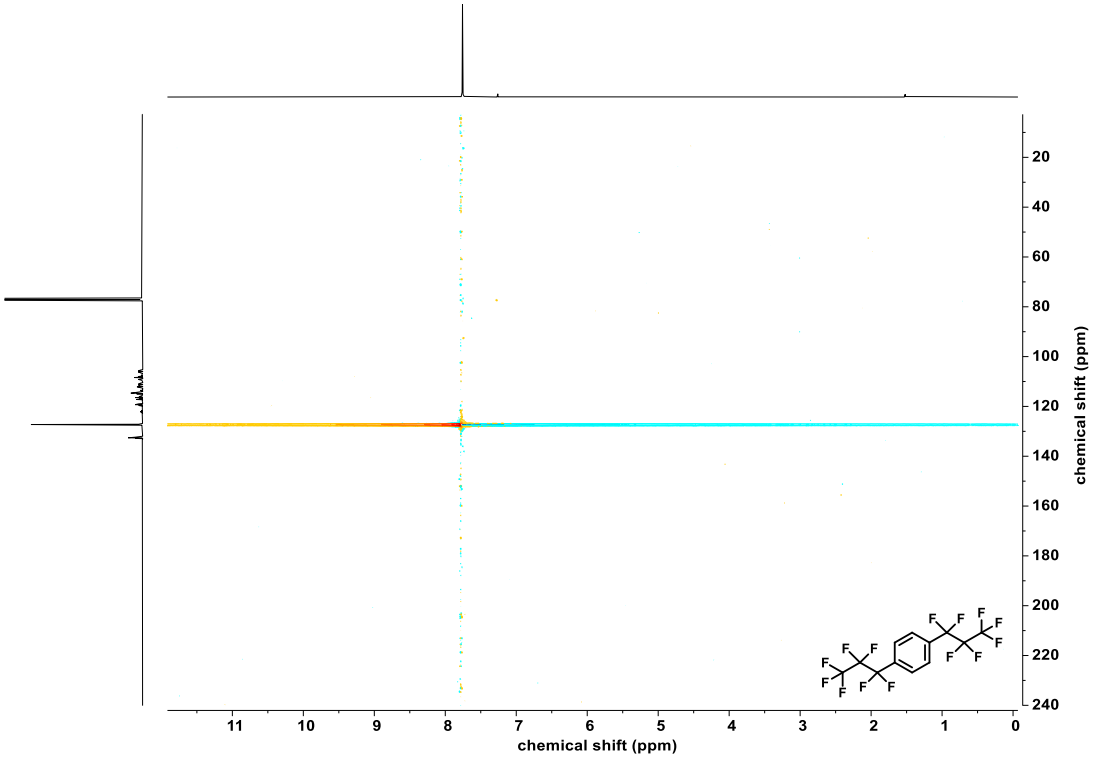

Figure 111. ^{1}H-^{13}C HSQC NMR spectrum of **57** ($CDCl_3$, 400 MHz, 101 MHz).

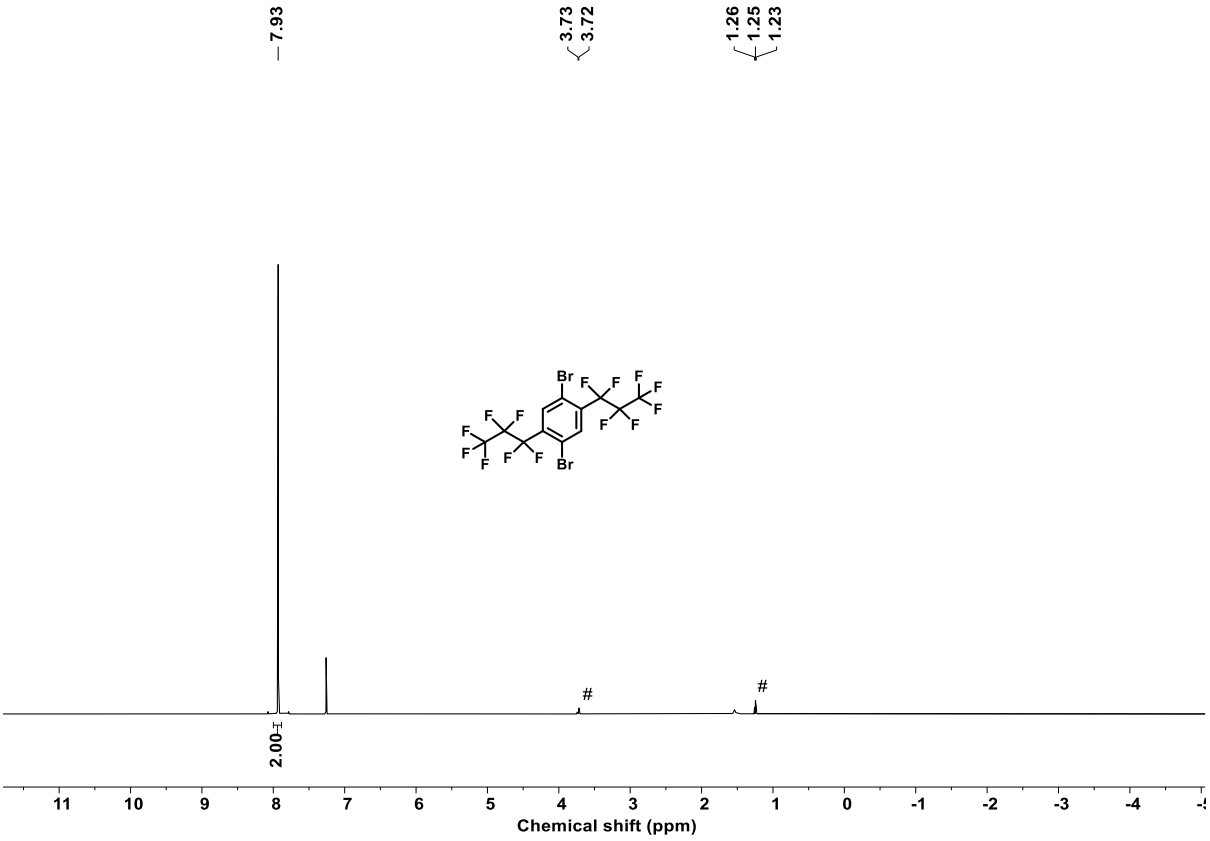

Figure 112. ^{1}H NMR spectrum of **66** ($CDCl_3$, 600 MHz). # = methanol

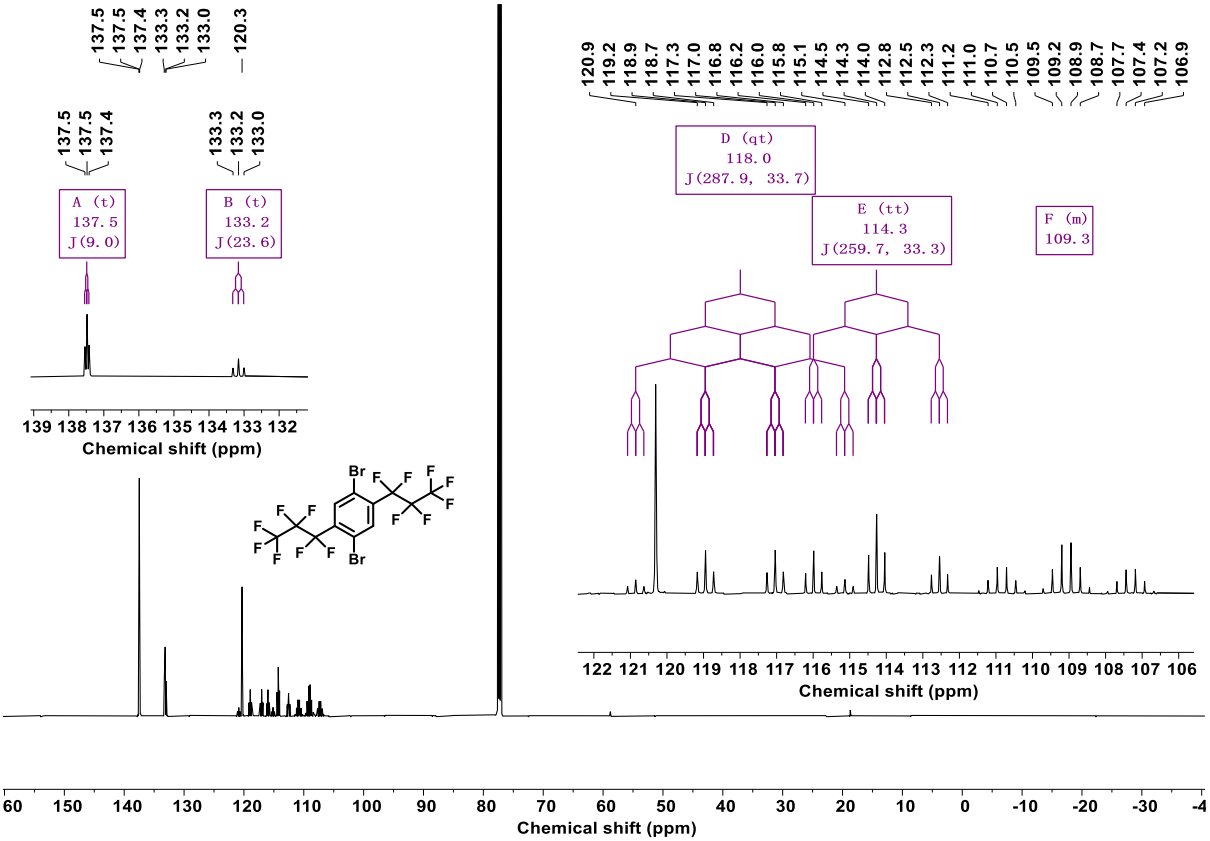

Figure 113. ^{13}C NMR spectrum of **66** ($CDCl_3$, 151 MHz).

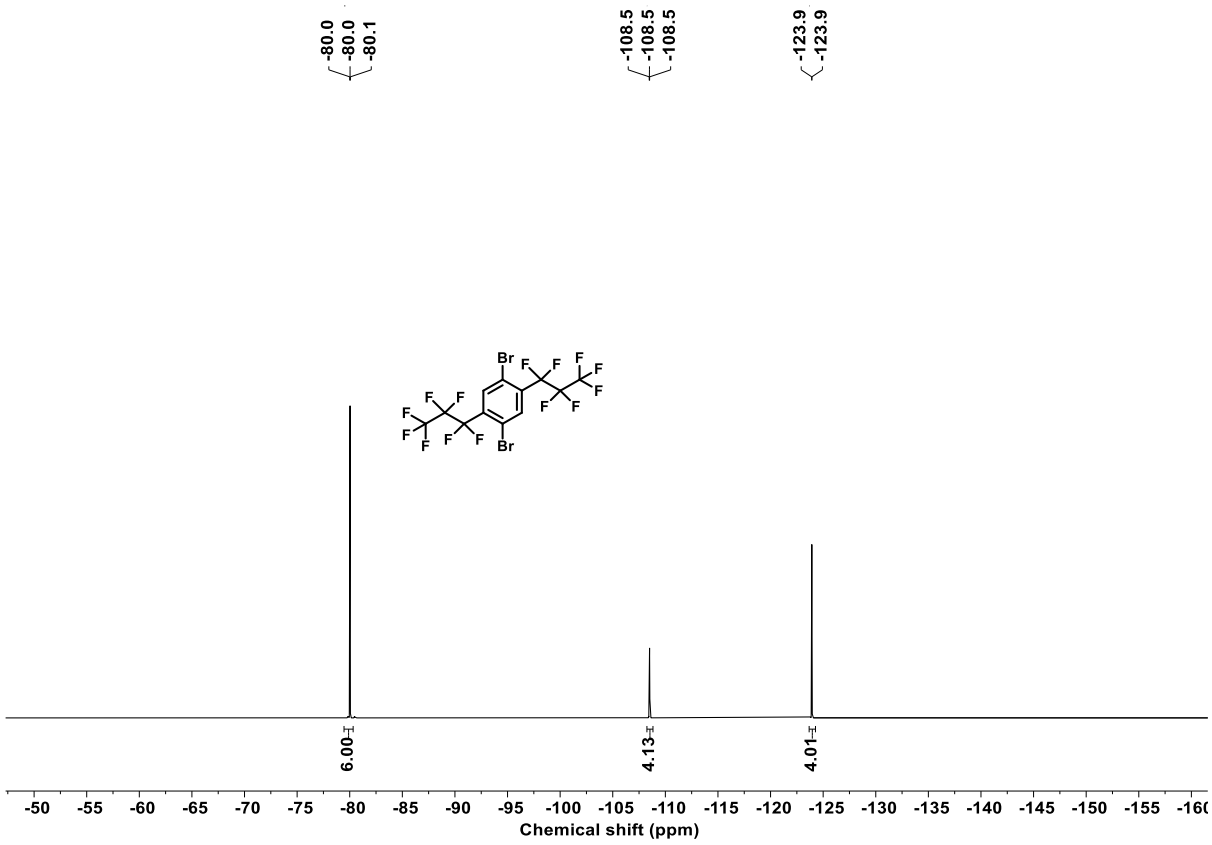

Figure 114. ^{19}F NMR spectrum of **66** ($CDCl_3$, 471 MHz).

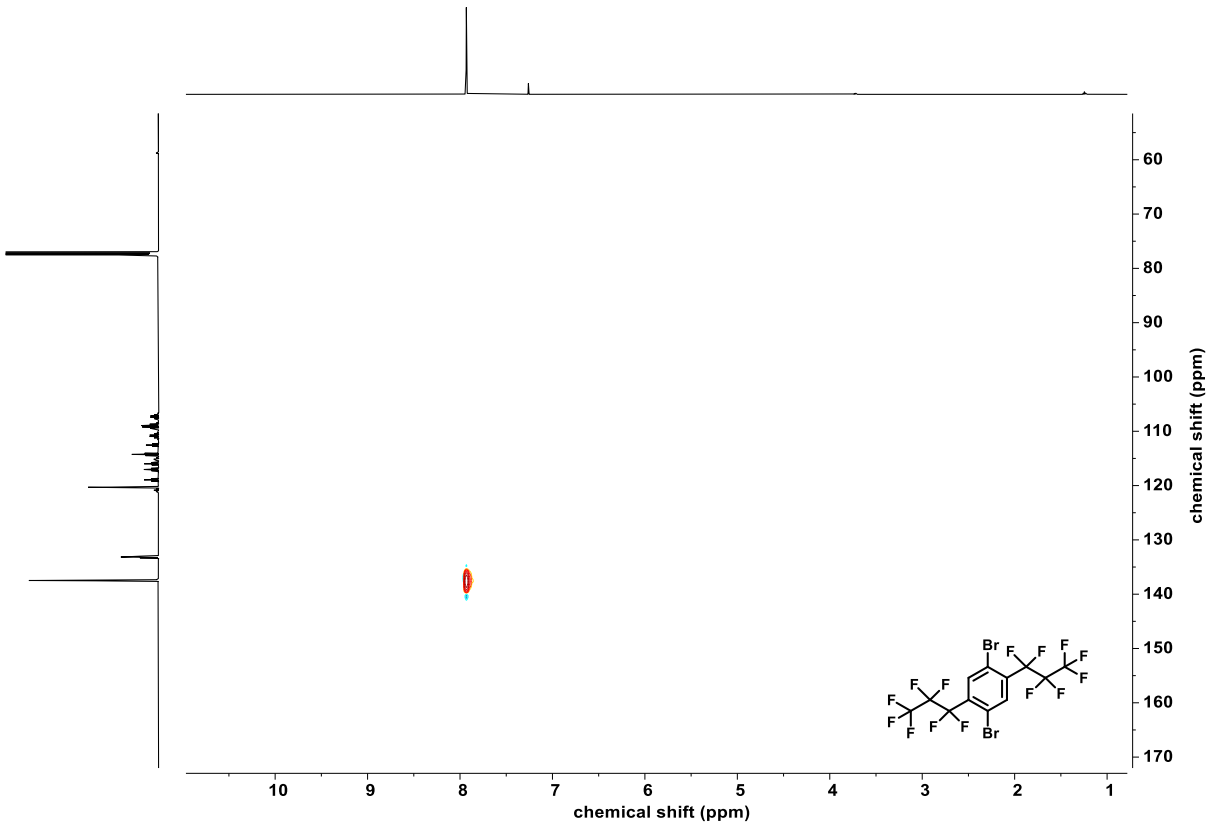

Figure 115. ^{1}H-^{13}C HSQC NMR spectrum of **66** ($CDCl_3$, 500 MHz, 126 MHz).

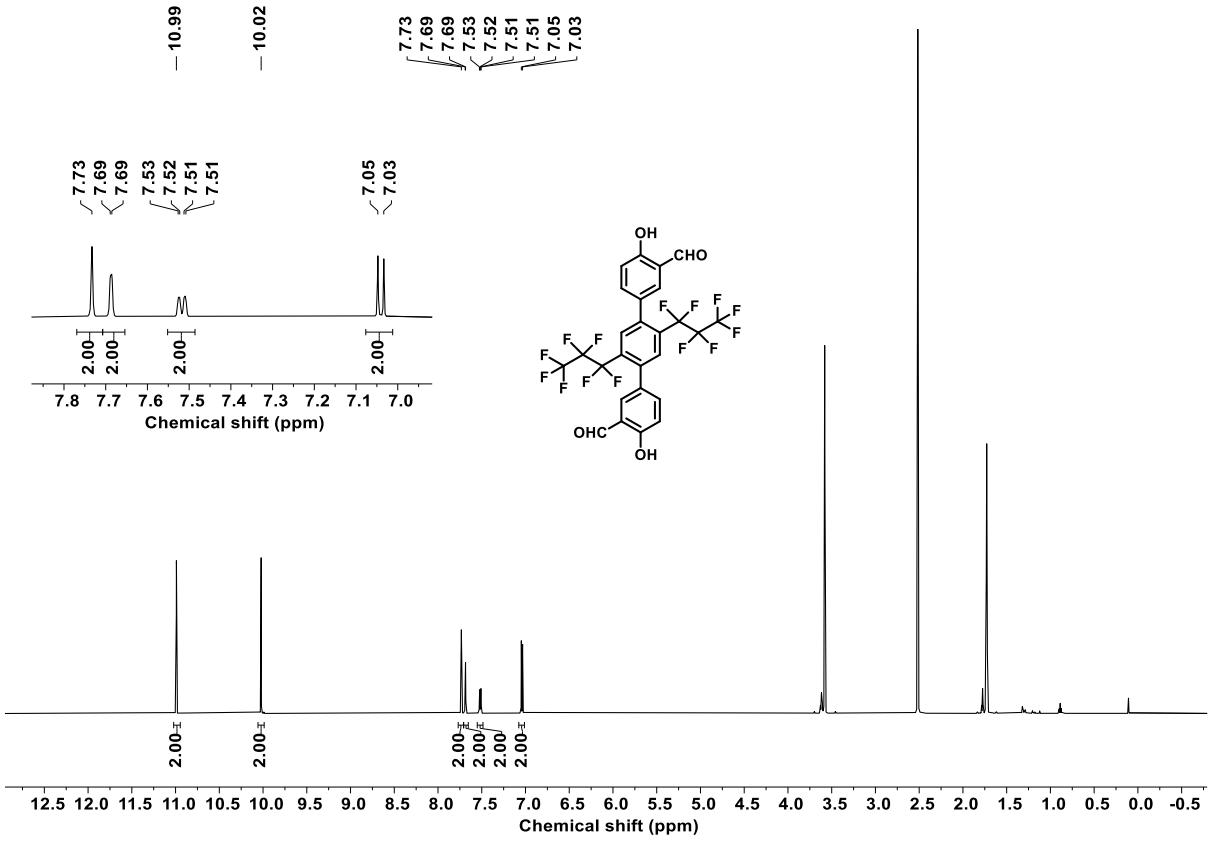

Figure 116. ^{1}H NMR spectrum of **71** (THF-d_8, 600 MHz).

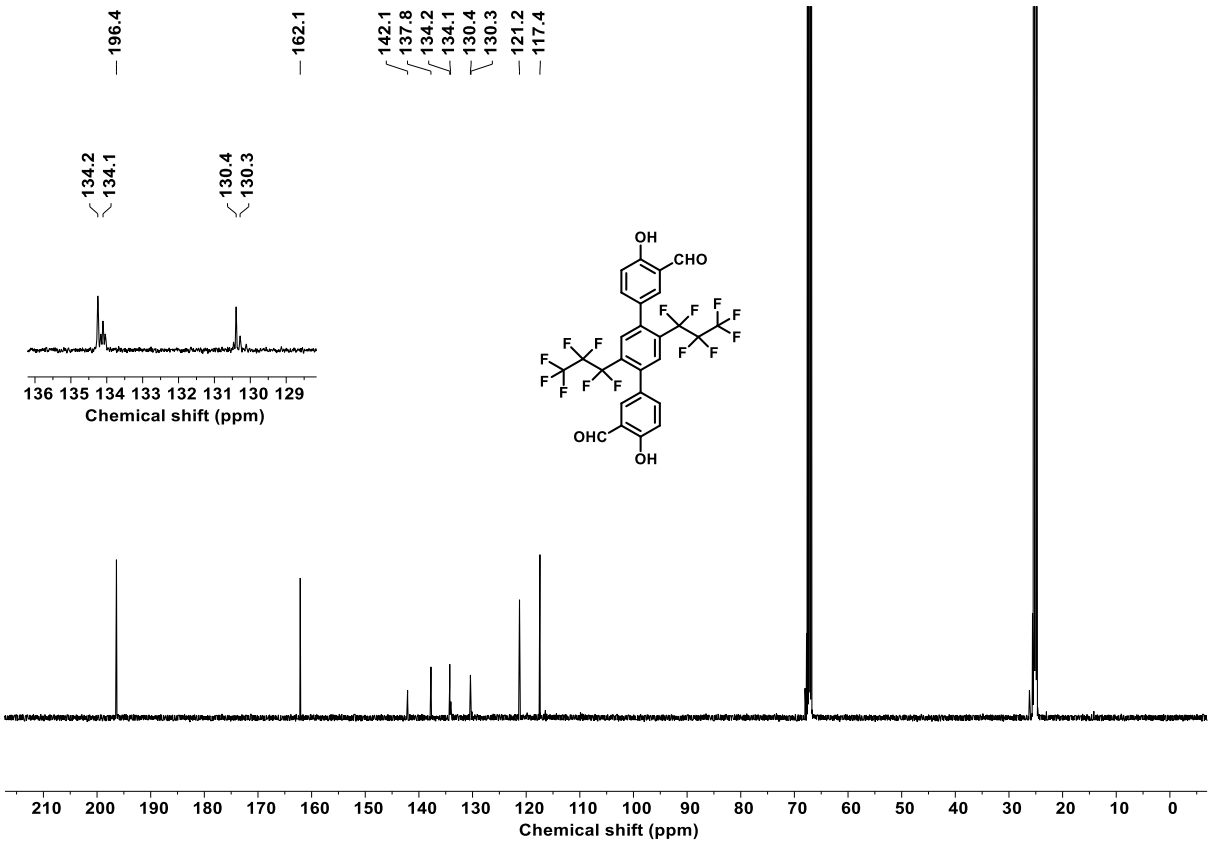

Figure 117. ^{13}C NMR spectrum of **71** (THF-d_8, 126 MHz).

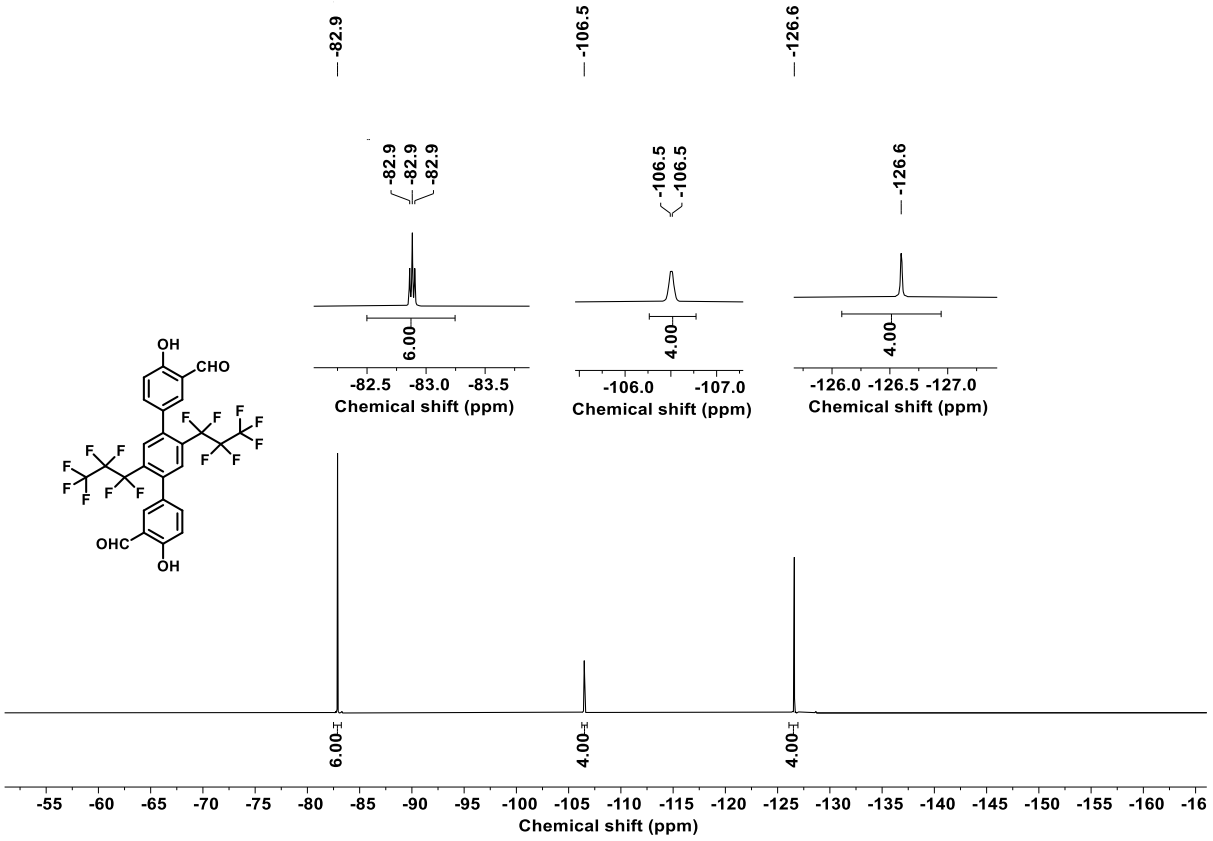

Figure 118. ^{19}F NMR spectrum of **71** (THF-d_8, 471 MHz).

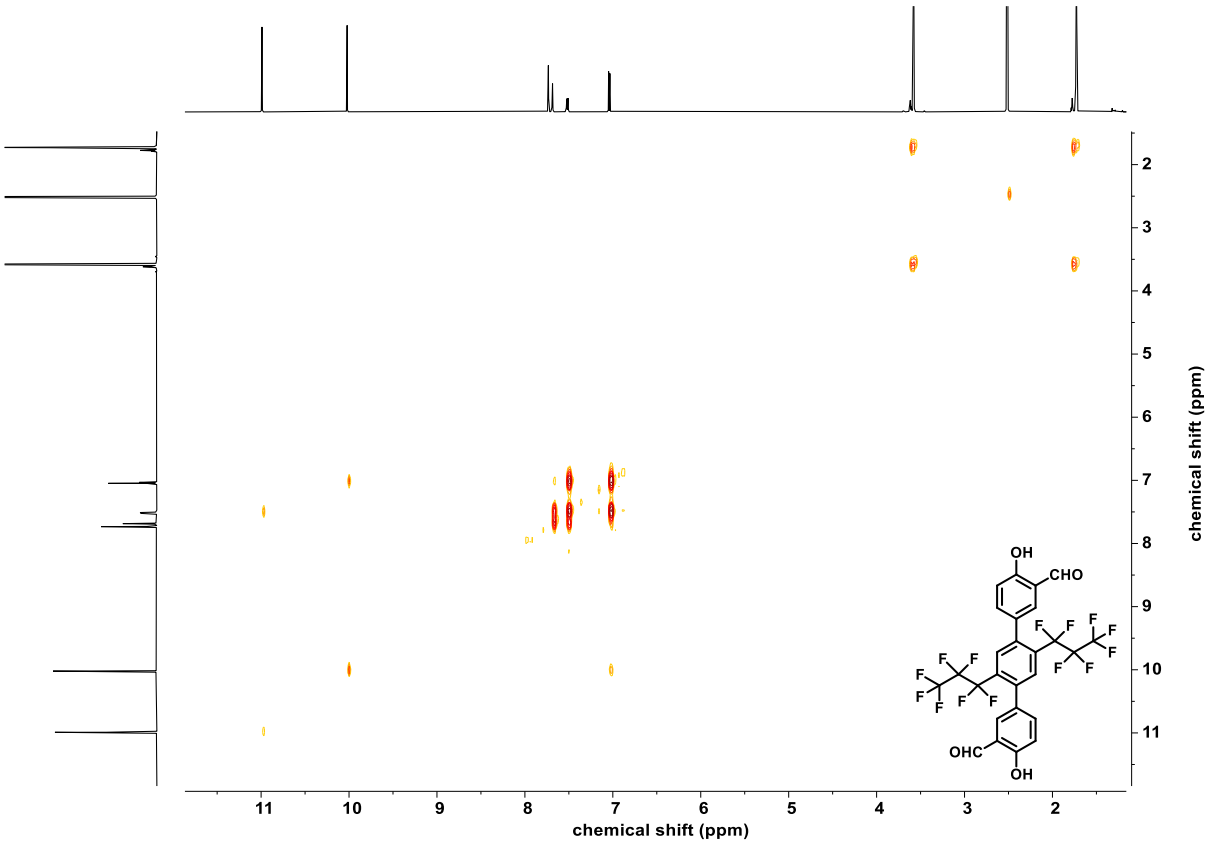

Figure 119. ^{1}H-^{1}H COSY NMR spectrum of **71** (THF-d_8, 600 MHz, 600 MHz).

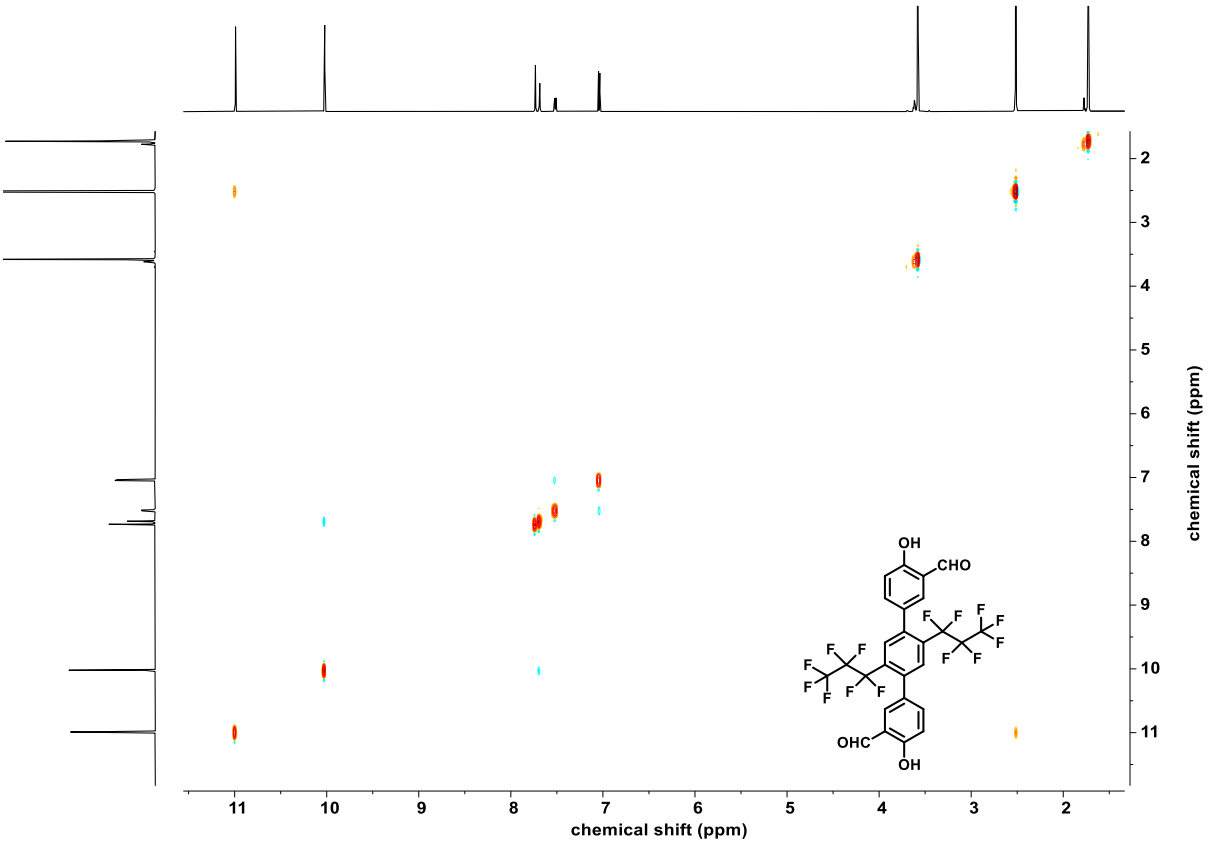

Figure 120. ^{1}H-^{1}H NOSY NMR spectrum of **71** (THF-d_8, 600 MHz, 600 MHz).

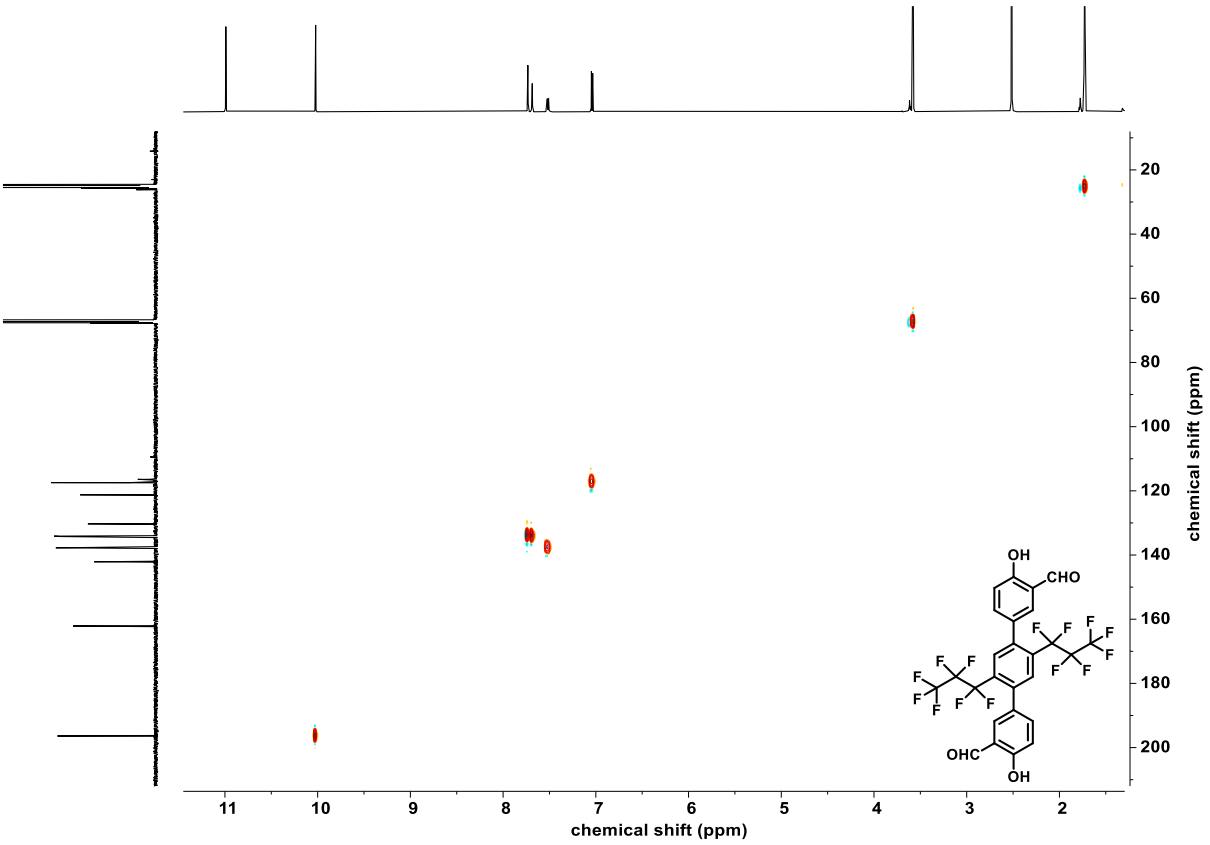

Figure 121. ^{1}H-^{13}C HSQC NMR spectrum of **71** (THF-d_8, 600 MHz, 126 MHz).

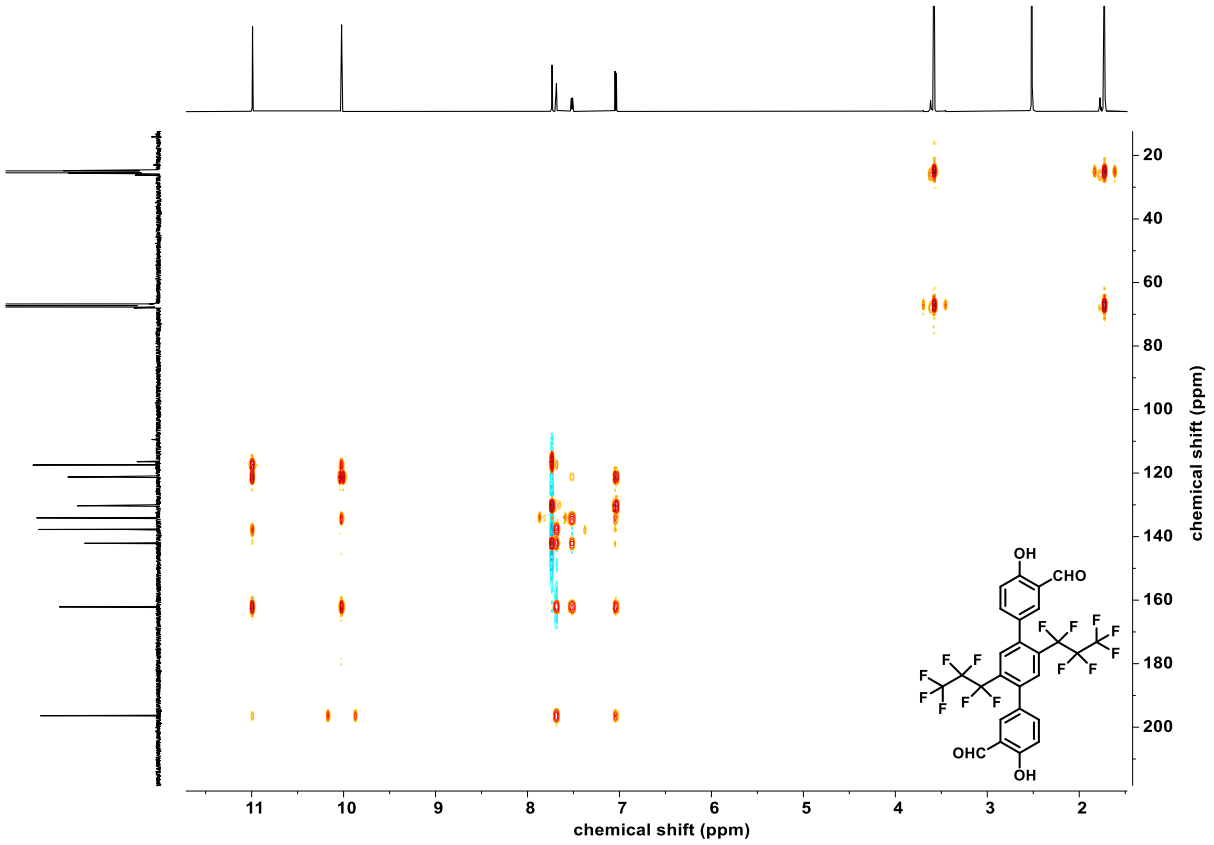

Figure 122. ^{1}H-^{13}C HMBC NMR spectrum of **71** (THF-d_8, 600 MHz, 126 MHz).

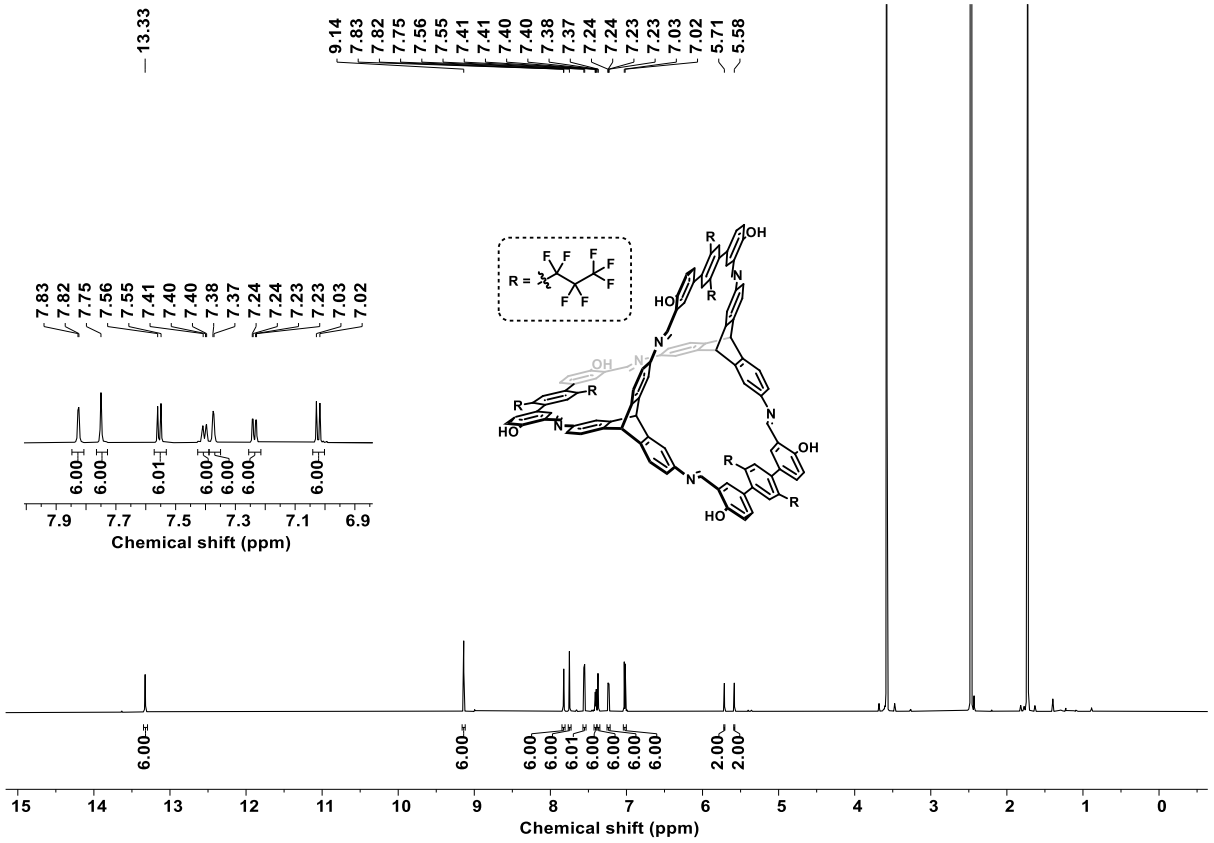

Figure 123. ^{1}H NMR spectrum of **cage-C_3F_7** (THF-d_8, 700 MHz).

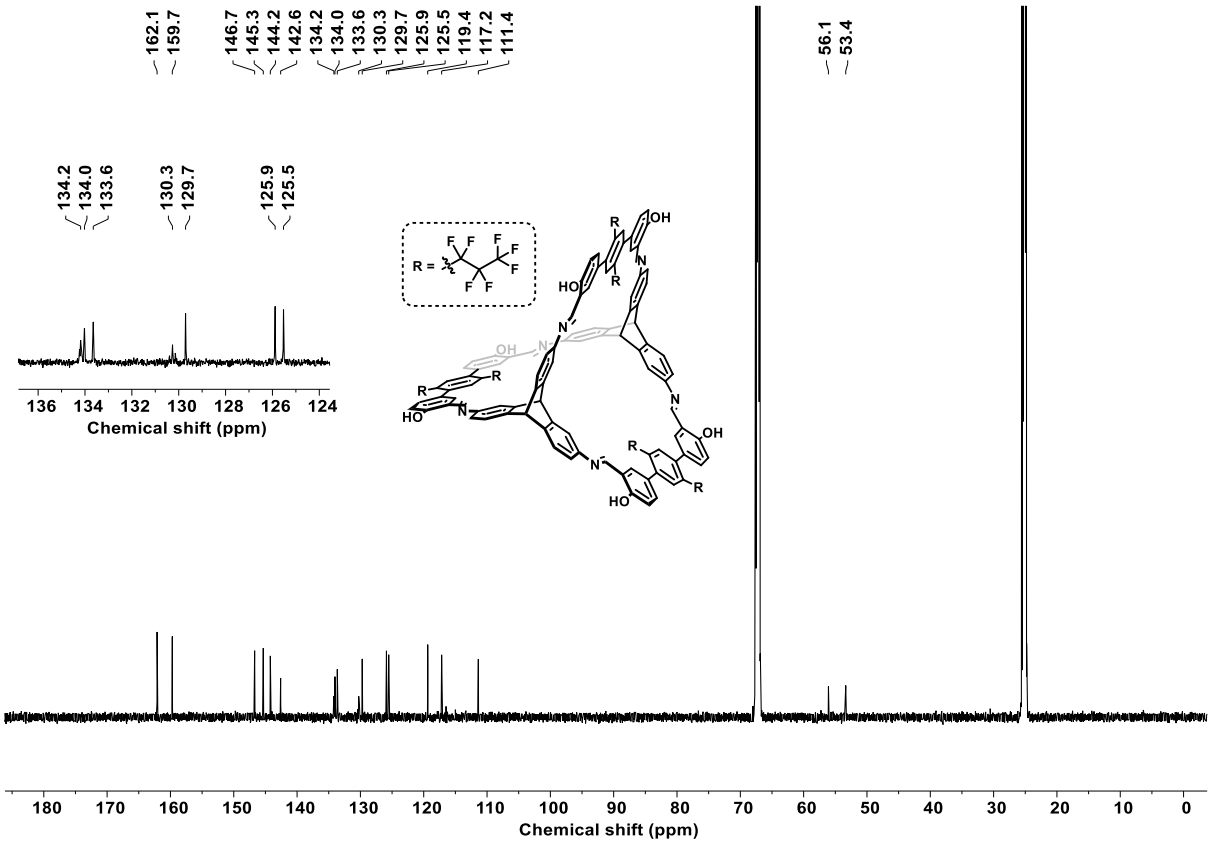

Figure 124. ^{13}C NMR spectrum of **cage-C_3F_7** (THF-d_8, 176 MHz).

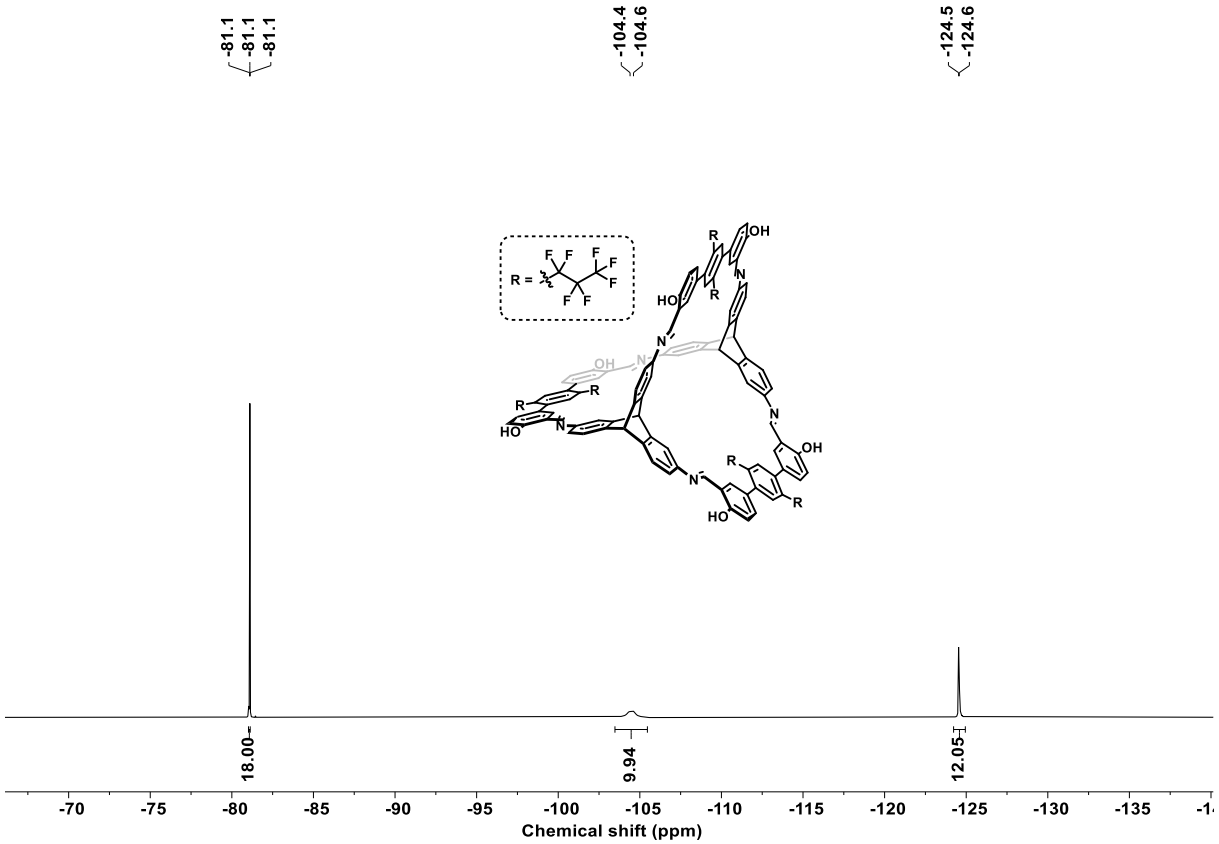

Figure 125. ^{19}F NMR spectrum of **cage-C_3F_7** (THF-d_8, 659 MHz).

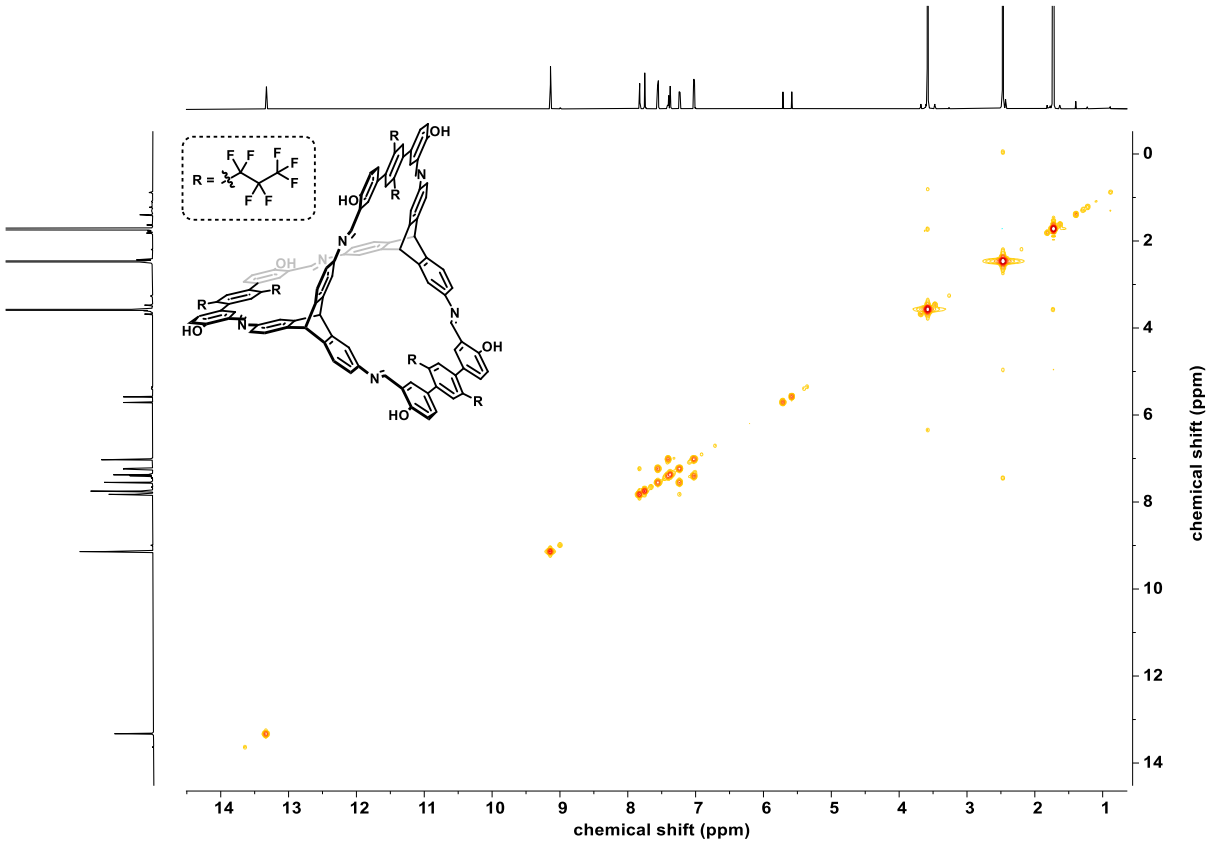

Figure 126. ^{1}H-^{1}H COSY NMR spectrum of **cage-C_3F_7** (THF-d_8, 700 MHz, 700 MHz).

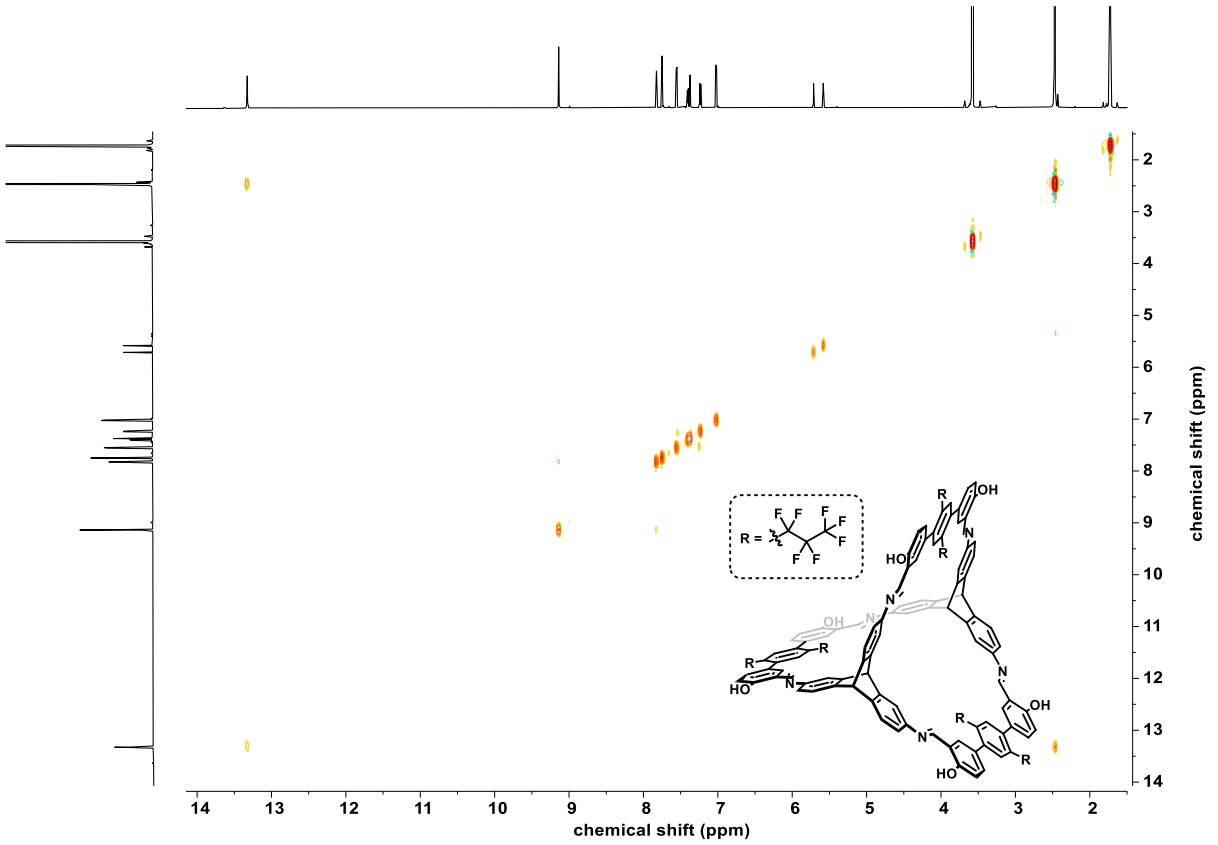

Figure 127. ^{1}H-^{1}H NOSY NMR spectrum of **cage-C_3F_7** (THF-d_8, 700 MHz, 700 MHz).

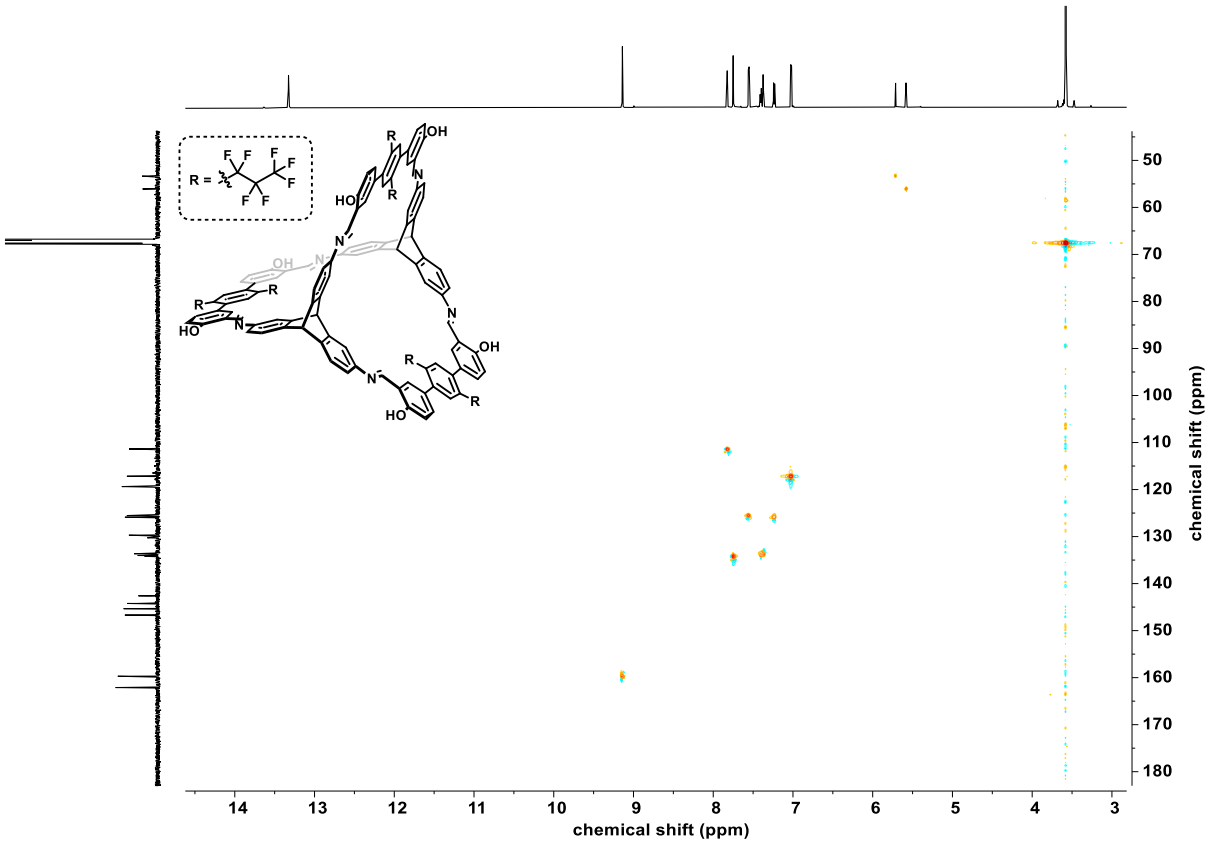

Figure 128. ^{1}H-^{13}C HSQC NMR spectrum of **cage-C_3F_7** (THF-d_8, 700 MHz, 176 MHz).

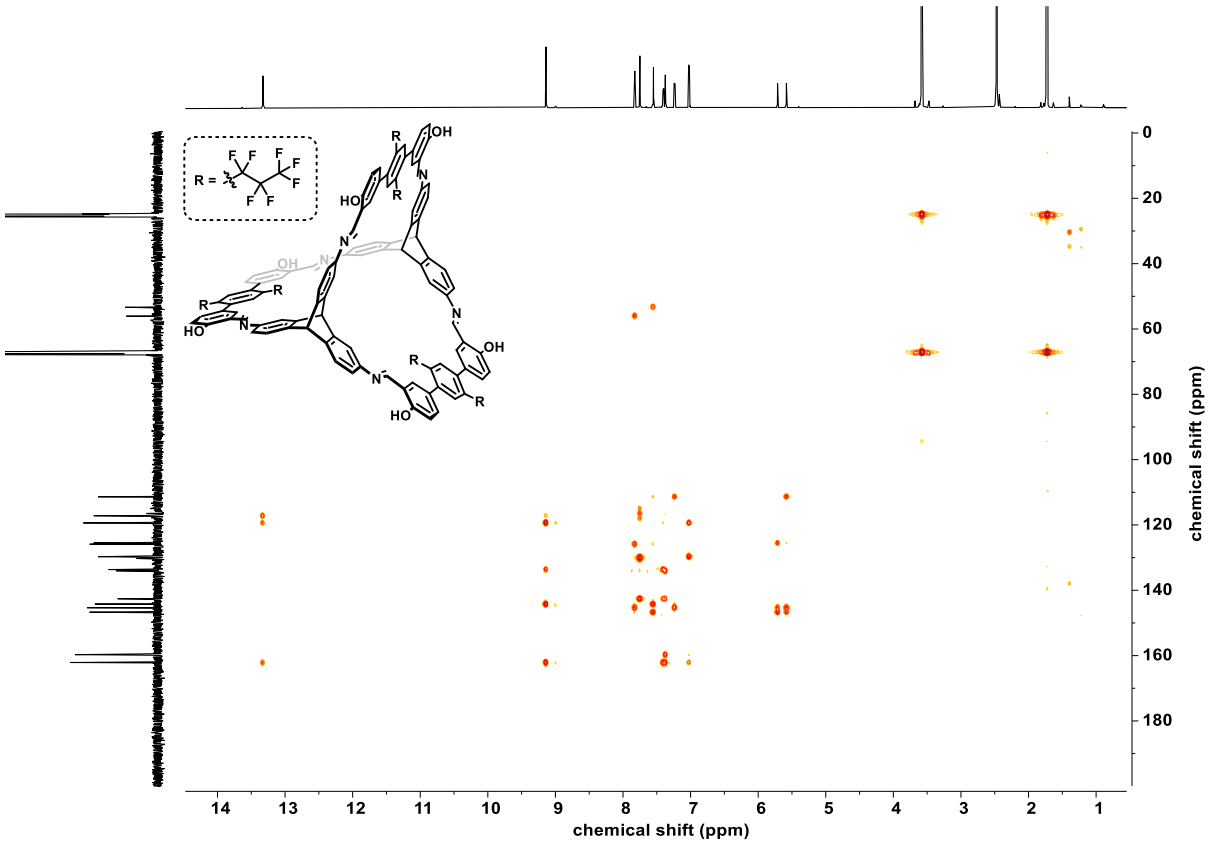

Figure 129. ^{1}H-^{13}C HMBC NMR spectrum of **cage-C_3F_7** (THF-d_8, 700 MHz, 176 MHz).

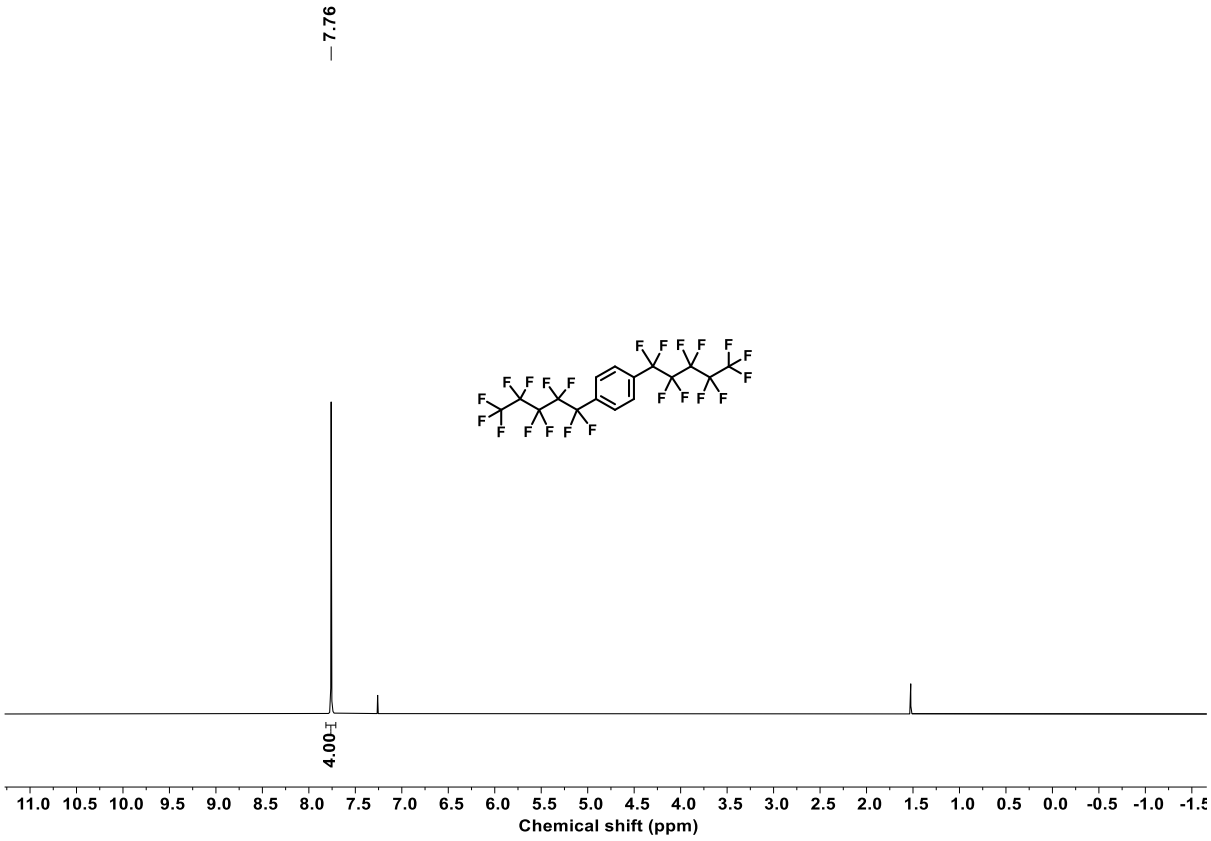

Figure 130. ^{1}H NMR spectrum of **58** ($CDCl_3$, 400 MHz).

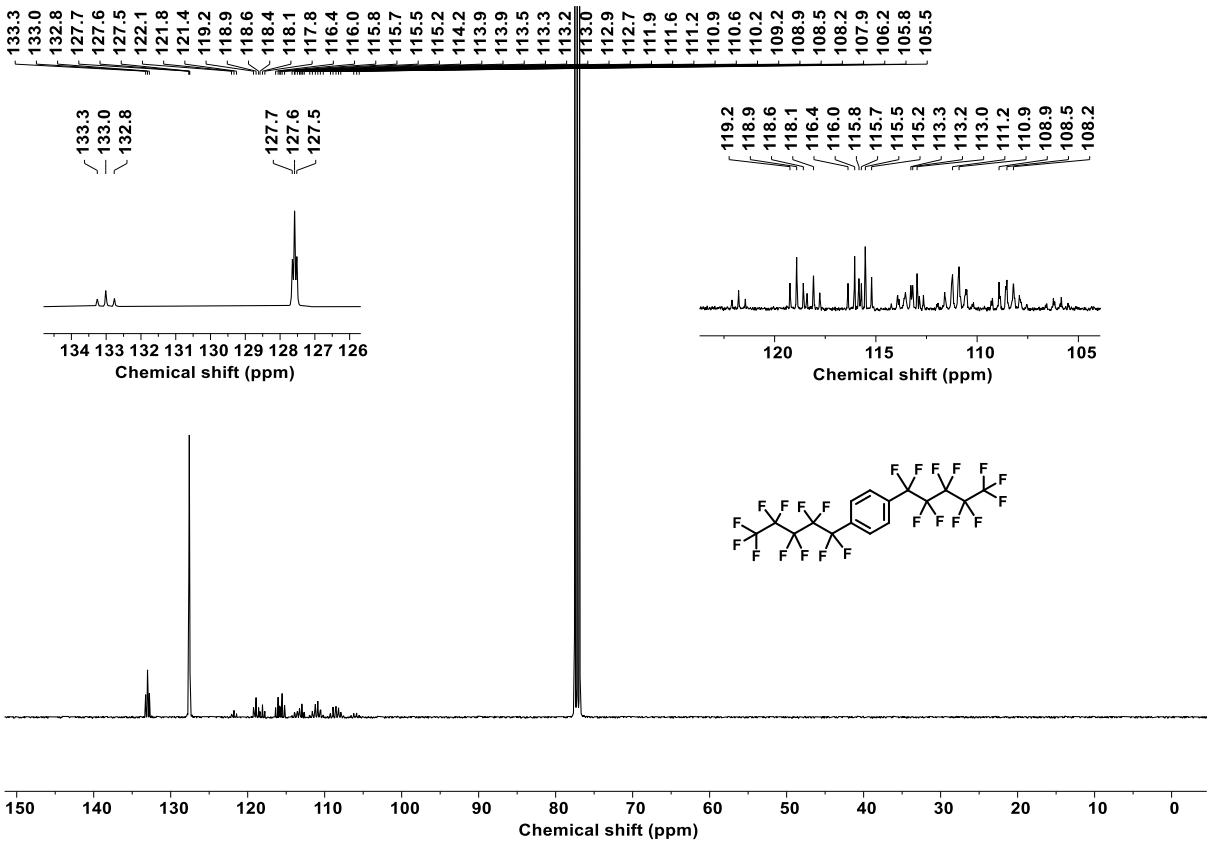

Figure 131. ^{13}C NMR spectrum of **58** ($CDCl_3$, 101 MHz).

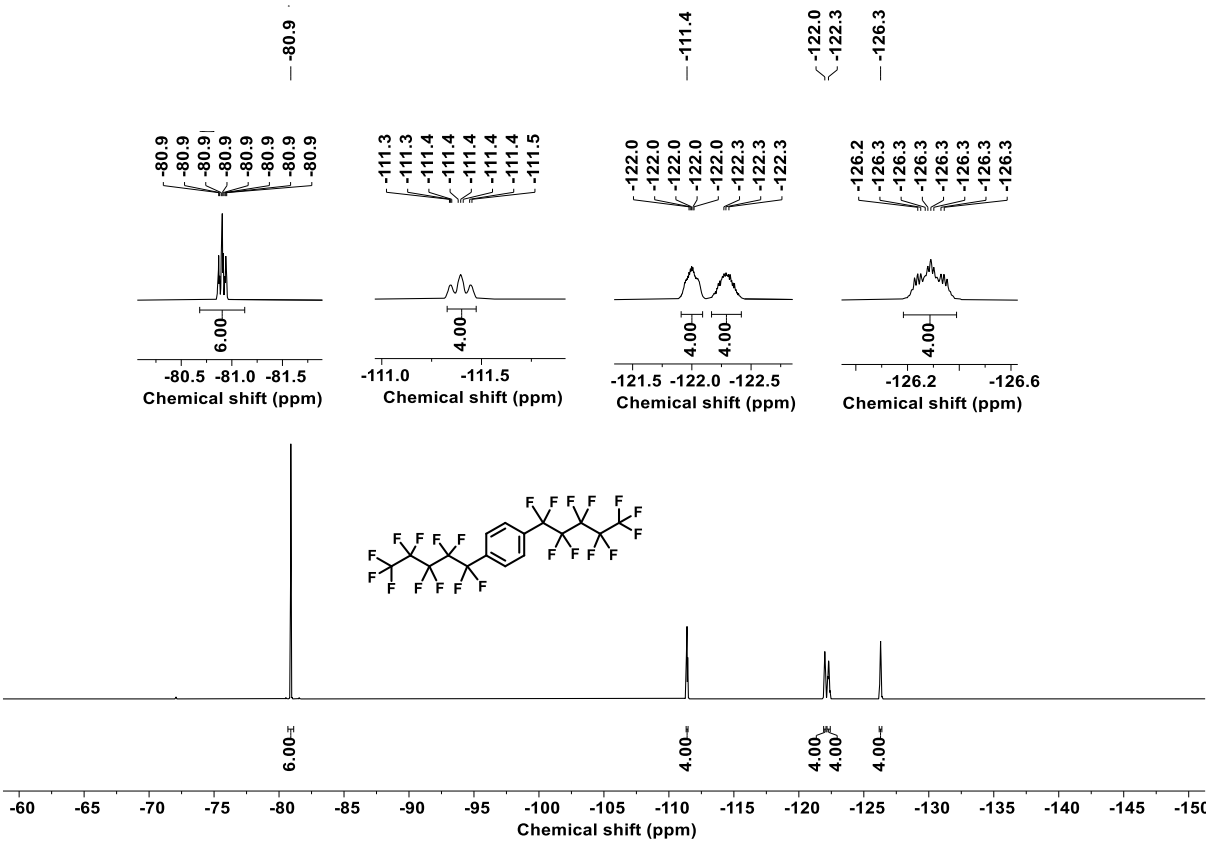

Figure 132. ^{19}F NMR spectrum of **58** ($CDCl_3$, 283 MHz).

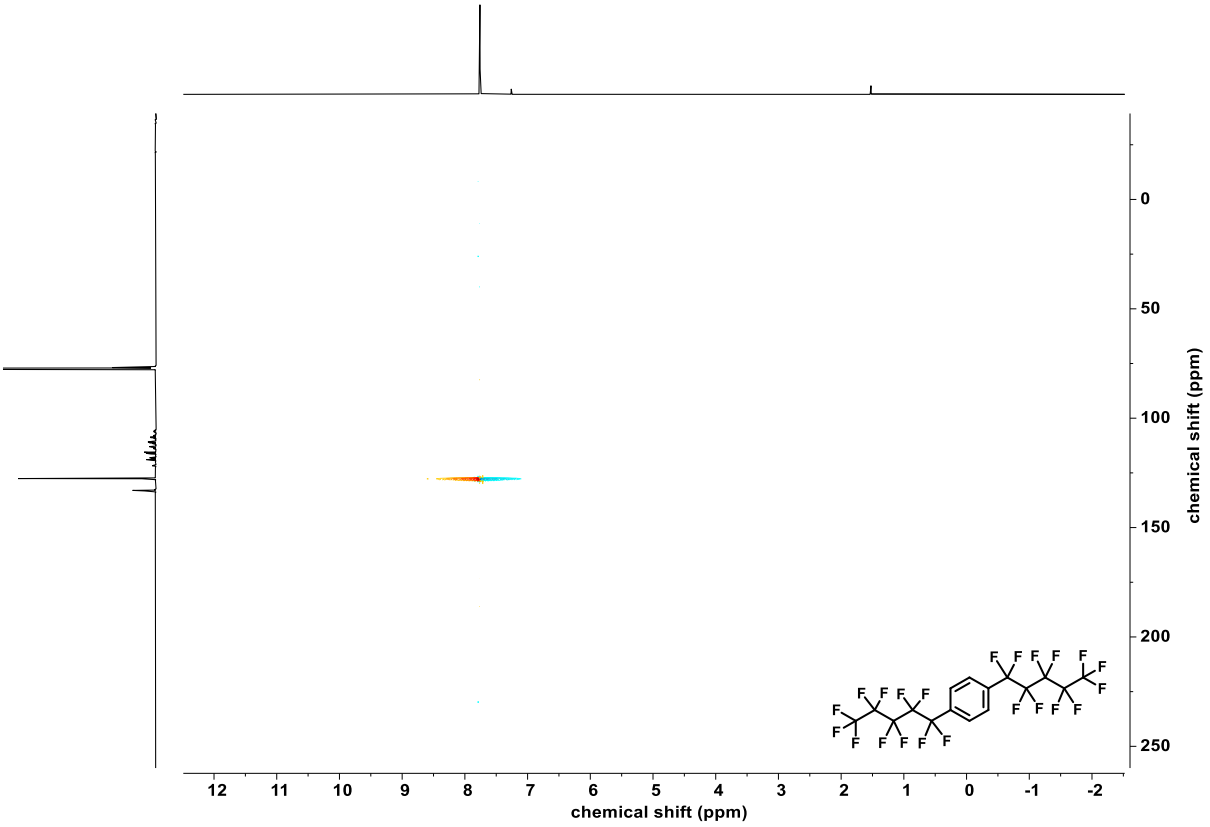

Figure 133. ^{1}H-^{13}C HSQC NMR spectrum of **58** ($CDCl_3$, 400 MHz, 101 MHz).

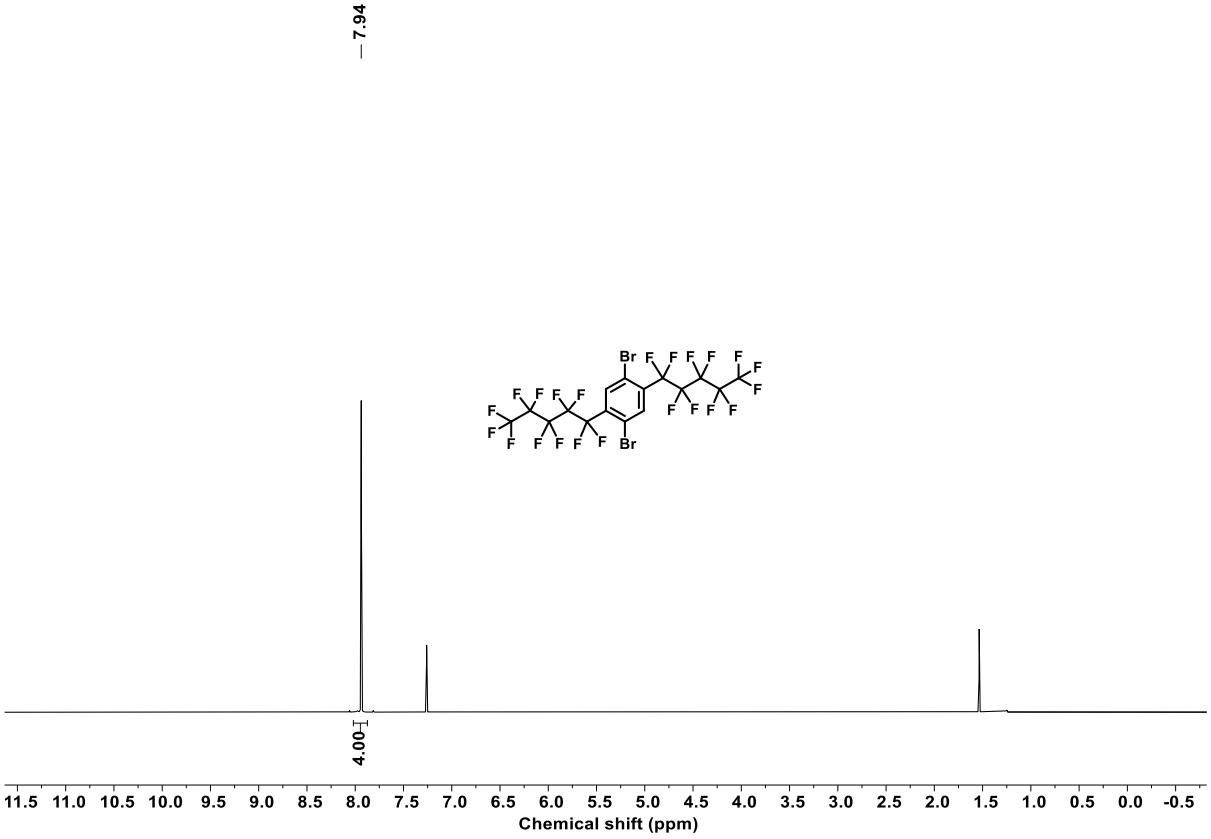

Figure 134. ^{1}H NMR spectrum of **67** ($CDCl_3$, 700 MHz).

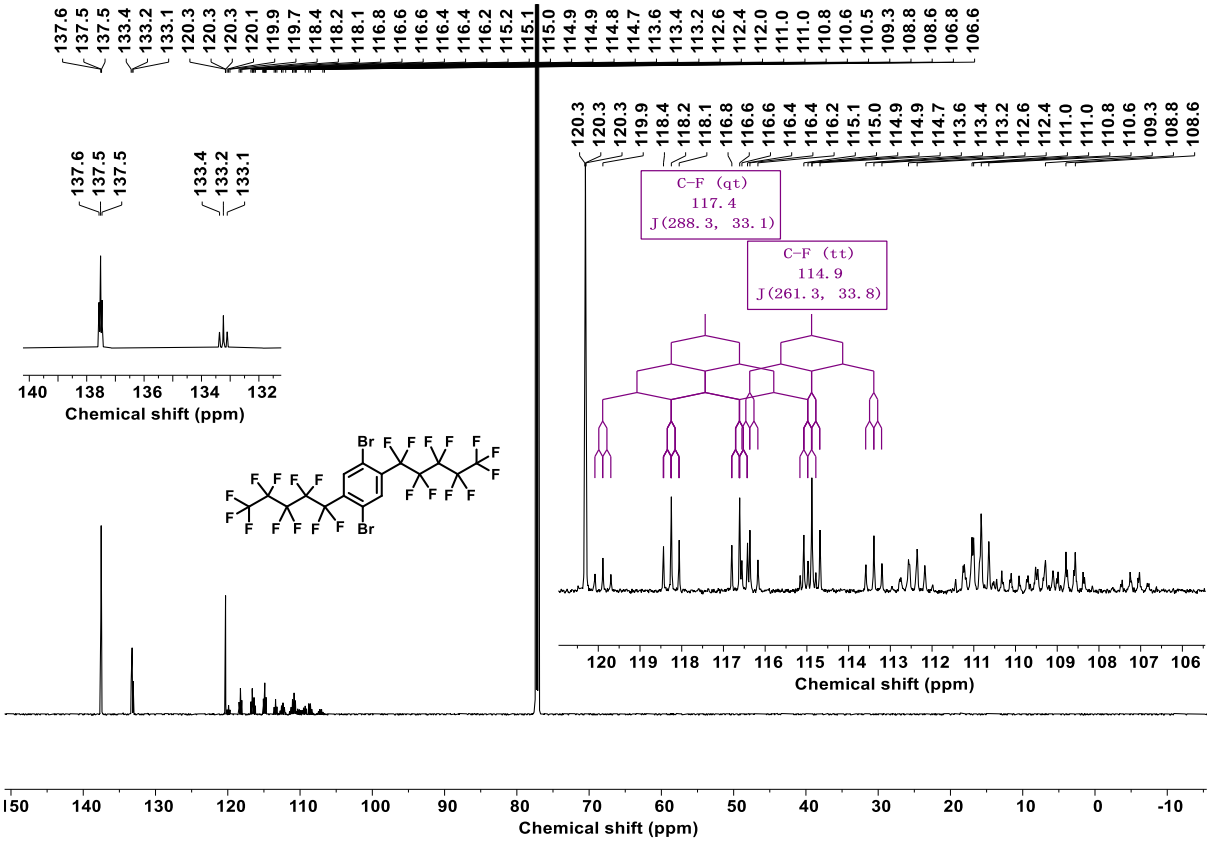

Figure 135. ^{13}C NMR spectrum of **67** ($CDCl_3$, 176 MHz).

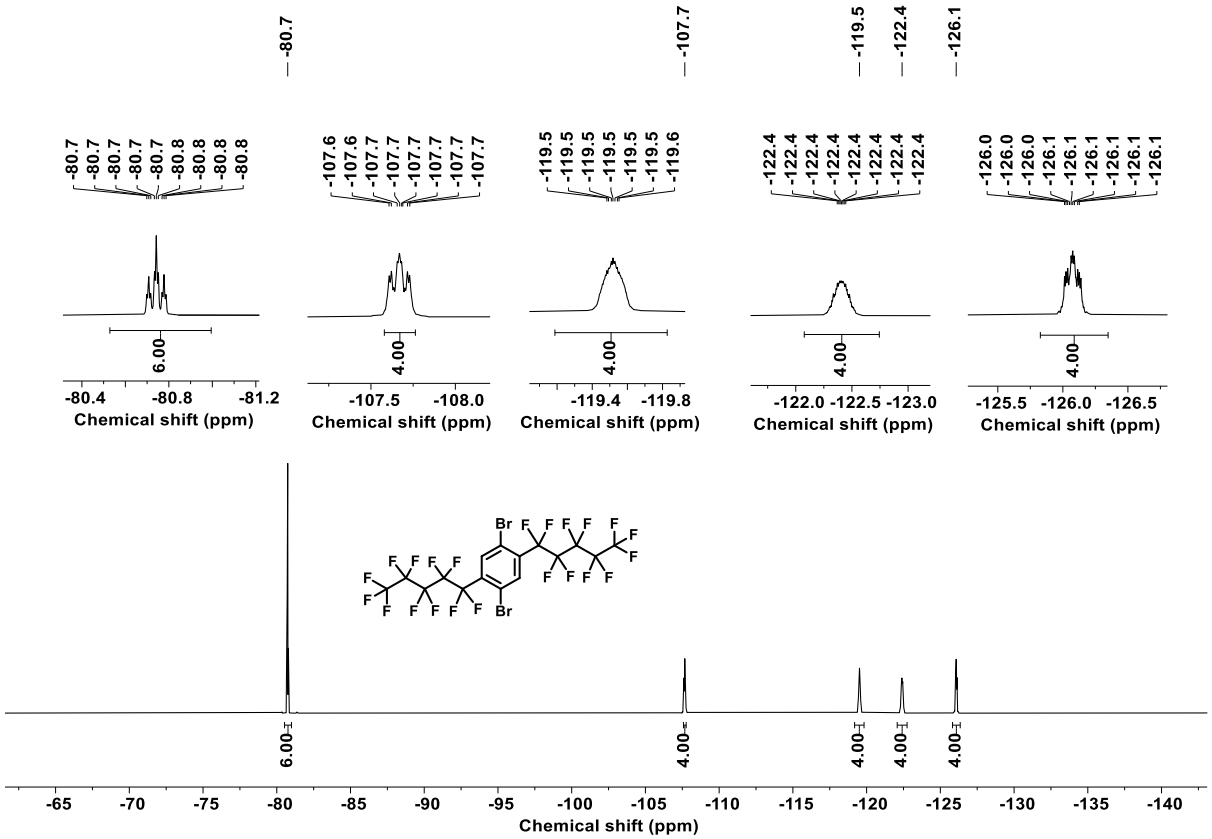

Figure 136. ^{19}F NMR spectrum of **67** ($CDCl_3$, 283 MHz).

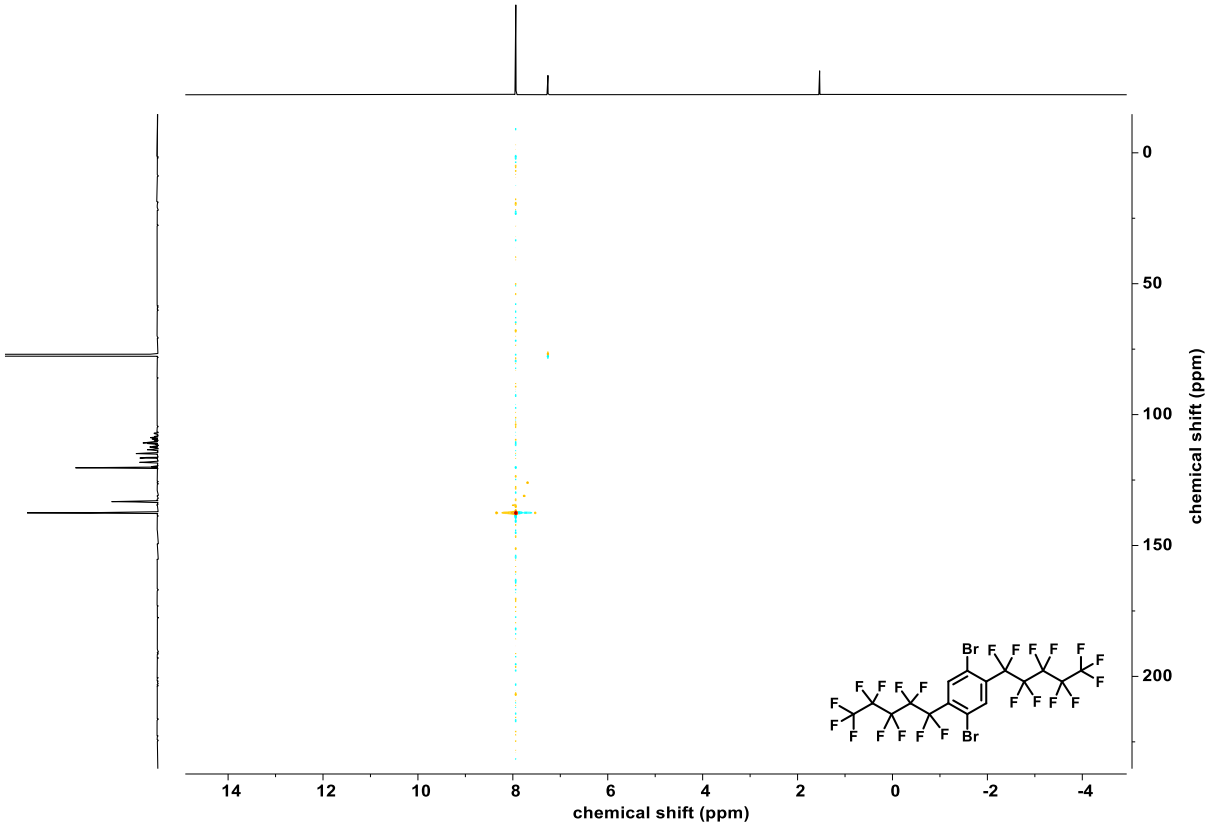

Figure 137. ^{1}H-^{13}C HSQC NMR spectrum of **67** ($CDCl_3$, 700 MHz, 176 MHz).

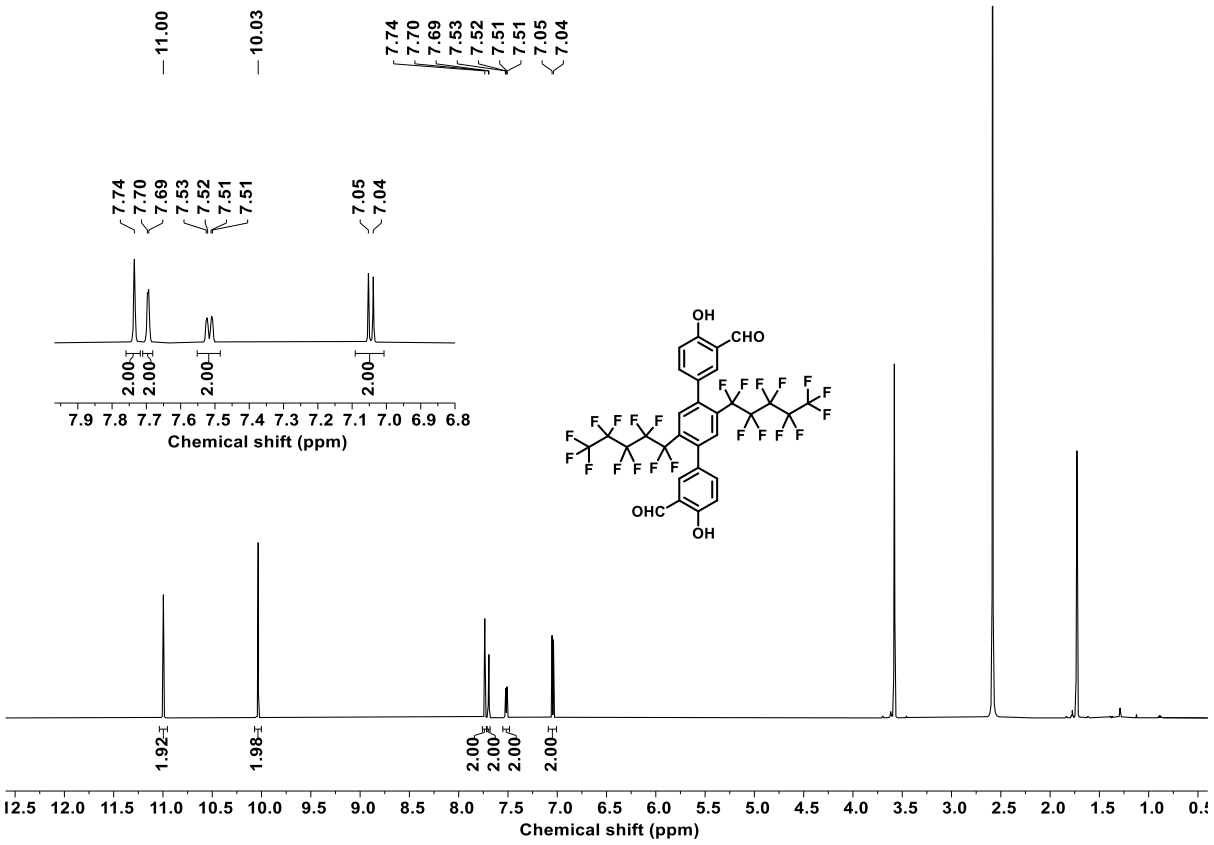

Figure 138. ^{1}H NMR spectrum of **72** (THF-d_8, 600 MHz).

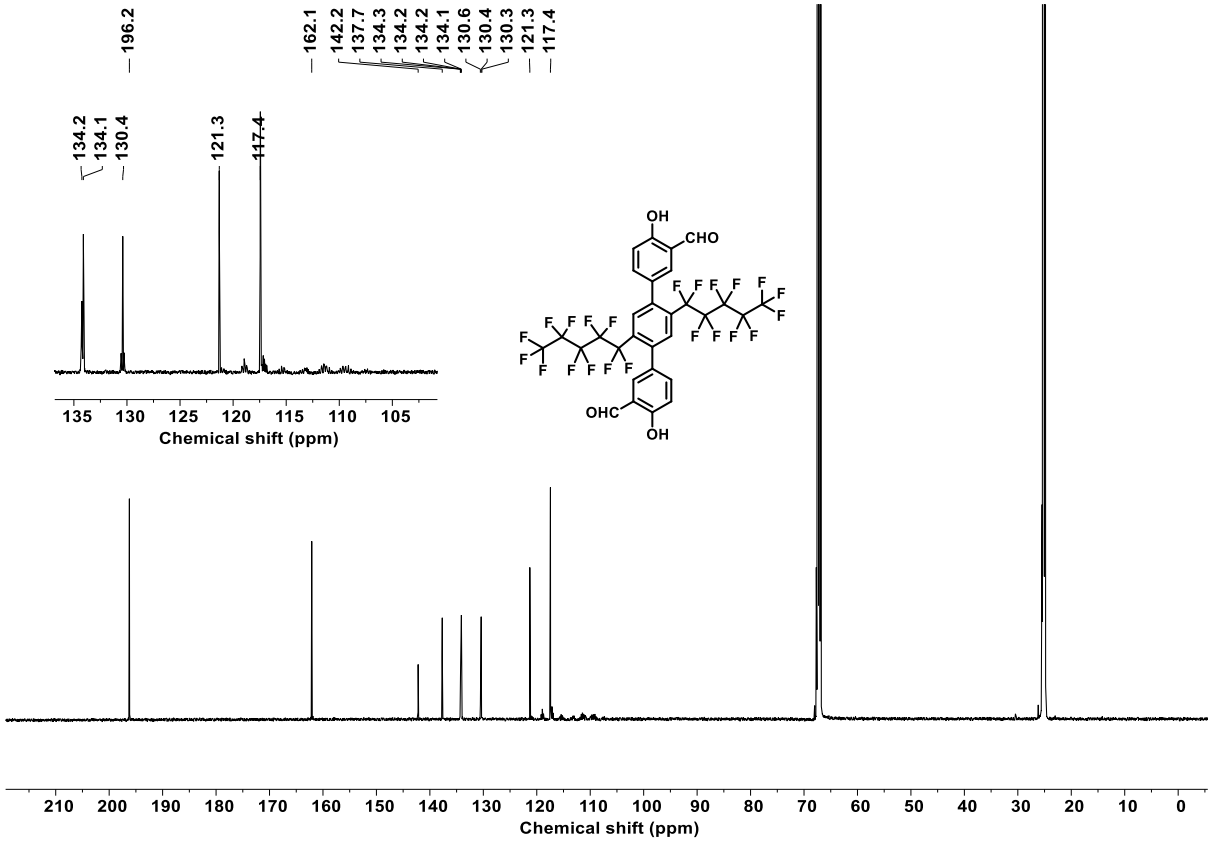

Figure 139. ^{13}C NMR spectrum of **72** (THF-d_8, 151 MHz).

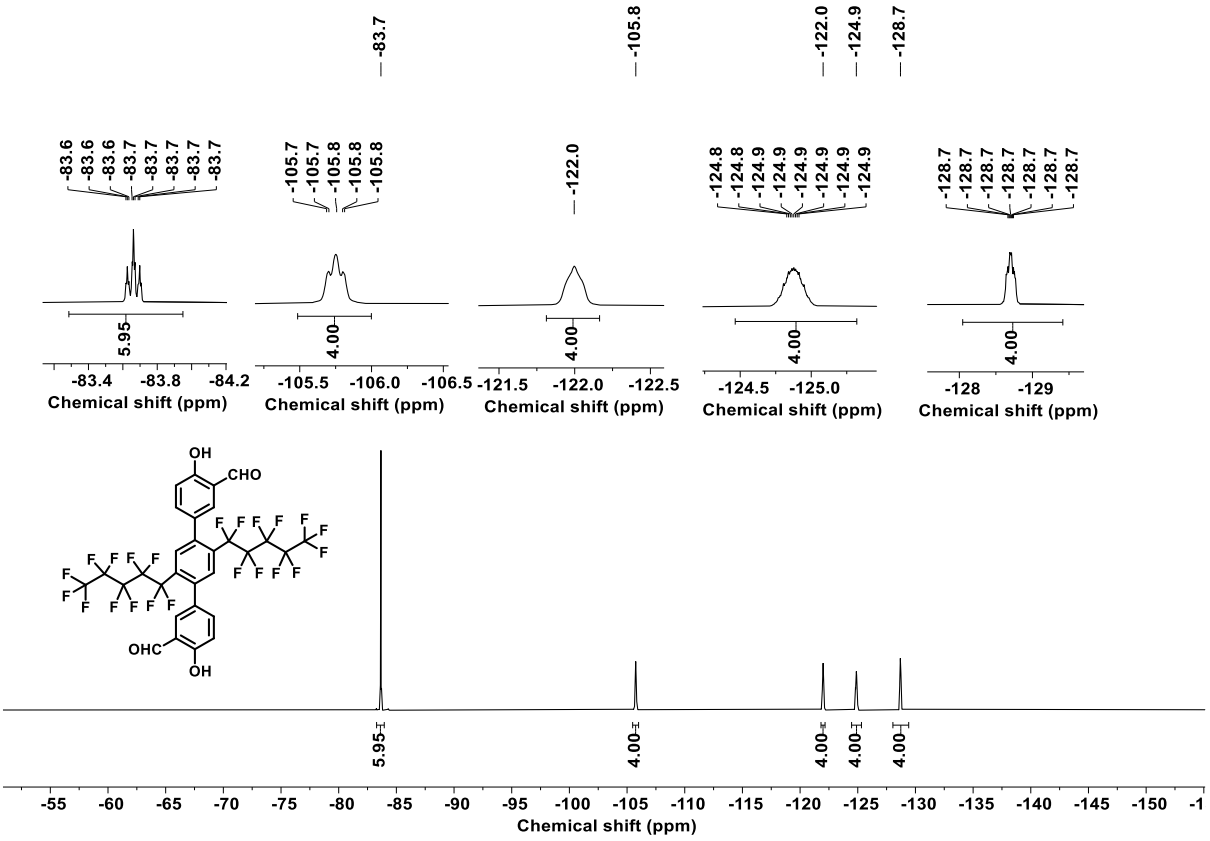

Figure 140. ^{19}F NMR spectrum of **72** (THF-d_8, 283 MHz).

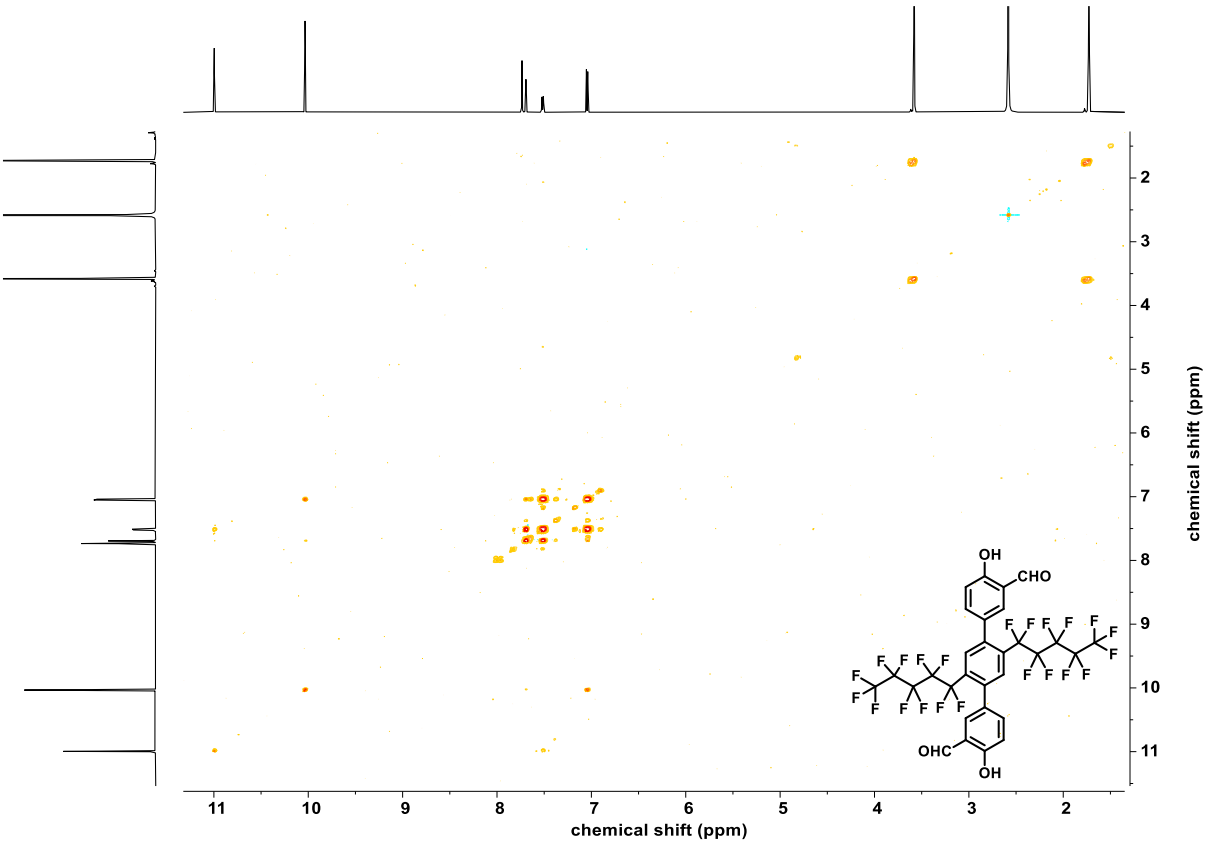

Figure 141. ^{1}H-^{1}H COSY NMR spectrum of **72** (THF-d_8, 600 MHz, 600 MHz).

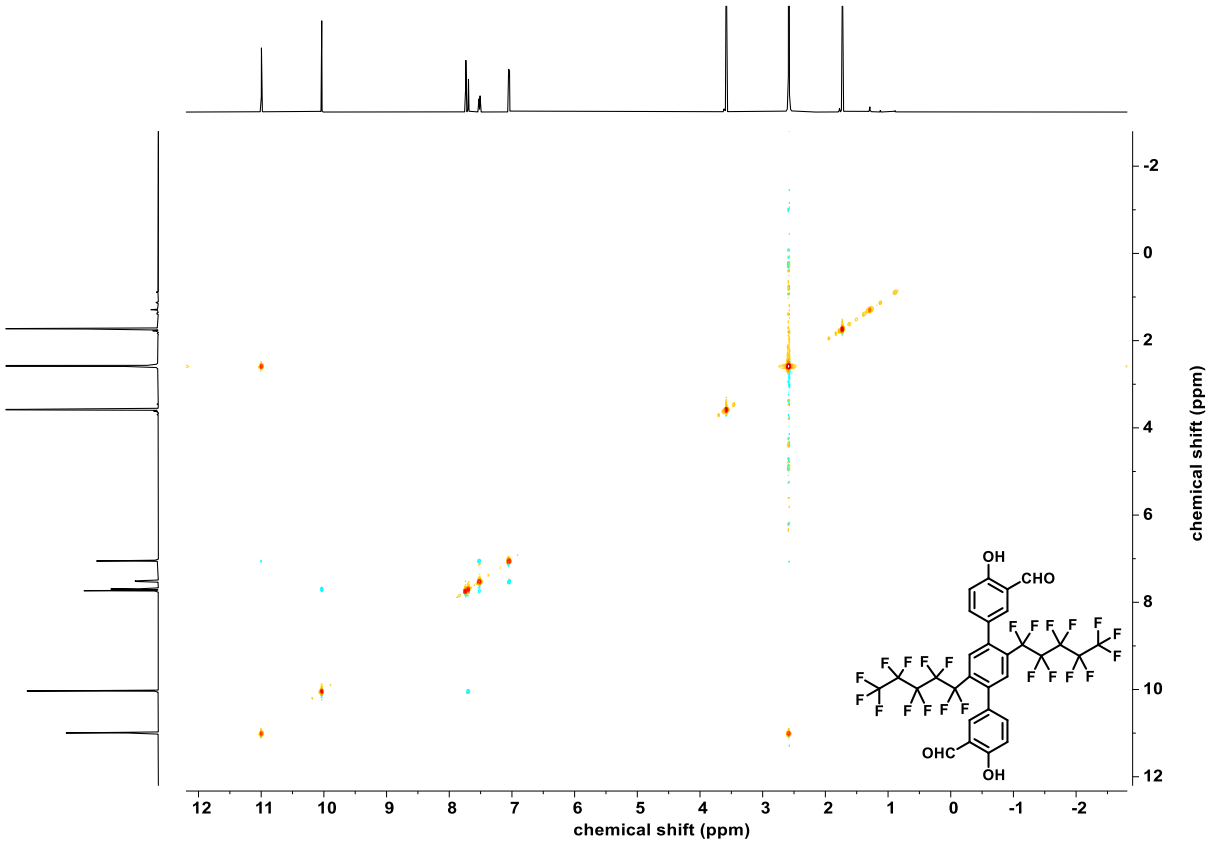

Figure 142. ^{1}H-^{1}H NOSY NMR spectrum of **72** (THF-d_8, 600 MHz, 600 MHz).

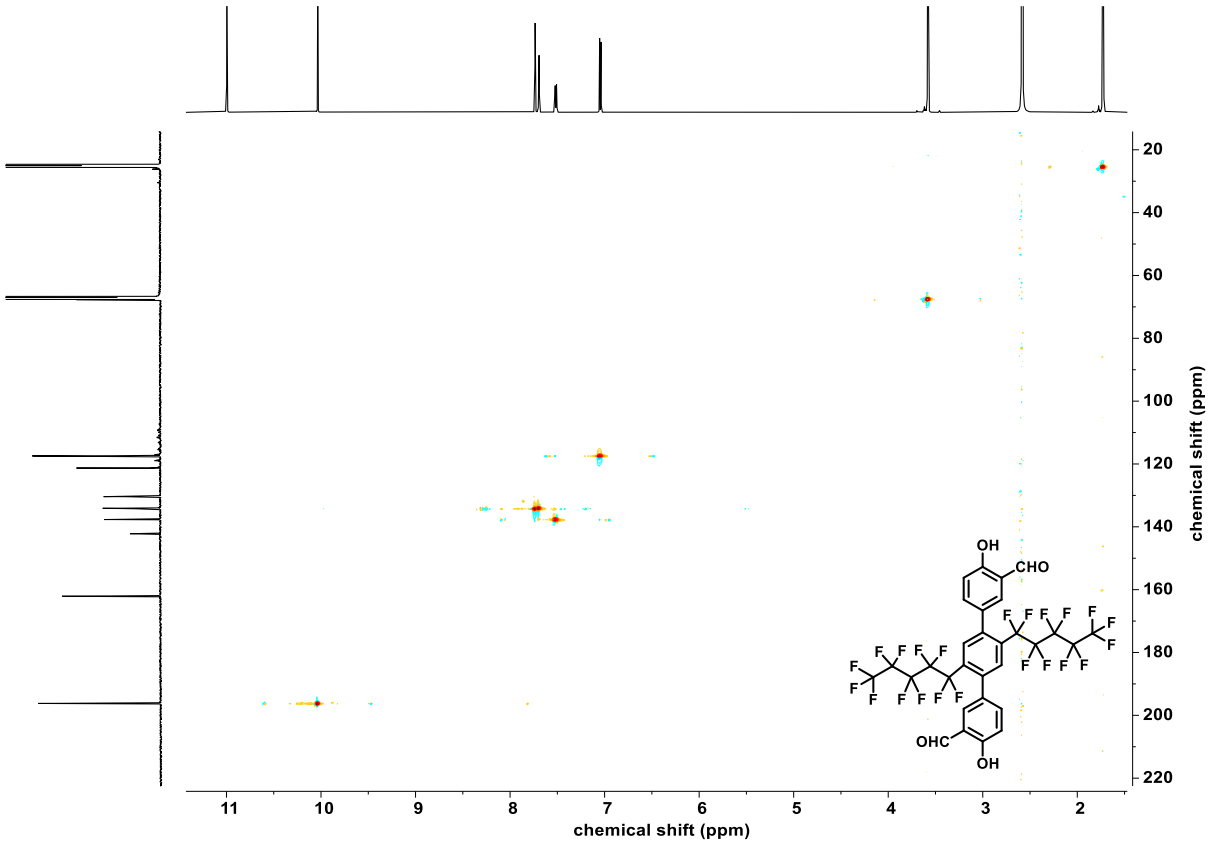

Figure 143. ^{1}H-^{13}C HSQC NMR spectrum of **72** (THF-d_8, 600 MHz, 151 MHz).

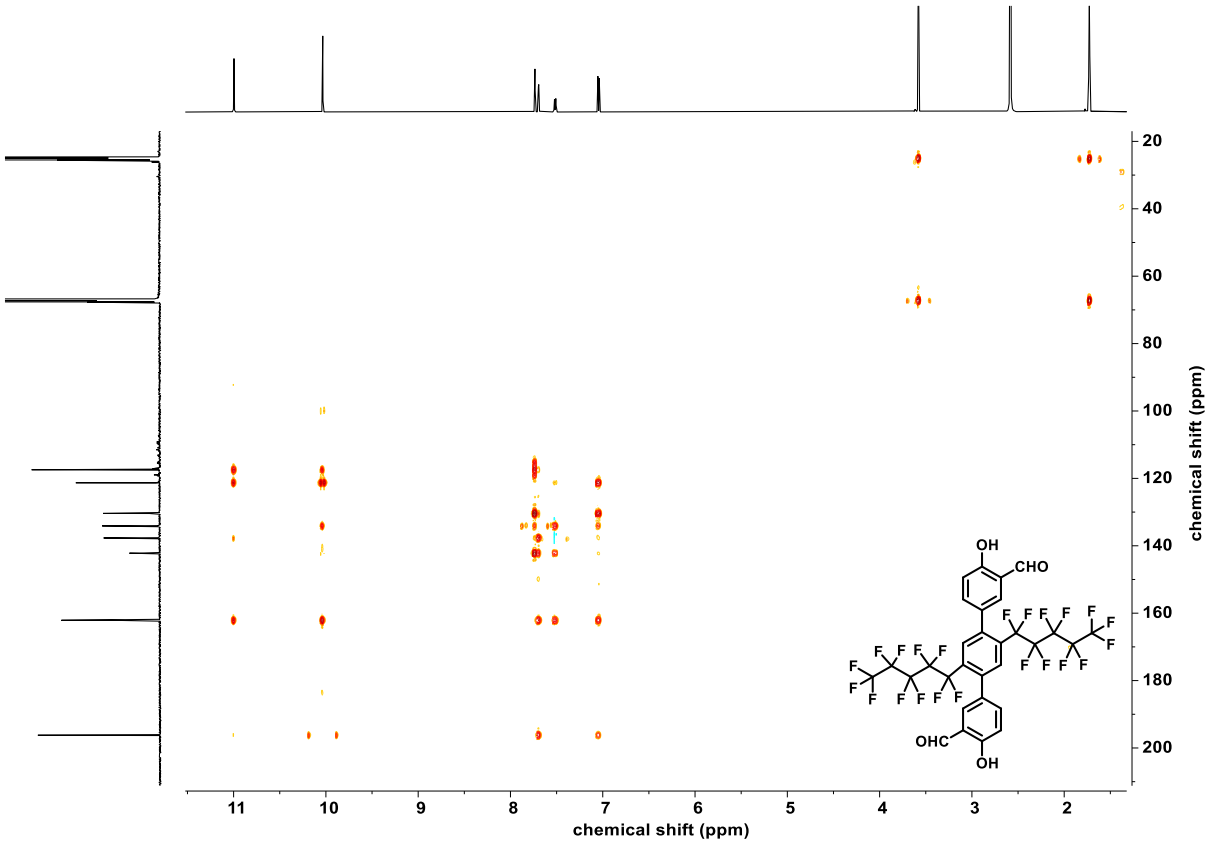

Figure 144. ^{1}H-^{13}C HMBC NMR spectrum of **72** (THF-d_8, 600 MHz, 151 MHz).

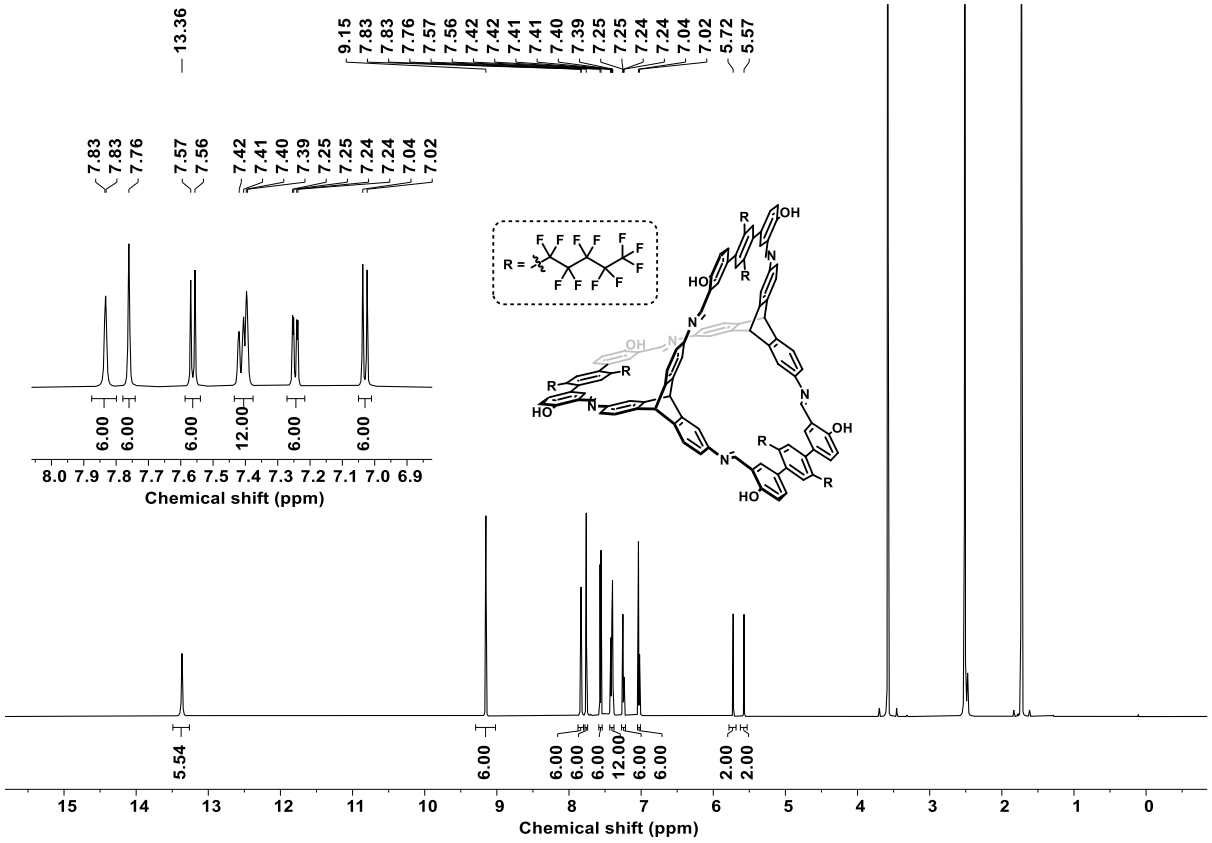

Figure 145. ^{1}H NMR spectrum of **cage-C_5F_{11}** (THF-d_8, 600 MHz).

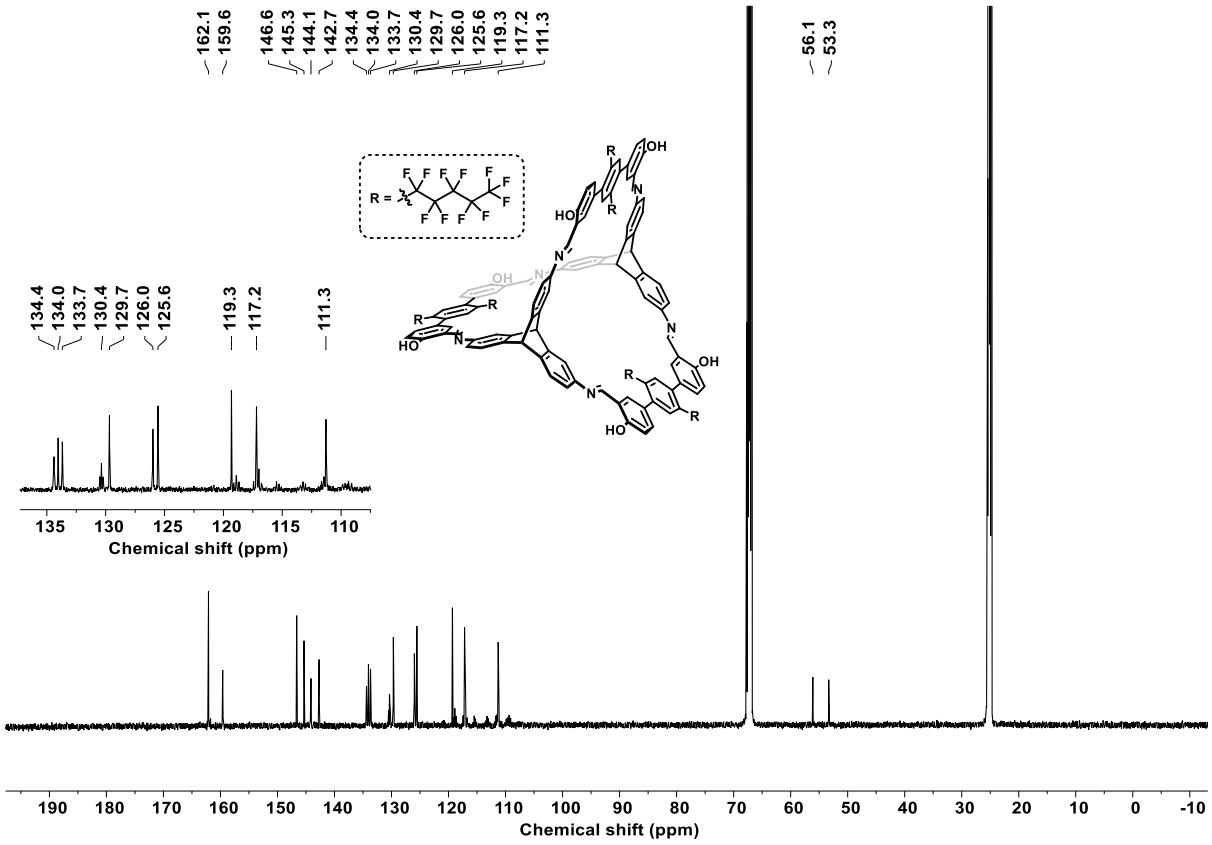

Figure 146. ^{13}C NMR spectrum of **cage-C_5F_{11}** (THF-d_8, 151 MHz).

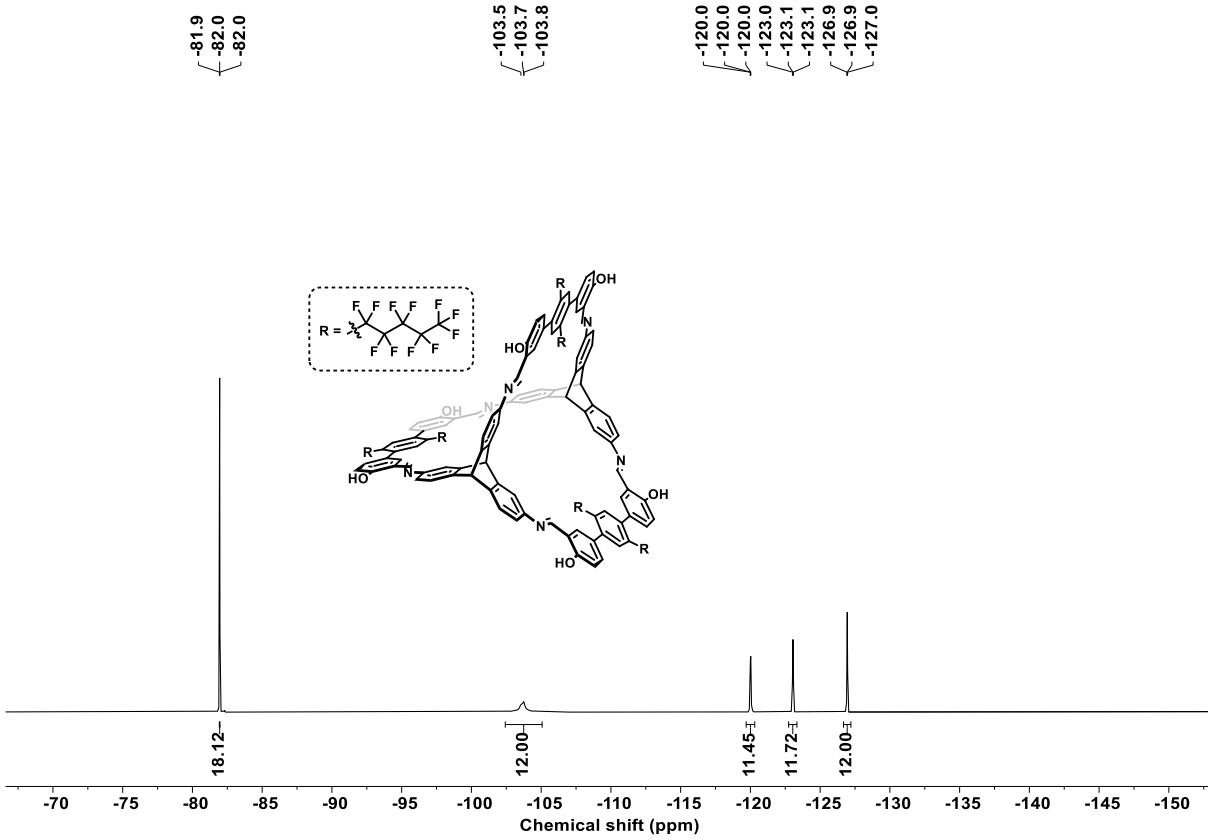

Figure 147. ^{19}F NMR spectrum of **cage-C_5F_{11}** (THF-d_8, 659 MHz).

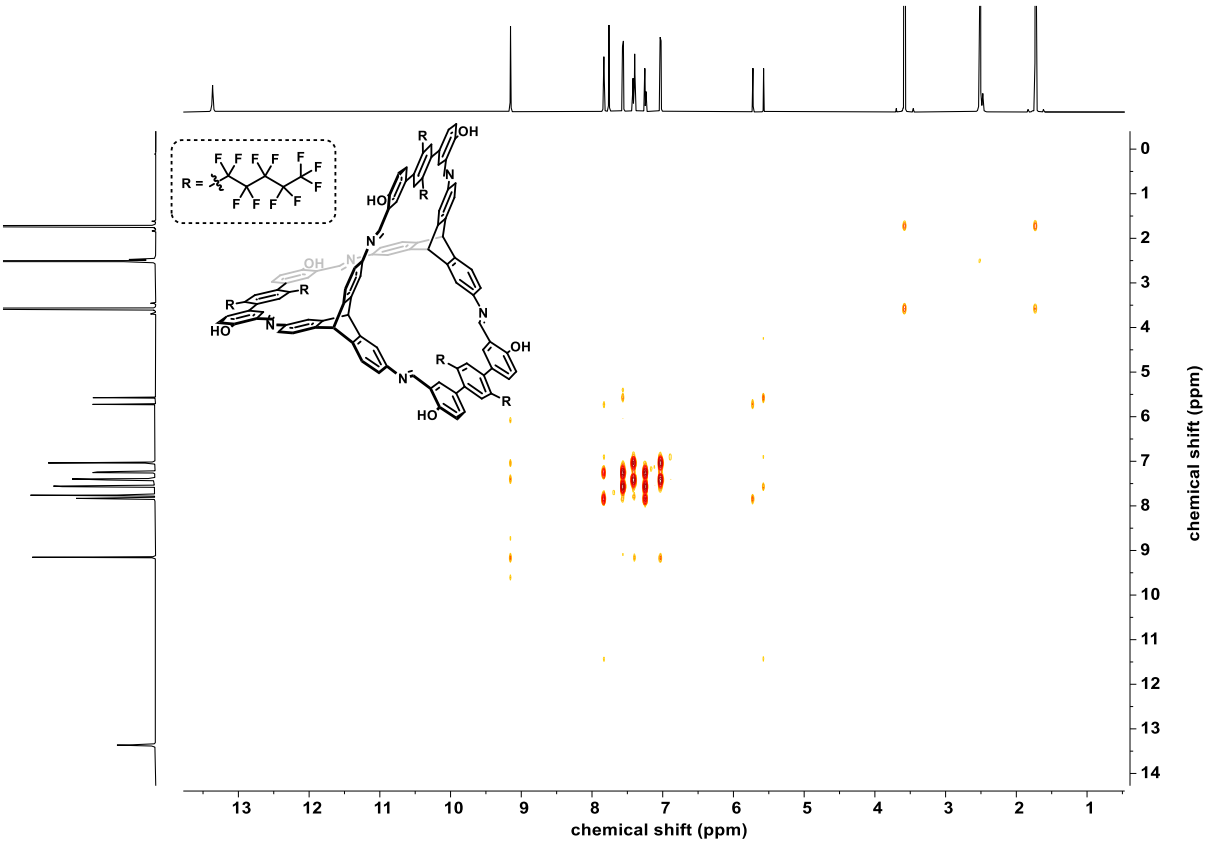

Figure 148. ^{1}H-^{1}H COSY NMR spectrum of **cage-C_5F_{11}** (THF-d_8, 600 MHz, 600 MHz).

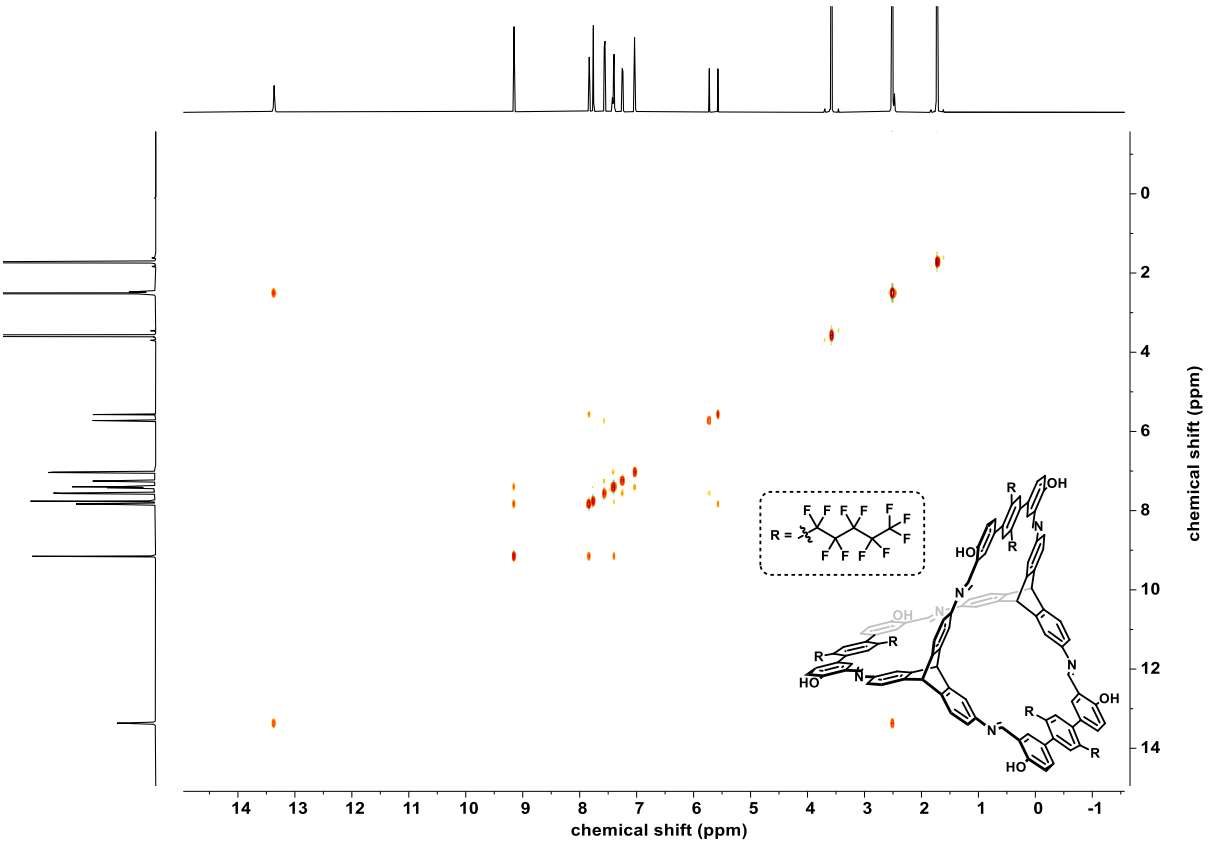

Figure 149. ^{1}H-^{1}H NOSY NMR spectrum of **cage-C_5F_{11}** (THF-d_8, 600 MHz, 600 MHz).

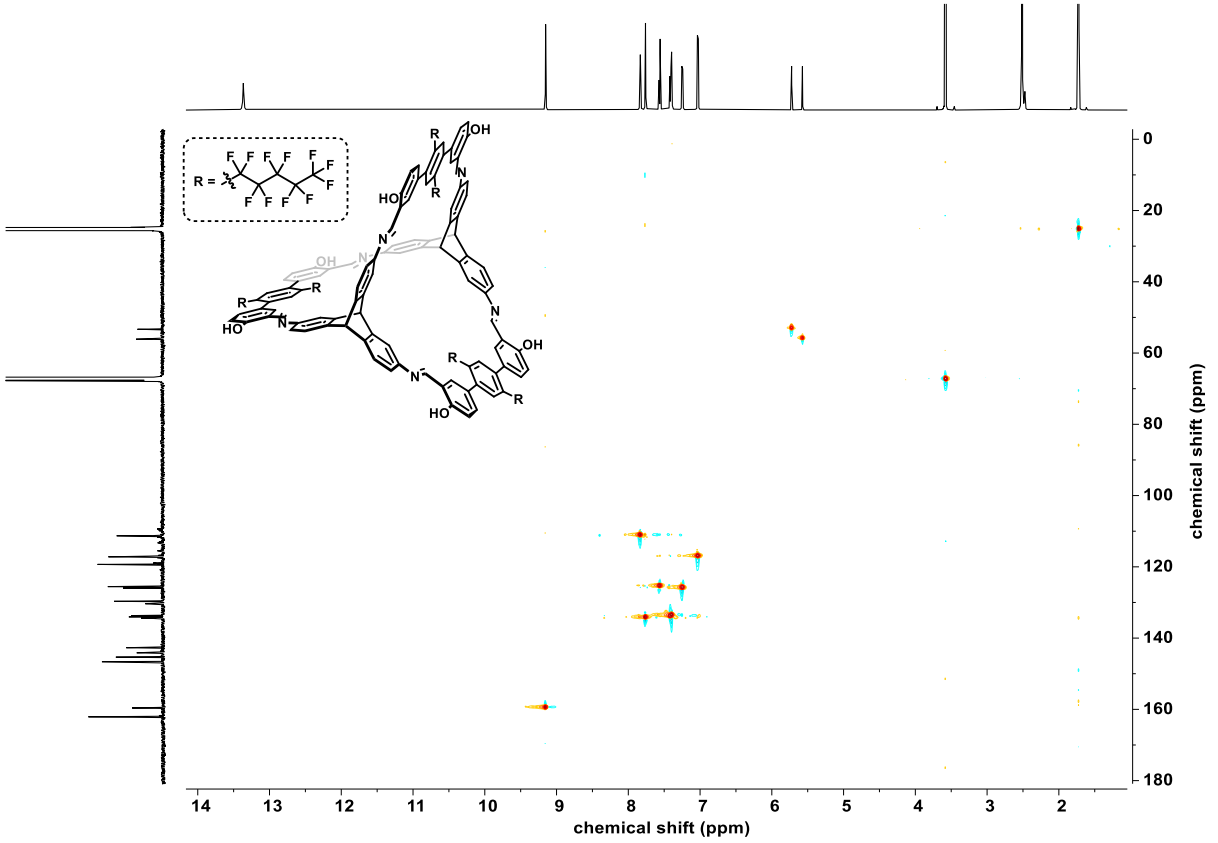

Figure 150. ^{1}H-^{13}C HSQC NMR spectrum of **cage-C$_5$F$_{11}$** (THF-d_8, 600 MHz, 151 MHz).

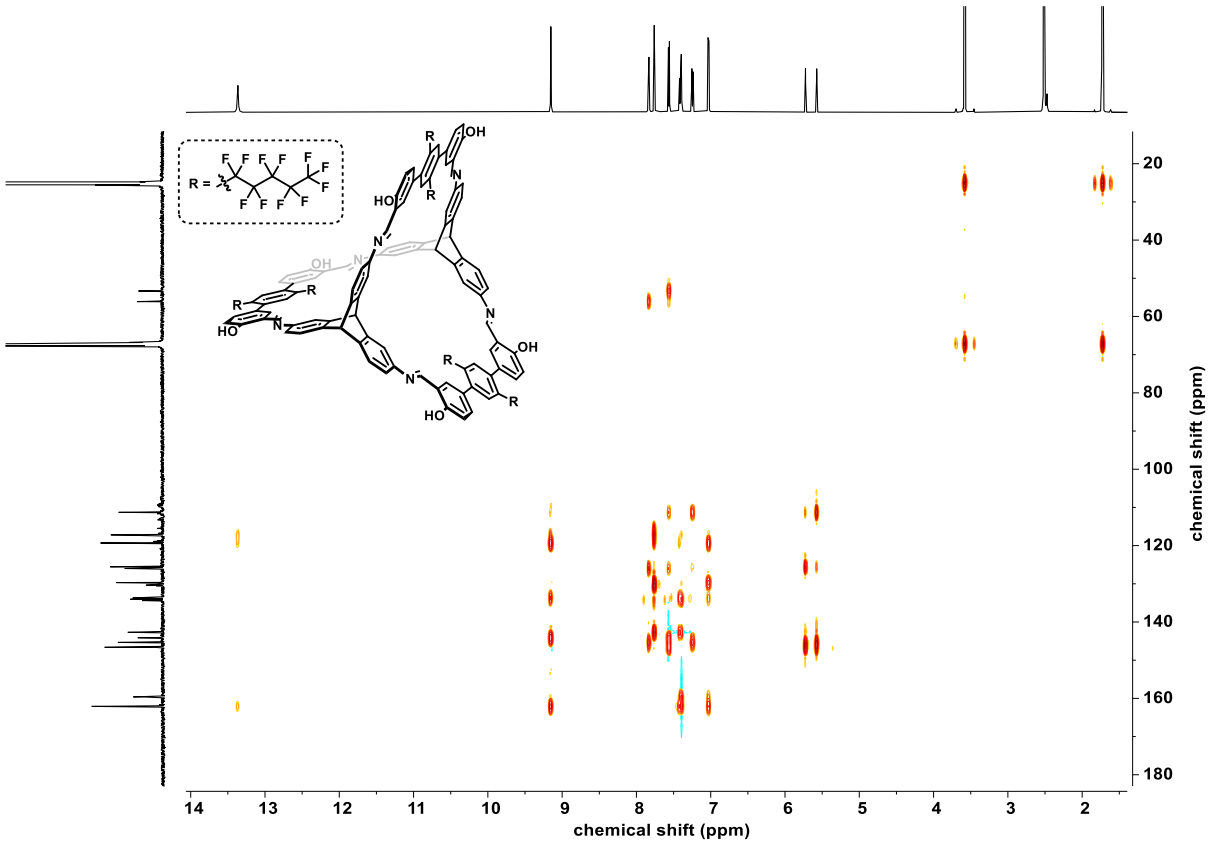

Figure 151. ^{1}H-^{13}C HMBC NMR spectrum of **cage-C$_5$F$_{11}$** (THF-d_8, 600 MHz, 151 MHz).

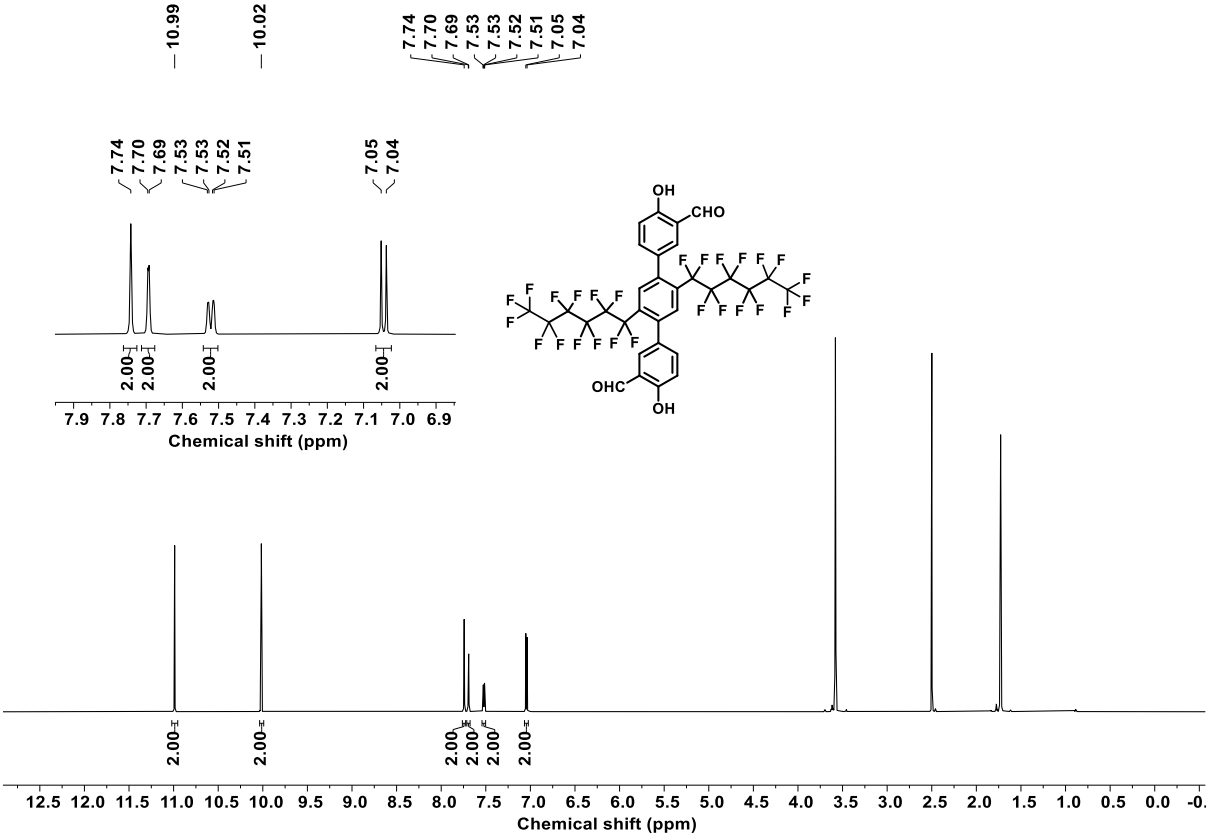

Figure 152. ^{1}H NMR spectrum of **73** (THF-d_8, 600 MHz).

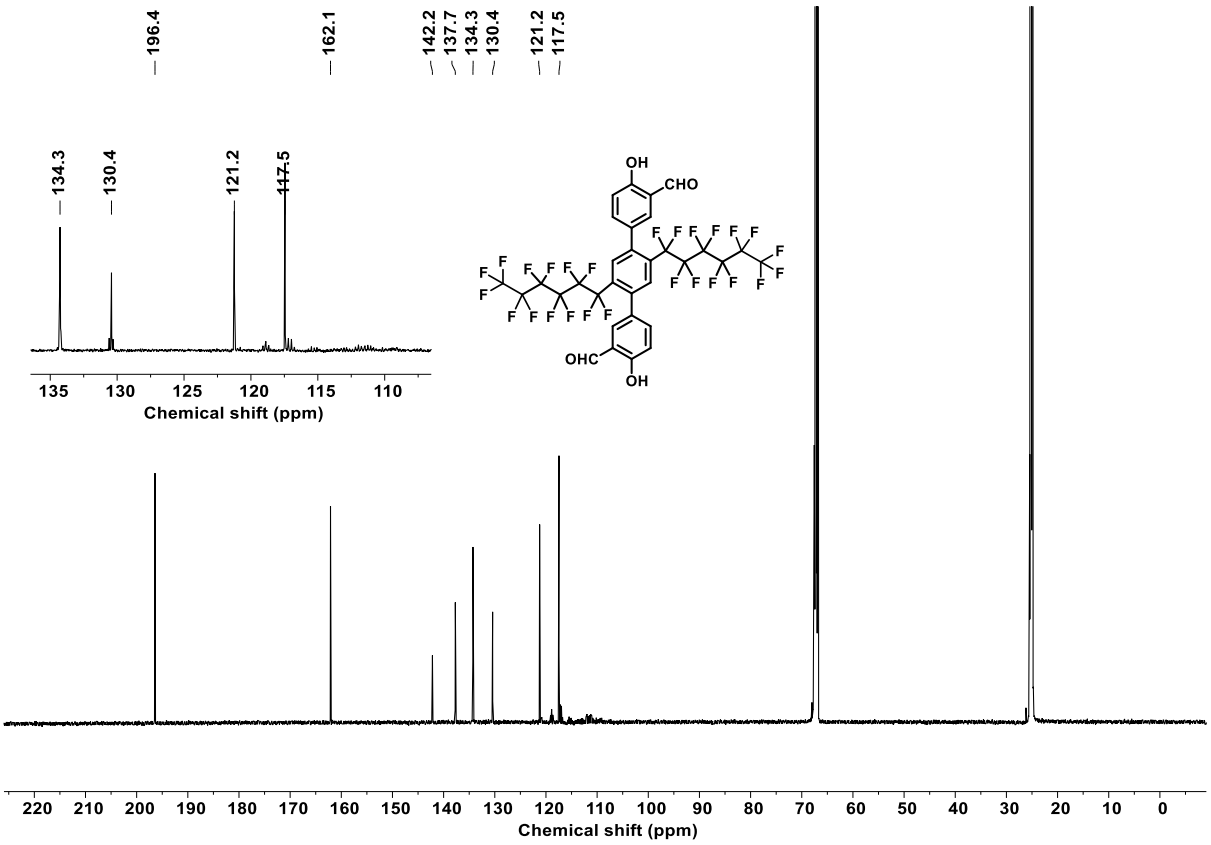

Figure 153. ^{13}C NMR spectrum of **73** (THF-d_8, 151 MHz).

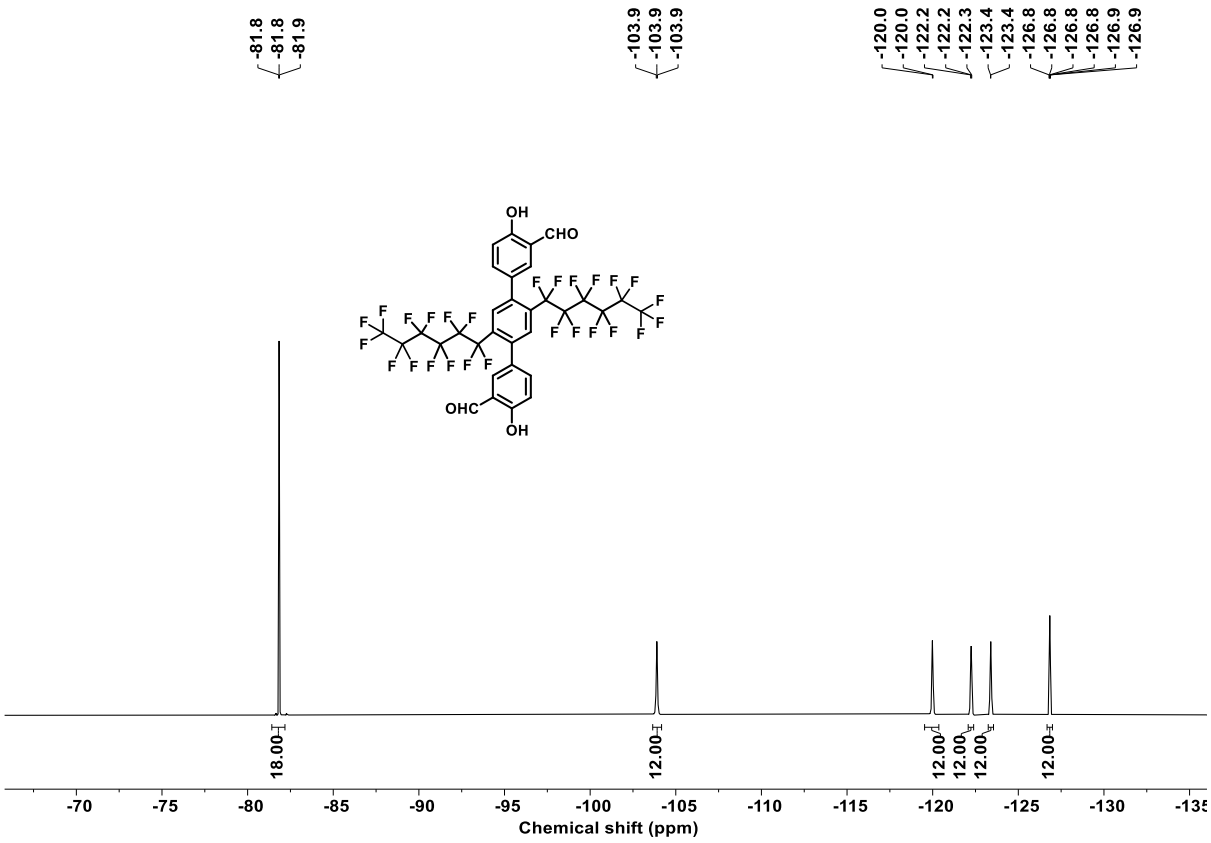

Figure 154. ^{19}F NMR spectrum of **73** (THF-d_8, 471 MHz).

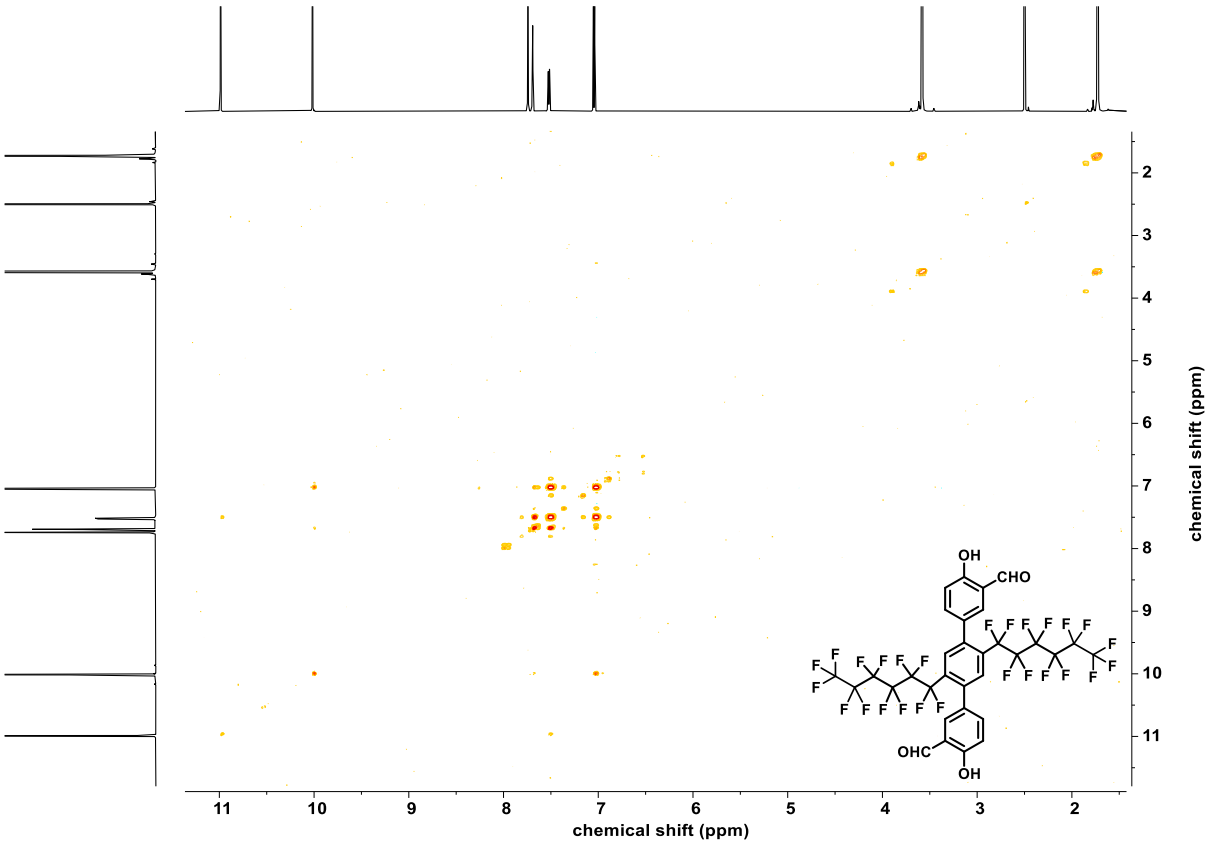

Figure 155. ^{1}H-^{1}H COSY NMR spectrum of **73** (THF-d_8, 600 MHz, 600 MHz).

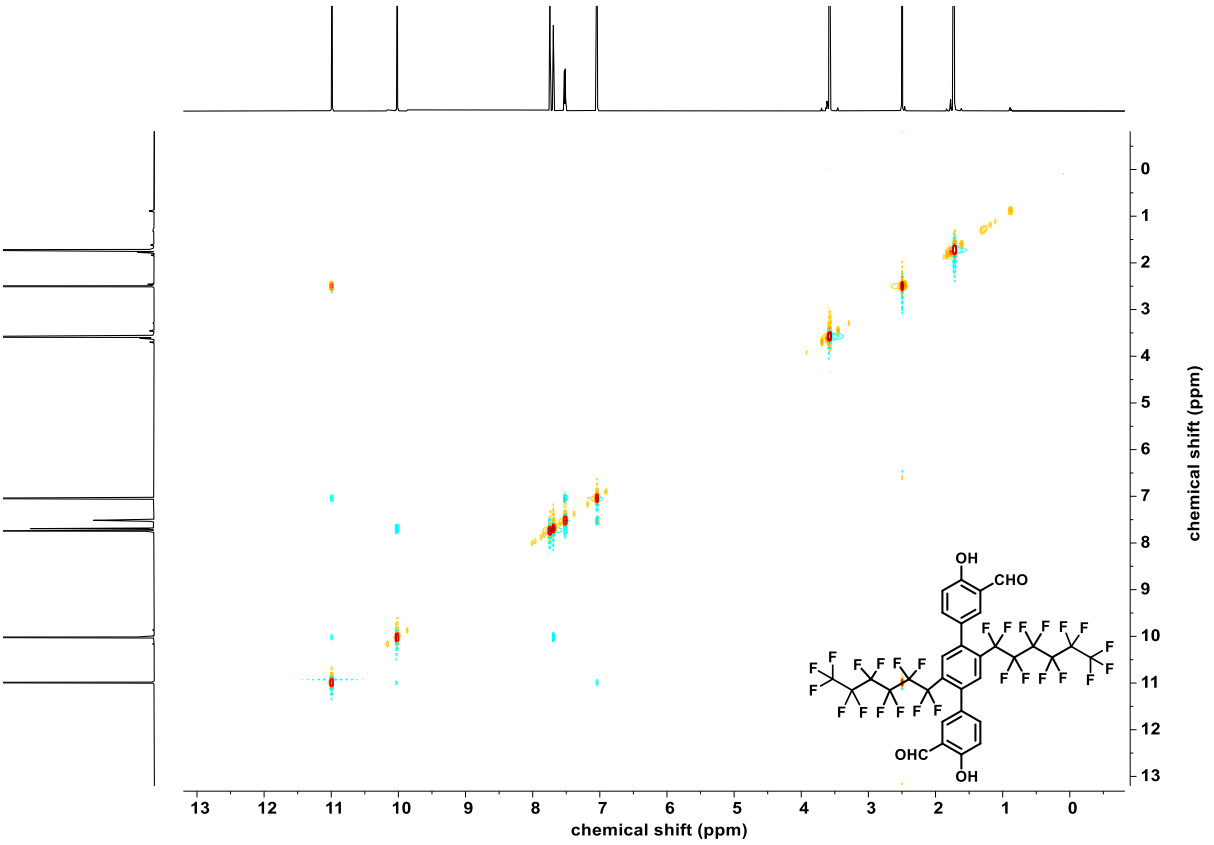

Figure 156. ^{1}H-^{1}H NOSY NMR spectrum of **73** (THF-d_8, 600 MHz, 600 MHz).

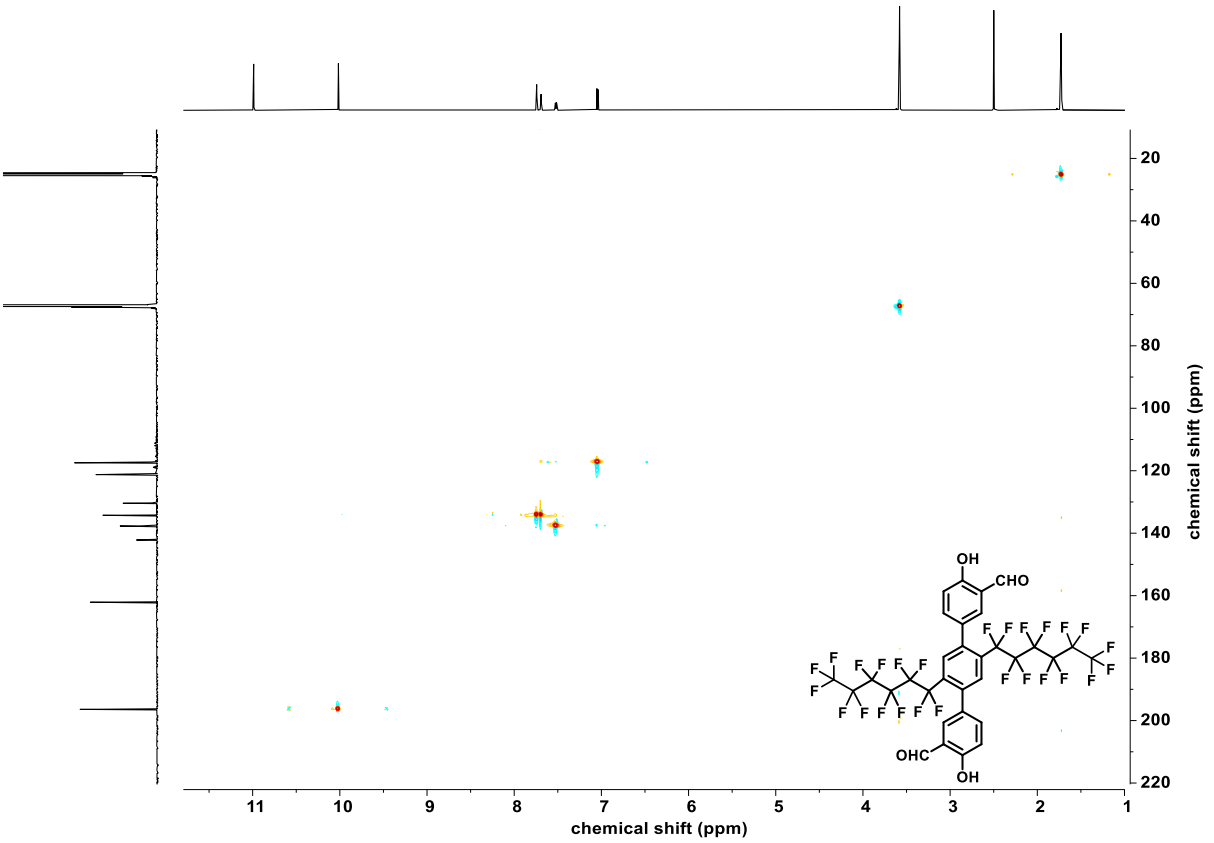

Figure 157. ^{1}H-^{13}C HSQC NMR spectrum of **73** (THF-d_8, 600 MHz, 151 MHz).

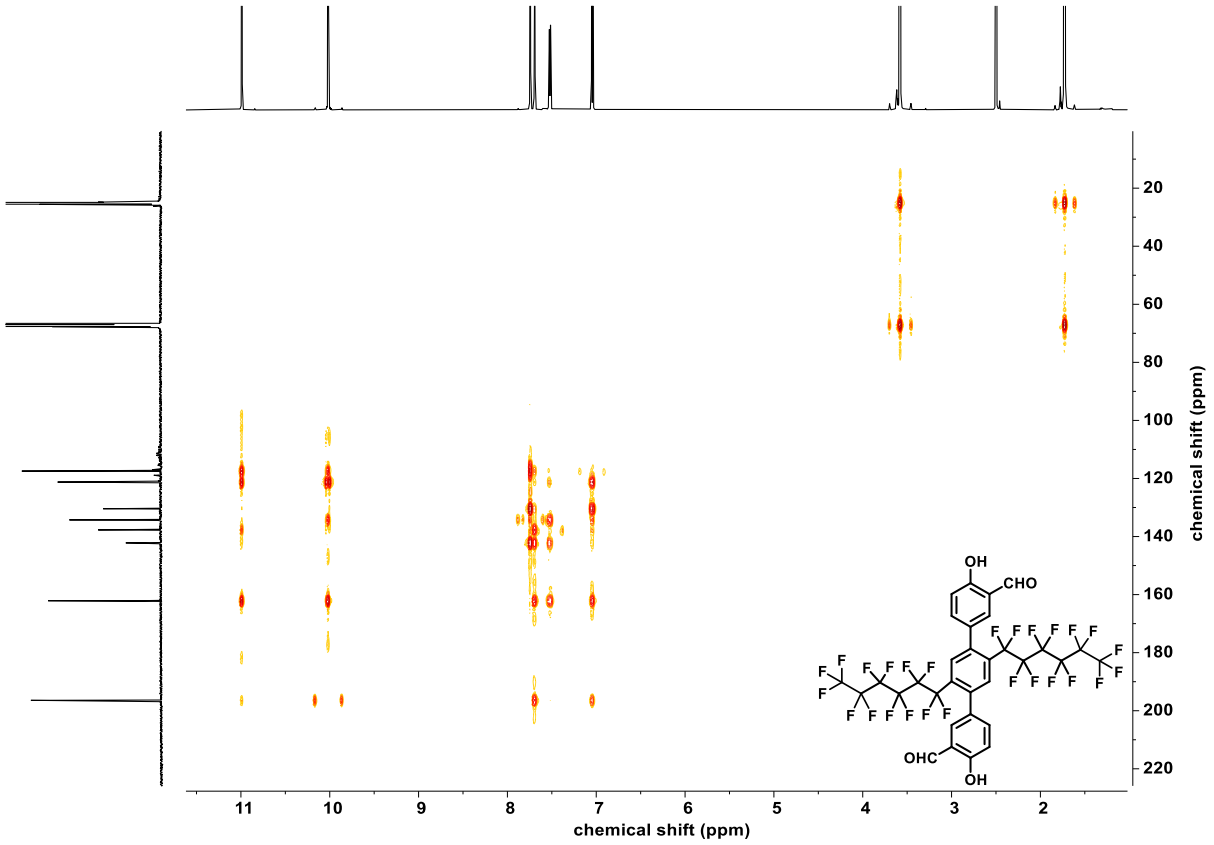

Figure 158. ^{1}H-^{13}C HMBC NMR spectrum of **73** (THF-d_8, 600 MHz, 151 MHz).

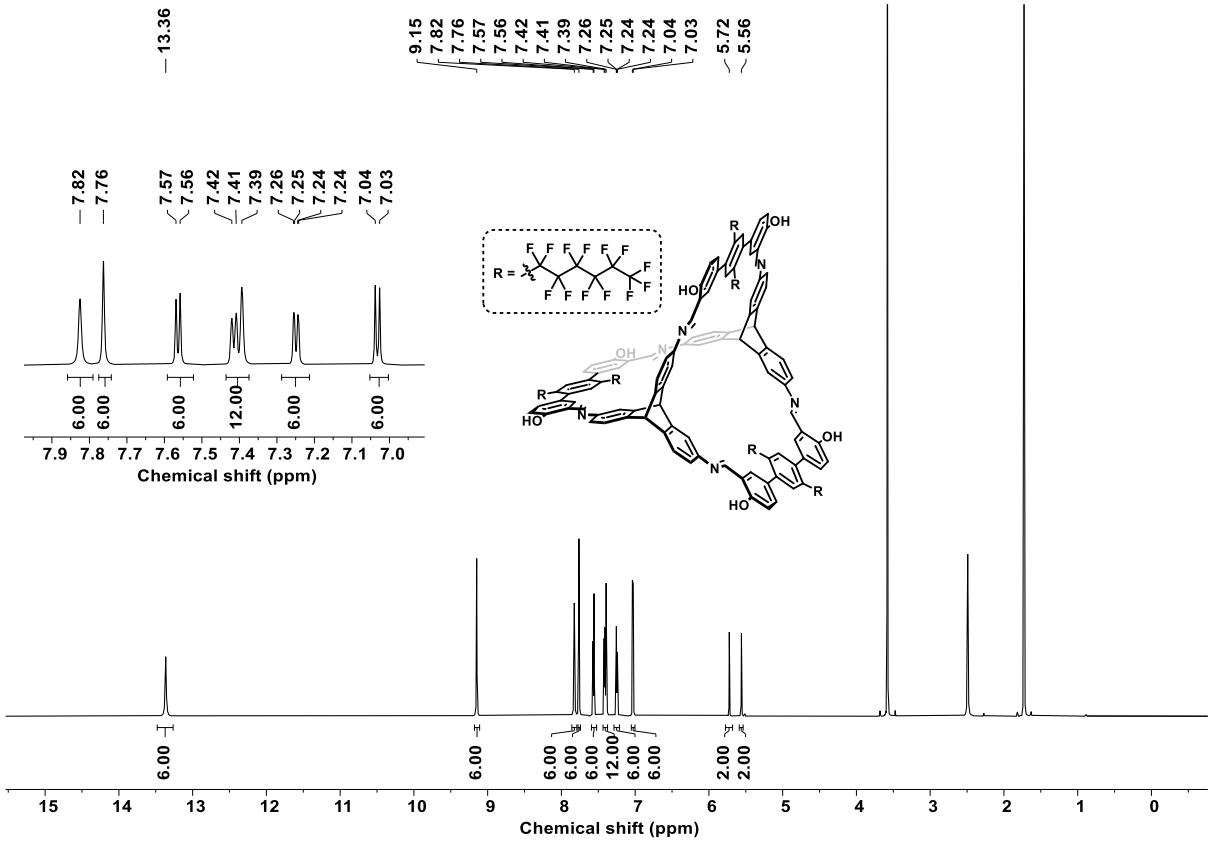

Figure 159. ^{1}H NMR spectrum of **cage-C_6F_{13}** (THF-d_8, 700 MHz).

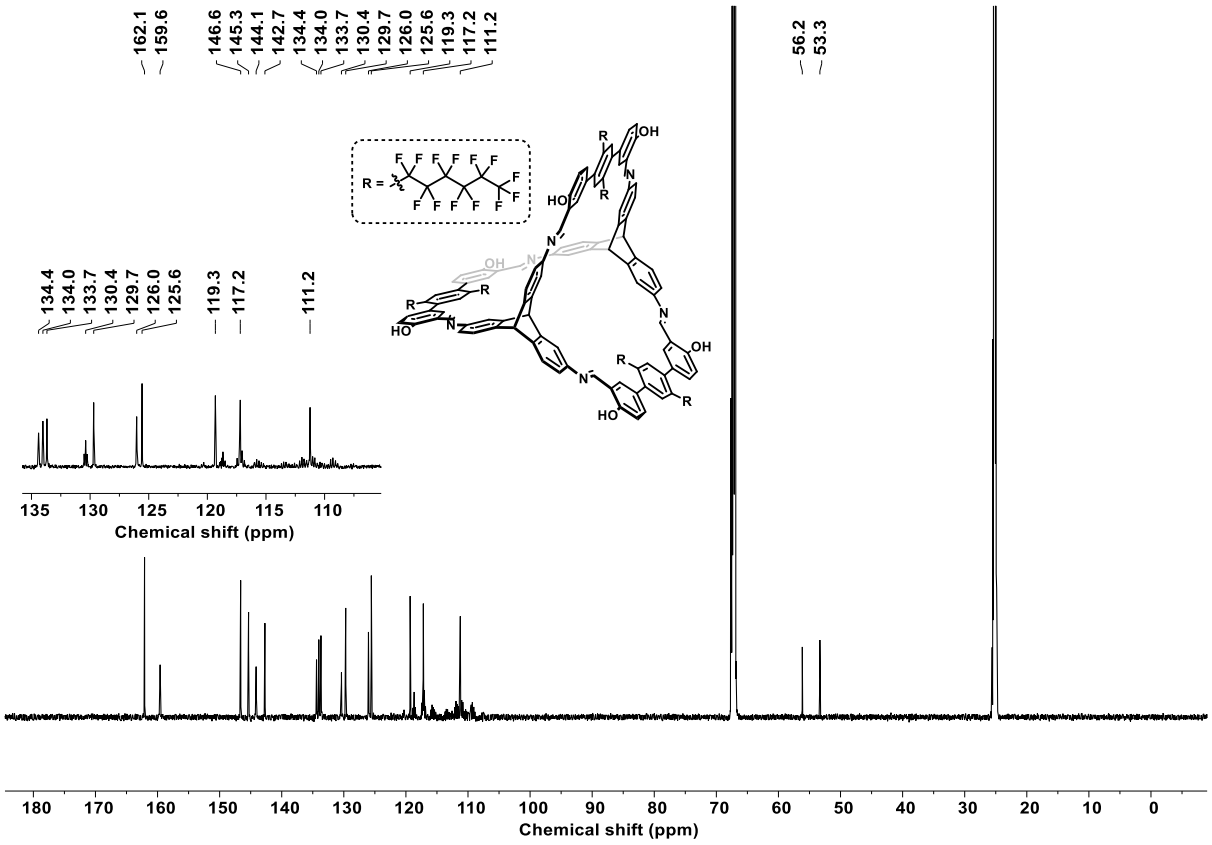

Figure 160. ^{13}C NMR spectrum of **cage-C_6F_{13}** (THF-d_8, 176 MHz).

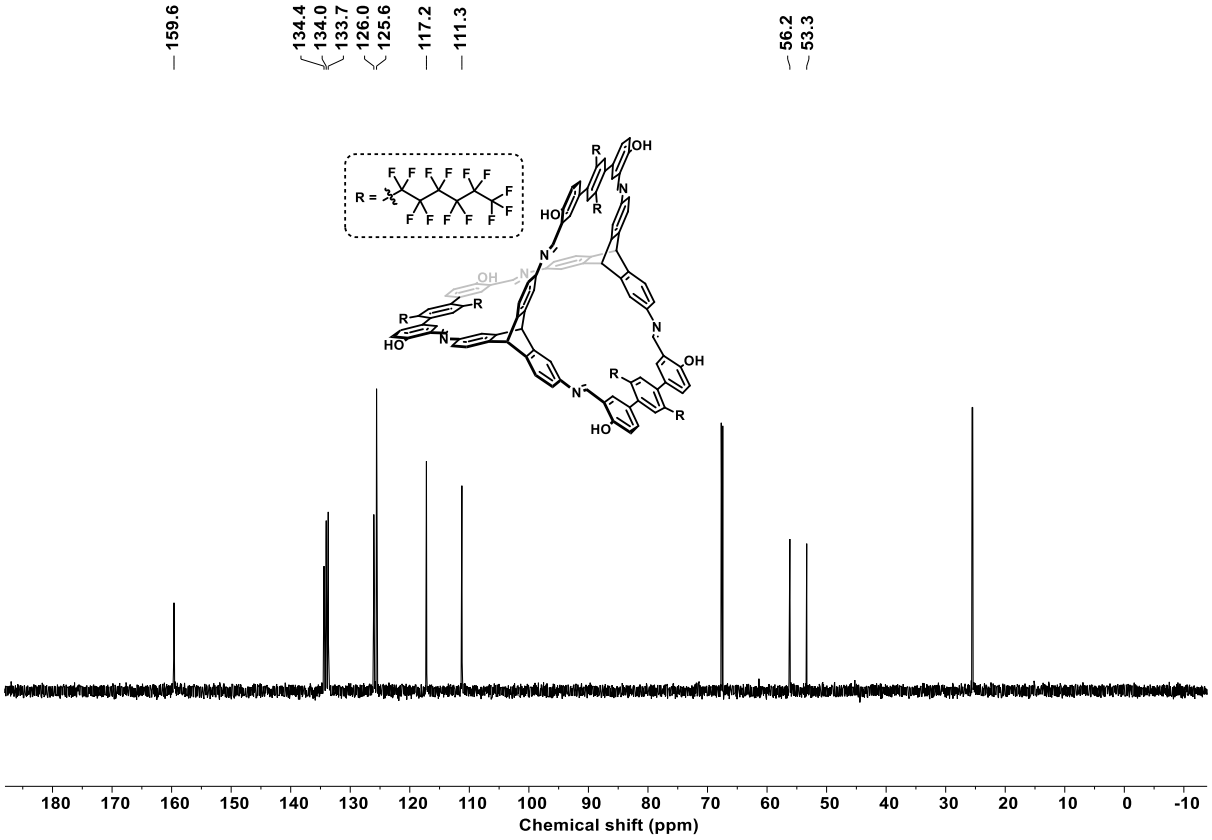

Figure 161. ^{13}C-DEPT135 NMR spectrum of **cage-C_6F_{13}** (THF-d_8, 176 MHz).

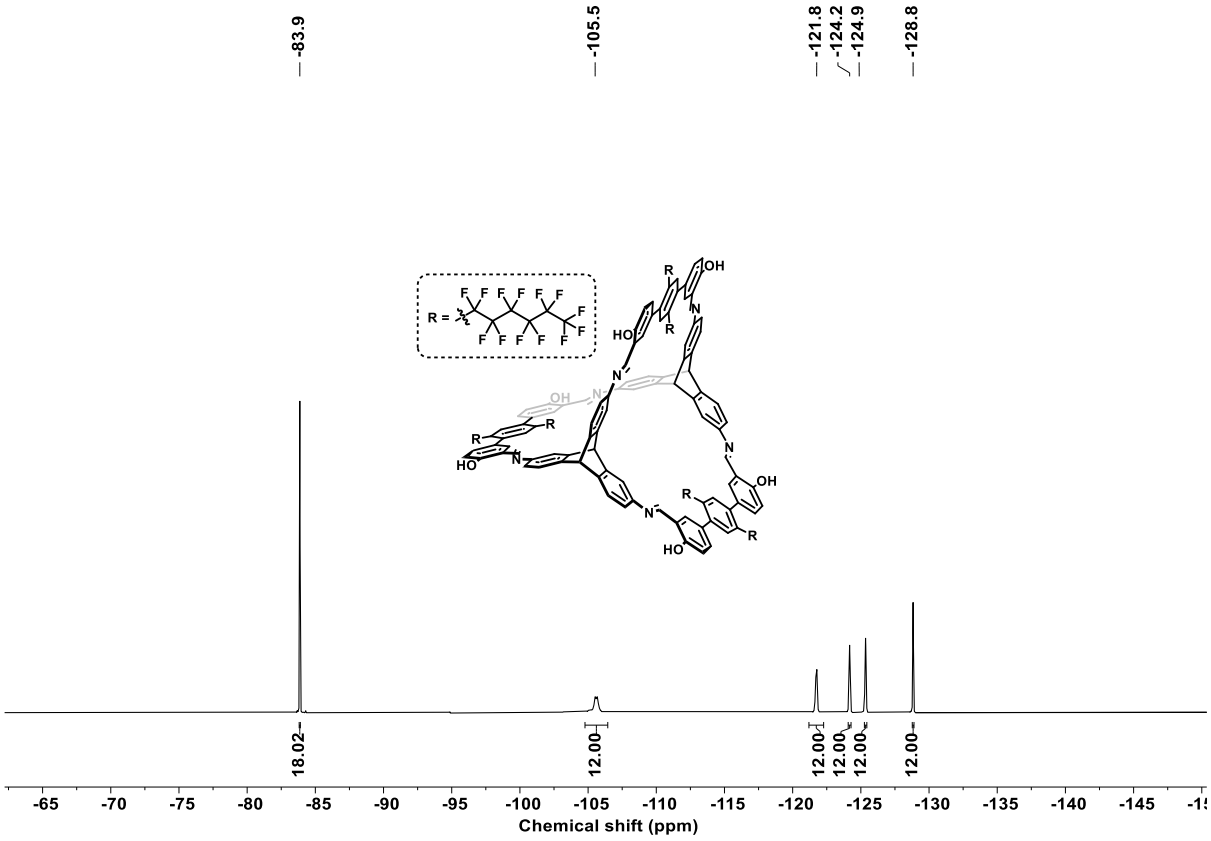

Figure 162. ^{19}F NMR spectrum of **cage-C$_6$F$_{13}$** (THF-d_8, 471 MHz).

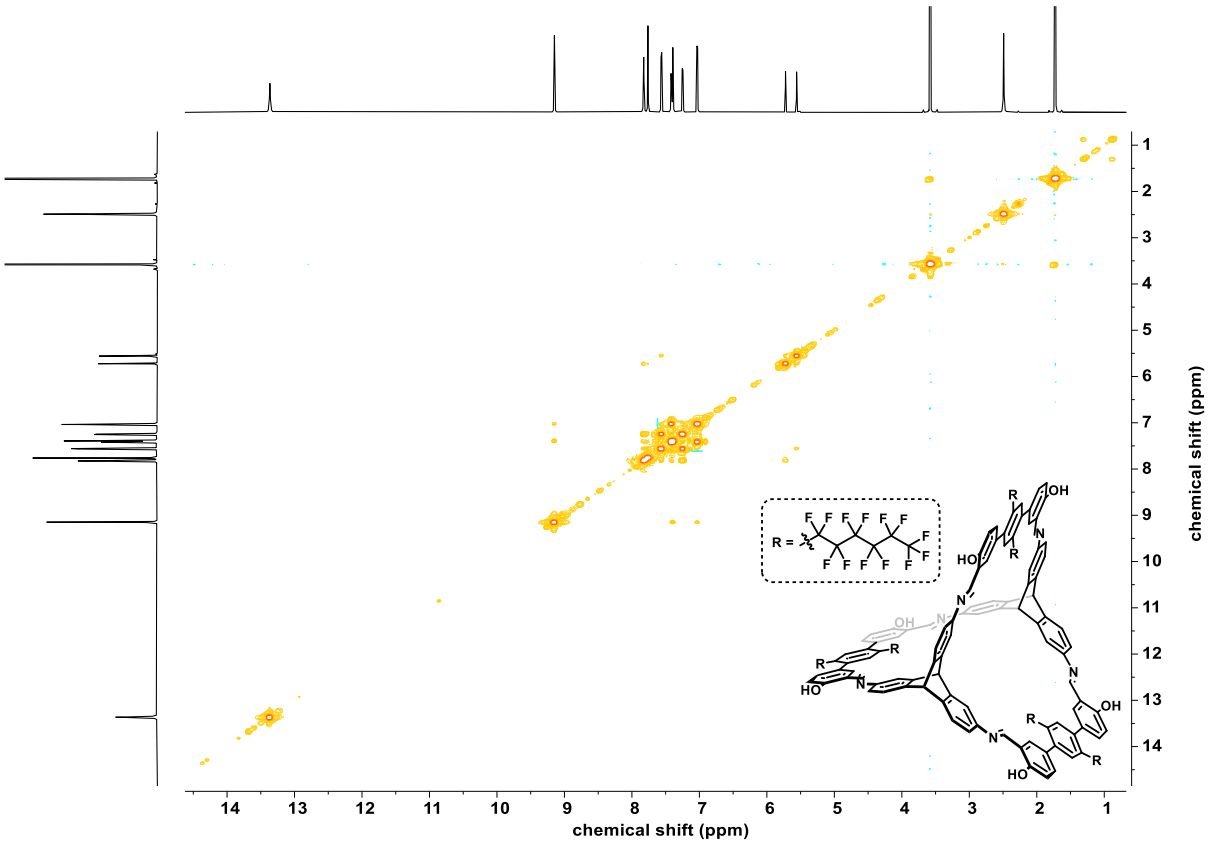

Figure 163. ^{1}H-^{1}H COSY NMR spectrum of **cage-C$_6$F$_{13}$** (THF-d_8, 700 MHz, 700 MHz).

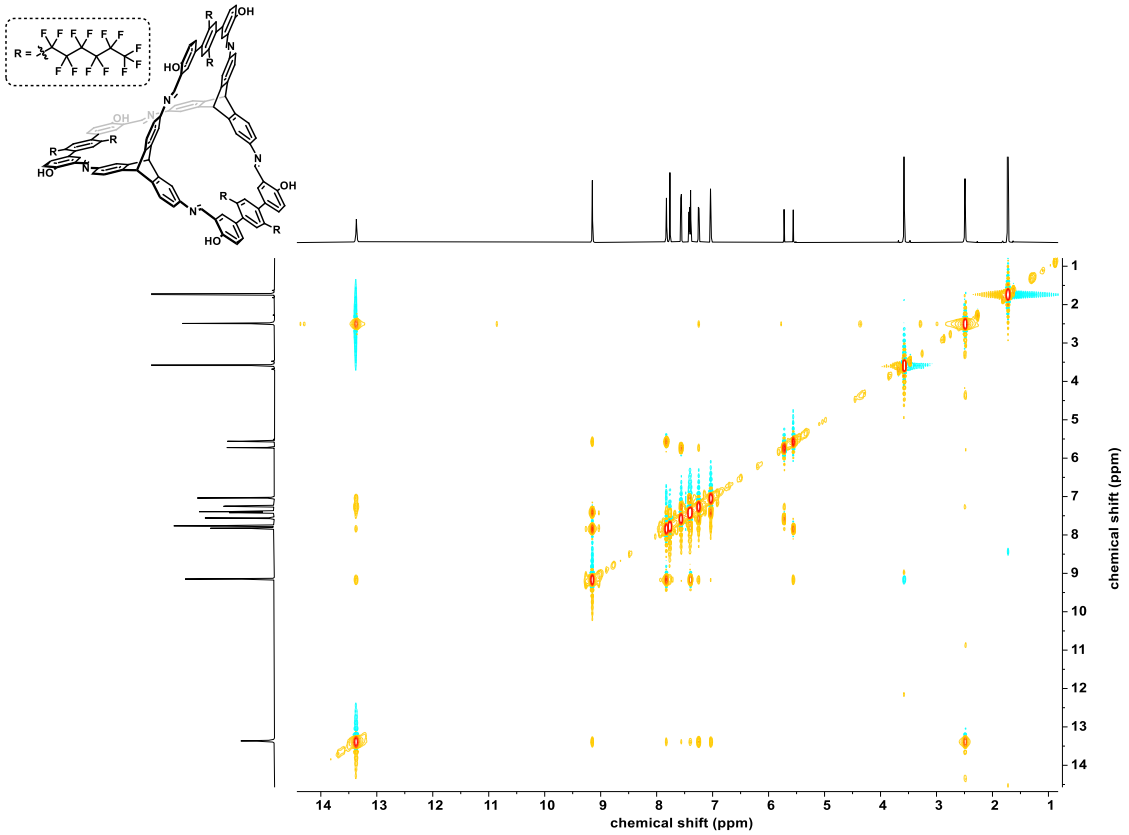

Figure 164. ^{1}H-^{1}H NOSY NMR spectrum of **cage-C$_6$F$_{13}$** (THF-d_8, 700 MHz, 700 MHz).

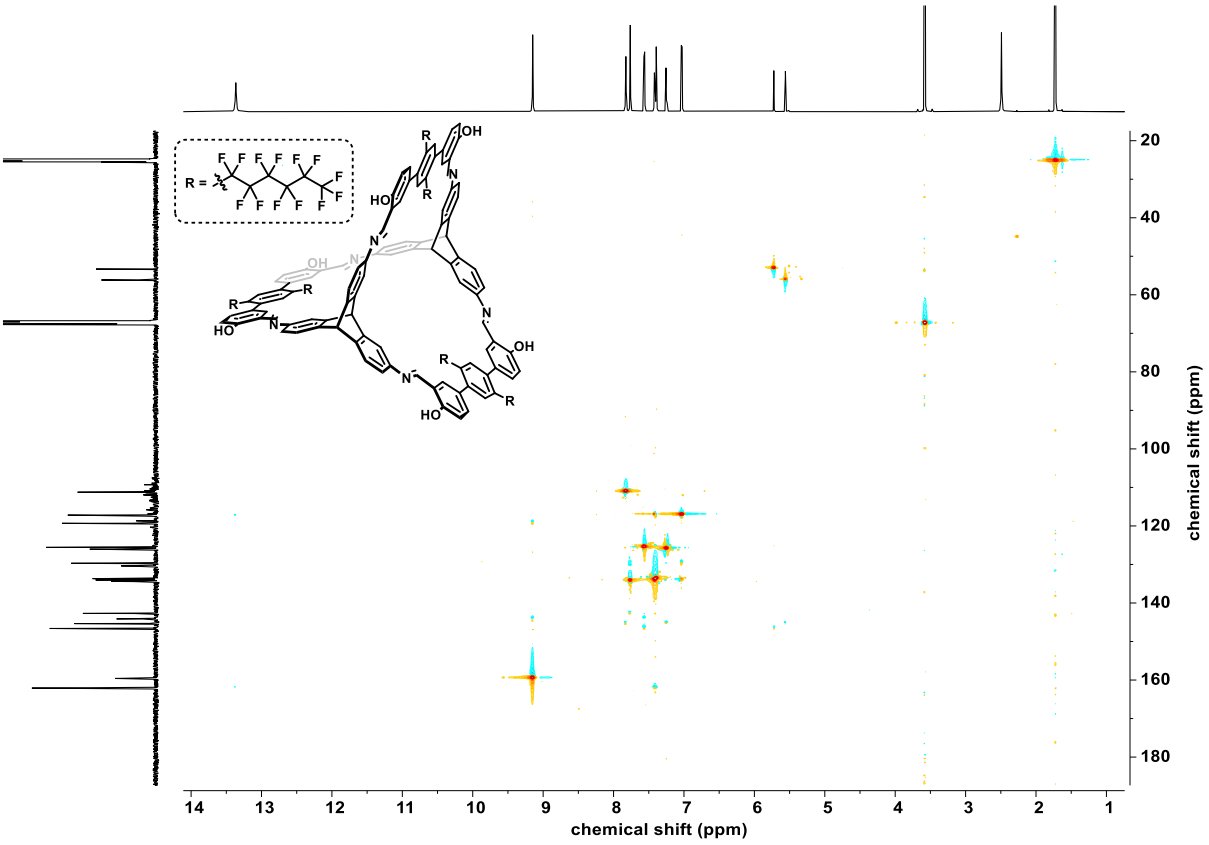

Figure 165. ^{1}H-^{13}C HSQC NMR spectrum of **cage-C$_6$F$_{13}$** (THF-d_8, 700 MHz, 176 MHz).

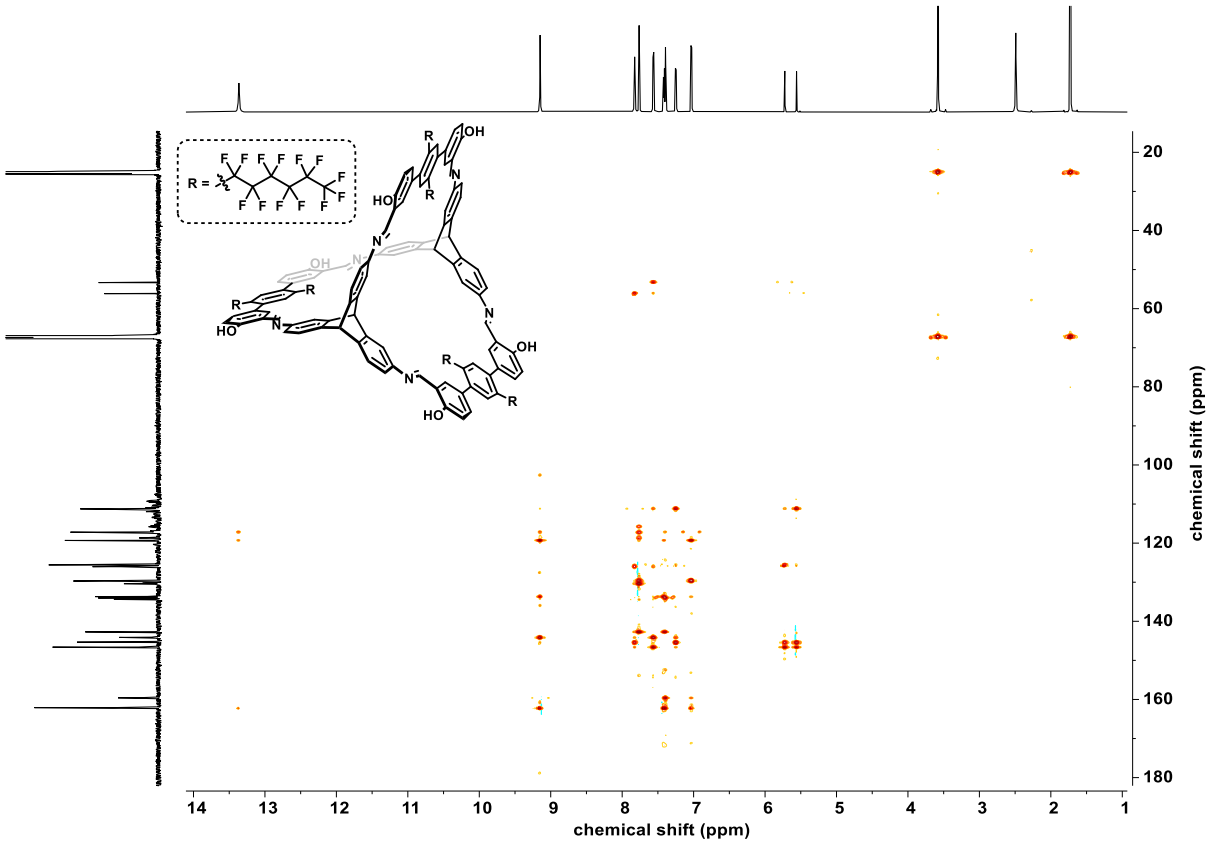

Figure 166. ^{1}H-^{13}C HMBC NMR spectrum of **cage-C$_6$F$_{13}$** (THF-d_8, 700 MHz, 176 MHz).

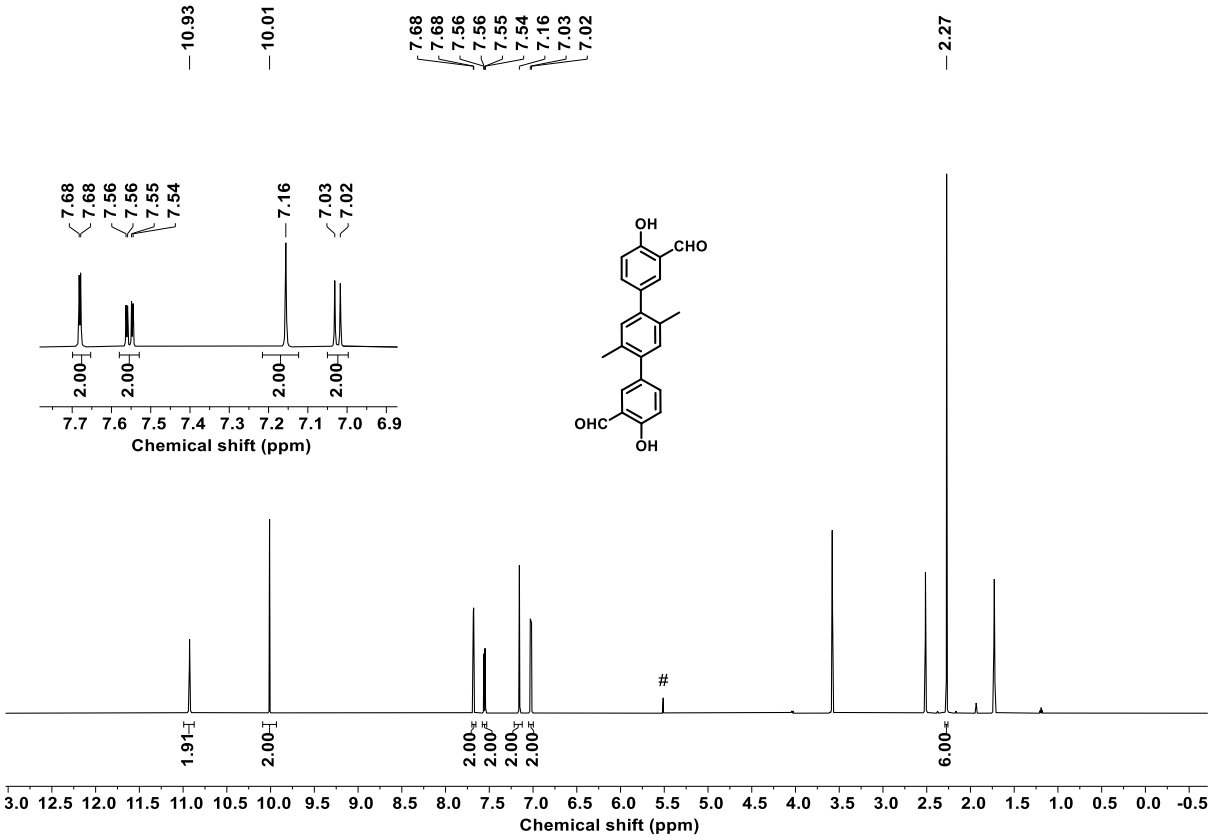

Figure 167. ^{1}H NMR spectrum of **75** (THF-d_8, 600 MHz).

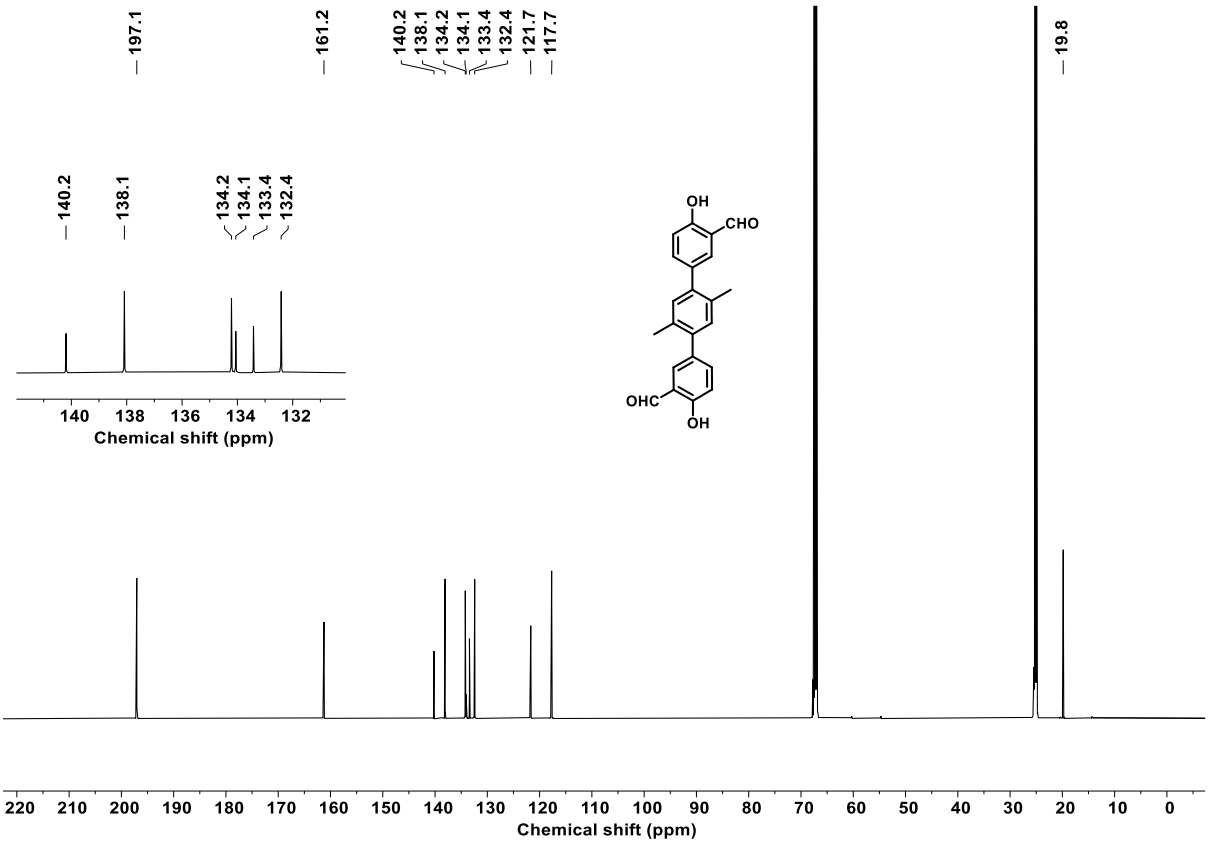

Figure 168. ^{13}C NMR spectrum of **75** (THF-d_8, 151 MHz).

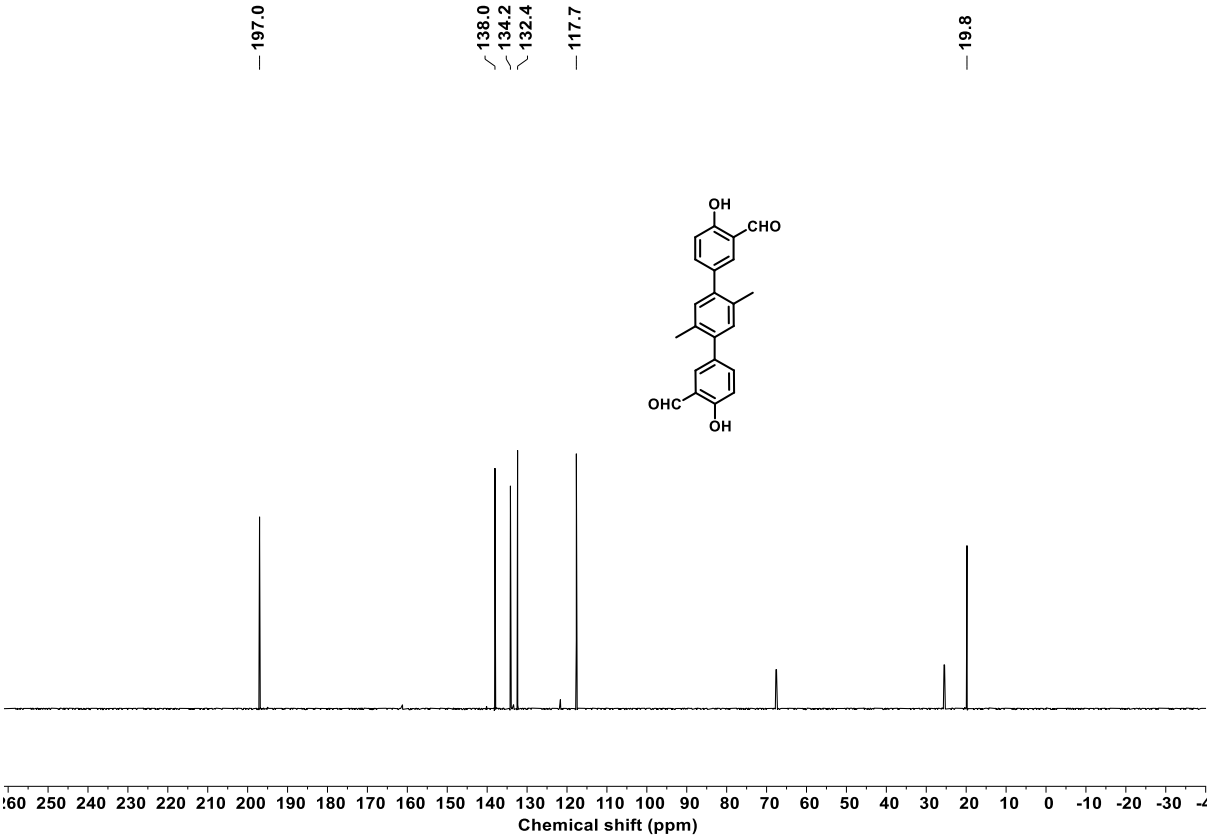

Figure 169. ^{13}C-DEPT135 NMR spectrum of **75** (THF-d_8, 151 MHz).

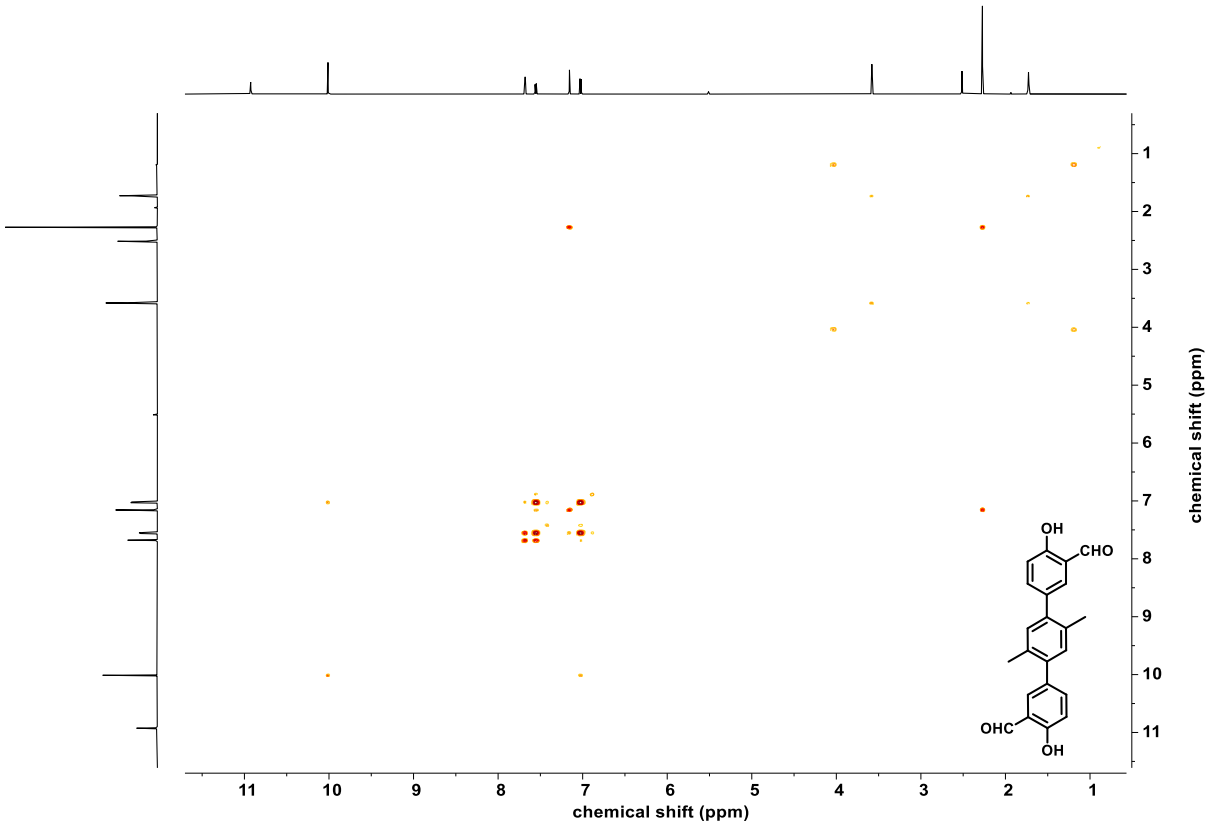

Figure 170. ^{1}H-^{1}H COSY NMR spectrum of **75** (THF-d_8, 600 MHz, 600 MHz).

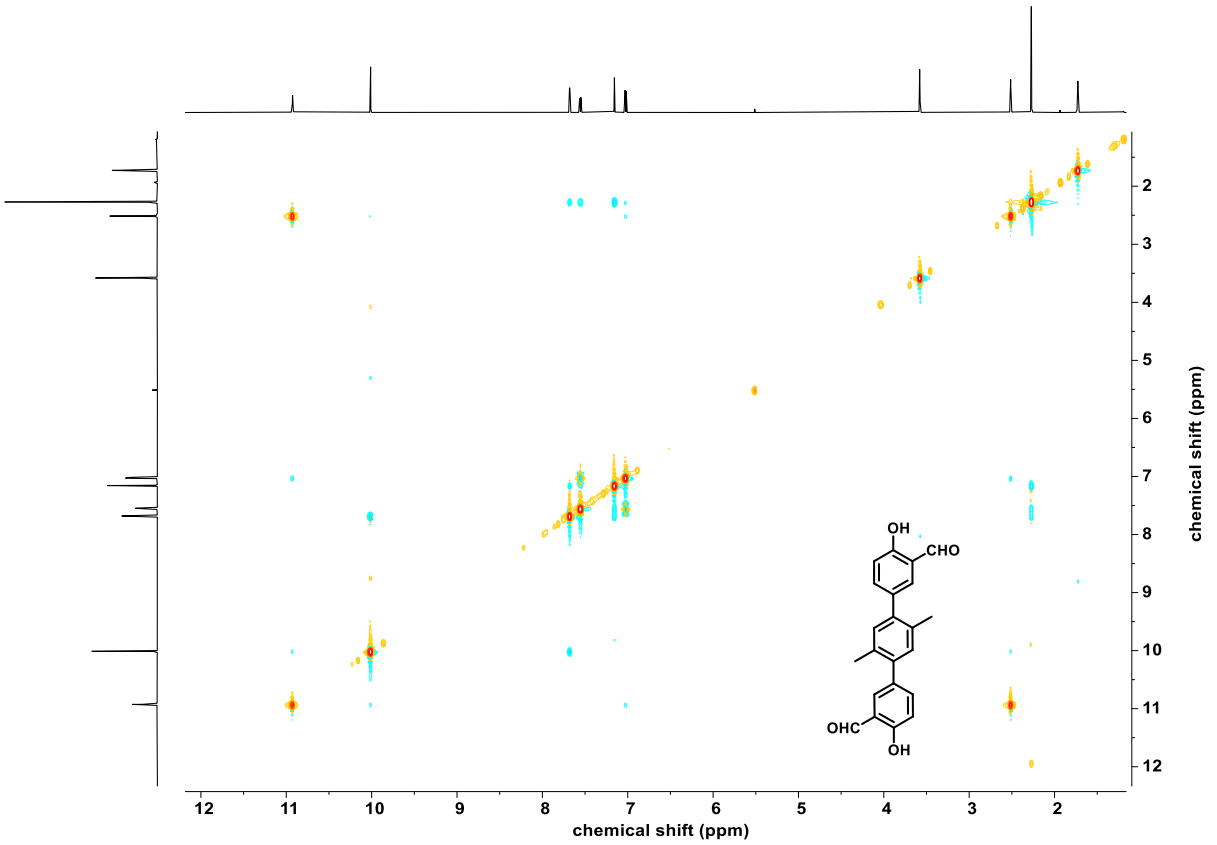

Figure 171. ^{1}H-^{1}H NOSY NMR spectrum of **75** (THF-d_8, 600 MHz, 600 MHz).

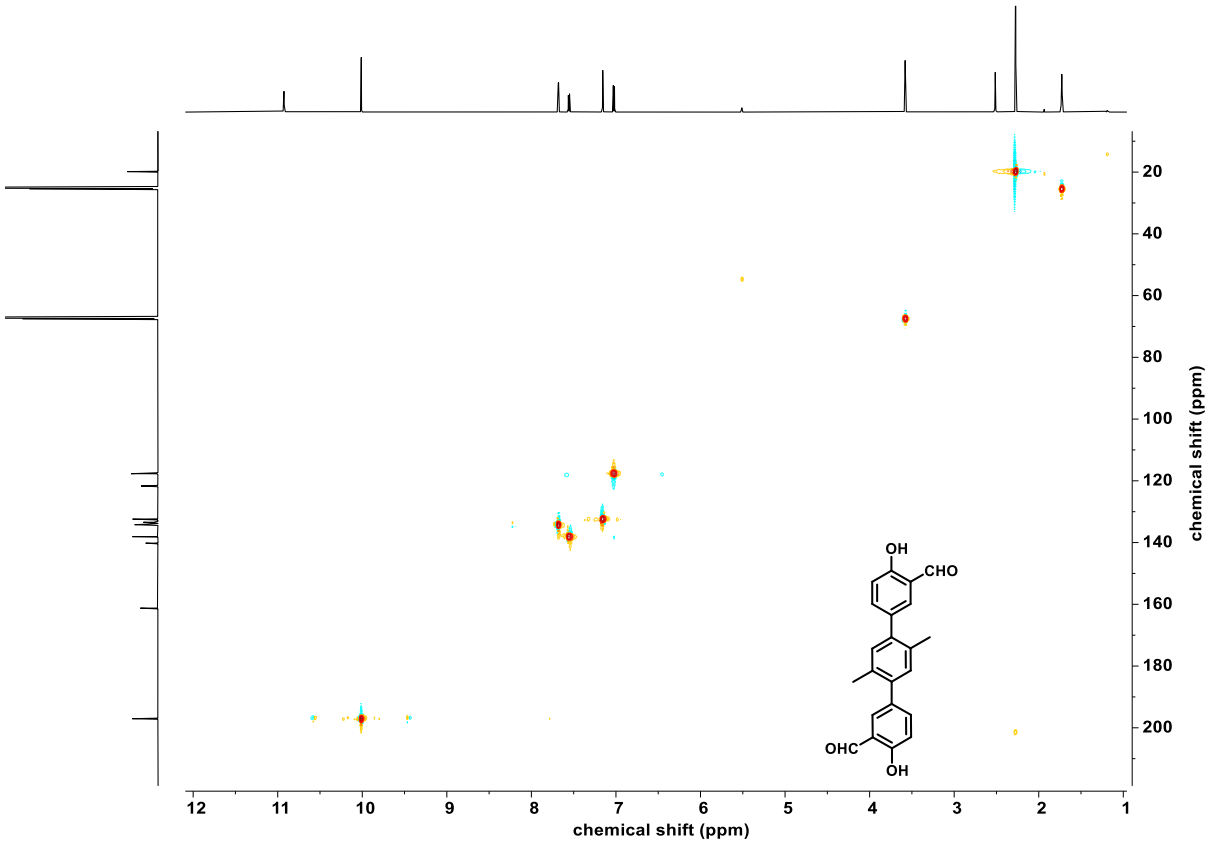

Figure 172. ^{1}H-^{13}C HSQC NMR spectrum of **75** (THF-d_8, 600 MHz, 151 MHz).

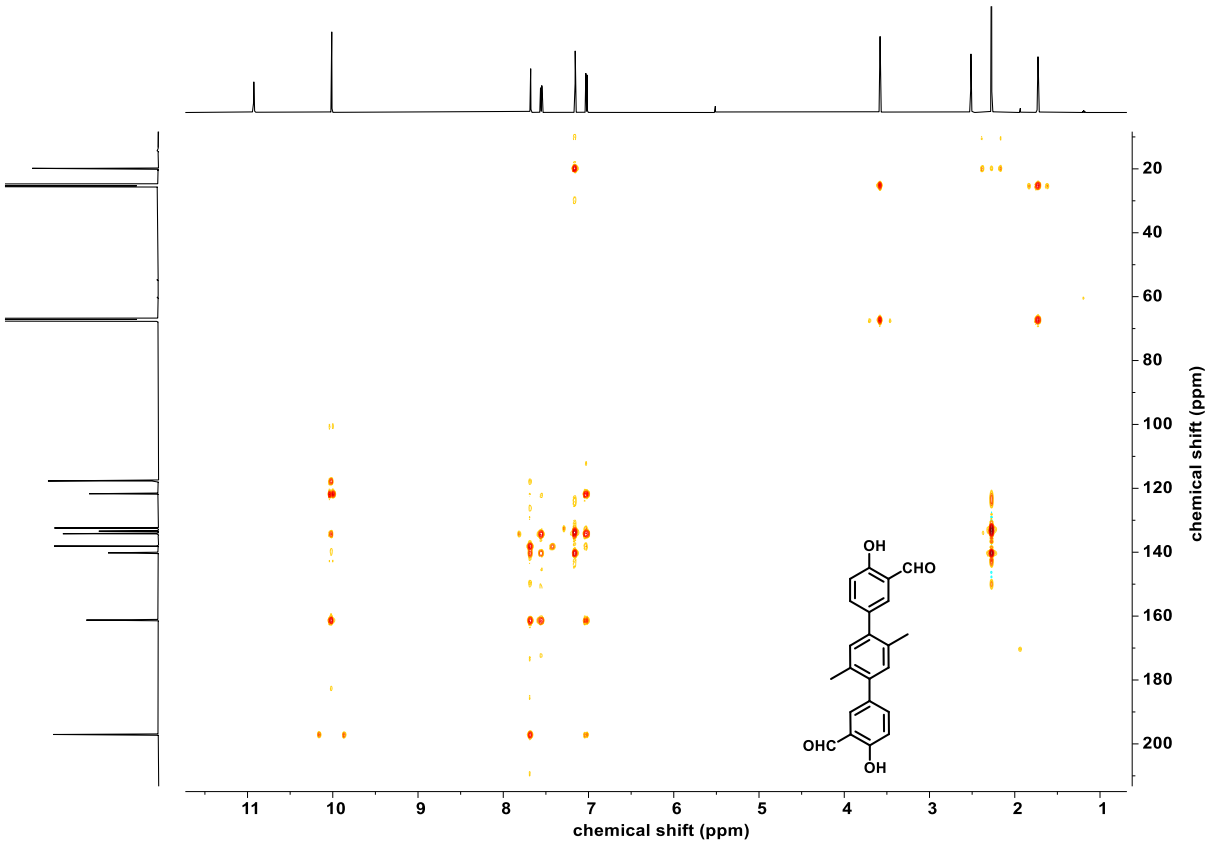

Figure 173. ^{1}H-^{13}C HMBC NMR spectrum of **75** (THF-d_8, 600 MHz, 151 MHz).

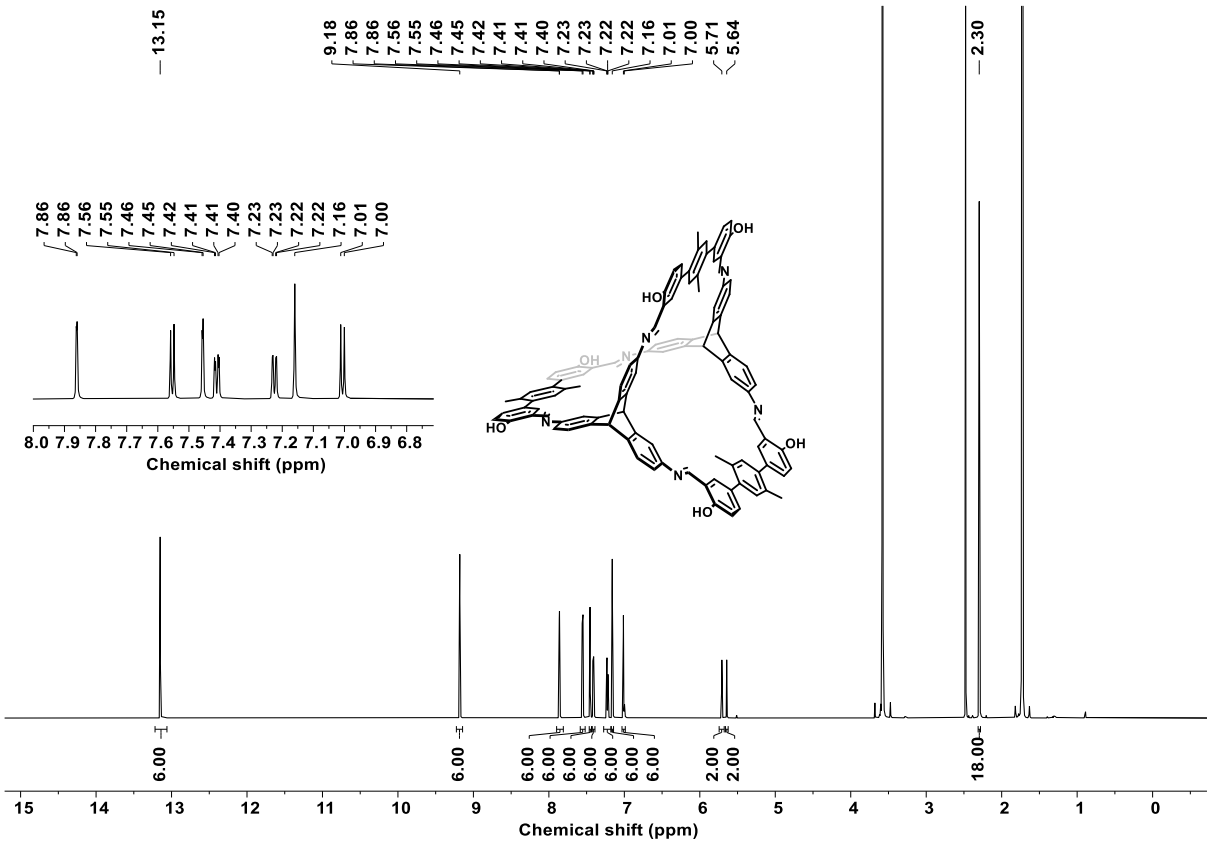

Figure 174. ^{1}H NMR spectrum of **cage-CH$_3$** (THF-d_8, 700 MHz).

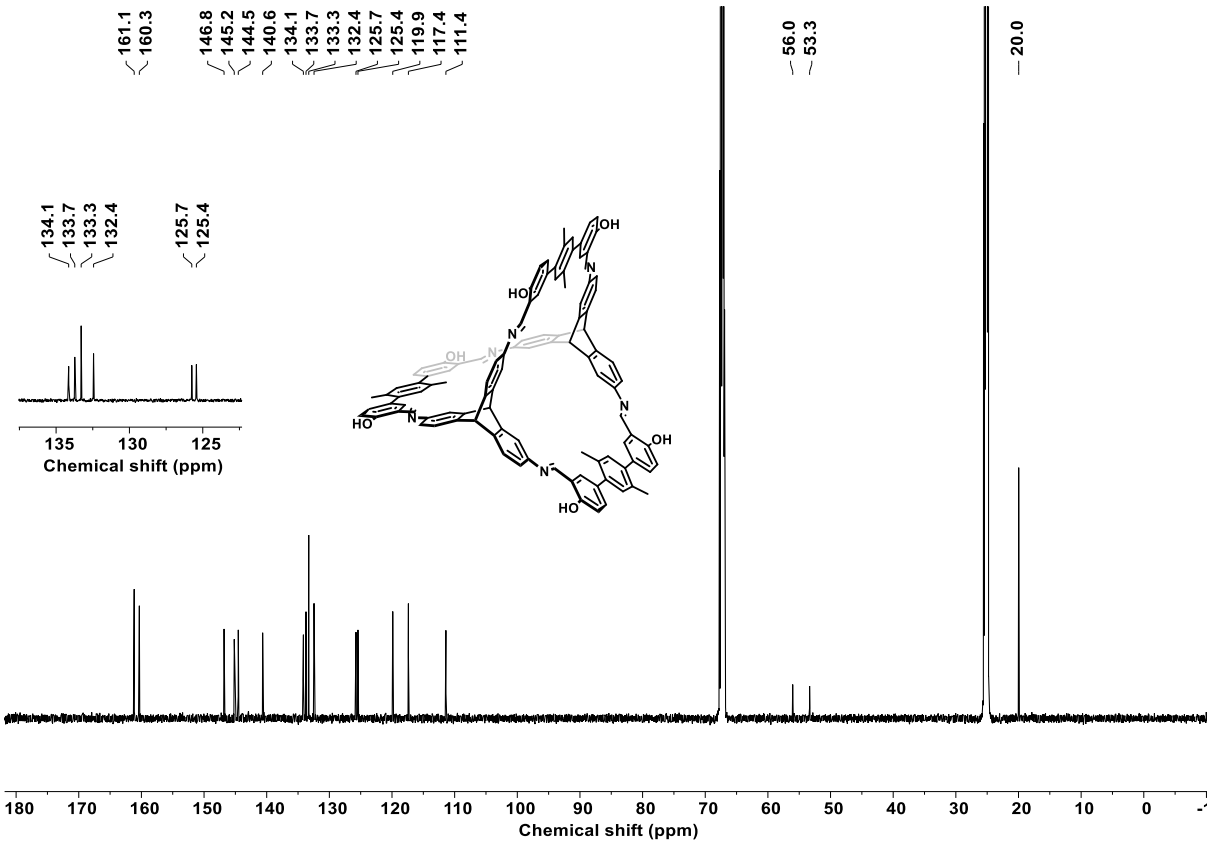

Figure 175. ^{13}C NMR spectrum of **cage-CH$_3$** (THF-d_8, 176 MHz).

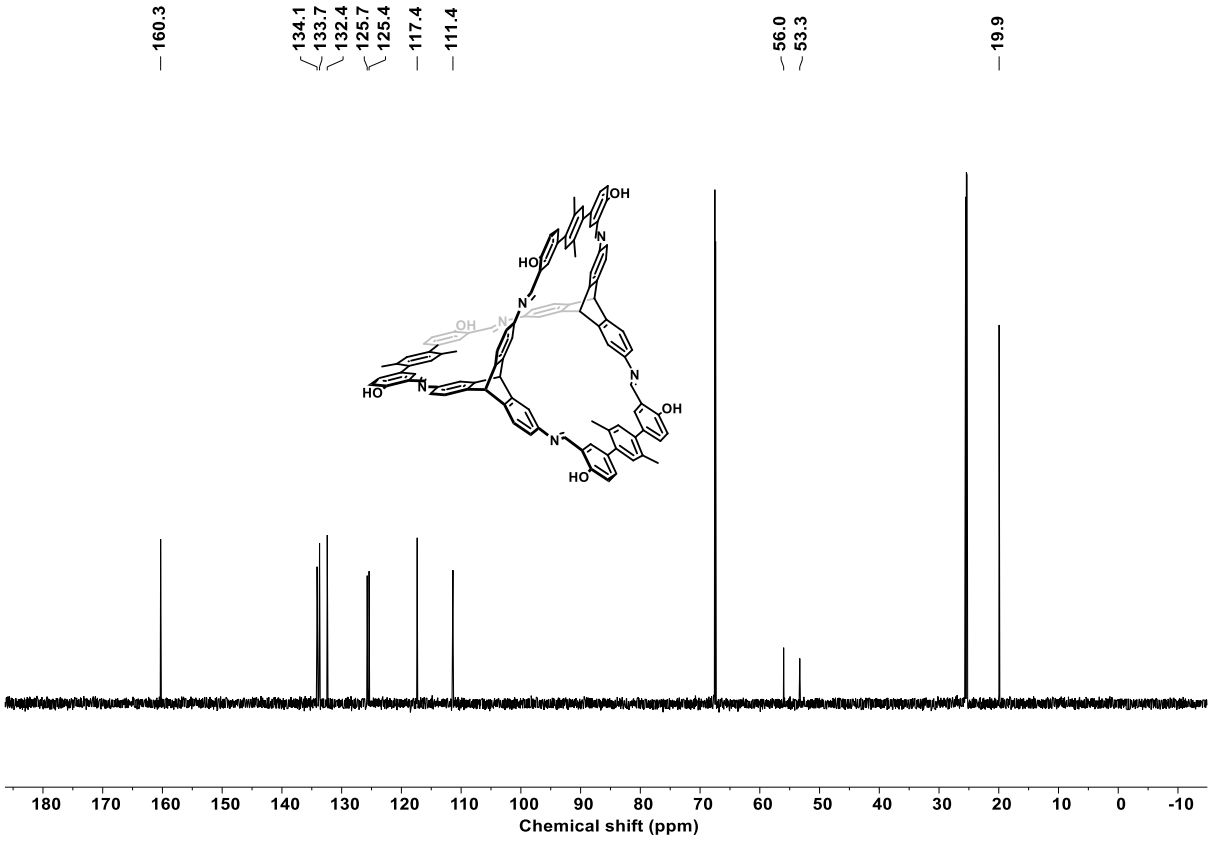

Figure 176. ^{13}C-DEPT135 NMR spectrum of **cage-CH$_3$** (THF-d_8, 176 MHz).

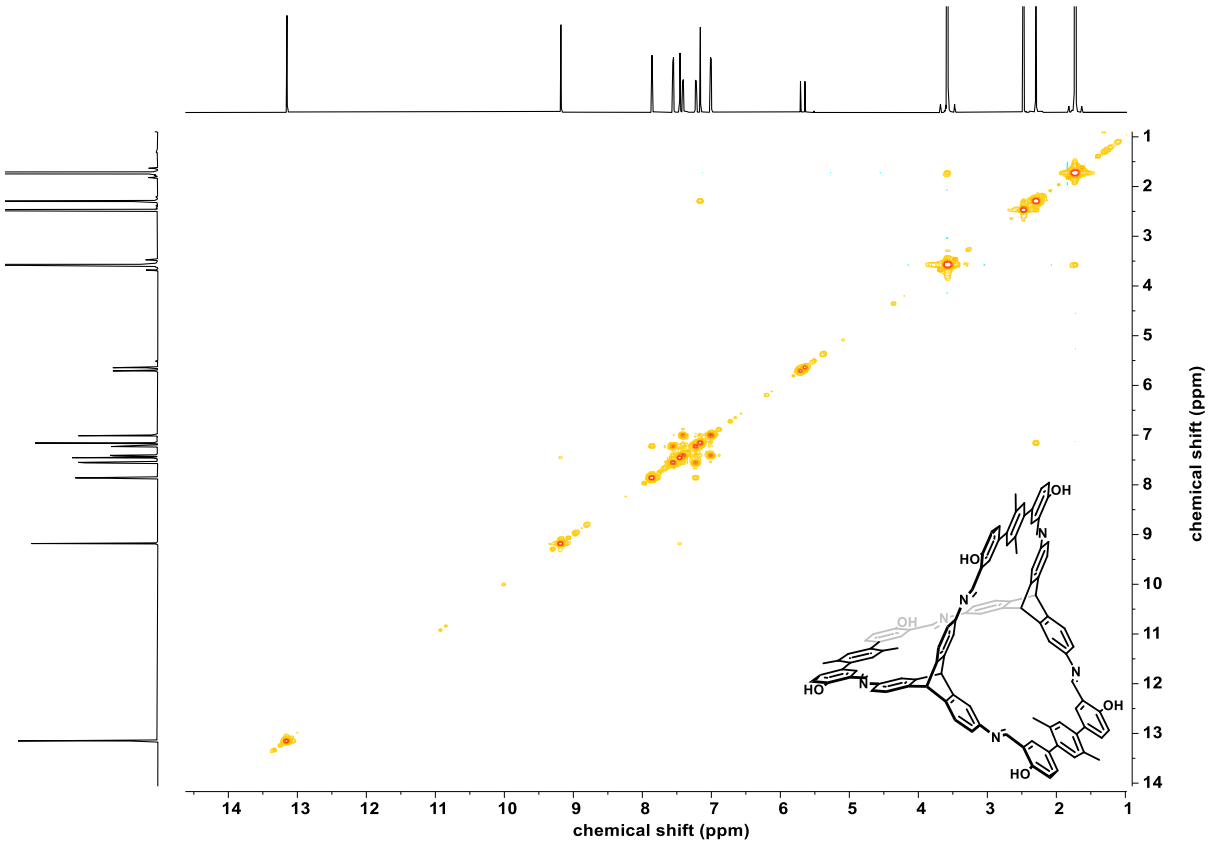

Figure 177. ^{1}H-^{1}H COSY NMR spectrum of **cage-CH$_3$** (THF-d_8, 700 MHz, 700 MHz).

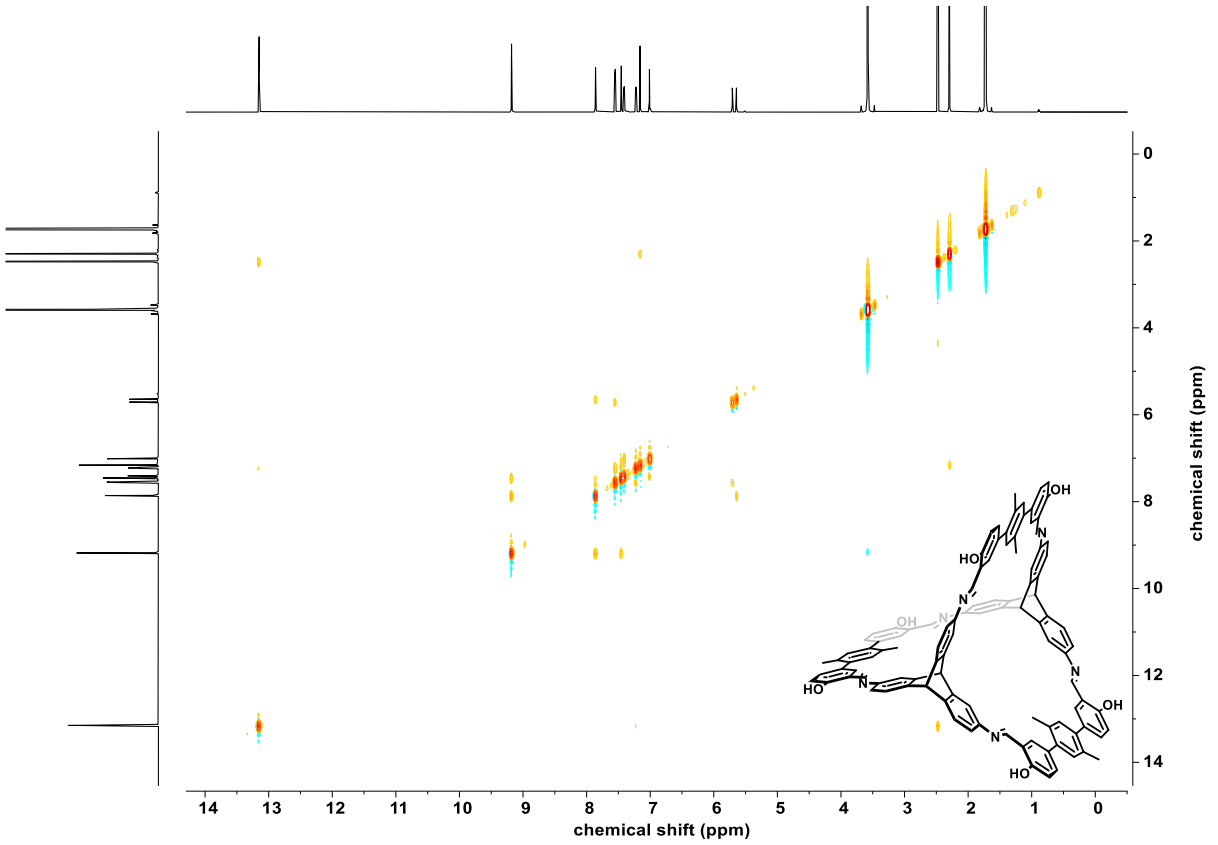

Figure 178. ^{1}H-^{1}H NOSY NMR spectrum of **cage-CH$_3$** (THF-d_8, 700 MHz, 700 MHz).

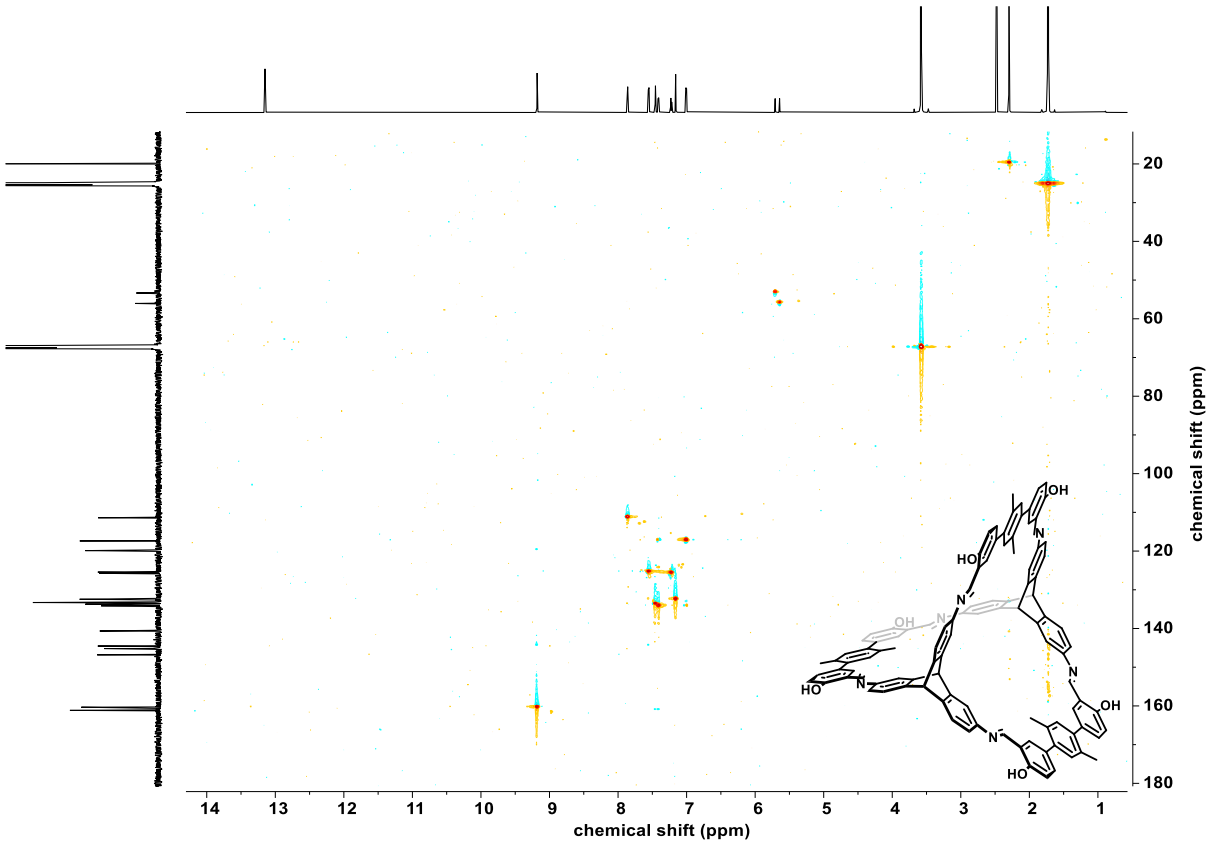

Figure 179. ^{1}H-^{13}C HSQC NMR spectrum of **cage-CH$_3$** (THF-d_8, 700 MHz, 176 MHz).

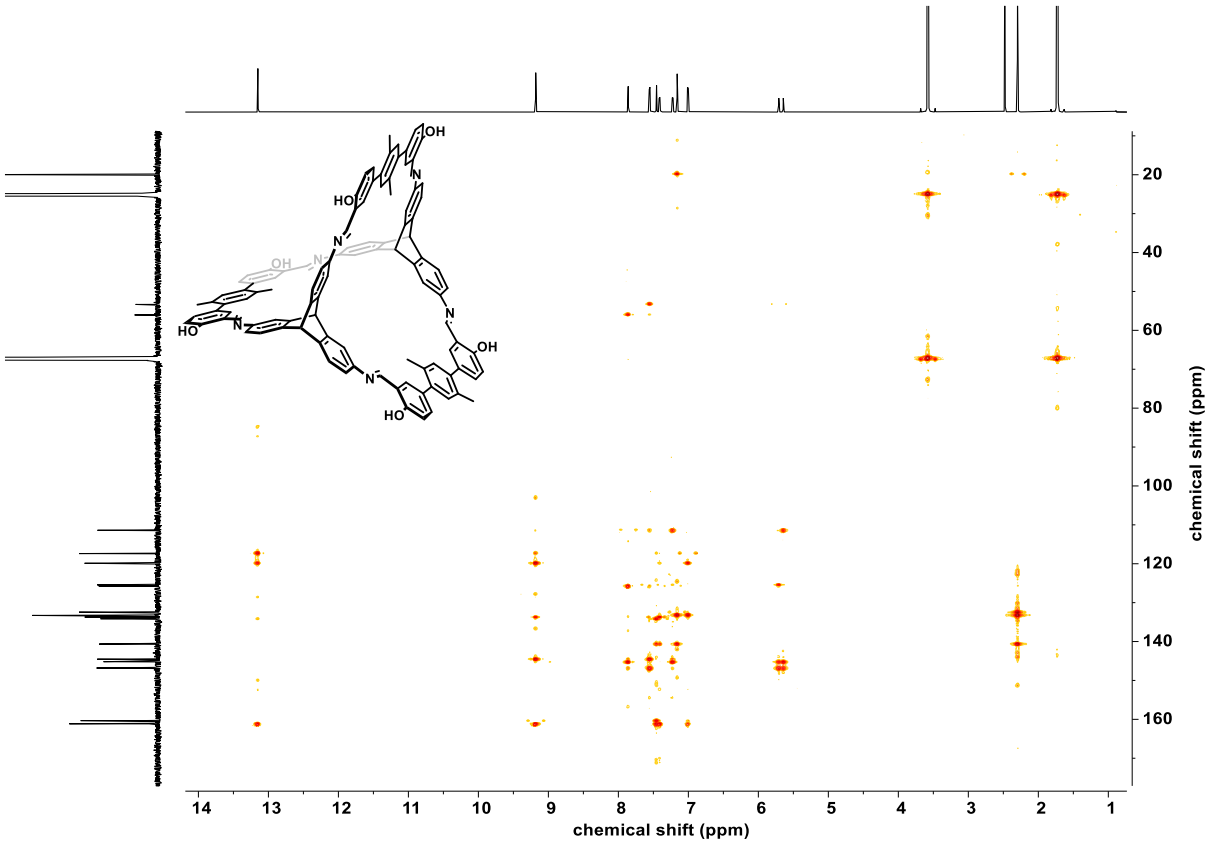

Figure 180. ^{1}H-^{13}C HMBC NMR spectrum of **cage-CH$_3$** (THF-d_8, 700 MHz, 176 MHz).

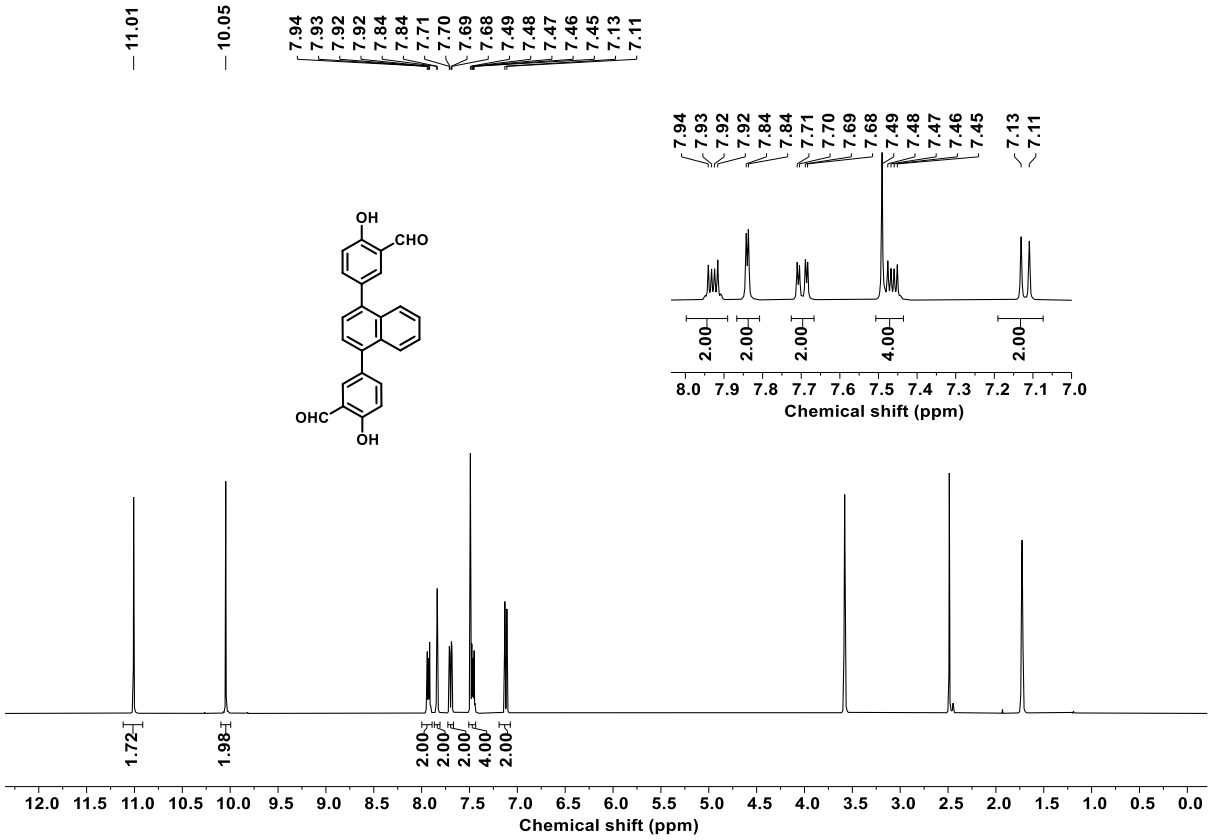

Figure 181. ^{1}H NMR spectrum of **77** (THF-d_8, 400 MHz).

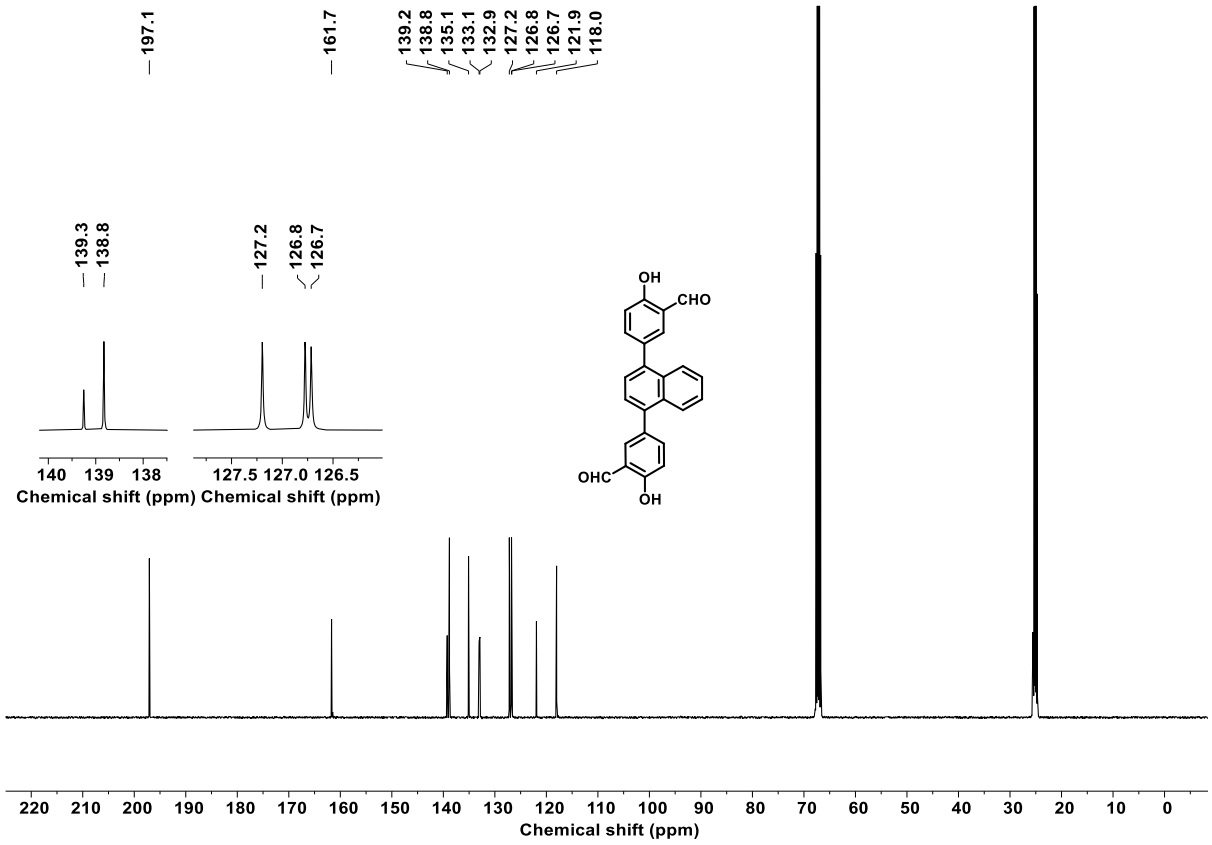

Figure 182. ^{13}C NMR spectrum of **77** (THF-d_8, 101 MHz).

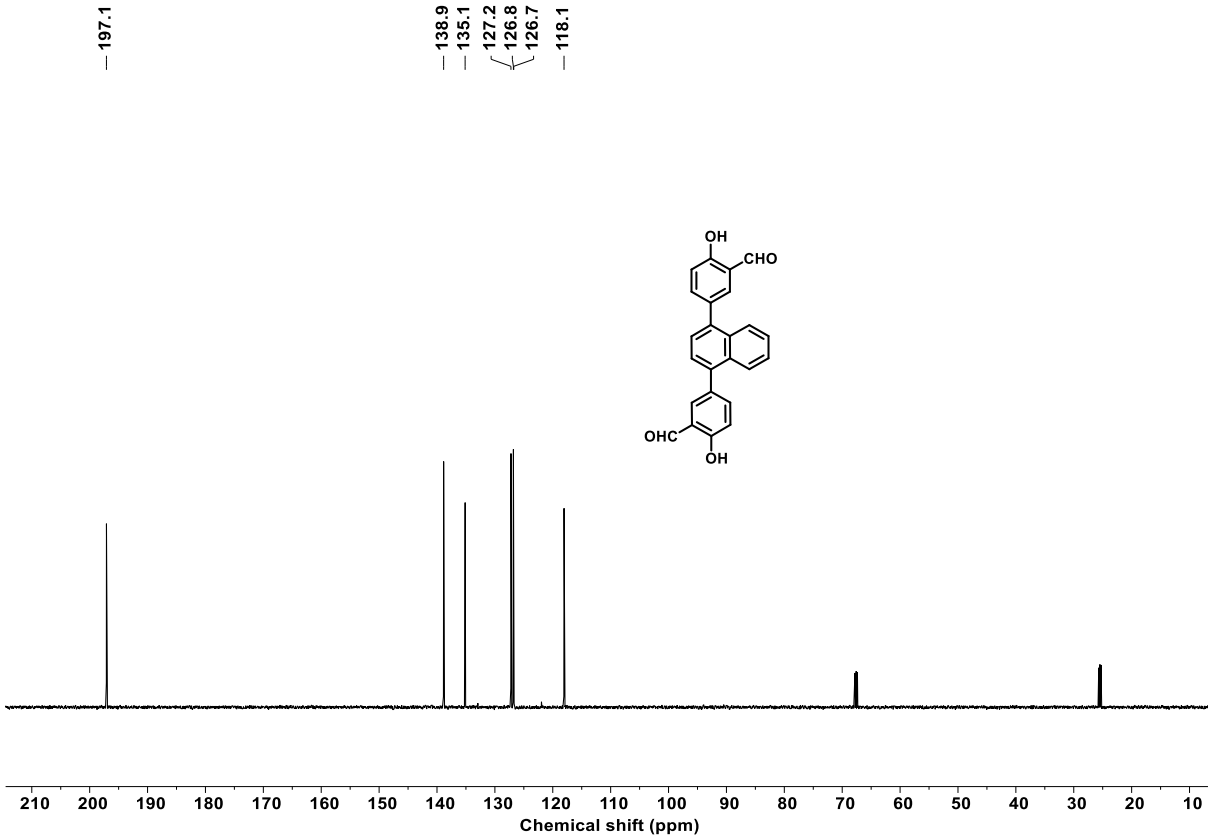

Figure 183. ^{13}C-DEPT135 NMR spectrum of **77** (THF-d_8, 101 MHz).

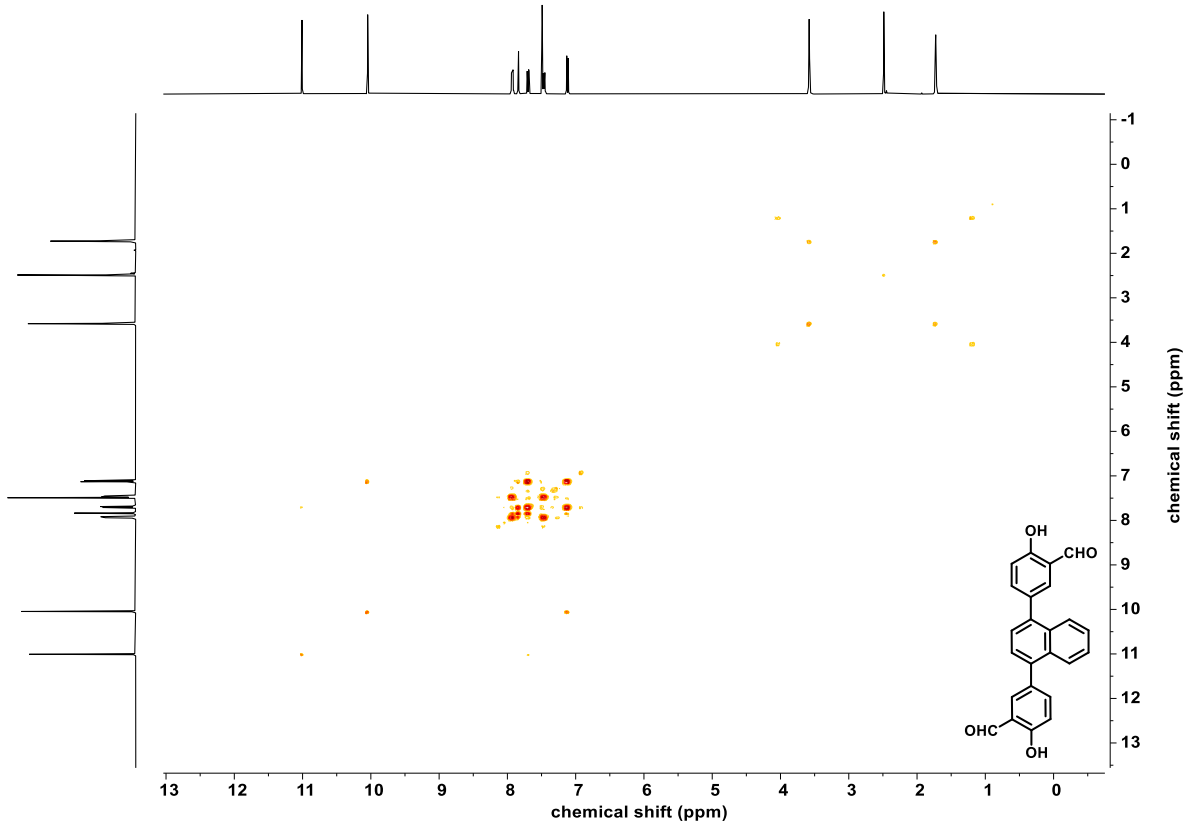

Figure 184. ^{1}H-^{1}H COSY NMR spectrum of **77** (THF-d_8, 400 MHz, 400 MHz).

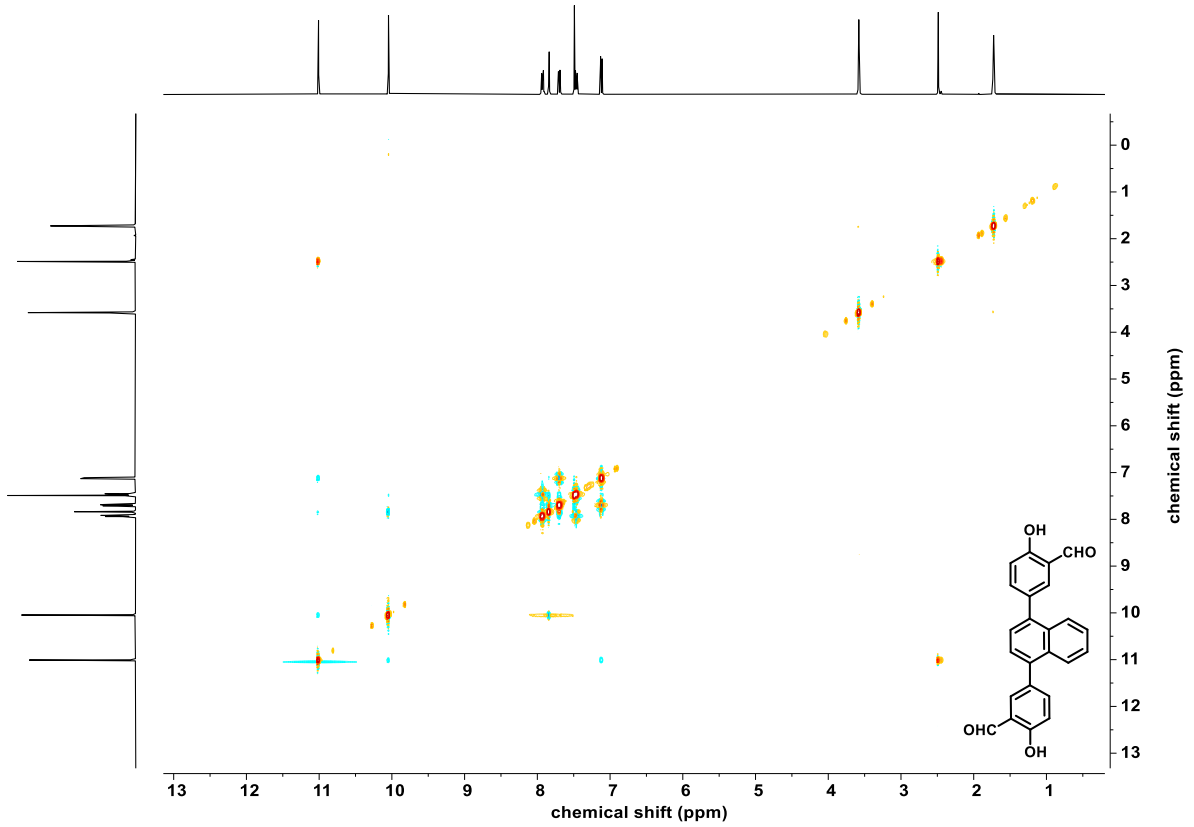

Figure 185. ^{1}H-^{1}H NOSY NMR spectrum of **77** (THF-d_8, 400 MHz, 400 MHz).

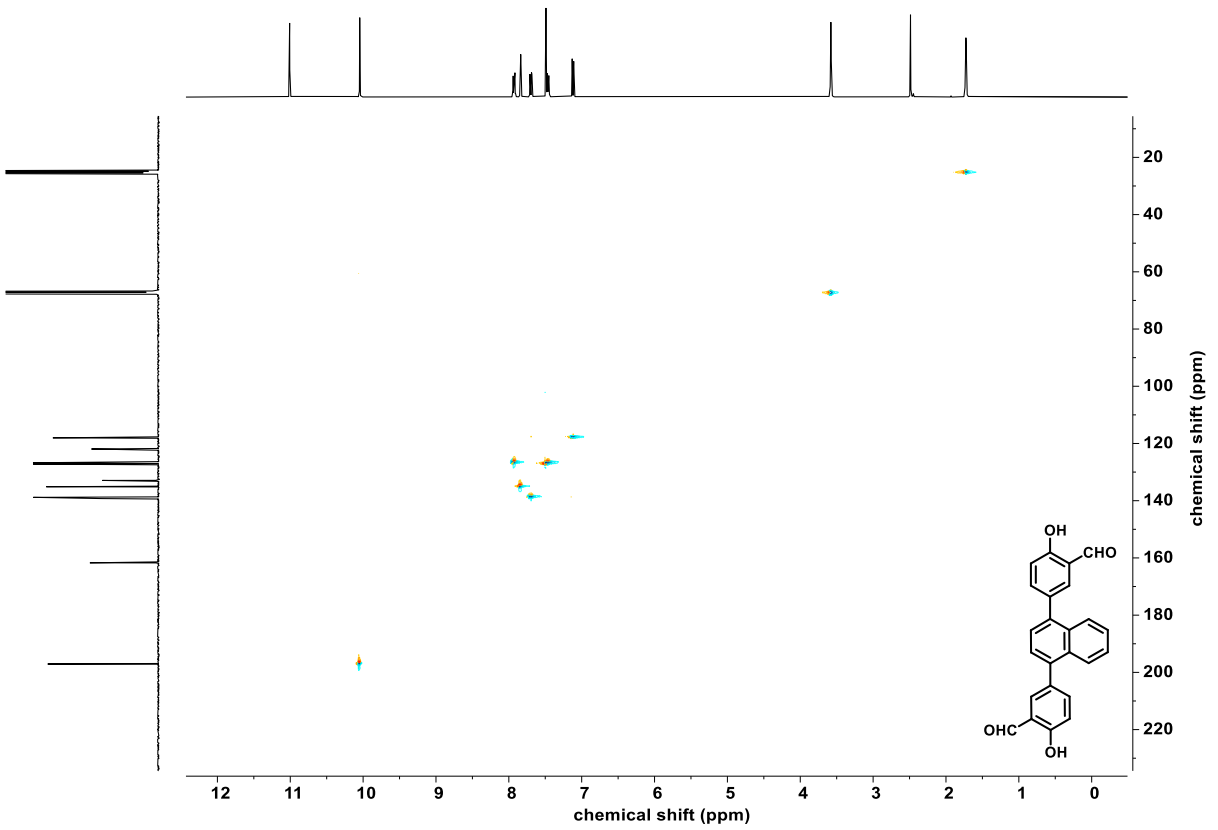

Figure 186. ^{1}H-^{13}C HSQC NMR spectrum of **77** (THF-d_8, 400 MHz, 101 MHz).

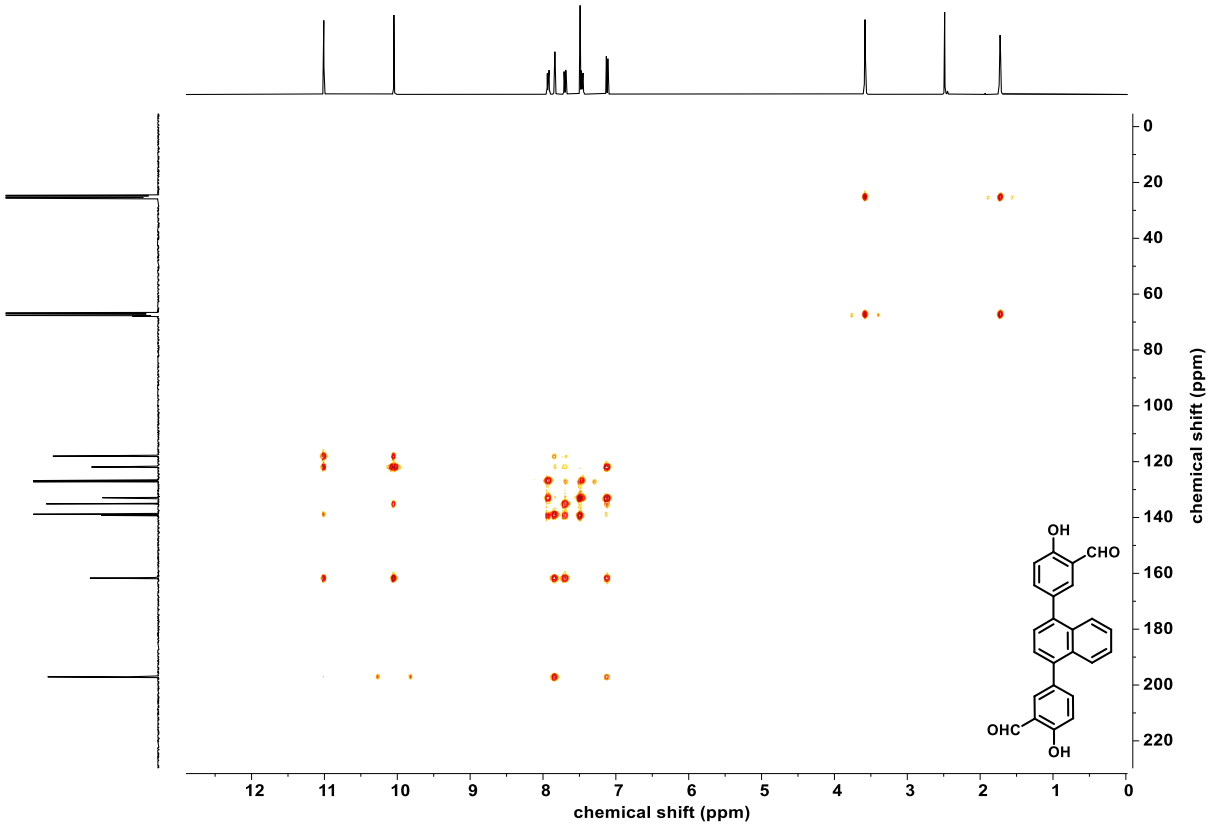

Figure 187. ^{1}H-^{13}C HMBC NMR spectrum of **77** (THF-d_8, 400 MHz, 101 MHz).

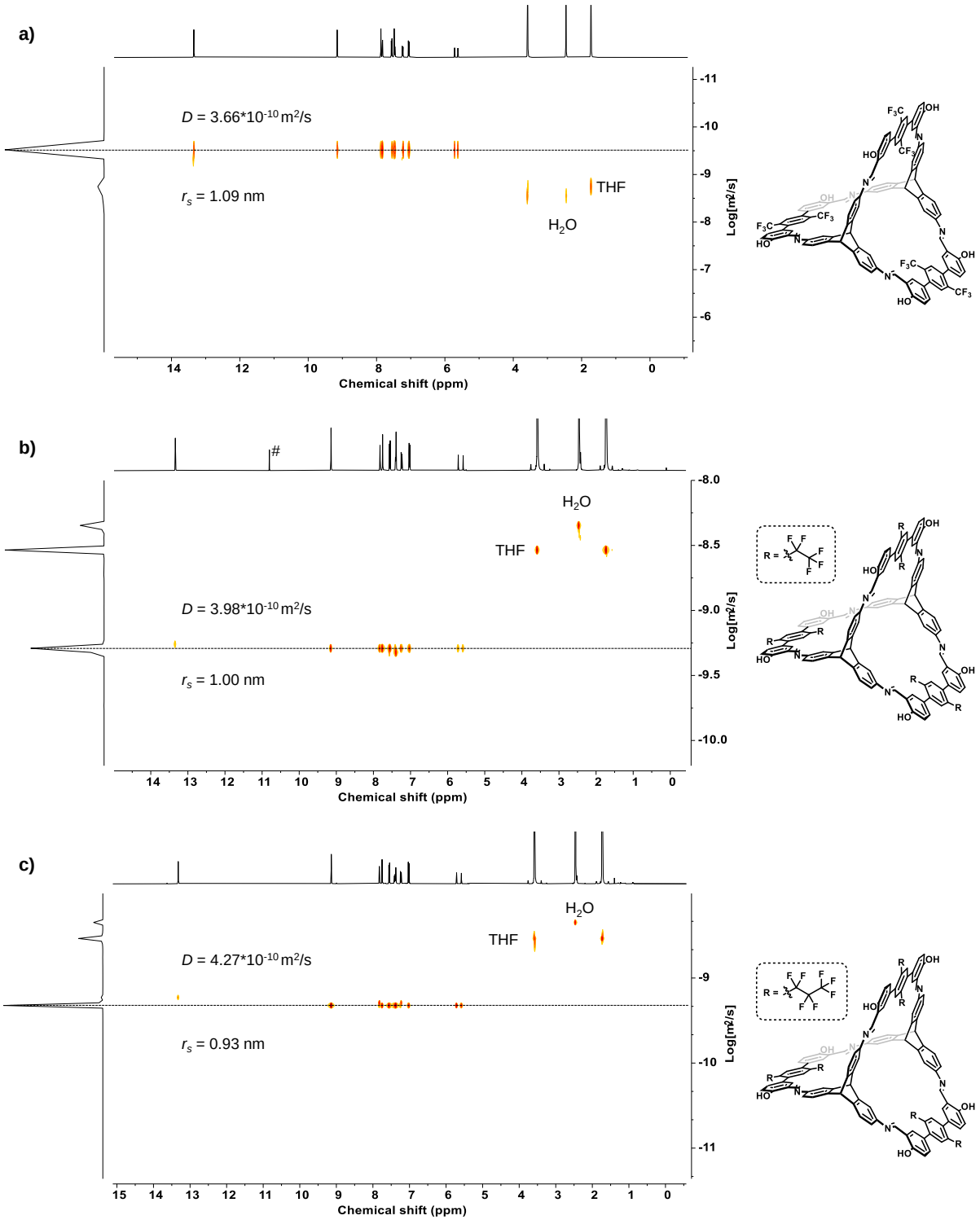

Figure 188. DOSY-NMR spectra (THF-d_8, 400 MHz, 295 K) of **cage-CF_3** (a), **cage-C_2F_5** (b), and **cage-C_3F_7** (c).

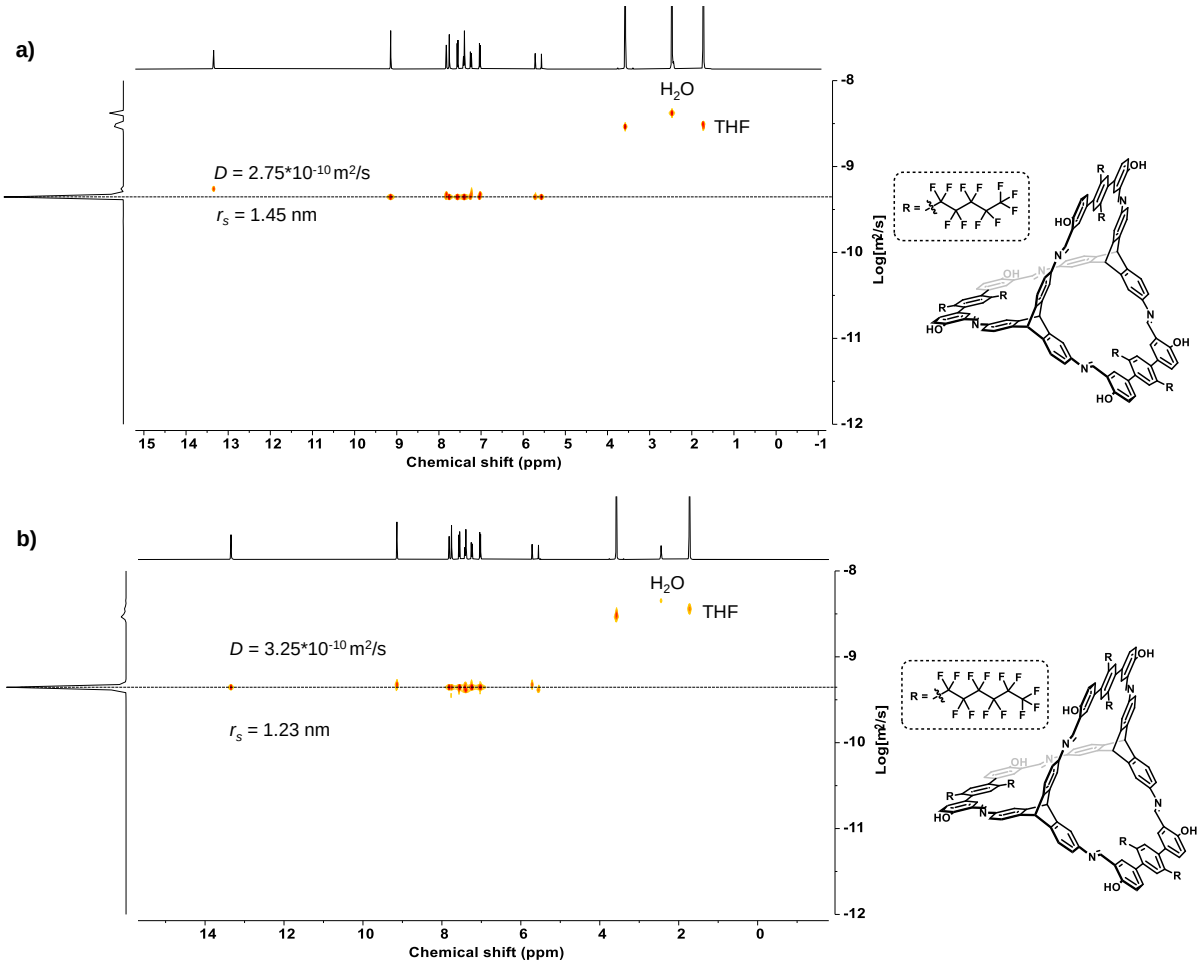

Figure 189. DOSY-NMR spectra (THF-d_8, 400 MHz, 295 K) of **cage-C_5F_{11}** (a) and **cage-C_6F_{13}** (b).

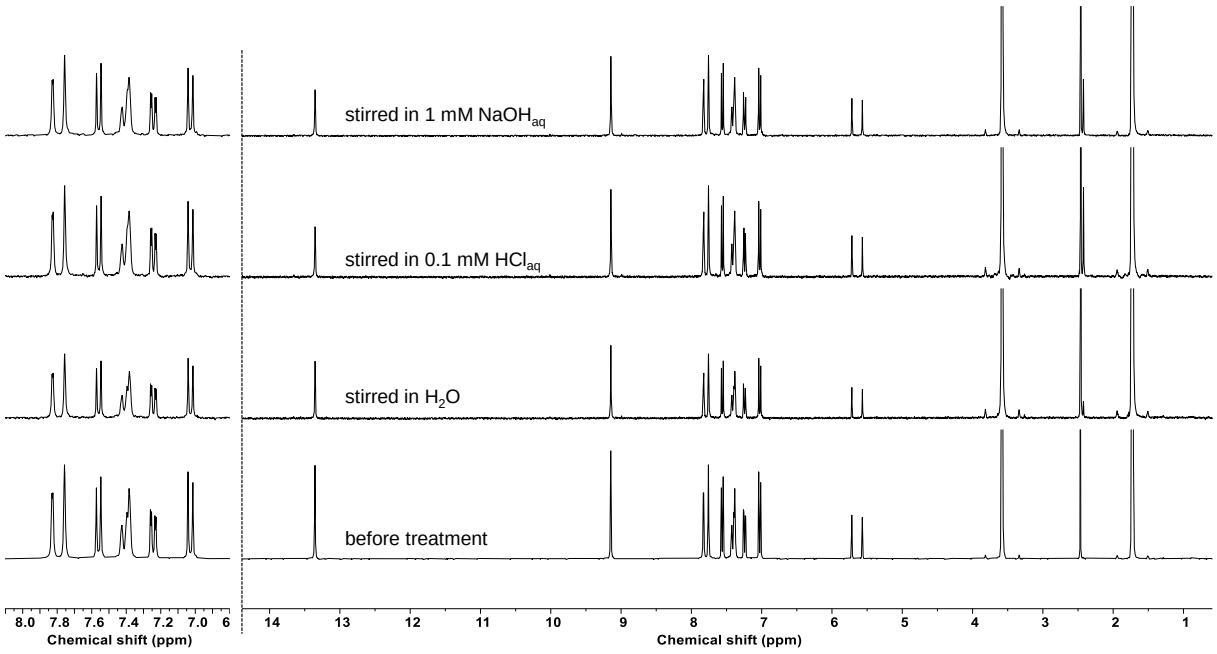

Figure 190. ^{1}H-NMR spectrum (right) of **F-cage** after water, acid, and base treatment (THF-d_8, 301 MHz) and zoomed in from 8.00 ppm to 7.00 ppm (left). Adapted with permission from Ref.[7]. Copyright © 2022 Wiley-VCH.

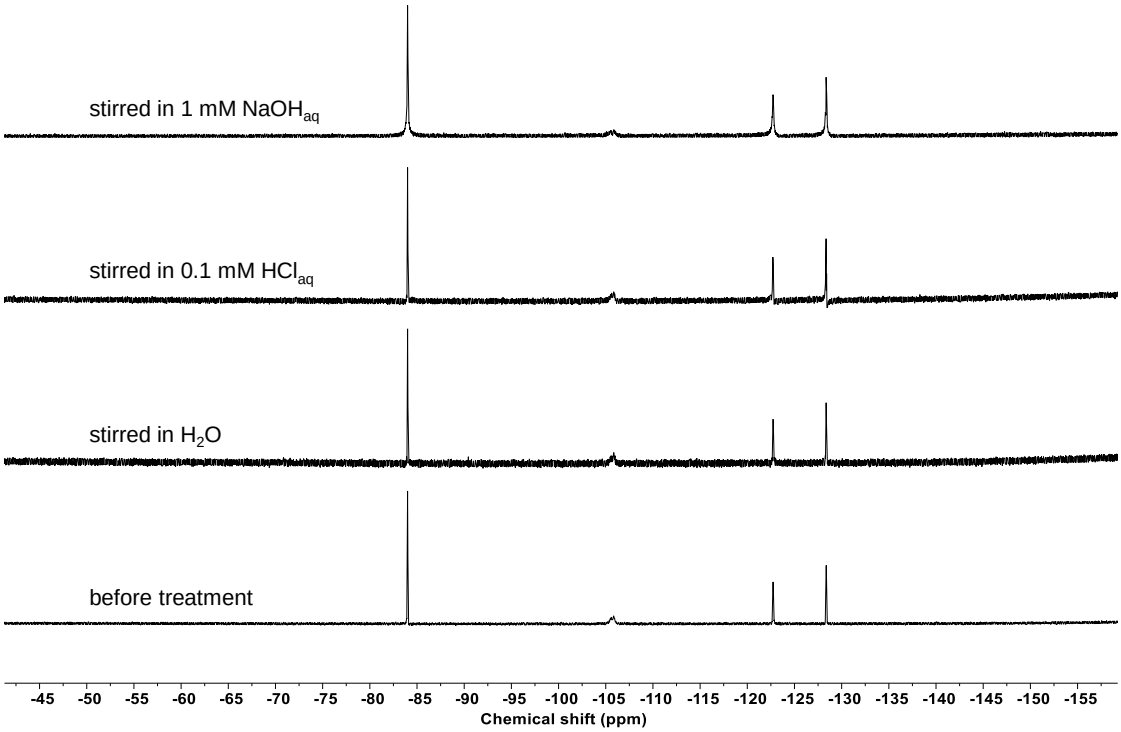

Figure 191. ^{19}F-NMR spectrum of **F-cage** after water, acid, and base treatment (THF-d_8, 283 MHz). Reproduced with permission from Ref.[7]. Copyright © 2022 Wiley-VCH.

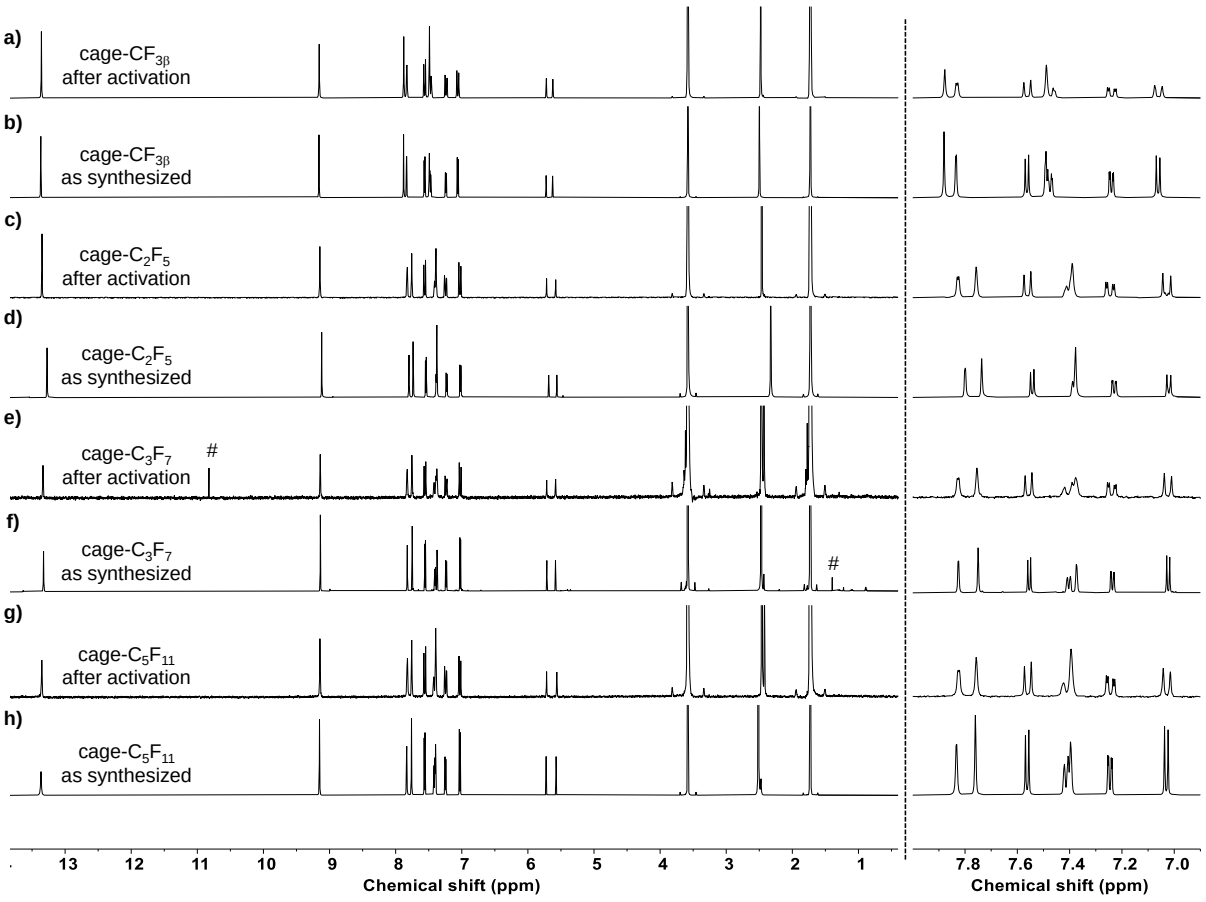

Figure 192. ^{1}H NMR spectrum comparision of fluorinated [2+3] cages after thermal activation and as synthesized in THF-d_8. (a-b) **cage-CF$_{3\beta}$**, (c-d) **cage-C$_2$F$_5$**, (e-f) **cage-C$_3$F$_7$**, and (g-h) **cage-C$_5$F$_{11}$**. # : impurity in THF-d_8. Left spectra zoom in to give right one.

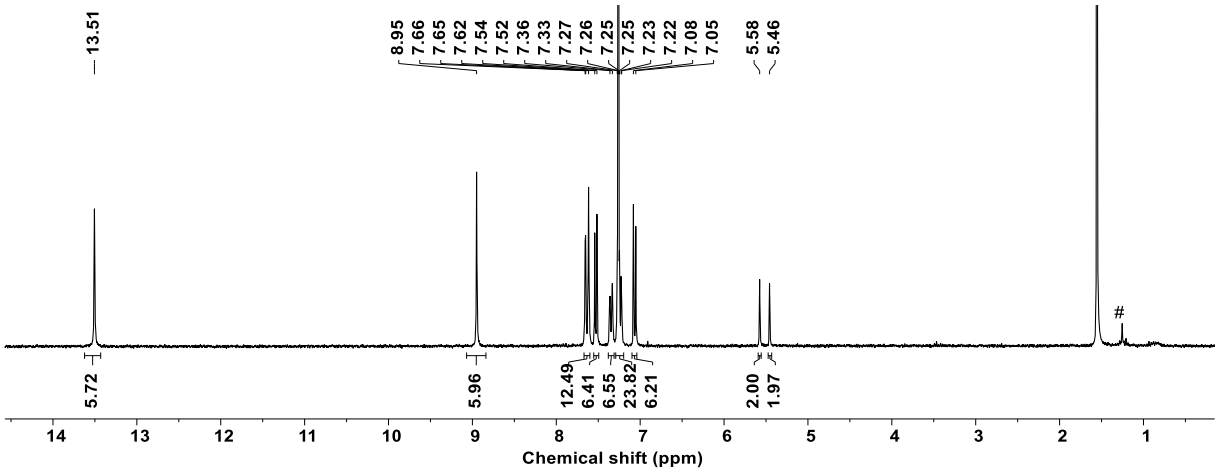

Figure 193. ^{1}H NMR spectrum of **cage-$C_6F_{13\alpha}$** after thermal activation ($CDCl_3$, 301 MHz). # : impurity in $CDCl_3$.

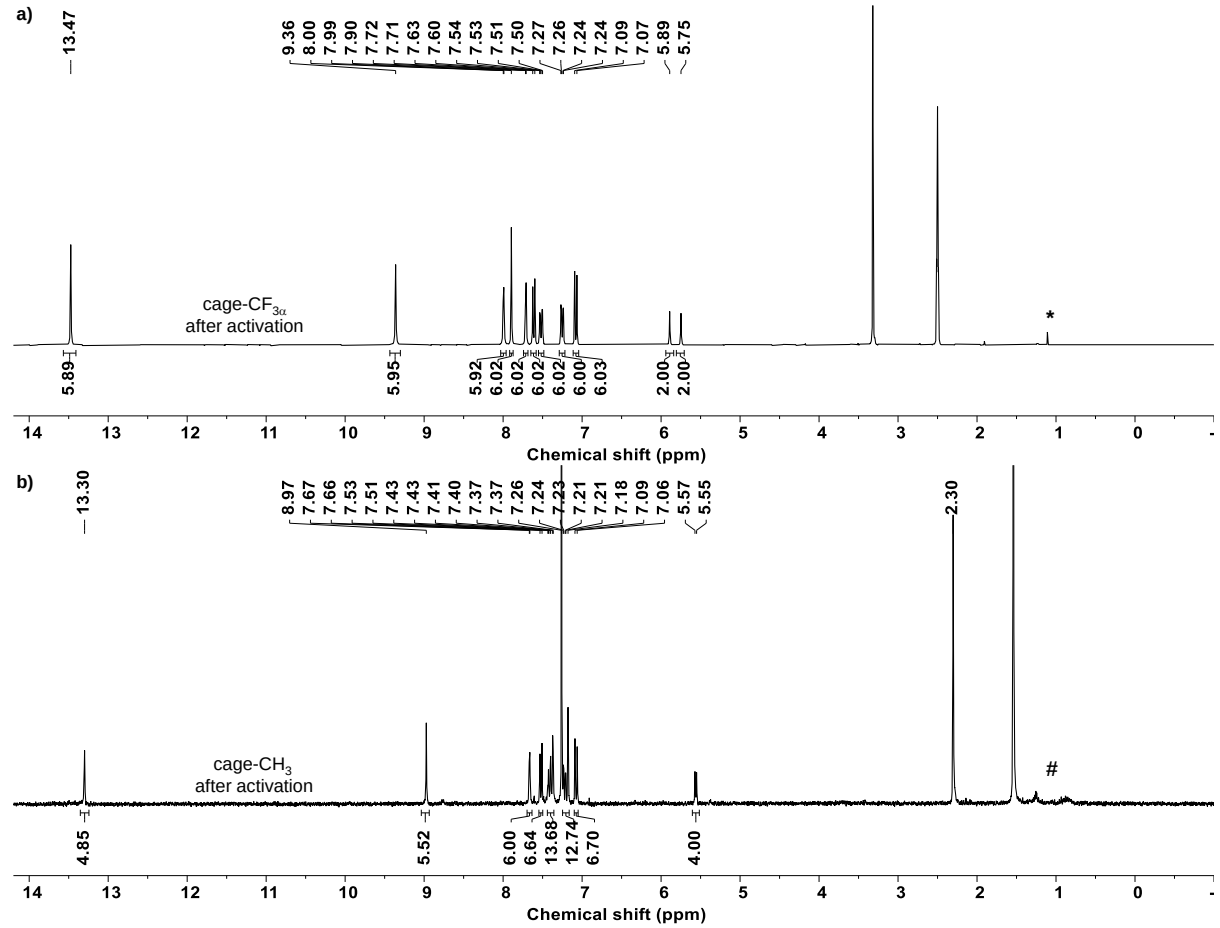

Figure 194. ^{1}H NMR spectra of solvate **cage-CF_3** in DMSO-d_6 and **cage-CH_3** after thermal activation in $CDCl_3$ (301 MHZ). *: impurity in DMSO-d_6, # : impurity in $CDCl_3$.

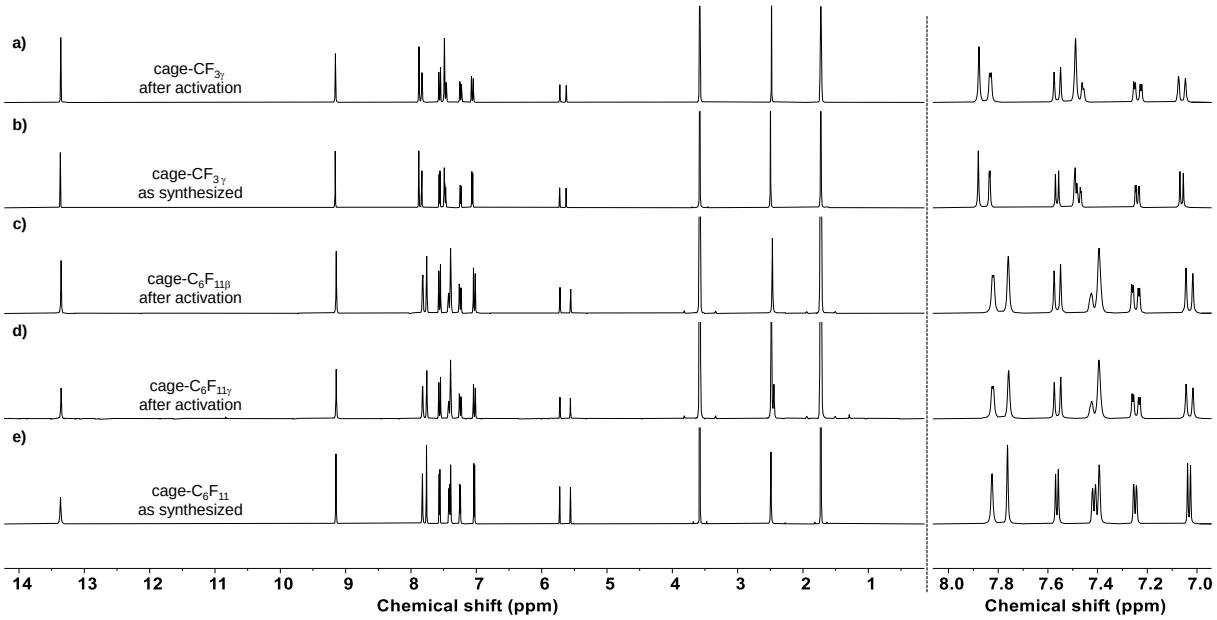

Figure 195. ^{1}H NMR spectrum comparison of [2+3] cages after thermal activation and as synthesized in THF-d_8. (a-b) **cage-CF$_{3\alpha}$**, (c-e) **cage-C$_6$F$_{13}$**. Left spectra zoom in to give the right one.

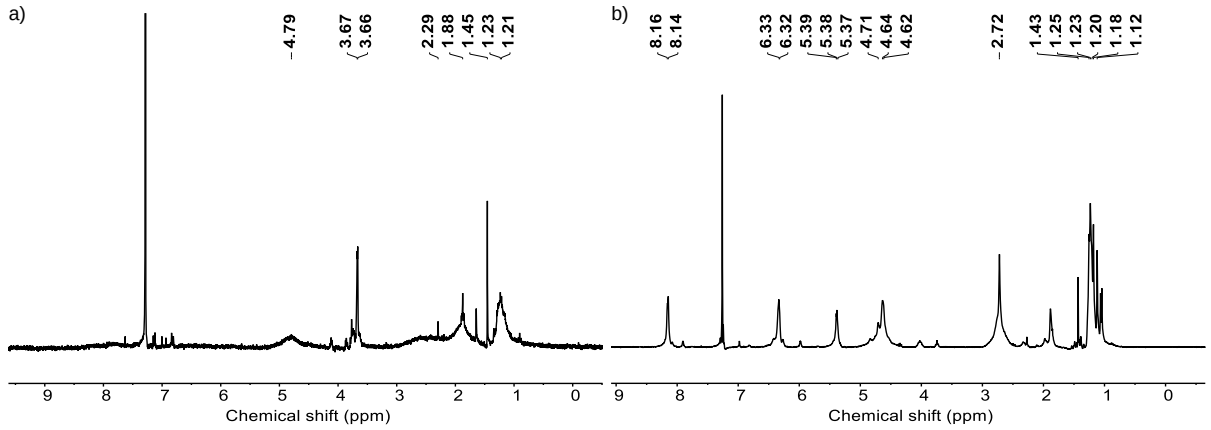

Figure 196. ^{1}H-NMR-spectra of the isolated (a) GPC-B fraction after seven cycles and (c) GPC-D fraction after 15 cycles in Figure 67. Adapted with permission from Ref.[140]. Copyright © 2023 Thieme Group.

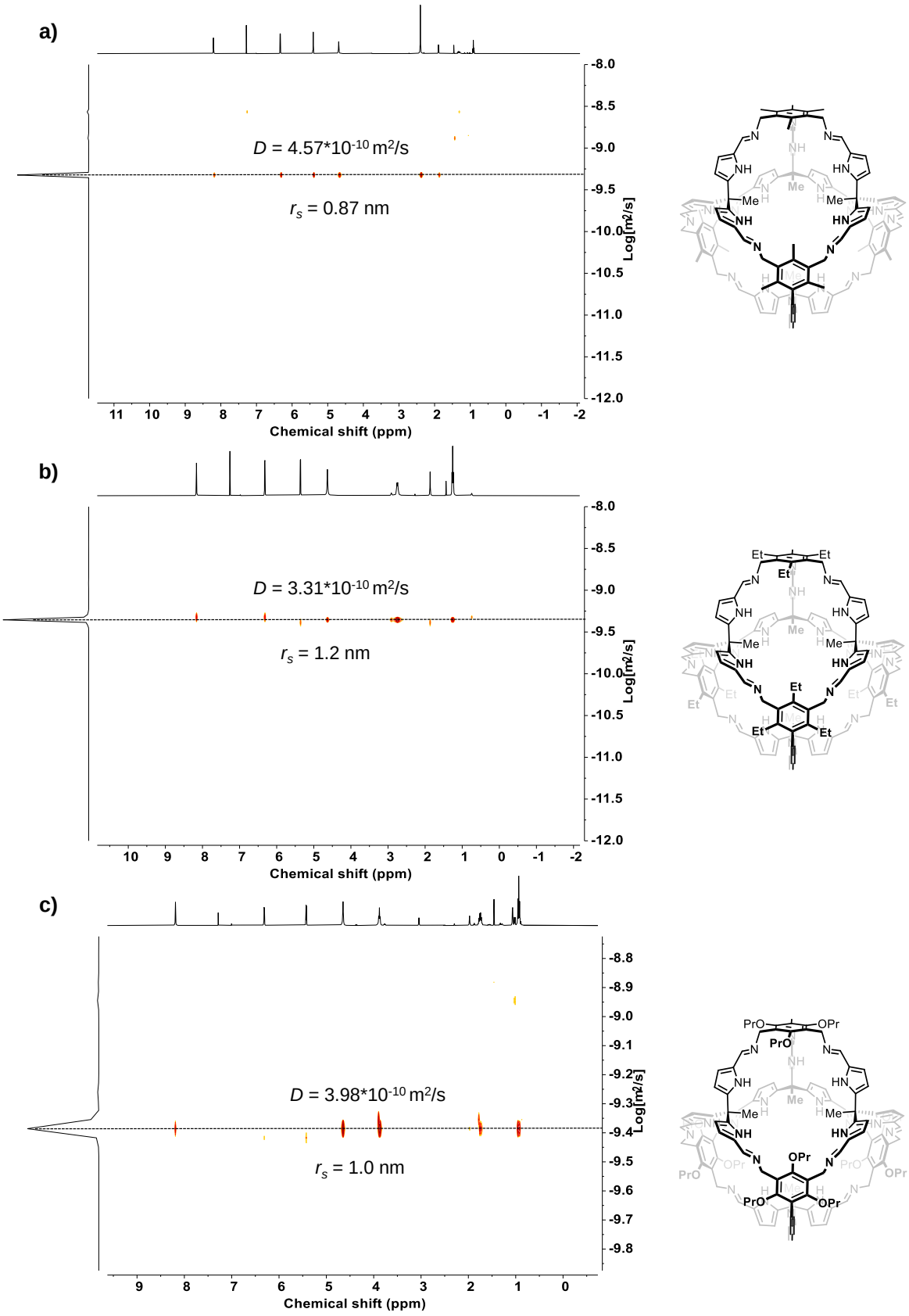

Figure 197. DOSY-NMR spectra ($CDCl_3$, 400 MHz, 295 K) of **cage-Me** (a), **cage-Et** (b), and **cage-OPr** (c). Adapted with permission from Ref.[140]. Copyright © 2023 Thieme Group.

2. TG Curve and GPC Trace

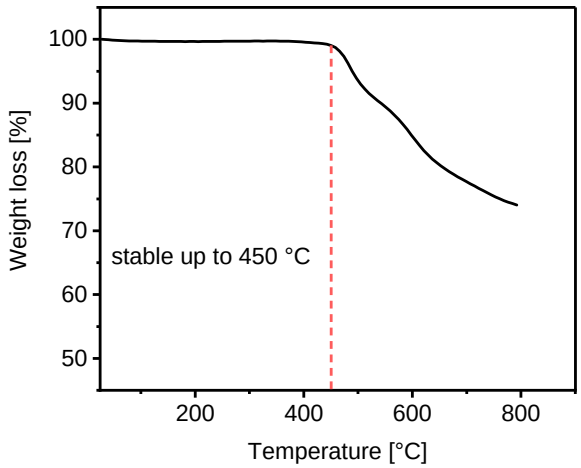

Figure 198. TGA curve of crystalline **cage-Nap** after activation (N_2, flow rate: 20 mL/min, heating rate: 10 K·min^{-1}).

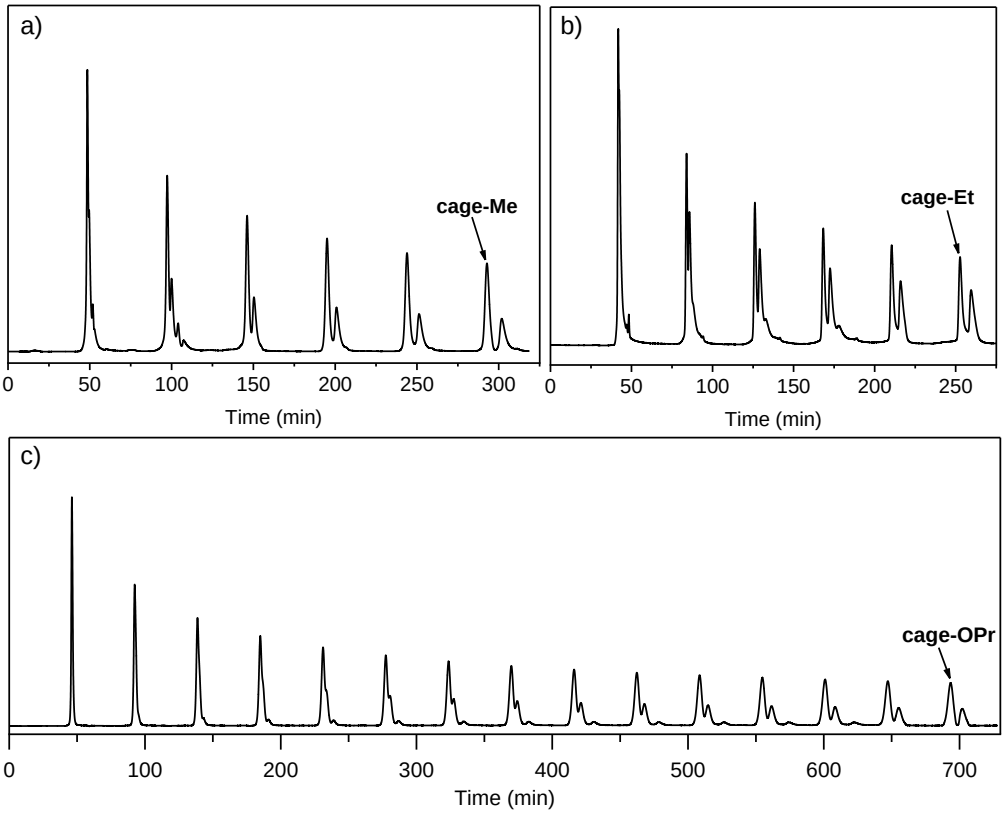

Figure 199. GPC trace of **cage-Me**, **cage-Et** and **cage-OPr** in THF. (flow rate: 5mL/min, temp: 40˚C, wavelength: 254 nm, GPC columns: 3 × 100 Å and 1 × 500 Å for **cage-Et**; 2 × 500 Å and 2 × 1000 for **cage-Me** and **cage-OPr**) Reproduced with permission from Ref.[140]. Copyright © 2023 Thieme Group.

3. MS Spectra

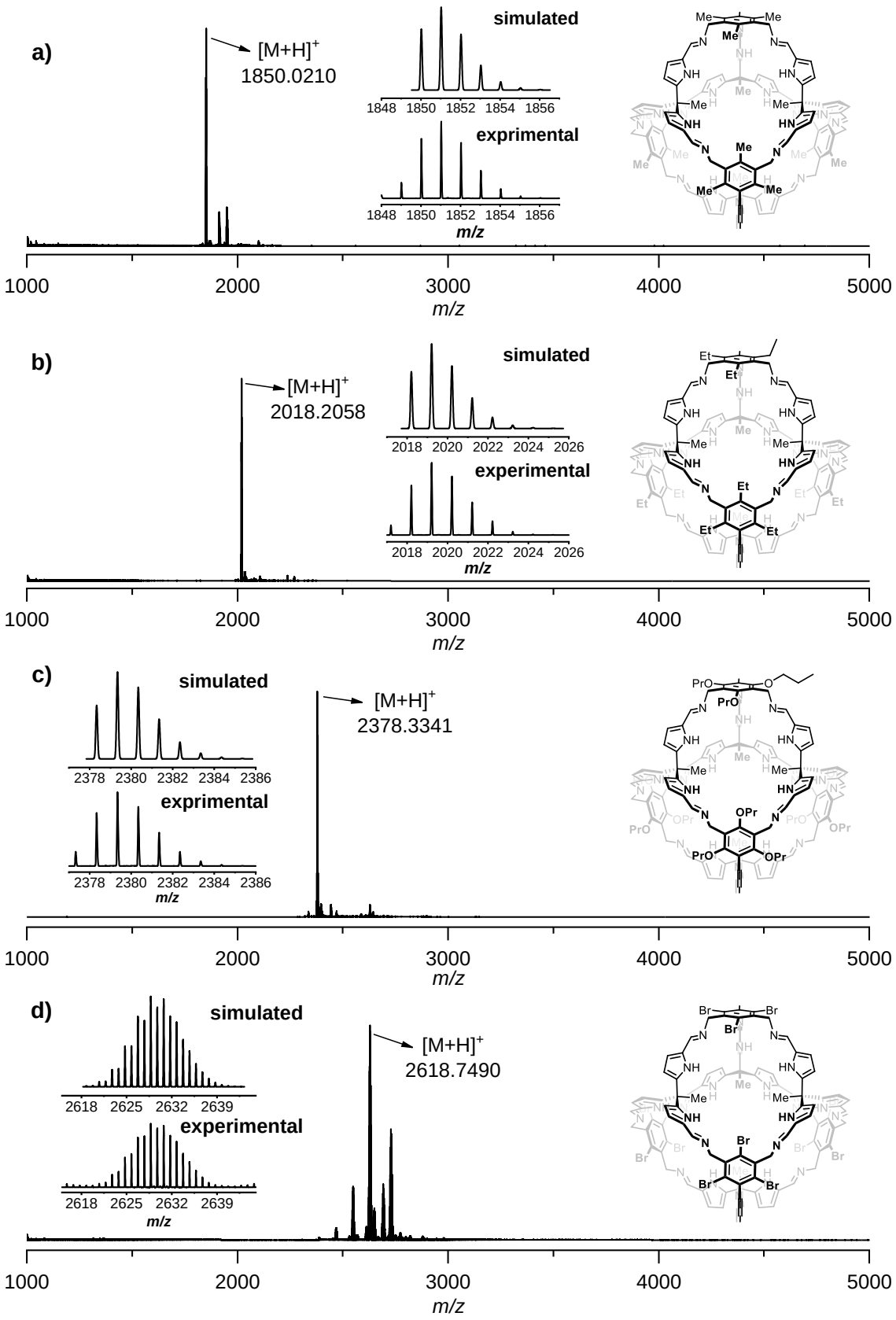

Figure 200. MALDI-TOF mass spectra of **cage-Me** (a), **cage-Et** (b), **cage-OPr** (c), and **cage-Br** (d). (matrix: DCTB) Adapted with permission from Ref.[140]. Copyright © 2023 Thieme Group.

4. Single Crystal X-ray Diffraction

Crystals of **cage-$CF_{3\alpha}$** suitable for single crystal X-ray diffraction have obtained by vapour diffusion of methanol in a saturated DMF-solution of **cage-CF_3**.

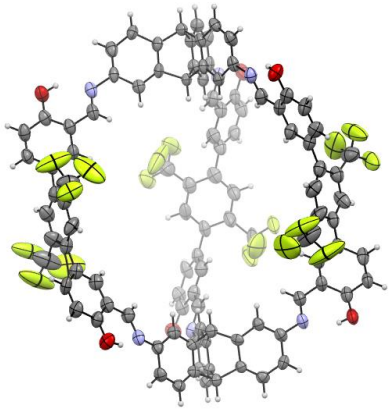

Table 17. Crystal data and structure refinement for **cage-$CF_{3\alpha}$**.

Identification code	tik15	
Empirical formula	$C_{106}H_{58}F_{18}N_6O_6$	
Formula weight	1853.58	
Temperature	200(2) K	
Wavelength	1.54178 Å	
Crystal system	trigonal	
Space group	$R\bar{3}c$	
Z	6	
Unit cell dimensions	a = 19.3976(2) Å	α = 90 deg.
	b = 19.3976(2) Å	β = 90 deg.
	c = 60.9238(14) Å	γ = 120 deg.
Volume	19852.4(6) $Å^3$	
Density (calculated)	0.93 g/cm^3	
Absorption coefficient	0.65 mm^{-1}	
Crystal shape	cuboid	
Crystal size	0.140 x 0.102 x 0.071 mm^3	
Crystal colour	orange	
Theta range for data collection	3.9 to 69.2 deg.	
Index ranges	$-19 \le h \le 20$, $-23 \le k \le 16$, $-51 \le l \le 72$	
Reflections collected	25240	
Independent reflections	5921 (R(int) = 0.0241)	
Observed reflections	4801 ($I > 2\sigma(I)$)	
Absorption correction	Semi-empirical from equivalents	
Max. and min. transmission	1.38 and 0.77	
Refinement method	Full-matrix least-squares on F^2	
Data/restraints/parameters	5921 / 445 / 411	
Goodness-of-fit on F^2	1.06	
Final R indices (I>2sigma(I))	R1 = 0.046, wR2 = 0.123	
Absolute structure parameter	0.51(8)	
Largest diff. peak and hole	0.26 and -0.24 $eÅ^{-3}$	

Crystals of **cage-CF$_{3\beta}$** suitable for single crystal X-ray diffraction have obtained by vapour diffusion of methanol in a saturated THF-solution of **cage-CF$_3$**.

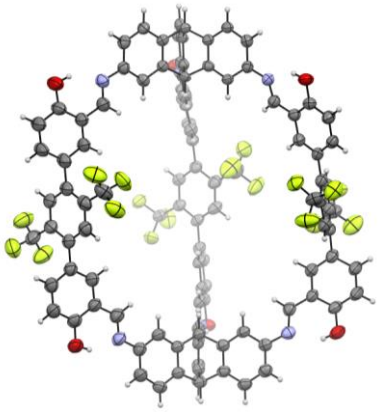

Table 18. Crystal data and structure refinement for **cage-CF$_{3\beta}$**.

Identification code	tik29sq	
Empirical formula	$C_{106}H_{58}F_{18}N_6O_6$	
Formula weight	1853.58	
Temperature	200(2) K	
Wavelength	1.54178 Å	
Crystal system	monoclinic	
Space group	*P2$_1$/c*	
Z	4	
Unit cell dimensions	a = 25.1178(7) Å	α = 90 deg.
	b = 34.1676(8) Å	β =102.130(2) deg.
	c = 15.5327(5) Å	γ = 90 deg.
Volume	13032.8(6) Å^3	
Density (calculated)	0.94 g/cm^3	
Absorption coefficient	0.66 mm^{-1}	
Crystal shape	rhombic	
Crystal size	0.090 x 0.089 x 0.050 mm^3	
Crystal colour	yellow	
Theta range for data collection	2.2 to 56.0 deg.	
Index ranges	-24≤h≤26, -36≤k≤36, -11≤l≤16	
Reflections collected	60464	
Independent reflections	16787 (R(int) = 0.0557)	
Observed reflections	9251 (I > 2σ(I))	
Absorption correction	Semi-empirical from equivalents	
Max. and min. transmission	0.97 and 0.55	
Refinement method	Full-matrix least-squares on F^2	
Data/restraints/parameters	16787 / 1206 / 1225	
Goodness-of-fit on F^2	1.05	
Final R indices (I>2sigma(I))	R1 = 0.060, wR2 = 0.156	
Largest diff. peak and hole	0.16 and -0.18 eÅ^{-3}	

Crystals of **cage-CF$_{3\gamma}$** suitable for single crystal X-ray diffraction have obtained by vapour diffusion of diethyl ether in a saturated DCM-solution of **cage-CF$_3$**.

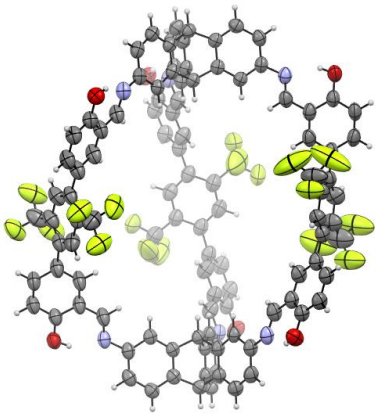

Table 19. Crystal data and structure refinement for **cage-CF$_{3\gamma}$**.

Identification code	tik14sq	
Empirical formula	$C_{106}H_{58}F_{18}N_6O_6$	
Formula weight	1853.58	
Temperature	200(2) K	
Wavelength	1.54178 Å	
Crystal system	monoclinic	
Space group	*C2/c*	
Z	4	
Unit cell dimensions	a = 35.1462(7) Å	α = 90 deg.
	b = 19.6140(5) Å	β =123.245(1) deg.
	c = 27.0324(9) Å	γ = 90 deg.
Volume	15585.1(7) Å^3	
Density (calculated)	0.79 g/cm^3	
Absorption coefficient	0.55 mm^{-1}	
Crystal shape	cuboid	
Crystal size	0.114 x 0.098 x 0.076 mm^3	
Crystal colour	orange	
Theta range for data collection	3.0 to 63.7 deg.	
Index ranges	-35≤h≤40, -22≤k≤17, -31≤l≤19	
Reflections collected	46603	
Independent reflections	12742 (R(int) = 0.0565)	
Observed reflections	8326 (I > 2σ(I))	
Absorption correction	Semi-empirical from equivalents	
Max. and min. transmission	1.47 and 0.68	
Refinement method	Full-matrix least-squares on F^2	
Data/restraints/parameters	12742 / 0 / 616	
Goodness-of-fit on F^2	1.05	
Final R indices (I>2sigma(I))	R1 = 0.065, wR2 = 0.190	
Largest diff. peak and hole	0.28 and -0.25 eÅ^{-3}	

Crystals of **cage-C_2F_5** suitable for single crystal X-ray diffraction have obtained by vapour diffusion of methanol in a saturated THF-solution of **cage-C_2F_5**.

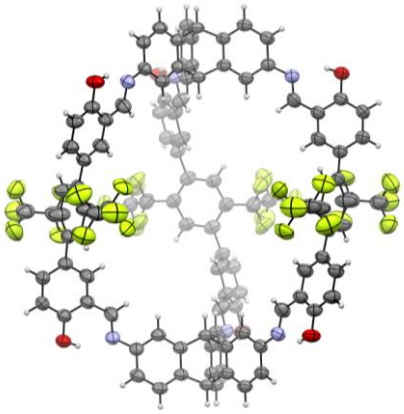

Table 20. Crystal data and structure refinement for **cage-C_2F_5**.

Identification code	tik12sq	
Empirical formula	$C_{112}H_{58}F_{30}N_6O_6$	
Formula weight	2153.64	
Temperature	200(2) K	
Wavelength	1.54178 Å	
Crystal system	trigonal	
Space group	$R\bar{3}c$	
Z	6	
Unit cell dimensions	a = 20.1547(4) Å	α = 90 deg.
	b = 20.1547(4) Å	β = 90 deg.
	c = 77.800(2) Å	γ = 120 deg.
Volume	27369.3(14) Å^3	
Density (calculated)	0.78 g/cm^3	
Absorption coefficient	0.61 mm^{-1}	
Crystal shape	brick	
Crystal size	0.083 x 0.078 x 0.068 mm^3	
Crystal colour	orange	
Theta range for data collection	2.8 to 56.0 deg.	
Index ranges	-21≤h≤14, -21≤k≤19, -83≤l≤63	
Reflections collected	29223	
Independent reflections	3965 (R(int) = 0.1002)	
Observed reflections	2276 (I > 2σ(I))	
Absorption correction	Semi-empirical from equivalents	
Max. and min. transmission	1.68 and 0.66	
Refinement method	Full-matrix least-squares on F^2	
Data/restraints/parameters	3965 / 335 / 297	
Goodness-of-fit on F^2	0.95	
Final R indices (I>2sigma(I))	R1 = 0.052, wR2 = 0.165	
Largest diff. peak and hole	0.23 and -0.20 eÅ^{-3}	

Crystals of **cage-C_3F_7** suitable for single crystal X-ray diffraction have obtained by vapour diffusion of methanol in a saturated THF-solution of **cage-C_3F_7**.

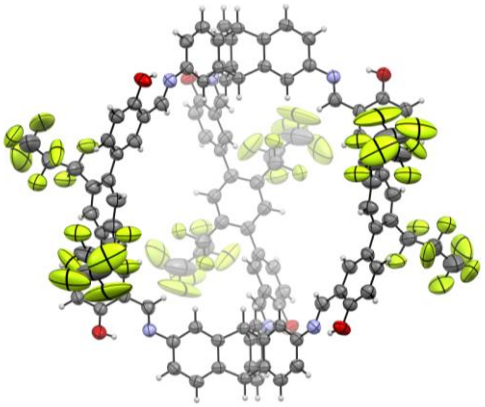

Table 21. Crystal data and structure refinement for **cage-C_3F_7**.

Identification code	tik24sq	
Empirical formula	$C_{118}H_{58}F_{42}N_6O_6$	
Formula weight	2453.70	
Temperature	200(2) K	
Wavelength	1.54178 Å	
Crystal system	trigonal	
Space group	$R\bar{3}c$	
Z	6	
Unit cell dimensions	a = 19.8267(1) Å	α = 90 deg.
	b = 19.8267(1) Å	β = 90 deg.
	c = 62.2239(11) Å	γ = 120 deg.
Volume	21183.1(5) Å^3	
Density (calculated)	1.15 g/cm^3	
Absorption coefficient	0.98 mm^{-1}	
Crystal shape	cuboid	
Crystal size	0.166 x 0.165 x 0.110 mm^3	
Crystal colour	yellow	
Theta range for data collection	3.8 to 71.7 deg.	
Index ranges	-20≤h≤24, -24≤k≤20, -42≤l≤75	
Reflections collected	33400	
Independent reflections	4536 (R(int) = 0.0425)	
Observed reflections	3394 (I > 2σ(I))	
Absorption correction	Semi-empirical from equivalents	
Max. and min. transmission	0.90 and 0.41	
Refinement method	Full-matrix least-squares on F^2	
Data/restraints/parameters	4536 / 591 / 351	
Goodness-of-fit on F^2	1.08	
Final R indices (I>2sigma(I))	R1 = 0.061, wR2 = 0.194	
Largest diff. peak and hole	0.26 and -0.34 eÅ^{-3}	

Crystals of **cage-C_5F_{11}** suitable for single crystal X-ray diffraction have obtained by vapour diffusion of methanol in a saturated THF-solution of **cage-C_5F_{11}**.

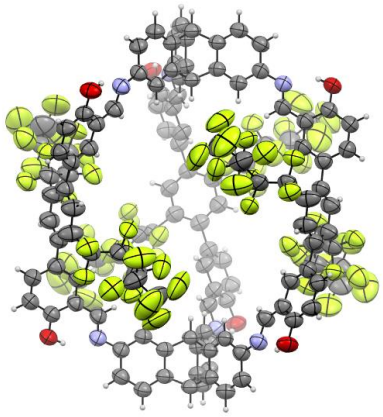

Table 22. Crystal data and structure refinement for **cage-C_5F_{11}**.

Identification code	tik31sq	
Empirical formula	$C_{130}H_{58}F_{66}N_6O_6$	
Formula weight	3053.82	
Temperature	200(2) K	
Wavelength	1.54178 Å	
Crystal system	trigonal	
Space group	$R\bar{3}c$	
Z	6	
Unit cell dimensions	a = 19.5342(4) Å	α = 90 deg.
	b = 19.5342(4) Å	β = 90 deg.
	c = 66.037(2) Å	γ = 120 deg.
Volume	21822.8(12) Å^3	
Density (calculated)	1.39 g/cm^3	
Absorption coefficient	1.30 mm^{-1}	
Crystal shape	cuboid	
Crystal size	0.170 x 0.080 x 0.077 mm^3	
Crystal colour	yellow	
Theta range for data collection	3.7 to 57.9 deg.	
Index ranges	-20≤h≤19, -17≤k≤21, -42≤l≤72	
Reflections collected	16543	
Independent reflections	3375 (R(int) = 0.0314)	
Observed reflections	2361 (I > 2σ(I))	
Absorption correction	Semi-empirical from equivalents	
Max. and min. transmission	0.96 and 0.74	
Refinement method	Full-matrix least-squares on F^2	
Data/restraints/parameters	3375 / 2920 / 605	
Goodness-of-fit on F^2	1.03	
Final R indices (I>2sigma(I))	R1 = 0.079, wR2 = 0.227	
Largest diff. peak and hole	0.25 and -0.19 eÅ^{-3}	

Crystals of **cage-CH$_3$** suitable for single crystal X-ray diffraction have obtained by vapour diffusion of methanol in a saturated THF-solution of **cage-CH$_3$**.

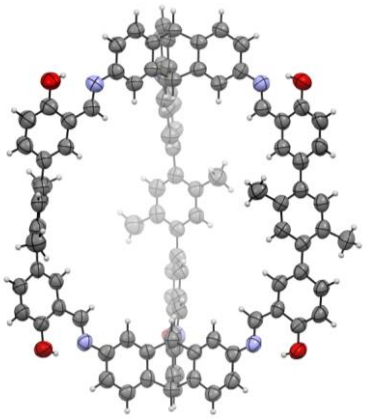

Table 23. Crystal data and structure refinement for **cage-CH$_3$**.

Identification code	tik23sq	
Empirical formula	$C_{106}H_{76}N_6O_6$	
Formula weight	1529.72	
Temperature	200(2) K	
Wavelength	1.54178 Å	
Crystal system	trigonal	
Space group	$R\bar{3}$	
Z	9	
Unit cell dimensions	a = 18.2241(4) Å	α = 90 deg.
	b = 18.2241(4) Å	β = 90 deg.
	c = 57.1701(19) Å	γ = 120 deg.
Volume	16443.4(8) Å^3	
Density (calculated)	1.39 g/cm^3	
Absorption coefficient	0.68 mm^{-1}	
Crystal shape	cuboid	
Crystal size	0.108 x 0.094 x 0.092 mm^3	
Crystal colour	orange	
Theta range for data collection	3.2 to 62.0 deg.	
Index ranges	-15≤h≤20, -20≤k≤19, -64≤l≤33	
Reflections collected	17475	
Independent reflections	5600 (R(int) = 0.0364)	
Observed reflections	3496 (I > 2σ(I))	
Absorption correction	Semi-empirical from equivalents	
Max. and min. transmission	0.95 and 0.58	
Refinement method	Full-matrix least-squares on F^2	
Data/restraints/parameters	5600 / 392 / 359	
Goodness-of-fit on F^2	1.06	
Final R indices (I>2sigma(I))	R1 = 0.088, wR2 = 0.251	
Largest diff. peak and hole	0.35 and -0.26 eÅ^{-3}	

Crystals of the C_3F_8-saturated **cage-C_3F_7** suitable for single crystal X-ray diffraction have been obtained by vapour diffusion of methanol into a saturated THF-solution of **cage-C_3F_7**. The supernatant mother liquor was removed and the residual single crystalline material dried at high vacuum for 14 h at room temperature and further activated at a kugelrohr oven at 50 °C under reduced pressure ($7 \cdot 10^{-2}$ mbar). After subsequent activation under reduced pressure ($1 \cdot 10^{-3}$ mbar) for 19 h at room temperature, activated **cage-C_3F_7** was subjected to an atmosphere of C_3F_8 for 24 h at room temperature and submitted to SCXRD analyses.

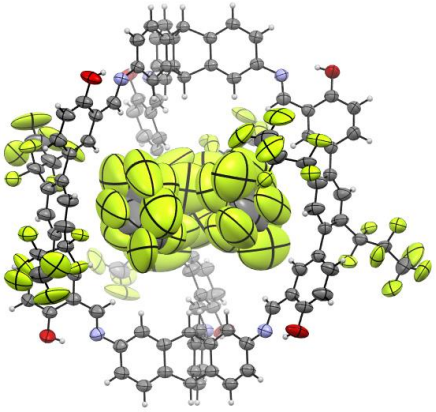

Table 24. Crystal data and structure refinement for **cage-C3F7**.

Identification code	tik35	
Empirical formula	$C_{127}H_{58}F_{66}N_6O_6$	
Formula weight	3017.79	
Temperature	200(2) K	
Wavelength	1.54178 Å	
Crystal system	trigonal	
Space group	$R\bar{3}$	
Z	6	
Unit cell dimensions	a = 19.2816(3) Å	α = 90 deg.
	b = 19.2816(3) Å	β = 90 deg.
	c = 61.7128(16) Å	γ = 120 deg.
Volume	19869.7(8) Å^3	
Density (calculated)	1.51 g/cm^3	
Absorption coefficient	1.42 mm^{-1}	
Crystal shape	cuboid	
Crystal size	0.107 x 0.088 x 0.054 mm^3	
Crystal colour	yellow	
Theta range for data collection	2.7 to 65.1 deg.	
Index ranges	-22≤h≤16, -16≤k≤22, -72≤l≤60	
Reflections collected	24649	
Independent reflections	7401 (R(int) = 0.0443)	
Observed reflections	4490 (I > 2σ(I))	
Absorption correction	Semi-empirical from equivalents	
Max. and min. transmission	0.95 and 0.77	
Refinement method	Full-matrix least-squares on F^2	
Data/restraints/parameters	7401 / 3137 / 840	
Goodness-of-fit on F^2	1.04	
Final R indices (I>2sigma(I))	R1 = 0.094, wR2 = 0.254	
Largest diff. peak and hole	0.53 and -0.39 eÅ^{-3}	

Crystals of the C_3F_8-saturated **cage-C_5F_{11}** suitable for single crystal X-ray diffraction have been obtained by vapour diffusion of methanol into a saturated THF-solution of **cage-C_5F_{11}**. The supernatant mother liquor was removed and the residual single crystalline material dried at high vacuum for 10 h at room temperature and further activated at a kugelrohr oven at 50 °C under reduced pressure ($2.1 \cdot 10^{-1}$ mbar). After subsequent activation under reduced pressure ($1 \cdot 10^{-3}$ mbar) for 21 h at room temperature, activated **cage-C_5F_{11}** was subjected to an atmosphere of C_3F_8 for 19 h at room temperature and submitted to SCXRD analyses.

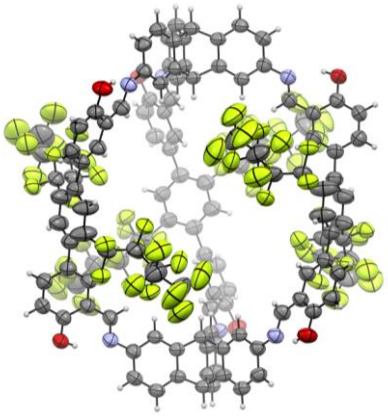

Table 25. Crystal data and structure refinement for C_3F_8-saturated **cage-C_5F_{11}**.

Identification code	tik34sq	
Empirical formula	$C_{130}H_{58}F_{66}N_6O_6$	
Formula weight	3053.82	
Temperature	200(2) K	
Wavelength	1.54178 Å	
Crystal system	trigonal	
Space group	$R\bar{3}c$	
Z	6	
Unit cell dimensions	a = 19.6121(2) Å	α = 90 deg.
	b = 19.6121(2) Å	β = 90 deg.
	c = 65.7479(17) Å	γ = 120 deg.
Volume	21900.8(7) Å^3	
Density (calculated)	1.39 g/cm^3	
Absorption coefficient	1.30 mm^{-1}	
Crystal shape	cuboid	
Crystal size	0.275 x 0.150 x 0.140 mm^3	
Crystal colour	yellow	
Theta range for data collection	2.9 to 68.5 deg.	
Index ranges	-22≤h≤23, -22≤k≤22, -57≤l≤78	
Reflections collected	23066	
Independent reflections	4333 (R(int) = 0.0296)	
Observed reflections	3276 (I > 2σ(I))	
Absorption correction	Semi-empirical from equivalents	
Max. and min. transmission	0.75 and 0.57	
Refinement method	Full-matrix least-squares on F^2	
Data/restraints/parameters	4333 / 2920 / 605	
Goodness-of-fit on F^2	1.06	
Final R indices (I>2sigma(I))	R1 = 0.090, wR2 = 0.264	
Largest diff. peak and hole	0.30 and -0.24 eÅ^{-3}	

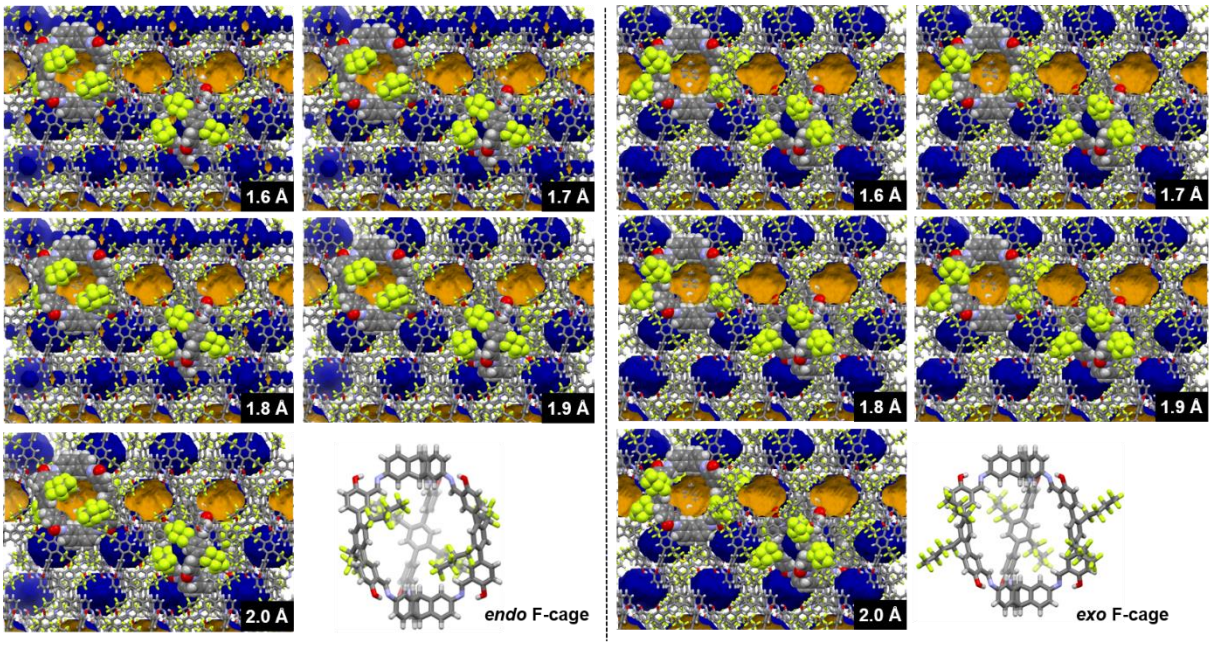

Figure 201. Void analyses of the single crystal X-ray structure of **F-cage** in *endo*-(left) and *exo*-(right) conformation with an approx. grid spacing of 0.5 Å (blue outer surface, yellow inner surface) viewed along a axis. Adapted with permission from Ref.[7]. Copyright © 2022 Wiley-VCH.

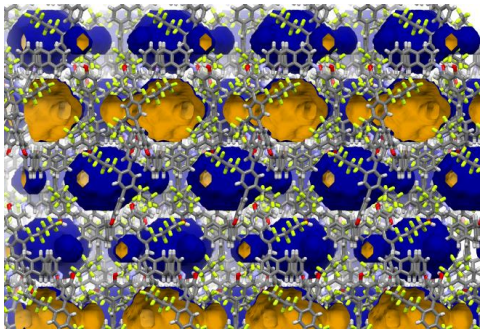

Figure 202. Void analyses of the single crystal X-ray structure of **F-cage** in *endo*-conformation with an approx. grid spacing of 0.5 Å and probe radius 1.6 Å in a slight side view.

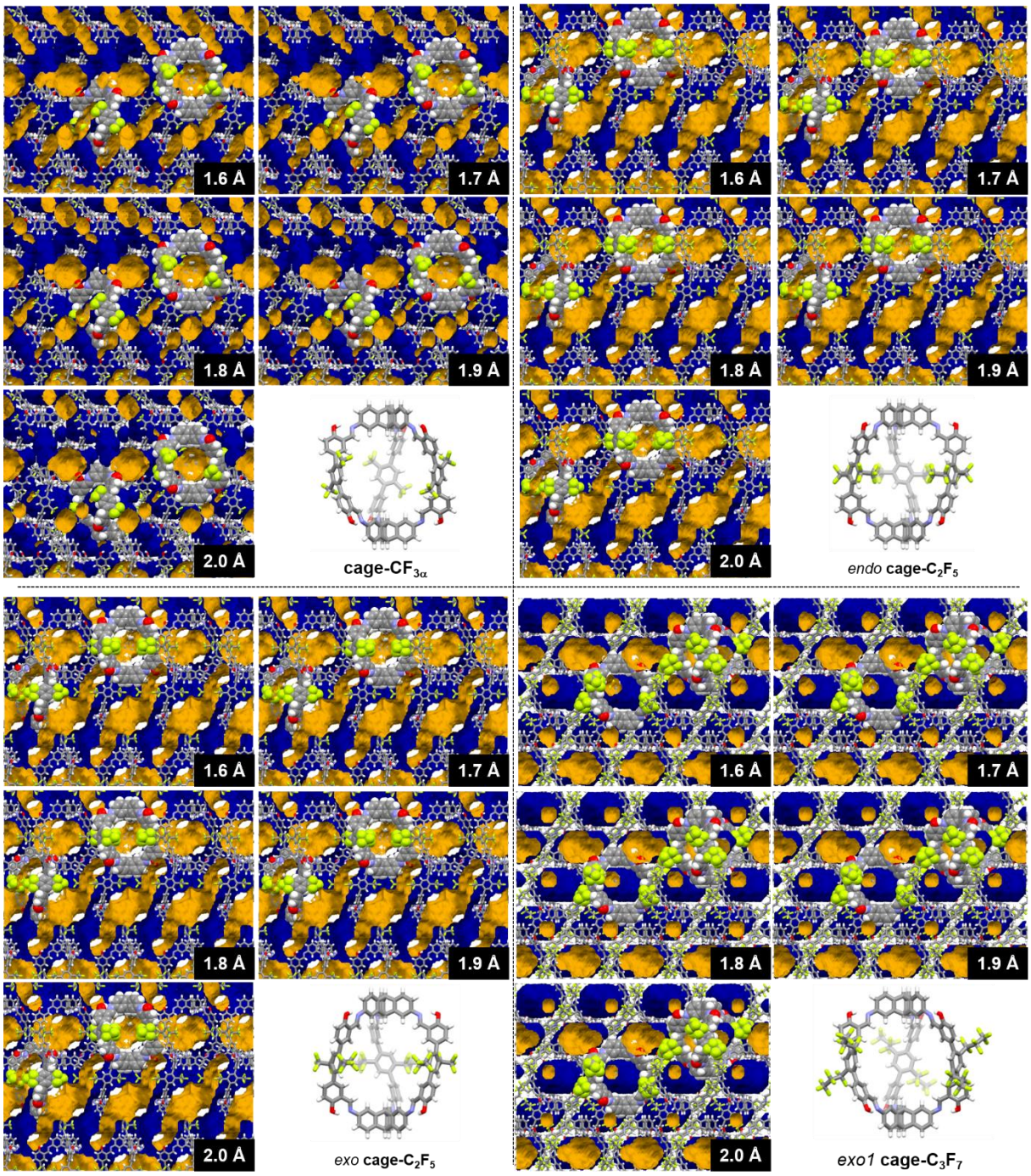

Figure 203. Void analyses of the single crystal X-ray structure of **cage-$CF_{3\alpha}$**, full *endo* **cage-C_2F_5**, full *exo* **cage-C_2F_5** , full *exo1* **cage-C_3F_7** with an approx. grid spacing of 0.5 Å.

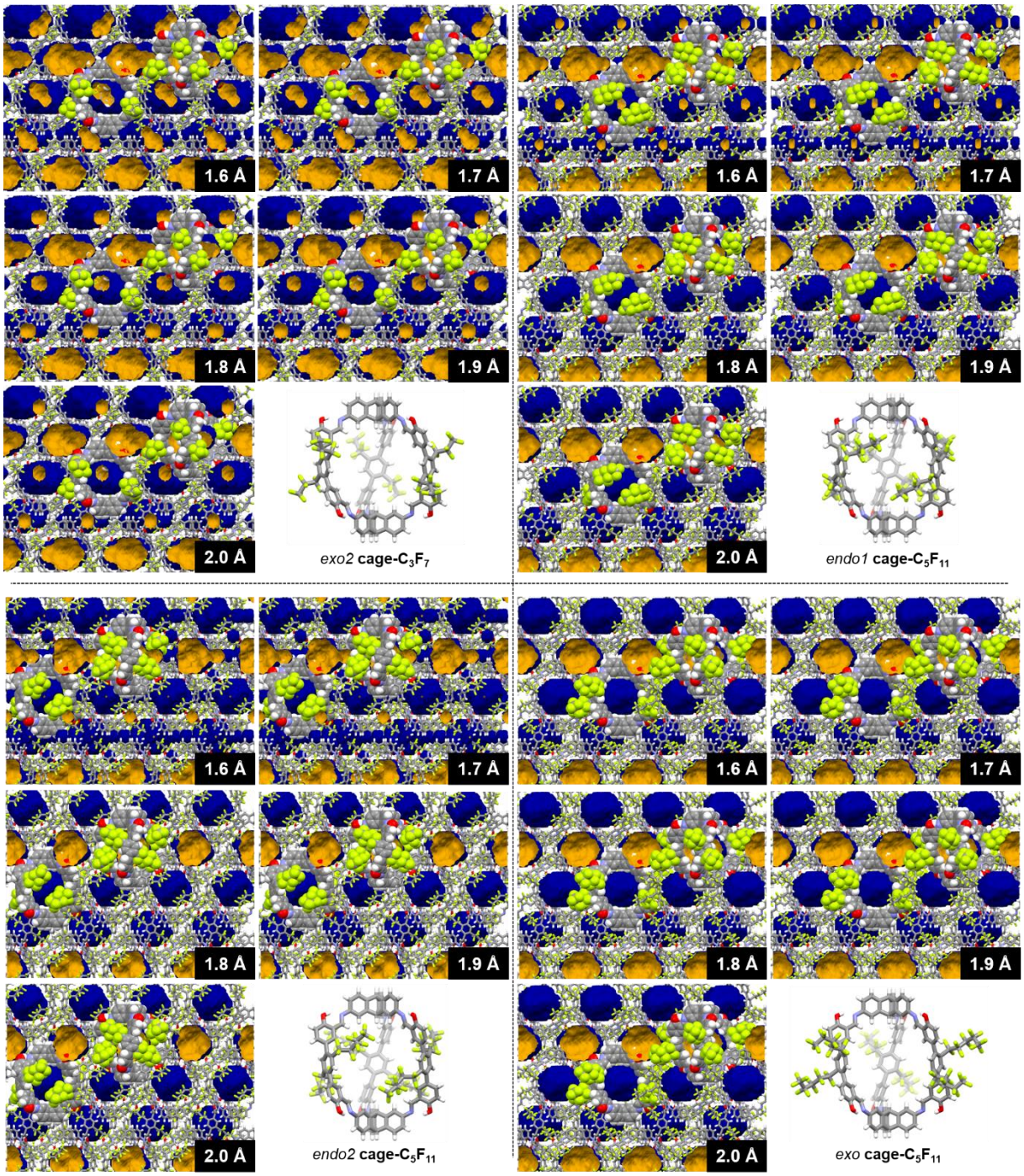

Figure 204. Void analyses of the single crystal X-ray structure of full *exo2* **cage-C_3F_7**, full *endo1* **cage-C_5F_{11}**, full *endo2* **cage-C_5F_{11}**, full *exo* **cage-C_5F_{11}** with an approx. grid spacing of 0.5 Å.

5. Gas Sorption

5.1. N_2-Sorption at 77 K

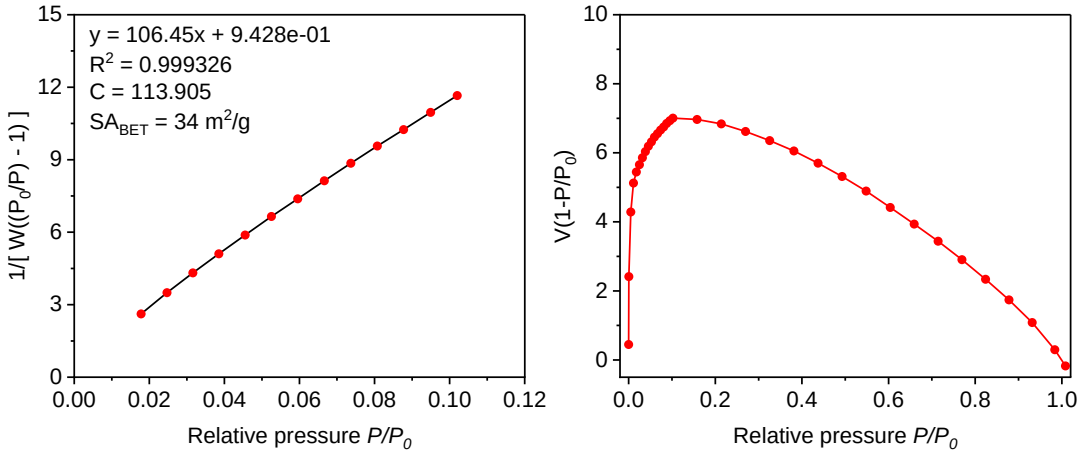

Figure 205. BET-plot (left) and corresponding Rouquerol-plot (right) of **cage-CF$_{3\alpha}$** from nitrogen sorption isotherm at 77 K.

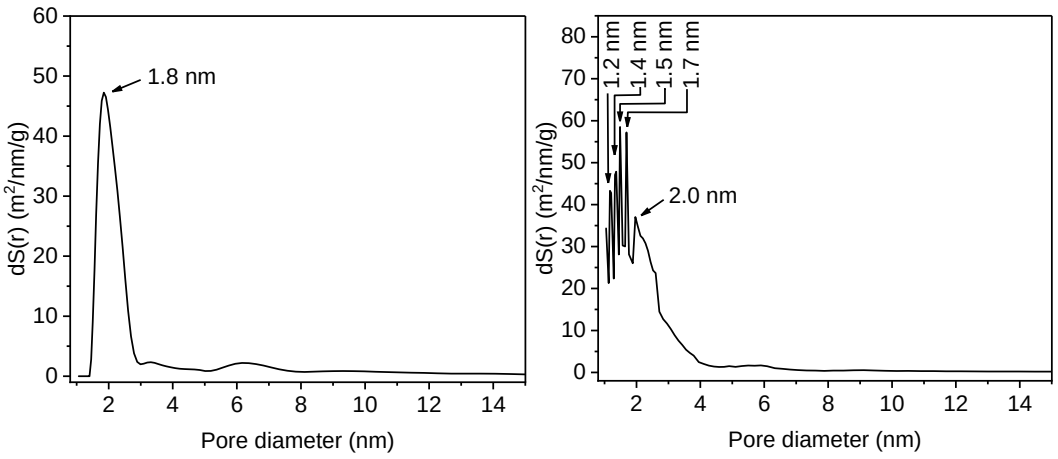

Figure 206. QSDFT pore size distribution (left) (cylindr./spher. pores on carbon, adsorption branch, fitting error: 1.036%) and NLDFT pore size distribution (right) (cylindr. pores on carbon, equilibrium model, fitting error: 4.109%) of **cage-CF$_{3\alpha}$** from nitrogen sorption isotherm at 77 K.

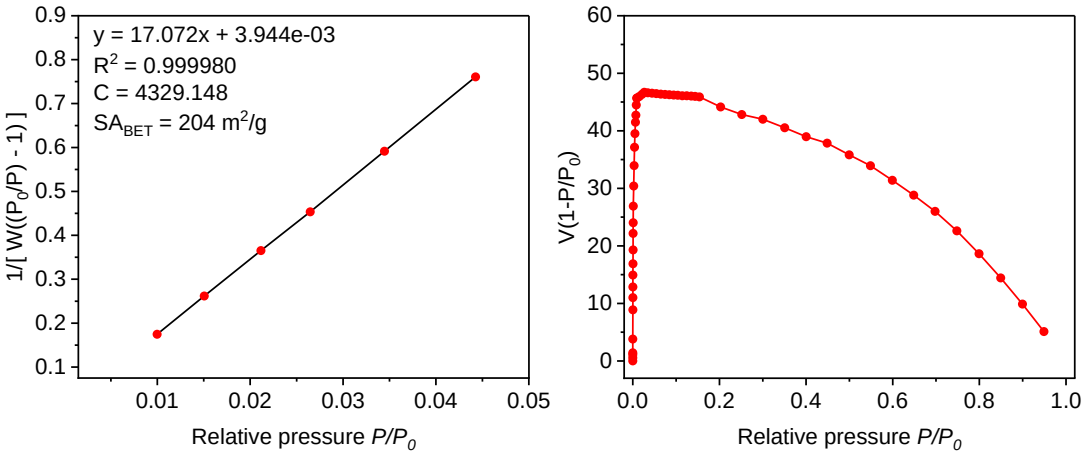

Figure 207. BET-plot (left) and corresponding Rouquerol-plot (right) of **cage-CF$_{3\beta}$** from nitrogen sorption isotherm at 77 K.

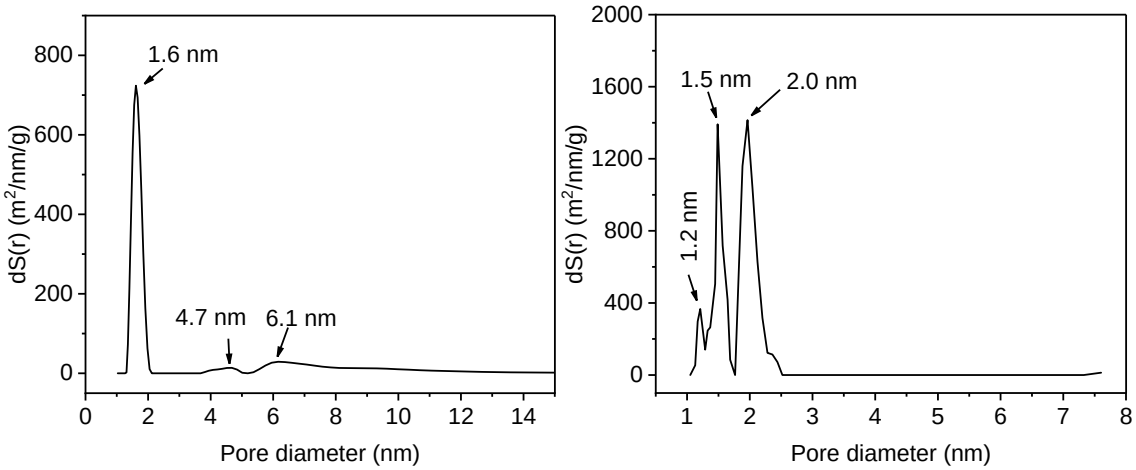

Figure 208. QSDFT pore size distribution (left) (cylindr./spher. pores on carbon, adsorption branch, fitting error: 2.615%) and NLDFT pore size distribution (right) (cylindr. pores on carbon, equilibrium model, fitting error: 7.715%) of **cage-CF$_{3\beta}$** from nitrogen sorption isotherm at 77 K.

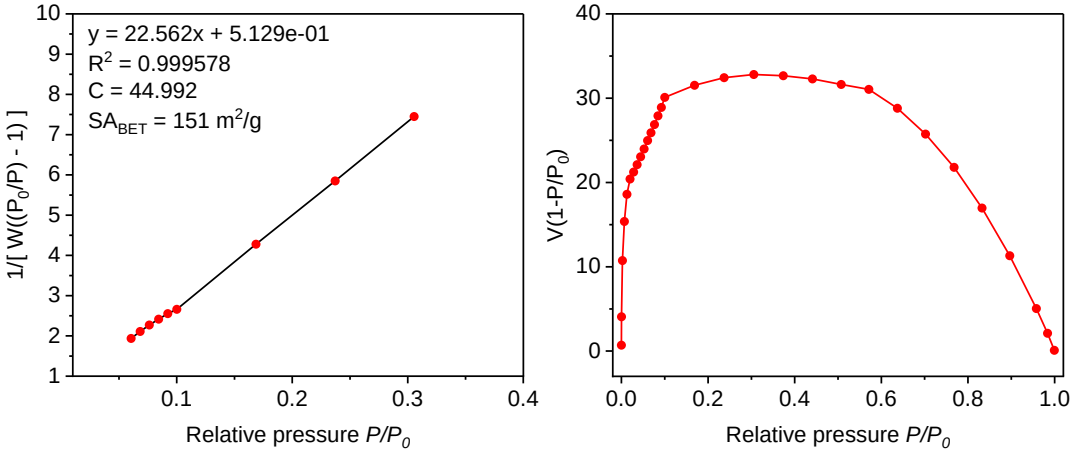

Figure 209. BET-plot (left) and corresponding Rouquerol-plot (right) of **cage-CF$_{3\gamma}$** from nitrogen sorption isotherm at 77 K.

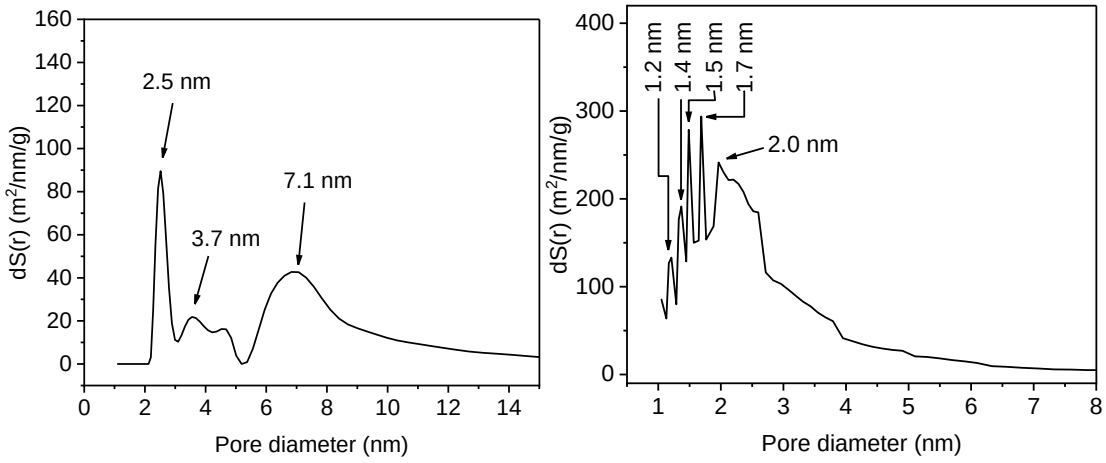

Figure 210. QSDFT pore size distribution (left) (cylindr./spher. pores on carbon, adsorption branch, fitting error: 2.166%) and NLDFT pore size distribution (right) (cylindr. pores on carbon, equilibrium model, fitting error: 5.000%) of **cage-CF$_{3\gamma}$** from nitrogen sorption isotherm at 77 K.

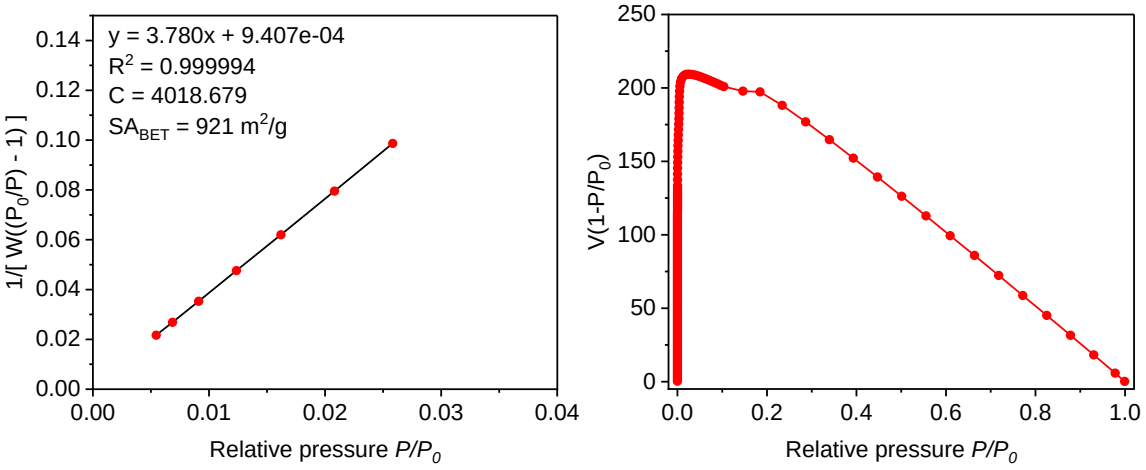

Figure 211. BET-plot (left) and corresponding Rouquerol-plot (right) of **cage-C_2F_5** from nitrogen sorption isotherm at 77 K.

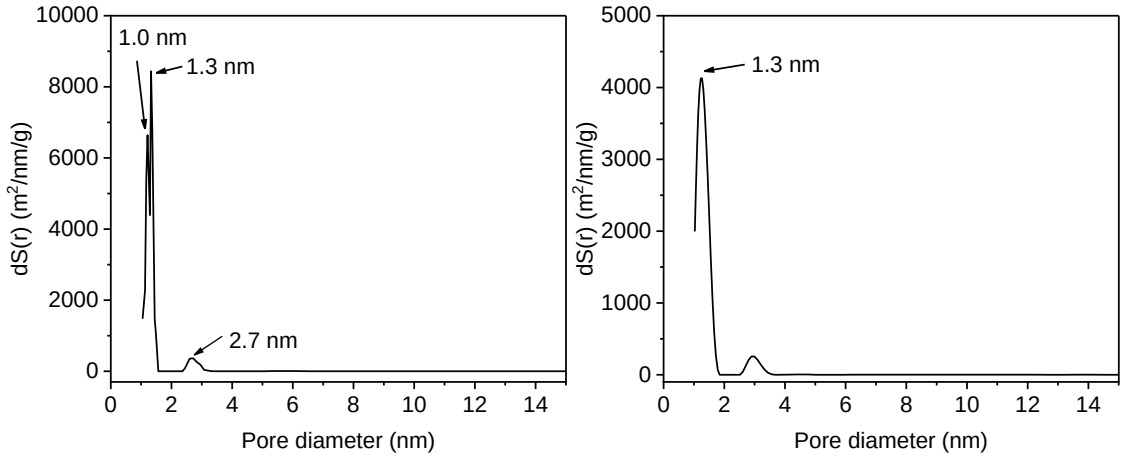

Figure 212. QSDFT pore size distribution (left) (cylindr./spher. pores on carbon, adsorption branch, fitting error: 1.243%) and NLDFT pore size distribution (right) (cylindr. pores on carbon, equilibrium model, fitting error: 0.882%) of **cage-C_2F_5** from nitrogen sorption isotherm at 77 K.

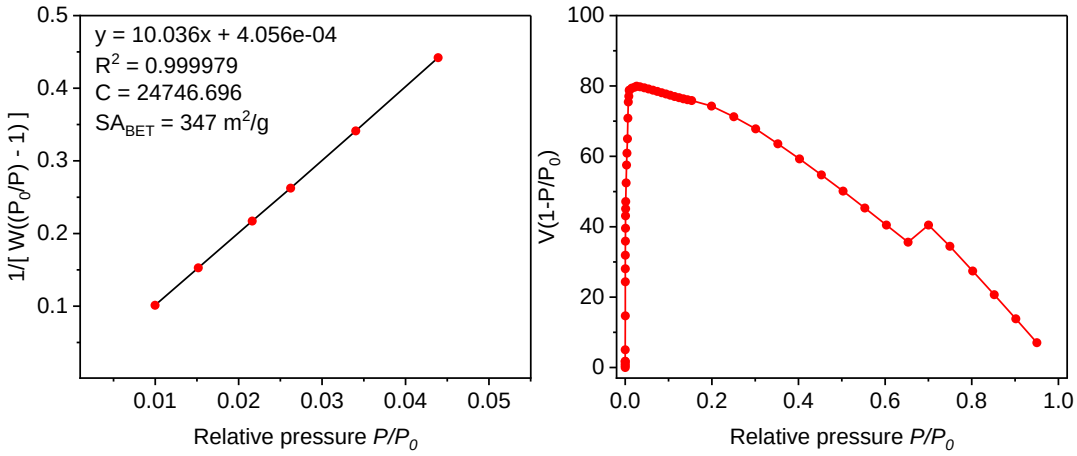

Figure 213. BET-plot (left) and corresponding Rouquerol-plot (right) of **cage-C_3F_7** from nitrogen sorption isotherm at 77 K.

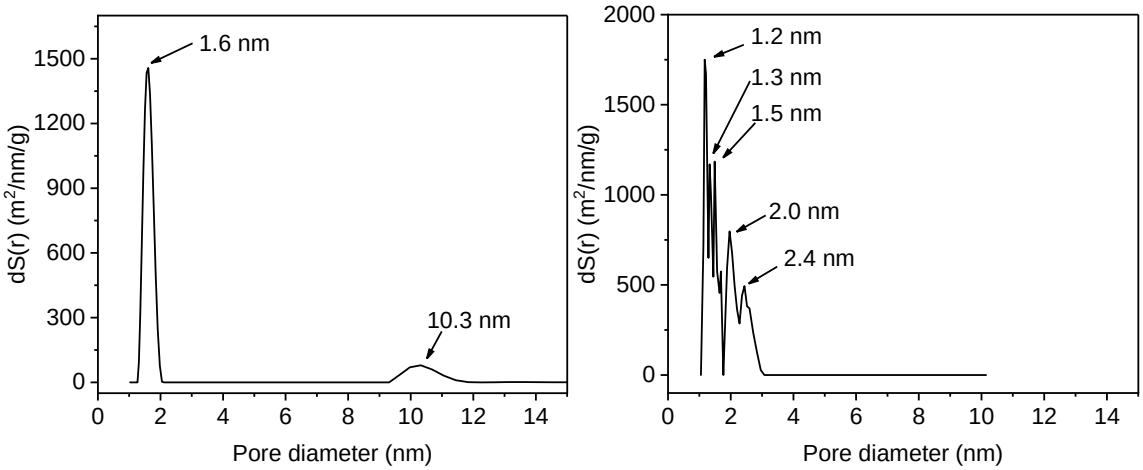

Figure 214. QSDFT pore size distribution (left) (cylindr./spher. pores on carbon, adsorption branch, fitting error: 3.556%) and NLDFT pore size distribution (right) (cylindr. pores on carbon, equilibrium model, fitting error: 6.777%) of **cage-C_3F_7** from nitrogen sorption isotherm at 77 K.

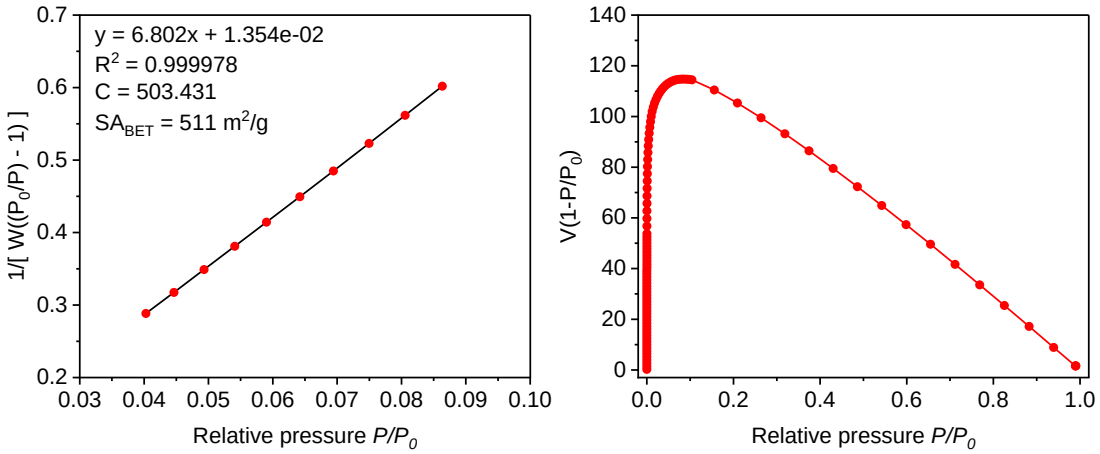

Figure 215. BET-plot (left) and corresponding Rouquerol-plot (right) of **cage-C_5F_{11}** from nitrogen sorption isotherm at 77 K.

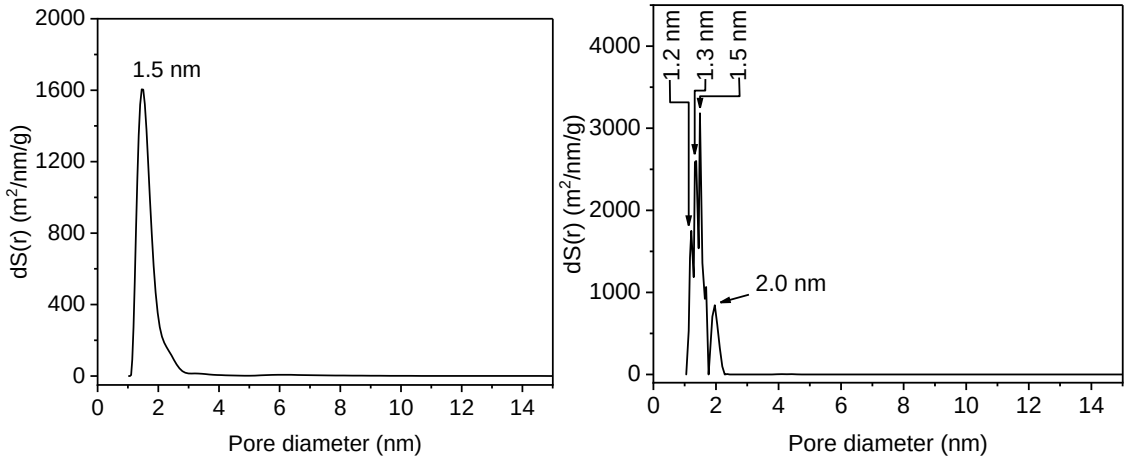

Figure 216. QSDFT pore size distribution (left) (cylindr./spher. pores on carbon, adsorption branch, fitting error: 1.964%) and NLDFT pore size distribution (right) (cylindr. pores on carbon, equilibrium model, fitting error: 1.495%) of **cage-C_5F_{11}** from nitrogen sorption isotherm at 77 K.

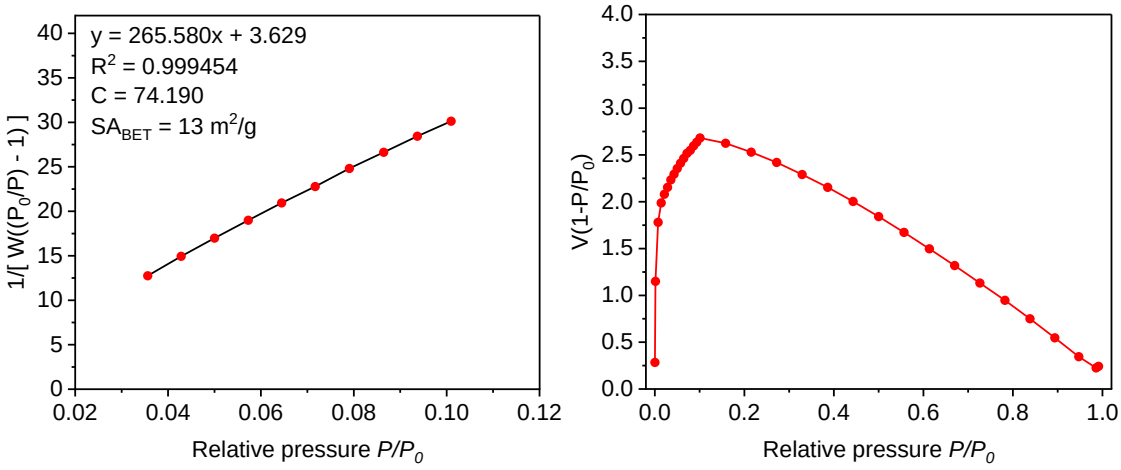

Figure 217. BET-plot (left) and corresponding Rouquerol-plot (right) of **cage-$C_6F_{13\alpha}$** from nitrogen sorption isotherm at 77 K.

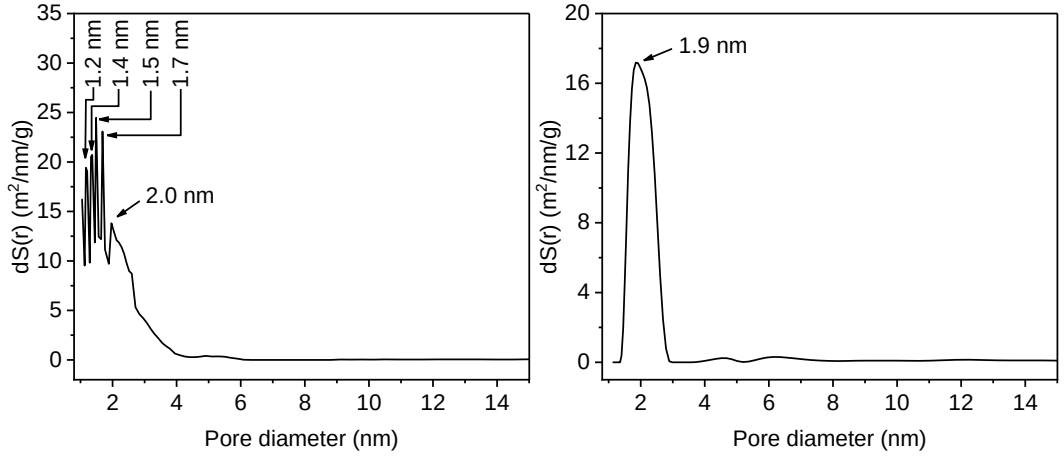

Figure 218. QSDFT pore size distribution (left) (cylindr./spher. pores on carbon, adsorption branch, fitting error: 5.246%) and NLDFT pore size distribution (right) (cylindr. pores on carbon, equilibrium model, fitting error: 6.776%) of **cage-$C_6F_{13\alpha}$** from nitrogen sorption isotherm at 77 K.

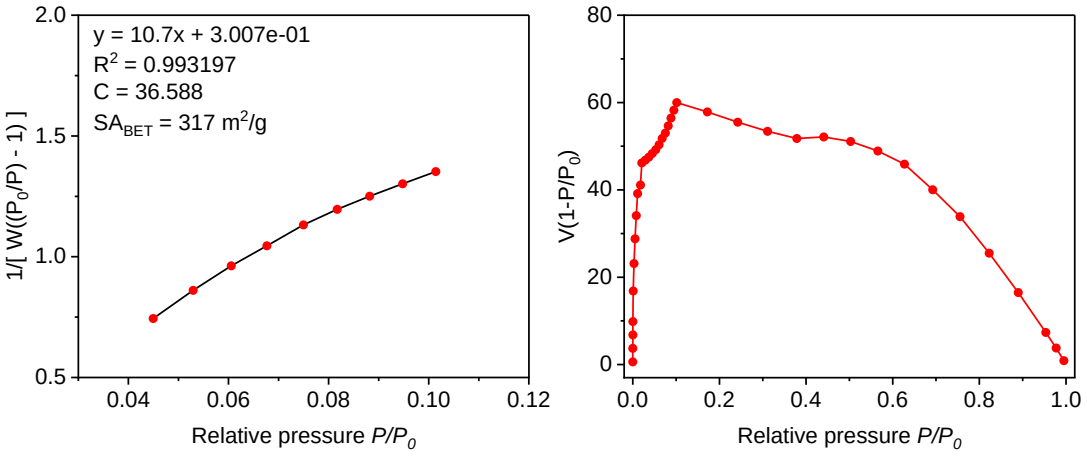

Figure 219. BET-plot (left) and corresponding Rouquerol-plot (right) of **cage-$C_6F_{13\beta}$** from nitrogen sorption isotherm at 77 K.

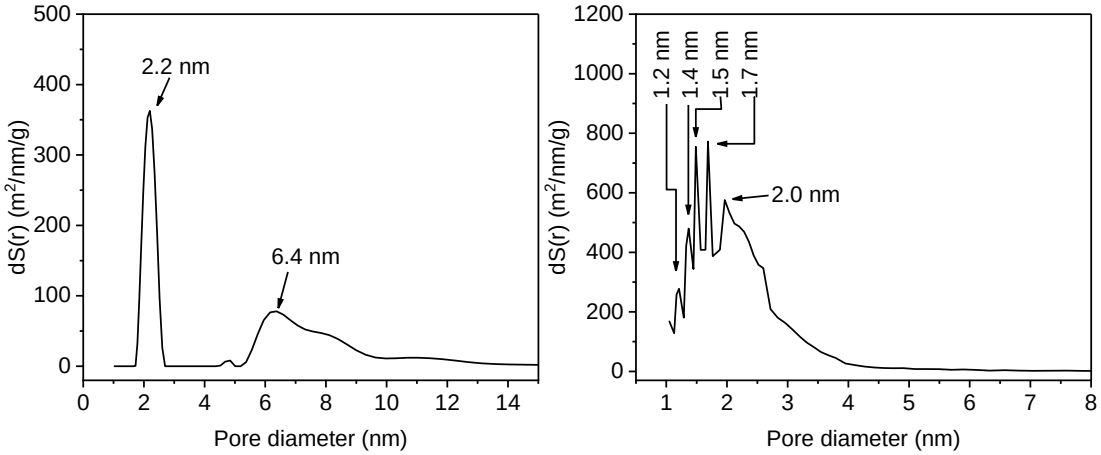

Figure 220. QSDFT pore size distribution (left) (cylindr./spher. pores on carbon, adsorption branch, fitting error: 2.394%) and NLDFT pore size distribution (right) (cylindr. pores on carbon, equilibrium model, fitting error: 7.678%) of **cage-$C_6F_{13\beta}$** from nitrogen sorption isotherm at 77 K.

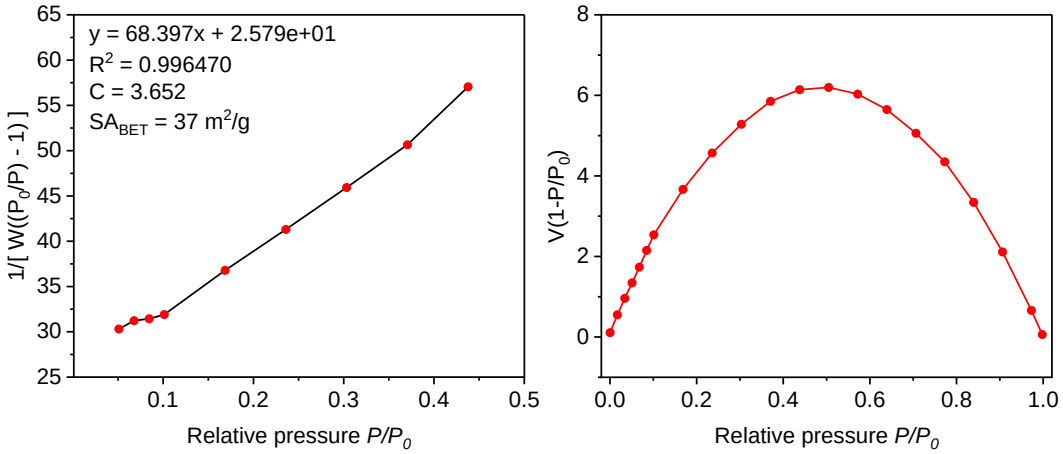

Figure 221. BET-plot (left) and corresponding Rouquerol-plot (right) of **cage-$C_6F_{13\gamma}$** from nitrogen sorption isotherm at 77 K.

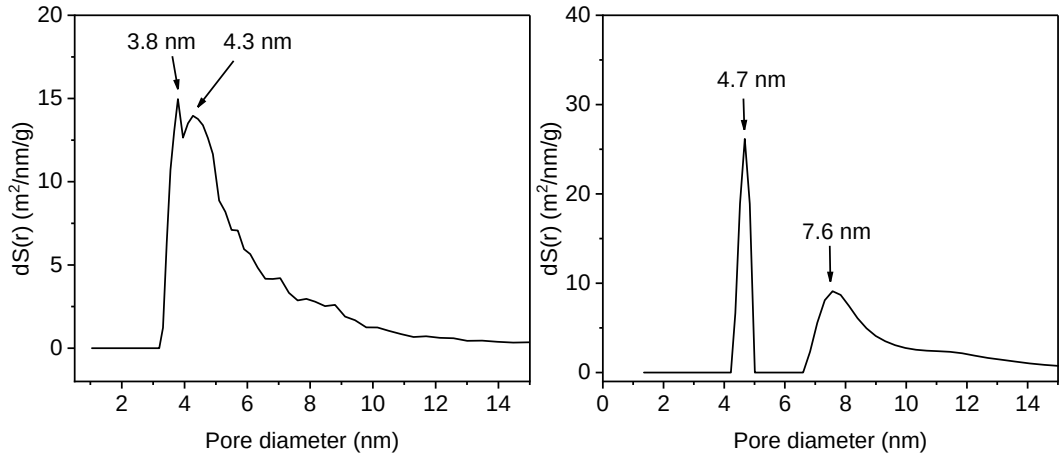

Figure 222. QSDFT pore size distribution (left) (cylindr./spher. pores on carbon, adsorption branch, fitting error: 8.697%) and NLDFT pore size distribution (right) (cylindr. pores on carbon, equilibrium model, fitting error: 6.563%) of **cage-$C_6F_{13\gamma}$** from nitrogen sorption isotherm at 77 K.

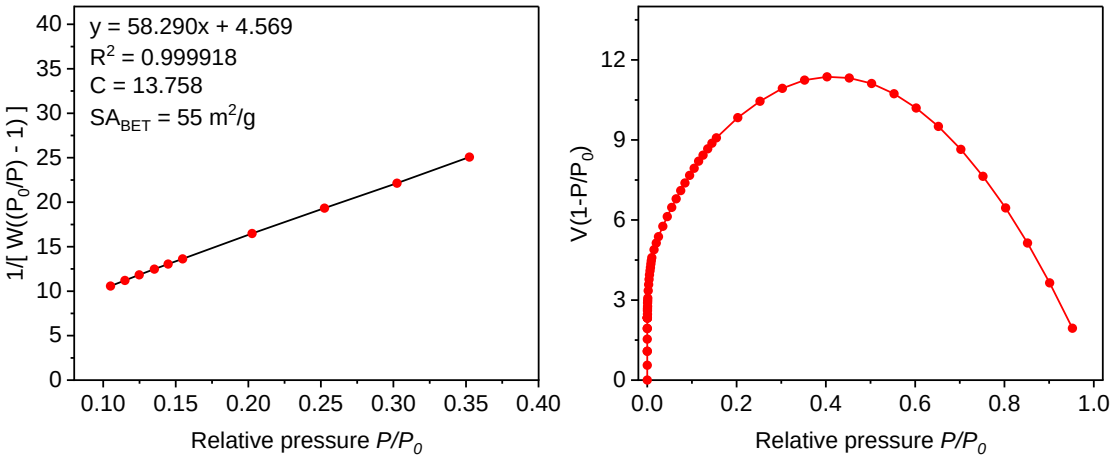

Figure 223. BET-plot (left) and corresponding Rouquerol-plot (right) of **cage-CH₃** from nitrogen sorption isotherm at 77 K.

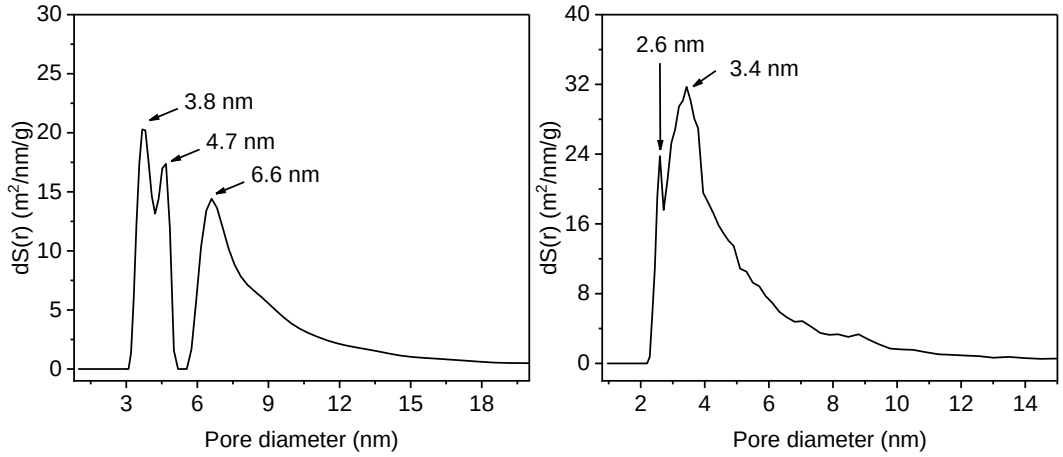

Figure 224. QSDFT pore size distribution (left) (cylindr./spher. pores on carbon, adsorption branch, fitting error: 2.741%) and NLDFT pore size distribution (right) (cylindr. pores on carbon, equilibrium model, fitting error: 1.680%) of **cage-CH₃** from nitrogen sorption isotherm at 77 K.

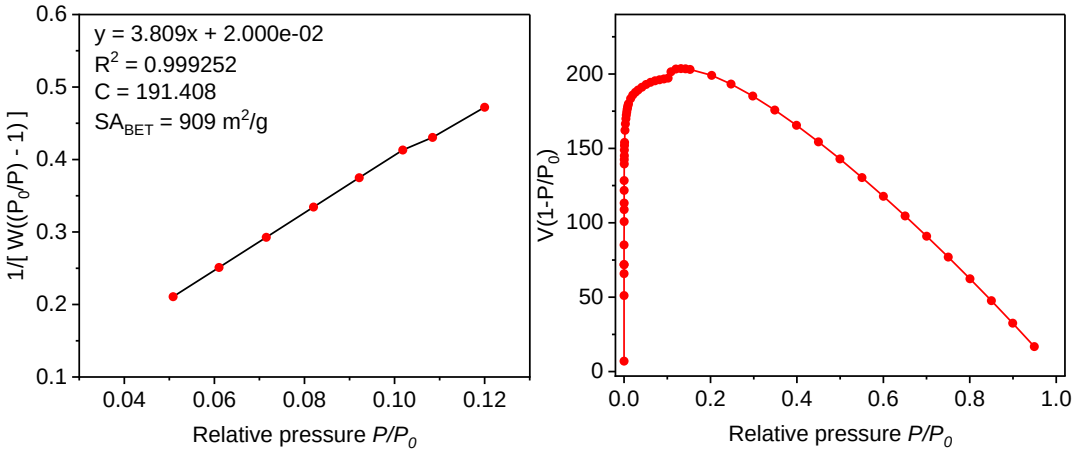

Figure 225. BET-plot (left) and corresponding Rouquerol-plot (right) of **cage-Nap** from nitrogen sorption isotherm at 77 K.

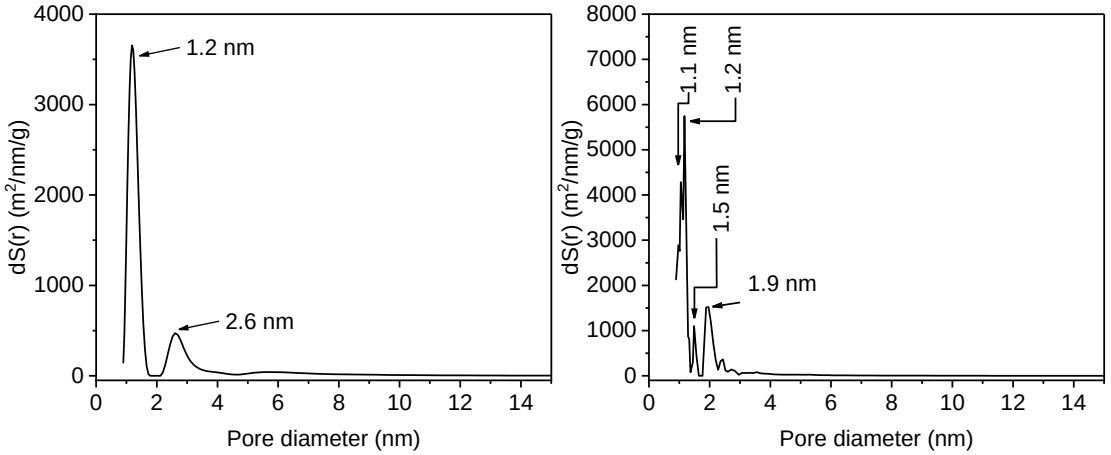

Figure 226. QSDFT pore size distribution (left) (cylindr./spher. pores on carbon, adsorption branch, fitting error: 0.574%) and NLDFT pore size distribution (right) (cylindr. pores on carbon, equilibrium model, fitting error: 0.505%) of **cage-Nap** from nitrogen sorption isotherm at 77 K.

5.2. Ar-Sorption at 87 K

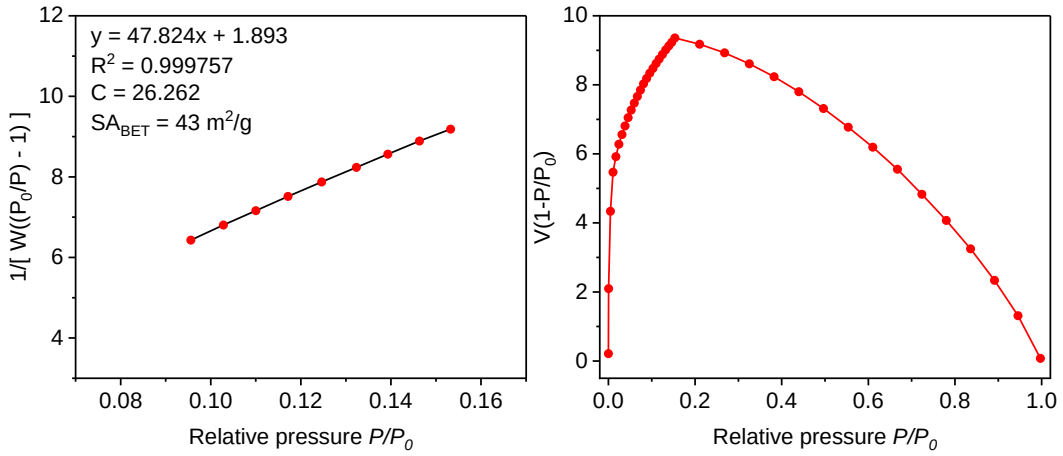

Figure 227. BET-plot (left) and corresponding Rouquerol-plot (right) of **cage-CF$_{3\alpha}$** from argon sorption isotherm at 87 K.

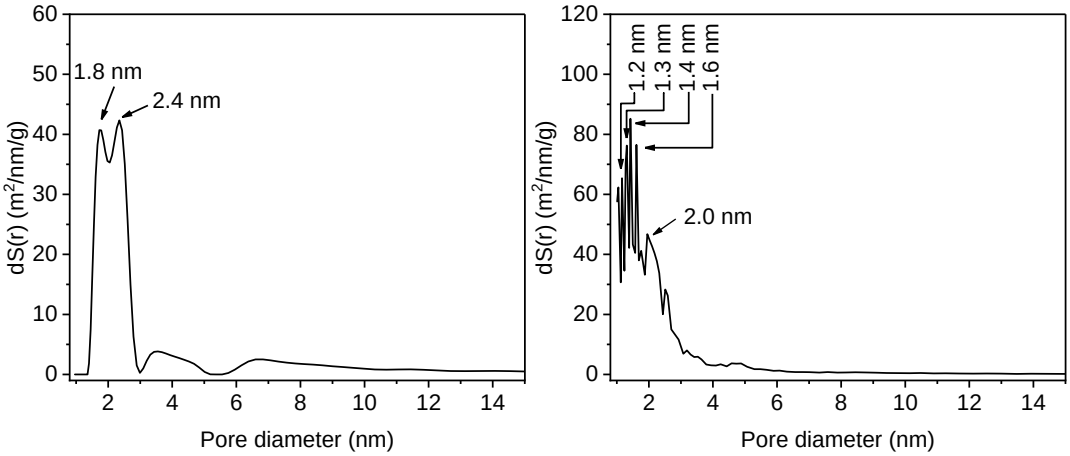

Figure 228. QSDFT pore size distribution (left) (cylindr./spher. pores on carbon, adsorption branch, fitting error: 0.730%) and NLDFT pore size distribution (right) (cylindr. pores on carbon, equilibrium model, fitting error: 3.816%) of **cage-CF$_{3\alpha}$** from argon sorption isotherm at 87 K.

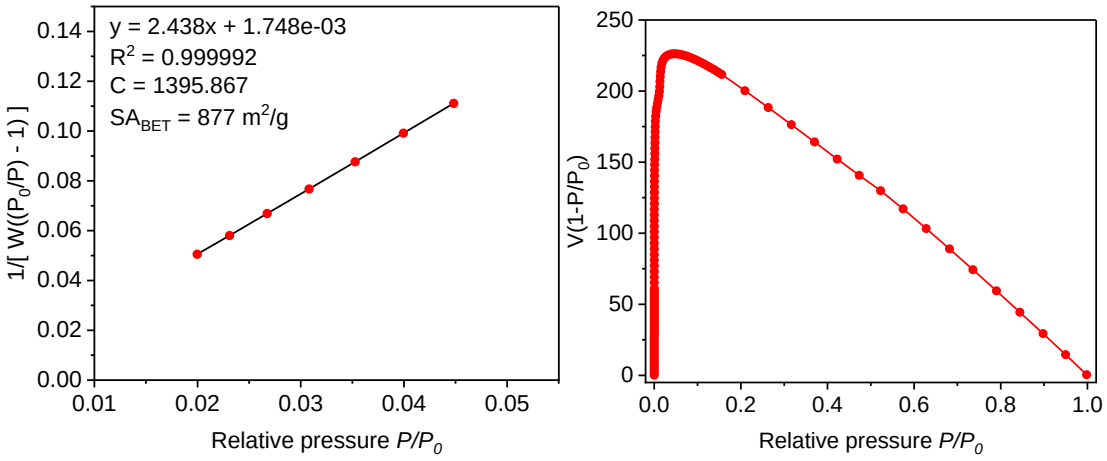

Figure 229. BET-plot (left) and corresponding Rouquerol-plot (right) of **cage-C_2F_5** from argon sorption isotherm at 87 K.

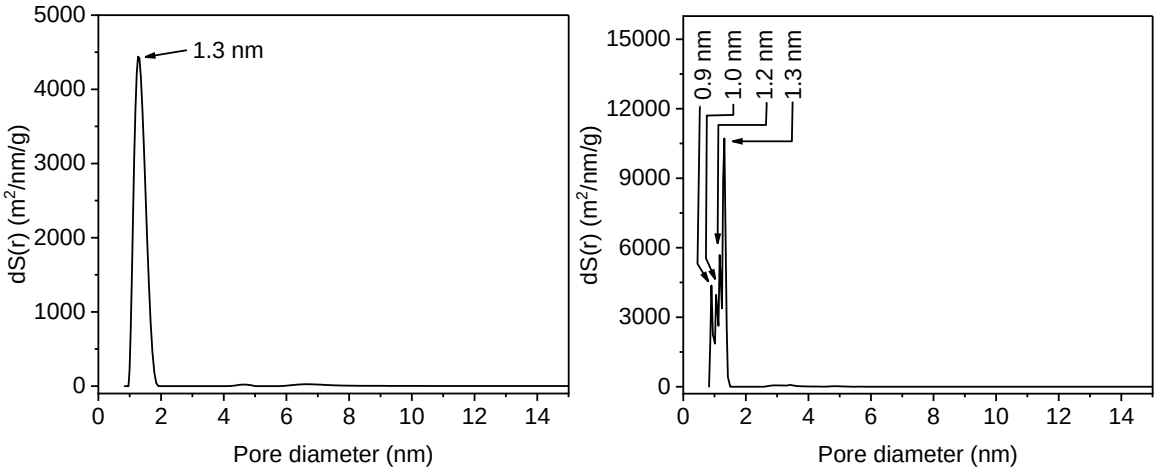

Figure 230. QSDFT pore size distribution (left) (cylindr./spher. pores on carbon, adsorption branch, fitting error: 1.772%) and NLDFT pore size distribution (right) (cylindr. pores on carbon, equilibrium model, fitting error: 0.354%) of **cage-C_2F_5** from argon sorption isotherm at 87 K.

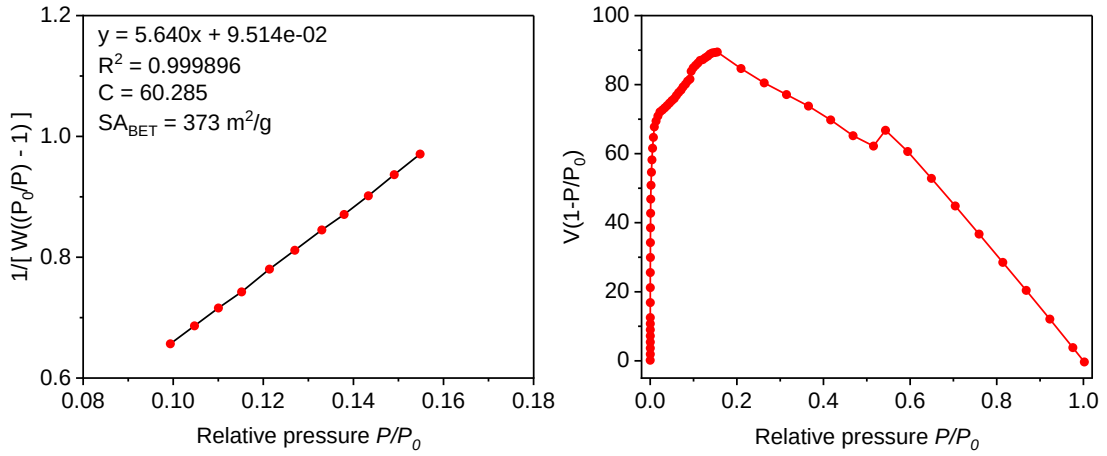

Figure 231. BET-plot (left) and corresponding Rouquerol-plot (right) of **cage-C_3F_7** from argon sorption isotherm at 87 K.

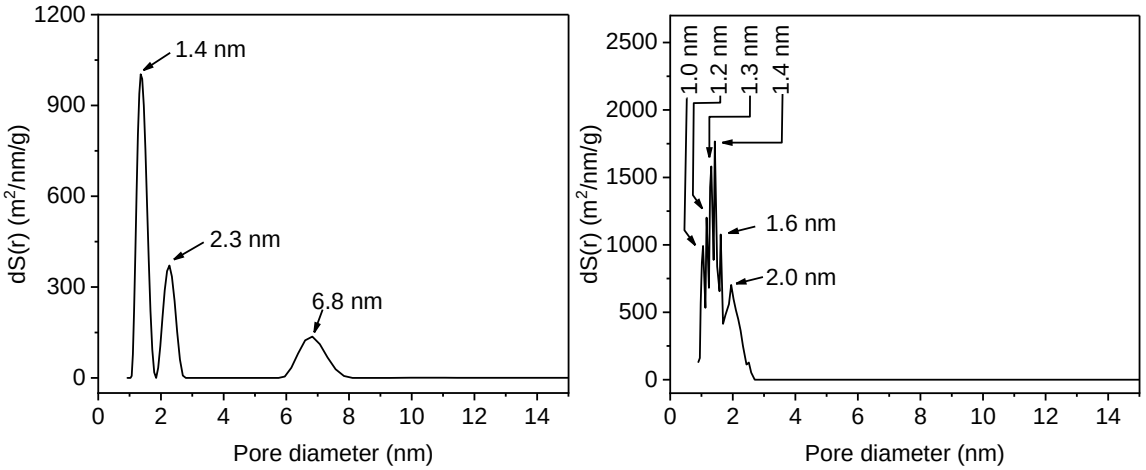

Figure 232. QSDFT pore size distribution (left) (cylindr./spher. pores on carbon, adsorption branch, fitting error: 1.591%) and NLDFT pore size distribution (right) (cylindr. pores on carbon, equilibrium model, fitting error: 3.542%) of **cage-C_3F_7** from argon sorption isotherm at 87 K.

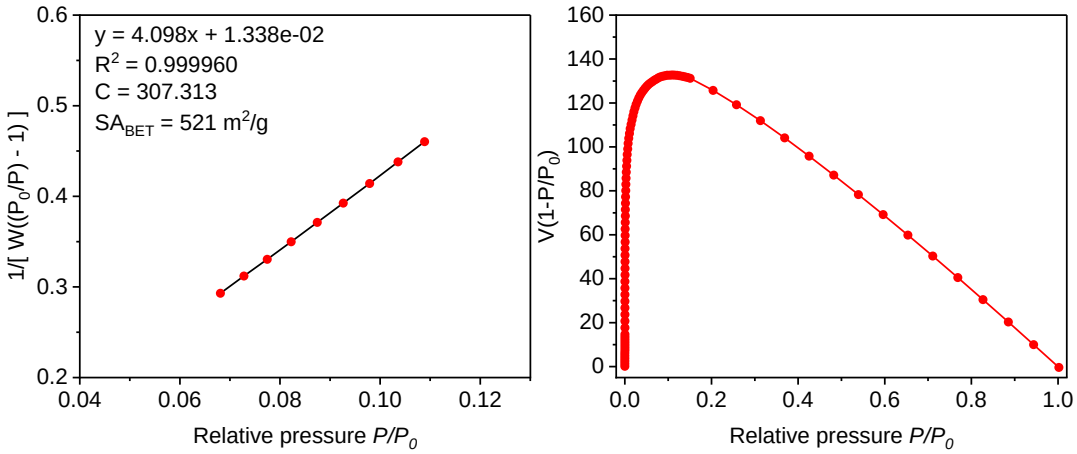

Figure 233. BET-plot (left) and corresponding Rouquerol-plot (right) of **cage-C_5F_{11}** from argon sorption isotherm at 87 K.

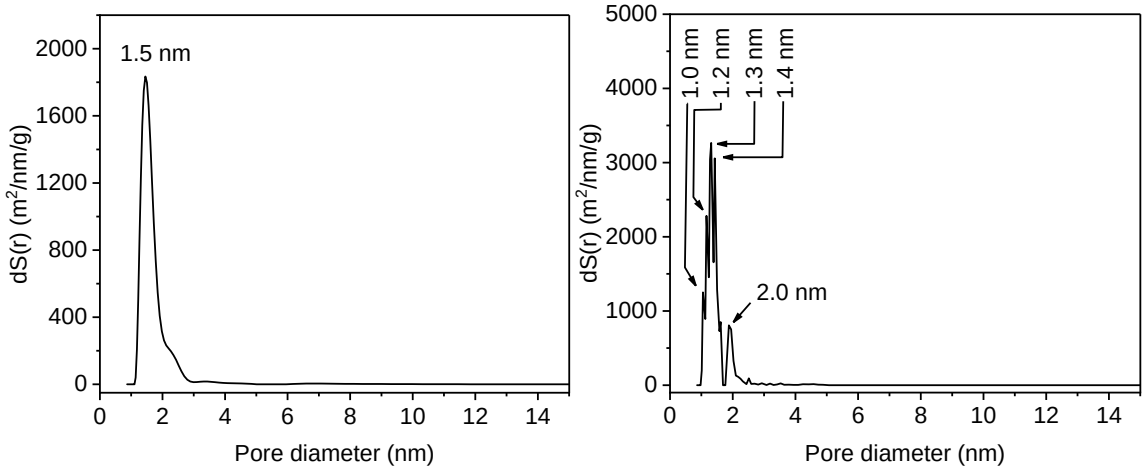

Figure 234. QSDFT pore size distribution (left) (cylindr./spher. pores on carbon, adsorption branch, fitting error: 1.886%) and NLDFT pore size distribution (right) (cylindr. pores on carbon, equilibrium model, fitting error: 1.124%) of **cage-C_5F_{11}** from argon sorption isotherm at 87 K.

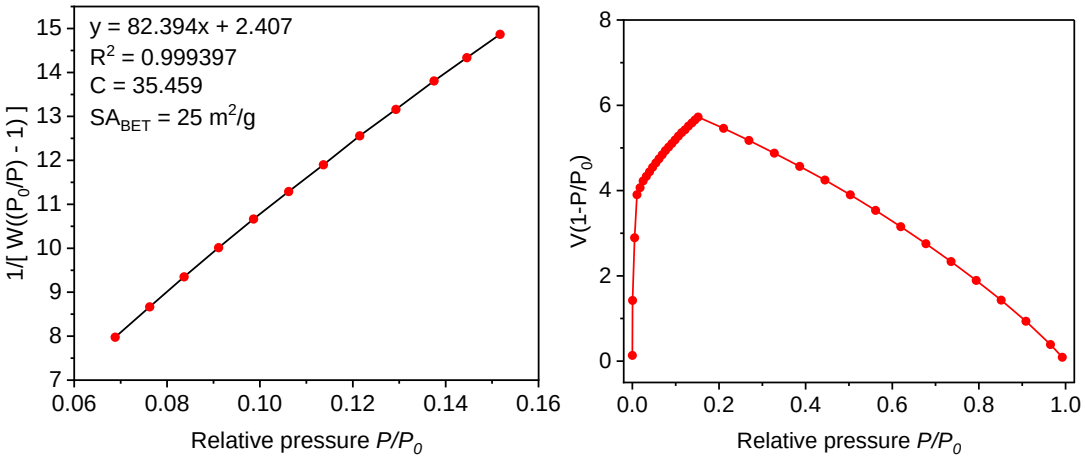

Figure 235. BET-plot (left) and corresponding Rouquerol-plot (right) of **cage-$C_6F_{13\alpha}$** from argon sorption isotherm at 87 K.

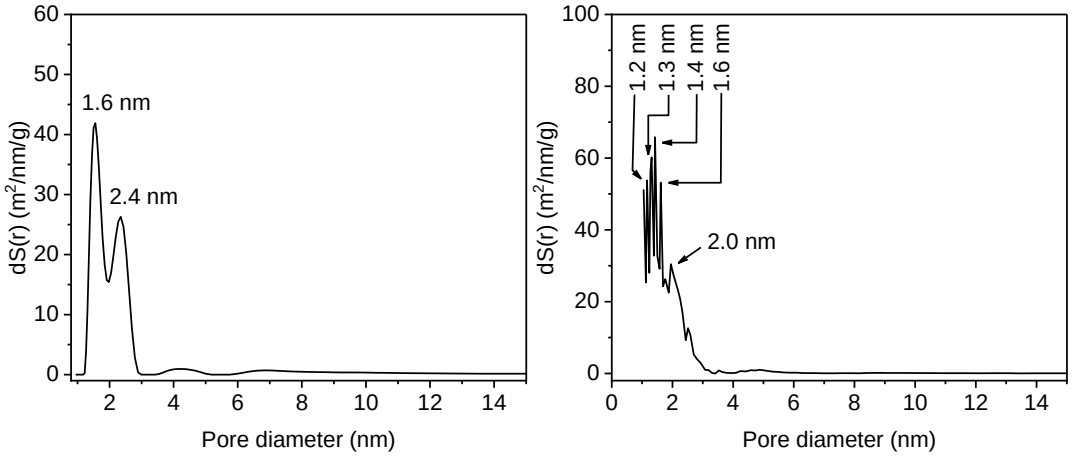

Figure 236. QSDFT pore size distribution (left) (cylindr./spher. pores on carbon, adsorption branch, fitting error: 1.035%) and NLDFT pore size distribution (right) (cylindr. pores on carbon, equilibrium model, fitting error: 6.106%) of **cage-$C_6F_{13\alpha}$** from argon sorption isotherm at 87 K.

5.3. CO_2-Sorption at 195 K

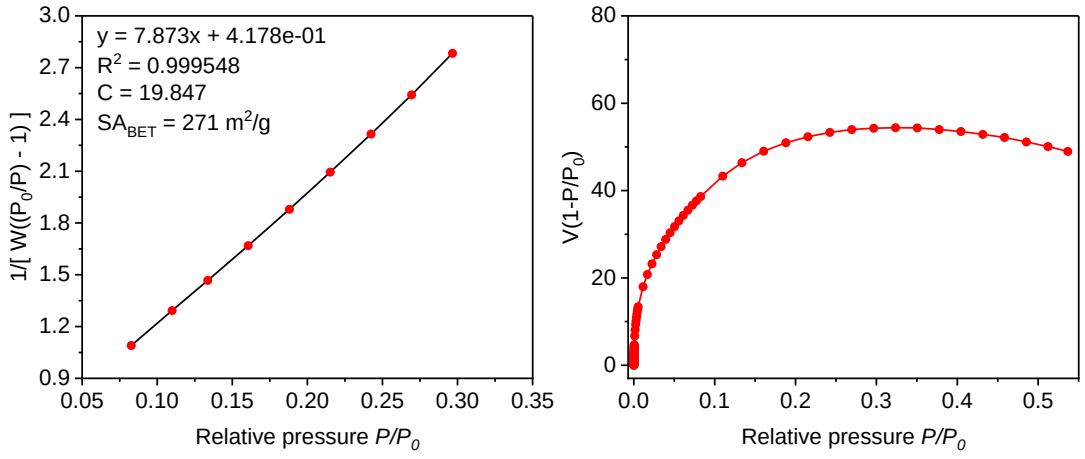

Figure 237. BET-plot (left) and corresponding Rouquerol-plot (right) of **cage-$CF_{3\alpha}$** from CO_2 sorption isotherm at 195 K.

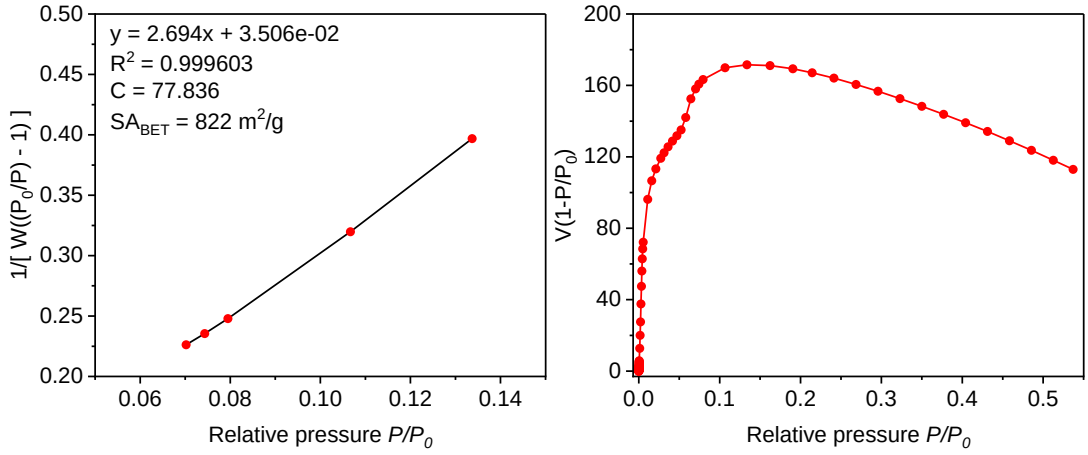

Figure 238. BET-plot (left) and corresponding Rouquerol-plot (right) of **cage-C_2F_5** from CO_2 sorption isotherm at 195 K.

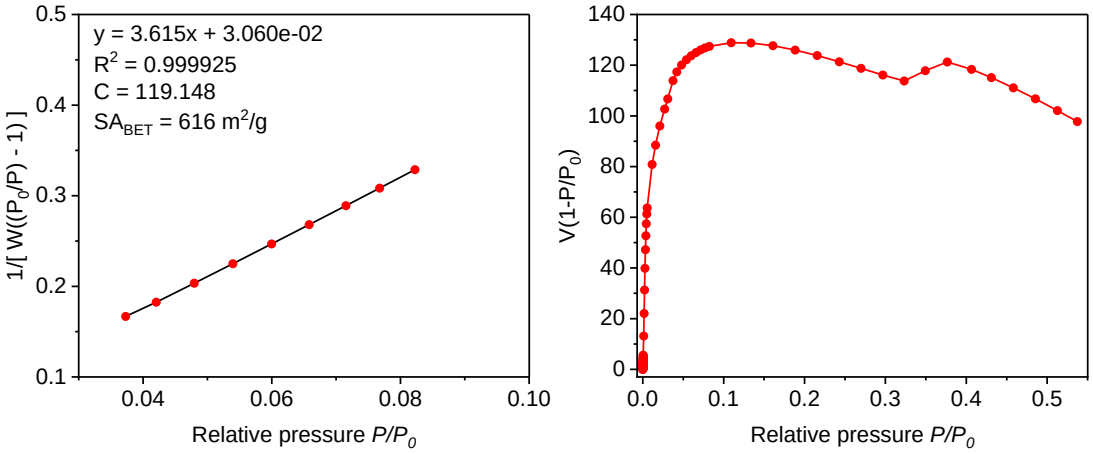

Figure 239. BET-plot (left) and corresponding Rouquerol-plot (right) of **cage-C_3F_7** from CO_2 sorption isotherm at 195 K.

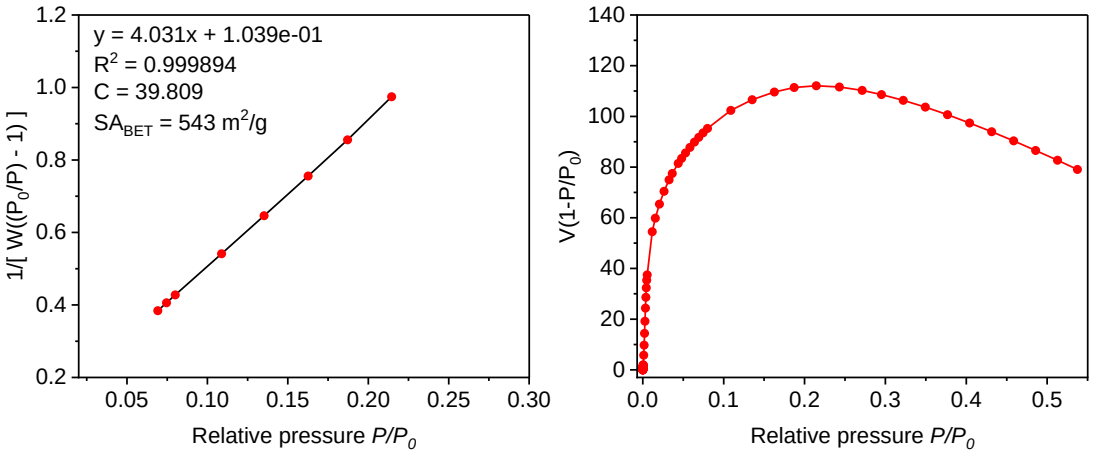

Figure 240. BET-plot (left) and corresponding Rouquerol-plot (right) of **cage-C_5F_{11}** from CO_2 sorption isotherm at 195 K.

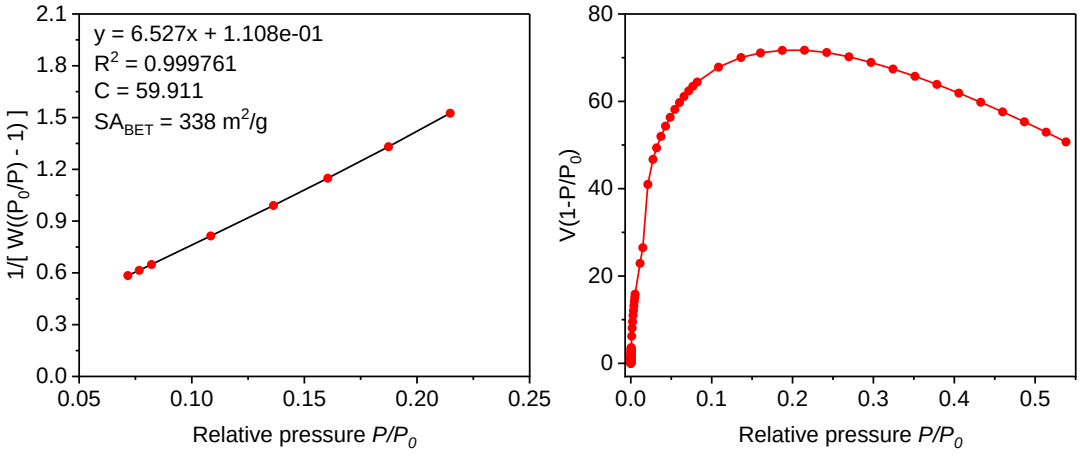

Figure 241. BET-plot (left) and corresponding Rouquerol-plot (right) of **cage-$C_6F_{13\alpha}$** from CO_2 sorption isotherm at 195 K.

5.4. Gas Sorption Isotherms and IAST Selectivity Curves

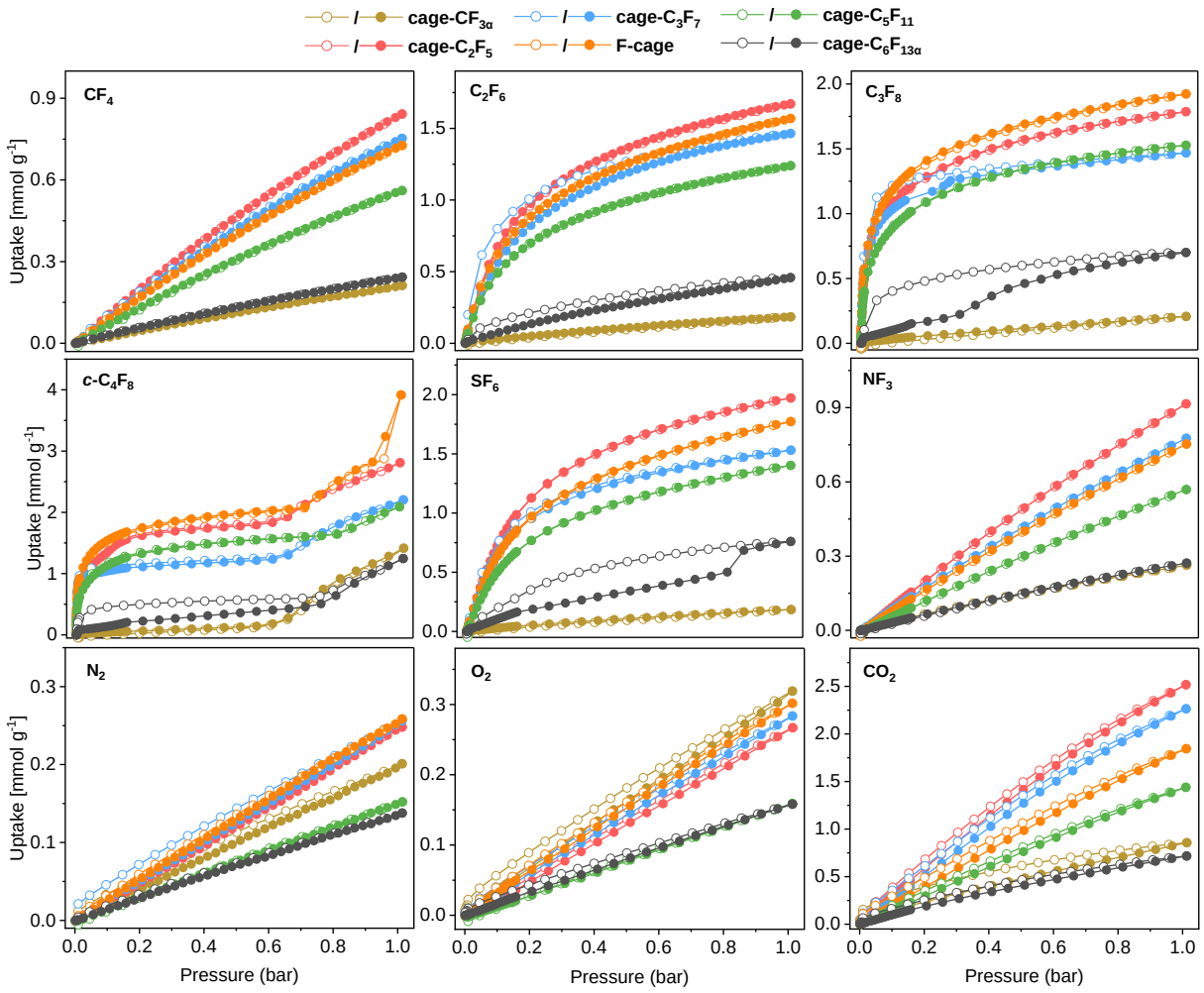

Figure 242. Gas sorption isotherms of **cage-CF$_{3α}$** (brown), **cage-C$_2$F$_5$** (red), **cage-C$_3$F$_7$** (blue), **F-cage** (orange), **cage-C$_5$F$_{11}$** (green), **cage-C$_6$F$_{13}$** (black) at 283 K. Note: The isotherm shapes of *c*-C$_4$F$_8$ are related to pore condensation processes.

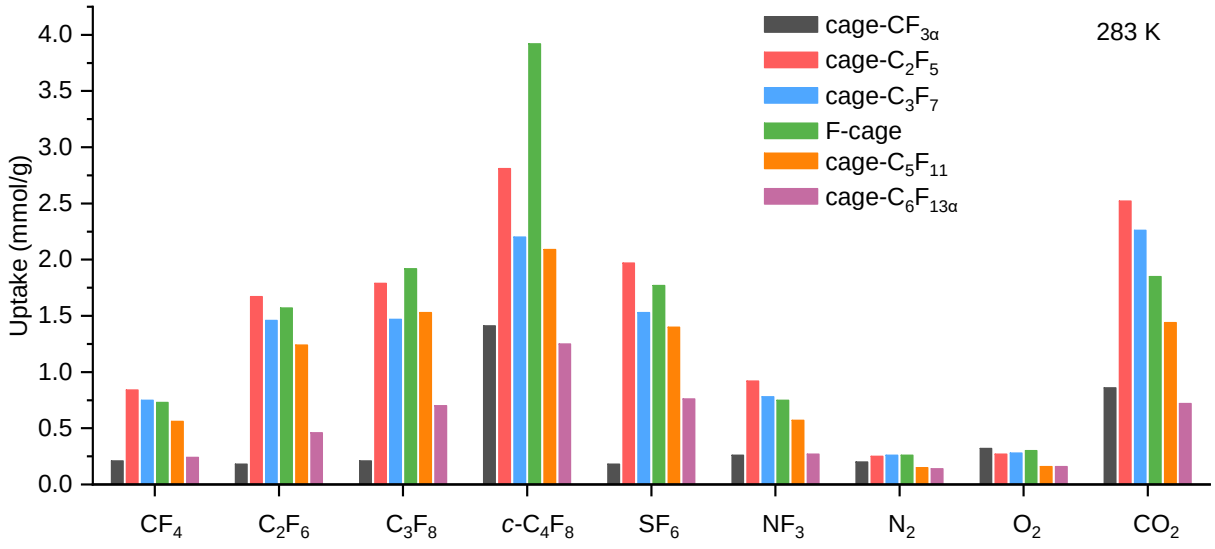

Figure 243. Gas uptake of **cage-CF$_{3α}$** (black), **cage-C$_2$F$_5$** (red), **cage-C$_3$F$_7$** (blue), **F-cage** (green), **cage-C$_5$F$_{11}$** (orange), and **cage-C$_6$F$_{13α}$** (purple) at 283 K and 1 bar.

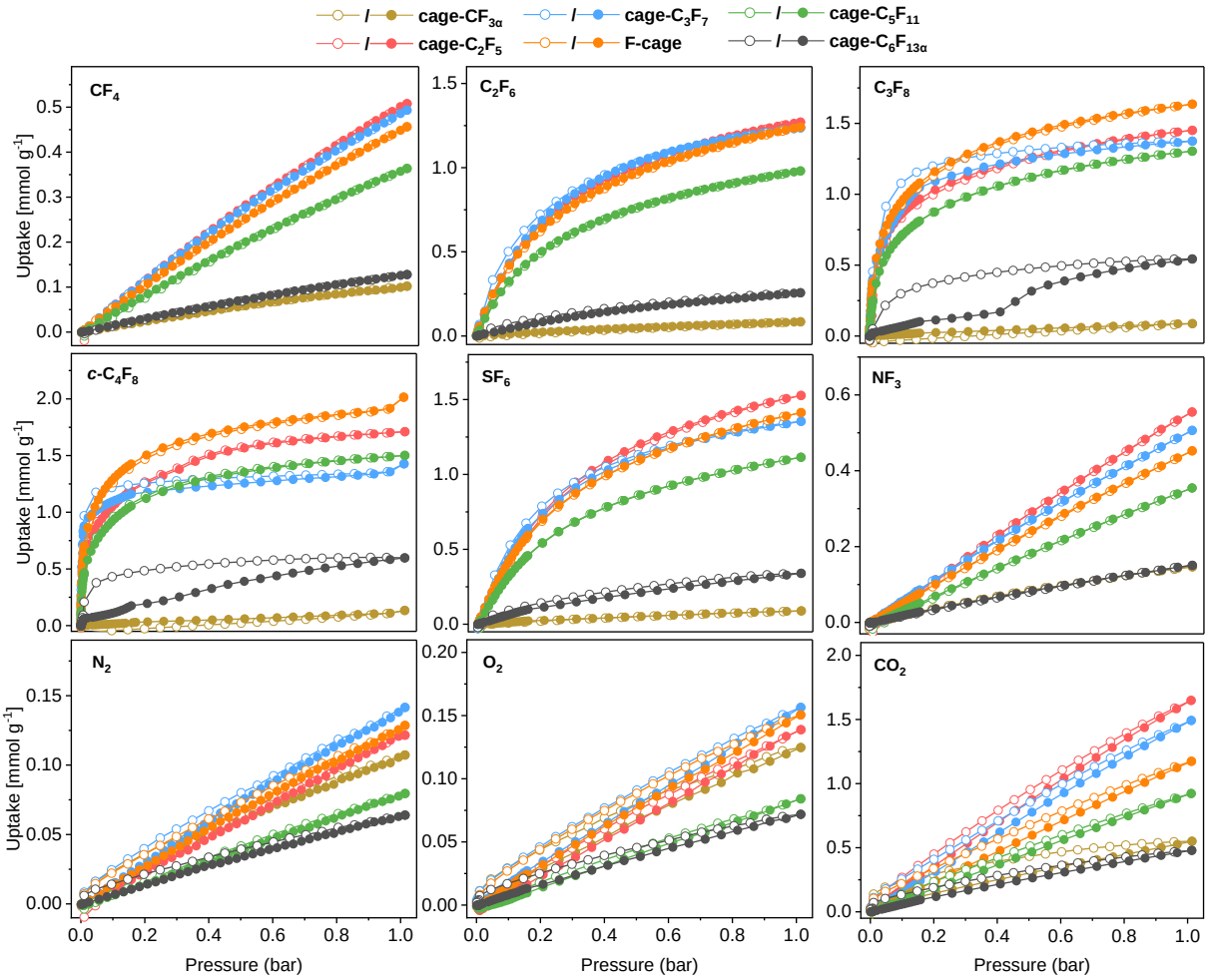

Figure 244. Gas sorption isotherms of **cage-CF$_{3α}$** (brown), **cage-C$_2$F$_5$** (red), **cage-C$_3$F$_7$** (blue), **F-cage** (orange), **cage-C$_5$F$_{11}$** (green), **cage-C$_6$F$_{13α}$** (black) at 298 K. The measurements at 298 K were performed by Dr. Anjana Kunhumbadukka Othayoth (OCI, Heidelberg University) under my help.

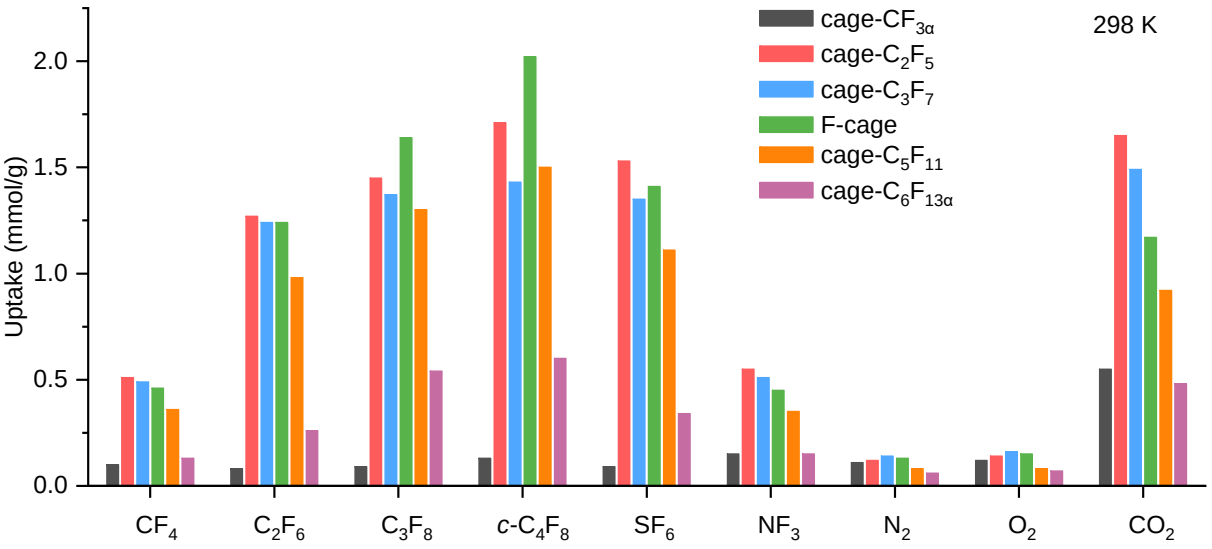

Figure 245. Gas uptake of **cage-CF$_{3α}$** (black), **cage-C$_2$F$_5$** (red), **cage-C$_3$F$_7$** (blue), **F-cage** (green), **cage-C$_5$F$_{11}$** (orange), and **cage-C$_6$F$_{13α}$** (purple) at 298 K and 1 bar.

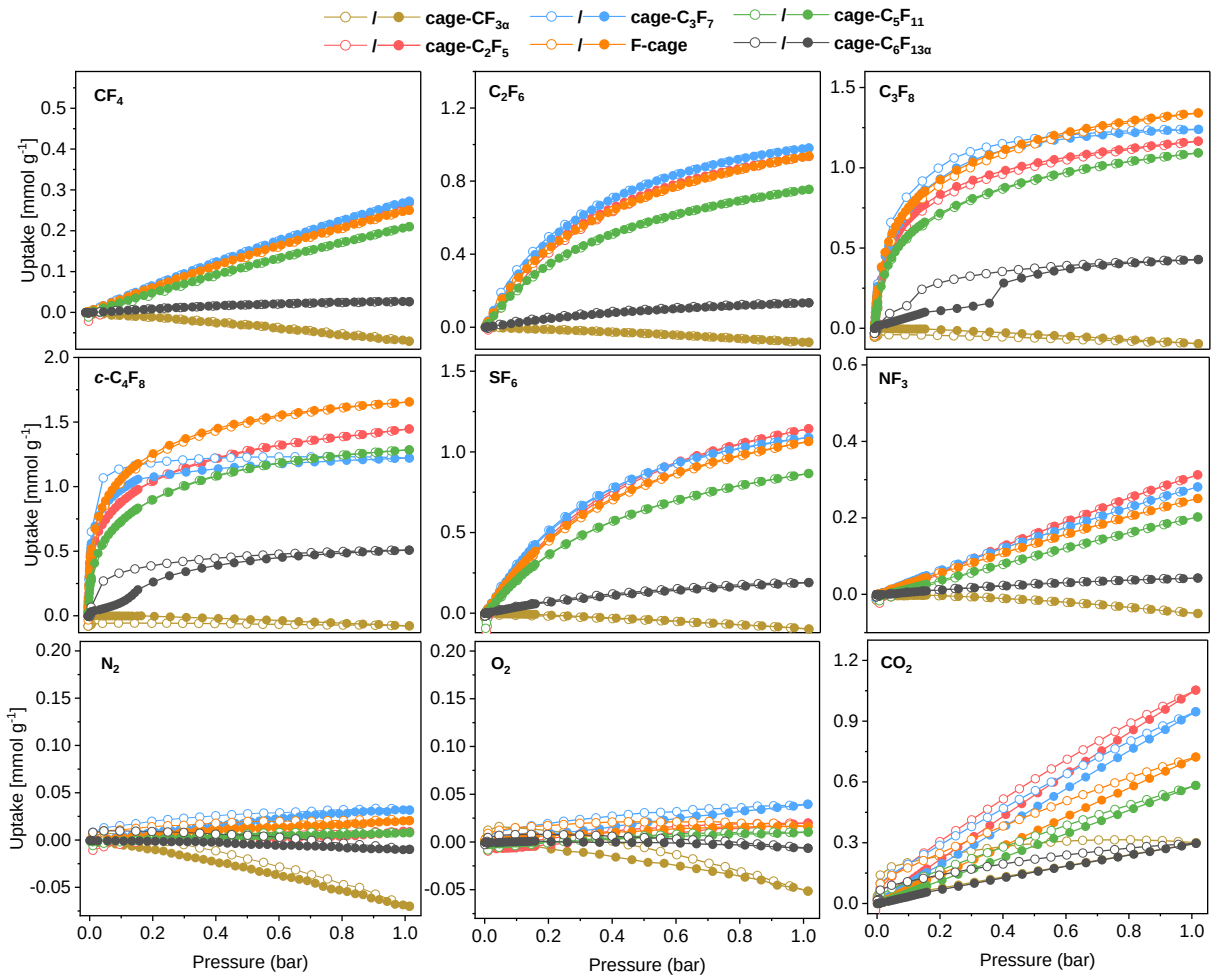

Figure 246. Gas sorption isotherms of **cage-CF$_{3\alpha}$** (brown), **cage-C$_2$F$_5$** (red), **cage-C$_3$F$_7$** (blue), **F-cage** (orange), **cage-C$_5$F$_{11}$** (green), **cage-C$_6$F$_{13\alpha}$** (black) at 313 K. Note: the negative gas uptake observed for **cage-CF$_{3\alpha}$** and **cage-C$_6$F$_{13\alpha}$** can be attributed to the extremely low uptake at 313 K, which falls below the accurate measurement range of the instrument. The measurements at 313 K were performed by Dr. Anjana Kunhumbadukka Othayoth (OCI, Heidelberg University) under my help.

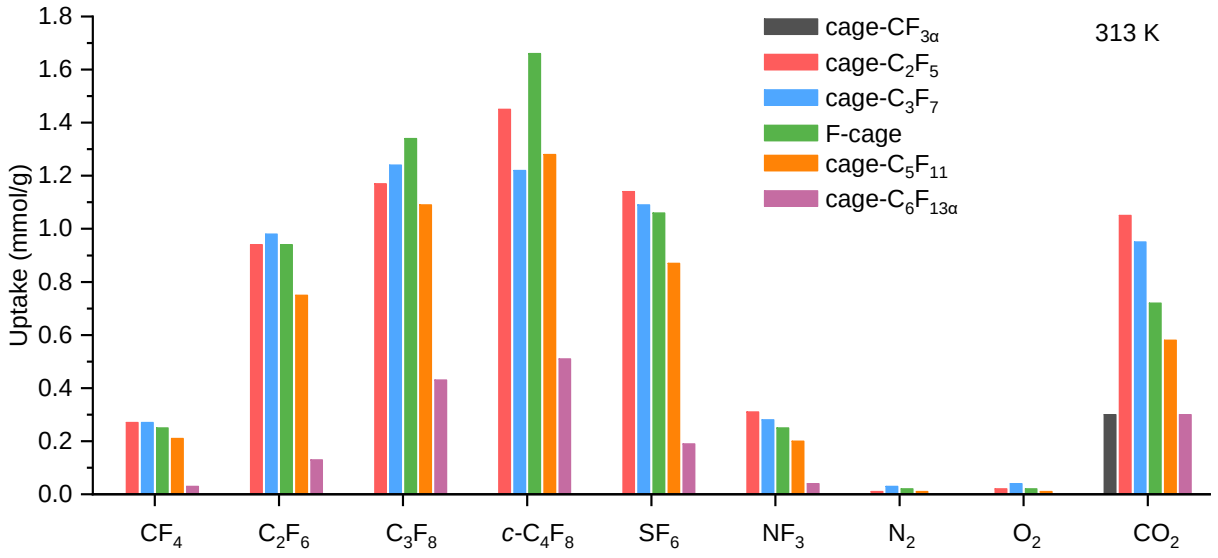

Figure 247. Gas uptake of **cage-CF$_{3\alpha}$** (black), **cage-C$_2$F$_5$** (red), **cage-C$_3$F$_7$** (blue), **F-cage** (green), **cage-C$_5$F$_{11}$** (orange), and **cage-C$_6$F$_{13\alpha}$** (purple) at 313 K and 1 bar.

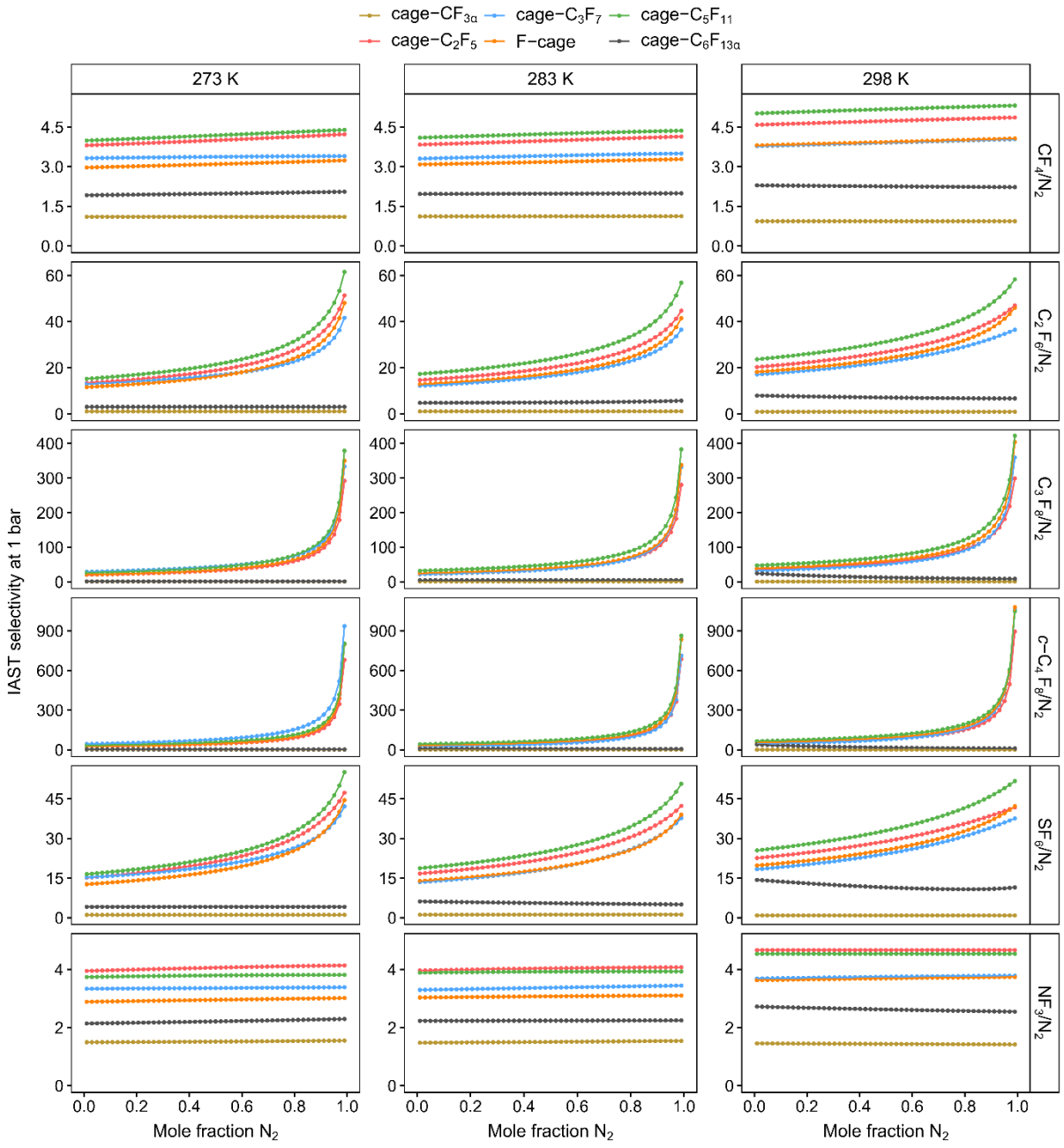

Figure 248. IAST curves (F-gas over nitrogen) of **cage-CF$_{3\alpha}$** (brown), **cage-C$_2$F$_5$** (red), **cage-C$_3$F$_7$** (blue), **F-cage** (orange), **cage-C$_5$F$_{11}$** (green), **cage-C$_6$F$_{13\alpha}$** (black) at 273 K (left column) 283 K (middle column), and 298 K (right column) at 1 bar.

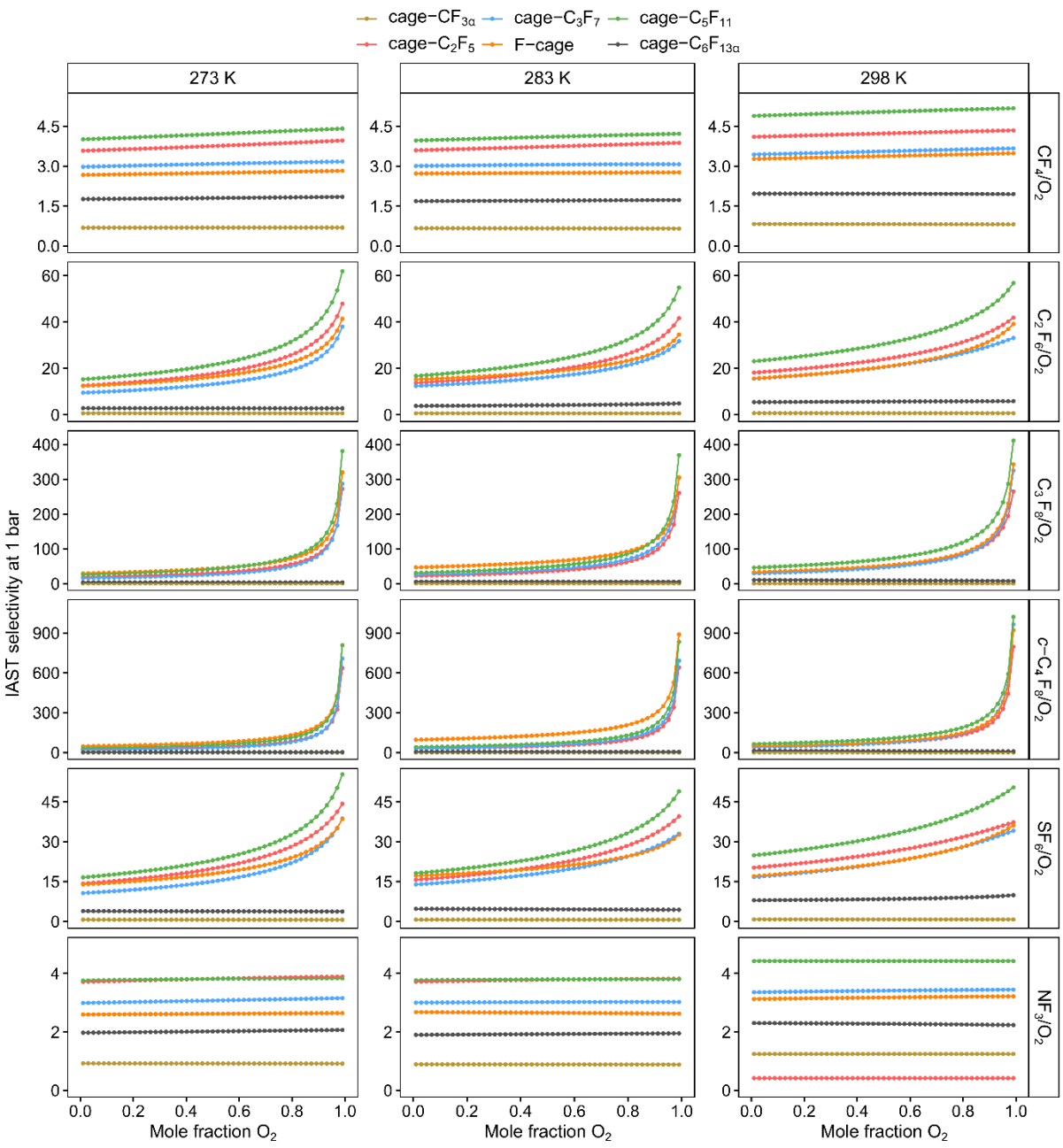

Figure 249. IAST curves (F-gas over oxygen) of **cage-$CF_{3\alpha}$** (brown), **cage-C_2F_5** (red), **cage-C_3F_7** (blue), **F-cage** (orange), **cage-C_5F_{11}** (green), **cage-$C_6F_{13\alpha}$** (black) at 273 K (left column) 283 K (middle column), and 298 K (right column) at 1 bar.

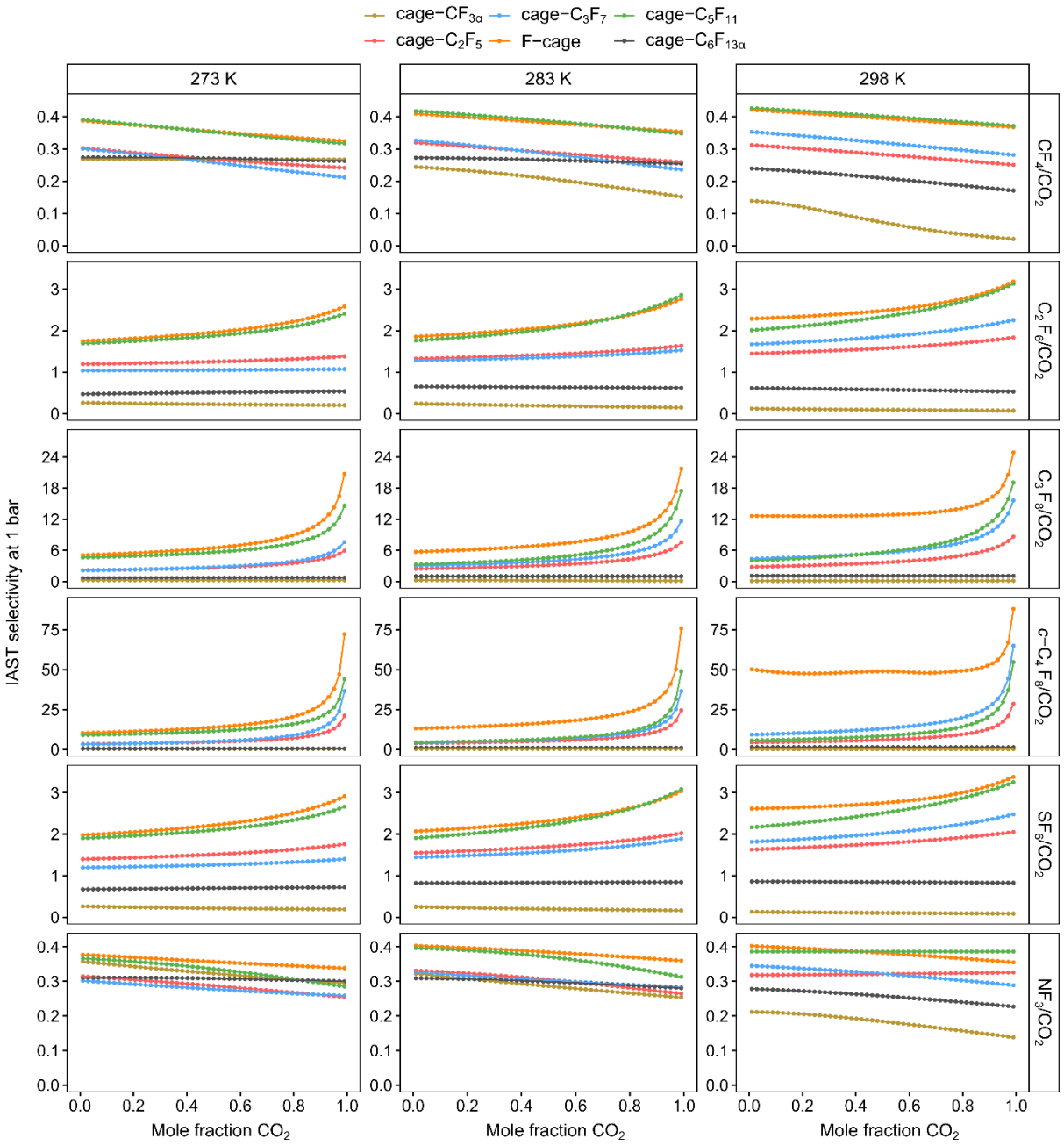

Figure 250. IAST curves (F-gas over carbon dioxide) of **cage-CF$_{3\alpha}$** (brown), **cage-C$_2$F$_5$** (red), **cage-C$_3$F$_7$** (blue), **F-cage** (orange), **cage-C$_5$F$_{11}$** (green), **cage-C$_6$F$_{13\alpha}$** (black) at 273 K (left column) 283 K (middle column), and 298 K (right column) at 1 bar.

5.5. Fitting and IAST Parameters

Table 26. Fitting and IAST parameters of Tóth and LAI isotherms as well as R^2 -values and Henry constants at 273 K

Cages	Gas	Affinity const. *K* [1/bar]	Max. uptake q_{max} [mmol/g]	Heterogenity Parameter *t*	R^2	*Model*	K_H
cage-$CF_{3\alpha}$	CF_4	0.000311	1000	1	0.999464	LAI	0.311
	C_2F_6	0.001411	423.945005	0.2356	0.999981	Tóth	0.598186402
	C_3F_8	0.000298	1000	1	0.988971	LAI	0.298
	c-C_4F_8	0.000426	1000	1	0.943371	LAI	0.426
	SF_6	0.001766	443.854573	0.2086	0.999846	Tóth	0.783847176
	NF_3	0.050550	10.827757	0.4995	0.999891	Tóth	0.547343116
	N_2	0.412943	0.686558	3.0421	0.999968	Tóth	0.283500932
	O_2	0.022671	20.558043	0.7893	0.999914	Tóth	0.466071393
	CO_2	0.001163	1000	1	0.981509	LAI	1.163
cage-C_2F_5	CF_4	0.332331	4.399286	1.0086	0.999989	Tóth	1.462019116
	C_2F_6	9.161702	2.690105	0.6254	0.999205	Tóth	24.64594036
	C_3F_8	273.250874	2.755367	0.3516	0.996523	Tóth	752.9064409
	c-C_4F_8	3640.315942	2.764162	0.2900	0.989907	Tóth	10062.42299
	SF_6	6.944563	2.622415	0.8715	0.999270	Tóth	18.21152618
	NF_3	0.506885	2.730789	1.8048	0.999872	Tóth	1.384195982
	N_2	0.000333	1000	1	0.999799	LAI	0.333
	O_2	0.000354	1000	1	0.998255	LAI	0.354
	CO_2	0.879734	4.793023	2.0790	0.999994	Tóth	4.216585296
cage-C_3F_7	CF_4	0.586949	2.024832	1.7041	0.999987	Tóth	1.188473118
	C_2F_6	9.964861	2.972831	0.4563	0.999741	Tóth	29.62384769
	C_3F_8	447.866500	1.624146	0.4379	0.992885	Tóth	727.4005845
	c-C_4F_8	1088.025197	1.204675	0.9150	0.991086	Tóth	1310.716754
	SF_6	9.527190	1.995162	0.7541	0.998833	Tóth	19.00828745
	NF_3	0.298820	3.986254	1.2328	0.999994	Tóth	1.190231231
	N_2	0.086438	4.039532	1.3672	0.999972	Tóth	0.349169067
	O_2	0.000370	1000	1	0.999952	LAI	0.37
	CO_2	0.969902	3.785917	2.5471	0.999918	LAI	3.67196847
F-cage	SF_6	7.760347	2.793672	0.6516	0.999268	Tóth	21.67986412
	NF_3	0.293659	3.680172	1.3249	0.999993	Tóth	1.080715629
	O_2	0.071192	5.697315	1.3297	0.999976	Tóth	0.405603249
cage-C_5F_{11}	CF_4	0.405172	2.324879	1.1619	0.999988	Tóth	0.941975874
	C_2F_6	9.060382	2.231758	0.5458	0.999237	Tóth	20.22058001
	C_3F_8	295.111200	2.736046	0.3084	0.998459	Tóth	807.4378183
	c-C_4F_8	3003.227683	2.678307	0.2657	0.994893	Tóth	8043.565726
	SF_6	6.569322	2.251886	0.6731	0.998764	Tóth	14.79336424
	NF_3	0.650189	1.226555	2.9882	0.999786	Tóth	0.797492569
	N_2	0.000209	1000	1	0.999871	LAI	0.209
	O_2	0.000208	1000	1	0.997428	LAI	0.208
	CO_2	0.917522	2.323443	4.0001	0.999843	Tóth	2.131810068
cage-$C_6F_{13\alpha}$	CF_4	0.191404	2.313105	0.8075	0.999981	Tóth	0.442737549
	C_2F_6	0.000601	1000	1	0.987473	LAI	0.601
	C_3F_8	0.000792	1000	1	0.985066	LAI	0.792
	c-C_4F_8	0.000581	1000	1	0.870642	LAI	0.581
	SF_6	0.00081	1000	1	0.971679	LAI	0.81
	NF_3	0.259592	1.852260	0.9454	0.999961	Tóth	0.480831878
	N_2	0.000196	1000	1	0.999485	LAI	0.196
	O_2	0.002186	102.473703	0.5643	0.999966	Tóth	0.224007515
	CO_2	0.065206	30.400168	0.3842	0.999932	Tóth	1.982273355

Table 27. Fitting and IAST parameters of Tóth and LAI isotherms as well as R^2 -values and Henry constants at 283 K.

Cages	Gas	Affinity const. *K* [1/bar]	Max. uptake q_{max} [mmol/g]	Heterogenity Parameter *t*	R^2	*Model*	K_H
cage-$CF_{3\alpha}$	CF_4	0.472838	0.483754	2.0519	0.999872	Tóth	0.228737274
	C_2F_6	0.212376	1.408269	0.6407	0.999931	Tóth	0.299082537
	C_3F_8	0.561981	0.543932	1	0.995350	LAI	0.305679449
	c-C_4F_8	0.000286	1000	1	0.945654	LAI	0.286
	SF_6	0.037641	12.017168	0.3281	0.999697	Tóth	0.452338221
	NF_3	0.163496	2.111046	0.7694	0.999867	Tóth	0.345147577
	N_2	0.000198	1000	1	0.999764	LAI	0.198
	O_2	0.000431	868.848044	0.3493	0.999908	Tóth	0.374473507
	CO_2	0.000906	1000	1	0.987066	LAI	0.906
cage-C_2F_5	CF_4	0.330856	3.106560	1.1652	0.999983	Tóth	1.027824015
	C_2F_6	5.723274	2.372526	0.7068	0.999600	Tóth	13.57861637
	C_3F_8	123.440331	2.548337	0.3854	0.997915	Tóth	314.5675628
	c-C_4F_8	2240.091296	3.268557	0.2578	0.993329	Tóth	7321.866086
	SF_6	4.616735	2.440404	0.9317	0.999645	Tóth	11.26669856
	NF_3	0.548072	1.807858	2.3323	0.999804	Toth	0.99083635
	N_2	0.000243	1000	1	0.999447	LAI	0.243
	O_2	0.000259	1000	1	0.997700	LAI	0.259
	CO_2	0.598023	4.890996	1.9680	0.999984	Tóth	2.924928101
cage-C_3F_7	CF_4	0.551931	1.606279	1.7280	0.999990	Tóth	0.886555175
	C_2F_6	5.307452	2.311466	0.6417	0.999965	Tóth	12.26799484
	C_3F_8	230.435241	1.751803	0.4388	0.997961	Tóth	403.6771465
	c-C_4F_8	533.711144	1.125576	0.8793	0.985814	Tóth	600.7324546
	SF_6	5.98532	1.768669	0.9618	0.999454	Tóth	10.58604994
	NF_3	0.254510	3.442872	1.2614	0.999990	Tóth	0.876245353
	N_2	0.000251	1000	1	0.999960	LAI	0.251
	O_2	0.015008	19.545120	0.7764	0.999951	Tóth	0.293333161
	CO_2	0.818138	3.102252	3.2278	0.999959	Tóth	2.538070247
F-cage	SF_6	4.816870	2.561754	0.7176	0.999582	Tóth	12.33963599
	NF_3	0.411658	1.949939	2.0129	0.999910	Tóth	0.802707989
	O_2	0.088627	3.507033	1.2056	0.999914	Tóth	0.310817814
	CO_2	0.700949	2.770941	3.7256	0.999982	Tóth	1.942288323
cage-C_5F_{11}	CF_4	0.418420	1.579806	1.4423	0.999967	Tóth	0.661022427
	C_2F_6	5.754379	1.975468	0.6126	0.999543	Tóth	11.36759157
	C_3F_8	134.043627	2.582908	0.3341	0.998884	Tóth	346.2223565
	c-C_4F_8	1427.025306	2.767037	0.2672	0.997638	Tóth	3948.631822
	SF_6	4.527728	1.922501	0.7853	0.999304	Tóth	8.704561608
	NF_3	0.675958	0.872322	3.8768	0.999721	Tóth	0.589653034
	N_2	0.000150	1000	1	0.999728	LAI	0.15
	O_2	0.000155	1000	1	0.996517	LAI	0.155
	CO_2	0.001471	1000	1	0.999458	LAI	1.471
cage-$C_6F_{13\alpha}$	CF_4	0.209546	1.411045	0.9697	0.999975	Tóth	0.295678836
	C_2F_6	0.025736	61.985353	0.2585	0.999779	Tóth	1.595255045
	C_3F_8	1.239187	0.717459	5.3626	0.993351	Tóth	0.793189
	c-C_4F_8	0.000872	1000	1	0.896120	LAI	0.872
	SF_6	0.000707	1000	1	0.000707	LAI	0.707
	NF_3	0.357706	0.911527	1.2471	0.999949	Tóth	0.326058677
	N_2	0.147481	0.979210	1.2678	0.999905	Tóth	0.14441487
	O_2	0.026959	6.137539	0.8380	0.999906	Tóth	0.165461914
	CO_2	0.076282	15.623667	0.4839	0.999940	Tóth	1.191804566

Table 28. Fitting and IAST parameters of Tóth and LAI isotherms as well as R^2 -values and Henry constants at 298 K.

Cage	Gas	Affinity const. *K* [1/bar]	Max. uptake q_{max} [mmol/g]	Heterogenity Parameter *t*	R^2	*Model*	K_H
cage-$CF_{3\alpha}$	CF_4	0.850296	0.139306	2.7578	0.999778	Tóth	0.118451335
	C_2F_6	0.170242	0.825927	0.5788	0.999380	Tóth	0.140607464
	C_3F_8	0.000094	1000	1	0.986629	LAI	0.094
	c-C_4F_8	0.000117	1000	1	0.987248	LAI	0.117
	SF_6	0.136811	1.146133	0.5269	0.997205	Tóth	0.156803602
	NF_3	0.567979	0.310577	1.6958	0.999089	Tóth	0.176401214
	N_2	0.504992	0.260533	1.4028	0.999439	Tóth	0.131567081
	O_2	0.099299	1.528161	0.7575	0.999573	Tóth	0.151744859
	CO_2	0.005244	225.331802	0.2721	0.999726	Tóth	1.18163997
cage-C_2F_5	CF_4	0.326651	1.803608	1.3161	0.999919	Tóth	0.589150357
	C_2F_6	3.499437	1.749462	0.8787	0.999908	Tóth	6.122132053
	C_3F_8	38.957936	1.867406	0.5143	0.998754	Tóth	72.75028343
	c-C_4F_8	1004.438627	3.564064	0.2401	0.994988	Tóth	3579.883551
	SF_6	2.673166	1.92104	1.1516	0.999676	Tóth	5.135258813
	NF_3	0.000560	1000	1	0.998406	LAI	0.56
	N_2	0.000120	1000	1	0.998635	LAI	0.12
	O_2	0.000134	1000	1	0.990129	LAI	0.134
	CO_2	0.357166	4.944781	1.8253	0.999963	Tóth	1.766107651
cage-C_3F_7	CF_4	0.358753	1.635699	1.2804	0.999981	Tóth	0.586811923
	C_2F_6	3.654933	1.491902	1.1120	0.999958	Tóth	5.452801853
	C_3F_8	84.307189	1.764594	0.4682	0.998467	Tóth	148.7679599
	c-C_4F_8	493.206605	1.327921	0.6051	0.988462	Tóth	654.9394081
	SF_6	3.499626	1.585550	1.1874	0.999798	Tóth	5.548832004
	NF_3	0.403285	1.344989	1.9266	0.999951	Tóth	0.542413889
	N_2	0.000143	1000	1	0.998066	LAI	0.143
	O_2	0.000157	1000	1	0.999350	LAI	0.157
	CO_2	0.652520	2.339628	4.3115	0.999986	Tóth	1.526654063
F-cage	SF_6	2.947954	1.999962	0.8929	0.999904	Tóth	5.895795978
	NF_3	0.361158	1.351230	1.7351	0.999976	Tóth	0.488007524
	O_2	0.000151	1000	1	0.999346	LAI	0.151
	CO_2	0.769543	1.522797	8.6377	0.999722	Tóth	1.171857772
cage-C_5F_{11}	CF_4	0.323811	1.290617	1.3325	0.999940	Tóth	0.417915981
	C_2F_6	3.374284	1.512821	0.7557	0.999785	Tóth	5.104687695
	C_3F_8	45.461665	2.136778	0.3953	0.999256	Tóth	97.14148562
	c-C_4F_8	406.573776	2.734229	0.2824	0.998325	Tóth	1111.665809
	SF_6	2.774246	1.521278	0.9667	0.999659	Tóth	4.220399406
	NF_3	0.000354	1000	1	0.998138	LAI	0.354
	N_2	0.000078	1000	1	0.998214	LAI	0.078
	O_2	0.000080	1000	1	0.988874	LAI	0.08
	CO_2	0.000917	1000	1	0.999793	LAI	0.917
cage-$C_6F_{13\alpha}$	CF_4	0.429452	0.357446	1.3926	0.999912	Tóth	0.1535059
	C_2F_6	0.914142	0.523446	1.0093	0.999731	Tóth	0.478503973
	C_3F_8	0.000580	1000	1	0.984279	LAI	0.58
	c-C_4F_8	0.000686	1000	1	0.960270	LAI	0.686
	SF_6	0.227727	5.474476	0.3522	0.999243	Tóth	1.246685996
	NF_3	0.404280	0.428583	1.4960	0.999768	Tóth	0.173267535
	N_2	0.310284	0.224044	1.5623	0.999702	Tóth	0.069517268
	O_2	0.047015	1.799040	0.6751	0.999757	Tóth	0.084581866
	CO_2	0.046559	14.011624	0.5408	0.999931	Tóth	0.652367202

Table 29. Fitting and IAST parameters of Tóth and LAI isotherms as well as R^2 -values and Henry constants at 313 K.

Cage	Gas	Affinity const. *K* [1/bar]	Max. uptake q_{max} [mmol/g]	Heterogenity Parameter *t*	R^2	*Model*	K_H
cage-C_2F_5	CF_4	0.400693	0.745486	1.6339	0.999527	Tóth	0.298711022
	C_2F_6	2.447332	1.238452	1.1074	0.999954	Tóth	3.03090321
	C_3F_8	18.755356	1.377738	0.6850	0.999370	Tóth	25.83996666
	c-C_4F_8	281.046362	2.502930	0.3004	0.997555	Tóth	703.4393708
	SF_6	1.941321	1.479070	1.3112	0.999811	Tóth	2.871349651
	NF_3	0.000313	1000	1	0.995711	LAI	0.313
	N_2	0.000006	1000	1	0.595314	LAI	0.006
	O_2	0.000017	1000	1	0.461232	LAI	0.017
	CO_2	0.347510	3.095555	2.3563	0.999905	Tóth	1.075736318
cage-C_3F_7	CF_4	0.328627	0.967731	1.2989	0.999959	Tóth	0.318022535
	C_2F_6	2.669151	1.273271	1.1090	0.999988	Tóth	3.398552563
	C_3F_8	32.407683	1.707008	0.5177	0.998952	Tóth	55.32017414
	c-C_4F_8	219.230297	1.319643	0.555	0.998940	Tóth	289.3057268
	SF_6	2.407464	1.329566	1.336	0.999965	Tóth	3.200882281
	NF_3	0.181015	1.721956	1.1523	0.999851	Tóth	0.311699865
	N_2	0.000035	1000	1	0.984478	LAI	0.035
	O_2	0.000040	1000	1	0.997520	LAI	0.04
	CO_2	0.000941	1000	1	0.999966	LAI	0.941
F-cage	SF_6	2.062049	1.506985	1.0701	0.999987	Tóth	3.107476912
	NF_3	0.198136	1.407462	1.1823	0.999899	Tóth	0.278868891
	O_2	0.000021	1000	1	0.927206	LAI	0.021
	CO_2	0.000713	1000	1	0.999932	LAI	0.713
cage-C_5F_{11}	CF_4	0.430785	0.530247	1.8875	0.999833	Tóth	0.228422454
	C_2F_6	2.363392	1.149219	0.8897	0.999905	Tóth	2.716054991
	C_3F_8	21.387619	1.609088	0.4953	0.999439	Tóth	34.41456108
	c-C_4F_8	80.115084	2.274630	0.3481	0.998370	Tóth	182.2321735
	SF_6	1.940461	1.206979	1.1286	0.999797	Tóth	2.342095677
	NF_3	0.0002	1000	1	0.995571	LAI	0.2
	N_2	0.000007	1000	1	0.960242	LAI	0.007
	O_2	0.000010	1000	1	0.851279	LAI	0.01
	CO_2	0.000573	1000	1	0.999597	LAI	0.573
cage-$C_6F_{13\alpha}$	CF_4	0.000032	1000	1	0.940966	LAI	0.032
	C_2F_6	1.241528	0.219958	1.1358	0.999815	Tóth	0.273084016
	C_3F_8	0.000525	1000	1	0.960249	LAI	0.525
	c-C_4F_8	2.343624	0.509496	2.9125	0.995371	Tóth	1.194067054
	SF_6	1.048473	0.442444	0.7834	0.999615	Tóth	0.463890588
	NF_3	1.108199	0.048717	3.31	0.997440	Tóth	0.053988131
	CO_2	0.008602	43.893866	0.4428	0.999848	Tóth	0.377575035

5.6. Gas Sorption Fitting Curves

Gas sorption fitting curves at 273 K

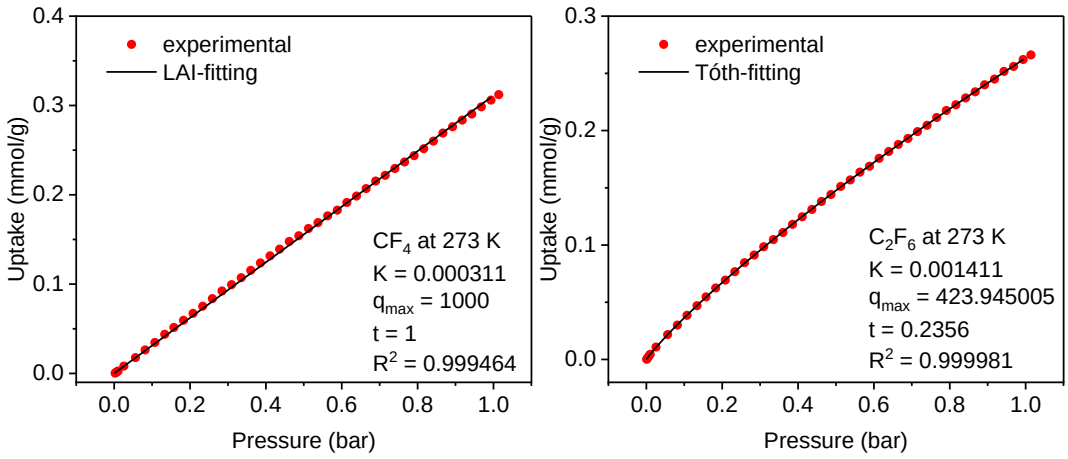

Figure 251. CF_4 (left) and C_2F_6 (right) isotherms and fitting curves of **cage-$CF_{3\alpha}$** at 273 K.

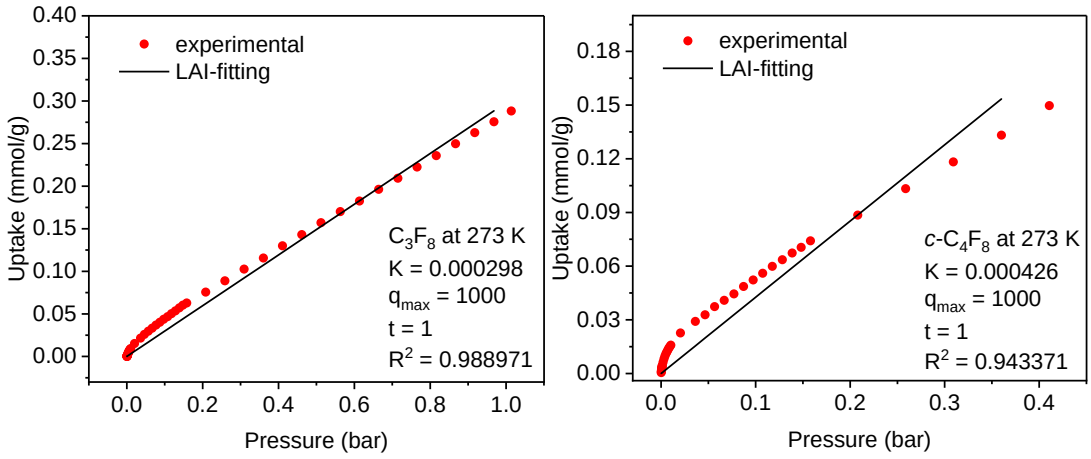

Figure 252. C_3F_8 (left) and *c*-C_4F_8 (right) isotherms and fitting curves of **cage-$CF_{3\alpha}$** at 273 K. (*Note*: Only the pressure range for *c*-C_4F_8 from 0-0.4 bar was taken into account due to pore condensation >0.4 bar)

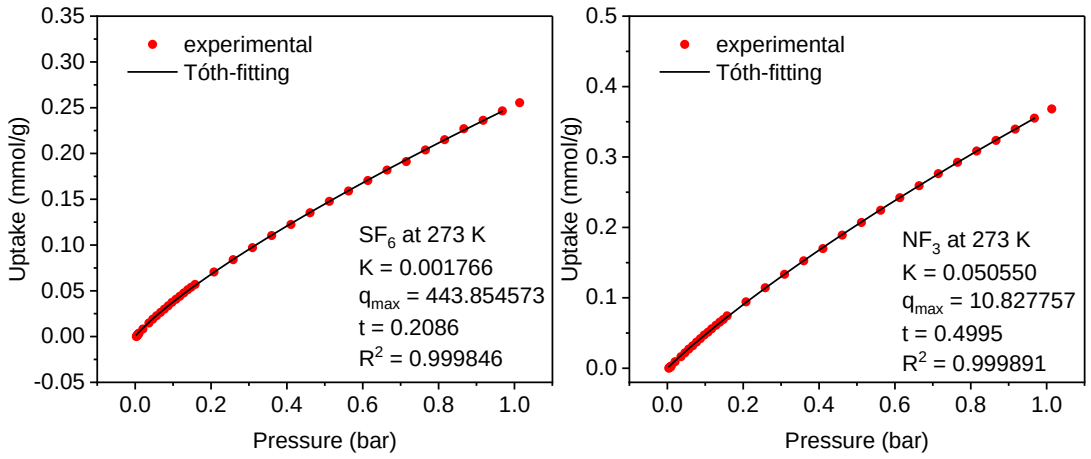

Figure 253. SF_6 (left) and NF_3 (right) isotherms and fitting curves of **cage-$CF_{3\alpha}$** at 273 K.

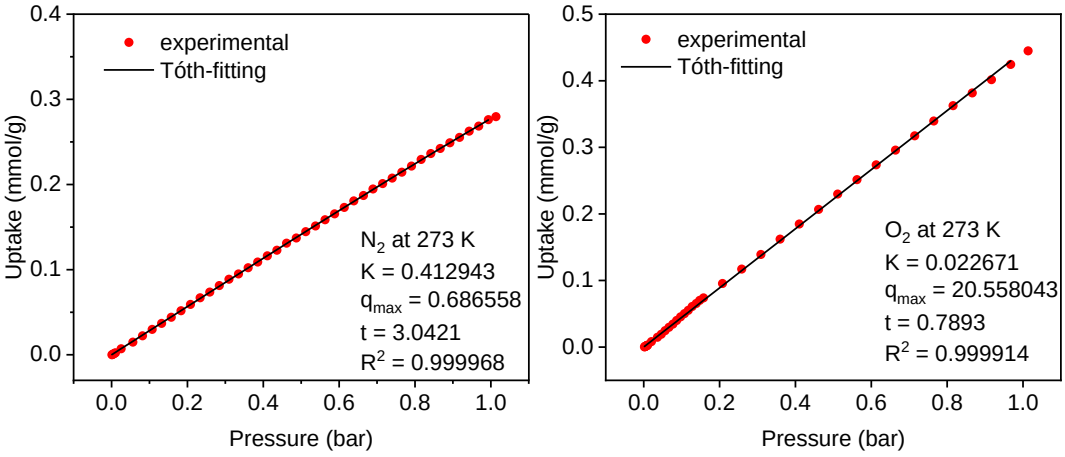

Figure 254. N_2 (left) and O_2 (right) isotherms and fitting curves of **cage-$CF_{3\alpha}$** at 273 K.

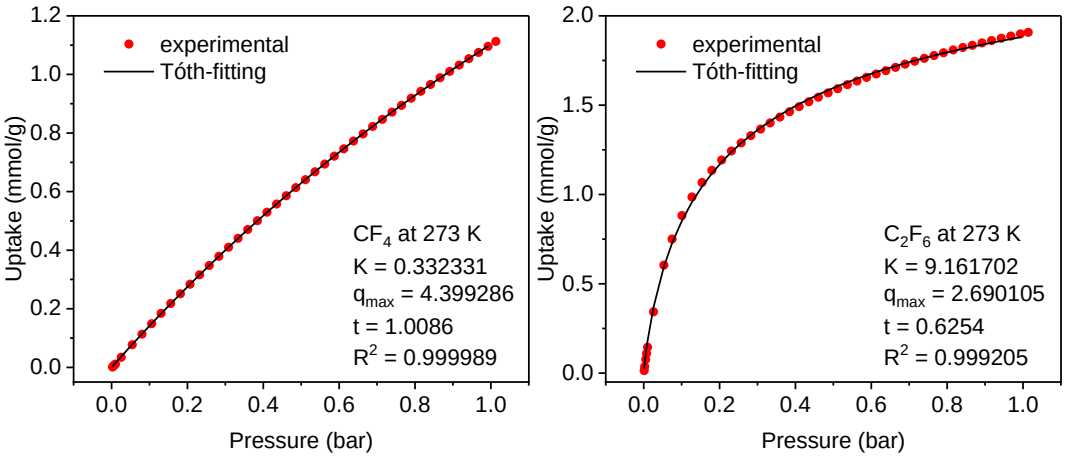

Figure 255. CF_4 (left) and C_2F_6 (right) isotherms and fitting curves of **cage-C_2F_5** at 273 K.

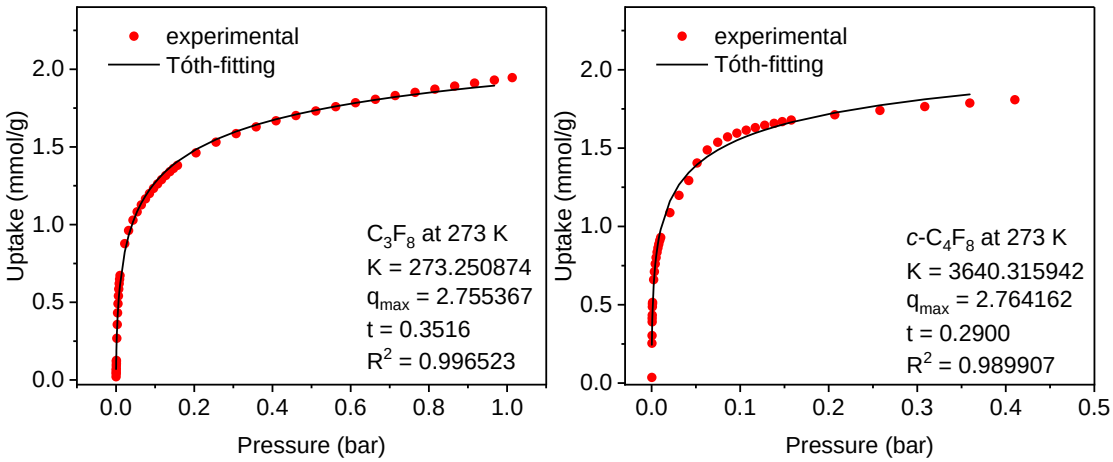

Figure 256. C_3F_8 (left) and *c*-C_4F_8 (right) isotherms and fitting curves of **cage-C_2F_5** at 273 K. (*Note*: Only the pressure range for *c*-C_4F_8 from 0-0.4 bar was taken into account due to pore condensation >0.4 bar)

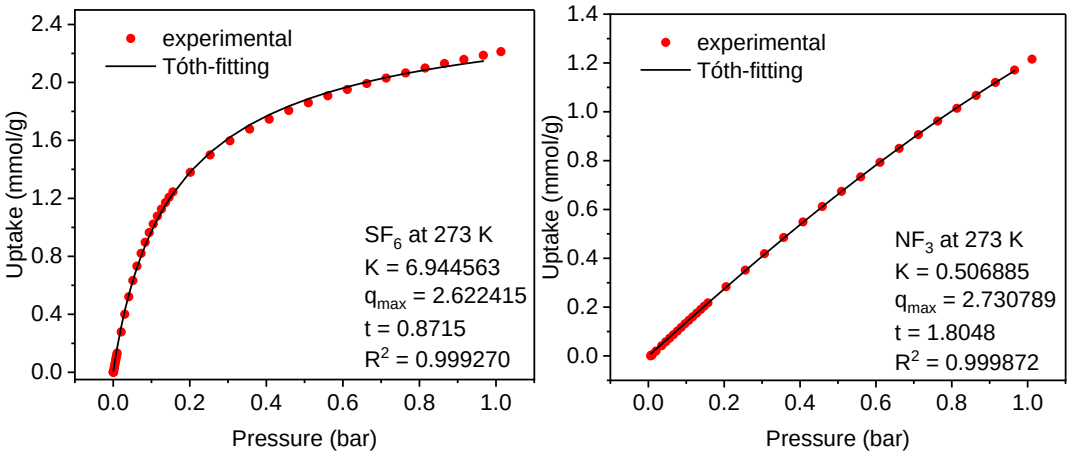

Figure 257. SF_6 (left) and NF_3 (right) isotherms and fitting curves of **cage-C_2F_5** at 273 K.

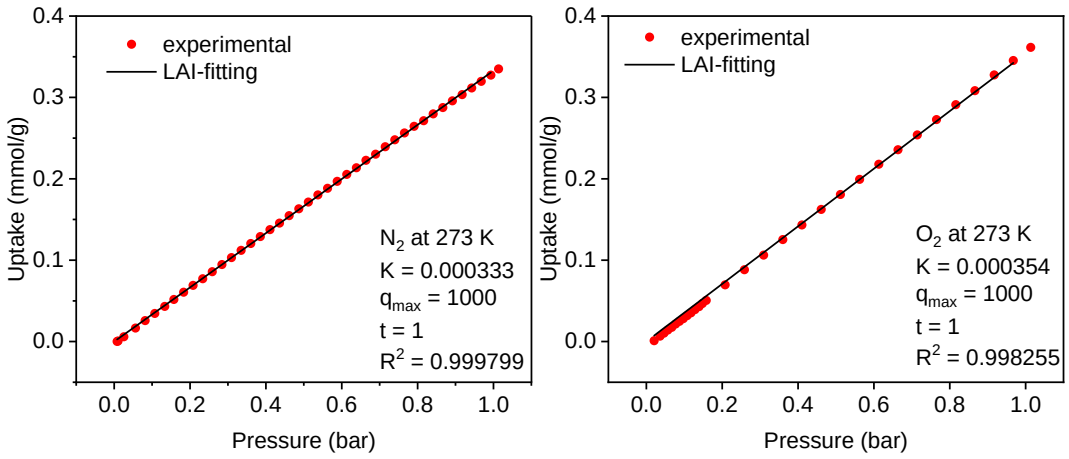

Figure 258. N_2 (left) and O_2 (right) isotherms and fitting curves of **cage-C_2F_5** at 273 K.

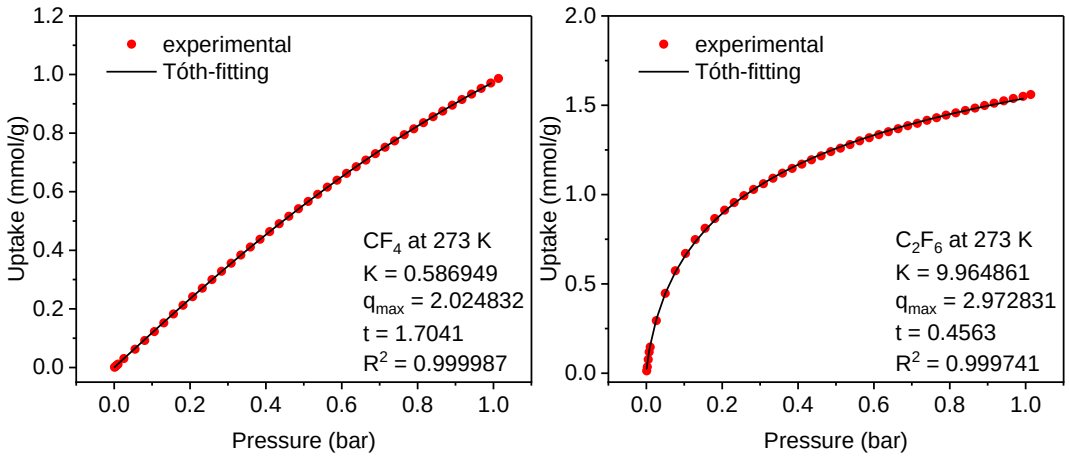

Figure 259. CF_4 (left) and C_2F_6 (right) isotherms and fitting curves of **cage-C_3F_7** at 273 K.

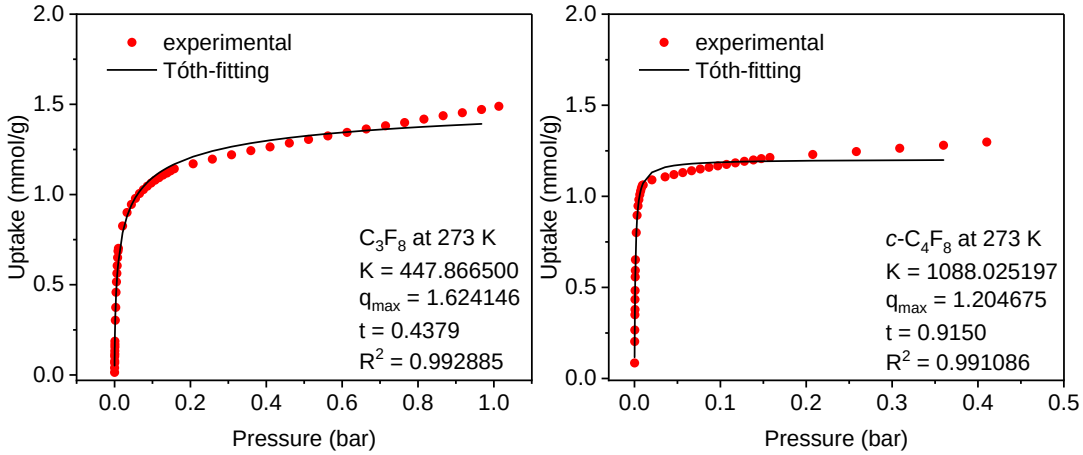

Figure 260. C_3F_8 (left) and *c*-C_4F_8 (right) isotherms and fitting curves of **cage-C_3F_7** at 273 K. (*Note*: Only the pressure range for *c*-C_4F_8 from 0-0.4 bar was taken into account due to pore condensation >0.4 bar)

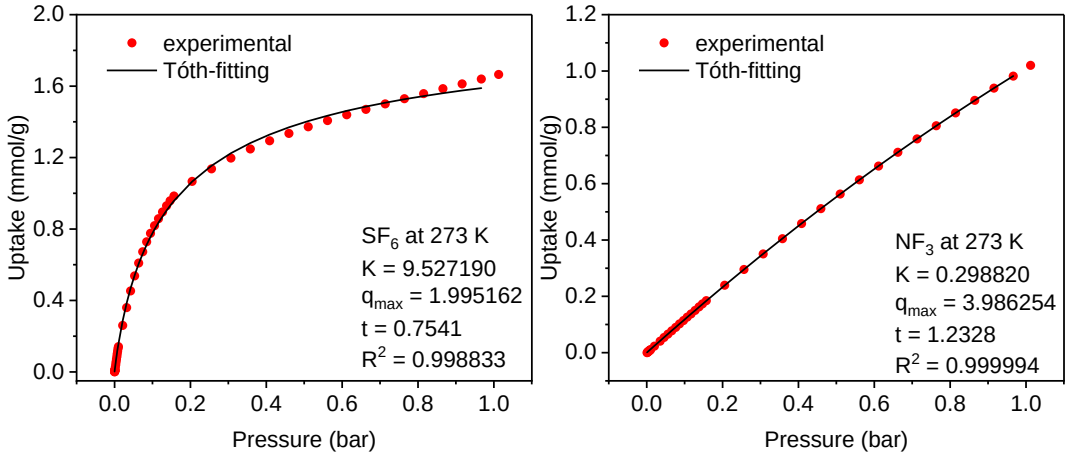

Figure 261. SF_6 (left) and NF_3 (right) isotherms and fitting curves of **cage-C_3F_7** at 273 K.

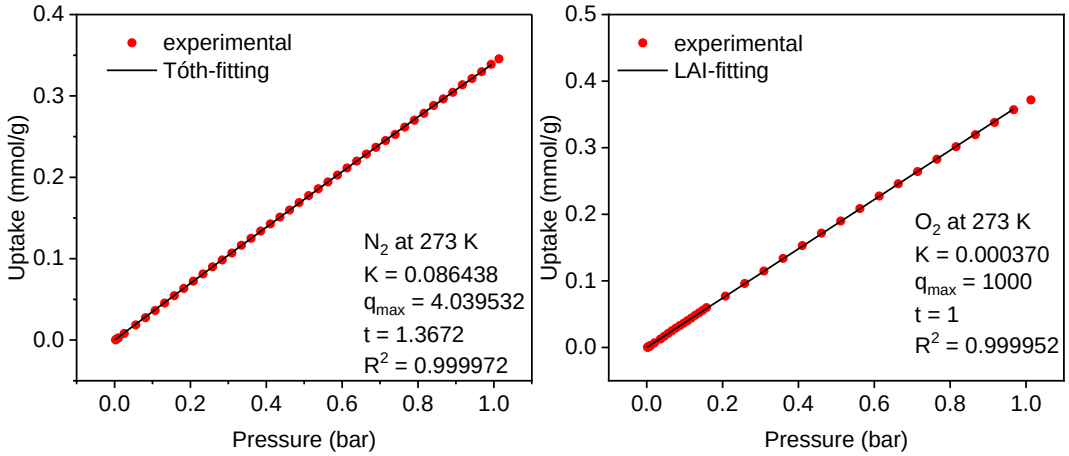

Figure 262. N_2 (left) and O_2 (right) isotherms and fitting curves of **cage-C_3F_7** at 273 K.

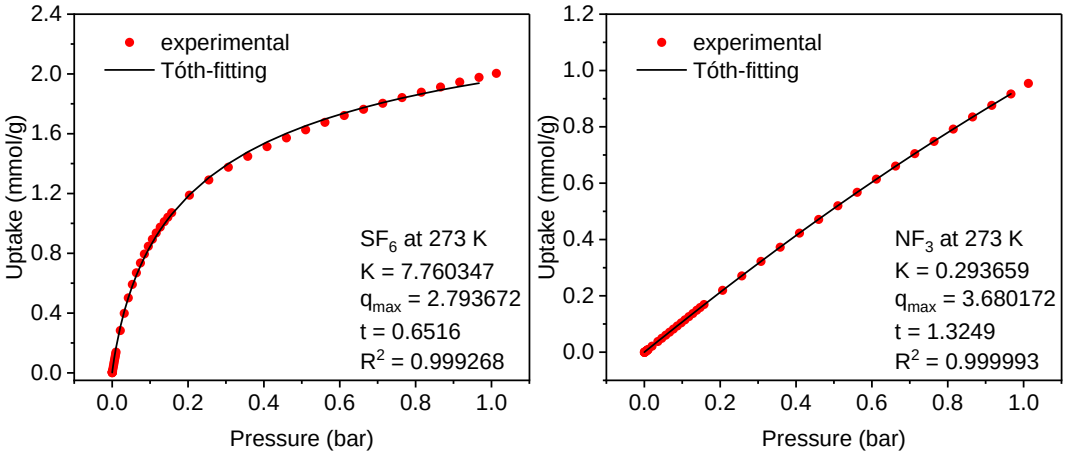

Figure 263. SF_6 (left) and NF_3 (right) isotherms and fitting curves of **F-cage** at 273 K.

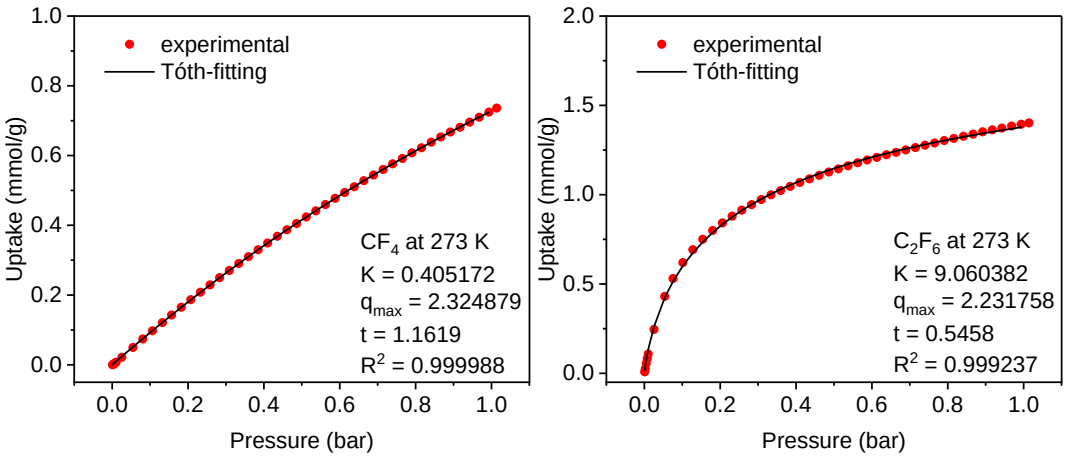

Figure 264. CF_4 (left) and C_2F_6 (right) isotherms and fitting curves of **cage-C_5F_{11}** at 273 K.

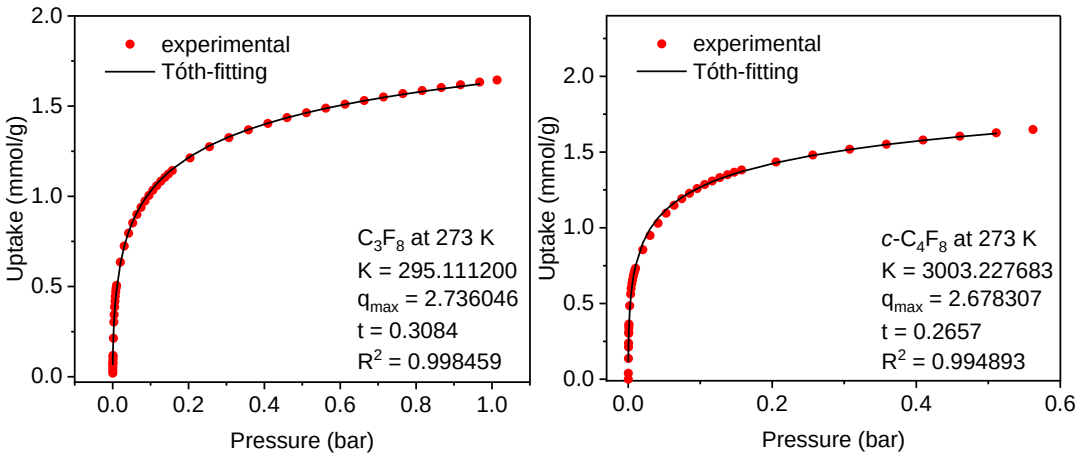

Figure 265. C_3F_8 (left) and *c*-C_4F_8 (right) isotherms and fitting curves of **cage-C_5F_{11}** at 273 K. (*Note*: Only the pressure range for *c*-C_4F_8 from 0-0.55 bar was taken into account due to pore condensation >0.55 bar)

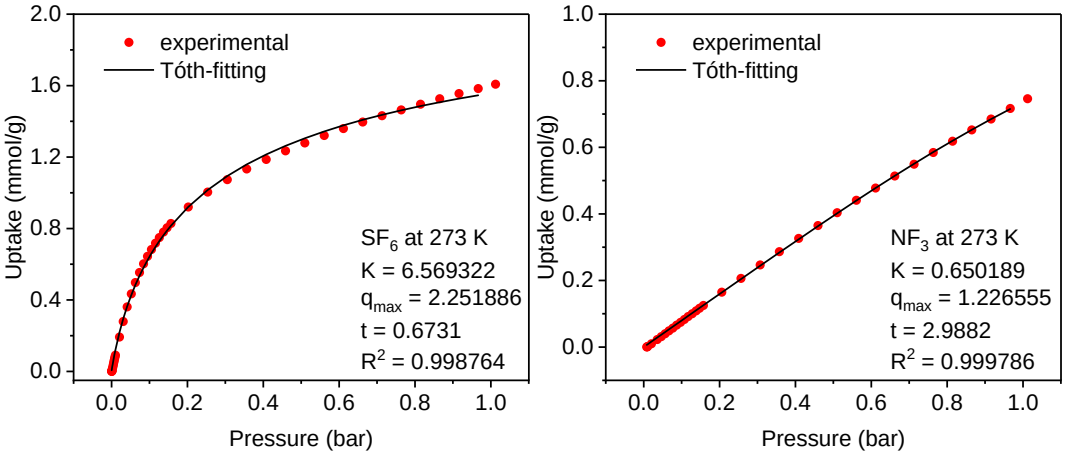

Figure 266. SF_6 (left) and NF_3 (right) isotherms and fitting curves of **cage-C_5F_{11}** at 273 K.

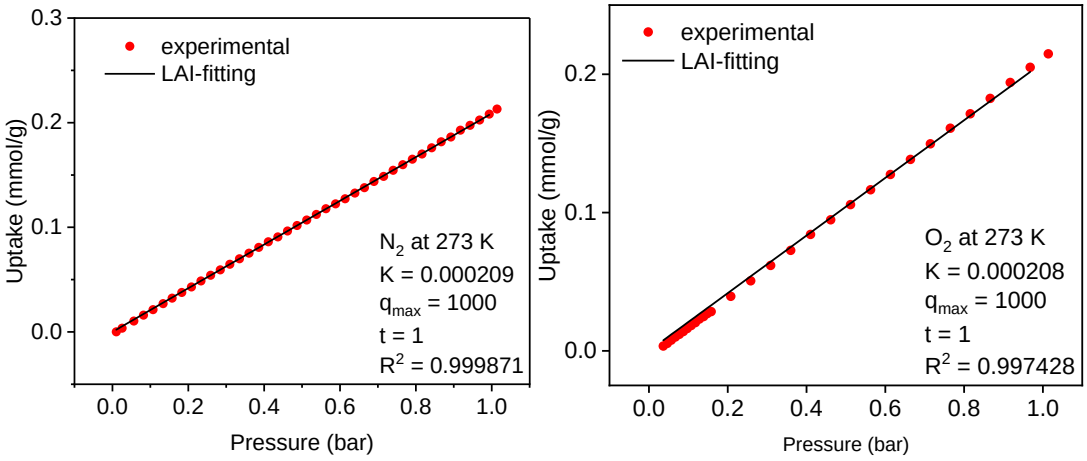

Figure 267. N_2 (left) and O_2 (right) isotherms and fitting curves of **cage-C_5F_{11}** at 273 K.

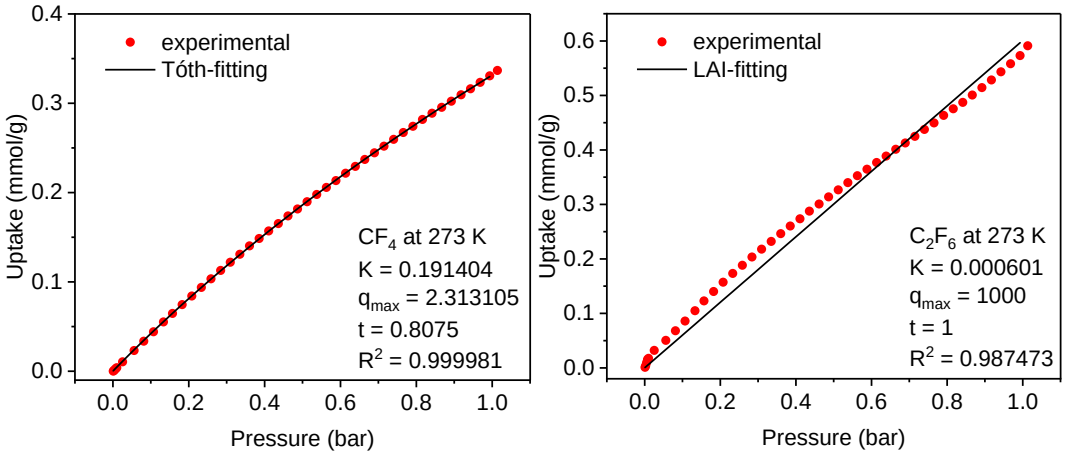

Figure 268. CF_4 (left) and C_2F_6 (right) isotherms and fitting curves of **cage-$C_6F_{13\alpha}$** at 273 K.

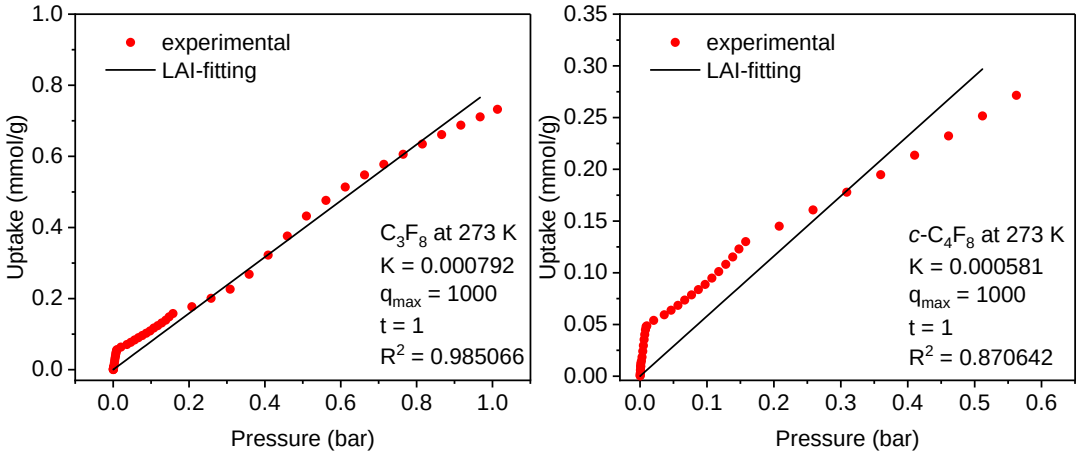

Figure 269. C_3F_8 (left) and *c*-C_4F_8 (right) isotherms and fitting curves of **cage-C$_6$F$_{13\alpha}$** at 273 K. (*Note*: Only the pressure range for *c*-C_4F_8 from 0-0.55 bar was taken into account due to pore condensation >0.55 bar)

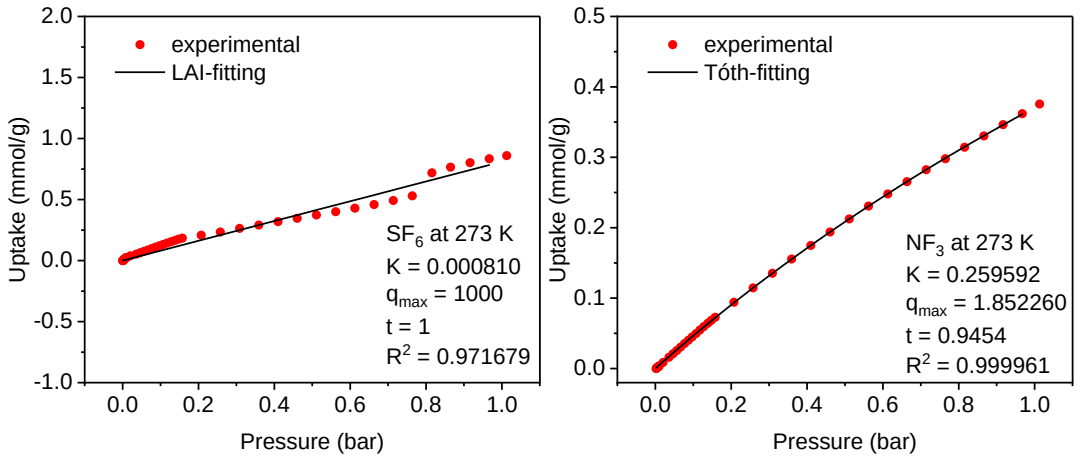

Figure 270. SF_6 (left) and NF_3 (right) isotherms and fitting curves of **cage-C$_6$F$_{13\alpha}$** at 273 K.

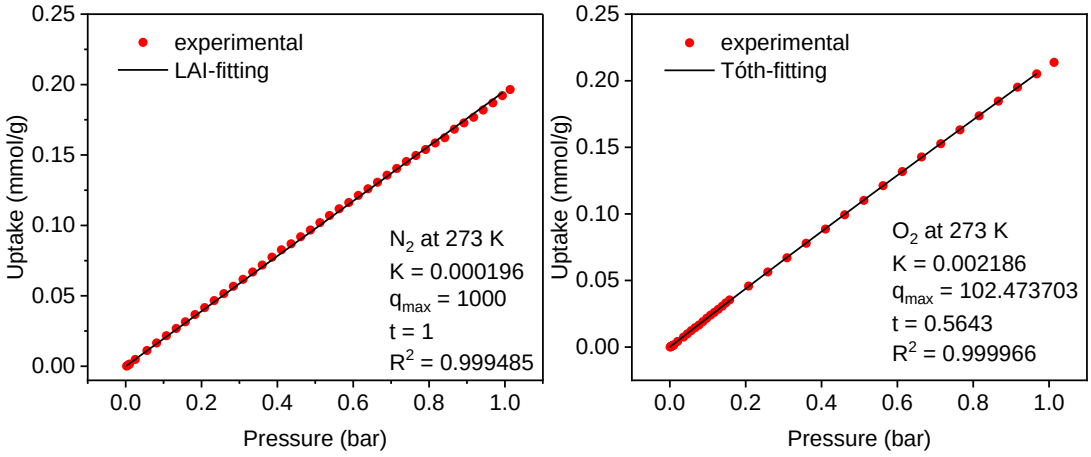

Figure 271. N_2 (left) and O_2 (right) isotherms and fitting curves of **cage-C$_6$F$_{13\alpha}$** at 273 K.

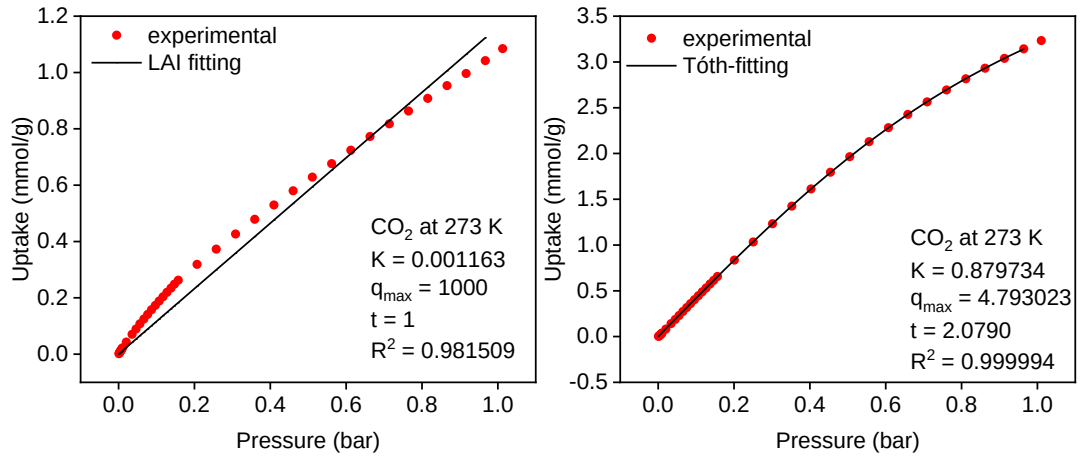

Figure 272. CO_2 isotherms and fitting curves of **cage-$CF_{3\alpha}$** (left) and **cage-C_2F_5** (right) at 273 K.

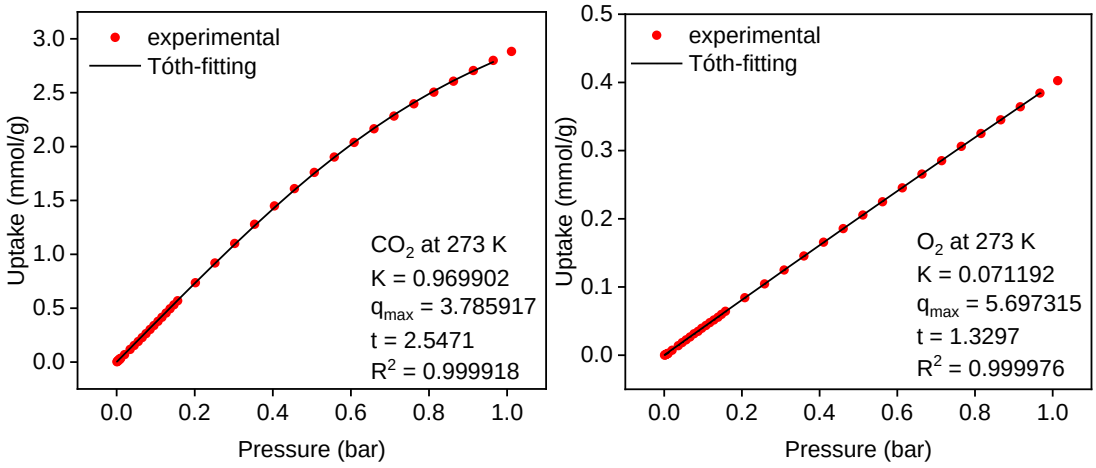

Figure 273. CO_2 isotherm and fitting curve of **cage-C_3F_7** (left) and O_2 isotherm and fitting curve of **F-cage** (right) at 273 K.

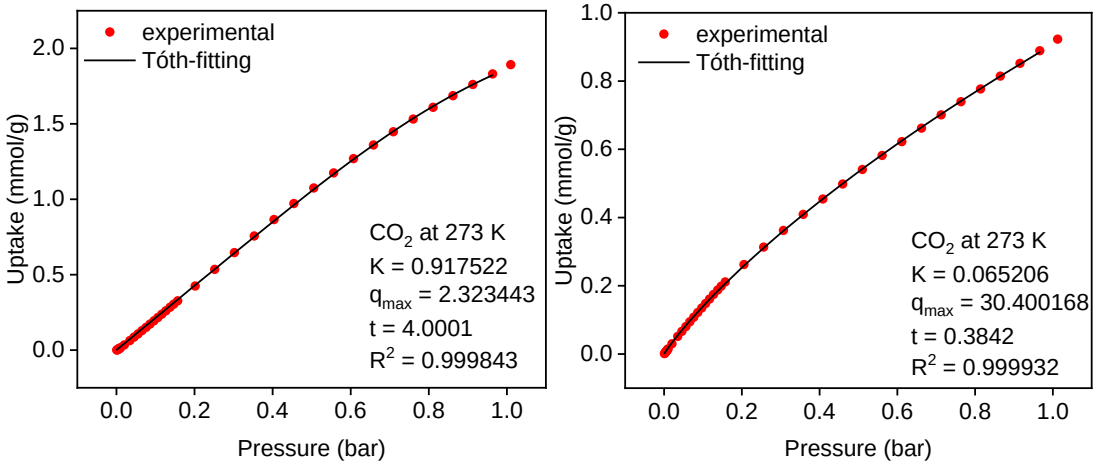

Figure 274. CO_2 isotherms and fitting curves of **cage-C_5F_{11}** (left) and **cage-$C_6F_{13\alpha}$** (right) at 273 K.

Gas sorption fitting curves at 283 K

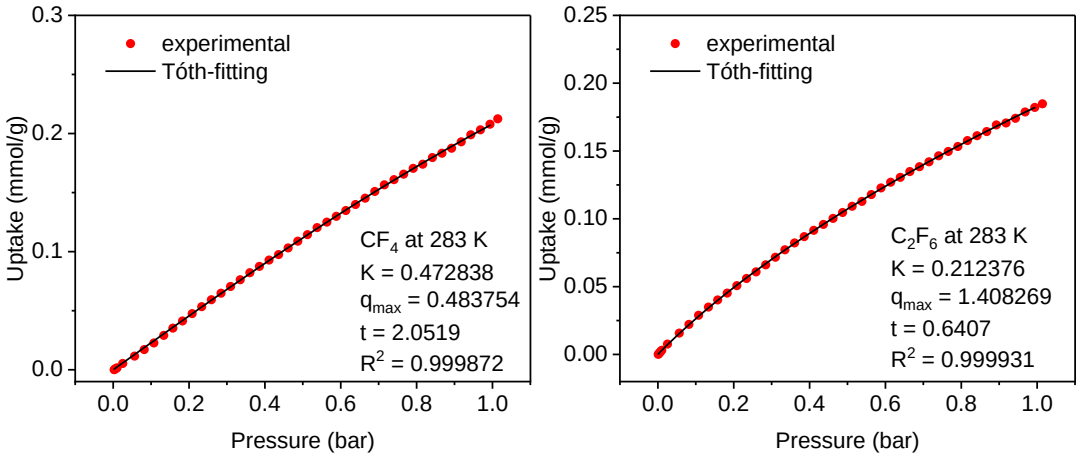

Figure 275. CF_4 (left) and C_2F_6 (right) isotherms and fitting curves of **cage-CF$_{3\alpha}$** at 283 K.

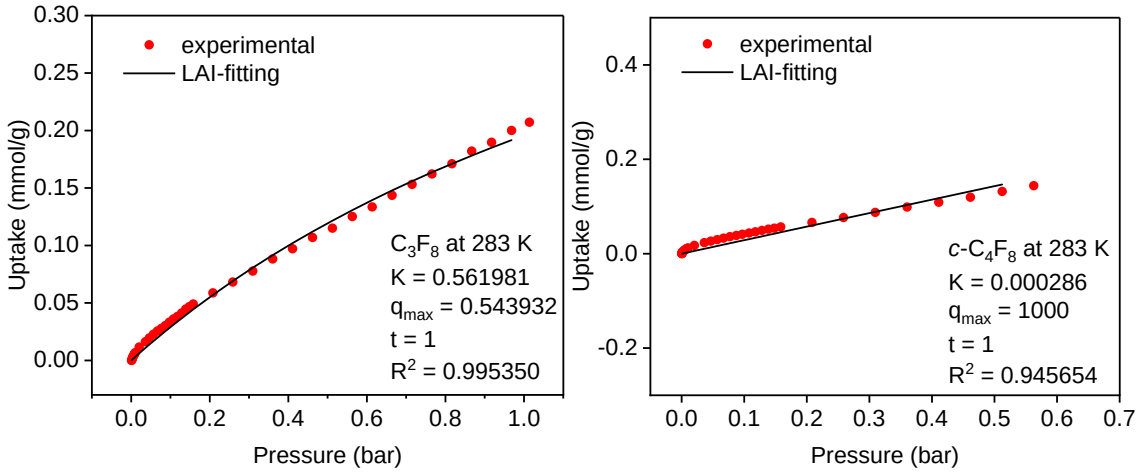

Figure 276. C_3F_8 (left) and *c*-C_4F_8 (right) isotherms and fitting curves of **cage-CF$_{3\alpha}$** at 283 K. (Note: Only the pressure range for *c*-C_4F_8 from 0-0.6 bar was taken into account due to pore condensation >0.6 bar)

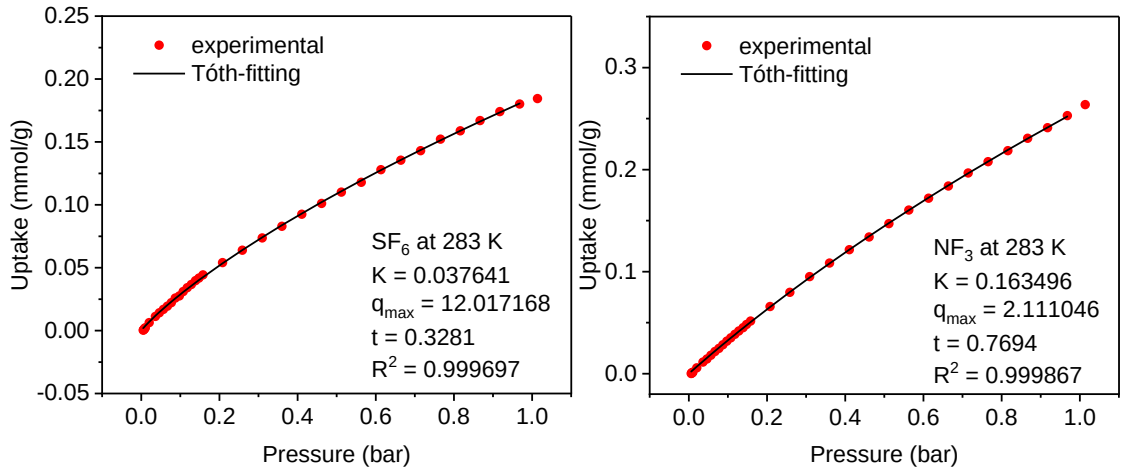

Figure 277. SF_6 (left) and NF_3 (right) isotherms and fitting curves of **cage-CF$_{3\alpha}$** at 283 K.

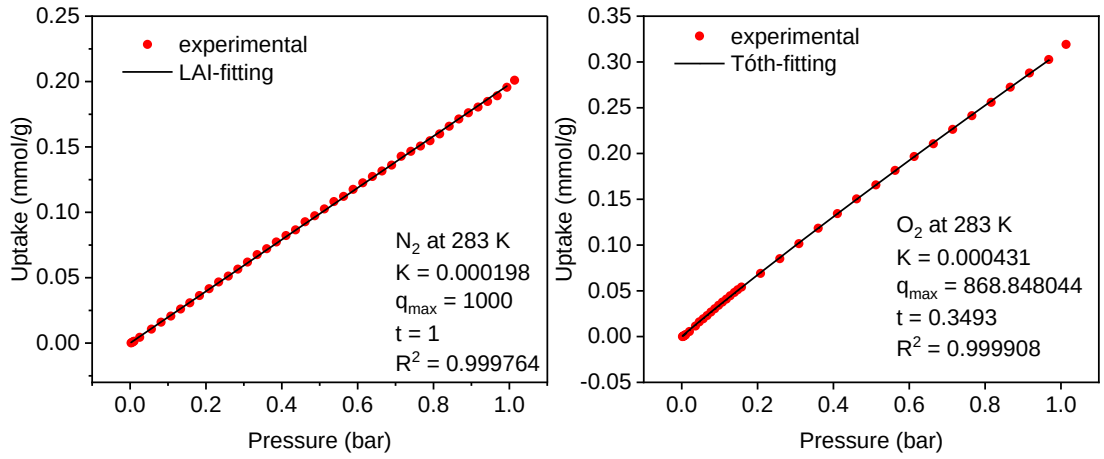

Figure 278. N_2 (left) and O_2 (right) isotherms and fitting curves of **cage-CF$_{3\alpha}$** at 283 K.

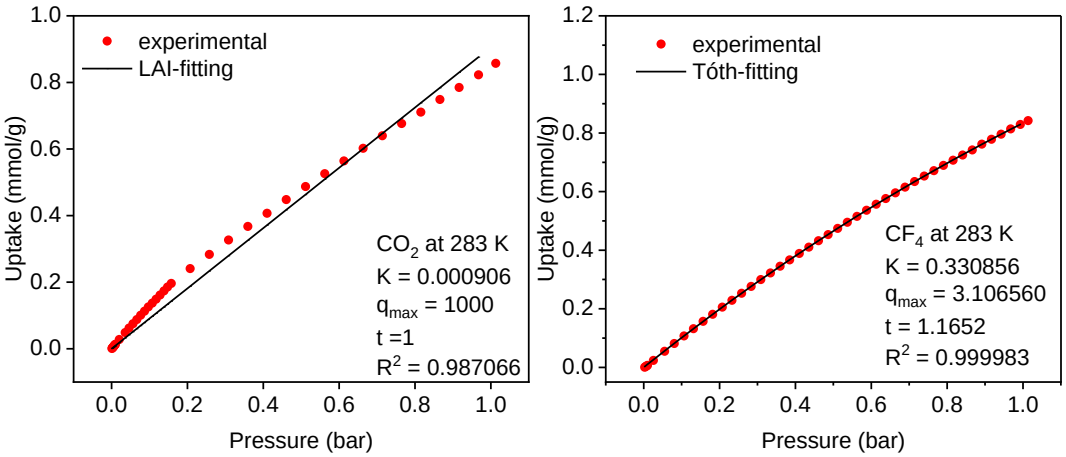

Figure 279. CO_2 isotherm and fitting curve of **cage-CF$_{3\alpha}$** (left) and CF_4 isotherm and fitting curve of **cage-C$_2$F$_5$** (right) at 283 K.

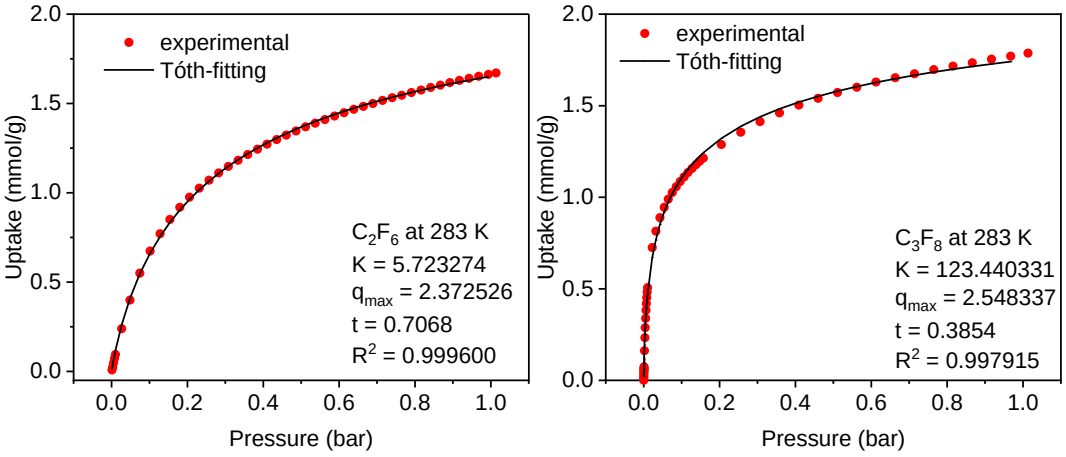

Figure 280. C_2F_6 (left) and C_3F_8 (right) isotherms and fitting curves of **cage-C$_2$F$_5$** at 283 K.

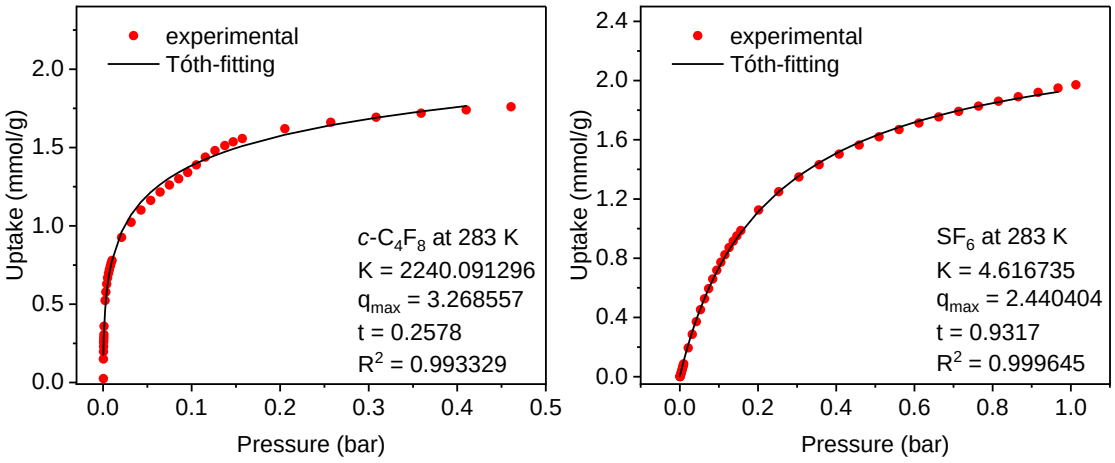

Figure 281. *c*-C_4F_8 (left) and SF_6 (right) isotherms and fitting curves of **cage-C_2F_5** at 283 K. (Note: Only the pressure range for from *c*-C_4F_8 0-0.6 bar was taken into account due to pore condensation >0.6 bar)

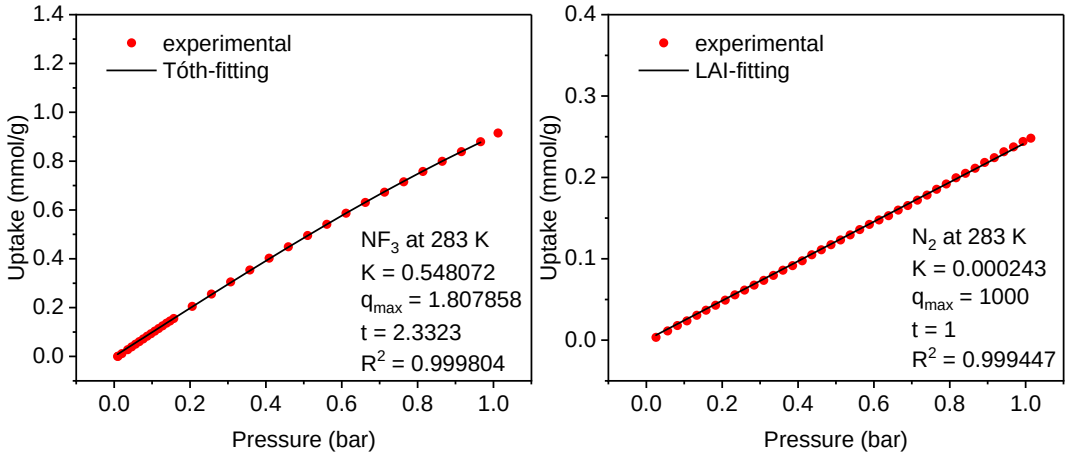

Figure 282. NF_3 (left) and N_2 (right) isotherms and fitting curves of **cage-C_2F_5** at 283 K.

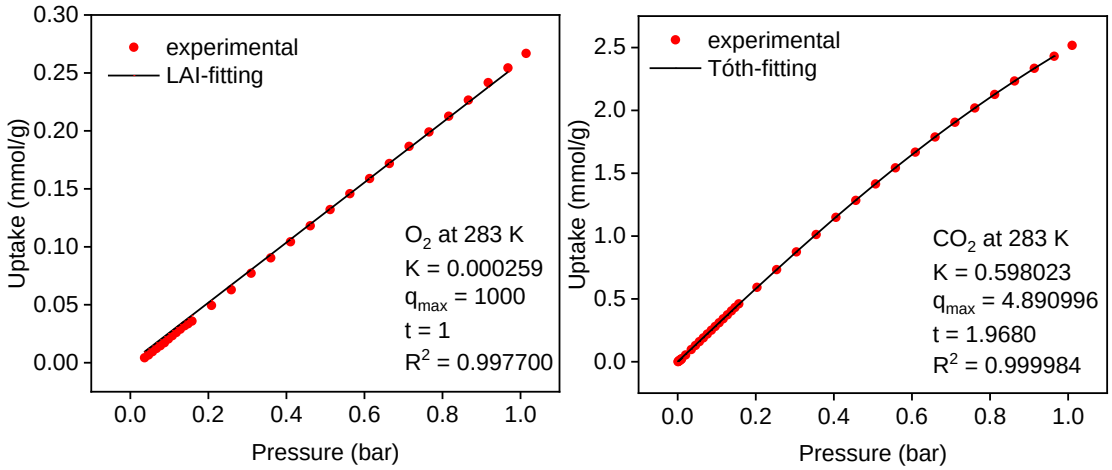

Figure 283. O_2 (left) and CO_2 (right) isotherms and fitting curves of **cage-C_2F_5** at 283 K.

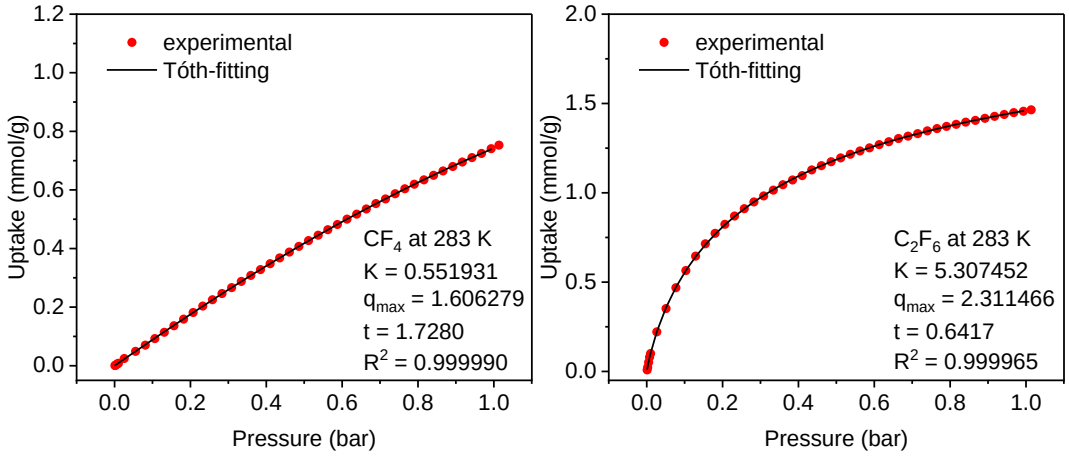

Figure 284. CF_4 (left) and C_2F_6 (right) isotherms and fitting curves of **cage-C_3F_7** at 283 K.

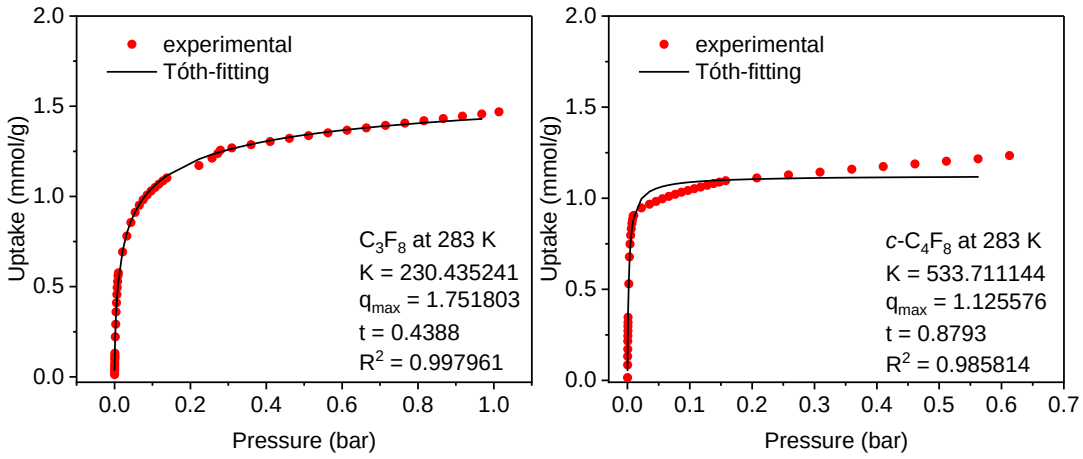

Figure 285. C_3F_8 (left) and *c*-C_4F_8 (right) isotherms and fitting curves of **cage-C_3F_7** at 283 K. (Note: Only the pressure range for from *c*-C_4F_8 0-0.6 bar was taken into account due to pore condensation >0.6 bar)

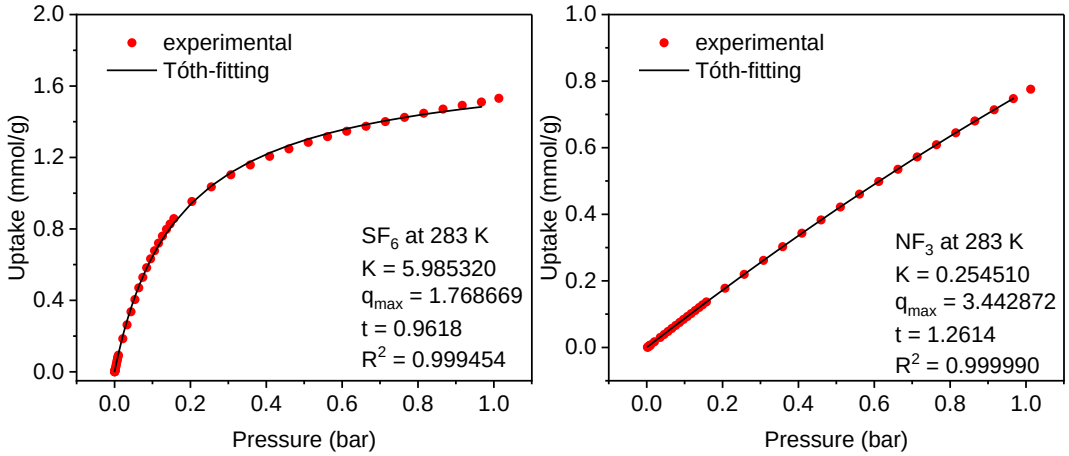

Figure 286. SF_6 (left) and NF_3 (right) isotherms and fitting curves of **cage-C_3F_7** at 283 K.

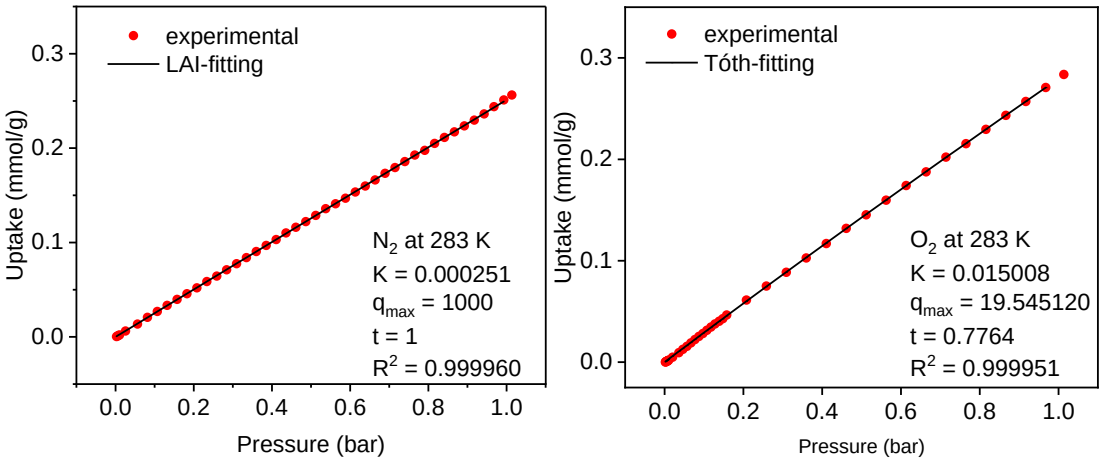

Figure 287. N_2 (left) and O_2 (right) isotherms and fitting curves of **cage-C_3F_7** at 283 K.

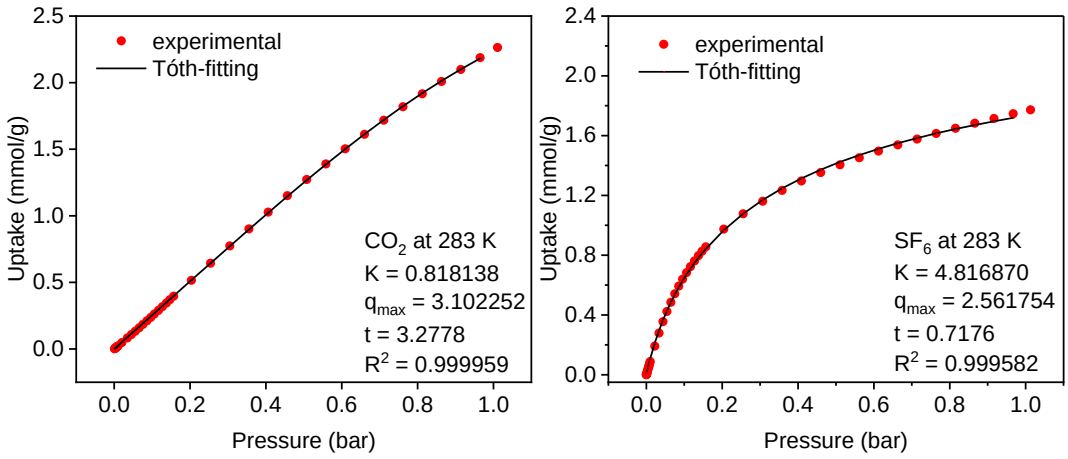

Figure 288. CO_2 isotherm and fitting curve of **cage-C_3F_7** (left) and SF_6 isotherm and fitting curve of **F-cage** (right) at 283 K.

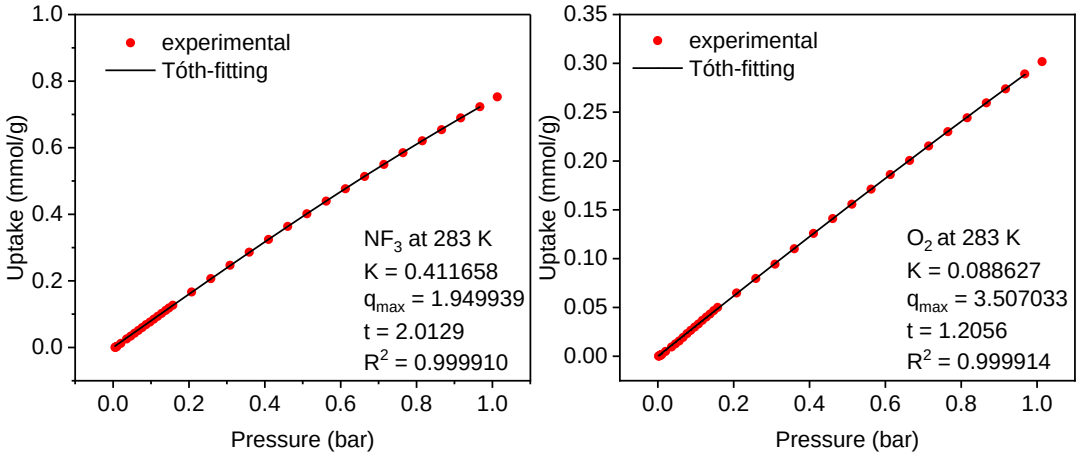

Figure 289. NF_3 (left) and O_2 (right) isotherms and fitting curves of **F-cage** at 283 K.

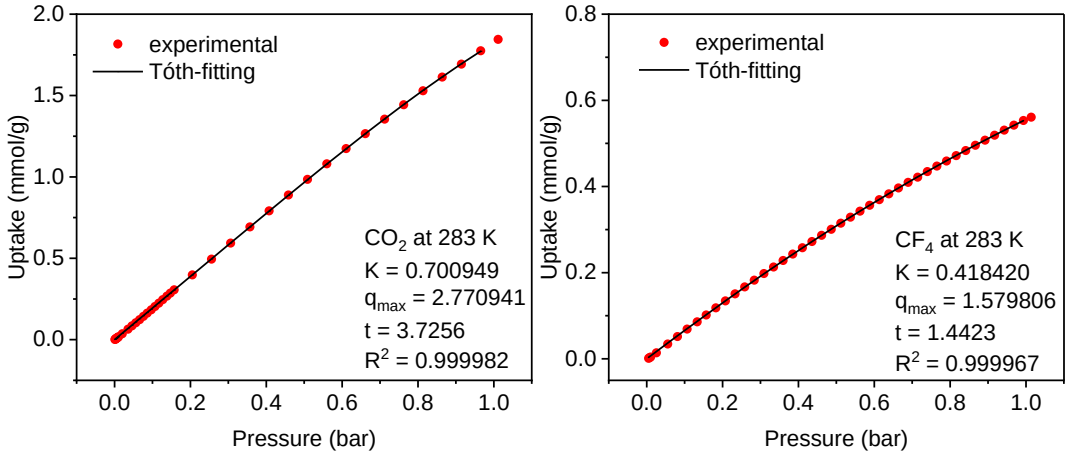

Figure 290. CO_2 isotherm and fitting curve of **F-cage** (left) and CF_4 isotherm and fitting curve of **cage-C_5F_{11}** (right) at 283 K.

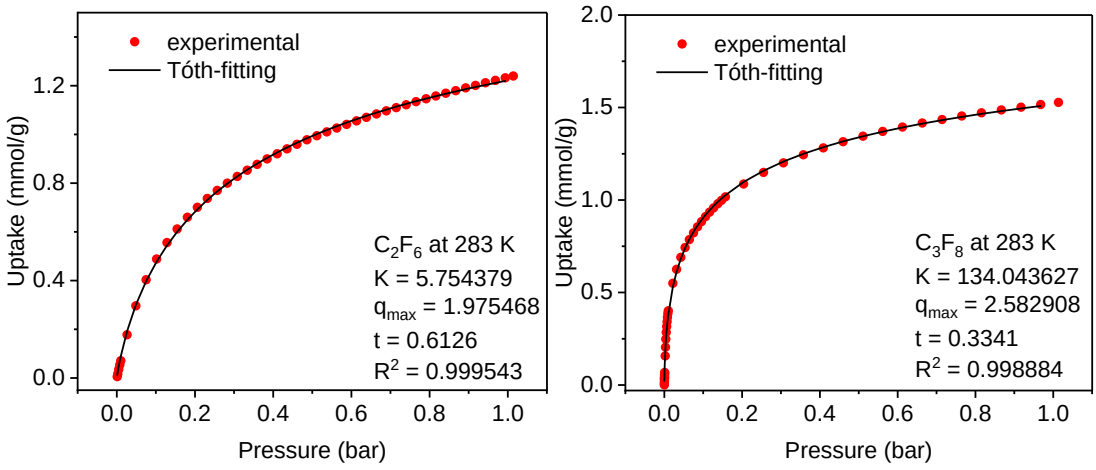

Figure 291. C_2F_6 (left) and C_3F_8 (right) isotherms and fitting curves of **cage-C_5F_{11}** at 283 K.

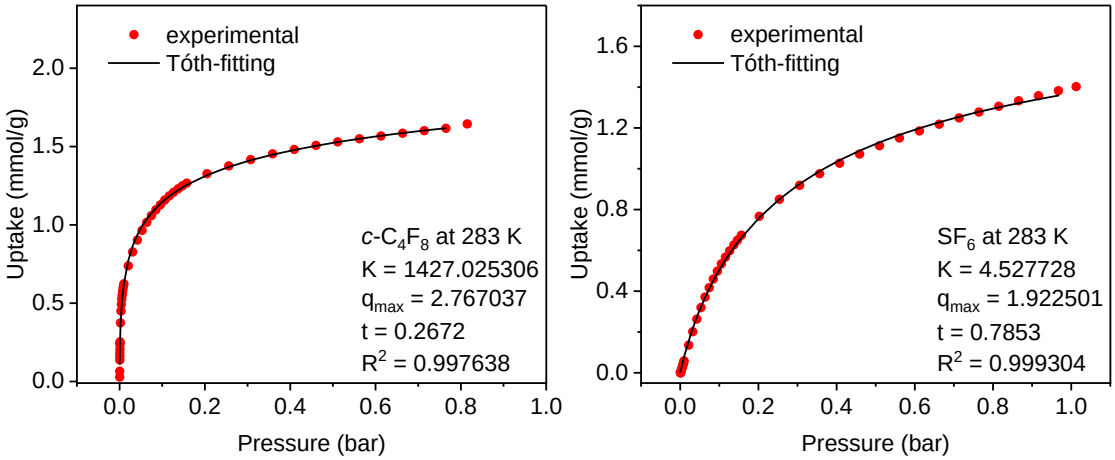

Figure 292. *c*-C_4F_8 (left) and SF_6 (right) isotherms and fitting curves of **cage-C_5F_{11}** at 283 K. (Note: Only the pressure range for from *c*-C_4F_8 0-0.6 bar was taken into account due to pore condensation >0.6 bar)

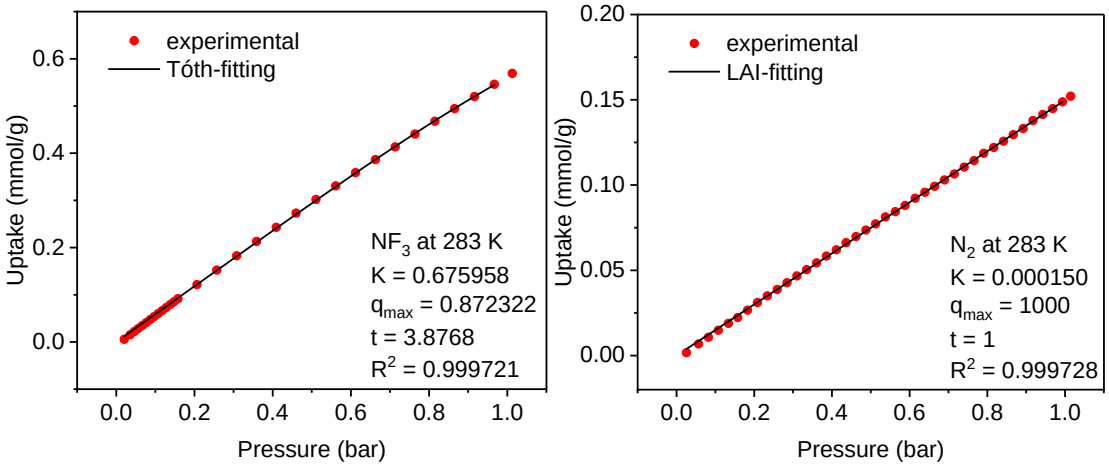

Figure 293. NF_3 (left) and N_2 (right) isotherms and fitting curves of **cage-C_5F_{11}** at 283 K.

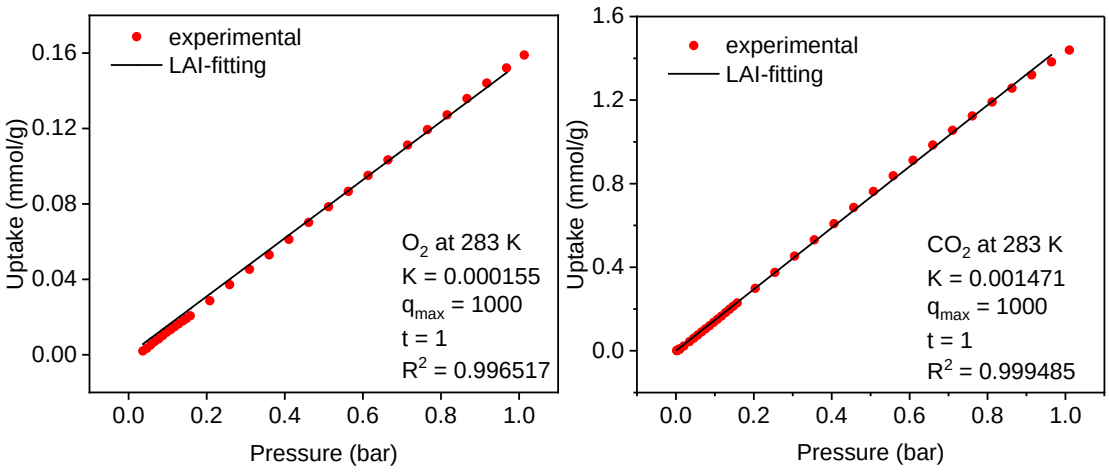

Figure 294. O_2 (left) and CO_2 (right) isotherms and fitting curves of **cage-C_5F_{11}** at 283 K.

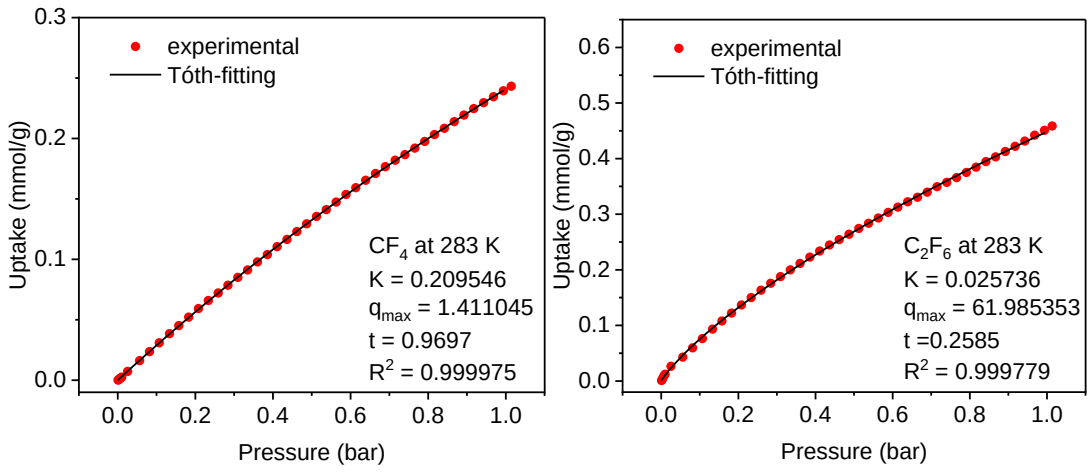

Figure 295. CF_4 (left) and C_2F_6 (right) isotherms and fitting curves of **cage-$C_6F_{13\alpha}$** at 283 K.

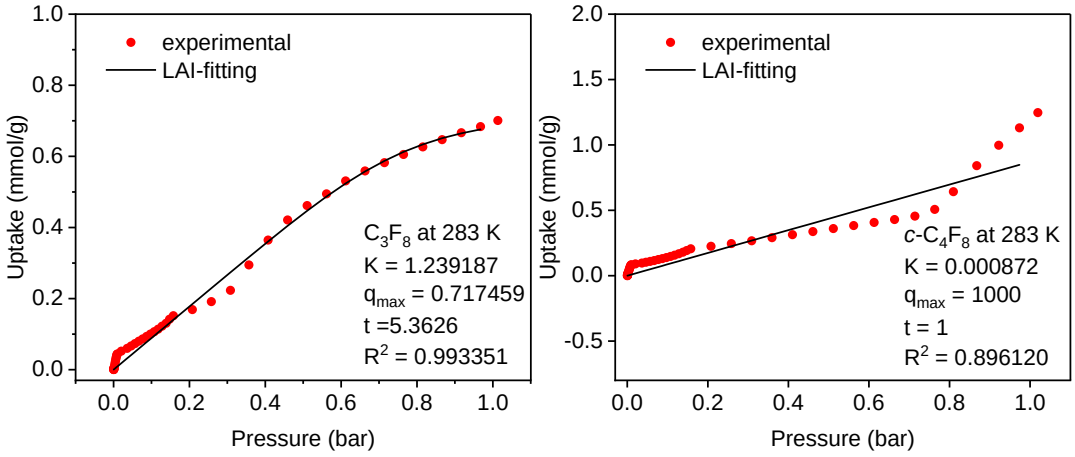

Figure 296. C_3F_8 (left) and *c*-C_4F_8 (right) isotherms and fitting curves of **cage-$C_6F_{13\alpha}$** at 283 K.

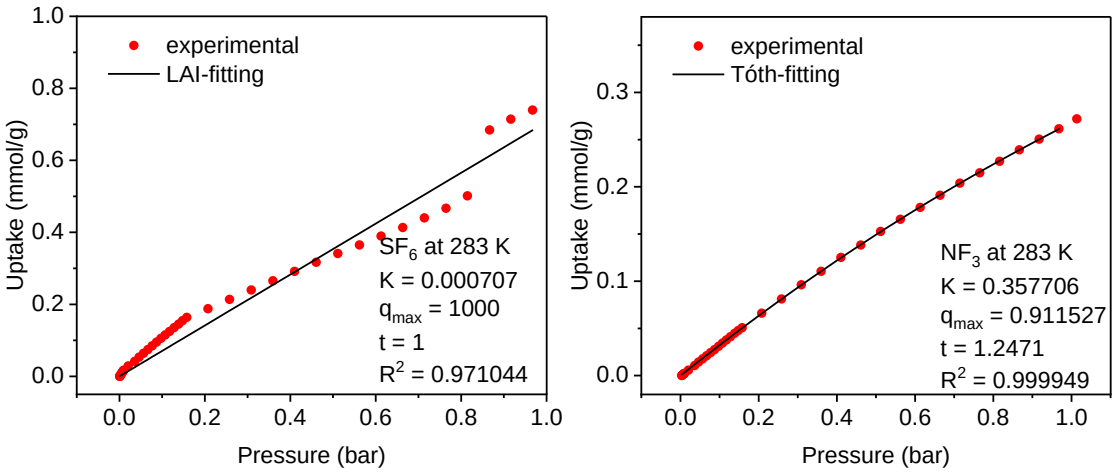

Figure 297. SF_6 (left) and NF_3 (right) isotherms and fitting curves of **cage-$C_6F_{13\alpha}$** at 283 K.

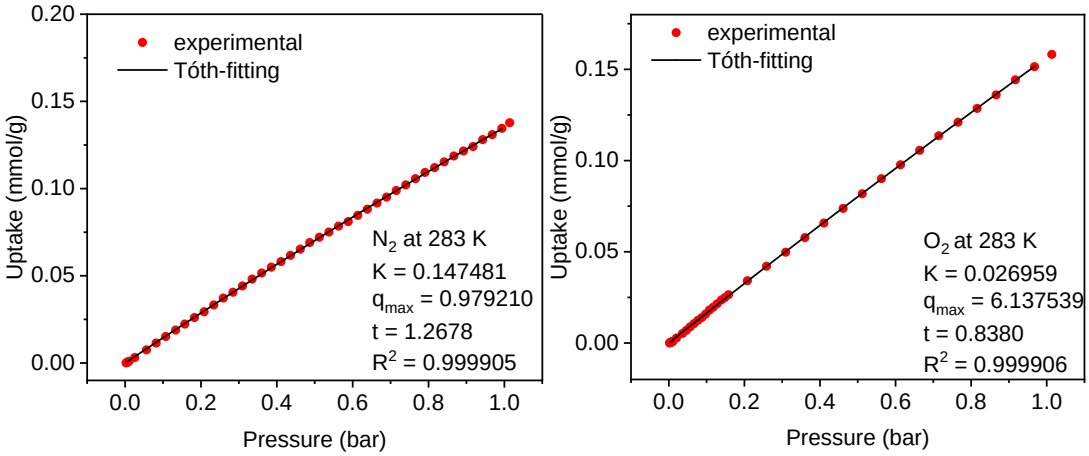

Figure 298. N_2 (left) and O_2 (right) isotherms and fitting curves of **cage-$C_6F_{13\alpha}$** at 283 K.

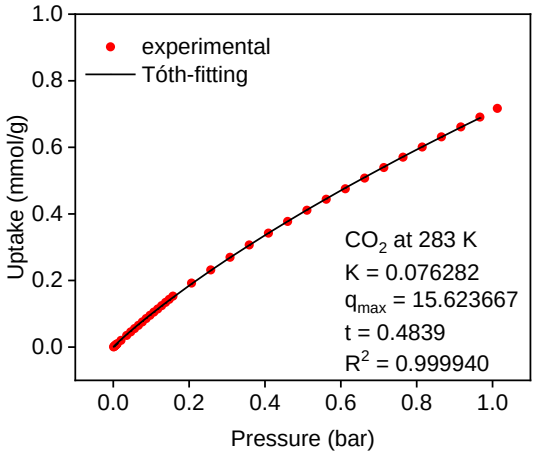

Figure 299. CO_2 isotherm and fitting curve of **cage-$C_6F_{13\alpha}$** at 283 K.

Gas sorption fitting curves at 298 K

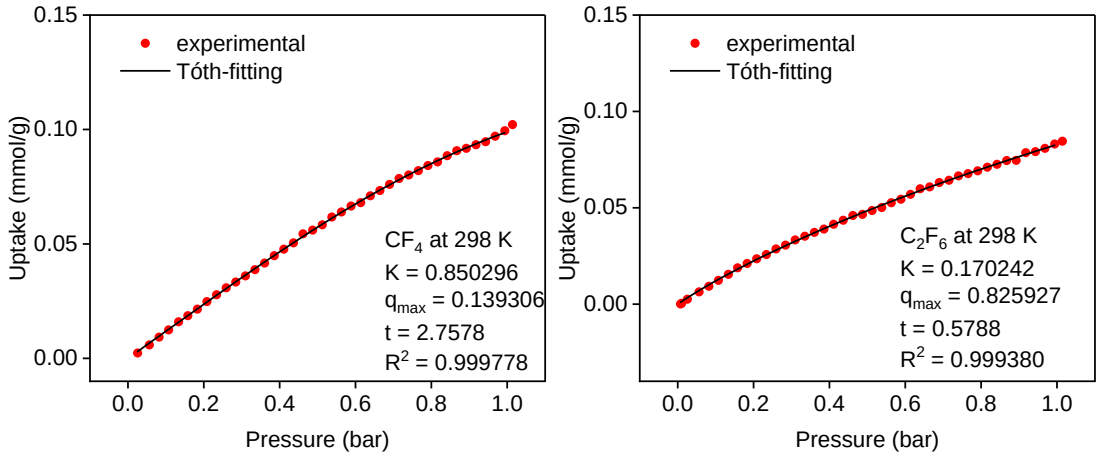

Figure 300. CF_4 (left) and C_2F_6 (right) isotherms and fitting curves of **cage-$CF_{3\alpha}$** at 298 K.

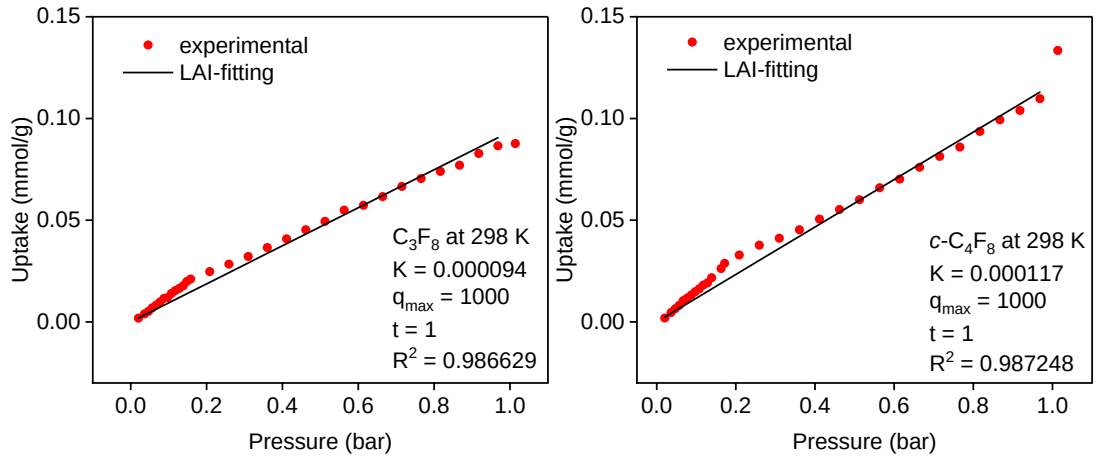

Figure 301. C_3F_8 (left) and *c*-C_4F_8 (right) isotherms and fitting curves of **cage-$CF_{3\alpha}$** at 298 K.

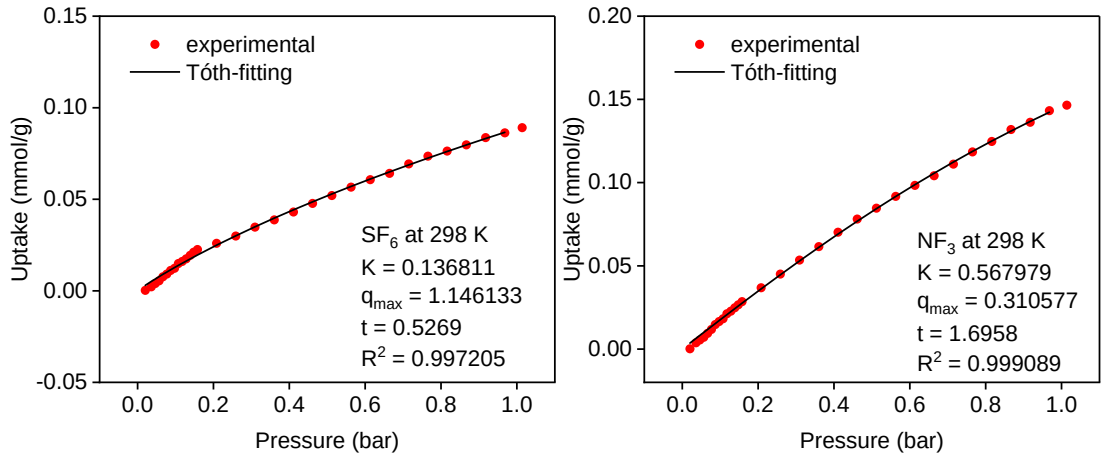

Figure 302. SF_6 (left) and NF_3 (right) isotherms and fitting curves of **cage-CF$_{3\alpha}$** at 298 K.

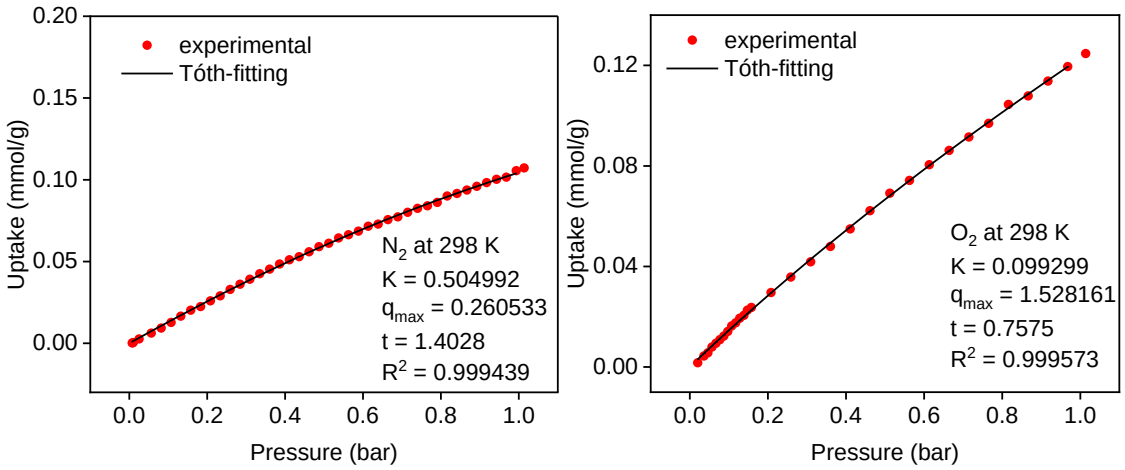

Figure 303. N_2 (left) and O_2 (right) isotherms and fitting curves of **cage-CF$_{3\alpha}$** at 298 K.

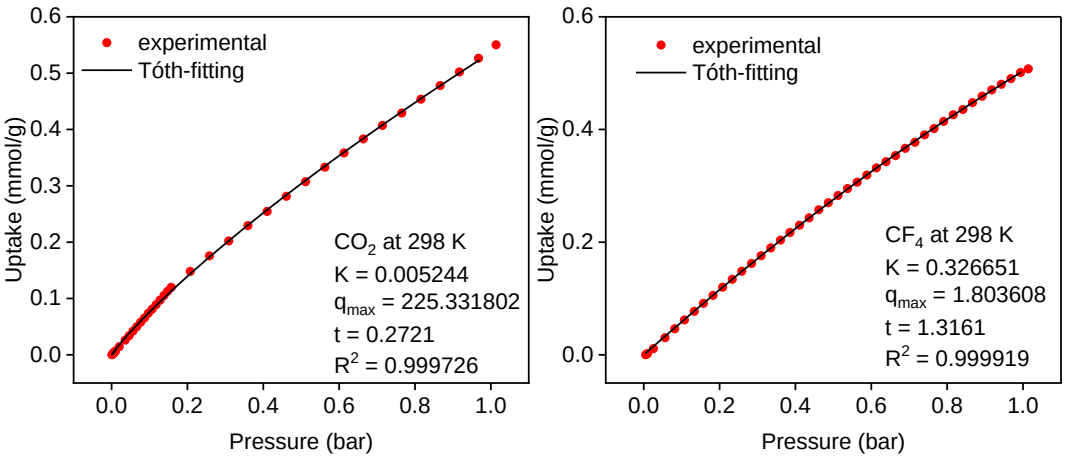

Figure 304. CO_2 isotherm and fitting curve of **cage-CF$_{3\alpha}$** (left) and CF_4 isotherm and fitting curve of **cage-C$_2$F$_5$** (right) at 298 K.

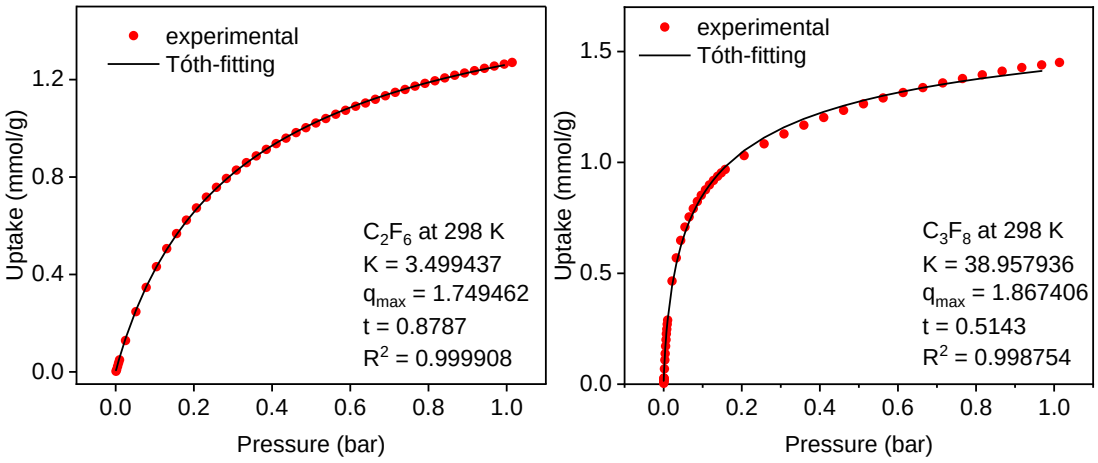

Figure 305. C_2F_6 (left) and C_3F_8 (right) isotherms and fitting curves of **cage-C_2F_5** at 298 K.

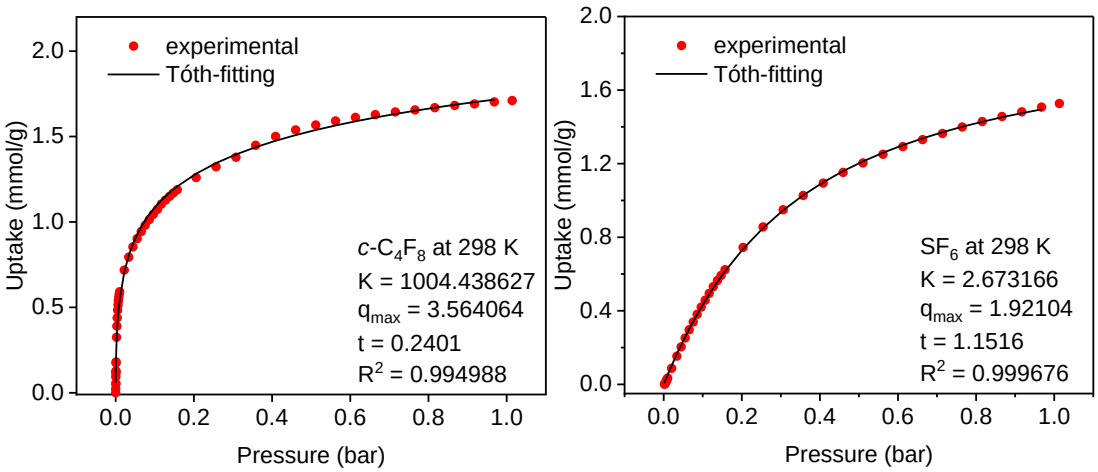

Figure 306. *c*-C_4F_8 (left) and SF_6 (right) isotherms and fitting curves of **cage-C_2F_5** at 298 K.

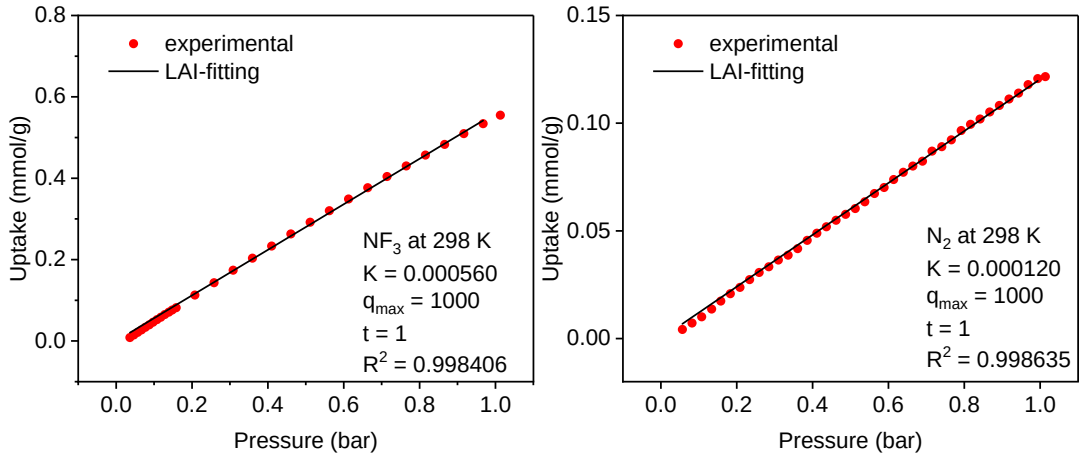

Figure 307. NF_3 (left) and N_2 (right) isotherms and fitting curves of **cage-C_2F_5** at 298 K.

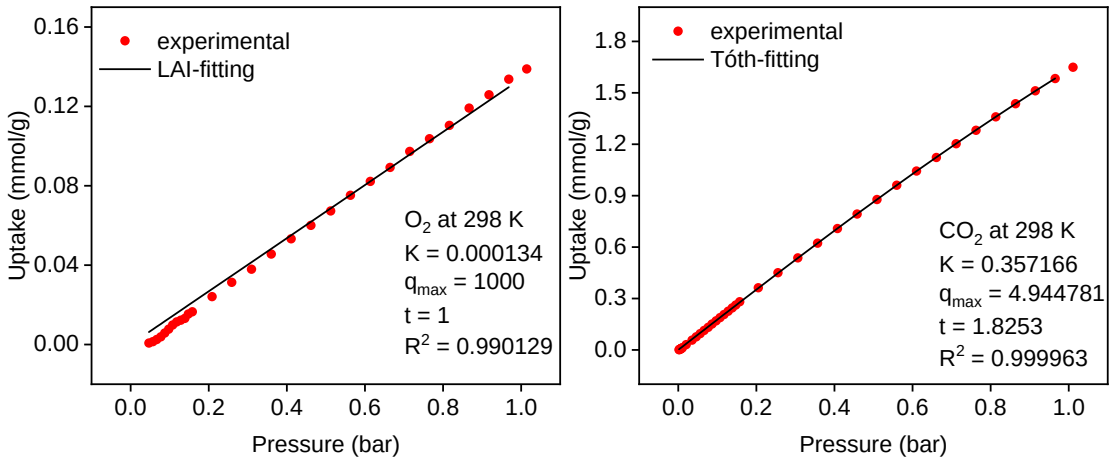

Figure 308. O_2 (left) and CO_2 (right) isotherms and fitting curves of **cage-C_2F_5** at 298 K.

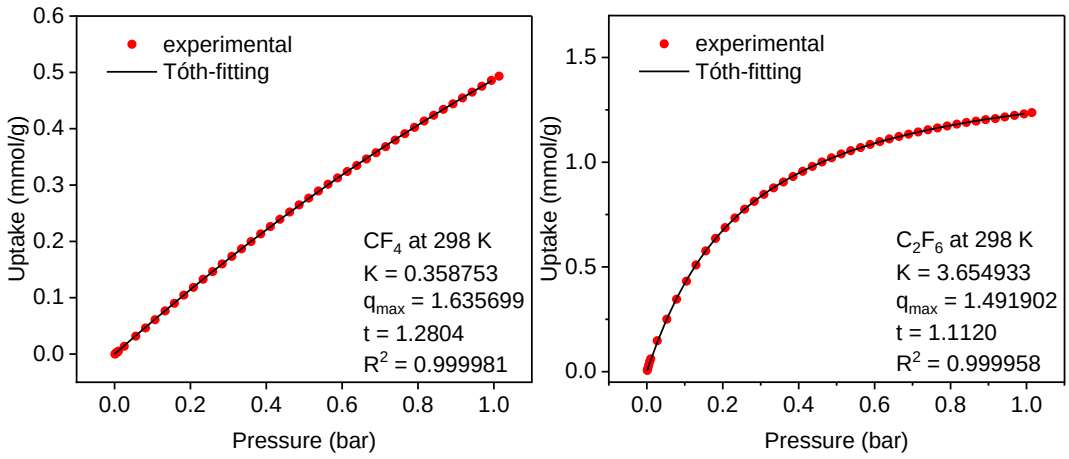

Figure 309. CF_4 (left) and C_2F_6 (right) isotherms and fitting curves of **cage-C_3F_7** at 298 K.

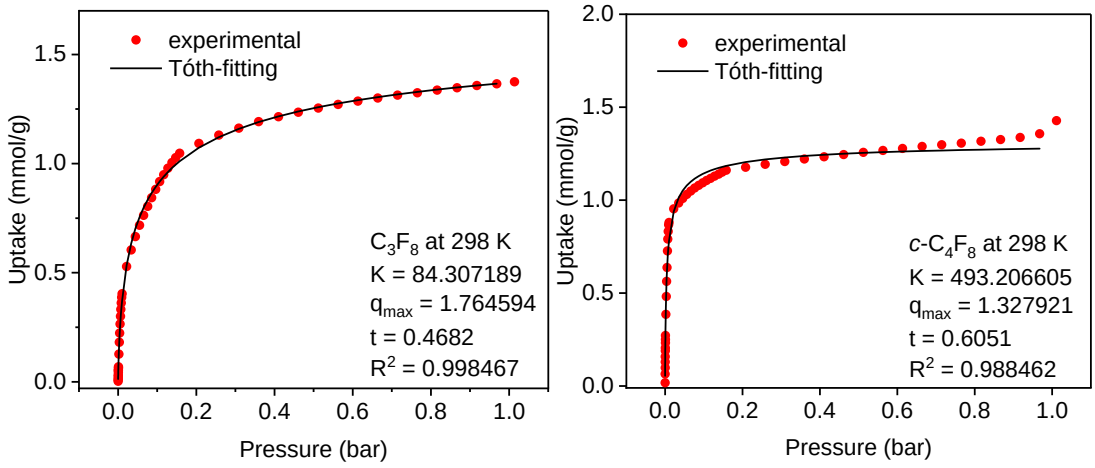

Figure 310. C_3F_8 (left) and *c*-C_4F_8 (right) isotherms and fitting curves of **cage-C_3F_7** at 298 K.

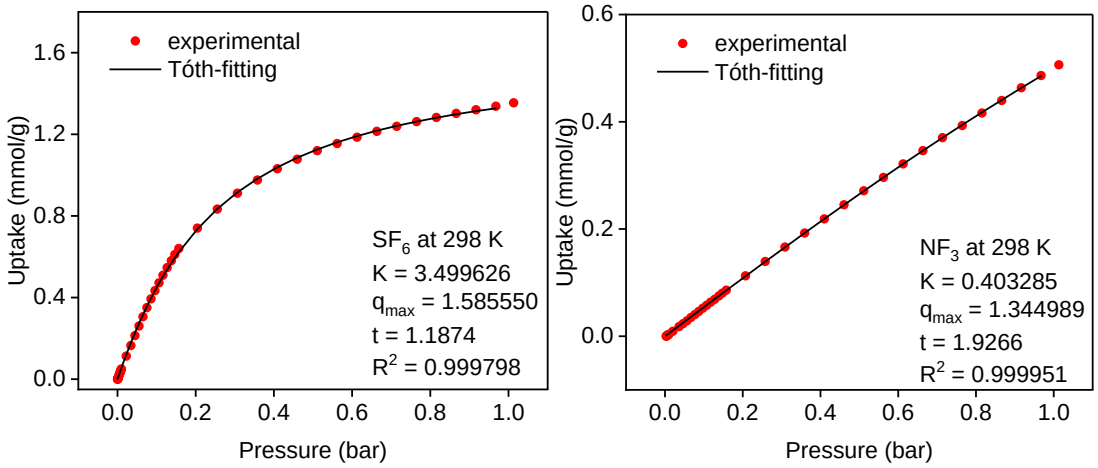

Figure 311. SF_6 (left) and NF_3 (right) isotherms and fitting curves of **cage-C_3F_7** at 298 K.

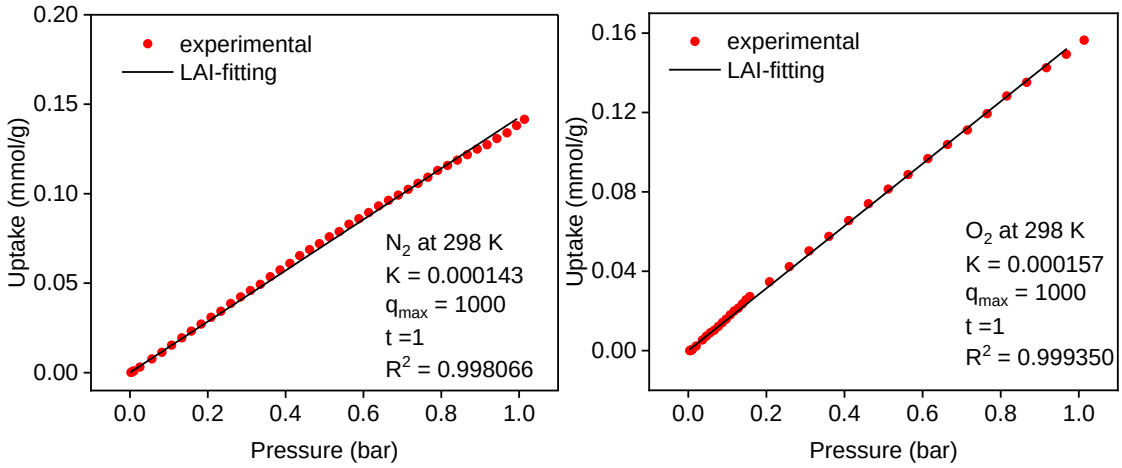

Figure 312. N_2 (left) and O_2 (right) isotherms and fitting curves of **cage-C_3F_7** at 298 K.

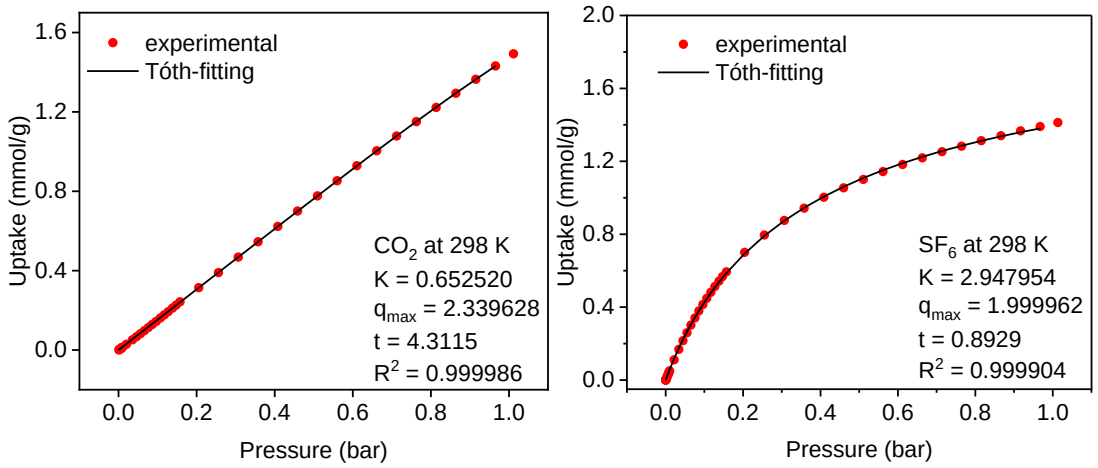

Figure 313. CO_2 isotherm and fitting curve of **cage-C_3F_7** (left) and SF_6 isotherm and fitting curve of **F-cage** (right) at 298 K.

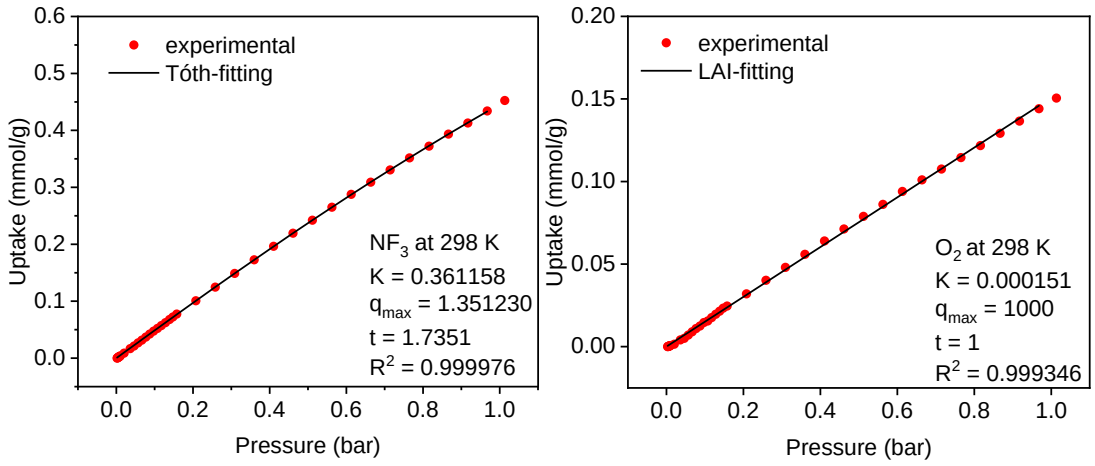

Figure 314. NF_3 (left) and O_2 (right) isotherms and fitting curves of **F-cage** at 298 K.

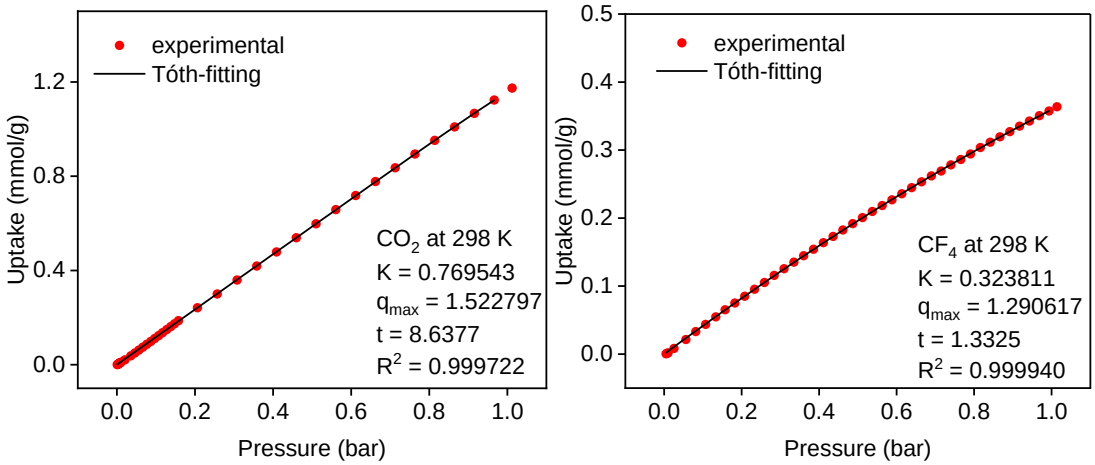

Figure 315. CO_2 isotherm and fitting curve of **F-cage** (left) and CF_4 isotherm and fitting curve of **cage-C_5F_{11}** (right) at 298 K.

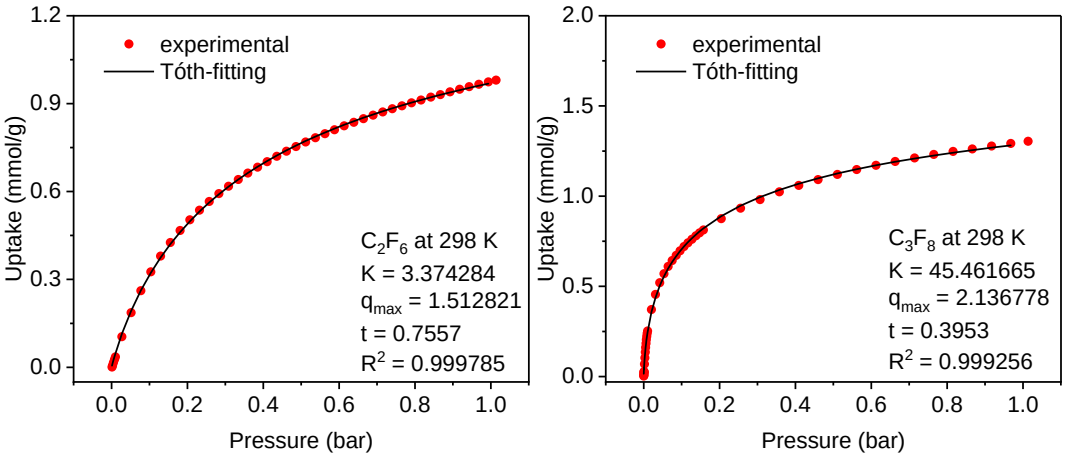

Figure 316. C_2F_6 (left) and C_3F_8 (right) isotherms and fitting curves of **cage-C_5F_{11}** at 298 K.

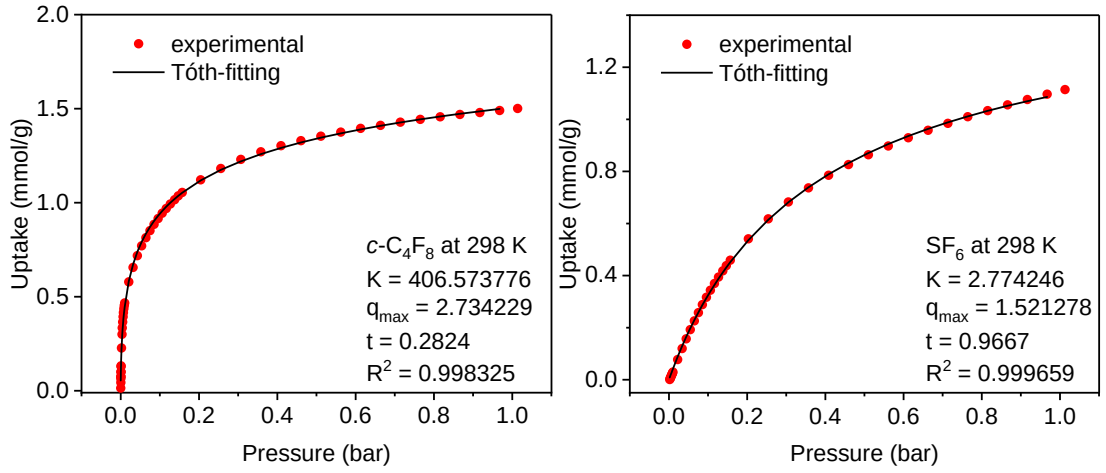

Figure 317. *c*-C_4F_8 (left) and SF_6 (right) isotherms and fitting curves of **cage-C_5F_{11}** at 298 K.

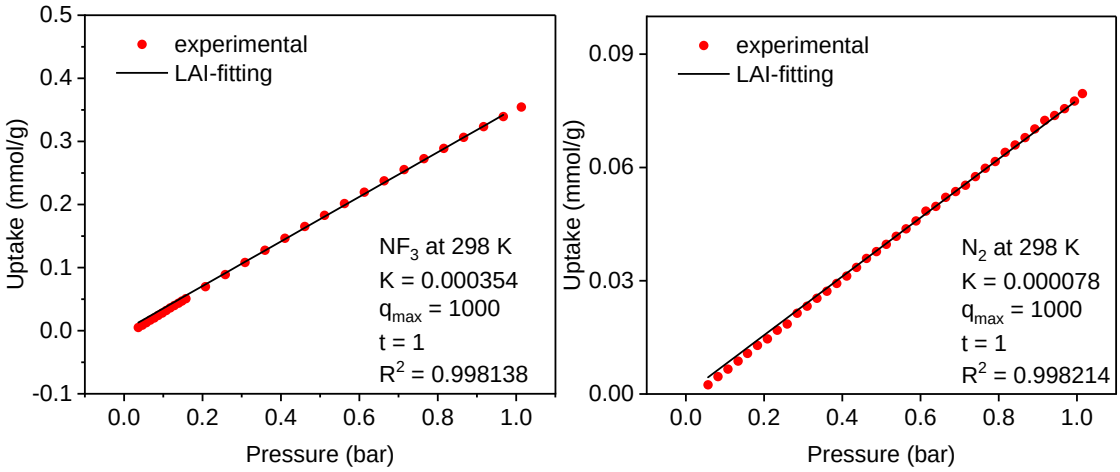

Figure 318. NF_3 (left) and N_2 (right) isotherms and fitting curves of **cage-C_5F_{11}** at 298 K.

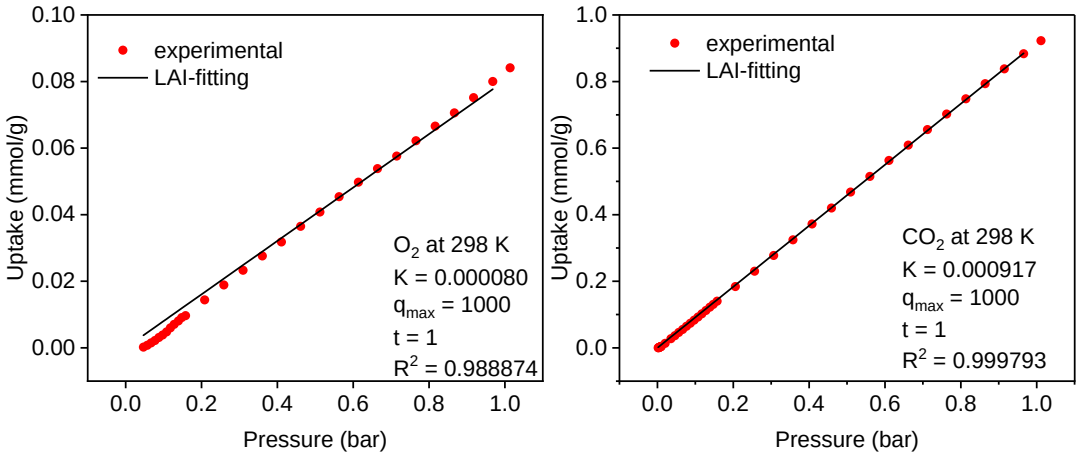

Figure 319. O_2 (left) and CO_2 (right) isotherms and fitting curves of **cage-C_5F_{11}** at 298 K.

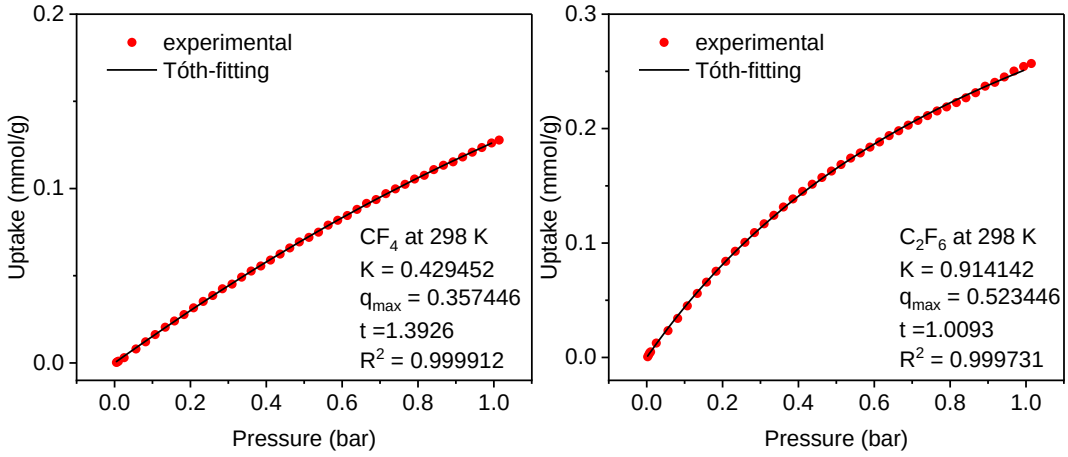

Figure 320. CF_4 (left) and C_2F_6 (right) isotherms and fitting curves of **cage-$C_6F_{13\alpha}$** at 298 K.

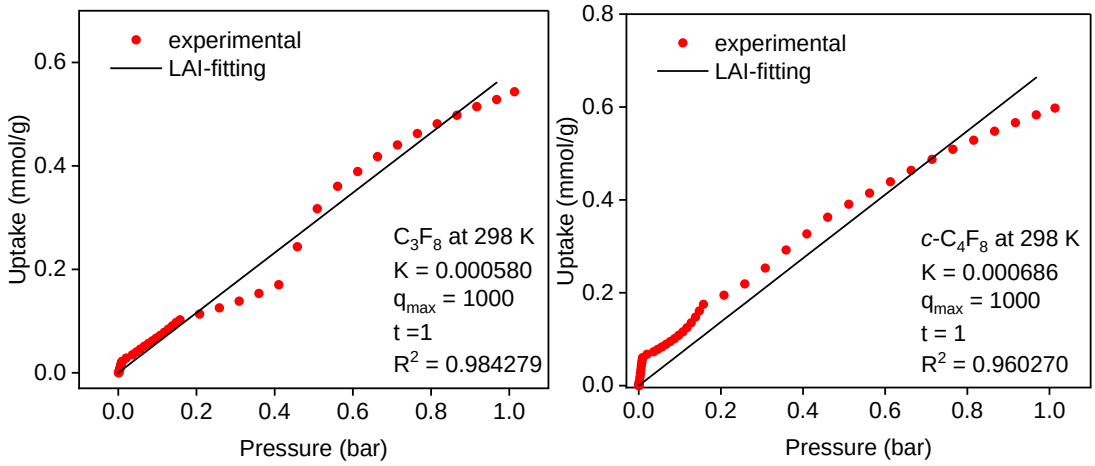

Figure 321. C_3F_8 (left) and *c*-C_4F_8 (right) isotherms and fitting curves of **cage-$C_6F_{13\alpha}$** at 298 K.

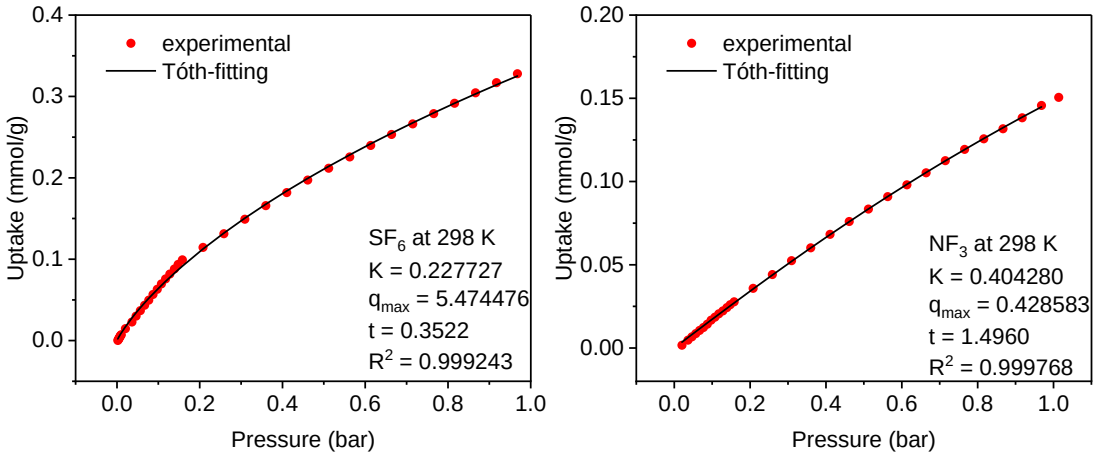

Figure 322. SF_6 (left) and NF_3 (right) isotherms and fitting curves of **cage-$C_6F_{13\alpha}$** at 298 K.

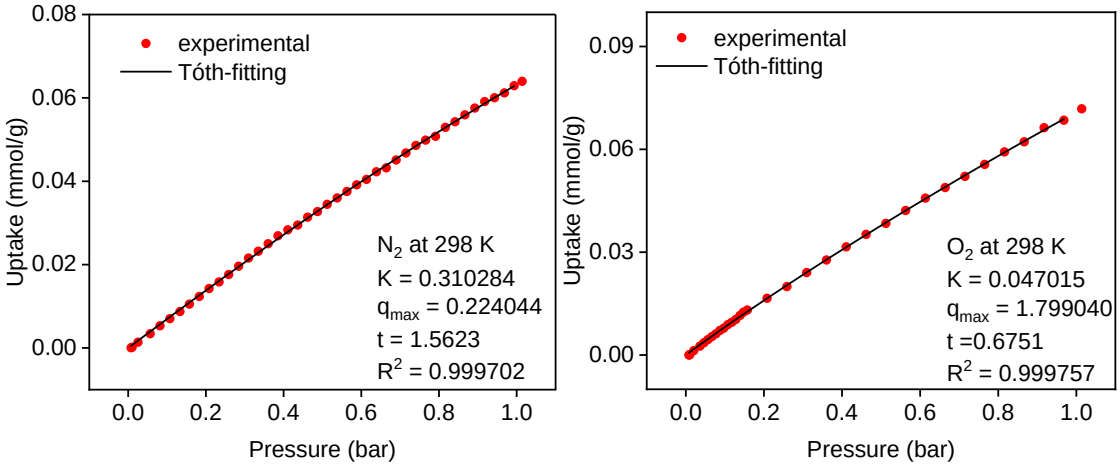

Figure 323. N_2 (left) and O_2 (right) isotherms and fitting curves of **cage-$C_6F_{13\alpha}$** at 298 K.

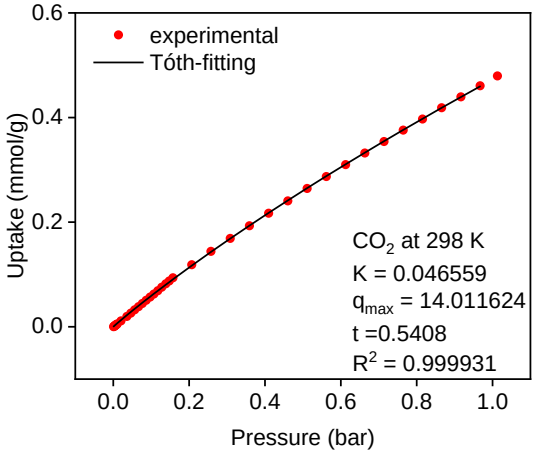

Figure 324. CO_2 isotherm and fitting curve of **cage-$C_6F_{13\alpha}$** at 298 K.

Gas sorption fitting curves at 313 K

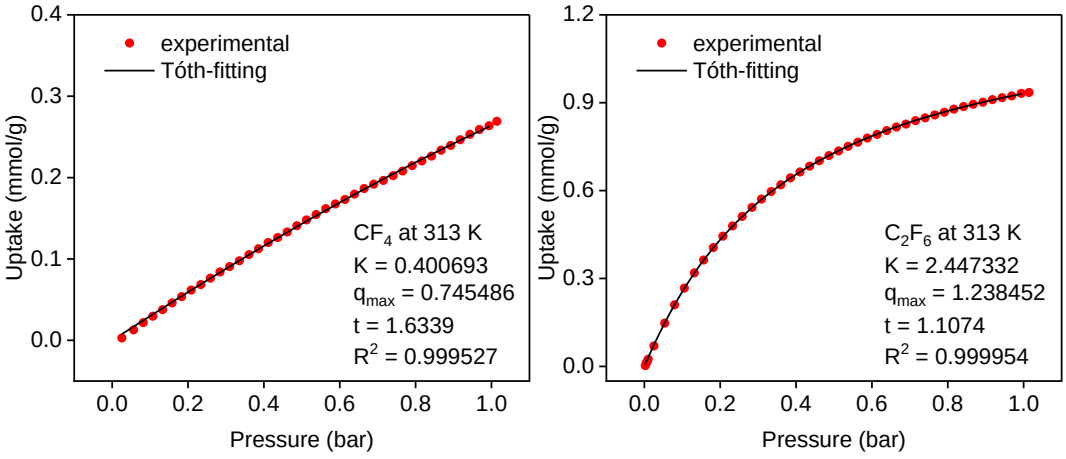

Figure 325. CF_4 (left) and C_2F_6 (right) isotherms and fitting curves of **cage-C_2F_5** at 313 K.

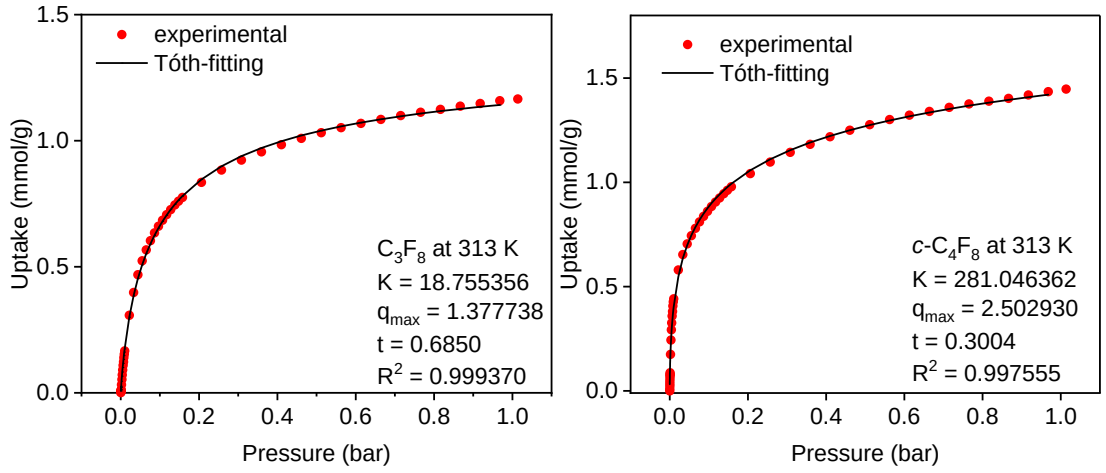

Figure 326. C_3F_8 (left) and *c*-C_4F_8 (right) isotherms and fitting curves of **cage-C_2F_5** at 313 K.

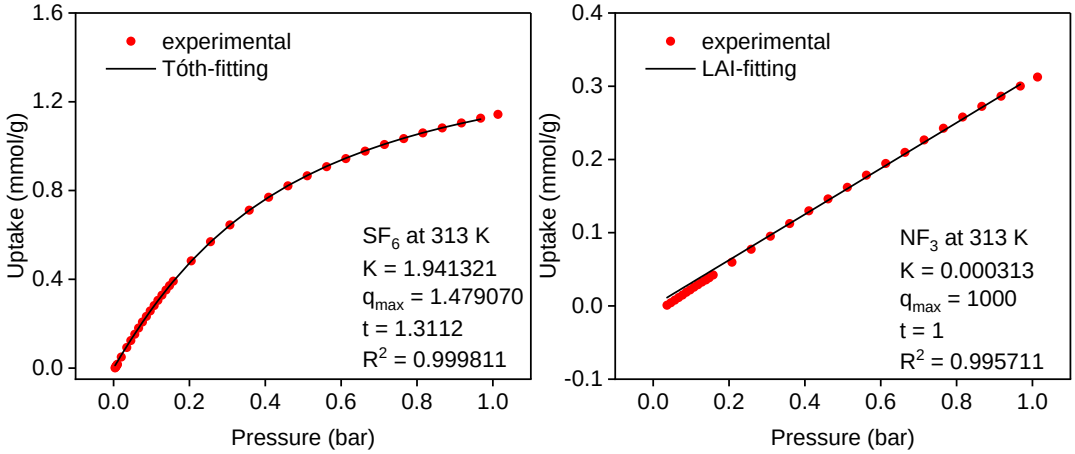

Figure 327. SF_6 (left) and NF_3 (right) isotherms and fitting curves of **cage-C_2F_5** at 313 K.

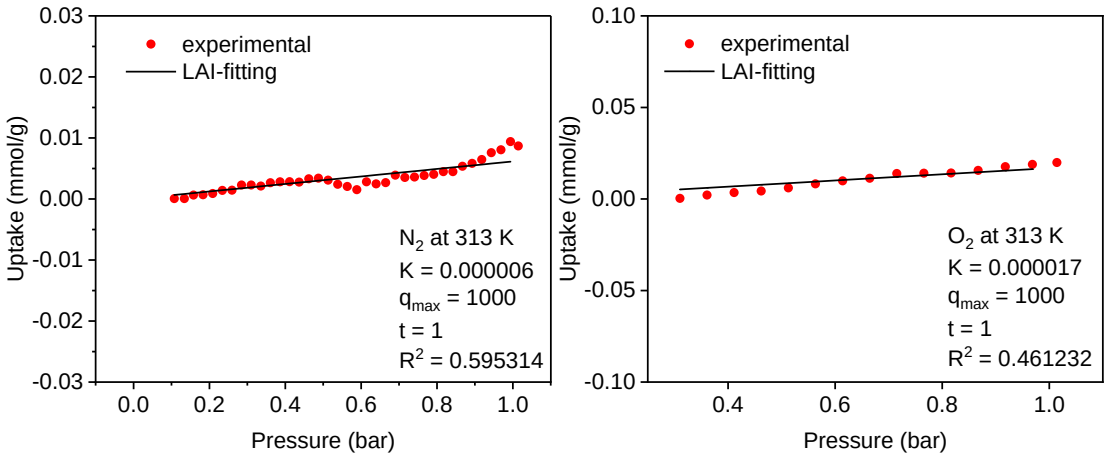

Figure 328. N_2 (left) and O_2 (right) isotherms and fitting curves of **cage-C_2F_5** at 313 K.

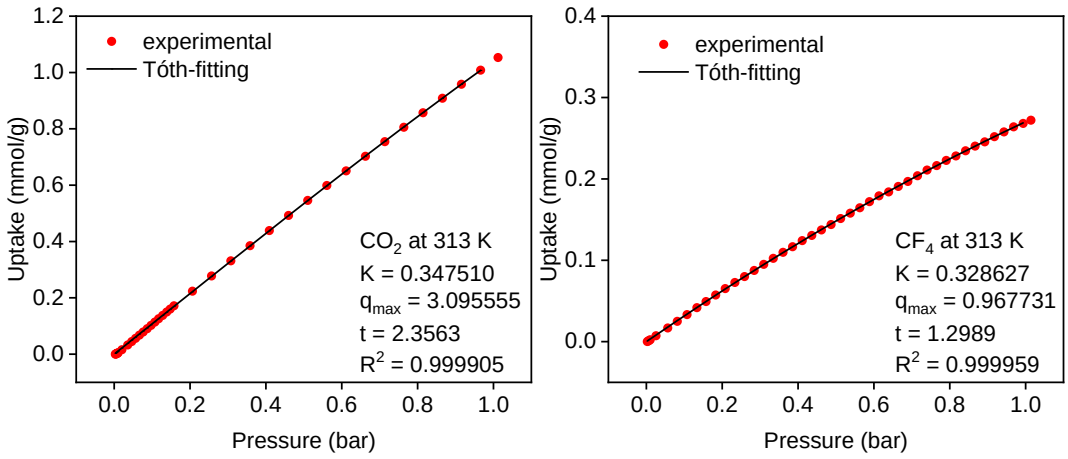

Figure 329. CO_2 isotherm and fitting curve of **cage-C_2F_5** (left) and CF_4 isotherm and fitting curve of **cage-C_3F_7** (right) at 313 K.

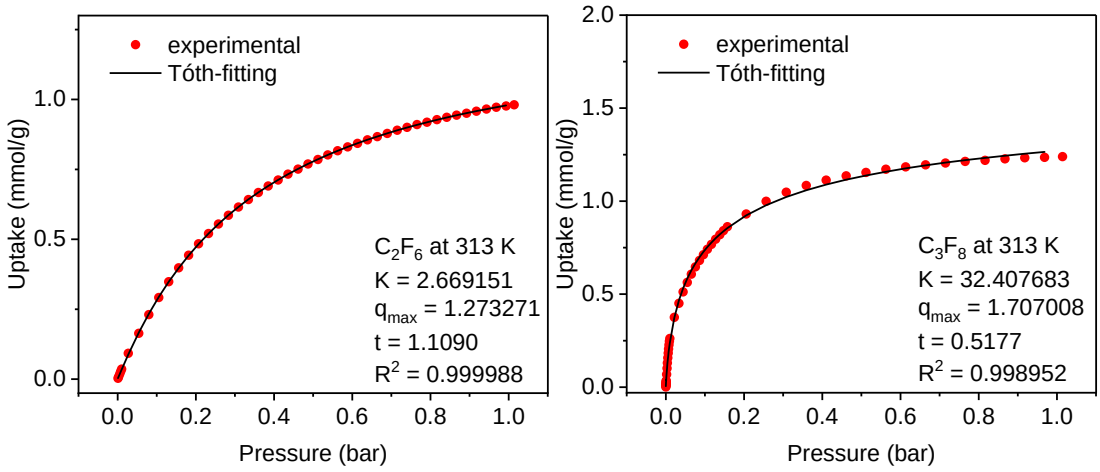

Figure 330. C_2F_6 (left) and C_3F_8 (right) isotherms and fitting curves of **cage-C_3F_7** at 313 K.

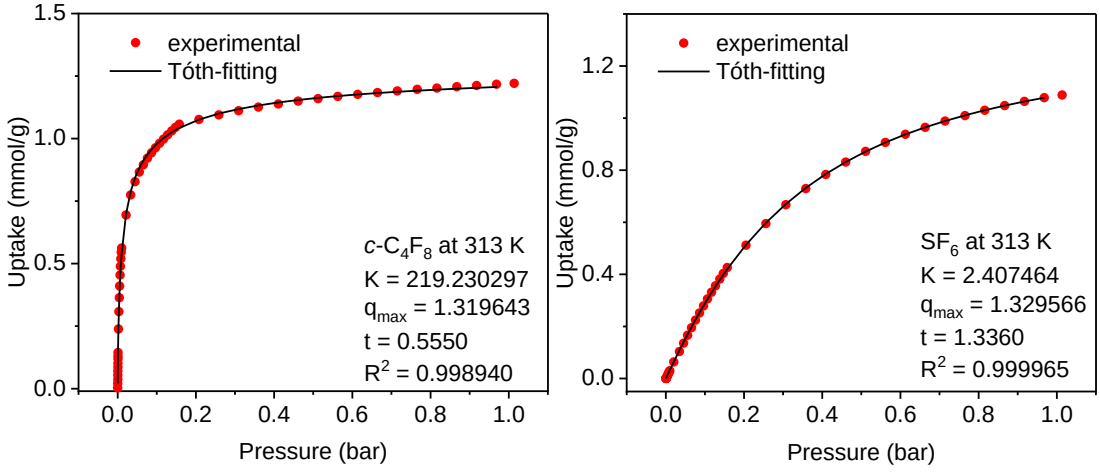

Figure 331. *c*-C_4F_8 (left) and SF_6 (right) isotherms and fitting curves of **cage-C_3F_7** at 313 K.

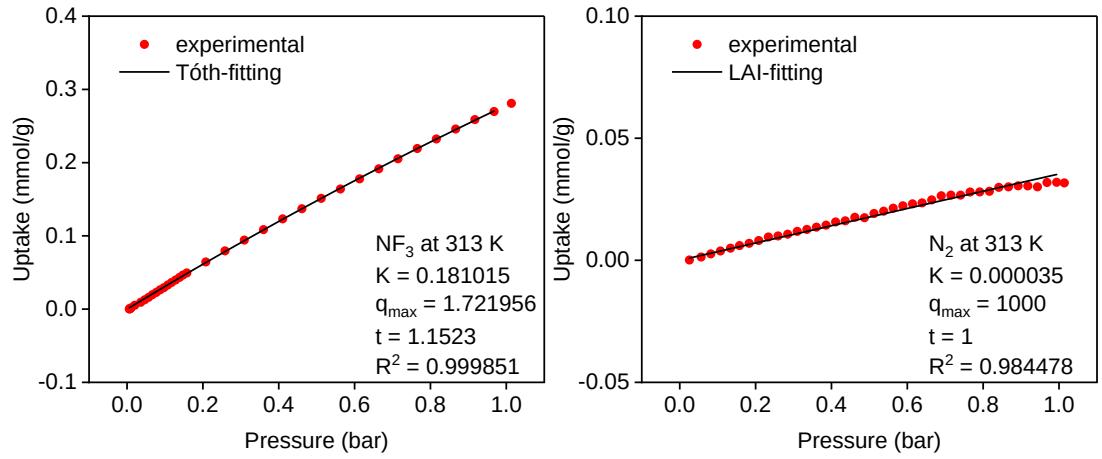

Figure 332. NF_3 (left) and N_2 (right) isotherms and fitting curves of **cage-C_3F_7** at 313 K.

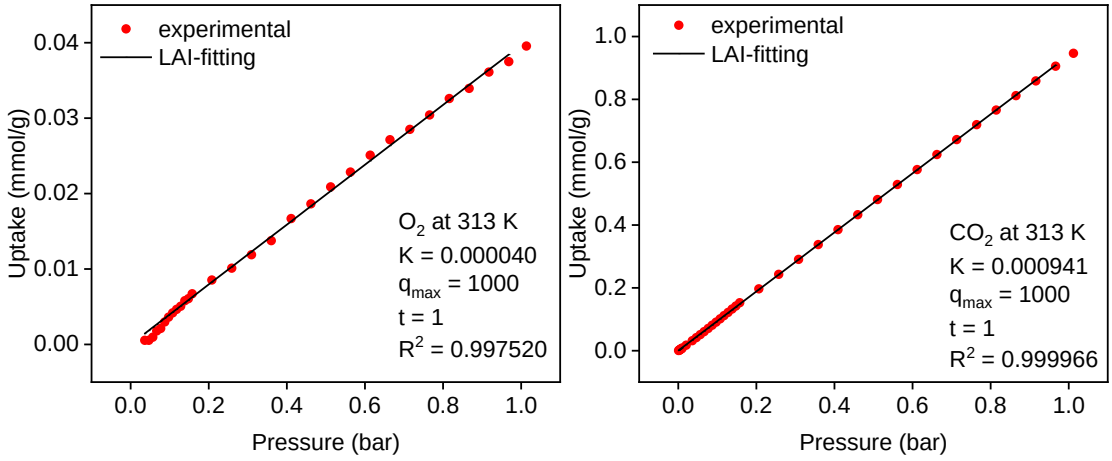

Figure 333. O_2 (left) and CO_2 (right) isotherms and fitting curves of **cage-C_3F_7** at 313 K.

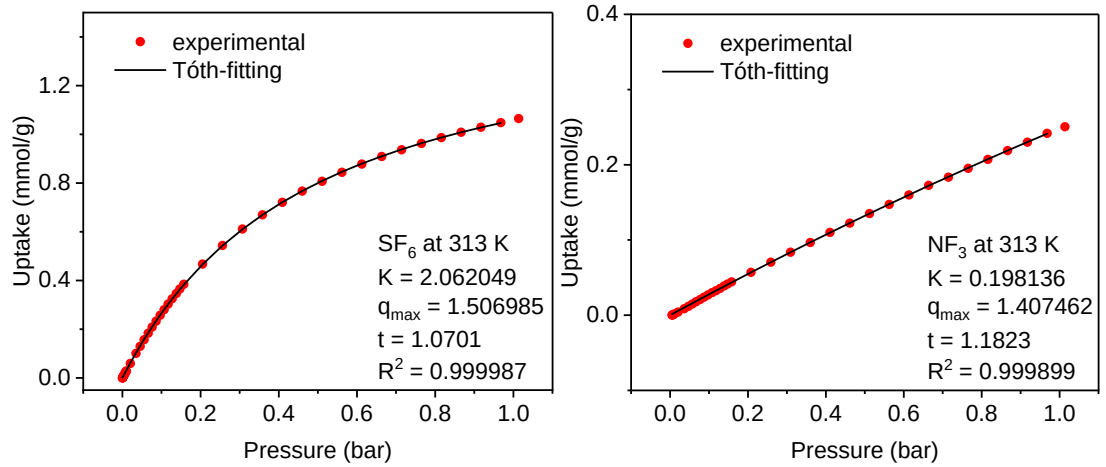

Figure 334. SF_6 (left) and NF_3 (right) isotherms and fitting curves of **F-cage** at 313 K.

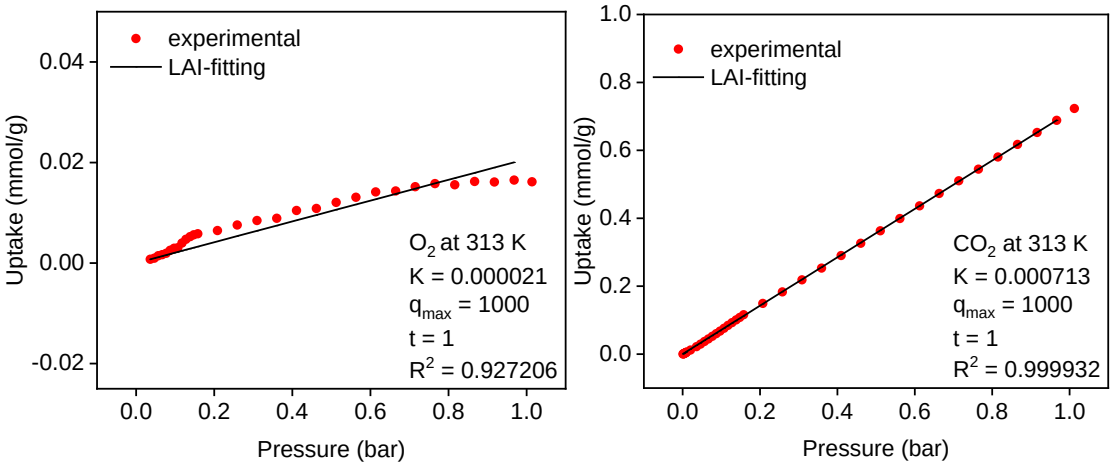

Figure 335. O_2 (left) and CO_2 (right) isotherms and fitting curves of **F-cage** at 313 K.

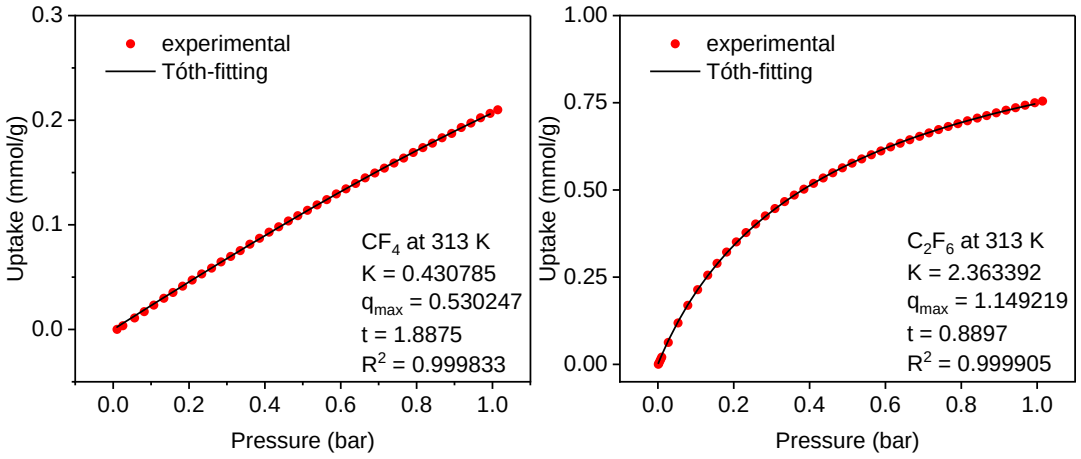

Figure 336. CF_4 (left) and C_2F_6 (right) isotherms and fitting curves of **cage-C_5F_{11}** at 313 K.

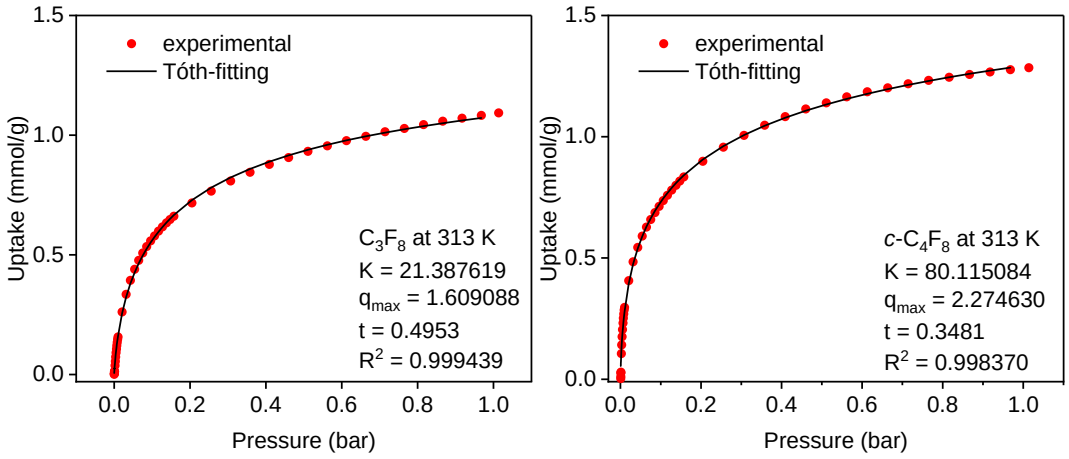

Figure 337. C_3F_8 (left) and *c*-C_4F_8 (right) isotherms and fitting curves of **cage-C_5F_{11}** at 313 K.

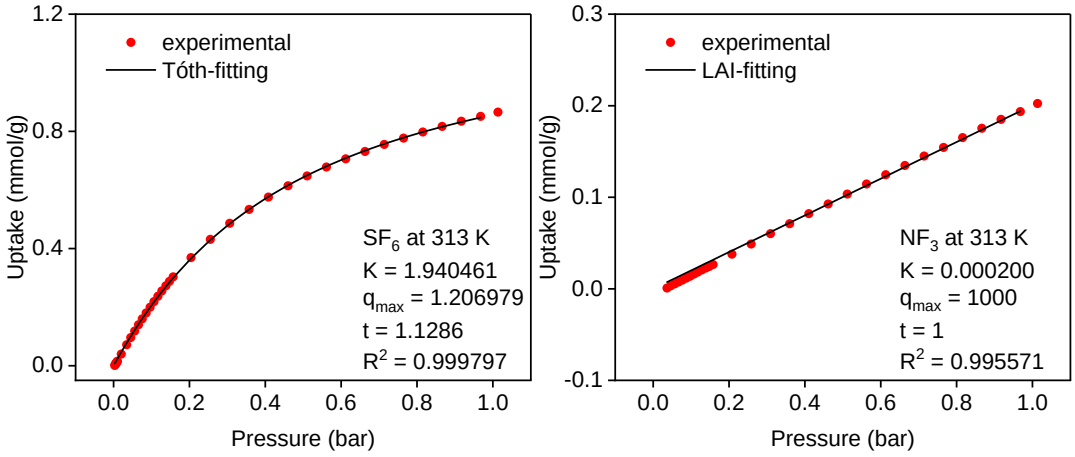

Figure 338. SF_6 (left) and NF_3 (right) isotherms and fitting curves of **cage-C_5F_{11}** at 313 K.

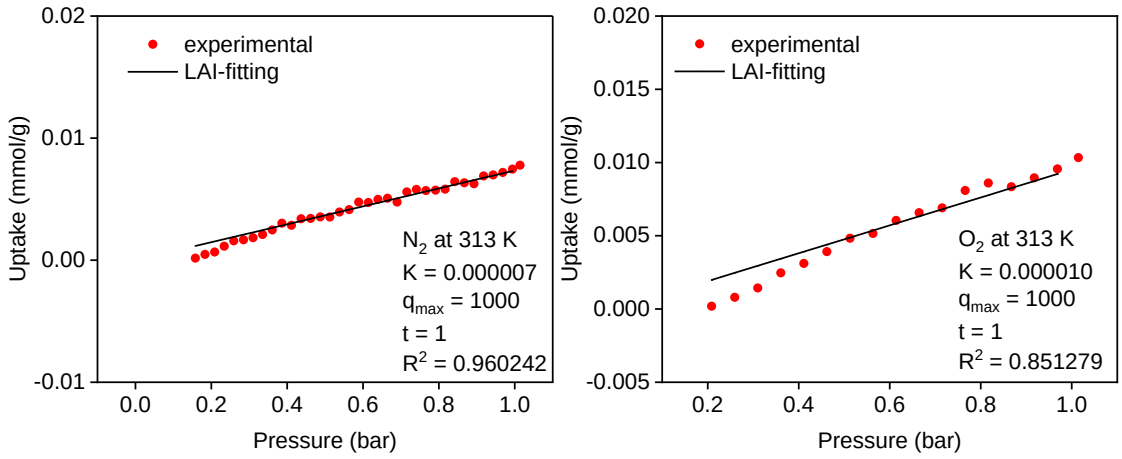

Figure 339. N_2 (left) and O_2 (right) isotherms and fitting curves of **cage-C_5F_{11}** at 313 K.

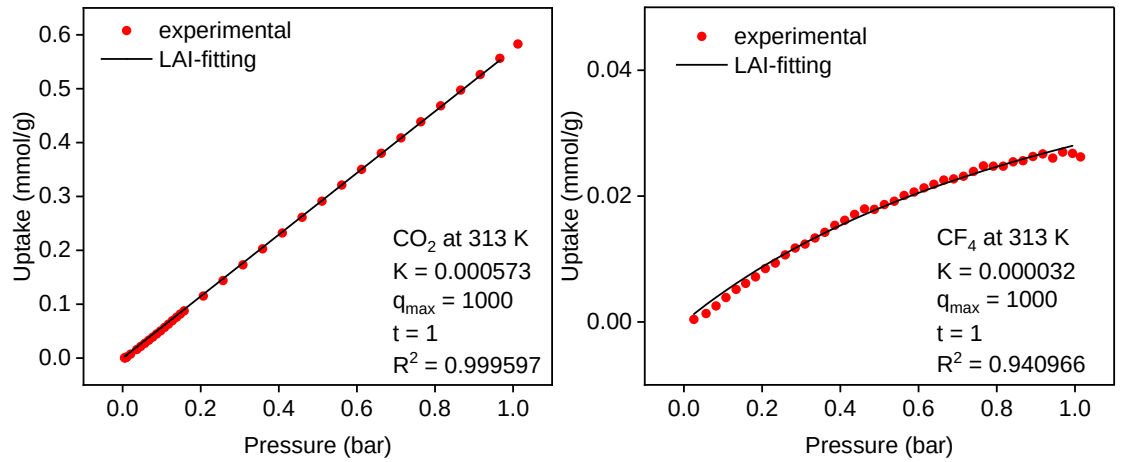

Figure 340. CO_2 isotherm and fitting curve of **cage-C_5F_{11}** (left) and CF_4 isotherm and fitting curve of **cage-$C_6F_{13\alpha}$** (right) at 313 K.

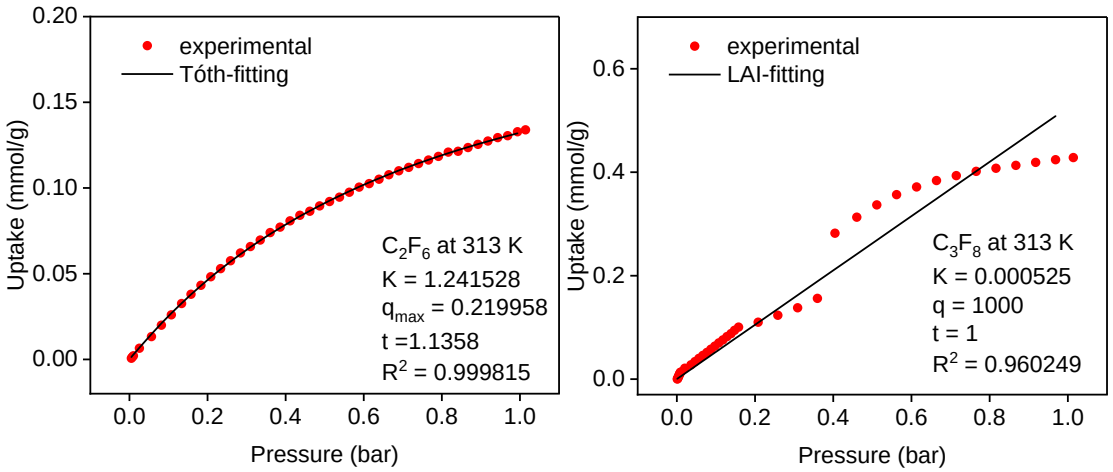

Figure 341. C_2F_6 (left) and C_3F_8 (right) isotherms and fitting curves of **cage-$C_6F_{13\alpha}$** at 313 K.

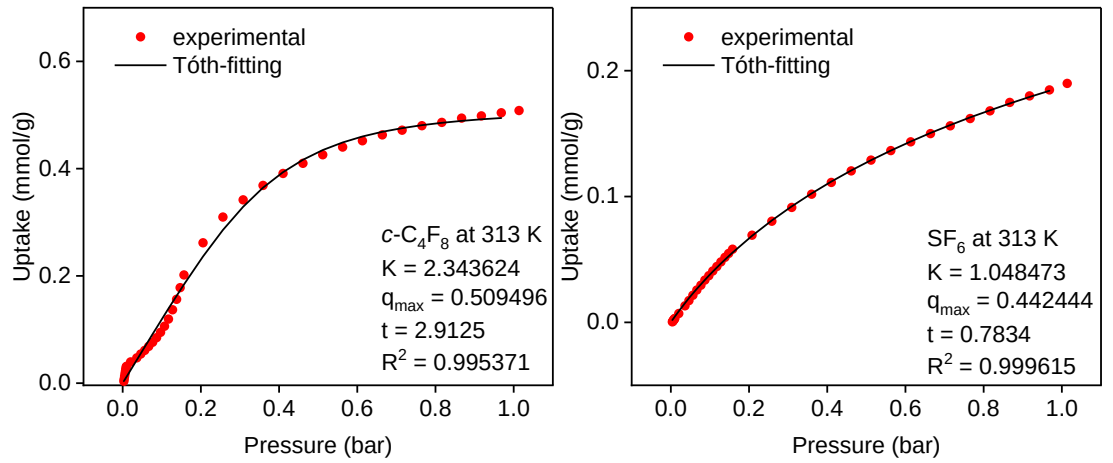

Figure 342. *c*-C_4F_8 (left) and SF_6 (right) isotherms and fitting curves of **cage-$C_6F_{13\alpha}$** at 313 K.

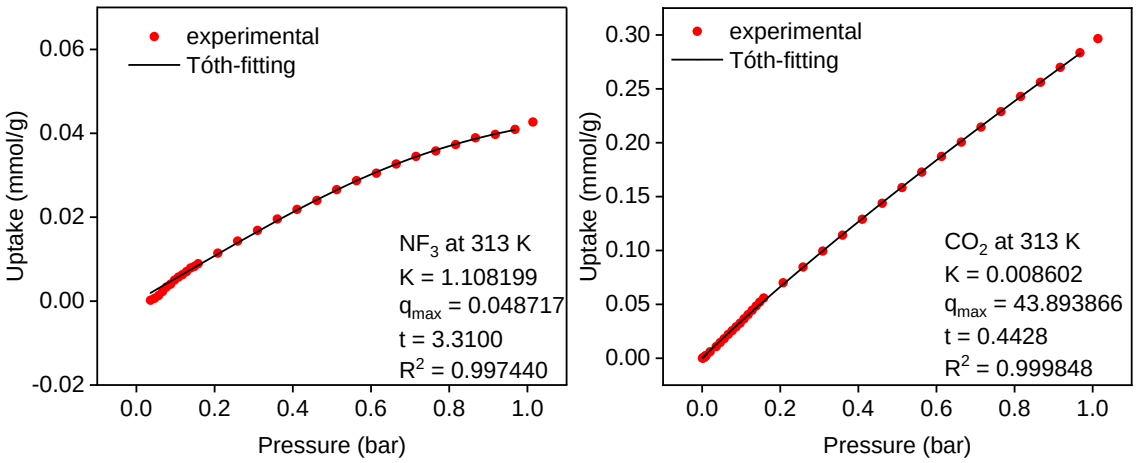

Figure 343. NF_3 (left) and CO_2 (right) isotherms and fitting curves of **cage-$C_6F_{13\alpha}$** at 313 K.

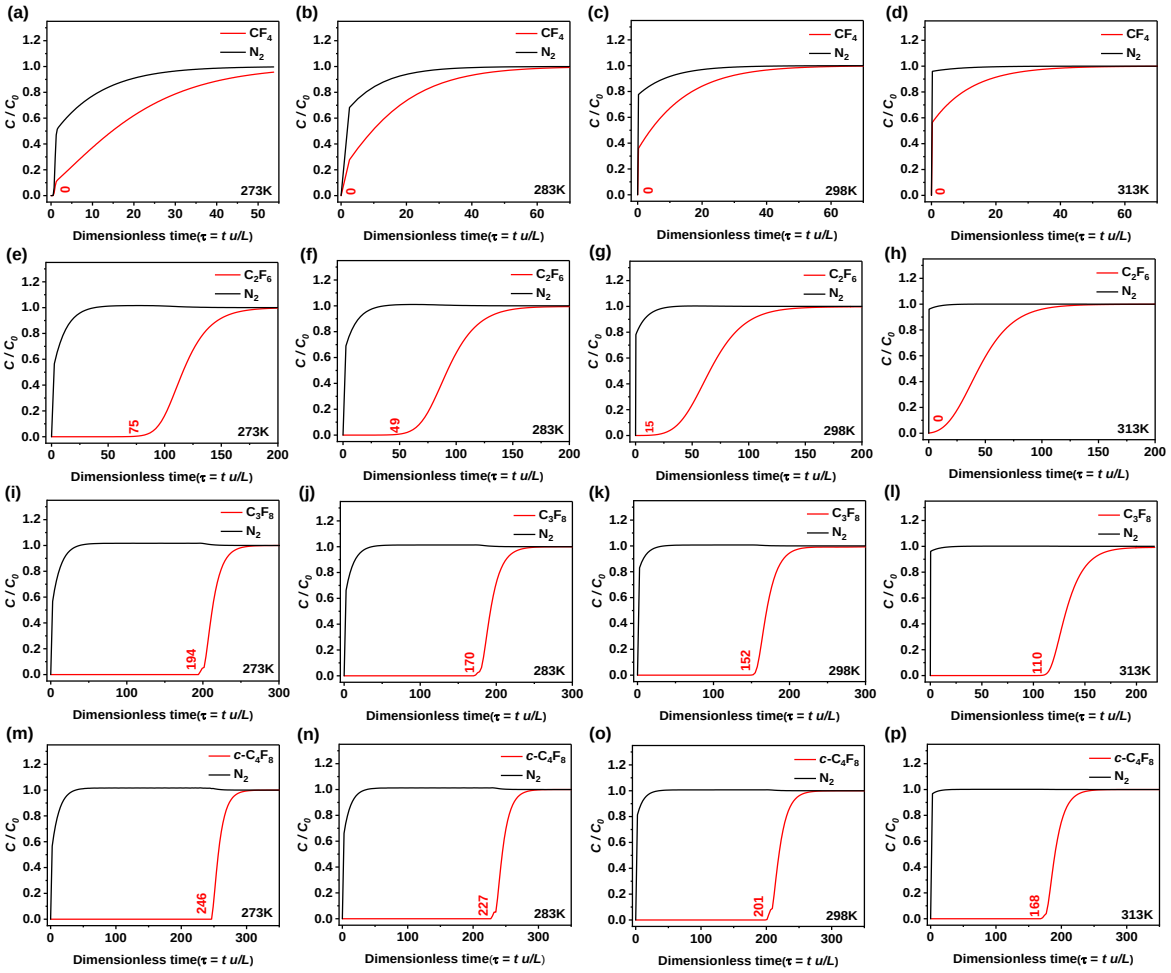

Figure 344. Calculated breakthrough curves of **F-cage** for 10:90 PFC/N_2 mixtures. a-d: CF_4/N_2; e-h: C_2F_6/N_2; i-l: C_3F_8/N_2; m-p: *c*-C_4F_8/N_2. Temperatures are given in the bottom right corner. Red curves: corresponding PFC; black curve: nitrogen. PFC breakthrough times are given. Reproduced with permission from Ref.[7]. Copyright © 2022 Wiley-VCH.

Theoretical breakthrough curves of **F-cage** were generated at various temperatures for 10:90 PFC/N_2 mixtures, utilizing single-gas isotherm fitting parameters. It was hypothesized that a PFC/N_2 gas mixture would traverse a packed column ($d \times L$ = 3 cm × 20 cm), containing 30 g of **F-cage**, under an overall pressure of 1 bar and a flow rate of 1000 mL/min. By plotting the dimensionless time of adsorption against the concentration of individual gases, breakthrough curves were produced. The breakthrough time increases with lower temperature and larger PFC. The longest dimensionless time is 246 for *c*-C_4F_8 at 273 K.

VIII. Abbreviations

°C	degree centigrade
°	degree
1D	one-dimensional
2D	two-dimensional
3D	three-dimensional
Å	angstrom
ATR	attenuated total reflection
BET	Brunauer, Emmett and Teller
B_2pin_2	bis(pinacolato)diboron
B3LYP	Becke, 3-parameter, Lee-Yang-Parr
BHT	butylated hydroxytoluene
Bpin	boronic acid pinacol ester
^tBu	tertiary butyl
Calcd.	calculated
CCDC	Cambrigde Crystallographic Data Centre
CD	circular dichroism
cm	centimeter
conc.	concentrated
COSY	correlation spectroscopy
DCM	dichloromethane
dec.	decomposition
DFT	density functional theory
DMF	*N*,*N*-dimethylformamide
DMSO	dimethylsulphoxide
EA	elemental analysis
Et	ethyl
OPr	propoxy
EtOH	ethanol
FT-IR	Fourier transform-infrared
g	gram
gegenüber	ggü.
HR	high resolution
IAST	ideal adsorbed solution theory
h	hour
HMBC	heteronuclear multiple-bond correlation spectroscopy

HRMS	high resolution mass spectrometry
HSQC	heteronuclear single-quantum correlation spectroscopy
K	Kelvin
kcal	kilocalorie
kJ	kilojoule
M	mol per liter
MALDI	matrix-assisted laser desorption
Me	methyl
MHz	megahertz
min	minute
MS	mass spectrometry
$MgSO_4$	magnesium sulphate
m.p.	melting point
NBS	*N*-bromosuccinimide
nm	nanometer
Na_2SO_4	sodium sulphate
NMR	nuclear magnetic resonance
NOESY	nuclear Overhauser effect spectroscopy
Nap	naphthyl
ns	nanosecond
ORTEP	oak ridge thermal ellipsoid plot
Ph	phenyl
PXRD	powder X-ray diffraction
PM6	parametrisiertes Modell 6
ppm	parts per million
rt	room temperature
Ref.	reference
R_f	retention factor
r-GPC	recycling gel permeation chromatography
ROESY	rotating frame nuclear overhauser effect spectroscopy
s	second
SCXRD	single crystal X-ray diffraction
SEM	scanning electron microscopy
Temperature	Temp.
TGA	thermogravimetric analysis
t-Bu	*tert*-butyl
TFA	trifluoroacetic acid

THF	tetrahydrofuran
TLC	thin layer chromatography
TOF	time of flight
δ	chemical shift
µm	micrometer

Acknowledgements

The culmination of this extensive journey prompts me to express my deepest gratitude to the individuals who have supported and helped me.

My foremost appreciation goes to my advisor, Prof. Dr. Michael Mastalerz, whose expert guidance, boundless patience, and perceptive insights have been my guiding stars. His mentorship has not only refined the course of my research but has also enriched my understanding of the “organic cage” domain. I am profoundly thankful for his provision of essential resources, access to laboratory facilities, and the creation of an environment conducive to meaningful research. My sincere thanks also go to Prof. Dr. Milan Kivala for graciously serving as the second examiner of my thesis.

I am deeply thankful to Dr. Sven M. Elbert, who, as my true “second advisor”, has shared invaluable lessons from experiment design to data analysis. His perceptive critiques and thoughtful suggestions have elevated the quality of my work. His contributions have been an essential cornerstone of my research journey.

I am indebted to the China Scholarship Council for their generous financial support, which has made it possible for me to thrive in this academic pursuit. Furthermore, I would also like to thank Heidelberg University for awarding me a completion grant within the framework of the “Stipendien-und Betreuungsprogramms (STIBET)” of the DAAD in the final phase of my doctoral training.

A special note of gratitude extends to my colleagues within my research group, whose stimulating discussions, collaborative endeavors, and camaraderie have made this journey more enriching. My gratitude goes to Lisa Roß for the German translation of the abstract, and to Dr. Sven M. Elbert, Dr. Zishou Zhou, Dr. Bahiru Punja Benke, and Dr. Sviatoslav Batsyts for their invaluable suggestions on this thesis. I also acknowledge Moritz Schuldt and Dr. Tobias Kirschbaum for their contributions to quantum chemical calculations and cage model creation. I am grateful for the invaluable contributions of Dr. Jochen C. Lauer, who provided essential support in calculating gas molecule volumes, and Dr. Bernd M. Schmidt from Heinrich-Heine-Universität, who generously shared the SCXRD data.

The technical and administrative team, including Ute Gärtner, Nicole Rast, and Janine Tornow-Gaisbauer, deserve my heartfelt thanks for their exceptional support in managing bureaucratic matters, allowing me to dedicate my focus to research. The collaborative efforts of Dr. Jürgen Graf and his team (OCI) for NMR measurements, Dr.

Jürgen Gross and his team (OCI) for MS measurements, and Dr. Frank Rominger and Margit Brückner (OCI) for SCXRD measurements are deeply appreciated. I am also grateful to Dr. Sebastian Ehrling and Francesco Walenszus (3P instruments) for their contributions to experimental breakthrough investigations, and to Dr. Wen-shan Zhang (BioQuant) for SEM measurements. Dr. Anjana Kunhumbadukka Othayoth's expertise in gas sorption measurements has been indispensable, and Dr. Sven Elbert's assistance with gas sorption and PXRD measurements has been invaluable.

I would also like to express my heartfelt gratitude to Dr. Gangxiang Zhou, Dr. Xubin Wang, Dr. Zishou Zhou, Dr. Xuan Yang, Dr. Xin-yue Hu, Dan Wang, and Xupin Yan (equal with Dan) for their unwavering support and help in both academic pursuits and life's endeavors.

Lastly, the steadfast encouragement of friends and family has fortified my resolve, with a special place reserved for my girlfriend, Qun Liu, whose presence has illuminated even the darkest passages of this journey.

As I look back, I see a small boat navigating through countless mountains. Looking ahead, the road stretches endlessly, filled with boundless possibilities and captivating horizons.

Ke Tian
田科
October 21st, 2023
Heidelberg

Eidesstattliche Versicherung gemäß § 8 der Promotionsordnung für die Gesamtfakultät für Mathematik, Ingenieur- und Naturwissenschaften der Universität Heidelberg

1. Bei der eingereichten Dissertation zu dem Thema „The Influence of Side Chain Modifications on the Properties of Imine Based Organic Cage Compounds“ handelt es sich um meine eigenständig erbrachte Leistung.

2. Ich habe nur die angegebenen Quellen und Hilfsmittel benutzt und mich keiner unzulässigen Hilfe Dritter bedient. Insbesondere habe ich wörtlich oder sinngemäß aus anderen Werken übernommene Inhalte als solche kenntlich gemacht.

3. Die Arbeit oder Teile davon habe ich bislang nicht an einer Hochschule des In- oder Auslands als Bestandteil einer Prüfungs- oder Qualifikationsleistung vorgelegt.

4. Die Richtigkeit der vorstehenden Erklärungen bestätige ich.

5. Die Bedeutung der eidesstattlichen Versicherung und die strafrechtlichen Folgen einer unrichtigen oder unvollständigen eidesstattlichen Versicherung sind mir bekannt.

Ich versichere an Eides statt, dass ich nach bestem Wissen die reine Wahrheit erklärt und nichts verschwiegen habe.

_____ _____

Ort und Datum Unterschrift